NASA CR 71490

JULY 30, 1965

DIN: 65SD4388

VOYAGER SPACECRAFT SYSTEM
PRELIMINARY DESIGN

ALTERNATE DESIGNS CONSIDERED

System Alternates

VOLUME B (Book 1 of 3)

PERFORMED UNDER
CONTRACT NO. 951112 NAS-7-100

for

CALIFORNIA INSTITUTE OF TECHNOLOGY
JET PROPULSION LABORATORY
4800 OAK GROVE DRIVE
PASADENA, CALIFORNIA

GENERAL ELECTRIC
SPACECRAFT DEPARTMENT
A Department of the Missile and Space Division
Valley Forge Space Technology Center
P. O. Box 8555 • Philadelphia, Penna. 19101

ALTERNATES CONSIDERED FOR THE 1971 FLIGHT SPACECRAFT

INTRODUCTION

This volume presents the design approaches considered and the rationale used in selecting the preferred design. It satisfies the requirements of section (ii) (i) (B) of the work statement, JPL Contract No. 951112. Alternates considered are divided into the same basic categories as the description of the preferred design in Volume A, that is:

I Alternate Mission Objectives and Design Criteria

II Alternate Design Characteristics and Restraints

III System Functional Alternatives

IV Subsystem Functional Alternatives

V Alternate Schedule and Implementation Plans

Insofar as is practical, individual documents within this volume correspond to the individual Functional Descriptions in Volume A.

In conducting the Phase IA study, several propulsion companies participated and carried out preliminary design studies under General Electric direction. Their reports are included as appendices to this volume as further description of alternate designs considered. The companies who participated were:

- Aerojet General
- Space Technology Laboratories
- Rocketdyne
- Thiokol
- Rocket Research

CII - VB211AA101

ALTERNATE MISSION OBJECTIVES AND ALTERNATE DESIGNS CONSIDERED

MISSION OBJECTIVES AND DESIGN CRITERIA

Index

1 General
2 Orbiter Lifetime
3 Arrival Date Separation

1.0 GENERAL

The Mission Objectives and Design Criteria are intimately related to the scientific objectives of the mission. To define or anticipate the scientific mission is beyond the scope of this study. At best, a discussion of mission objectives must be limited to the feasible types of missions including launch vehicles with conclusions left in abeyance until the specific scientific mission is defined.

Since 1962, the General Electric Company, Missile and Space Division has participated in several JPL and NASA sponsored Voyager studies as well as conducting in house Mars mission studies for Voyager, Mariner B, and Advanced Mariner. From these studies and other data, the possibilities that exist for a Mars mission, depending on the scientific mission, consist of the following:

a. Space Vehicle

   1. Capsule transported by a bus which flies by Mars after release of the capsule

   2. Orbiter which orbits Mars after release of a capsule

   3. Orbiter only

   4. Capsule released from a Mars orbit by an orbiter which continues to orbit Mars after release of the capsule

b. Launch Vehicle

   1. Atlas Centaur

   2. Titan IIIC

   3. Saturn IB/Centaur

   4. Saturn V

c. Program

   1. Single opportunity, multiple flights

   2. Continuing program for several opportunities

The three categories -- space vehicle, launch vehicle, and program -- are all interrelated and dependent upon the scientific mission.

It may be concluded that during the scientific investigation of Mars, both orbiters and capsules will be required - orbiters and capsules for making atmospheric measurements

to determine the type of life which may conceivably be supported on Mars, and orbiters for mapping of the surface variations with time and location, and for determining the topographical characteristics. The actual determination of life requires the utilization of surface measurements, hence capsules.

On the basis of the results of the previous studies, it is concluded that the mission objectives as defined in JPL Document 45, "Preliminary 1971 VOYAGER Mission Specifications" are a feasible and logical approach to the investigation of Mars. The final conclusions in reference to the definition of the Voyager Mission objectives must wait for the definition of the Voyager scientific mission(s).

2.0 ORBITER LIFETIME

It is important to recognize which time varying features of the Martian seasons will be accessible to observation during the six-month period of the 1971 mission. These features appear at certain times of the season at certain points on the surface and to observe them under best conditions will influence the approach trajectory, orbit and landing site. Some of these relationships are shown in Figure 1-1 in which to depict the correlation of events on the Martian surface with the seasons, the areocentric latudes the subsolar point and seasonal waves are plotted against the heliocentric longitude.

In the right-hand part of Figure 1-1, the trace of the wave of darkening is shown moving from the south to the north during the southern spring (heliocentric longitude of 267° to 357°). For reference the subsolar point is also shown for the right half of the Figure. In the left-hand part of the Figure the wave of darkening is shown moving in the opposite direction. The heliocentric longitude at arrival as well as six months later is noted on Figure 1-1. Thus the wave of darkening, being a spring time feature, has moved to the northern hemisphere and has nearly completed its course before the arrival of the spacecraft. The north polar cap has started forming but is, of course, far from the subsolar point (90°) and therefore receives essentially no illumination. Near the middle of the orbit phase, the southward moving wave of darkening is observable near Utopia and Acidalium Mare but similarly these areas have rather poor illumination. Extension of orbiter life to 8 or 9 months would allow the latitude of the wave of darkening (from north to south) and the subsolar point to approach each other during orbiter life and would provide much improved lighting conditions for viewing the north polar cap. Enhancement of the darkness of Syrtis Major (an important event) could be observed by an orbiter of about nine months life. Extension of the orbiter lifetime to nine months can be easily accomplished if a reduced probability of success and mission capability is accepted for the extra lifetime. The reduced capability would be in the areas of planet scan platform pointing, power, and data rate. However, even without design changes a data return sufficient to describe the wave moment would be possible.

3.0 ARRIVAL DATE SEPARATION

As a design criteria, the minimum time between arrival at Mars of the two spacecraft is 10 days. As shown in VB220AA101, optimization of the trajectories for engineering

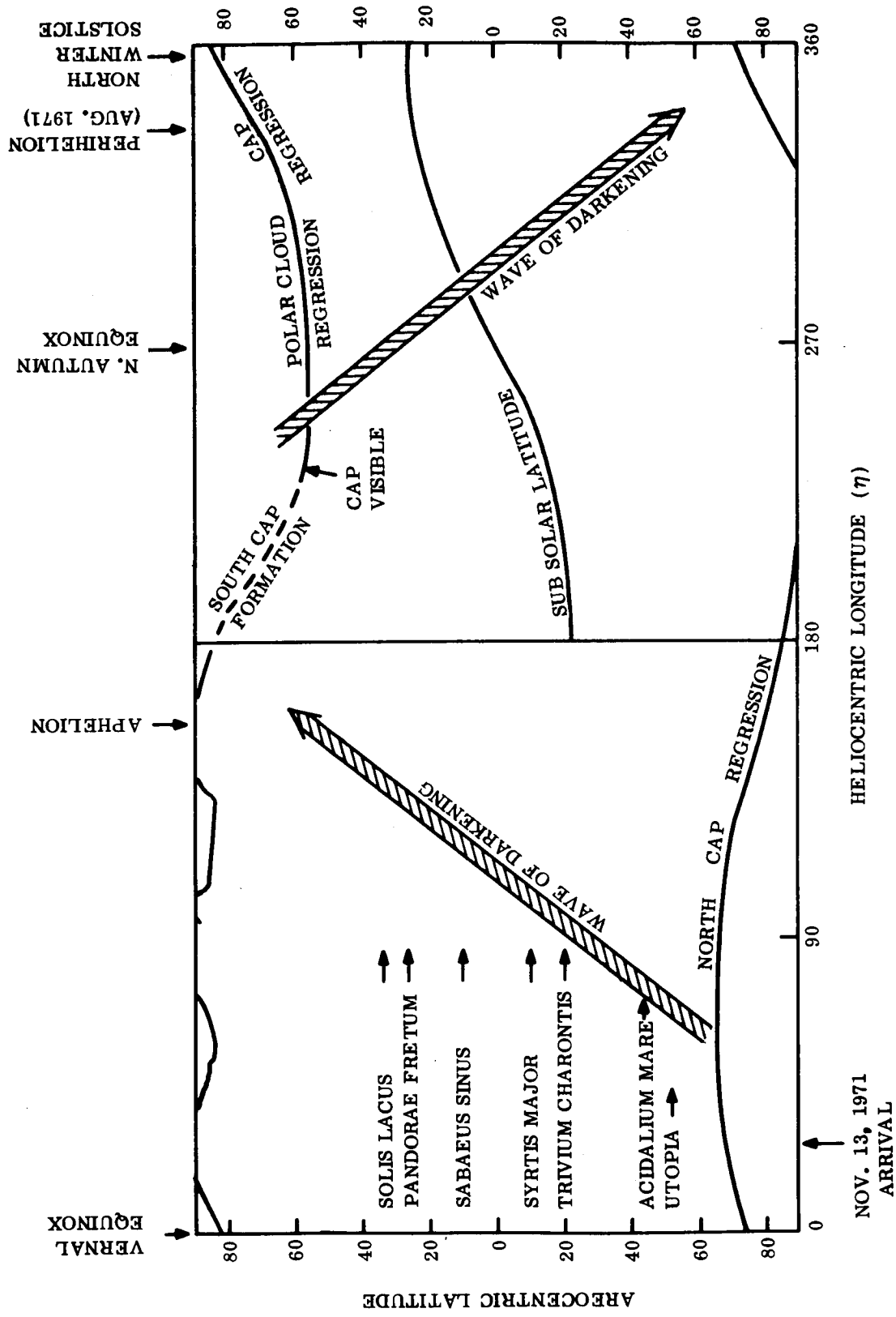

Figure 1-1. Seasonal Variation of Martian Features

and scientific requirements, assuming a Syrtis Major capsule landing area, is accomplished by maintaining a constant approach velocity of 3.5 km/sec. However, this trajectory selection law must be violated if 10 days between arrival of the two spacecraft is maintained and the first launch occurs after May 28, 1971. For this condition, either shorter time between arrivals must be accepted, a different impact area selected, or a mid-December arrival for the second spacecraft be accepted. The mid-December arrival date results in an orbit of lesser desirability from both an engineering (occultations) and scientific viewpoint. It is therefore suggested that the 10 days between arrival design criteria be reviewed so as to maximize the mission return.

In the above, a capsule landing area of Syrtis Major was assumed. The same conflict will probably exist for any other pre-determined landing area if nearly constant approach geometry and velocity are to be obtained. This is desirable for the maximum utilization of propulsion weight and optimization of scientific sensor motion and placement.

CII - VB220AA010

ALTERNATE DESIGN CHARACTERISTICS AND RESTRAINTS CONSIDERED

FLIGHT SPACECRAFT UTILIZING EARTH (TWO AXES) AND MARS (ONE AXIS) FOR ATTITUDE CONTROL REFERENCES

Index

1.0 General Description
- 1.1 Guidance and Control Subsystem
- 1.2 Power Subsystem
- 1.3 Telecommunications Subsystem
- 1.4 Propulsion Subsystem
- 1.5 Vehicle
- 1.6 Summary and Conclusions

1.0 GENERAL DESCRIPTION

A Flight Spacecraft system utilizing the Earth and Mars as attitude control references was examined as an alternate to the recommended Sun-Canopus referenced system. During the orbital phase of the mission, the roll axis of the spacecraft is oriented to the Earth and attitude about roll is controlled by an infrared Mars sensor. With this control scheme, the high-gain antenna may be rigidly mounted to the spacecraft structure and the Mars instrument pointing function can be accomplished, with no blockage, by a single degree of freedom platform with a total excursion of ± 90 degrees. With the recommended Sun-Canopus oriented spacecraft, scan platform blockage is encountered during most orbits and effort is expended to configure the vehicle so that the blockage occurs only when a minimum of information will be lost. To a large degree, a spacecraft using the Earth-Mars reference scheme transfers responsibility for articulation of the high-gain antenna and scan platform to the attitude control subsystem. During the interplanetary cruise mission phase, this spacecraft will use the Sun and Canopus as attitude control references. A conceptual layout of this spacecraft follows (Figure 1-1).

During the orbital operations phase of the mission, the spacecraft roll axis and the coincident high gain antenna beam are aligned to the Earth. As the spacecraft progresses through an orbit, the vehicle performs a rolling motion to maintain Mars within the field-of-view of the scan platform. Because of this rolling motion, it is not feasible to bias the solar array to the Sun; the solar array is pointed along the spacecraft roll axis, and the rather small loss incurred by pointing away from the Sun is accepted. This loss is obviously not a consideration for an RTG powered spacecraft. In this section, however, consideration will be restricted to a spacecraft using solar cells as the source of prime power. A later section (VB220AA030) discusses in detail the adaptation of a Sun-Canopus stabilized vehicle to RTG power and such a conversion for an Earth-stabilized vehicle will involve very similar considerations.

1.1 GUIDANCE AND CONTROL SUBSYSTEM

For time periods of the order of the orbital period, the Mars-Earth line, to which the spacecraft roll axis is aligned, is virtually inertial. The required vehicle roll motions as the spacecraft traverses its orbit are indicated by Figure 1-2 for the important case where the scan platform is aligned to the local vertical. An attitude reference singularity occurs when the Mars-Earth line lies in the orbit plane ($\Psi = 90°$). As this singularity is approached, the vehicle must sustain high roll rates in order to track the center of Mars with small error. Since the spacecraft must traverse this singularity in certain orbits, the roll control loop must be designed to cope with the problem. Figure 1-3 specifies the pointing direction of the scan platform required for local vertical alignment as a function of orbit position.

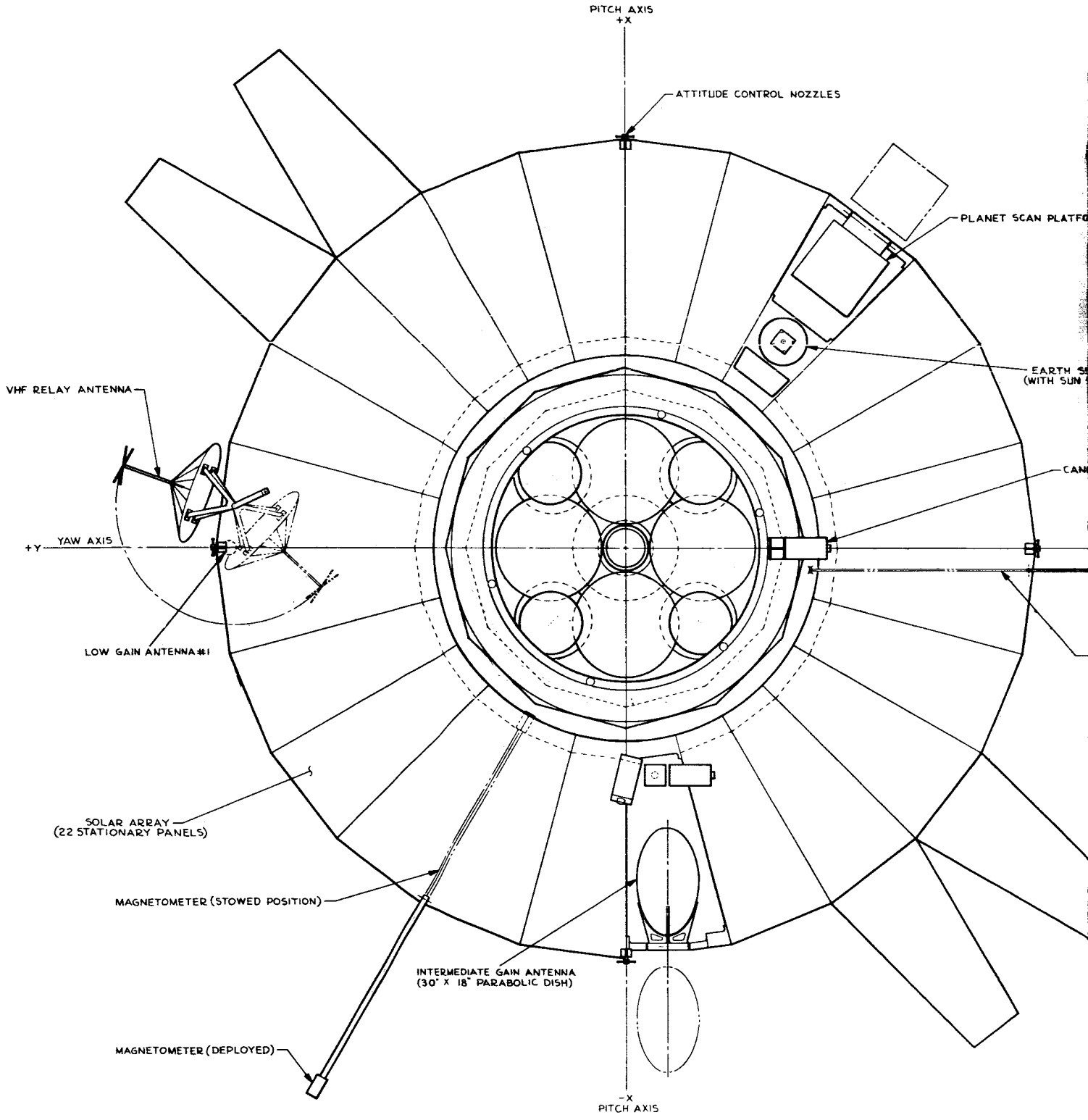
PITCH AXIS
+X
ATTITUDE CONTROL NOZZLES
PLANET SCAN PLATFO
EARTH S
(WITH SUN
VHF RELAY ANTENNA
CAN
+Y
YAW AXIS
LOW GAIN ANTENNA #1
SOLAR ARRAY
(22 STATIONARY PANELS)
MAGNETOMETER (STOWED POSITION)
INTERMEDIATE GAIN ANTENNA
(30" X 18" PARABOLIC DISH)
MAGNETOMETER (DEPLOYED)
-X
PITCH AXIS

3

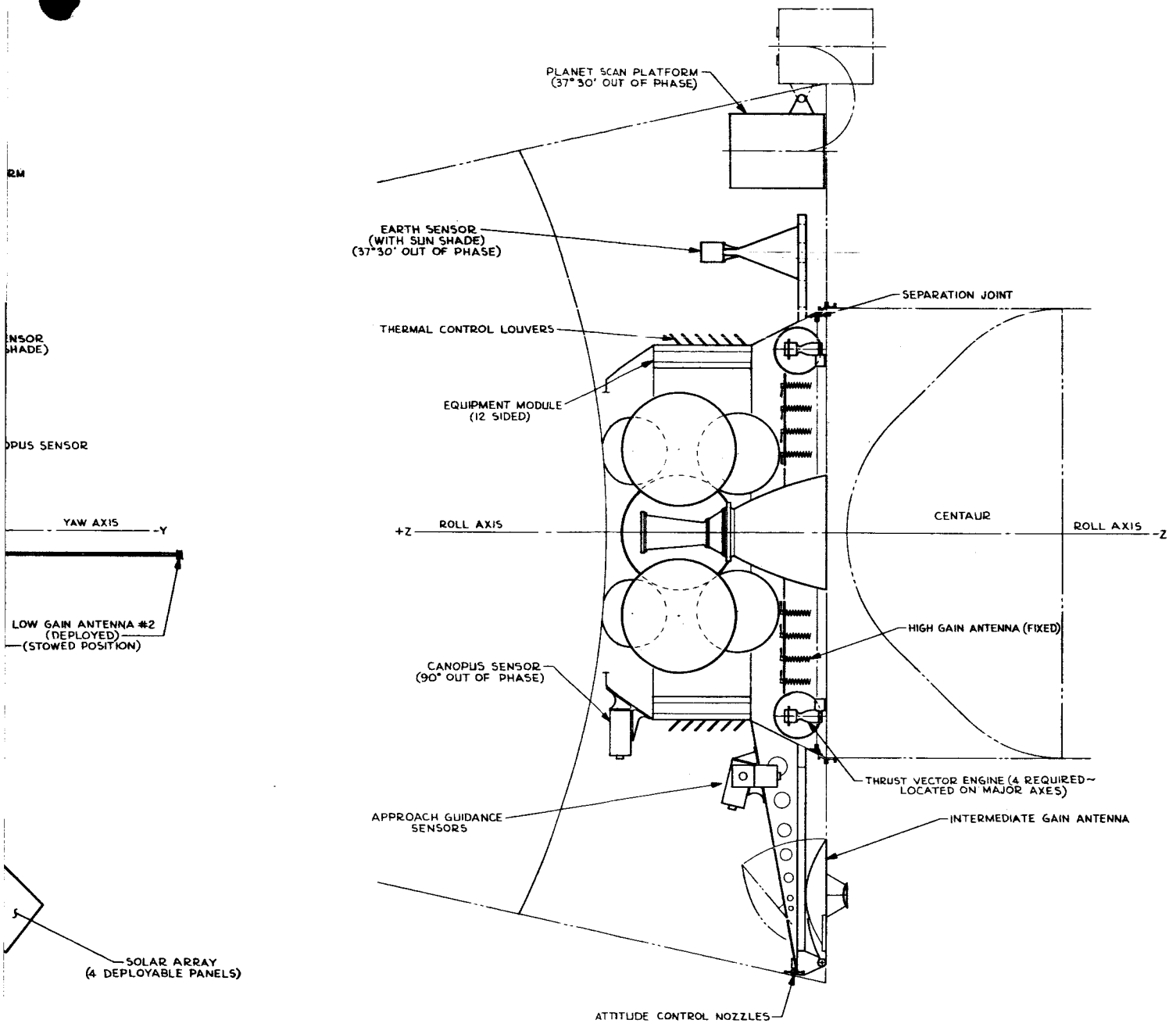

Figure 1-1. Flight Spacecraft Utilizing Earth (Two Axes) and Mars (One Axis) for Attitude Control References

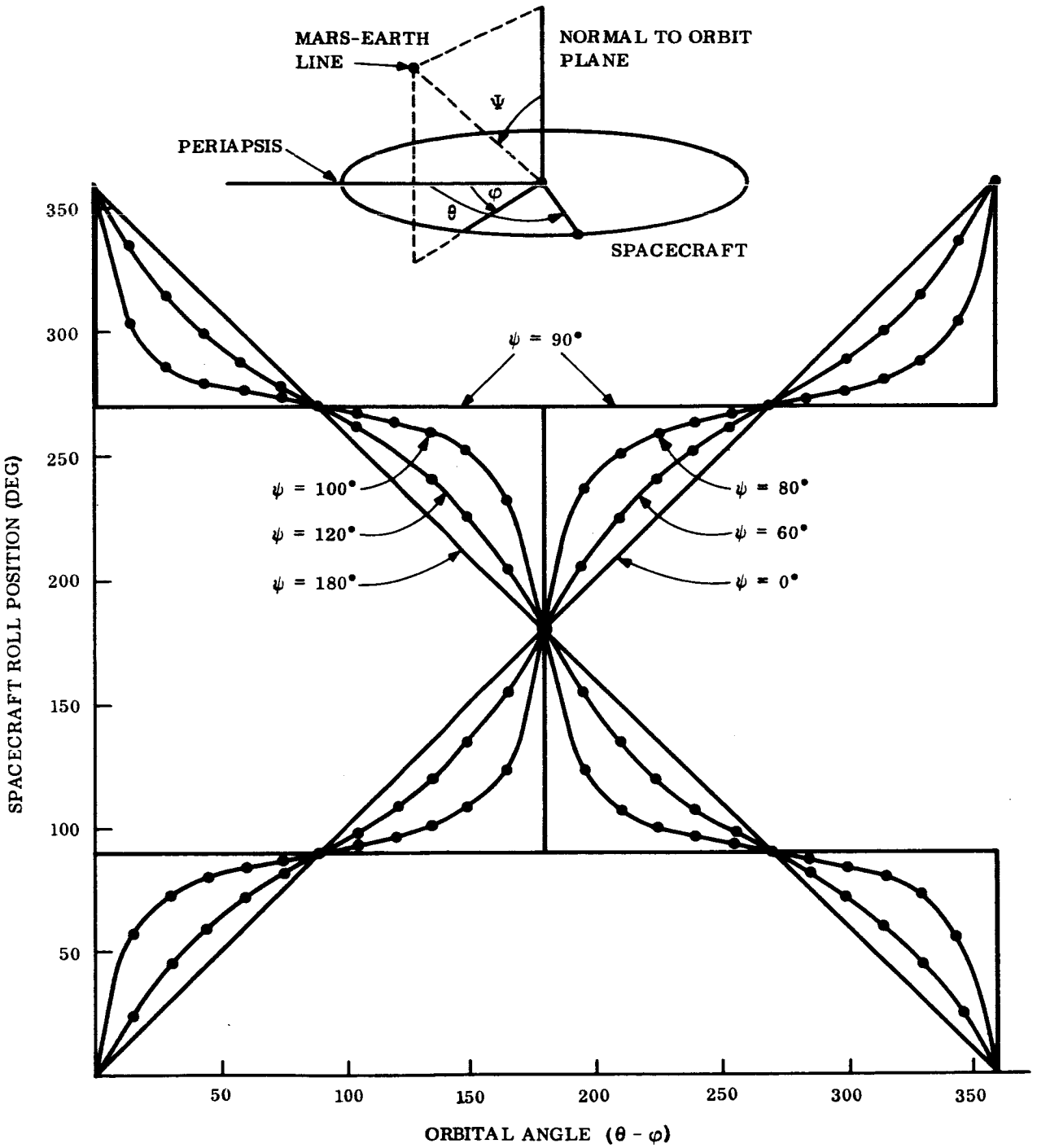

Figure 1-2. Spacecraft Roll Position Required for Plane Pointing Function on Two Axes - Earth, One-Axis Mars, Stabilized Vehicle

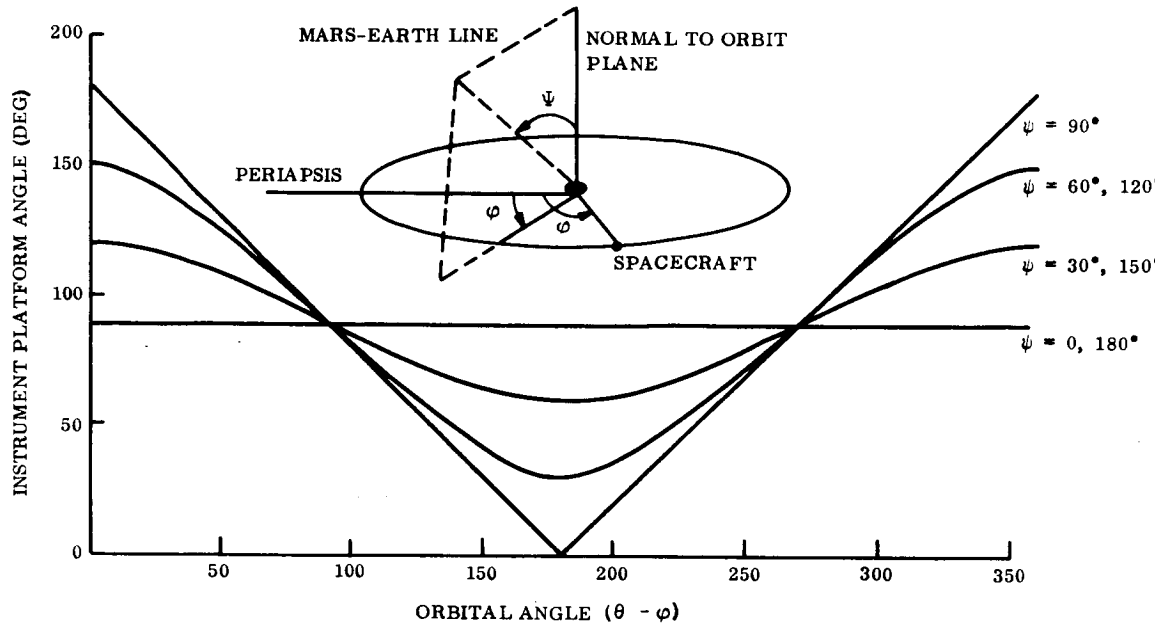

Figure 1-3. Angle Between Vehicle Roll Axis and Instrument Platform Pointing Direction (Local Vertical Pointing) vs. Spacecraft Orbital Position

Two general types of Earth sensor were studied for controlling the pitch and yaw axes, an optical star tracker and an RF phase monopulse scheme used in conjunction with the high-gain antenna. Both sensor types have significant disadvantages; both have very poor Earth acquisition capability and are prone to loss of reference during Earth occultation. Although the Earth will appear as a very bright star (between -1.8 and -2.3 visual magnitude), the optical tracker is subject to interference in the form of Mars' albedo, the Sun, planets other than the Earth, and the star background. At the end of the orbital mission, the Sun-Mars-Earth angle is small so that a large sun shade is required. The sun shade represented in Figure 1-1 is designed to permit the Earth to be tracked when it is only 8-1/2 degrees from the Sun. RF angle sensing adds complexity to the telecommunications subsystem, and more important, it requires continuous transmission from the Earth, which is probably an unreasonable burden on the DSIF. The recommended approach to Earth sensing utilizes both sensor types, an optical star tracker to be used for the majority of the orbital mission with RF phase monopulse equipment for use during times of intolerable optical interference and in event of optical sensor failure. Figure 1-4 is a block diagram of the yaw and pitch attitude control systems for the orbital mission phase. To keep the diagram simple, adaptation of the control system for interplanetary cruise or for engine burn is not illustrated. It is anticipated that these functions would be performed as indicated for the preferred design in Volume A. This block diagram and those which follow represent a minimum of analysis and are not presented as optimum techniques.

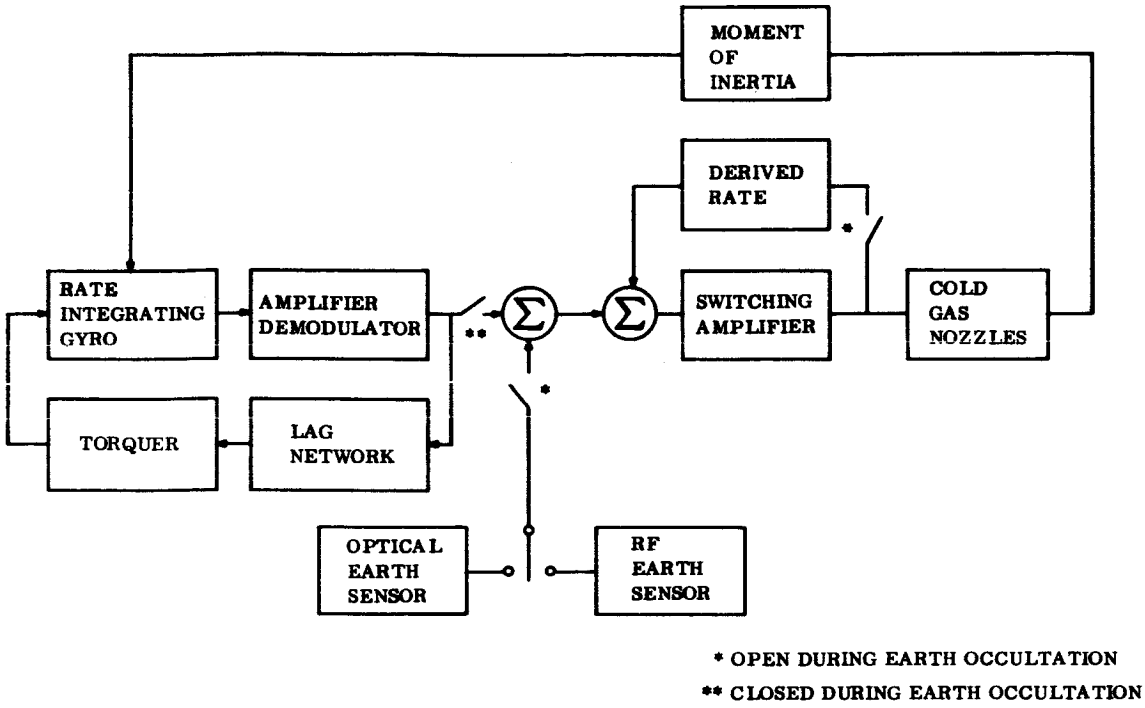

Figure 1-4. Pitch-Yaw Attitude Control Loop, Orbital Operations Mission Phase, Earth-Oriented Flight Spacecraft

They do represent approaches which, based on the analysis which has been performed, will work.

Earth occultation is the only occultation that affects the attitude control system. Occultation is handled by programming or sensing its occurrence and transferring the vehicle pitch and yaw attitude reference to high quality gyros, which will retain the vehicle within the acquisition capability of the Earth sensors through the period of occultation. Impending occultation may also be "sensed" by comparison of Mars subtended angle as measured by the Mars sensor and the position of the scan platform. This method of sensing impending occultation is not too attractive, particularly if sensing must occur in advance to permit gyro warm-up; the false alarm rate would be high.

The sensor for Flight Spacecraft roll control as well as scan platform pointing is a two-axes, infrared, dither-type planet sensor mounted on the scan platform. The field of view of this sensor is a 90 degree cone (45 degrees half angle) which must not view the spacecraft for any scan platform position. Depending on its size, the portion of the biological barrier that remains with the spacecraft may violate this constraint and have to be separated as in the preferred 1971 design. A possible roll attitude control scheme is illustrated by Figure 1-5. Figure 1-2 shows that vehicle roll rate is a combination of a constant rate equal to the average spacecraft orbital rate and a relatively large cyclic perturbation. These are classic conditions where the momentum

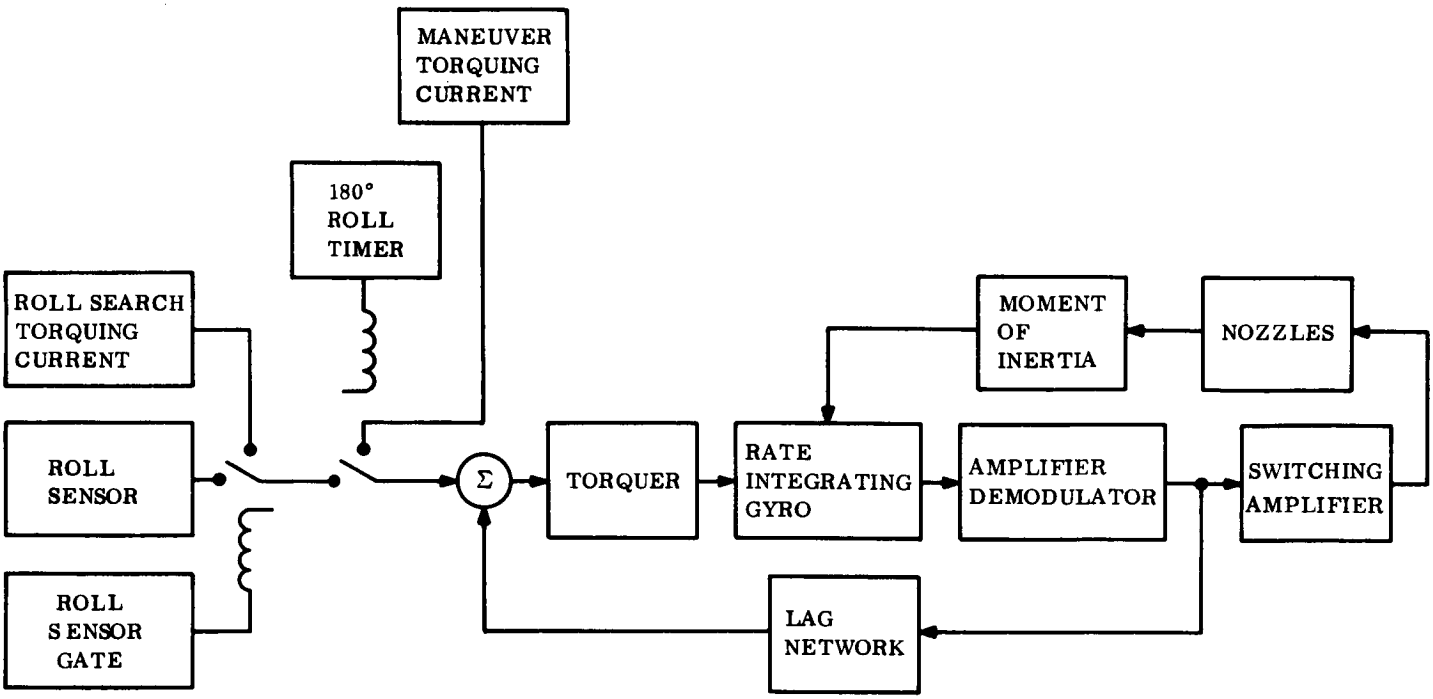

Figure 1-5. Roll Attitude Control Loop, Orbital Operations Mission Phase, Earth Oriented Flight Spacecraft

storage function of a momentum wheel is applied; however, the weight of gas saved does not appear to justify the weight and added complexity of a momentum wheel. To illustrate, a flight spacecraft with a 2000 slug-feet^2 roll moment of inertia in a 3000 kilometer by 25,000 kilometer orbit (above surface of Mars) is considered. A six-month orbital mission will consist of approximately 230 orbits. For one-half of these orbits, the Mars-Earth line will be assumed to make an angle larger than 25 degrees with the orbit plane so that (refer to Figure 1-2) the Flight Spacecraft roll rate in the worst case will vary from practically zero to two times the orbital angular rate. The remaining orbits will be assumed to require two 180 degree roll maneuvers at a rate limited to 1.75×10^{-3} radians per second (six degrees per minute). With these assumptions, the total torque impulse required to handle the planet tracking function is 1360 foot-pound-seconds. The nozzles have a torquing radius of ten feet, so the impulse required is 136 pound seconds which, with a Freon system, represents about 4.1 pounds including tanks. To do the same job with a momentum wheel would require five foot-pound-second capacity at a probable weight of at least 25 pounds as well as additional complexity. The above gas consumption calculation assumes that roll rates not greater than six degrees per minute will not introduce enough cross-coupling between control axes to significantly increase gas consumption in pitch and yaw control. A momentum wheel will save the gas required to overcome cyclic roll disturbance torques but this saving is felt to be small.

As already indicated, a roll control reference singularity occurs when Mars, Earth, and the Flight Spacecraft lie in a line; the performance of the roll control system will become sluggish as this point is approached and the gain of the roll sensor approaches zero. The roll attitude control loop is implemented to "put up" with this poor performance rather than to add sophistication to design around it. During most orbits, the roll sensor has gain and torques the gyro so that Mars is properly tracked. Feedback around the gyro is used to develop a mix of rate and position information. In the orbits which closely approach the reference singularity, the roll sensor output will perform an inertial hold function. The scan platform will hit its stop in attempting to track Mars which will initiate a 180 degree vehicle roll at a rate of six degrees per minute. The time required for the maneuver gets the Flight Spacecraft through the singular point.

If the planet sensor loses Mars, an automatic reacquisition occurs; the Flight Spacecraft is commanded into a slow roll and the scan platform sweeps back and forth in a search mode. The scan platform moves in discrete steps of 1/4 degree per second. Figure 1-6 illustrates the control logic required to move the scan platform. No specific implementation is indicated for pointing the scan platform away from the local vertical. For most purposes, this can probably be accomplished by biasing the output of the Mars sensor.

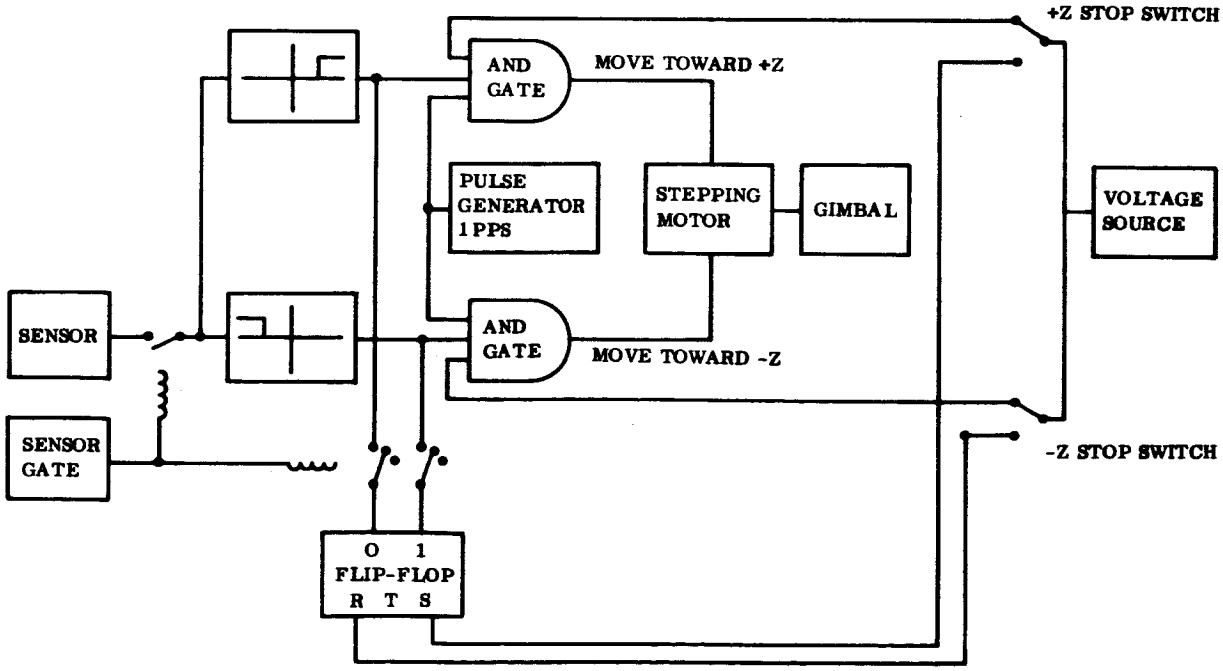

Figure 1-6. Scan Platform Position Control, Orbital Operations Mission Phase, Earth Oriented Flight Spacecraft

The significant advantages and disadvantages of this spacecraft are pretty well confined to the attitude control and articulation functions. For the interplanetary cruise mission phase, this vehicle requires Sun and Canopus sensors in addition to its Earth and Mars sensing equipment. Furthermore, its roll control loop incorporates a gyro which must function during the orbital period. Although this equipment is well developed and reasonably reliable, attitude control of the Earth oriented vehicle is more complex than for the recommended Sun-Canopus configuration. Use of the Sun as a pitch and yaw control reference is considerably easier than using the Earth. On the other hand, reliable mechanical gimbals for long term space operation are a genuine design problem. The recommended Sun-Canopus vehicle requires five essential mechanical gimbals and associated control loops to perform the orbital mission while the Earth-oriented vehicle requires one. Motion of the scan platform of the Earth-oriented spacecraft is less desirable for the planet oriented science (line scanning instruments in particular) as the scan platform is rotated about the local vertical as the Flight Spacecraft progresses around the orbit.

1.2 POWER SUBSYSTEM

The power subsystem of the two-axes, Earth-oriented vehicle is identical to that for a Sun-oriented vehicle except for a reduction of design margin or an equivalent increase of array area. For Voyager power profiles, the array is sized by the orbital load; a plot of relative available power for 1971 and 1973 orbital missions follows as Figure 1-7. The Earth oriented vehicle must carry 16% greater solar array area in order to provide a minimum power level equal to the minimum of the Sun-oriented array in 1973; thus, four deployable panels of nine square feet each are shown on Figure 1-1. These panels represent an estimated increase in vehicle weight of 35 pounds. This attitude stablization concept is readily adapted to RTG power (refer to VB220AA030).

1.3 TELECOMMUNICATIONS SUBSYSTEM

Use of the Earth as an attitude control reference during the orbital mission phase has considerable impact on the telecommunication subsystem. The high-gain antenna is fixed to the vehicle structure and the intermediate gain antenna must be gimballed to provide better data rate during transit and maneuvers than the low-gain antennas. Angle tracking capability is incorporated.

The tradeoff on the high-gain antenna is basically a selection between a deployed parabolic reflector and an array fixed on the roll axis and fitted around the engine nozzle. The parabolic reflector is easier to implement but requires flexible RF cabling and a deployment mechanism; alignment is more of a problem when a deployment is involved. Thermal distortion due to radiation and plumming from the engine is a potential problem with the array. Both antennas are believed comparable from a gain and weight standpoint (as the array does not require a deployment mechanism). Use of an array preserves symmetry of the spacecraft. The choice to illustrate the design with an array is quite arbitrary. A waveguide fed slot array was not used since it would not provide sufficient bandwidth for both transmission and reception.

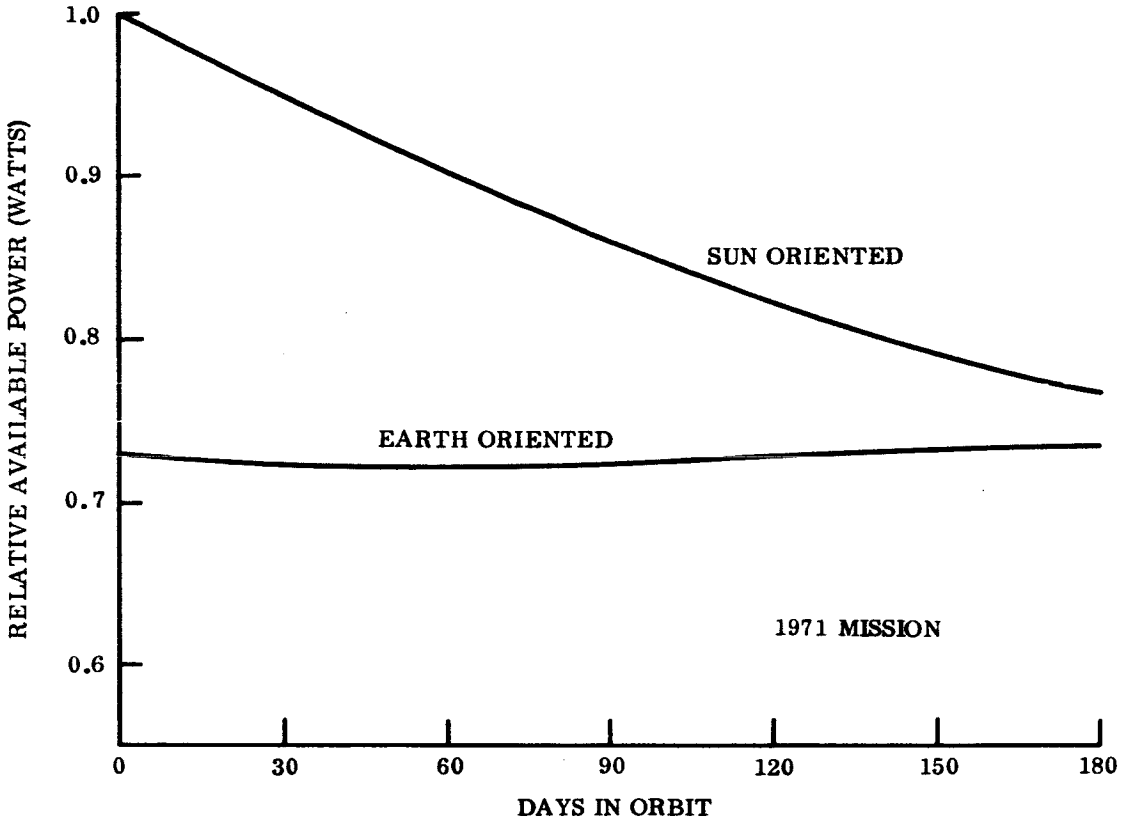

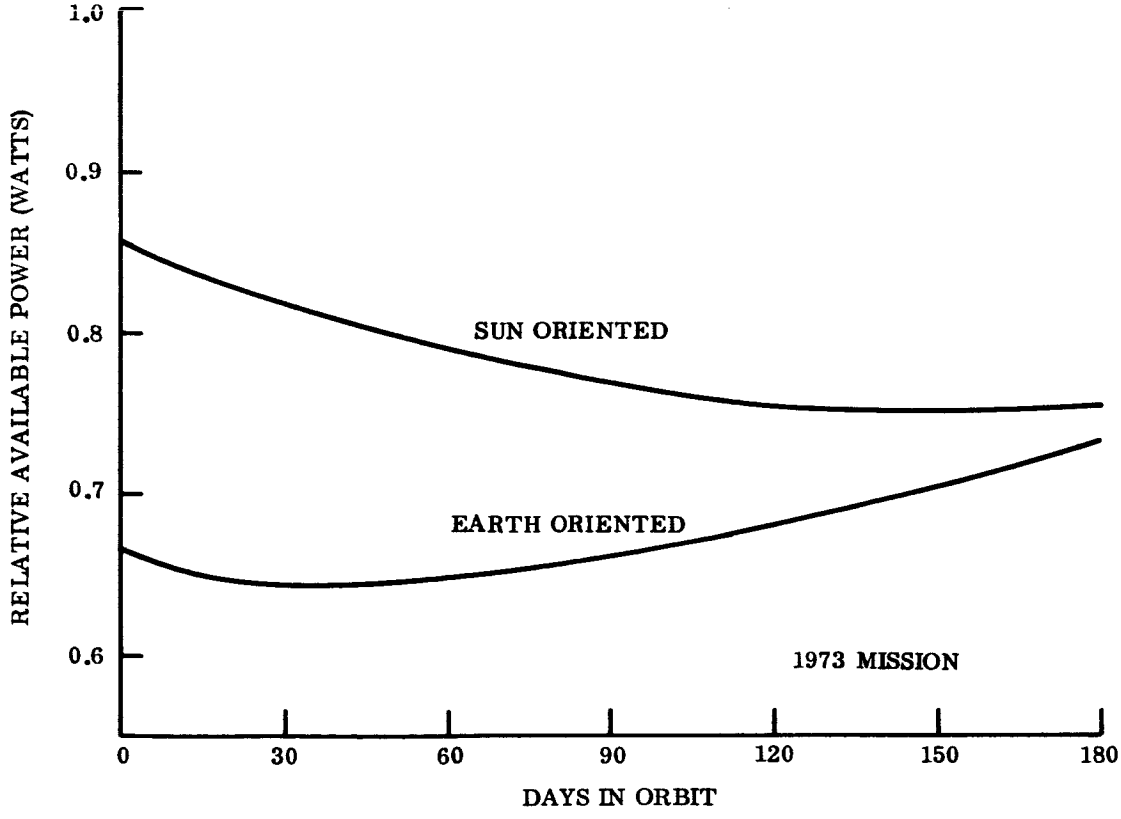

Figure 1-7. Available Power Relative to Equal Area Array Oriented to Sun at 1971 Encounter

The antenna shown in Figure 1-8 is an array of 96 endfire helices. Each element is 1-1/2 wavelengths long and provides a gain of approximately 13 db. A corporate feed network consisting of coaxial cables and stripline power dividers is mounted behind the radiator base screen. Four tracking beams are provided by the four quadrant arrays. A summary of the estimated high gain antenna characteristics follows:

Frequency	2295 mc
Element gain	13 db
Array gain	32.8 db
Half power beamwidth	3.6 degrees
Worst sidelobes	-8.5 db
Acquisition beamwidth (null beamwidth on sum pattern)	7 degrees

Data rates obtained with this high gain antenna will be comparable to the prime downlink of the recommended Sun-Canopus configuration.

Angle error detection is accomplished using a phase monopulse scheme as illustrated by Figure 1-9. This angle tracking implementation has a minimal impact on the reliability of the prime downlink as the active elements are isolated from the transmitter; the angle sensing equipment can fail with little impact on the downlink (providing that the optical Earth sensor is operable).

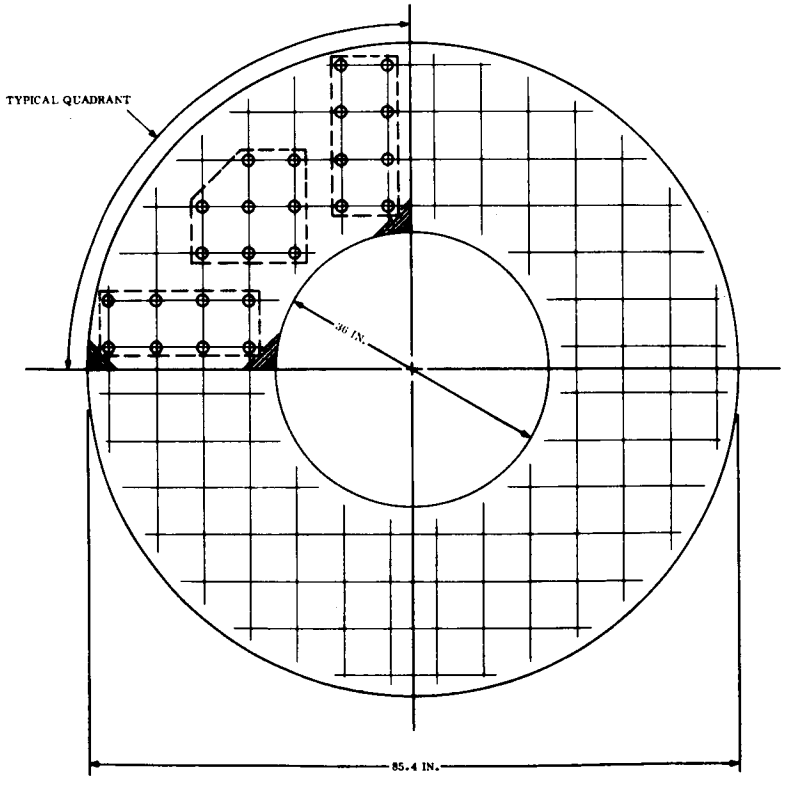

Figure 1-8. High Gain Antenna (Endfire Array) 96 Elements (6.1-inch Division)

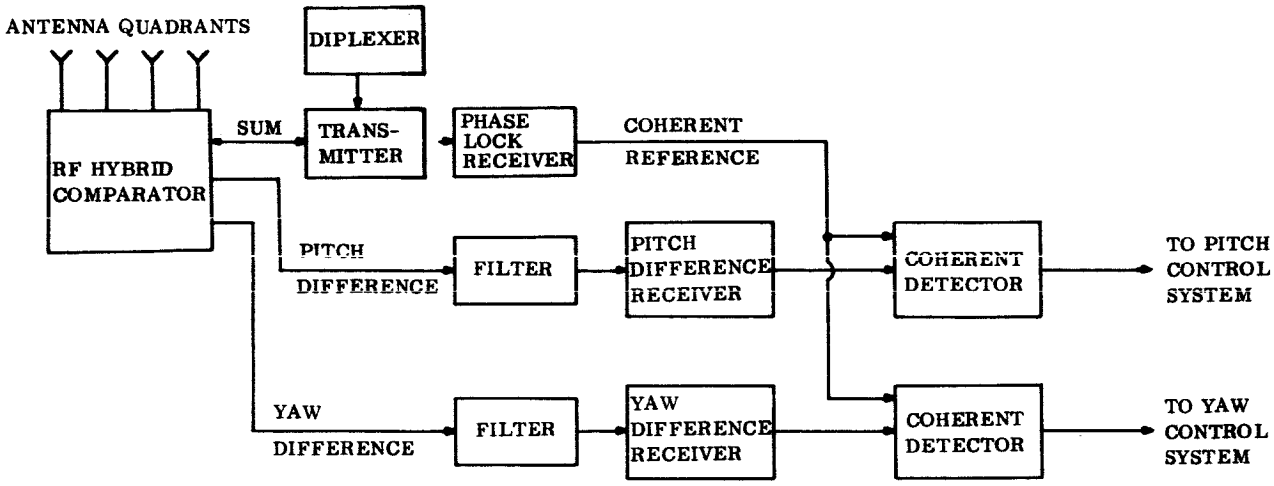

Figure 1-9. RF Angle Tracking System, Orbital Operations Mission Phase, Earth-Oriented Flight Spacecraft

With a fixed high-gain antenna, some means of sustaining communication at reasonable data rates during transit and maneuvers must be implemented. This requirement is satisfied by a 30-inch by 18-inch Cassegrain fed elliptical antenna which can be rotated on a single gimbal. Downlink data rate at encounter with this antenna and 50 watts transmitted to the 85-foot dish is over 50 bits per second. When the array is turned away from the Sun for maneuvers, a 25 bits per second downlink can be maintained using the 20-watt transmitter. It is intended that the gimbal position of this antenna be commanded from Earth. Very limited analysis has been performed on this antenna to maximize gain while maintaining the required coverage and the configuration presented is probably not optimum.

The low gain and VHF capsule relay antennas on the Earth oriented spacecraft are identical to those on the recommended Sun-Canopus vehicle.

1.4 PROPULSION SUBSYSTEM

The propulsion subsystem in the two-axes Earth oriented vehicle is practically identical to the recommended Sun-Canopus vehicle. To obtain space for the high-gain antenna, the propellent tanks have been reoriented. The result is slightly more complex propulsion structure and poorer propulsion subsystem accessibility. As previously indicated, the effect of engine thermal radiation and plume on the high-gain antenna has not been evaluated.

1.5 VEHICLE

Vehicle layout considerations for the Earth-oriented vehicle are much the same as for the recommended Sun-Canopus configuration. The Earth-oriented vehicle will have slightly higher moments of inertia and slightly lower ballistic parameter, but the differences are insignificant. A summary of estimated weight differences between the recommended Sun-oriented vehicle and the alternate Earth-oriented vehicle is shown in Table 1-1. Minus signs designate greater weight in the Sun-oriented system:

Table 1-1. Estimated Weight Differences Between the Recommended Sun-oriented Vehicle and Ultimate Earth-oriented Vehicle

	Pounds
Gimballed high-gain antenna versus high-gain array	-5.9
Fixed Mariner-C antenna versus smaller gimballed intermediate gain antenna	-2.1
Three-gimbal scan platform versus one-gimbal scan platform	-34.0
Earth sensor including sun shade	+11.0
Angle tracking equipment	+13.0
Additional Freon gas including tanks and factor of three for redundancy	+12.3
Solar array required for equal power margin	+35.0
	+29.3

The Earth-oriented vehicle would be approximately 30 pounds heavier neglecting additional propulsion fuel requirements.

In normal attitude, the equipment module of both the Sun-oriented and Earth-oriented spacecraft is completely shaded from the Sun, and the thermal control problems for the two systems are identical.

1.6 SUMMARY AND CONCLUSIONS

Assuming that a solar array is used as an electrical power source, the Earth-oriented concept requires a relatively small Sun-Spacecraft-Earth angle and the approach is not practical for a Venus mission. Both the recommended Sun-Canopus vehicle and the Earth-oriented vehicle present similar difficulties for an Atlas-Centaur test shot.

Thermal control of both vehicles is identical; as in both cases, the equipment module is shaded from the sun. The Earth-oriented vehicle is more symmetrical and has slightly higher moments of inertia, but the differences are thought not to be significant.

The motions, relative to Mars, of the scan platform of the Earth-oriented vehicle may be inconvenient for the planet oriented science. While the scan platform experiences no blockage for any orbit, it does rotate about the local vertical at rates as high as six degrees per minute which is certainly undesirable for planet oriented science. The recommended Sun-Canopus vehicle does not experience this rotation, but it does encounter blockage during portions of most orbits. Furthermore, the location of the scan platform on the Sun-Canopus vehicle will probably have to be adjusted for other missions requiring different orbits.

The ultimate choice between the recommended Sun-Canopus vehicle and the alternate Earth oriented vehicle depends on an assessment of relative probability of mission success. Furthermore, the essential difference in the reliability of the two vehicles involves a comparison of the reliability of the more complex attitude control subsystem of the Earth-oriented vehicle and the more complex articulation subsystem of the Sun-Canopus vehicle. More specifically, attitude control of the Earth-oriented vehicle requires additional sensors as well as full time use of a gyro in the roll control loop during the orbital mission. Attitude control is a vital vehicle function and this degradation of reliability is undersirable. On the other hand, the recommended Sun-Canopus vehicle employs five essential mechanical gimbals with associated control loops as opposed to two essential mechanical gimbals on the Earth-oriented vehicle (intermediate gain antenna is not essential) for the orbital mission. Failure of these gimbals, especially the antenna articulation subsystem, is virtually as serious as loss of attitude control. An adequate quantitative reliability comparison of these two approaches in this important area cannot be generated; the decision to recommend the Sun-Canopus approach was based on the following factors:

In favor of recommended Sun-Canopus vehicle:

a. Estimated to be 29.3 pounds lighter (neglecting fuel for propulsion system)

b. Less complex attitude control system using techniques proven on Mariner

c. Uses the Sun as an attitude control reference. Easy acquisition

d. Scan platform motions are more favorable for planet oriented science.

In favor of an Earth-oriented vehicle:

a. Relatively simple articulation

b. Scan platform position need not be altered for different orbits

c. Earth eclipse is the only occultation that affects attitude control

d. Vehicle will not block the scan platform.

CII - VB220AA020

ALTERNATE DESIGN CHARACTERISTICS AND RESTRAINTS CONSIDERED

FLIGHT SPACECRAFT UTILIZING MARS LOCAL VERTICAL STABILIZATION

Index

1.0 General Description
1.1 Guidance and Control
1.2 Thermal Control
1.3 Summary and Conclusions

1.0 GENERAL DESCRIPTION

The feasibility of using two axis attitude stabilization to Mars during the mission orbital phase was examined with the general conclusion that the approach is possible, but not very practical in light of Voyager mission requirements. Study of this system was confined to examination of attitude control and temperature control implications. Results of these studies are that this system configuration compares poorly to all other techniques examined. Therefore, no integrated Flight Spacecraft concept was developed.

Articulation of solar panels to the Sun from a two-axis Mars vehicle is considered impractical and this stabilization concept would require radioisotope thermoelectric generator (RTG) power. Pointing of the high-gain antenna to the Earth could be accomplished using an azimuth-elevation arrangement and rolling the vehicle body about the local vertical to eliminate the azimuth gimbal. Antenna elevation would then require a gimbal with 180-degree rotation capability. This single gimbal antenna articulation technique has a significant problem due to a control reference singularity when Mars, the Flight Spacecraft, and Earth are nearly in a straight line. When this singularity is approached, the required vehicle angular rates increase drastically (several orders of magnitude) and, very likely, it will not properly track the Earth. The control problems associated with this reference singularity are reduced if a second rotational degree of freedom is added to the antenna articulation control system.

1.1 GUIDANCE AND CONTROL

The recommended control axis configuration for a Flight Spacecraft using two-axis Mars stabilization is symbolically represented by Figure 1-1. Stabilization references for the transit phase of the mission are Canopus and the Sun. Reference vectors for body axis alignment during the orbital mission phase are: the local vertical, and the perpendicular to the orbit plane. Antenna articulation is obtained using two mechanical gimbals. The body fixed (outer) gimbal axis lies in the orbit plane, while the inner gimbal axis is perpendicular to the outer gimbal axis and the Mars-Earth line.

Local vertical reference is supplied by means of a pair of IR horizon scanners which provide voltage outputs proportional to angular displacements about two orthogonal axes lying in the local horizontal plane. The angular displacement about the local vertical vector (rotational error about the yaw axis) is determined by a semi-open loop technique in which the Mars-Earth line is utilized as the prime reference. As the perpendicular to the orbit plane and the Mars-Earth line are inertial on a day-to-day basis, and a heuristic relation exists between them; the perpendicular to the orbit plane can be determined from the Mars-Earth line. Furthermore, the Mars-Earth line is known in body axes through the antenna gimbal angles. Construction of the body yaw control reference is a difficult implementation problem.

The primary antenna pointing reference is an Earth sensor. Two general types have been considered for this application: an optical star tracker, and RF simultaneous lobing equipment associated with the high-gain antenna. The choice between these sensors is examined in VB220AA010 with the conclusion that the prime Earth sensor

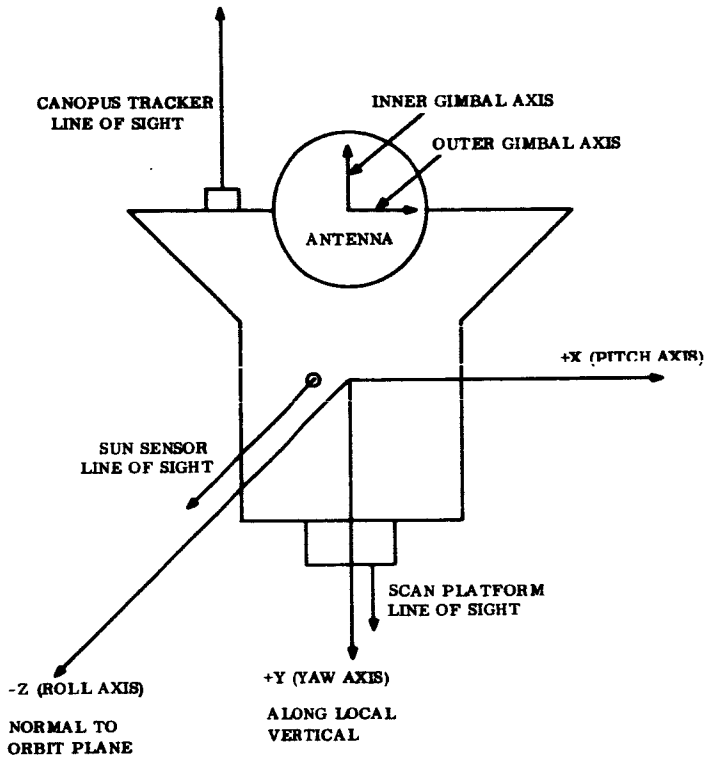

Figure 1-1. Conceptual Control Axis Configuration, Two-Axis Mars Stabilization

should be optical with the RF technique implemented for use during times of optical interference (for example, a conjunction of Venus and Earth as seen from Mars), or in case of failure of the optical sensor. This approach causes minimal degradation of the reliability of the telecommunications subsystem and makes low the probability that the DSIF will be required to provide an RF beacon signal for an extensive time interval. Both sensing techniques will experience short periods of Earth occulation during certain orbits. The limited acquisition-capability of these sensors makes a second shorter term reference necessary to avoid an antenna search mode after each occultation. Further, antenna reference must be continuous since this reference supplies information for body yaw control. To provide continuous reference, two single degree-of-freedom precision gas bearing (for long life) rate integrating gyros are mounted on the antenna to sense angular displacements about the same axes as the prime Earth sensor. These gyros are torqued by the prime reference sensor to maintain orientation. When loss of reference occurs, the torquing loop is opened and the antenna is pointed inertially.

1.2 THERMAL CONTROL

A two-axis Mars oriented vehicle creates very difficult temperature control problems in that it can assume any orientation with respect to the Sun. A simple thermal analysis assuming no conduction around the equipment module, 480 watts of heat dissipation, 48 square feet of radiating area, and temperature limits of 40° F to 80° F within the

equipment module (these values are typical of the recommended 1971 design), was performed. The zero conduction assumption is not too bad for a worst-case analysis as the narrow temperature range and light-weight construction preclude efficient heat conduction. This analysis indicates that active shutters could not maintain the part of the equipment module which is illuminated by the Sun below 80° F.

The equipment module can be maintained within the 40° F to 80° F range using a thermal coating with absorptivity of 0.1 and emissivity of 0.39, but about 100 watts of heater power is required whenever the equipment module is completely shaded. These very gross thermal studies permit only the conclusion that a two-axis Mars oriented vehicle is undesirable from a temperature control standpoint.

1.3 SUMMARY AND CONCLUSIONS

When compared with the other system concepts studied, the two-axis Mars vehicle is unattractive. A list of specific advantages and disadvantages of this system concept follows:

a. Advantages

1. Planet sensors may be body mounted. This provides flexibility in changing or adding experiments and simplifies field-of-view problems.

2. Out-of-orbit-plane pointing is easily accomplished by biasing the planet sensor.

3. Antenna pointing error is independent of limit cycle deadband. Larger vehicle deadbands are permissible resulting in control gas savings.

b. Disadvantages

1. Requires five long-life precision gyros.

2. Solar power cannot be used.

3. Requires a continuous Earth reference.

4. Requires a very complex yaw control loop.

5. Extreme dependence on proper gyro function.

6. Thermal control may impose unreasonable heater power requirements.

CII - VB220AA030

ALTERNATE DESIGN CHARACTERISTICS AND RESTRAINTS CONSIDERED

FLIGHT SPACECRAFT UTILIZING RADIOISOTOPE THERMOELECTRIC GENERATORS FOR PRIMARY POWER

Index

1 General Description
2 Guidance and Control Subsystem
3 Power Subsystem
4 Telecommunications Subsystem
5 Propulsion Subsystem
6 Vehicle
7 Other Considerations
8 Summary and Conclusions

1.0 GENERAL DESCRIPTION

The Preliminary Voyager Mission Specification states that solar cells shall be used as the source of primary power. Past Voyager studies have indicated that a radioisotope thermoelectric generator (RTG) power subsystem is competitive with solar cells; this fact led to re-examination of RTG power in light of the Phase 1A constraints. Most important details concerning the RTG units are classified and such items as estimated isotope availability, choice of thermoelectric junctions, and current state of development of RTG units similar to the type recommended for Voyager are covered in a classified appendix. The unclassified comments will necessarily be vague as to specific RTG performance.

Figure 1-1 is a layout of the Flight Spacecraft as modified for RTG power. Except for power subsystem, this vehicle is virtually identical to the prime Sun-Canopus vehicle. RTG power is applicable to the other alternate systems concepts presented in Volume B.

2.0 GUIDANCE AND CONTROL SUBSYSTEM

The change from solar array to RTG power has minimal impact on the Guidance and Control Subsystem. A small reduction in the moments of inertia of the Flight Spacecraft results, which will tend to conserve control gas. Some increase in the ballistic parameter is achieved which permits lower orbits without violating the contamination constraint. Of course, spacecraft orientation to the Sun is no longer required, permitting leisurely maneuvers and consideration of other attitude control references. Temporary loss of vehicle attitude control ceases to be a critical problem.

3.0 POWER SUBSYSTEM

A Radioisotope Thermoelectric Generator consists of several series strings of thermoelectric junctions surrounding a removable isotope thermal energy source. To some degree, the electrical properties of an RTG can be shaped by selection of the number of junctions in series in each string, the number of strings in parallel, and the characteristics of the individual junctions. A typical voltage current relationship for an 85-watt RTG is given in Figure 3-1. In general, an RTG should be operated at its maximum power; hence, a shunt regulator is used which operates the RTG near its maximum power point and dissipates power not required by the load. RTG units using plutonium 238 as fuel are recommended for this application; as these devices are only about five percent efficient, provision must be made in the vehicle design to permit direct radiation of large amounts of excess energy from the RTG.

The choice of six 85-watt RTG units was determined by the power profile indicated below, by the dimensional configurations of the vehicle, and by the goal to keep the unit power level low enough to be comparable with designs currently under development. The high isotope cost makes it desirable to keep the power requirements low

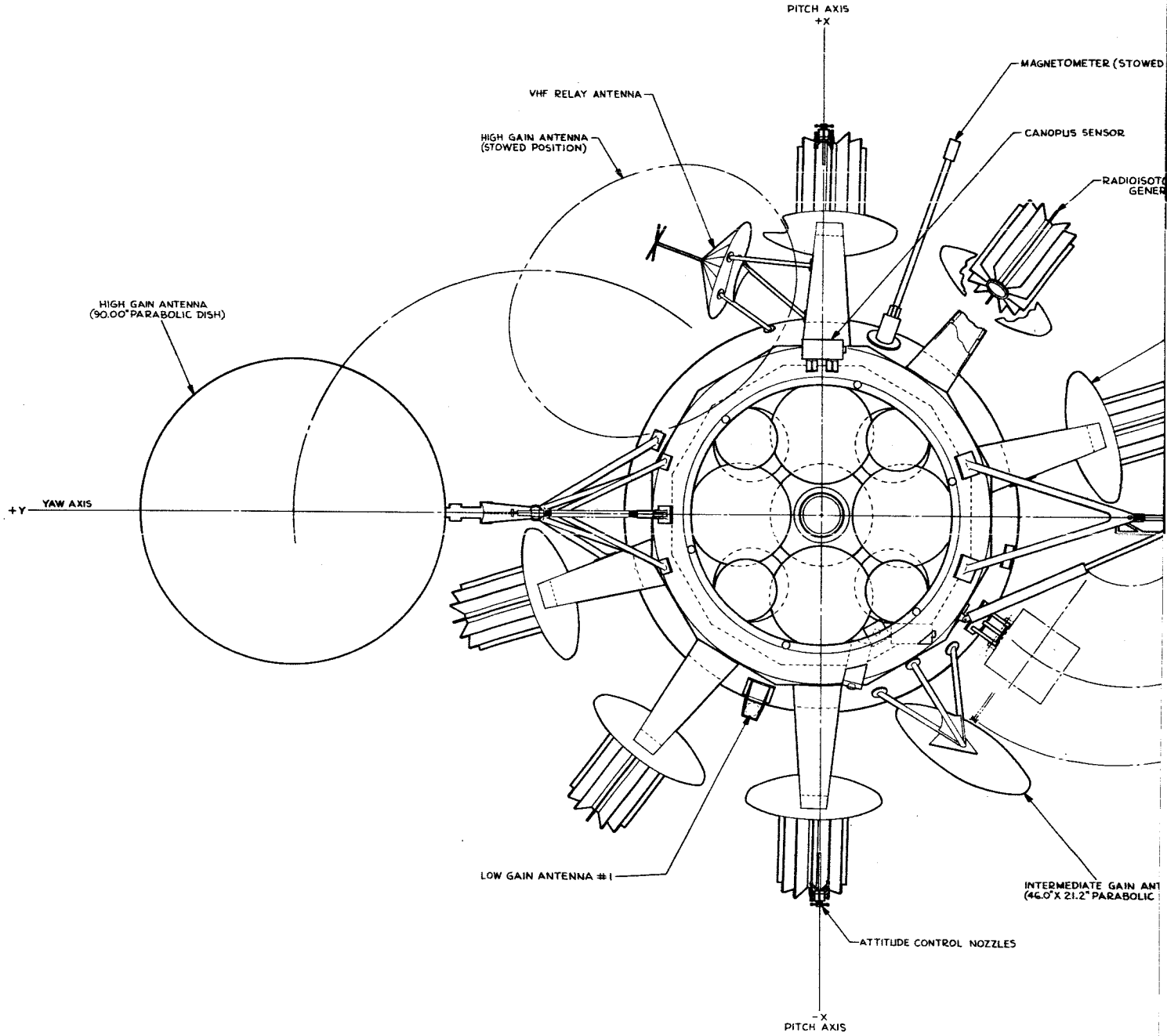

FLIGHT SPACECRAFT UTILI

3

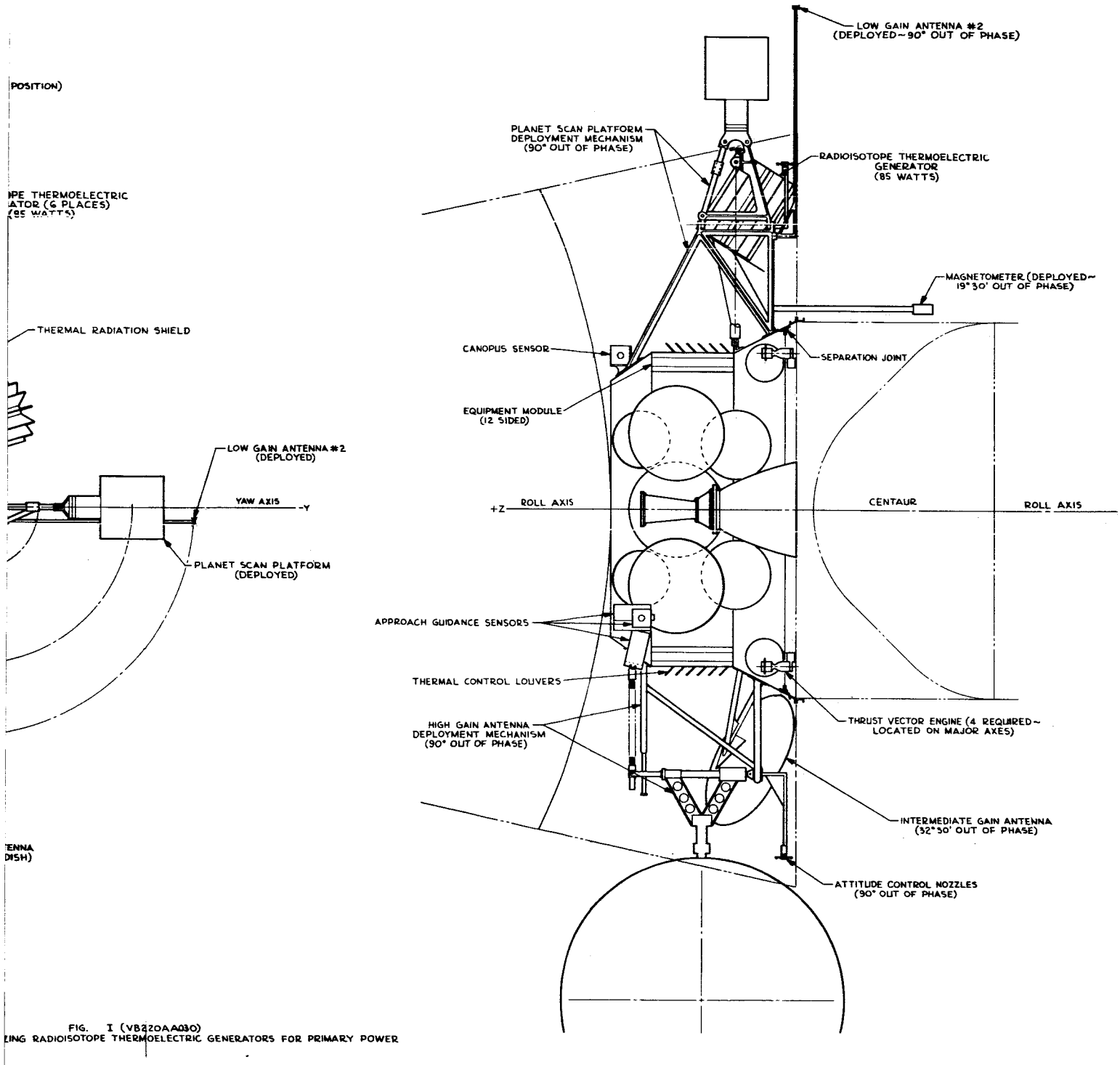

Figure 1-1. Flight Spacecraft as Modified for RTG Power

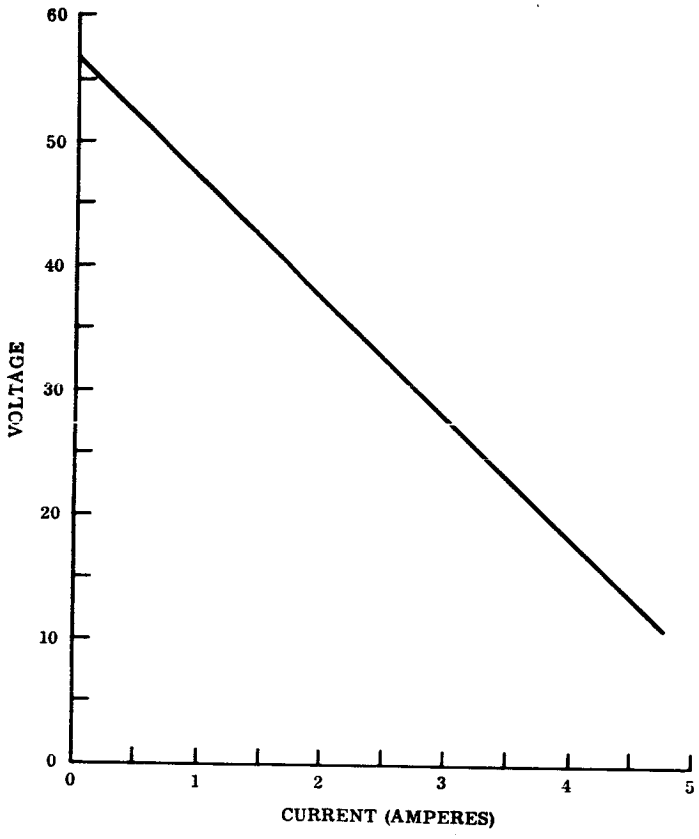

Figure 3-1. Typical Characteristic of an 85-Watt RTG

and the power profile constant throughout the mission. The following profile gives the assumed RTG power output requirements for the various mission phases:

	Watts
Launch to acquisition	317
Early cruise	451
Late cruise	453
Mid-course maneuver	435
Approach	476
Separation maneuver	440
Post separation cruise	368
Orbit Insertion	440
Orbit with full science	438
Orbit with partial science	354
Orbit solar eclipse	374

This profile is essentially that for the prime Sun-Canopus vehicle except for the very obvious modification of using the 20-watt transmitter during early cruise and the 50-watt transmitter during sun occultation. Use of six 85-watt power units gives a minimum margin of 34 watts during the approach phase. Certainly, this represents a minimal effort in optimization of the load profile and much more effort would be required if RTG's were the power source for the recommended 1971 vehicle.

Figure 3-2 is the block diagram of the RTG Power Subsystem. This arrangement has very high power conditioning efficiency and inherent reliability, but has the deficiency that loads above the capacity of the RTGs will pull the voltage down. Use of such a system is dependent on the ability to predict loads which are characterized by large power requirements for short time periods and operate them from the topping battery. Furthermore, all electrical components must sustain without damage a low voltage transient if an electrical fault occurs in the vehicle. If these conditions are intolerable, the alternate system indicated by Figure 3-3 will, at a sacrifice of efficiency, maintain voltage in the presence of an overload. Both systems utilize inverters and synchronizer identical to those described for the recommended 1971 design.

Both power subsystem approaches provide inherent redundancy in the shunt regulators. As the minimum vehicle power requirement is above the capacity of three RTGs, any three power units can be connected directly to the load and the shunt regulators on the remaining three power units will perform the regulating function. If provision is made to switch the output of each RTG directly into the load, the power subsystem can sustain the failure of any shunt regulator with no degradation of the ability of the vehicle to perform the mission. The estimated weight of each shunt regulator is four pounds, so that this redundancy does not invoke a large weight penalty. Due to isotope cost and the relatively high reliability of an RTG, these power units are not redundant. They are isolated by diodes so that the impact of loss of a power unit is 85 watts less raw power available to the spacecraft. The power profile previously presented shows that failure of a single power unit will not seriously degrade the orbital mission.

Figure 3-4 is the circuit of the shunt regulator, a high frequency (about ten kilocycles per second) switching device which, because of simplicity and small number of parts, should be very reliable. This component has the interesting property that its efficiency improves as it is required to deliver more power to the load. If the RTG becomes fully loaded, its entire output is delivered to the load except for small diode loss and the power required by the regulator. In the fully loaded state, regulating efficiency should be around 95%. A parts count reliability analysis for the shunt regulator yielded a failure rate of 1.07×10^{-7} failures per hour, which implies a probability of successful operation for 5000 hours of 0.99947. Proper voltage regulation requires only three of the four shunt regulators.

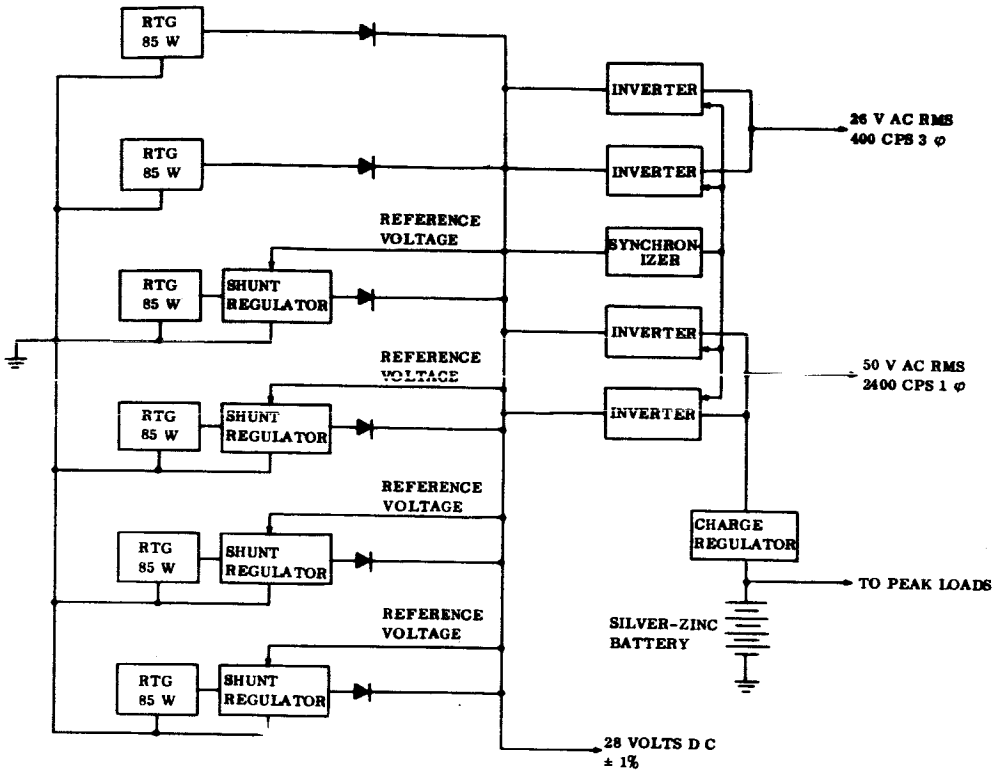

Figure 3-2. RTG Power Subsystem

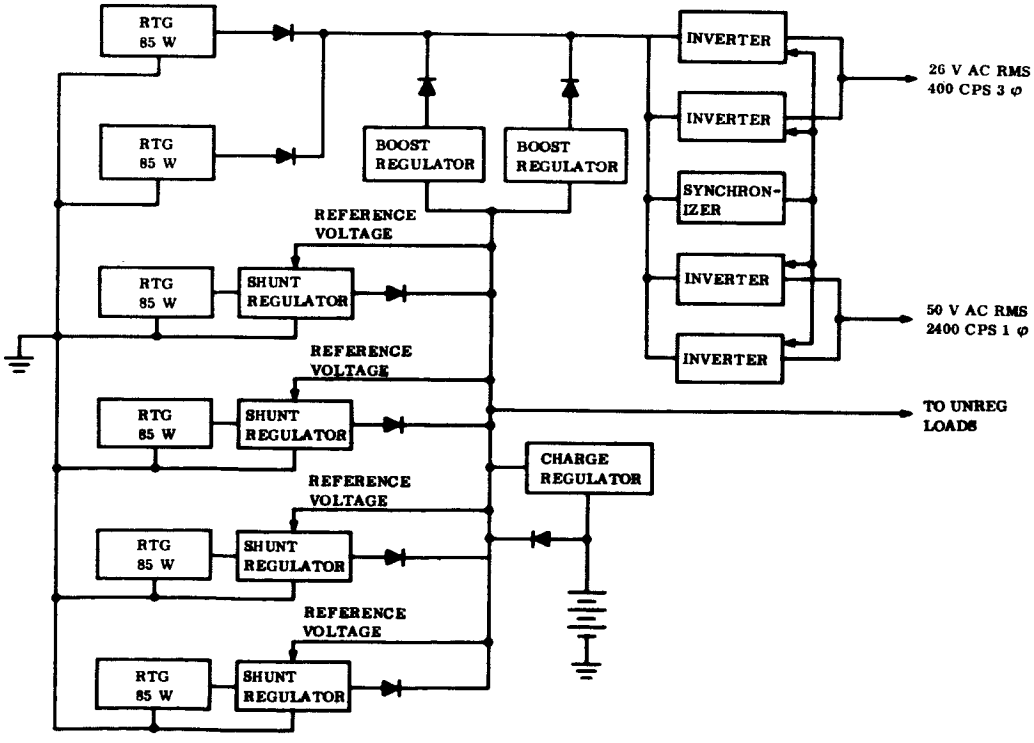

Figure 3-3. Alternate RTG Power Subsystem

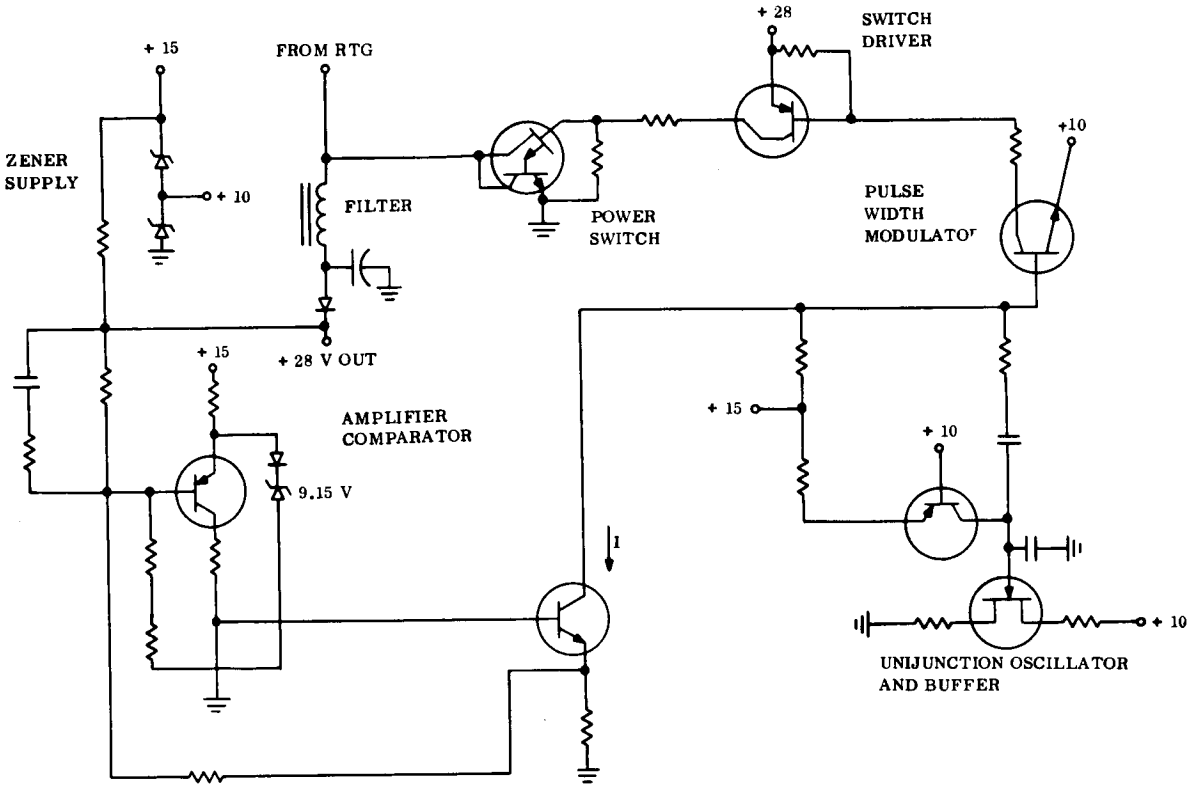

Figure 3-4. Shunt Regulator

No specific requirement for the topping battery has been identified so the battery has been selected arbitrarily to be composed of twenty two 6-ampere-hour silver zinc cells (as the battery will be practically fully charged for the entire mission) with a capacity of 200 watt-hours. The series charge regulator will limit charging current to 0.2 ampere and will limit battery voltage to any of three levels - 42.9 volts, 41 volts, or 39 volts (voltage level selected by command).

Any analysis of the reliability of the power subsystem of an RTG powered vehicle is questionable as little test data is available on RTG units. The failure modes of a thermoelectric generator consist of gradual deterioration as well as random open circuit failures which result in complete loss of power. Those failure modes that effect a gradual or minor loss of performance may be best circumvented by providing sufficient margin in thermopile design to assure adequate performance over design life.

Open circuit failures in the thermopile are a major source of concern in achieving long life and high reliability; with improper design, this type of failure results in complete loss of power. To reduce the problem of open circuit failures, the RTG units will be wired as shown in Figure 3-5. A total of 800 thermocouples will be connected in ladder fashion to obtain 400 stages in series (these numbers are unclassified approximations). Failure of any stage requires failure of both thermocouples in that stage and constitutes total failure of the power unit. With this

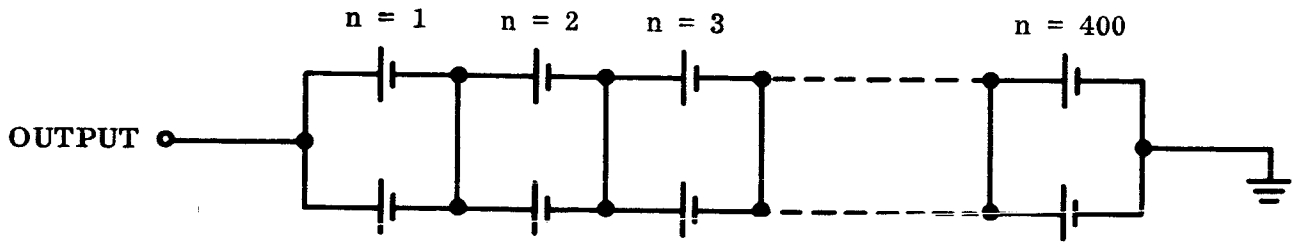

Figure 3-5. RTG Internal Wiring

arrangement, a probability of 0.995 that a given RTG will not fail open circuit in 5000 hours (duration of transit plus one month in orbit) requires a thermocouple failure rate not greater than 7×10^{-7} failures per hour, a rate which probably can be realized.

These reliability numbers do not have a very firm basis; probably more important is the fact that solar cell power subsystems are well developed and have worked well in the past. On the other hand, RTGs are not so well developed, but are felt to hold considerable promise as highly reliable, extremely long life, power sources.

RTG power units are insensitive to particle radiation at any intensity expected on a Mars mission. In the event of extreme solar activity or very intense Mars radiation belts, degradation of solar cells can curtail the data producing capability of a Voyager probe (refer to VB236FD101 - Appendix).

If a solar array powered vehicle loses its ability to orient to the Sun, the batteries will provide only a few hours communication at very low data rates to accomplish trouble-shooting. A vehicle with RTG units does not depend on Sun orientation for life and under conditions of attitude control loss, the only significant constraint will be very low data transmission capability-very relaxed troubleshooting should provide the maximum likelihood of identifying and circumventing the malfunction.

4.0 TELECOMMUNICATIONS SUBSYSTEM

Use of RTGs for prime power has, in itself, no impact on the telecommunications subsystem.

5.0 PROPULSION SUBSYSTEM

The propulsion subsystem is, for practical purposes, independent of the choice of prime power source.

6.0 VEHICLE

Conversion of the recommended 1971 vehicle to RTG power involves little more than removing the solar panels and configuring the RTGs so that their radiating surfaces have a maximum view of space. Thermal radiation shields are employed to prevent direct radiation from the RTG to the equipment module and reduce the problem of temperature control of the equipment module. The scan platform implementation shown in Figure 1-1 permits the scan platform to view Mars without separation of the lower section of the biological barrier. Removal of the biological barrier and use of a scan platform design similar to the recommended 1971 design is a superior approach. Furthermore, the antenna can be moved off the +y axis as for the prime 1971 design so as to completely eliminate blockage of the altitude control nozzles. A potential configuration problem is the proximity of the yaw altitude control nozzles to the radiating surfaces of the RTGs.

Placement of the power units on the spacecraft permits fuel loading through an access port in the shroud. Once the power units are fueled, cooling air is required and this inconvenience makes on the pad fueling attractive. An estimate of the cooling air requirement is 80 pounds per minute of air at 40°F. No allowance is made for cooling any RTG units in the capsule. The thermal time constant of an RTG is such that it can sustain, without damage, the temperature rise which occurs between launch and shroud separation.

A summary of estimated weight differences between the recommended 1971 design and an RTG powered vehicle follows. Minus signs designate greater weight of the recommended 1971 design.

	Pounds
Increased weight of high-gain antenna support structure	+8.0
Solar array	-204.2
RTG power units including support structure	+311.4
Increased weight of attitude control nozzle support structure	+3.0
Increased weight of support structure of medium gain and relay antennas	+3.0
Batteries	-117.0
Main buck regulators	-23.0
Shunt regulators	+16.0
Charge regulators	-4.5
Topping battery with charge regulator	+10.0
	+2.7

The fact that all power from the RTG Power Subsystem is regulated may result in some weight saving in other subsystems. Nevertheless, the weight difference between an RTG powered vehicle and a solar cell powered vehicle appears negligible.

Lack of a solar array reduces the frontal area of the spacecraft and increases the ballistic parameter. The consequence is that lower orbits are possible without violation of the Mars contamination constraint.

7.0 OTHER CONSIDERATIONS

The isotope cost is substantial - approximately $22,500 per electrical watt. It seems probable that spare RTGs would be manufactured, but a minimum number of spare fuel elements would be fabricated. Assuming that one spare fuel element would be fabricated for each launch opportunity, a total of twenty six 85-electrical-watt fuel elements would be required for the 1971 and 1973 opportunities at a cost of approximately $50,000,000. Fuel availability and cost is further explored in the classified appendix.

Handling of nuclear materials is a significant safety problem although Plutonium produces relatively low radiation levels. Using established techniques, fuel capsules of the size suggested can be handled by an individual for about three hours without exceeding his allowable exposure for a calendar quarter. The high temperature of the fuel capsules also presents safety problems. Most system testing would probably be accomplished by substituting electrical heaters for the fuel capsules and thus avoiding the difficulties of handling nuclear materials. Current practice is to design the RTG so it will contain the fuel through re-entry at any attitude or through any launch abort.

RTG power units tend to complicate the magnetic design of the spacecraft. Thermopiles may use small iron parts to inhibit undesirable chemical reactions; these parts can be made very thin to reduce the total amount of iron. RTG's are direct current generators, but they can be constructed so as to largely eliminate the resulting magnetic field.

The estimated radiation level from an 85-electrical-watt Plutonium 238 RTG is:

0.020 rads/hour neutrons at one meter

0.002 rads/hour gamma at one meter

175 rads/year neutrons at one meter

18 rads/year gamma at one meter

Typical one year dosages experienced by a spacecraft in Earth orbit are:

Radiation belt	10^{12} rads
Solar flare	10^{6} rads
Cosmic rays	5 rads

Radiation from the RTGs is insignificant compared to background radiation as far as damage to electronics is concerned, but it may affect scientific measurements. An Atlas - Centaur test flight would require a minimum of three 85 watt RTG units which would pose a configuration problem. Although this problem has not been pursued in detail, it appears that the units could not be fueled with the shroud in place and would require a simple deployment in order to provide a sufficient view factor to space. For the 1975-77 opportunities, the Flight Spacecraft apparently has a very limited scientific mission and it is undesirable to use RTGs for just the transit mission phase. The ideal approach for these later missions would seem to be to depend on capsule RTGs for power during transit as this energy should be readily available. Use of RTG units on Voyager would provide excellent experience for design of probes to the outer planets, which will almost certainly require nuclear power sources.

8.0 SUMMARY AND CONCLUSIONS

Use of Plutonium 238 Radioisotope Thermoelectric Generators is an attractive alternative to the recommended 1971 design. In favor of the recommended 1971 design:

a. Batteries and solar cells are well proven components.

b. No radioactive materials or high temperature surfaces are required. Safety of personnel is less of a problem.

c. Easier temperature control. Does not require a large volume of cooling air on the launch pad.

d. No availability problem.

e. Lower hardware cost.

In favor of an RTG powered vehicle:

a. Inherently resistant to radiation. Solar flares and Mars radiation belts are not a problem.

b. Has potential for higher reliability.

c. Temporary loss of attitude control is not a critical problem.

d. Increases ballistic parameter.

Both approaches are comparable from a weight standpoint and present about the same level of difficulty in adaptation to a 1969 Atlas-Centaur flight.

CII - VB220AA050

ALTERNATE DESIGN CHARACTERISTICS AND RESTRAINTS CONSIDERED

TRADEOFF STUDY: MICROELECTRONIC VERSUS ELECTRONIC PIECE PART CIRCUITS

Index

1	Summary
2	Introduction
3	Available Microelectronic Techniques
4	Reliability of Microcircuits
5	Design Experiences with Microelectronics
6	Microelectronic Tradeoff Studies
7	Conclusions
I	Derivation of Temperature Acceleration Factors For Integrated Circuits
II	Attitude Control Loop Tradeoff Analysis
III	Telemetry Processor Tradeoff Analysis

1.0 SUMMARY

The reliability of microcircuits has been demonstrated by more than 216 million hours of silicon integrated life test data by vendors and users. A reasonable failure rate for silicon integrated circuits (SIC) is 0.005%/1000 hours at 40°C. Digital microcircuits are preferred over piece-part implementations. As there is limited data on film circuits and analog integrated microcircuits, use of these circuits must be justified on the basis of each application. A listing of some of the applications of microcircuitry shows a proven capability does exist for production and use of microelectronic equipment.

A tradeoff analysis of a microelectronic versus cordwood attitude control loop and a 61-channel telemetry processor shows that significant improvements in reliability are obtained through redundancy. The redundant microcircuit version of the equipment is no larger or heavier than the non-redundant cordwood version. In the case of the telemetry processor, the redundant microcircuit version is approximately 40 times more reliable and one-third the size and weight of the non-redundant cordwood version.

Standard microcircuits for use throughout the Voyager Spacecraft will be specified on the approved parts list. The number of microcircuit types will be kept to a minimum. Selection will be made on the basis of history of reliability, performance and usage. The selection of the approved microcircuits will be made after Phase IA on the basis of analysis of subsystem functions and requirements.

2.0 INTRODUCTION

To use or not use microelectronics for implementing Voyager electronic functions is a decision requiring a careful analysis of all pertinent information and data. The most important factor in this decision is reliability. On the one hand, conservatism indicates the use of older techniques (standard electronic piece parts) because of a longer history of experience. On the other hand, the desire to improve Spacecraft Systems indicates the use of microelectronics wherever possible to gain possible improvements in reliability, size, and weight. The study on the following pages was made to resolve the differences between these two schools of thought and to determine the best approach for implementing Voyager electronic functions.

The report first describes microelectronic techniques that might be applicable to Voyager, and then discusses the basic underlying reasons for the generally expected improvement in reliability of microcircuits over the older piece part electronic techniques.

Next, an analysis is made of available microcircuits life testing data to determine if microcircuits have been able to demonstrate a history of reliability, and to determine a reasonable failure rate number for microcircuits. This failure rate number will then be used in subsequent microelectronic versus piece part equipment tradeoff analyses (Section 6.0). The next question to be answered, then, assuming the

demonstrated reliability of the microcircuits, is, - does industry, in general, and GE, Motorola, and Texas Instruments, in particular, have sufficient experience in the design and fabrication of microelectronic equipment to be able to reliably implement electronic equipment with microelectronic circuits? Tables are shown listing equipment already or being converted to microelectronic form. Section 6.0 then contains the results of detailed tradeoff studies of a piece part cordwood construction versus a microelectronic implementation of a typical attitude control loop and a 61-channel PCM Telemetry Processor. The intent here is to show improvement, if any, in reliability, size, weight, and cost of microelectronic equipment.

Finally, based on the preceding studies, conclusions are made about the reliability of microcircuits, where advantages are to be gained by their use, and their recommended use on Voyager.

3.0 AVAILABLE MICROELECTRONIC TECHNIQUES

The microelectronic techniques possibly applicable to the Voyager Program can be divided into several basic groups depending on the process used in fabrication. These are: The micro-modular, thin-film, and silicon-integrated approaches (Figure 3-1). The molecular approach is another basic group but the development of this process is much slower than originally expected and, therefore, not considered here.

3.1 MICRO-MODULAR APPROACH

This technique uses discrete miniature component parts, sometimes of the same form factor, interconnected in various ways (wires, conductive cements, thin films, etc.), and packaged in small modules or transistor packages.

The U.S. Army micro-modular development uses standard size ceramic wafers each containing a single or dual component part interconnected by riser wires and metallized leads. Another technique interconnects tiny pellets, each containing a component part, on a copper clad board (Hughes, P.R. Mallory). Still another micro-modular approach is simply a reduction in size of standard type component parts and interconnecting them with miniature semiconductors (Centralab-PEC).

This effort is generally considered an interim technique to realize size and weight reductions. It has the advantages of piece part circuit techniques, but offers limited potential for improvements in system reliability and cost.

3.2 THIN-FILM APPROACH

This classification includes all techniques whereby circuit elements are deposited or formed on substrates by methods other than diffusion techniques. In other words, the substrate itself is passive, supporting active parts and circuit elements formed on its surface. Here full potential exists for a significant improvement in all factors including reliability. However, the technology is at present limited to forming

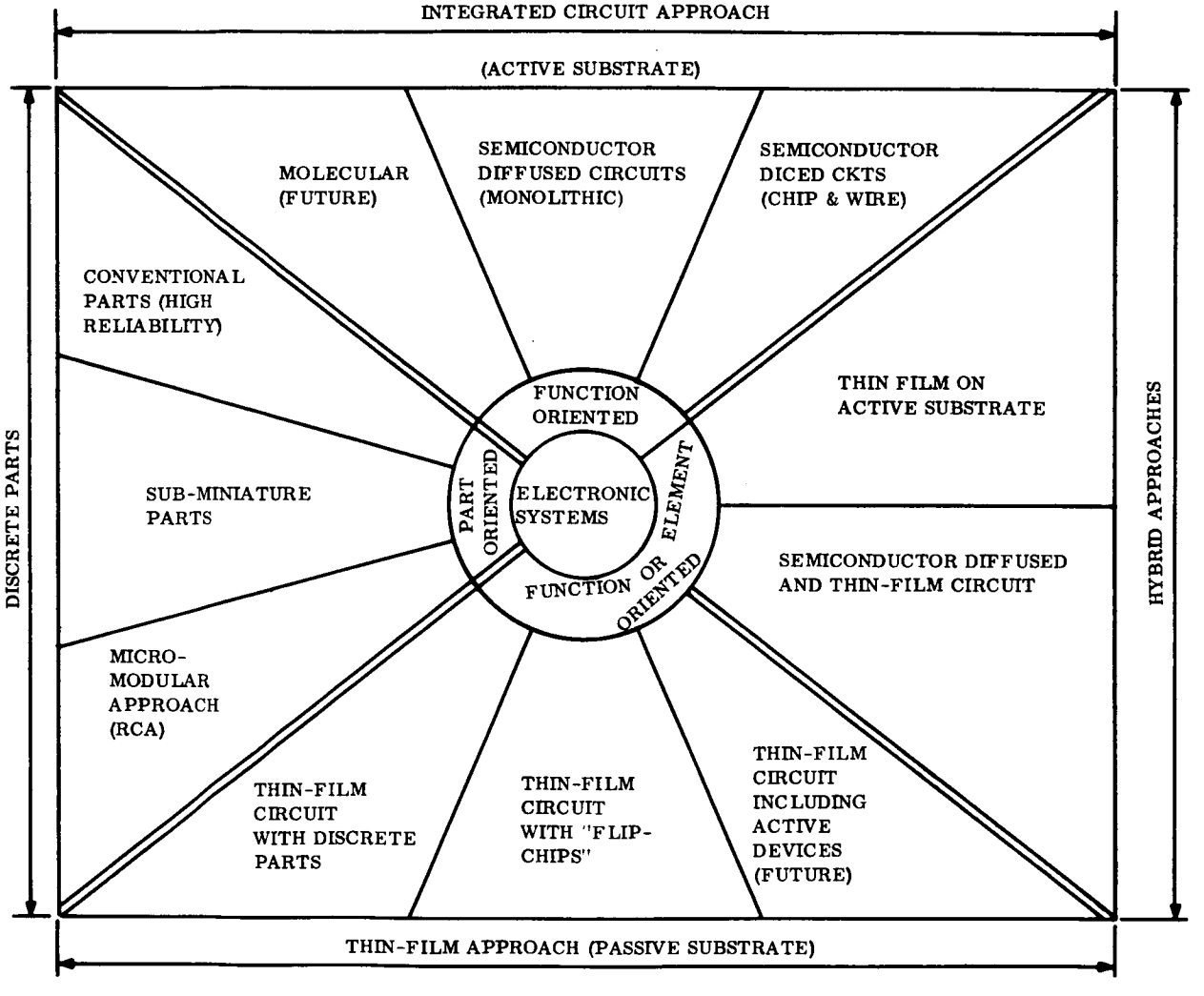

Figure 3-1. Electronic System Design Approaches

conductors and passive components, with discrete active component parts attached separately. There is considerable research into the development of thin-film active devices which could be formed simultaneously with the other parts of the circuit. The potential of this technique for significant gains in reliability probably rests on the success of this research. Several companies are developing thin-film circuits with inverted "flip-chip" semiconductor devices to reduce the intraconnections and thus improve the reliability of the thin-film circuits. Tight tolerances and greater electrical performance range are the most lucrative aspects of thin-film circuits.

3.3 SILICON-INTEGRATED CIRCUITS (SIC)

These circuits are formed within a monolithic silicon substrate by a combination of diffusion and growth processes, with deposited overlays for intraconnections. Some of the abbreviations used by vendors for this type of circuit are IC, FEB, and SIC, which mean, respectively, integrated circuit, functional electrical block, and silicon-integrated circuit. They are also called solid circuits or semi-conductor networks.

Theoretically, this type of circuit is capable of maximum improvement in reliability, cost, size, and weight over circuits made with discrete parts. However, the manufacturing process is such that all circuit elements cannot be optimized simultaneously. The diced semiconductor circuits (sometimes called chip and wire), are intended to improve electrical performance; however, the reliability of the diced circuit is reduced by the additional interconnections.

3.4 HYBRID CIRCUIT APPROACH

A hybrid circuit is defined here as an arrangement consisting of combinations of thin film, silicon integrated, and/or piece parts. There is a significant trend toward exploring a hybrid form wherein the silicon substrate contains diffused transistors and diodes, and the passive circuit elements are deposited in thin films on the passivation layer of the silicon wafer surface. The intraconnections are also deposited on the silicon substrate and are an integral part of the circuit. This technique can increase manufacturing yield and optimize circuit performance. Another form of hybrid approach is a combination of silicon integrated circuits with thin-film circuits using one or both sides of a passive substrate.

4.0 RELIABILITY OF MICROCIRCUITS

4.1 WHY SHOULD MICROCIRCUITS BE MORE RELIABLE?

It has been claimed that significant gains in reliability can be achieved through the use of the microelectronic techniques. Investigations have shown that microelectronic circuits have fewer failure mechanisms than are found in conventional designs with component parts. Some of the basic factors contributing to the higher reliability of microelectronic equipment are:

a. Reduction of interconnections and parts

b. Improved connection techniques

c. The use of redundancy becomes more practical through size and weight savings

d. Monolithic structure of silicon integrated circuits

e. Less handling.

4.1.1 REDUCTION OF INTERCONNECTIONS AND PARTS

It is well known that many of the failures in electronic equipment can be traced to failures of interconnections. The following tabulation shows the reduction ratio of interconnections which might be expected as a result of using silicon integrated circuits (SIC).

	Cordwood (Conventional Parts)	μE (SIC)	Reduction Ratio
Circuit Level (RCTL Flip-Flop)	125	20	6/1
Component Level (32-Stage Counter)	1536	305	5/1

4.1.2 IMPROVED CONNECTION TECHNIQUES

The reduction of the varieties of connections when using SIC's is a major factor contributing to improved reliability of electronic equipment. Discussing the connection reliability, both the interconnections between microelectronic μE circuit elements and interconnections between the component parts or the integrated circuits must be considered.

In a circuit, with discrete component parts, in addition to internal part connections, each part must be individually interconnected to the rest of the circuit. For example to connect the emitter region of a transistor through a resistor to a bias terminal requires a minimum of 11 connections. These include evaporated, thermal compression, welded, crimped and soldered connections. These connections involve a number of different materials and are made by at least four different manufacturers; the transistor suppliers, the resistor manufacturer, the circuit board fabricator, and the circuit assembler.

In a silicon monolithic circuit, the same process requires only seven connections. About two-thirds of these are evaporated intraconnections made by an automatic process. Because of the automatic process controls used and the essential nature of

this type of connection, its reliability is much greater than most of the connections made to conventional parts.

Another, less obvious reliability improvement will result because the material, size, and shape of the external leads will become uniform. At this time, considerable effort is being expended to standardize on methods of assembly for discrete component circuitry. This effort can achieve only partial success because of the great differences in the parts used. The standardization possible with integrated circuits will permit simplified equipment assembly.

4.1.3 REDUNDANCY

The use of redundancy for significantly increased reliability becomes more practical with microelectronics because some of the size and weight savings can be converted to adding redundant circuits or black boxes. Doubling circuit elements to perform individual functions or dual black boxes can be used and still the microelectronic redundant equipment will be smaller and lighter than the nonredundant discrete part version of the same equipment. The tradeoff study of the telemetry processor (see Section 6.3) clearly demonstrates this point.

4.1.4 ADDITIONAL IMPROVEMENT FACTORS

Reliability evaluation testing, test certification, and control of vendors are all simplified since they are performed on a circuit level rather than a part level. Handling, identification, and polarity errors are reduced. The manufacturing simplicity is a key to higher reliability and lower costs.

Misapplication of component parts contributes to poor equipment reliability. The nature of integrated circuits is such that functional parameters and bias conditions are closely specified. The application will, therefore, duplicate the particular conditions of use for which the circuit was designed, manufactured, and tested. This set of circumstances does not generally exist for discrete piece parts. For example, transistors, from economic necessity, are tested only under specific conditions. However, the actual operating conditions for transistors in equipment can vary over a wide range of conditions depending on the design restraints on the circuit.

4.2 WHAT DOES MICROCIRCUIT LIFE TEST DATA SHOW?

The availability and use of various microelectronic techniques has accelerated rapidly during the past two to three years. A review of some of the current programs where these techniques have been applied, is given in Section 5.0. In this section, a review of available microelectronics reliability data is presented. As will be seen, this data substantiates the claim that microelectronic circuits have achieved failure rate levels equal to or better than those for equivalent circuits made with discrete parts.

By far, the most widely exploited microelectronic technique has been the silicon monolithic integrated circuit for digital applications, and a large amount of reliability data are currently available on these devices. These data have been derived from operating and storage life testing at various temperatures by vendors and from laboratory and field operation of equipment using integrated circuits.

More recently, linear (analog) integrated circuits of the monolithic type have become available from most major integrated circuit vendors. The linear circuits are being used on a number of current programs. However, because of their more recent introduction and much lower production volume, only a limited amount of reliability data are currently available. The data which exists, however, are very encouraging in that excellent parameter stability has been demonstrated, and no indications of a substantially higher failure rate than that achieved for digital circuits has been noted. In the next six to twelve months, considerably more reliability data on these devices will be available as a result of tests now in progress or about to be started.

Thin-film techniques have been available as long or longer than semiconductor integrated circuits. The technology for fabricating thin-film passive devices, particularly resistors and capacitors, is well developed; and thin-film devices are in use on several current programs. However, most thin-film circuits are custom designed and of low usage volume. Because of these factors, only limited reliability data are available; but the data that exists show circuit stabilities and failure rates comparable to or better than those obtained with the best discrete parts. In the case of hybrid devices, the same factors of low volume and custom circuits have precluded the generation of a significant quantity of reliability data.

In order to keep abreast of the reliability levels which have been demonstrated for the various microelectronic techniques, General Electric has developed an extensive file of microelectronic reliability data. Information obtained from each source is tabulated on a standard format which provides columns for the items of information necessary to investigate the reliability factors of interest. Follow up and personnal contacts are made to obtain data on items not included in the vendor reports, and the file is continuously updated as new vendor reports are received. This microelectronics data file provided the input data for this analysis of microelectronic reliability.

4.2.1 DIGITAL INTEGRATED CIRCUITS

A summary of the data available on digital semiconductor integrated circuits is given in Table 4-1. It is evident from Table 4-1 that a wealth of data has been accumulated, (over 200-million device hours of testing on 47,000 devices). However, the majority of the data were generated at accelerated test conditions.

In order to use the data in Table 4-1 to assess the failure rate indicated at typical spacecraft ambient temperatures such as 40°C, it is necessary to derive acceleration factors for failure rate versus temperature. The results of such an analysis are given in Appendix I. Using the acceleration factors of Appendix I, the data from

Table 4-1. Summary of Reliability Data - Digital Silicon Integrated Circuits

Source	Test Conditions	Number of Devices	Total Device Hours	Total Device Failures	Most Recent Report	Remarks
Amelco	125 °C oper.	676	1,890,000	0	October 1964	DCTL
Amelco	150 °C stor.	22	419,000	1	October 1964	DCTL
Fairchild	125 °C Ring Counter	2172	37,514,758	8	May 1965	Early production non-epitarial devices
Fairchild	125 °C Ring Counter	3626	38,338,644	0	May 1965	Current production, RTL, DTL devices
Fairchild	250 °C Computer	18,000	78,000,000	0	May 1965	Apollo Computer - RTL
Fairchild	25 °C, 75 °C Ring Counter	459	2,000,000	0	May 1965	Martin Orlando Module Test - RTL
Fairchild	125 °C Ring Counter	68	396,000	1	May 1965	Boeing evaluation test - DTL
Fairchild	125 °C oper.	1253	986,650	1	May 1965	FACT testing, RTL, DTL, TTL
Fairchild	150 °C stor.	610	418,600	1	May 1965	FACT testing, RTL, TTL
Fairchild	150 °C stor.	715	1,426,000	2	May 1965	Special tests, RTL

Table 4-1. Summary of Reliability Data - Digital Silicon Integrated Circuits (Continued)

Source	Test Conditions	Number of Devices	Total Device Hours	Total Device Failures	Most Recent Report	Remarks
GMe	125 °C operating		1,040,000	0	April 1964	RTL Gates
Motorola	25 °C Ring OSC.	1640	6,191,424	0	June 1965	Monolithic (MECL) and Hybrid devices
Motorola	125 °C Ring OSC.	977	3,998,836	9	June 1965	Monolithic (MECL) and Hybrid devices
Motorola	150 °C stor.	197	783,750	1	June 1965	Same as above
Motorola	175 °C stor.	946	1,719,625	5	June 1965	Same as above
Motorola	200 °C stor.	45	63,460	0	June 1965	Same as above
Motorola	250 °C stor.	35	40,000	0	June 1965	Same as above
Motorola	300 °C stor.	39	110,384	1	June 1965	Same as above
Motorola	25 °C oper. Max. rating*	890	1,046,265	5	June 1965	*175 °C junction temp
Motorola	125 °C oper.	344	446,105	3		
Philco	125 °C oper.		6,429,000	0	March 1965	RTL

Table 4-1. Summary of Reliability Data - Digital Silicon Integrated Circuits (Continued)

Source	Test Conditions	Number of Devices	Total Device Hours	Total Device Failures	Most Recent Report	Remarks
Philco	125°C		6,429,000	0	March 1965	RTL
Signetics	-55°C oper.	25	75,000	0	October 1965	DTL
Signetics	25°C oper. Ring counter	111	2,330,300	1	October 1964	DTL
Signetics	25°C oper.	460	2,682,300	0	October 1964	DTL
Signetics	25°C oper. equipment*	1303	4,732,200	0	October 1964	*Devices used in production test equipment
Signetics	70°C oper.	25	25,000	0	October 1964	DTL
Signetics	125°C oper.	710	1,628,000	4	October 1964	DTL
Signetics	125°C stor.	172	1,071,000	0	October 1964	DTL
Signetics	200°C stor.	450	810,000	4	October 1964	DTL
Signetics	300°C stor.	35	241,000	4	October 1964	DTL
Sylvania	125°C oper.	73	392,000	1	October 1964	
Sylvania	150°C oper.	55	147,000	0	October 1964	
Sylvania	200°C stor.	20	20,000	0	October 1964	
Sylvania	300°C stor.	23	32,000	0	October 1964	

Table 4-1. Summary of Reliability Data-Digital Silicon Integrated Circuits (Continued)

Source	Test Conditions	Number of Devices	Total Device Hours	Total Device Failures	Most Recent Report	Remarks
Texas Instruments	25 °C stor.	154	140,000	0	June 1965	Series 51 RCTL
Texas Instruments	25 °C Field Data	7116	5,643,492	1	June 1965	Series 51 RCTL
Texas Instruments	25 °C Field Data	1800	3,465,000	1	June 1965	Series 53 DTL
Texas Instruments	125 °C oper.	878	1,414,860	13	June 1965	Series 51 RCTL
Texas Instruments	125 °C oper.	45	90,000	0	June 1965	Series 53 DTL
Texas Instruments	125 °C stor.	293	1,267,000	4	June 1965	Series 51 RCTL
Texas Instruments	125 °C stor.	45	88,000	0	June 1965	Series 53 DTL
Texas Instruments	150 °C stor.	40	1,100	0	June 1965	Series 51 RCTL
Texas Instruments	200 °C stor.	589	910,140	13	June 1965	Series 51 RCTL
Texas Instruments	300 °C stor.	56	66,500	4	June 1965	Series 51 RCTL
Westinghouse	125 °C oper.		4,500,000	6	June 1965	
TOTALS		46,901	216,696,393	94		

Table 4-1 at various temperatures can be extrapolated to 40°C* operating conditions. The results of these calculations are shown in Table 4-2. The failure rate column gives the estimated failure rate, using the maximum likelihood estimator

$$\hat{\lambda} = \frac{10^5 F}{T} \quad \%/\text{K hours}$$

Where zero failures are recorded, the upper 50 percent confidence circuit is used as the failure rate estimator

$$\overline{\lambda} = \frac{0.695\ (10)^5}{T}$$

The failure rates indicated by the various vendors vary over a wide range. However, the range is no greater than that observed for other types of piece parts in various failure rate compendiums which have appeared in the literature. In order to reduce Table 4-2 to a single generic failure rate for digital integrated circuits, the geometric mean of the failure rates for the various vendors was calculated. As shown in Table 4-2, the geometric mean is 0.009 %/1000 hours. The geometric mean seems preferable to the arithmetic mean since the range of variation exceeds one order of magnitude.

Most of the reliability data upon which Table 4-2 is based, were derived from devices manufactured in 1963. It is, therefore, reasonable to believe that the current generic failure rate is less than 0.009 %/1000 hours. Limited data are available from which an estimate of actual reliability growth trends can be made. However, a failure rate of 0.005 %/1000 hours for microcircuits produced and screened for use on Voyager is considered to be conservative and well within the state-of-the-art capabilities.

4.2.2 LINEAR INTEGRATED CIRCUITS

A summary of the currently available data on linear integrated circuits is given in Table 4-3. As noted previously, it can be anticipated that the quantity of data available on linear circuits will increase sharply in the next several months. In particular, a sample of 500 Fairchild μA702A differential amplifiers is scheduled to begin a 2000-hour life test in the near future as part of the qualification test program for these devices on the Apollo LEM. The Fairchild FACT lot sampling program, from which the μA702 data in Table 4-3 was derived, will also continue to generate about 30,000 hours per month of data. While the data currently available are insufficient to establish a definite failure rate, there is no reason to believe that catastrophic failure rates as good as those observed for digital circuits cannot be achieved. Linear circuits are more sensitive to drift failure in the sense that system applications cannot withstand as high a parameter shift for linear circuits as for digital circuits. Data available to date, however, indicate extremely good parameter stability for these devices and, therefore, it appears that drift failures will not constitute a serious problem.

*The expected operating temperature of much of the Voyager electronic equipment.

Table 4-2. Achieved Failure Rates at 40 °C Ambient for Digital Semiconductor Integrated Circuits

Vendor	Equivalent Device Hr at 40 °C in K-Hr	Total Device Failures	Estimated Failure Rate-40 °C % (K-Hr)
Amelco	21,414	1	0.0047
Fairchild	814,774	12	0.0015
GMe	10,400	0	0.0066
Motorola	76,615	19	0.0250
Philco	64,290	0	0.0011
Signetics	51,903	13	0.0250
Sylvania	8,530	1	0.0117
Texas Instruments	41,199	31	0.0752
Westinghouse	45,000	6	0.0133
Geometric mean			0.009

4.2.3 FILM CIRCUITS

The reliability data available on film elements is summarized in Table 4-4. As noted previously, virtually no data on complete circuits are available due to the custom design and low usage. However, the element data in Table 4-2 show that failure rates as low or lower than those achieved for the analogous discrete part have been achieved. Furthermore, parameter stability has been shown to be equal to or better than that obtainable from most available discrete parts.

It is emphasized that the primary purpose of Tables 4-1 and 4-2 is to indicate the total quantity of data available on integrated circuits and to derive an overall state-of-the-art generic failure rate. The data in Table 4-2 does not provide a basis for comparison of vendors with respect to reliability. Such a comparison would require that many other factors in addition to operating temperature be taken into account, i.e., device data of manufacture; complexity and functional characteristics; type of package; operating conditions; failure definition; screening tests performed; etc. The performance of such an in-depth analysis is the next logical step in the application of microelectronic circuits to the Voyager Program. Such an analysis will permit the development of specific failure rates for individual vendors to assist in vendor selection.

Table 4-3. Summary of Available Reliability Data - Linear Integrated Circuits

Source	Test Conditions	Number of Devices	Total Device Hours	Total Device Failure	Most Recent Report	Remarks
Amelco	200 °C stor.	93	317,000	1	December 1964	Differential Amplifier
Fairchild	125 °C oper.	102	82,216	0	June 1965	702A
TI	85 °C oper.	140	280,000	0	June 1965	Series 52
TI	125 °C oper.	55	8,300	0	June 1965	Series 52
TI	150 °C stor.	45	53,300	0	June 1965	Series 52
TOTALS		435	440,816	1		

Table 4-4. Failure Rate of Thin-Film Elements

Vendor	Type of Test		Device-Hr	Failure Rate		Report Dated	Remarks
	Conditions	°C		$\%/10^3$ Hr	C.L.		
CORNING							
R-Networks	2 1/2 x Std Pwr	25	163×10^6	0.0006	60%	3/64	Tin Oxide Resistors - MM (HNR)
	2 1/2 x Std Pwr	70	1.404×10^3	0.0660	60%	3/64	
CTS							
Resistors	Load Life	85	36×10^6	0.0002	60%	9/64	Cermet
Capacitors	75V dc	85	2.3×10^6	0.03 - 0.05	60%	9/64	
MEPCO				0.0002	Observed	11/62	Resistor
RCA							
Resistor	Full Load	70	3.686×10^6	0.0249	60%	9/62	Cermet
Capacitors	2X Rated Volt.	85	2.560×10^6	0.0358	60%	9/62	Precision - Multilayer
Capacitor	2X Rated Volt.	85	1.997×10^6	0.101	60%	9/62	General Purpose - Multilayer
Inductors	Rated	85	1.674×10^6	0.055	60%	9/62	
TEXAS INST.							
Resistors	Operating	25 to 175	30×10^6	0.003	60%	6/62	Extended Life

5.0 DESIGN EXPERIENCES WITH MICROELECTRONICS

The objective of this Section is to assess the degree of usage and experience in applying microelectronic techniques to military and space applications.

5.1 INDUSTRY EXPERIENCE

The programs wherein a great amount of experience with microelectronics has been obtained are the Air Force advanced Minuteman and F-111 fighter-plane projects, and the Navy programs such as Polaris-A-3, TACAN, LORAN-C, etc. NASA is using microcircuits in the Interplanetary Monitoring Probe (IMP) Program, and is considering microcircuits for OAO, AOSO, OGO, Apollo, etc. Initial applications have been directed mainly at digital equipment. For each of these projects, the reliability of the integrated circuit - as well as its size and weight factor - has been judged superior to conventional circuits. Tables 5-1 and 5-2 list equipment designed with microelectronic circuits, the general application, and the numbers of circuits used.

5.1.1 GE-MSD MICROELECTRONIC ACTIVITIES

5.1.1.1 SPACECRAFT DEPARTMENT (GE-SD) ACTIVITIES

a. Gravity Gradient Test Satellite

Earth Sensor - Uses low-power, silicon-integrated circuits developed by GE and Westinghouse integrated differential detectors.

Telemetry Processor - Being fabricated with GE-developed, low-power logic (1 mw/ckt) plus additional specially developed microcircuits. This processor will be flown in a redendant form for increased reliability (as described in Section 6.3).

Redundant PN Generator - Uses low-power microcircuits and majority logic redundancy techniques for increased reliability.

b. Biosatellite

Jet Controller - Modules have been fabricated using Texas Instruments SN51 and SN 52 Series integrated circuits.

Power Supply Timer - Digital silicon integrated circuits are used to measure energy consumption.

5.1.1.2 RE-ENTRY SYSTEMS DEPARTMENT (GE-RSD) ACTIVITIES

The Re-entry Systems Department has developed microelectronic data handling, telemetry processing, and command equipment for MBRV, Biosatellite, and Advanced Minuteman programs.

Table 5-1. Microelectronic Activities by Industry

Program	Company	Equipment	No. of IC Ckts	Remarks
Loran-C	Sperry Gyroscope	Receiver Converter	900 580	Flight in 1964, IC represents 95% of total circuitry
Apollo	MIT Instrumentation Lab	Guidance Computer	4000	Fairchild IC's
IMP-NASA	JPL	Optical Orientation Sensor	45	Flight in 1963, SN51 Series
Interplanetary System	JPL/NASA	Radio Ranging	150	TI & Fairchild IC's
Minuteman II-D37B	NAA-Autonetics	Airborne Computer	1950	Flight in 1964, MM Series by TI
Monica-C	NAA-Autonetics	Airborne Computer	3600	Flight in 1964
XR-45 & XR-47	NAA/Autonetics	Terrain-Following Radar	*	9 types of IC circuits, 12 types of TF circuits
MAGIC	AC Spark Plug	Airborne Computer	2098	
AN/ASA-27	Litton Industries	Computer Indicator	2000	6% of system circuits SN 51 Series
AN/ASN-44	Litton Industries	Inertial Navigator	200	Cost reduced 25% - TI Ckts
Phoenix	Litton Industries	Computer System	6000	
MMRBM - USAF	Sperry Rand	Guidance Computer	1200	Feasibility Model
SABLE - USAF	Univac	Central Computer	*	For Re-entry Vehicles
Data System-Navy	Univac	Computer	*	Multi-Chip Circuits
USAF - Proposed	GE - LMED	Display Generator	560	Fairchild 930 Series (DTL)
USAF - Navy	GE - LMED	Computer (Airborne)	150	IC Ckts (Motorola MECL)
F-111A	GE - LMED	Attack Radar Set	750	IC SN51 Pilot Production
F-111A	GE - LMED	Attack Radar Set	225	2/3 IC and 1/3 Hybrid-Production
USAF - Classified	GE - LMED	Counter Measure	4000	IC Circuits
A-NEW (Navy)	GE - LMED	Control Board	1830	Fairchild 930, SE160, & 124 & Custom
L-90	Librascope	Gen. Purpose Comp.	1200	20 MC Clock Rate IC
USAF	General Precision Aerospace	Transceivers & Comp. for Doppler Radar	*	70% of system in IC

* Exact Count Not Known

Table 5-2. Microelectric Activities by Subcontractors

Program	Equipment	No. of IC Circuits	Remarks
TEXAS INST.			
USAF/Classified	Guidance Computer	2750	Feasibility Model-SN51, SN52
AOSO	Data Handling Command & Timing	768 1011	SN51 Series
USAF-Class II Aircraft	PCM Telemetry Encoder	285	Series 51,52 (100% IC)*
APN/149	Radar Computer Signal Conditioner	217 102	Series 51 & 52 plus Conventional* Conventional & IC
NASA	Counter/Scanner Programmer	36	Space Vehicle Application*
Mariner C-JPL	Encoder Simulator	200	Series 51*
NASA, Huntsville	Counters (UP-Down)	16	Up/Down Binary*
TERCOM	Arithmetic Unit	542	Packaged on 49 Etched Boards*
USAF	Demonstration Computer	587	
NASA	Time Code Generator		For Manned Spacecraft
JPL/Space Applicator	Pseudo-Noise Generator	23	Temp Range -55 to 85°C
MOTOROLA Apollo-NASA	Up Data Link (UDL)	160	Feasibility Model (Fairchild)
Apollo-NASA	Digital Test Command System	30,000	Ground Equipment
NAVY	Transceiver	100	Redundant - All μE Approaches
AROD-NASA	Doppler Radar (Airborne)	3,000	Size limitation Dictates IC (Philco-Motorola)
DIGICOM-USAF	PCM Telemetry	100 Analog 200 Digital	

*See Figure 5-1 for packaging configurations.

GE – MSD has a centralized microelectronic facility specifically charged with general microelectronic applications, evaluation, custom circuit development, and integration of information among departments.

5.1.2 MOTOROLA AND TEXAS INSTRUMENTS ACTIVITIES

Motorola, Inc. (Military Electronics Division) and Texas Instruments (Apparatus Division) have been working with microelectronic approaches for several years. Their experience in design, development, packaging, and fabrication of aerospace equipments for high reliability programs is extensive and well documented. Table 5-2 contains a partial listing of microelectronic equipment built by Motorola and Texas Instruments.

Each equipment is a development or production model filling a specific need of a Defense Department or NASA customer. To date, more than 25 contracts for subsystems or equipment using integrated semiconductor networks have been completed or are underway.

The advantages of increased reliability and reduced size, weight, power-consumption and, in some cases, cost have stimulated the production of these equipments using semiconductor networks. Figure 5-1 shows Texas Instruments microelectronic packaging configurations.

6.0 MICROELECTRONIC TRADEOFF STUDIES

6.1 INTRODUCTION

Whether a component should be designed with integrated or hybrid microcircuits or conventional piece parts, depends on an analysis of performance requirements of the specific component. Usually a detailed evaluation of the electrical characteristics will indicate the proper design approach. If not, additional analysis of reliability, weight, available power, size, cost, etc., will narrow the selection of the proper design approach.

Each design approach offers certain technical advantages, but the tradeoff must be carefully approached with the objective of the final usage. In the following sections a comparative analysis between microelectronic and conventional (discrete) part approaches is presented for two specific equipments: an attitude control loop and a telemetry processor.

6.2 ATTITUDE CONTROL LOOP

In this section both a redundant and a non-redundant mechanization of an attitude control loop are described. A comparative analysis is thus made of each mechanization for several possible design approaches using combinations of discrete parts, digital integrated circuits, and linear integrated circuits.

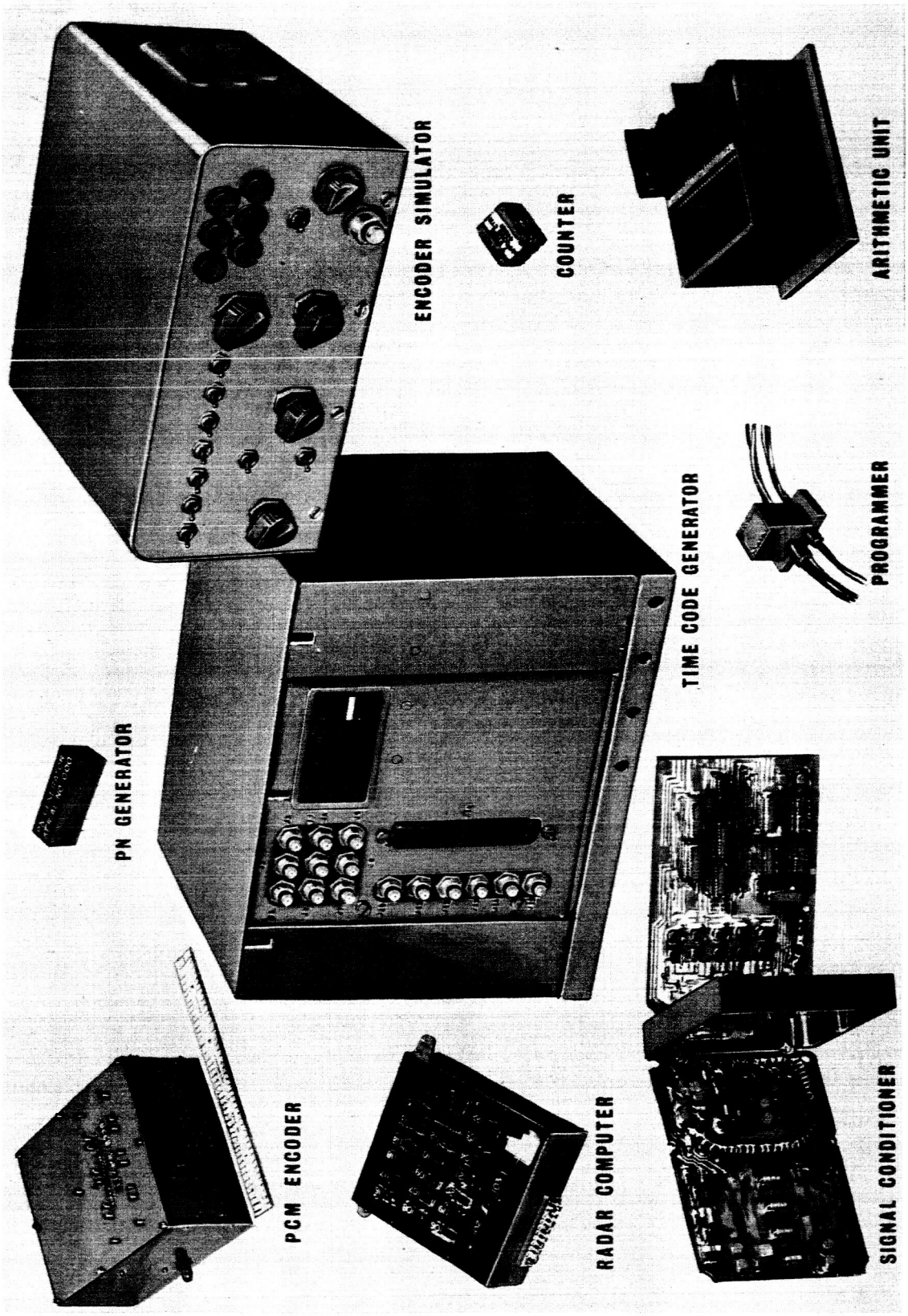

Figure 5-1. Texas Instruments Microelectronic Packaging Configurations

6.2.1 FUNCTIONAL DESCRIPTION

A functional block diagram for a single channel (e.g., pitch) of the redundant attitude control loop is shown in Figure 6-1. The loop receives input signals from the sun sensors and the rate gyro, together with disable command signals that determine which of the two sensor inputs will be used.

The input and control signals are fed to each of three identical (redundant) input signal processing circuits shown as blocks A_1, A_2 and A_3 in Figure 6-1. Each circuit contains a sun sensor amplifier, a reference source, a threshold detector, and a null detector. The outputs from the three signal processing circuits are fed to majority logic circuits where the triple redundant outputs X, Y, and Z are combined into a single output F according to the relation

(1) $F = XY + XZ + YZ$

The majority logic is performed in two logic stages, an AND stage and an OR stage. In general, single failures in the AND stage will not disable the control loop. The output of the majority logic circuit is fed to the solenoid amplifiers which are non-redundant and are shown as block D as Figure 6-1.

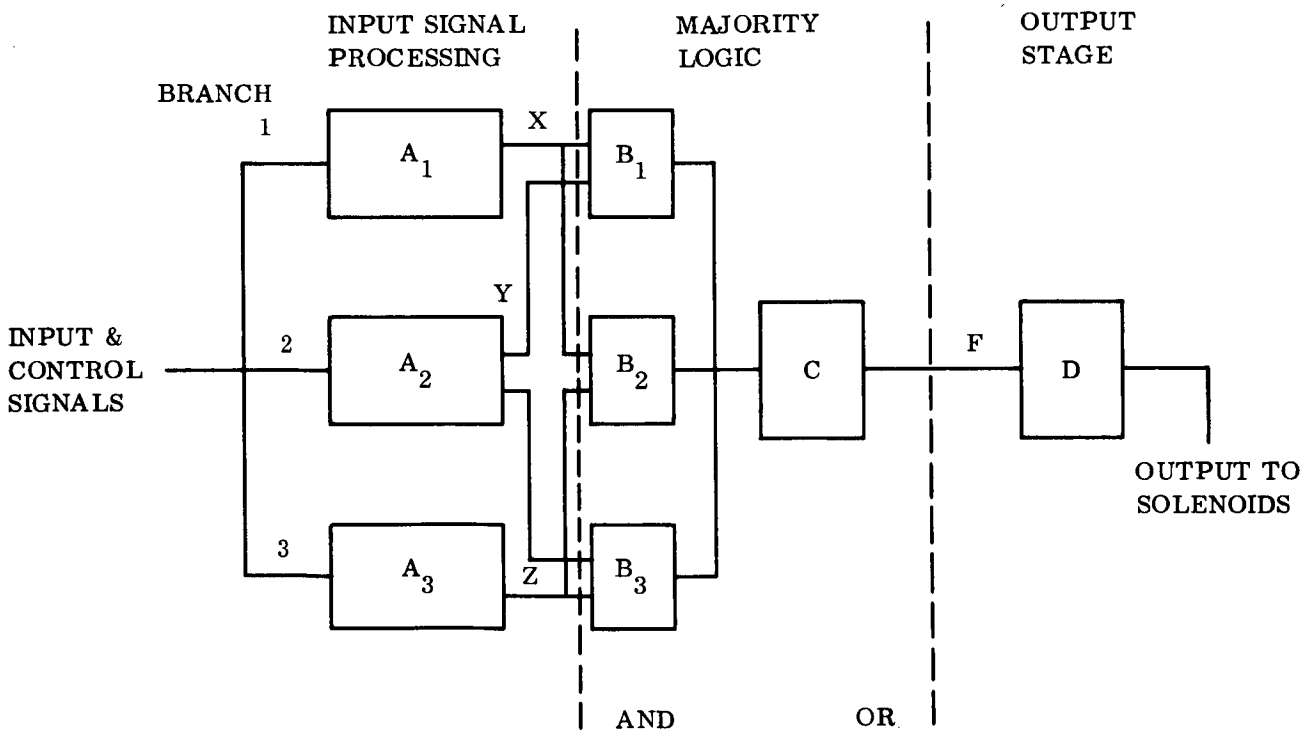

Figure 6-1. Reliability Block Diagram
Attitude Control Loop (one channel)

In the non-redundant mechanization of the control loop, blocks A_1, A_2, and A_3 are replaced by a simple input signal processing circuit (e.g., block A_1), and the majority logic circuits (blocks B_1, B_2, B_3 and C) are deleted. Thus, the non-redundant mechanization consists of blocks A_1 and D in series.

As noted, Figure 6-1 applies to a single channel of the attitude control loop. There will be three such channels (pitch, roll, and yaw), which are essentially independent in a probability sense. Since the purpose of this analysis is to compare the relative reliability of different design configurations it will be sufficient to carry out the analysis for a single channel of the attitude control loop.

6.2.2 DESIGN APPROACHES

The design configurations considered for each of the two control loop mechanizations (redundant and non-redundant) are:

a. All discrete parts

b. Discrete parts + digital integrated circuits (IC) wherever possible

c. Discrete parts + linear integrated circuits wherever possible

d. Discrete parts + digital and linear integrated circuits wherever possible.

The only portion of the control loop amenable to the application of currently available "standard" (as opposed to "custom") digital integrated circuits is the majority logic function. Linear integrated circuits, such as the Fairchild μ A702 and the TI SN522 differential amplifiers, can be applied in the input signal processor, block A (A_1, A_2, A_3). However, some discrete parts are still required for feedback, biasing and reference purposes.

6.2.3 ANALYSIS

The predicted failure rate, λ in %/1000 hours, and the number of parts, N, for each block in Figure 6-1 is shown in Table 6-1. In calculating N, each integrated circuit was counted as a single part. The failure rate of external connections was included in λ. Since the majority logic function is not required in the non-redundant mechanization, configurations (b) and (d) are not applicable for the non-redundant case. A breakdown of Table 6-1 to the piece part level is given in Appendix II.

From Table 6-1, the probability of failure for each configuration can be calculated for a mission time t from the following equations:

Redundant Mechanization:

(2) $Q \cong 3\,(\lambda_A + \lambda_B)^2 t^2 + (\lambda_C + \lambda_D)\,t$

Table 6-1. Attitude Control Loop, Failure Rate & Parts Count Data

Design Configuration	Block A λA	Block A N_A	Block B λB	Block B N_B	Block C λC	Block C N_C	Block D λD	Block D N_D
Redundant								
a. Discrete	0.371	162	0.013	6	0.027	18	0.048	8
b. Digital IC	0.371	162	0.020	3	0.014	2	0.048	8
c. Linear IC	0.177	79	0.013	6	0.027	18	0.048	8
d. Dig. & Lin. IC	0.177	79	0.020	3	0.014	2	0.048	8
Non-Redundant								
a. Discrete	0.371	162	N/A		N/A		0.048	8
b. Linear IC	0.177	79	N/A		N/A		0.048	8

Non-redundant Mechanization:

(3) $Q \cong (\lambda_A + \lambda_D)\, t$

The derivation of these equations is given in Appendix II.

For either mechanization, reliability can be calculated as:

(4) $R = 1 - Q$

The total parts count for each configuration can also be calculated from Table 6-1 as follows:

<u>Redundant Mechanization</u>

(5) $N = 3N_A + 3N_B + N_C + N_D$

<u>Non-redundant Mechanization</u>

(6) $N = N_A + N_D$

Using equations (2) through (6) together with the data in Table 6-1, a comparison of the various design configurations was made for a mission time t of one year (8760 hours). The results are shown in Table 6-2. The assumption of a one-year mission of continuous operation and "space" environment is an approximation to the actual

Voyager mission profile. This approximation is sufficiently accurate for comparing the various design configurations.

Table 6-2. Attitude Control Subsystems
Comparison of Design Configurations - Single Channel

Configuration	Reliability	Total Parts	Size (In^3)	Weight (lb)
Redundant				
a. Discrete	0.99019	530	70	2.7
b. Digital IC	0.99105	505		
c. Linear IC	0.99255	281		
d. Digital & Linear IC	0.99370	256	33	1.2
Non-redundant				
a. Discrete	0.9633	170	33	1.2
b. Linear IC	0.9803	87		

The probability of failure and parts count data in Table 6-2 are shown graphically in Figure 6-2. It is seen from the graph that the use of integrated circuits yields a much greater reduction in failure probability for the non-redundant, than for the redundant mechanization. This is due to the fact that in the redundant case most of the failure probability can be attributed to the non-redundant solenoid output stage where the use of microelectronic approaches is not possible. However, it will be noted that even though the use of integrated circuits does not provide significant gain in reliability for the redundant configurations, a reduction in total parts count by a factor of about 2/1 is achieved. This reduction in parts count largely cancels out the increase in parts count which was incurred by the use of redundancy. Therefore, comparing the first and last points on Figure 6-2 and comparing sizes and weights in Table 6-2, it is seen that the use of both microelectronics and redundancy yields an overall decrease in failure probability of about 4 to 1, but requires no increase in overall size and weight.

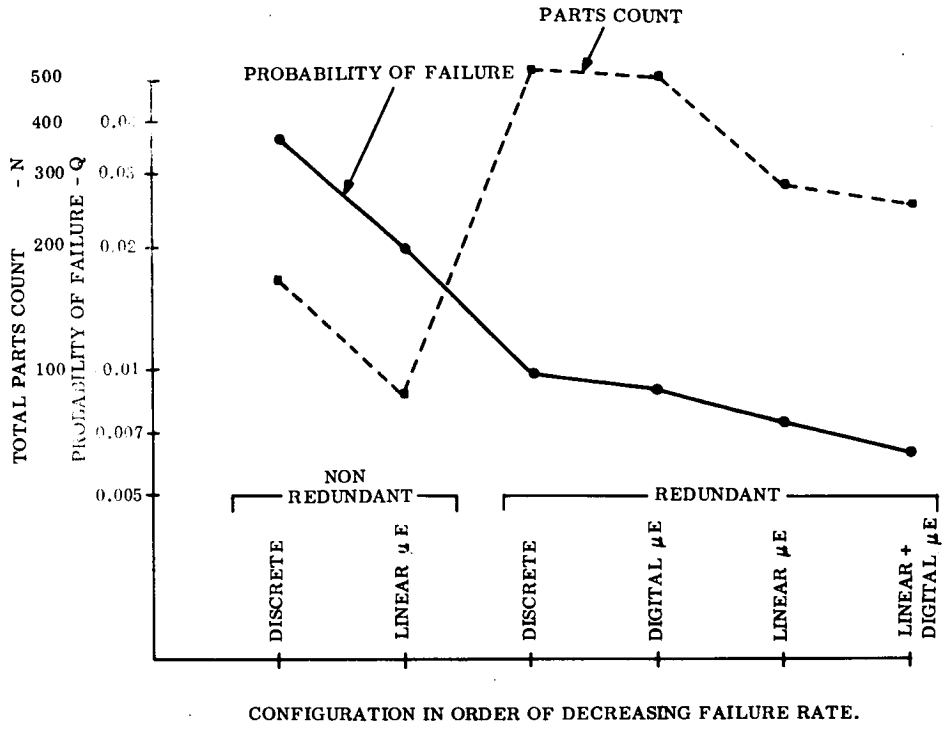

Figure 6-2. Comparison of Failure Probability and Parts Count for Various Control Loop Configurations (1 Year Mission)

6.3 TELEMETRY PROCESSOR

6.3.1 INTRODUCTION

A telemetry processor as designed and fabricated by GE is shown in block diagram form in Figure 6-3. This processor has been implemented with conventional piece parts and packaged cordwood style. A later version completely interchangeable with the cordwood design has been designed and fabricated with microelectronic circuits. A detailed comparison of the important parameters for each processor is made to determine their relative advantages. Additionally the parameters are shown for a redundant version of the microelectronic processor (Figure 6-4), similar to that applied on the Air Force Gravity Gradient Test Satellite Program.

6.3.2 FUNCTIONAL DESCRIPTION

Referring to the functional diagram, (Figure 6-3) the processor takes 61 analog input lines and converts each in turn to a 7-bit digital word. The operation proceeds as follows: The clock input steps the programmer through its various states. A new multiplexer channel is selected every eight clock pulses. The eight clock pulses between channel selection are used to convert the present analog channel input voltage to a 7 bit binary word. The conversion is the successive approximation

type in which the most significant bit of the digital-to-analog (D/A) converter is tried first. As each bit of the D/A converter is tried in turn, the analog comparator compares the analog input voltage against the D/A converter analog output voltage. As the next bit of the D/A converter is energized, the output of the comparator either removes or leaves the previous bit in the D/A converter depending upon the relative magnitude of the input and previous D/A output analog voltages. The control logic supplies the control signals for the D/A converter and generates two sync words and one satellite identification word per frame. The reference supplies an analog reference voltage for the D/A converter.

The only significant operational differences between the two processor versions are that the microelectronic version has a much greater input multiplexer impedance and the input multiplexer channels are broken up into 8-channel branches. This increases reliability because a single channel failure can cause the loss of at most eight additional channels. This is not true of the cordwood processor, i.e., all channels are in parallel. This fact was not taken into account when calculating the reliability of the two units.

In the redundant version (Figure 6-4) simple logic (simple compared to a telemetry processor) is used to alternate between the outputs of two or three processors at the telemetry data frame rate. It is not suggested that this is the best form of redundancy for every telemetry system. The best choice can only be made after a careful study of mission requirements and objectives.

6.3.3 TRADE OFF RESULTS

The parameters of interest are shown in Table 6-3. For both the microelectronic and the conventional telemetry processor, the numbers shown for size, weight and power are actual measured values. The method and calculations for obtaining the reliability numbers are shown in Appendix III.

Table 6-3. Trade Off Results

Processor Version	Reliability Ps. (1 yr.)	Size (in.^{3})	Weight (lb.)	Power (watts)	Cost (*)
Cordwood	0.885	500	12	1.2	1
Microelectronic	0.90	40	1.2	0.38	1/2
Microelectronic 2 units-Redundant**	0.99	81	2.5	0.78	1
Microelectronic 3 units-Redundant	0.997	121	3.7	1.2	1-1/2

*Normalized to cost of cordwood Processor.

**Similar to that being flown on the Gravity Gradient Test Satellite

6.3.4 CONCLUSIONS

In terms of probability of failure, the 2 unit redundant microelectronic telemetry processor provides an improvement factor of 12 to 1 (0.12/0.01), and the 3 unit redundant version provides an improvement factor of 40 to 1 (0.12/0.003). This increased reliability was obtained with no increase in power, a size reduction of 4 to 1 and a weight reduction of over 3 to 1, when compared to the non-redundant cordwood version. Although there appears little difference in reliability between the cordwood and non-redundant microelectronic processor, this example graphically points out how some of the savings in size and weight attributable to microelectronic techniques can be used to increase reliability significantly.

6.4 COST CONSIDERATIONS

At the present time, high reliability integrated microcircuits are considerably lower in cost than high reliability piece part cordwood circuits performing the same function. For example, it has been estimated that the cost of a high reliability potted module is between $300 and $600 depending upon complexity. Whereas the high reliability integrated microcircuit cost for the same function is between $50 and $100. Additionally, integrated microcircuits are continually declining in cost as process controls improve and mechanization and labor become more efficient.

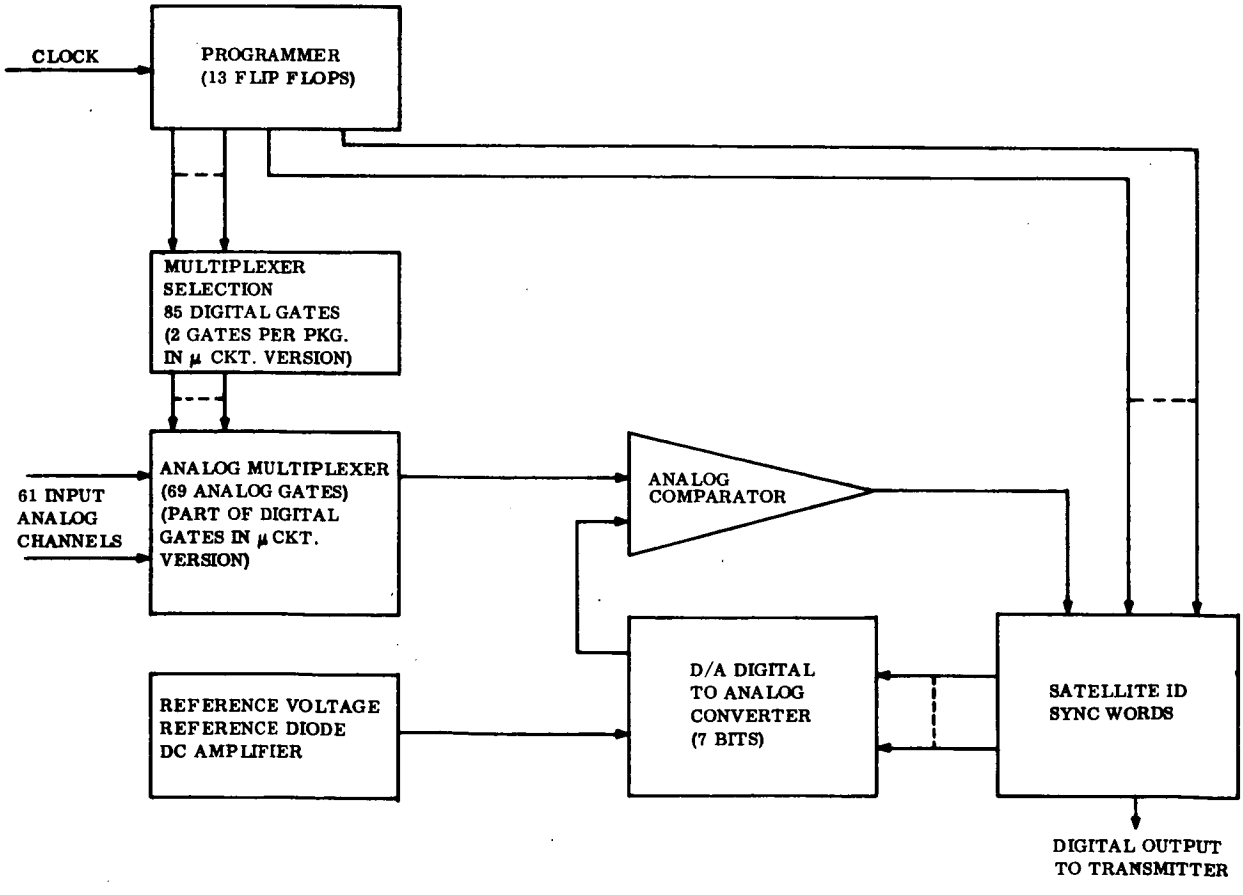

Figure 6-3. Telemetry Processor

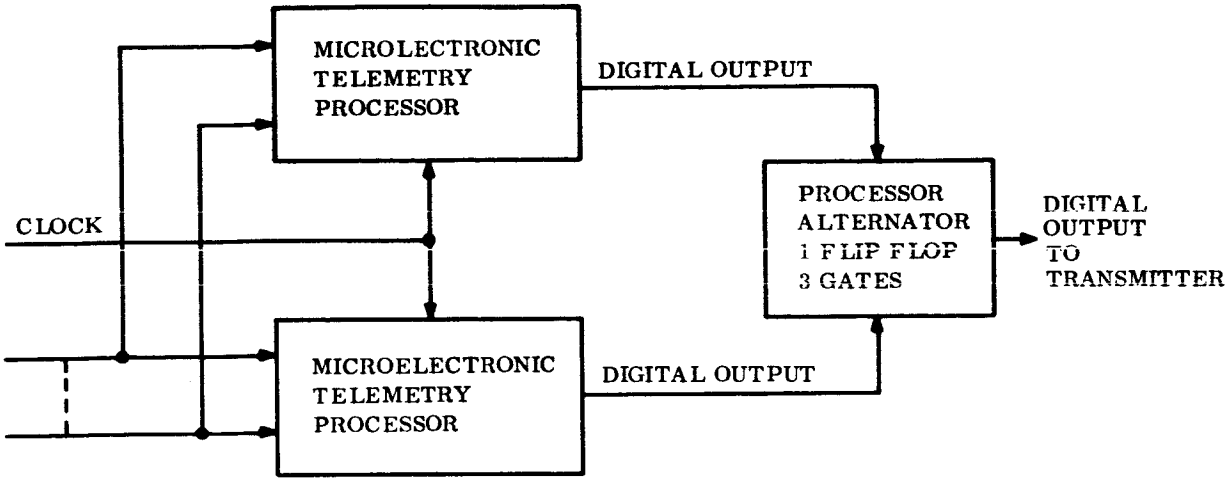

Figure 6-4. Redundant Microelectronic Telemetry Processor

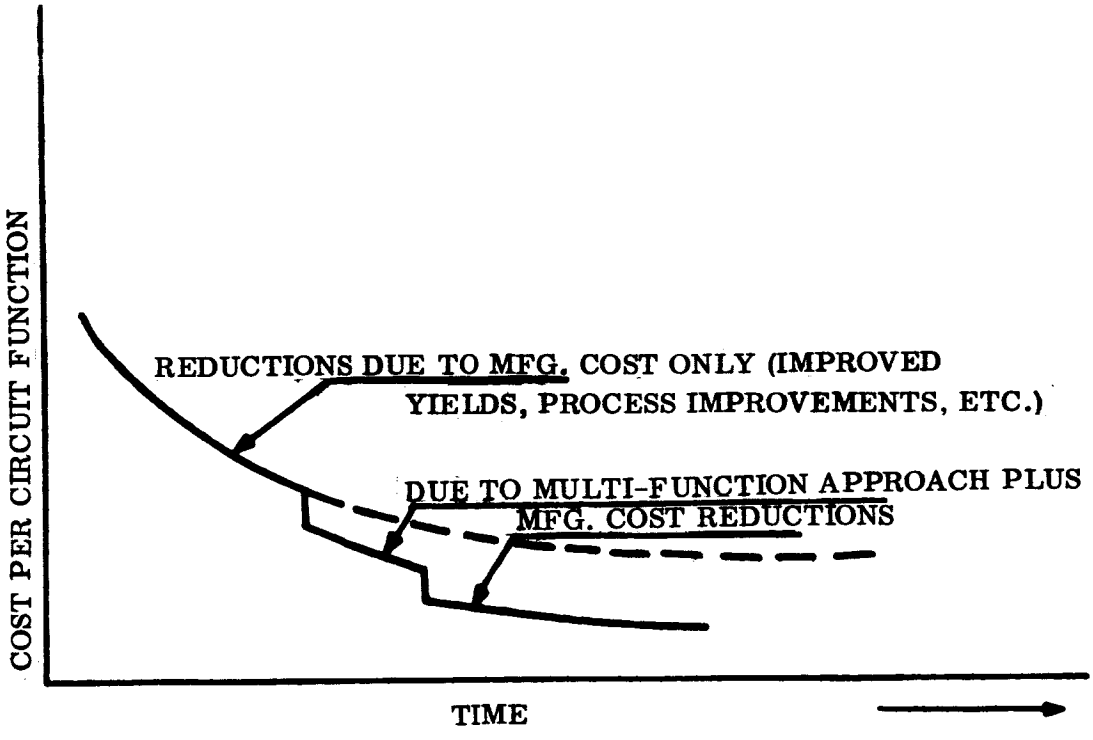

Figure 6-5. Cost Reduction with Multifunction Integrated Circuits

6.4.1 MULTIFUNCTION INTEGRATED CIRCUITS

Multifunction integrated circuits contain more than one circuit function per package. Substantial improvements in cost and reliability result from the smaller number of network packages required for a given system. Fewer packages mean less external interconnections and fewer opportunities for reliability problems. Fewer devices also mean lower system cost, since three or four circuits can be built simultaneously into a single structure with only a nominal manufacturing cost increase over that required to build one circuit.

The bulk of integrated microcircuit manufacturing costs is accumulated in the packaging stage, and these costs are virtually fixed regardless of the number of circuit functions performed by the substrate. The result is a step-function decrease in the effective cost of integrated circuits as shown in Figure 6-5.

An example of a typical multifunction microcircuit package is shown in Figure 6-6. Since the multi-function version can perform six NAND functions, package count is reduced from three to one. Because these functions are all internally connected and use common supply and return terminals, twelve connections are eliminated.

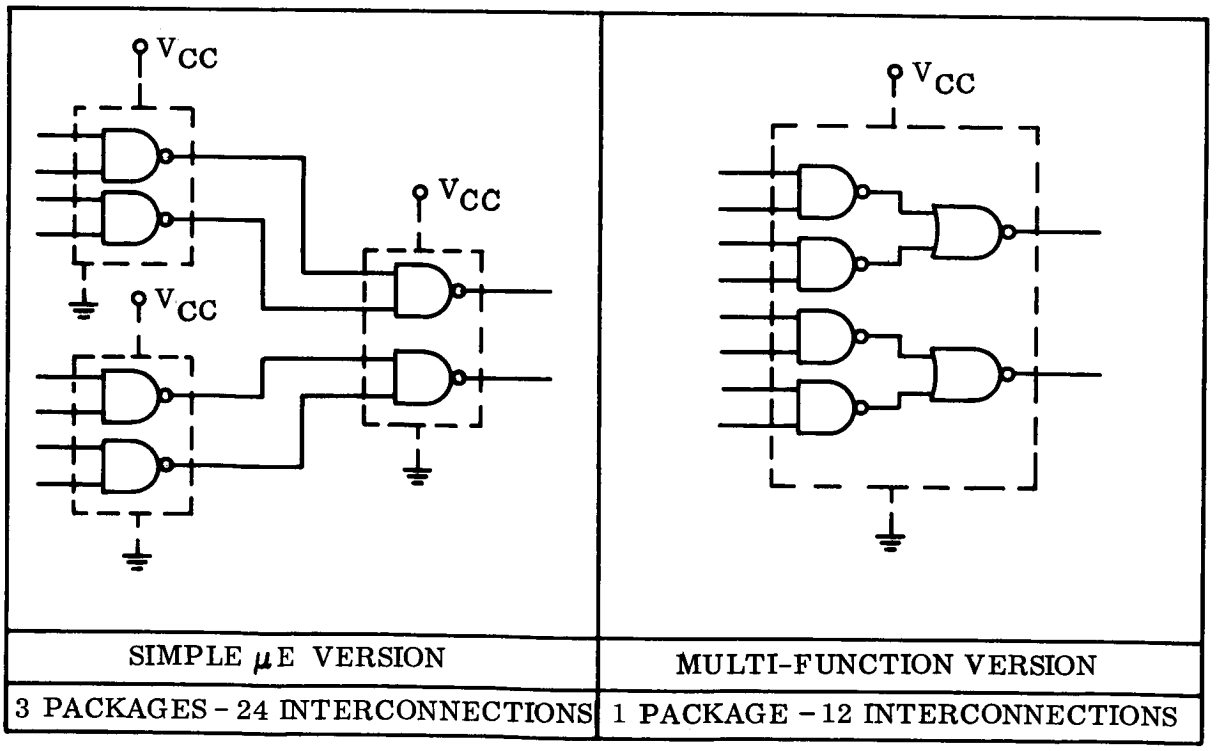

Figure 6-6. Multifunction Integrated Circuits (Two Exclusive OR Stages)

7.0 CONCLUSIONS

The basic question of this study is, "Should microcircuits be used on the Voyager Spacecraft Program?" The answer is that selected standard silicon integrated microcircuits should be used. The arguments favoring this conclusion are:

a. Over 216-million hours of life test data on digital silicon integrated circuits demonstrate a history of reliability. This is orders of magnitude more data than exists on applicable piece part circuits.

   Much less data is available on film and silicon integrated analog circuits. Although the available data looks good and more data is being generated, these circuits should be used in place of piece parts only if subsystem requirements make their use desirable. An example would be if size and weight constraints on a black box are such that redundancy is more practical through the use of these microcircuits.

b. From the generated reliability data on silicon microcircuits a present reasonable generic failure rate is only 0.005% / 1000 hr. Section 5 lists considerable experience by GE, Texas Instruments, and Motorola in designing, building, and testing microcircuit equipment and points out that the application of standard microcircuits is no longer in the development phase, but is to the point where microcircuits can be applied as easily (if not more so because of standard uniform packaging techniques) as piece part cordwood circuits.

c. Significant gains in equipment reliability, size, and weight are to be obtained through the use of microcircuits. The example microelectronic versus cordwood attitude control loop and telemetry processor tradeoff analyses (Section 6) proves these points. The redundant microcircuit processor is 40 times more reliable and 1/3 the size and weight of the cordwood processor. The improvement in digital equipment will generally be more dramatic than that for analog equipment since a larger number of circuits are generally utilized in digital equipment.

APPENDIX I. DERIVATION OF TEMPERATURE ACCELERATION FACTORS FOR INTEGRATED CIRCUITS.

Texas Instruments and Signetics Corporation have each accumulated a sufficient quantity of data at several different temperatures so that an investigation of failure rate versus temperature can be made.

The test conditions at which a significant quantity of data is available are 25°C and 125°C operating, and 125°C, 200°C, and 300°C storage. Data from Signetics and Texas Instruments for each of these conditions is shown in Table I-1.

Examination of the data in Table I-1 shows that there is a difference in failure rate between operating and storage conditions at 125°C. This is contrary to the often stated view that the failure rate of integrated circuits is substantially the same in either the operating or storage states because the power dissipated during normal operation is not sufficient to cause any appreciable increase in device temperature. For Texas Instruments, a storage-operating "K-factor" of 3/1, (at 125°C) is indicated; for Signetics the indicated K-factor is 2/1.

Table I-1. Data Summary for Selected Test Conditions
Signetics and Texas Instruments

Test Condition	Signetics			TI		
	T K-Hr.	F	λ %/K-Hr.	T Hr.	F	λ %/K Hr.
25°C oper	644	0	0.0072	5644	1	0.018
125°C oper	1628	2	0.123	1415	13	0.92
125°C storage	1071	0	0.065	1267	4	0.316
200°C storage	810	4	0.494	911	13	1.43
300°C storage	241	4	1.66	66	4	6.07

T = total device hours - thousands

F = total device failures

λ = measured failure rate %/K hrs.

$$\lambda = \frac{100F}{T} \quad \text{if } F > 0 \text{ (max. likelihood estimate)}$$

$$\lambda = \frac{6905}{T} \quad \text{If } F = 0 \text{ (50\% copper confidence limit)}$$

However, the Signetics data contains zero failures at 125° C storage, requiring the use of the 50% upper confidence limit to determine the measured failure rate. Therefore, the estimate based on the Texas Instruments data seems preferable.

To investigate the failure rate acceleration factor due to ambient temperature, the failure rate data in Table I-1 for 125° C, 200° C and 300° C storage is plotted in Figure I-1 on a log scale against reciprocal absolute temperature. The data for Texas Instruments yields an excellent fit to a straight line; the Signetics data gives a reasonably good straight line fit. Furthermore, the fitted lines for the two vendors are very close to being parallel, which suggests that the use of a single "generic" acceleration factor for all vendors may be valid.

Using Figure I-1 together with the 3/1 storage-operating factor previously discussed, acceleration factors for any operating temperature can be determined. Acceleration factors for several specific temperatures are:

Test Condition	Acceleration Factor
25° C operating	0.04
55° C operating	0.13
85° C operating	0.33
125° C operating	1.0 (base
125° C storage	0.34
200° C storage	1.5
300° C storage	6.6

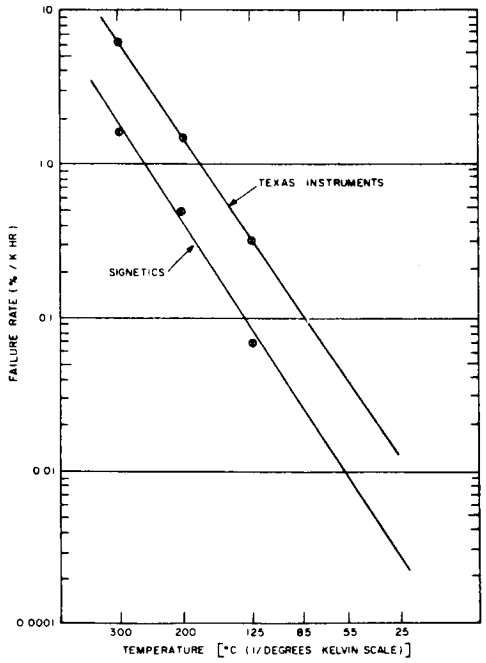

Figure I-1. Failure Rate Vs. Temperature Storage Conditions

APPENDIX II. ATTITUDE CONTROL LOOP TRADE OFF ANALYSIS

II-1. BREAKDOWN OF PARTS COUNT AND FAILURE RATE DATA

A breakdown of the parts count and failure rate data, which was given in Tabel 6-1, is shown in Tables II-1, II-2, and II-3.

Table II-1. Parts Count and Failure Rate Data Discrete Component Configuration

Function	Circuit/Part	No. Used N	Failure Rate %/K Hr. λ	Product Nλ
A	Input signal processing			
	Sun sensor amplifier			
	Transistor, signal	6	0.004	0.024
	Resistor film	16	0.0005	0.008
	Resistor, WW prec.	1	0.015	0.015
	Diodes, Gen. purpose	4	0.002	0.008
	Capacitor, tantalum	2	0.005	0.010
	Connections	64	0.0001	0.006
	Subtotal, S.S. Ampl.			0.071
	Reference Source			
	Resistor, film	5	0.0005	0.003
	Diode, zener	2	0.010	0.020
	Connections	14	0.0001	0.001
	Subtotal, ref. source			0.023
	Null detector			
	Transistor, signal	14	0.004	0.056
	Resistor, film	36	0.0005	0.018
	Diodes, gen. purpose	3	0.002	0.006
	Diodes, zener	2	0.010	0.020
	Capacitor, tantalum	3	0.005	0.015
	Connections	130	0.0001	0.013
	Subtotal, Null Detector			0.128

Table II-1. Parts Count and Failure Rate Data Discrete Component Configuration (Continued)

Function	Circuit/Part	No. Used N	Rate %/K Hr. λ	Product Nλ
	Threshold Detector			
	Transistor, signal	18	0.004	0.072
	Resistor, film	42	0.0005	0.021
	Diode, gen. purpose	3	0.002	0.006
	Diode, zener	2	0.010	0.020
	Capacitor, tantalum	3	0.005	0.015
	Connections	154	0.0001	0.015
	Subtotal, threshold det.			0.149
A	Total, input signal proc.			0.371
B	Majority logic, OR stage			
	Diodes, gen. purpose	6	0.002	0.012
	Connections	12	0.0001	0.001
B	Total, maj. logic OR stage			0.013
C	Majority logic, AND stage			
	Diodes, gen. purpose	9	0.002	0.018
	Resistors, film	9	0.0005	0.005
	Connections	36	0.0001	0.004
C	Total, maj. logic AND stage			0.027
D	Output stage			
	Transistors, power	4	0.008	0.032
	Diodes, gen. purpose	2	0.002	0.004
	Resistors, film	2	0.0005	0.010
	Connections	20	0.0001	0.002
D	Total, output stage			0.048

Table II-2. Majority Logic Failure Rates, Digital Microcircuit Configuration (Continued)

Function	Circuit/Part	No. Used N	Failure Rate %/K Hr. λ	Product Nλ
B	Majority Logic, OR stage			
	Microcircuit, FIC 946	2	0.005	0.010
	Microcircuit, FIC 930	1-1/2	0.005	0.007
	Connections	28	0.0001	0.003
	Total, maj. logic OR stage			0.020
C	Majority Logic, AND Stage			
	Microcircuit, FIC 932	2	0.005	0.010
	Microcircuit, FIC 930	1/2	0.005	0.002
	Connections	20	0.0001	0.002
	Total, maj. logic AND stage			0.014

Table II-3. Input Signal Processing Failure Rates, Linear Microcircuit Configuration

Function	Circuit/Part	No. Used N	Failure Rate %/K Hr. λ	Product Nλ
A	Input signal processing			
	Sun sensor amplifier			
	Linear ckt, FIC uA702A	1	0.005	0.005
	Resistor, film	6	0.0005	0.003
	Resistor, ww prec.	1	0.015	0.015
	Diode, gen. purpose	1	0.002	0.002
	Capacitor, taut	2	0.005	0.010
	Connections	28	0.0001	0.003
	Subtotal, S.S. Ampl.			0.038
	Reference Source			
	Resistor, film	5	0.0005	0.003
	Diode, zener	2	0.010	0.020
	Connections	14	0.0001	0.001
	Subtotal, ref. source			0.023

Table II-3. Input Signal Processing Failure Rates, Linear Microcircuit Configuration (Continued)

Function	Circuit/Part	No. Used N	Failure Rate %/K Hr. λ	Product N λ
	Null Detector			
	Linear ckt, FIC uA702A	1	0.005	0.005
	Linear ckt TI SN522	2	0.005	0.010
	Resistor, film	15	0.0005	0.008
	Diodes, gen purpose	3	0.002	0.006
	Capacitor, tantalum	2	0.005	0.010
	Capacitor, glass	1	0.0005	0.001
	Connections	66	0.0001	0.007
	Subtotal, null det.			0.047
	Threshold detector			
	Linear ckt, FIC uA702A	1	0.005	0.005
	Linear ckt, TI SN522	2	0.005	0.010
	Transistor, signal	4	0.004	0.016
	Resistor, film	23	0.0005	0.012
	Diode, gen purpose	3	0.002	0.006
	Capacitor, taunt.	2	0.005	0.010
	Capacitor, glass	1	0.0005	0.001
	Connections	94	0.0001	0.009
	Subtotal, threshold det.			0.069
A	Total, input signal processing			0.177

The failure rate estimates in Table II-3 are based on the assumption of a failure rate for linear microcircuits of 0.005 %/K hr., which is the same failure rate used for digital microcircuits. Since linear circuits are much more sensitive to parameter drift than digital circuits, it may be that linear circuits will display a higher failure rate than digital circuits due to a higher number of "drift" failures. From Table II-3, it is seen that the failure rate estimate of 0.177 %/K hr., can be broken down as follows:

Total failure rate	0.177 %/K hr.
Failure rate of linear microcircuits (7x0.05)	0.035 %/K hr.
Failure rate exclusive of linear microcircuits	0.142 %/K hr.

Thus, the total failure rate of the input signal processing circuits can be expressed as a function of the failure rate λ_L used for the linear microcircuits as:

(25) $\lambda_A = 0.142 + 7\lambda_L$

This relation is plotted in Figure II-1. From Figure II-1 it is seen that linear microcircuits will yield a reduction in failure rate over the discrete component configuration as long as $\lambda_L < 0.033$ - that is, as long as the linear microcircuit failure rate does not exceed six times the failure rate which has been achieved for digital microcircuits. Therefore, it seems reasonable to conclude that some reliability improvement would accrue from the use of linear microcircuits, although the increase may not be as great as that indicated by assuming a failure rate for linear circuits equal to that achieved for digital circuits.

II.2 DERIVATION OF RELIABILITY MODELS

II.2.1 REDUNDANT MECHANIZATION

A reliability block diagram for a single channel of the attitude control loop was previously given in Figure 6-1. The redundant portion of the channel consists of three parallel branches and associated majority logic such that control loop failure will occur only if failures occur in two or all three of the branches. Denoting the probability of failure for each branch br Q_b, the probability of failure for the redundant portion of the control loop is:

(1) $Q_r = 3Q_b^2 - 2Q_b^3$

Since Q_b is very small (< 0.1), equation (1) can be closely approximated by

(2) $Q_r \simeq 3Q_b^2$

Assuming a constant failure rate λ_b for each branch, Q_b can be expressed as

(3) $Q_b = 1 - e^{-\lambda_b t}$

Where t is the mission time over which the probability of failure applies. Again using the fact that Q_b is very small, equation (3) can be approximated by

(4) $Q_b \simeq \lambda_b t$

From Figure 6-1 it is seen that the branch failure rate λ_b is equal to

(5) $\lambda_b = \lambda_A + \lambda_B$

Combining equations (2), (4) and (5), the probability of failure for the redundant portion of the control loop becomes

$$(6) \qquad Q_r \cong 3\,(\lambda_A + \lambda_B)^2 t^2$$

For the non-redundant portion of the control loop, blocks C and D, the probability of failure is

$$(7) \qquad Q_n \cong (\lambda_C + \lambda_D)\, t$$

Hence, the total probability of failure for the entire control loop is

$$(8) \qquad Q \cong Q_r + Q_n$$

$$\cong 3(\lambda_A + \lambda_B)^2 t^2 + (\lambda_C + \lambda_D)\, t$$

II.2.2 NON-REDUNDANT MECHANIZATION

The non-redundant mechanization consists simply of blocks A and D in "series" - that is failure of either block will cause control loop failure. Hence

$$(9) \qquad Q \cong (\lambda_A + \lambda_D)\, t$$

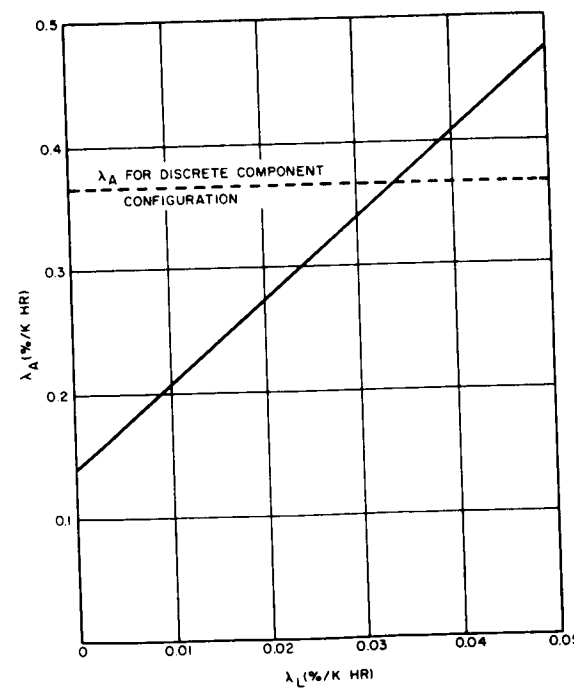

Figure II-1. Input Signal Processing Circuit Failure Rate vs. Linear Micro Circuit Failure Rate

APPENDIX III. TELEMETRY PROCESSOR TRADE OFF ANALYSIS

Tables III-1, III-2 and III-3 contain the detailed reliability calculations for the microelectronic and cordwood processor and the alternator circuitry.

Table III-1. Microelectronic Telemetry Processor

Circuit	N	λ	$N\lambda$	Remarks
Flip Flop	20	0.005	0.10	
Multiplex Switch/NOR	30	0.01	0.30	2 cts./flat pack
Nands	40	0.005	0.20	All integrated
Majority Gate	6	0.005	0.03	All integrated
D/A Switch/NOR	14	0.01	0.14	2 circuits per Flat Pack
Resistor Network (4 Res./Network)	4	0.002	0.01	
Differential Amplifier (multiple chip)	6	0.02	0.12	Failure Rate of microcircuit X4. because of chip and wire technique.
Reference Diode	1	0.01	0.01	5 volt reference
Capacitors (Tantalum)	8	0.005	0.04	Decoupling
Resistors (film)	7	0.0005	0.00	Decoupling
Interconnections	2994	0.0001	0.30	Includes every connection inside μE Telemetry Processor Box.
μETP Failure Rate, Total			1.25 %/K hr.	

N = Number of Circuits
λ = Failure Rate %/K hrs.
$N\lambda$ = Product

Failure Rate of Microelectronic Telemetry Processor from Table III-1

$$\lambda = 1.25\ (10)^{-5}$$

For a one year mission t = 8670 hr., $\lambda t = 0.108$

Reliability = $P_{SM} = e^{-\lambda t} = 0.90$

Probability of Failure = $P_{FM} = 0.10$

Table III-2. Cordwood Telemetry Processor

Part	N	λ	$N\lambda$
Switching Transistors	175	0.001	0.175
Small Signal Transistors	6	0.004	0.024
Diodes	369	0.001	0.369
Zener Regulator	1	0.01	0.01
Capacitors-Glass	45	0.0005	0.0225
Capacitors-Tantalum	23	0.005	0.115
Resistors-Metal Film	482	0.0005	0.241
Connections	4480	0.0001	0.448
Cordwood Processor Failure Rate Total			1.404 %/K hr.

Failure Rate of Cordwood Telemetry Processor from Table III-2

$\lambda = 1.405(10)^{-5}$

For a one-year mission t = 8670 hr.

$\lambda t = 0.122$

Reliability = $P_{SC} = e^{-\lambda t} = 0.885$

Probability of Failure = $P_{FC} = 0.115$

Table III-3. Processor Alternator Reliability
Microelectronic Processors

Circuit	N	λ	$N\lambda$
Flip Flop	1	0.01	0.01
Nand Gate	2	0.005	0.01
Nor Gate	1	0.005	0.005
Total Alternator Failure Rate (λ)			0.025 %/K hr.

For a one-year mission t = 8670 hr.

$\lambda t = 0.00217$

Reliability = $P_{SA} = e^{-\lambda t} = 0.9984$

Probability of Failure = $P_{FA} = 0.002$

Redundant Microelectronic Telemetry Processor (2 units) with Alternator.

The important failure modes are the failure of both Telemetry Processors or the failure of the alternator circuits. All other failure modes can be shown to be second order in in their effect on reliability.

The probability of failure of the two-unit redundant processor is then;

$$P_{F2} = P^2FM + P_{FA}$$

$$= (0.12)^2 + 0.002$$

$$= 0.012$$

$$P_{S2} = 0.988$$

Redundant Microelectronic Telemetry Processor (3 units) with Alternator.

All failure modes are second order compared to the probability of failure of all three Telemetry Processors plus the probability of failure of the Alternator NANDS and NOR.

$$P^3_{FM} = (0.10)^3 = 0.001$$

P_{FA3} = Probability of Failure of Alternator NANDS (3) and NOR (1).

$$= 0.015 + 0.005 = 0.02 \ \%/\text{Khr.}$$

For a 1-year mission:

$$P_{FA3} = 0.02\%/\text{Khr.} \times 8670 \text{ hr.}$$

$$= 0.00173$$

Probability of Failure of triply redundant system is then:

$$P_{F3} = P^3_{FM} + P_{FA3} = 0.0027$$

$$P_{S3} = 0.997$$

CII - VB220AA060

ALTERNATE DESIGN CHARACTERISTICS AND RESTRAINTS CONSIDERED

APPLICATION OF COMPUTERS TO CIRCUIT DESIGN

Index

1 Purpose
2 General
3 NET 1
4 PREDICT
5 SPARC
6 STANPAC
7 ECAP
8 CONCLUSIONS

1.0 PURPOSE

The Voyager mission dictates stringent design requirements to the circuit design engineer. The techniques of worst case design or of statistical design to meet these requirements are well known. The theory behind them is simple and straightforward. However, the implementation of these on complex circuits is frequently less than simple or straightforward. Often they are tedious and time consuming and are therefore, a frequent source of computational error. In addition, an ac or transient analysis of some of the more complex circuits by hand calculations is often next to impossible. To relieve the engineer of the burden of tedious computation and to minimize the chance for computational error, digital computer programs have been developed that are capable of automated circuit design analysis. This report describes five of these, their advantages and disadvantages in light of certain fundamental criteria, and draws some conclusions as to their use on Voyager. The five programs and the computers required are:

a.	NET-1	IBM 7094
b.	PREDICT	IBM 7094
c.	SPARC	RECOMP II (Autonetics)
d.	STANPAK	GE 225
e.	ECAP	IBM 1620

2.0 GENERAL

Circuit analysis programs, in general, can be classified as to the various operations they perform. Of interest here are the following:

2.1 EQUATION WRITING

The ability of the computer to form its own matrix equations upon receipt of the circuit topology---as opposed to requiring the designer to insert them.

2.2 STEADY STATE DC ANALYSIS

A summary of all voltages and currents in the circuit with all ac sources removed (either shorted or opened, as required).

2.3 STEADY STATE AC ANALYSIS

A summary of voltages and currents as a function of time and resulting from periodic generators, either external or internal, e.g., an oscillator.

2.4 TRANSIENT ANALYSIS

A time history of voltages and currents as a result of the application of an arbitrary non-periodic forcing function.

2.5 PARTIAL DERIVATIVES OR SENSITIVITY

The rate of change of a particular (dependent) variable with respect to an incremental change in another (independent) variable, all other variables held constant. This is a measure of the sensitivity of a circuit to a particular parameter and is useful in Worst Case Analysis.

2.6 WORST CASE ANALYSIS

An examination of the circuit when all variables have reached a predetermined "Worst Case" limit. The polarity of these limits may either be determined by paragraph 2.5 above, or by the designer externally.

2.7 STATISTICAL ANALYSIS

A determination of the probability of circuit failure given the distribution of all parameters, usually less stringent and more realistic than worst case analysis. An example is "Monte Carlo."

Several computer programs have been investigated in an effort to determine those most suited for Voyager application. These are NET-1, PREDICT, ECAP, SPARC, and STANPAK. NET-1, PREDICT and ECAP are all basically IBM programs adapted for particular uses. SPARC was developed by Autonetics for use on the Recomp II machine. STANPAK was developed by the GE computer division.

3.0 NET 1

NET-1 was developed for use at Los Alamos Scientific Laboratory for use on the MANIAC II computer. It has been rewritten for the IBM 7090/94.

Upon receipt of the network topology the program will determine the matrix equations necessary for solution. It will then proceed to the solution necessary for the steady state dc condition. The output for this solution lists the voltage at every node in the circuit and the current at inductor, transistor, and diode terminals. In addition, total current drain for each supply, total power dissipation, and the condition of every diode and transistor (on, off, saturated, etc.) will be listed. Special messages will be given if any semi-conductor device exceeds 75% of its voltage, current, or power rating. Upon completion of the dc analysis, a steady state ac analysis will be performed (if applicable). Then, if requested, a transient analysis in response to some arbitrarily specified forcing function will be performed. The output of this analysis is a time history of the parameters calculated in the dc analysis plus special messages indicating when a transistor or diode changed state (on to off, saturation to on, etc.).

It should be pointed out that all of these solutions are nominal solutions, that is, they are calculated on the basis of one set, the nominal set, of values for the circuit components. There is no provision in the program for parameter variation, consequently partial derivative calculation is not convenient and worst case analysis without designer intervention in the program is impossible. A worst case analysis becomes tedious because of the difficulty involved in parameter variation.

There are several other drawbacks to NET-1. First, it requires the use of "Library Tapes" on which are stored the parameters for all the semiconductor elements involved in a circuit. Some of these parameters are not readily available from manufacturers and must be either measured or calculated from other data. The Library must be constantly updated. Another significant requirement for the program is a 32K scratchpad memory. This is frequently the total memory capacity of the computer installation. Consequently this program cannot be run in conjunction with other programs and therefore requires more machine time. This can become expensive and difficult to schedule.

The outputs of the analysis can be printed on-line in real-time, that is, while the computer is running. Ordinarily, however, they are written on magnetic tape which is several orders of magnitude faster. This allows them to be printed off-line, thereby saving costly computer time.

NET-1 is capable of handling circuits composed of up to 200 nodes. It is anticipated that this will more than cover the needs of Voyager.

In summary, NET-1 is capable of solving rather complex circuit analysis problems (200 nodes). It will write its own equations, a point of no little significance when dealing with large, complicated circuits. However, as it provides only nominal solutions, it is of little value as a worst case end of life prediction tool. In addition, it requires a large computer installation and is therefore comparatively expensive.

4.0 PREDICT

PREDICT is another automated circuit analysis program using the 7094 computer. It was developed by IBM for the Air Force Weapons Laboratory to assist in the analysis of circuit operation in a radiation environment. In this capacity it is part of a larger system of programs which simulate radiation dosage and calculate the effect on semiconductor components. PREDICT itself is simply a circuit analysis program and as such can be extracted from the larger system.

PREDICT resembles NET-1 in several respects. It can handle circuits of the same general size. As a parenthetical note it should be mentioned that limitation of size is not a function of the technique employed or the computer used, but of the program itself. There is another limitation on size which is purely economic. The larger the circuit the more complex the mathematical operation and the more time consuming is the program.

Another similarity between NET-1 and PREDICT is the equation writing feature. The designer merely supplies a description of the circuit topology and the parameter values and the program does the rest.

Again, as in NET-1, PREDICT produces as its output a time history of various branch currents and node voltages. It differs in that it does not print all of these but only certain selected ones. This time history is in response to a non-periodic forcing function. PREDICT does not calculate ac or dc steady state solutions as such but in effect does somewhat the same thing as "initial conditions" for the transient solution. This requires a separate computer run, which means that the two computer runs are required for the complete solution. Some other features of PREDICT include:

a. An X-Y plot of the outputs if the required plotting equipment is available.

b. Machine requirements -

   1. Fortran II Monitor System

   2. 32K Memory

   3. 10 Tape Drives

   4. On-line Printer

   5. Off-line Tape to Printer equipment

c. Radiation effects are treated as parameter changes in equivalent circuits.

d. No built in semi-conductor model. This requires an externally determined equivalent circuit.

e. Allows the use of any arbitrary mathematical expression.

In summary, PREDICT is intended primarily to determine the nominal transient response to any arbitrary non-periodic forcing function. It does not easily generate dc or ac steady state solutions although these can be accomplished. Equation writing routines are provided. As only nominal solutions are computed it is of little value as a worst case end of life prediction tool. A large computer installation is required.

5.0 SPARC

SPARC was developed by Autonetics for use on their RECOMP II desk size computer. RECOMP II has been used quite extensively by GE for circuit design. Although limited in capability because of its relatively small size and slow speed (compared with, say, the IBM 7094), it makes maximum use of the man-machine interface. The operator in effect has the ability to "talk" to the machine during computational iterations.

Because of the small size of the computer involved, SPARC is much more restricted in the size of the matrices it can handle. This, of course, is reflected in the size of the circuit that can be analyzed. The maximum matrix order that can be handled is 16 and the number of parameters is limited to 60. A measure of the speed of the program can be ascertained from the fact that the estimated time to load the equations and data and calculate one set of answers for a 12 x 12 matrix can be over one hour. It is interesting to note that the major part of this time is taken up with the loading of the machine.

SPARC has the ability to generate its own matrix equations, with the same restrictions as above, for the dc steady state case only. It is understood that work is being done by Autonetics on the ac and transient equation writing routines but there is no indication at the present time that these are available.

The dc analysis portion of the program, in addition to solving the equations for the unknown circuit quantities, calculates partial derivatives. Using these partials to determine the use of the minimum or maximum part value, the computer can give a worst case solution for each of the unknowns. SPARC also permits parameter change and parameter iteration as dictated by the operator.

SPARC is also capable of performing ac and transient analyses although a new set of matrix equations must be generated for each. Because the solution of a matrix involving complex numbers is broken into two new matrices of the same order, one involving the real terms and one involving the imaginary terms, the maximum order of the complex matrix is reduced to eight. Therefore, the size of the circuit that can be accommodated is reduced.

In summary, because of its ability to take partial derivatives and make worst case calculations, SPARC can be an excellent worst case end of life prediction tool. However, for complex circuit analysis, it suffers from size limitations. A feature that is at once an asset and a liability is the amount of operator intervention required in the loading and execution of the program. A large installation is not required. A drawback is the lack of ac and transient equation writing techniques.

6.0 STANPAK

A statistical design approach is taken by a program called STANPAK developed by GE Computer Division. This program was written for a GE computer and makes use of several other programs maintained at the GET Library.

STANPAK is basically a reliability prediction and tolerance analysis tool. Given a circuit with predetermined topology, predetermined component values and their tolerances, and the distribution of the components, the program computes the mean and variance for each independent variable, the mean, variance, and tolerance limits for the dependent variable. It is then capable of relaxing or tightening component tolerances until a predetermined dependent variable tolerance is satisfied. In the process of this calculation partial derivatives are determined.

In addition a Monte Carlo analysis can be performed. In this portion of the program, component values are selected randomly from their distributions and the dependent variable computed. This procedure is repeated for a predetermined number of trials and the distribution of the result is tabulated. This result is a measure of the probability that the dependent variable will fall within predetermined limits.

STANPAK as it is presently constituted can handle thirty parameters and seven functions, a function being defined as an algebraic expression in which every variable except the dependent variable is either an input variable or a previously computed variable. In short, it handles equations in one unknown. It is not capable of ac or transient computations.

In summary, STANPAK would be useful as a worst case end of life prediction tool. It is limited to the dc case and to relatively simple circuits. In addition it can indicate where component tolerances can be relaxed and thereby show where cost savings can be made. This last is true for all techniques that compute partial derivatives.

7.0 ECAP

Another IBM circuit analysis program is called ECAP (Electronic Circuit Analysis Program). ECAP differs from NET-1 and PREDICT in that it uses the IBM 1620 computer system as opposed to the 7094 and the maximum circuit size that can be accommodated is smaller. However, ECAP does solve for partial derivatives and the worst case limits for all unknowns.

ECAP is capable of handling circuits of up to twenty-one nodes and sixty branches. It will write its own matrix equations requiring only a description of the network topology from the designer. It will perform a dc analysis in which it will supply the following outputs:

a. Node voltages, branch voltages, branch currents, and power dissipation.

b. Partial derivatives and sensitivity coefficients.

c. Worst Case analysis, given component tolerances.

d. Standard deviation of node voltages (assumption: circuit parameters statistically independent, random, and normally distributed about their nominal values).

e. Coefficients of the internally generated matrix equations.

ECAP will perform an ac analysis with the following outputs:

a. Node voltages, branch voltages and currents, and power dissipation.

b. Frequency response and phase angles.

c. Coefficients of the internally generated matrix equation.

The transient analysis program will supply:

a. Node voltages and branch element currents.

b. Switching times.

c. Equilibrium Solutions.

d. Initial Conditions.

e. Coefficients of the internally generated matrix equations.

In summary, ECAP provides a system for obtaining dc, ac, and transient response characteristics for circuits of modest size. It is limited to twenty-one nodes and sixty branches. These are fewer than either NET-1 or PREDICT, but are 25% more nodes than SPARC. In addition to the nominal solutions provided, partial derivatives are taken, worst case analysis can be made, and a statistical analysis can be obtained. Equation writing routines are included for all analyses. A disadvantage that could exist in the use of ECAP is the requirement for an IBM 1620 computer system including 1311 Disk File.

8.0 CONCLUSIONS

A number of programs for computer circuit analysis have been examined in light of the Voyager mission requirements. All have been found wanting for one reason or another.

NET-1 and PREDICT satisfy the equation writing and circuit complexity criteria, and perform a transient analysis. In addition, NET-1 will perform dc and ac analyses. Both, however, fail to produce anything more than nominal solutions. Neither will take partial derivatives or perform worst case or statistical analyses. Both require an IBM 7094 installation.

SPARC, on the other hand, performs partial derivative and worst case calculations as a matter of course, but requires its inputs in the form of matrix coefficients externally determined by the designer. It is limited in circuit complexity handling capability and is relatively slow.

STANPAK provides a statistical and worst case parameter variation solution for each unknown expressed as an equation. It will solve equations in one unknown and perform certain statistical operations on them. Its application is limited to small circuits and to dc evaluation only. It is the simplest of the methods studied.

ECAP satisfies all of the design criteria established: equation writing, dc, ac, and transient analyses, worst case and statistical routines, but is limited in the size of of the circuit that it can handle. A three stage differential amplifier exhausts its capacity.

In general for the Voyager Program, ECAP seems to be the most usable computer tool available for detailed circuit design. There are two possibilities for overcoming the ECAP limitation in circuit size handling capability. One possibility is that versions of this program adapted to larger computers can be obtained for use on Voyager. If this is impossible, a computer program will be generated during the next phase of the Voyager Program with a large capacity and the desirable features of ECAP.

Other computer programs are not to be arbitrarily ruled out, either for GE or subcontractor use. However, any method of circuit analysis selected must utilize the same parameter worst case end of life data that have been determined as suitable for the Voyager mission requirements. The important part of the analysis is the validity of the input data and the design information obtained from the analysis. The methods used or the computer tools themselves are of less importance.

CII - VB220AA070

ALTERNATE DESIGN CHARACTERISTICS AND RESTRAINTS CONSIDERED

RADIATION ANALYSIS

Index

1 Introduction
2 Radiation Environment
3 Effects on Subsystems
4 Effects on Semiconductor Electronics
5 References

1.0 INTRODUCTION*

This section discusses the external radiation environment defined in the mission specification. The effects of this radiation environment on solar cells and external thermal coatings are presented in VB236FD101 - Appendix A and VB235AA101, respectively. Utilizing the external environment, an analysis has been conducted to determine the environment that will exist in the spacecraft interior. The effect of this radiation level on the electronic equipment has been assessed and is presented in some detail in Section 3.

The assumptions concerning the intensity of a possible Martian radiation belt is, of course, the overall controlling factor in assessing the seriousness of the effects on the semiconductor electronics. The analysis is constructed as a parametric study with the intensity of the Martian radiation belt as the parameter. Various cases are treated where the Martian belt intensity varies from an intensity equal to that of the Earth's trapped radiation belt to a "worst-case" intensity equal to 10^4 times the intensity of the Earth's belt.

In summary, it appears that, assuming a shielding mass of one gram per square centimeter, the Martian radiation belt intensity will not contribute significantly to the total mission dose for the nominal mission (elliptical orbit) until it exceeds ten times the intensity of the Earth's belt. For a Martian belt intensity below this level, the main component of the radiation environment will be that due to the solar flare protons. As such, the effects on the semiconductor electronics do not appear to be very serious from both radiation induced bulk damage effects and also from radiation induced surface effects. Exceptions to this may exist for some low frequency ($f_{\alpha o} < 1.0$ mc.), high gain, silicon power transistors. Similarly, for a Martian belt intensity 100 times the intensity of the Earth's belt, the bulk damage in semiconductors would not pose a serious problem. The induced surface effects however would begin to take on a serious nature since the total mission ionization dose would be on the order of 10^4 Rads (air). Some consideration of shielding and device derating would have to be taken into account in particularly sensitive components.

For a Martian belt intensity 1000 times the intensity of the Earth's belt, the total mission dose would be equivalent to a dose of 10^{12} fast neutrons/cm^2 along with an ionization dose of approximately 10^5 Rads (air) (for the minimum shielding case of 1.0 gms/cm^2). This dose would cause serious effects both from a bulk damage and

*This section discusses in detail the effects of Martian radiation of various assumed intensities on the semiconductor electronic components. The recent preliminary results of the Mariner IV radiation detection experiment indicates little or no radiation in the vicinity of Mars. As such, the radiation environment would consist principally of solar flare protons. As is shown in the discussion, the solar flare protons alone do not pose any serious degrading effects in semiconductors except possibly for low frequency, high gain silicon power devices.

induced surface effects standpoint in transistors. Very definite considerations on shielding, device operating current levels, and device derating would be required.

For the assumed "worst case" environment, where the Martian belt intensity is 10^4 times the intensity of the Earth's belt, the radiation effects in transistors would be quite severe. The total mission dose would be equivalent to a dose of 10^{13} fast neutrons/cm^2 along with an ionization dose of 10^6 Rads (air). These radiation doses would create major degrading effects in all transistors. Specialized shielding, restrictions on device operating current levels, device derating, parts screening and/or device manufacturing process line monitoring would have to be imposed on the spacecraft design to ensure a reliable system. The increased application of microelectronic circuitry may reduce this problem considerably since it appears that very high frequency microcircuits would not be affected seriously at these doses. However, some further experimental work, particularly in the induced surface effects area, will probably be required for microcircuits to gain confidence in their radiation resistance.

2.0 RADIATION ENVIRONMENT

2.1 INTERNAL - 1971 MISSION

The significant charged particle radiation environment components encountered by the spacecraft during the various phases of its mission are as follows:

- Earth Trapped Radiation
- Solar Cosmic Radiation
- Mars Trapped Radiation
- Galactic Cosmic Radiation

Each of these components will now be discussed in detail.

2.1.1 EARTH TRAPPED RADIATION

The total integrated dose the spacecraft will encounter during the insertion and parking orbit phases is expected to be small compared to the overall mission exposure. As given in the Mission Specification, the time-integrated dose is estimated to be as follows:

Protons ($E > 30$ Mev)	1×10^7 protons/cm^2
Electrons ($E > 0.5$ Mev)	4×10^{10} electrons/cm^2

2.1.2 SOLAR COSMIC RADIATION

2.1.2.1 SOLAR FLARES

The solar flare environmental requirements given in the Mission Specification can be expressed as follows:

$$N(>E) = 4.5 \times 10^{10} E^{-1.12}, \text{ protons/cm}^2\text{/event}$$

$$N(>E) = 4.18 \times 10^{5} E^{-1.02}, \text{ protons/cm}^2\text{/sec (peak/event)}$$

$$N(>E) = 7.43 \times 10^{12} E^{-1.94}, \text{ protons/cm}^2\text{/year}$$

This represents the environment in the vicinity of the Earth. In determining the total mission integrated dose, a $(1/R)^2$ dependence on the intensity is used, where R is in terms of AU from the Sun to the spacecraft.

The above specification implies a flare occurrence of 10 flares per year based on the flux above 30 Mev. For the present analysis a conservative estimate of one flare per month is used.

It is of interest to compare the above estimates with the data from the last corresponding solar flare maximum period (1959-1960 period). Table 2-1 shows this comparison for the integrated proton flux of E >30 Mev. In Table 2-1, three different launch dates are considered; May 11, June 10, and June 25. The first column of dose estimates gives the particle flux greater than 30 Mev for the entire mission based on the flare occurrence and intensity observed during the corresponding 1959-60 yearly time period. The second column assumes the flare occurrence corresponding to the 1959-60 time period and the Specification value of 10^9 protons/cm^2/event, E > 30 Mev (Earth value). The third column assumes a flare occurrence of one flare per month each with the intensity of 10^9 protons/cm^2/event, E >30 Mev (Earth value).

As can be seen from the table, there is little difference between the total mission integrated dose for these three situations. For the present analysis, the one flare per month occurrence rate is assumed. This results in the vehicle accumulating two-thirds of its total mission dose during the cruise phase and the remaining one-third during the Mars orbital phase. Figure 2-1 shows the final assumed environment for the total mission integrated dose due to solar flares. The dose for E >30 Mev is taken as 10^{10} protons/cm^2 and for E >100 Mev as 10^9 protons/cm^2. These values are slightly higher than any of the corresponding values in Table 2-1.

2.1.2.2 SOLAR WIND

The values of the solar wind are assumed to be the following:

Mean density: 0.5 AU; 20 Hydrogen atoms/cc

1.0 AU; 5 Hydrogen atoms/cc

Table 2-1. Solar Flare Exposure (E >30 Mev)

Launch/Arrival Date	Cruise/Orbital Time (days)	Integrated Intensity for 1959-60 Solar Active Period (protons/cm^2)	Integrated Intensity 1959-60 Occ., 10^9 protons/cm^2/ event (protons/cm^2)	Integ. Intensity, One Flare/Month, 10^9 protons/cm^2/event (protons/cm^2)
5/11/71 12/17/71	220/180 Total	$6.1 \times 10^9 / 1.9 \times 10^7$ 6.12×10^9	$4.18 \times 10^9 / 4.96 \times 10^9$ 9.14×10^9	$6.0 \times 10^9 / 2.9 \times 10^9$ 8.9×10^9
6/10/71 12/19/71	192/180 Total	$5.2 \times 10^9 / 1.9 \times 10^7$ 5.22×10^9	$3.4 \times 10^9 / 4.96 \times 10^9$ 8.36×10^9	$4.9 \times 10^9 / 2.9 \times 10^9$ 7.8×10^9
6/25/71 12/28/71	186/180 Total	$5.2 \times 10^9 \times 10^7$ 5.22×10^9	$3.4 \times 10^9 / 4.96 \times 10^9$ 8.36×10^9	$4.3 \times 10^9 / 2.9 \times 10^9$ 7.2×10^9

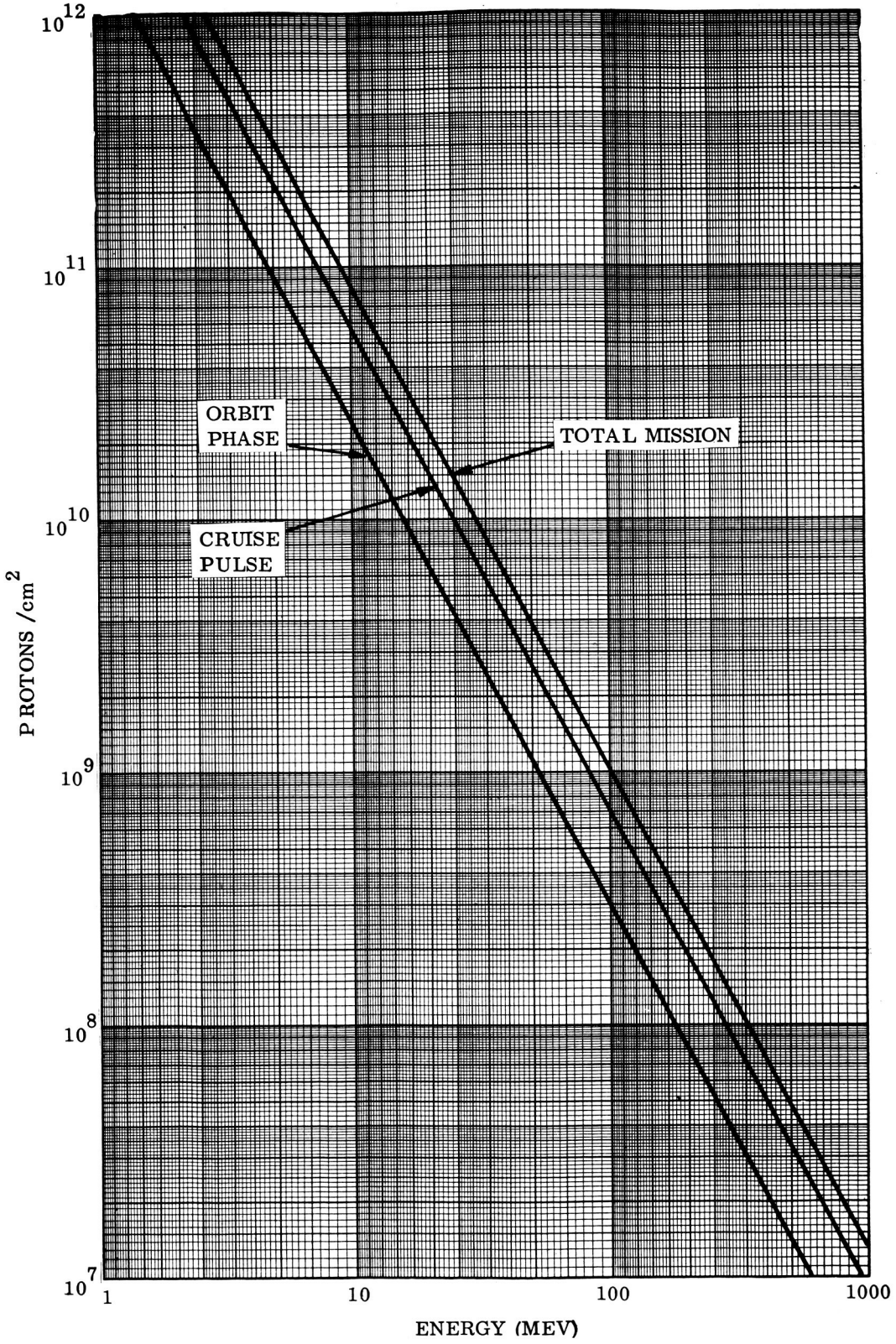

Figure 2-1. Solar Flare Protons Integral Isotopic Flux, Total Mission Dose

1.75 AU; 2 Hydrogen atoms/cc

Mean Flow: 0.5 AU; 8×10^8 Hydrogen atoms/cc/sec

1.0 AU; 2×10^8 Hydrogen atoms/cc/sec

1.75 AU; 1×10^8 Hydrogen atoms/cc/sec

The mean velocity of the solar wind from 0.5 AU to 1.75 AU, is assumed to be 450 to 500 Km/sec. The electron density for energies on the order of a few electron volts is assumed to be 10^3 electrons/cm^3.

2.1.3 MARS TRAPPED RADIATION

The speculation of a Martian Radiation Belt is not based on any direct experimental data at the present time. However, based on the planet's similarity to earth, it is quite probable that a belt exists. The intensity of such a belt would have to be as much as ten thousand times the intensity of the Earth's belt before it could be observed on Earth. Hopefully the Mariner IV spacecraft will shed some light on this question.

For the present analysis, a Martian radiation belt is assumed to exist. The structure of the belt is assumed to be identical to that of the Earth in relation to the planet size (i.e., in terms of planetary radii). Thus the peak of the inner belt is assumed at approximately 1.5 Martian radii (5000 km) from the center of Mars and the peak of the outer belt at approximately 4.7 Martian radii (16,000 km).

Based on these assumptions, the dose received in a given Martian orbit may be estimated utilizing present Earth Radiation Belt computer programs. Such an estimate has been made for the Mars elliptical orbit mission (nominal mission). The Mars orbit is assumed to have a periapsis of 3000 km and an apoapsis of 25,000 km with an inclination of 40 degrees. The radiation flux encountered in this Martian orbit would correspond to that encountered in an Earth orbit having a perigee at about 12000 km and an apogee at 54,200 km. The results of this calculation are shown in Figure 2-2 for the daily flux of electrons and protons that the vehicle would be exposed to in the elliptical Mars orbit. The curves shown in Figure 2-2 assume a Martian belt intensity equal to that of the Earth's belt. Any assumption on the Martian belt intensity relative to the Earth's belt would be a direct mutltiplying factor on the curves shown in Figure 2-2. For example, the worst case environment is assumed to be ten thousand (10^4) times the intensities shown in Figure 2-2. The energy spectrum shape is assumed to be independent of intensity however.

2.1.4 GALACTIC COSMIC RADIATION

The primary galactic cosmic radiation consists mostly of protons and heavier nuclei. The elemental composition is given in the Mission Specification. The maximum yearly flux is taken to be 1.2×10^8 particles/cm^2. The energy of these particles is 100 Mev

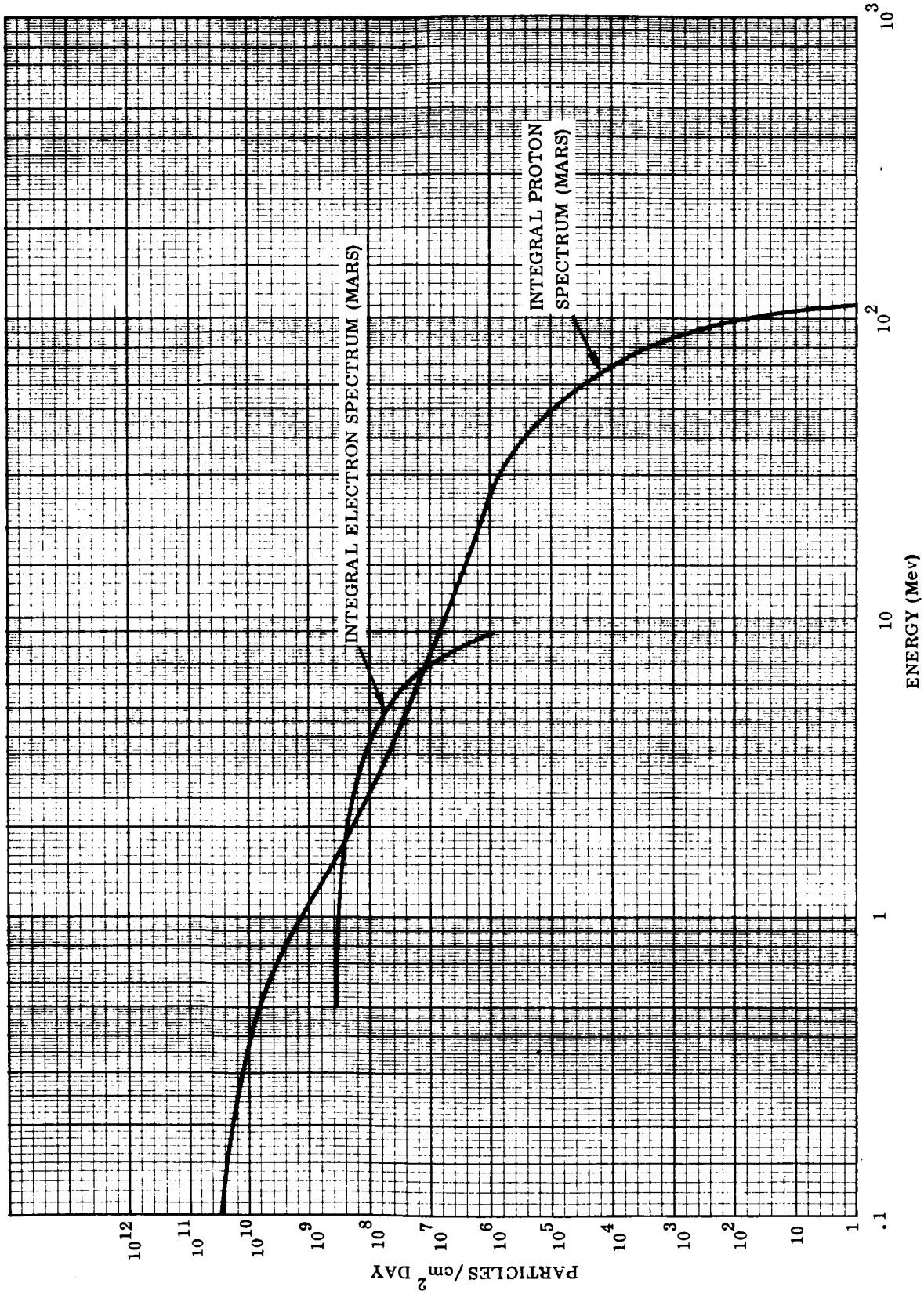

Figure 2-2. Mars Trapped Radiation

and greater. This radiation, though very penetrating, will be somewhat insignificant compared to the other environment components. The maximum integrated dose will be 20 rad/year.

2.2 INTERNAL - 1969 MISSION

The average daily electron and proton flux to be encountered by the vehicle during the two month earth orbiting phase of the 1969 mission is shown in Figure 2-3. A nominal orbit of 200 miles perigee, 6700 miles apogee, and 30° inclination has been assumed.

The solar cosmic radiation and primary galactic radiation described above for the 1971 mission is also assumed to apply to the 1969 mission.

2.3 INTERNAL RADIATION ENVIRONMENT

In order to assess the effects of the radiation environment on the internal satellite components, the shielding effect of the satellite structure must be taken into account. Such shielding calculations have been performed utilizing the external radiation environment for the 1971 mission described in the previous sections. The essential results are summarized in Figure 2-4, which shows the total accumulated ionization dose for the entire 1971 mission in terms of Rads (Air) as a function of shield thickness for various assumptions concerning the intensity of the Martian radiation belt.

The "A" curve, although it includes the effect of a Martian radiation belt equal to the intensity of the Earth's belt, is primarily due to the solar flare protons. Conversely, as the value of the Martian belt intensity is assumed to increase up to the maximum of 10^4 times the Earth's intensity, the solar flare protons become insigificant.

These dose estimates represent a maximum value from the geometrical shielding point of view since a simple slab geometry has been assumed with the isotropic flux incident on one side of the slab. However, similar work on other programs has shown that this technique does give a reasonable maximum dose estimate, particularly for components mounted close to the surface of the vehicle. The dose estimates given in Figure 2-4 also include the dose due to the Bremsstrahlung (X-rays) generated by the incident electrons.

Although computer shielding programs are available which can calculate detailed isodose contours within a given instrument cannister or a complete spacecraft structure, it is felt that this sort of detail is not required at this point in the program.

Figures 2-5 and 2-6 show the shapes of the electron and proton spectra for the Martian belt (Mars = Earth intensity) after passing through various shield thicknesses using the slab geometry.

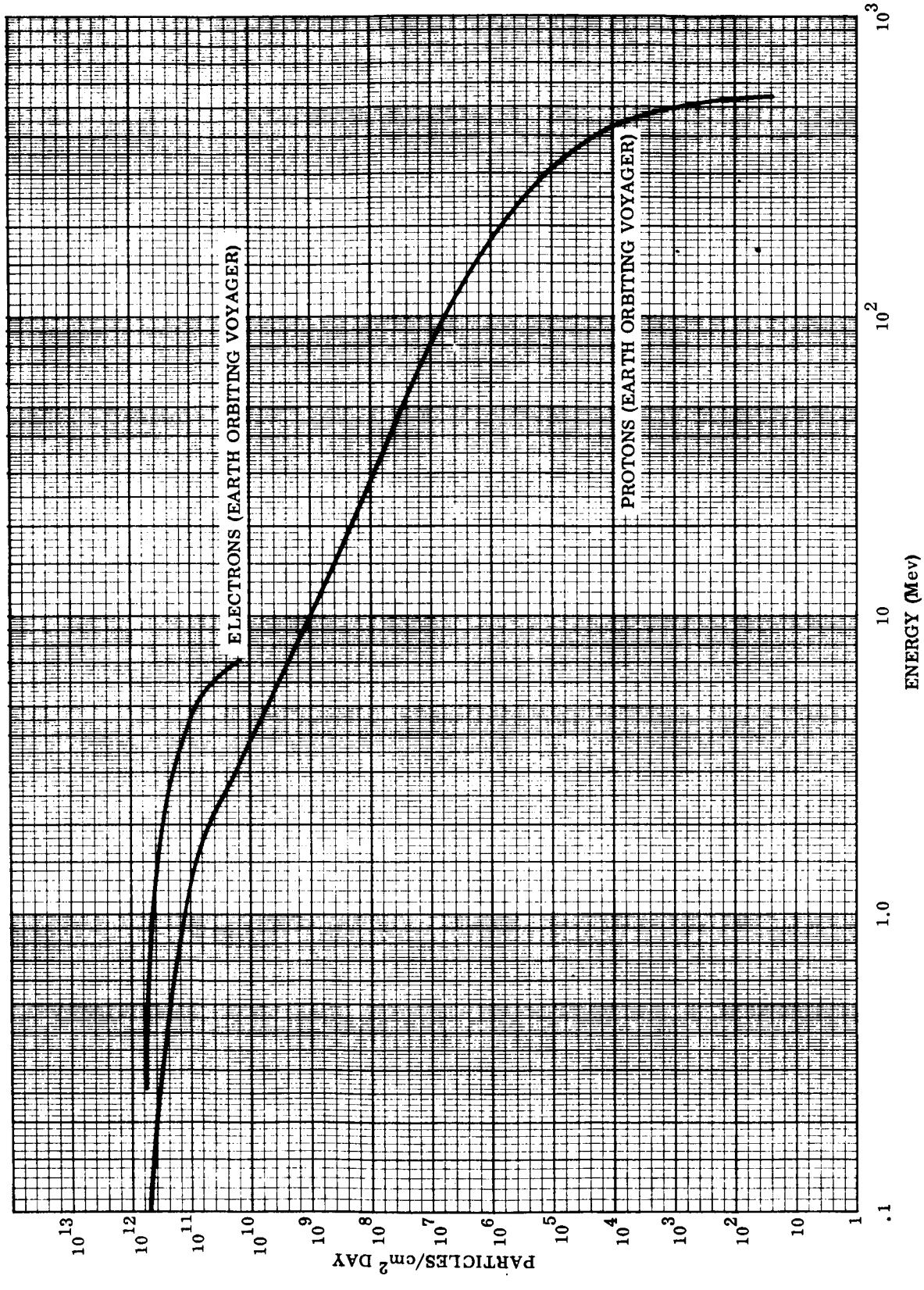

Figure 2-3. Earth Trapped Radiation, 1969 Mission

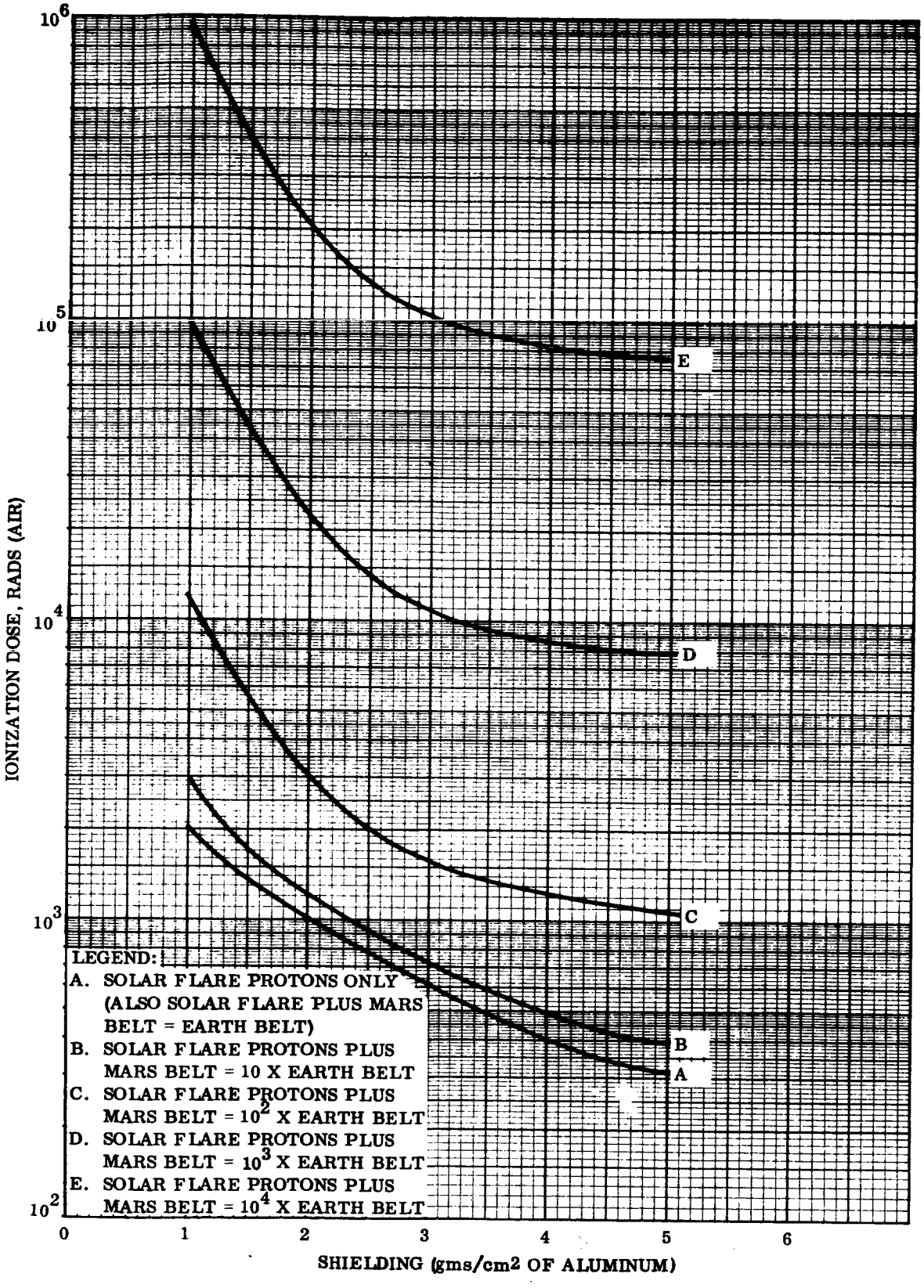

Figure 2-4. Ionization Dose vs Shielding, Total Mission Dose

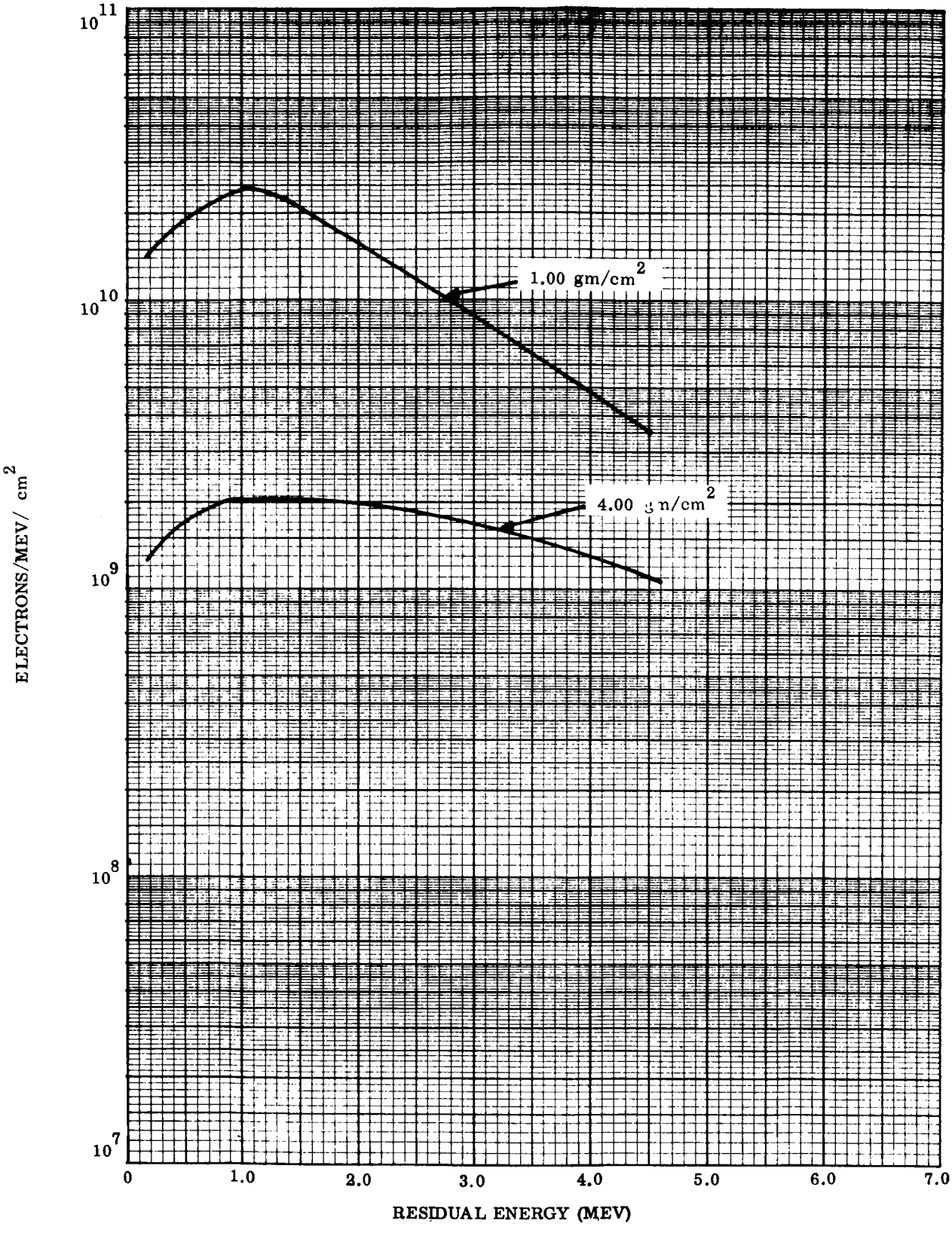

Figure 2-5. Residual Electron Flux, Mars Belt, Total Mission Dose

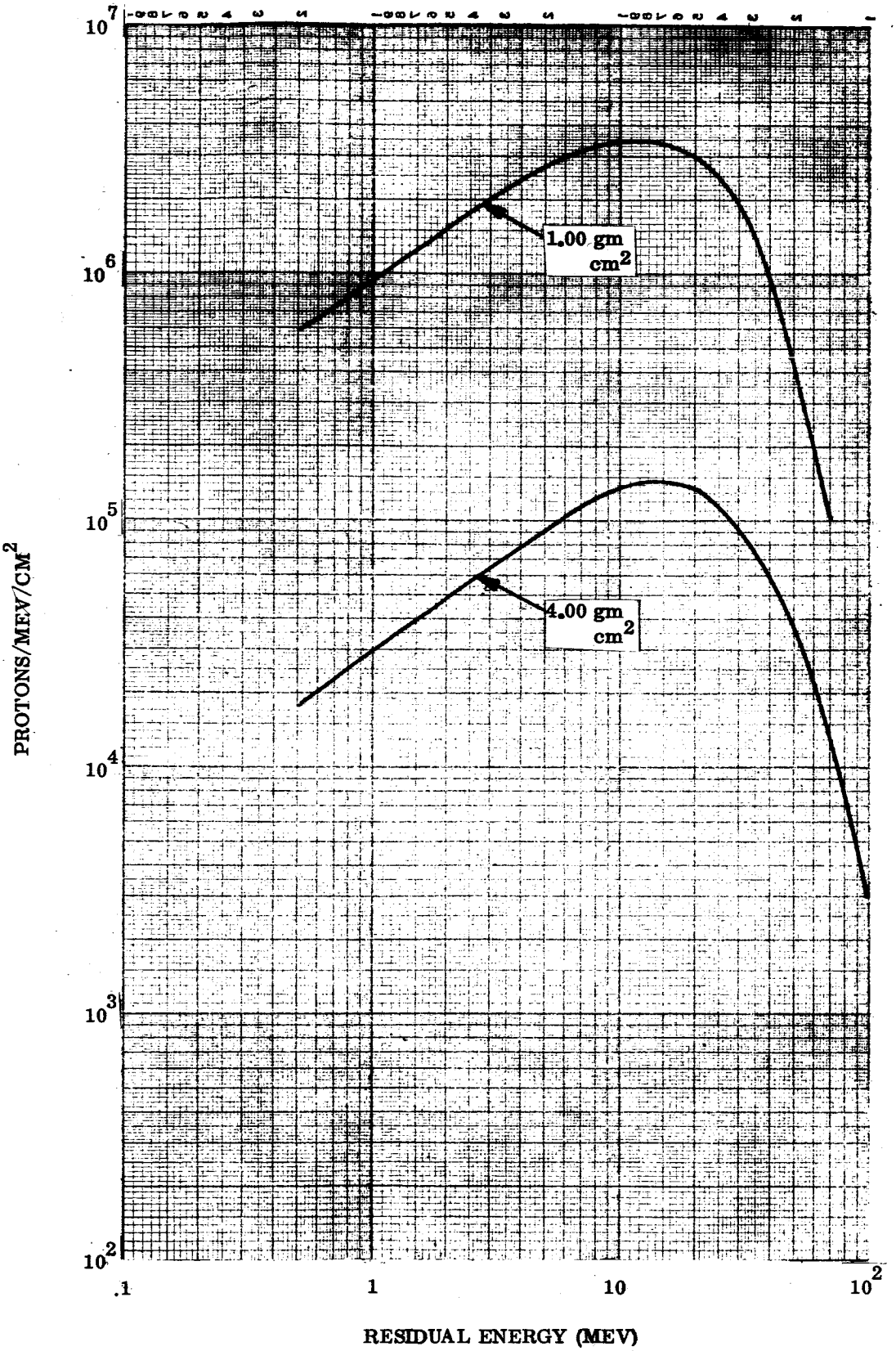

Figure 2-6. Residual Proton Flux, Mars Belt; - Total Mission Dose

3.0 EFFECTS ON SUBSYSTEMS

The effects of the radiation environment on the solar cell power system are given in detail in VB236FD101 - Appendix A. Similiarly, the effects on external thermal coatings are also given elsewhere, see VB235AA101. The effects of the solar wind and other very low energy components of the radiation environment are of particular concern to these surface coatings.

The remainder of this section will be devoted to a detailed discussion of the effects of the radiation environment on the internal semiconductor electronic components. These components are considered to be the most sensitive in the spacecraft system and will therefore serve as a basis to judge the seriousness of the radiation environment on the spacecraft system.

4.0 EFFECTS ON SEMICONDUCTOR ELECTRONICS

Radiation exposure of semiconductor components can result in two general classes of effects: bulk effects and surface effects. In what follows, bulk effects are defined as those damage processes which occur within the normal crystal lattice structure while surface effects refer to damage processes which alter the semiconductor surface properties. Both of these processes can radically affect the electrical characteristics of semiconductor devices.

It is the purpose of this section to describe in detail the effects of ionizing radiation on semiconductor devices, in particular transistors and diodes, and to present the calculational procedures and experimental data used to assess the effects of the environment on the Voyager electronic systems. The essential results on bulk damage are contained in Section 3.1 while that for surface effects is given in Section 3.2.

4.1 BULK EFFECTS

In general, there are two types of interactions between the semiconductor crystal lattice and the incident radiation. These are referred to as carrier production and lattice defect production. Carrier production results from the excitation of valence electrons to the conduction band by ionizing radiation propagating through the crystal. These generated electron-hole pairs produce an increase in conductivity, however, they tend to recombine with a time constant equal to the normal carrier lifetime, hence carrier production is a transient effect for pulsed radiation. This effect is independent of the integrated dose and varies only with dose rate. For the Voyager environment, the dose rate will be low ($<10^3$ rads/hr). In a typical silicon diode, this would produce an excess reverse current of less than 10^{-10} amps. Therefore carrier production can be regarded as an insignificant effect.

Lattice defect production represents a more serious problem and results from collistions between higher energy particles and lattice atoms. Essentially, this is a three-phase process. First there is a primary interaction between the incident particle and an atom of the crystal lattice. If the energy of the incident particle is

sufficient, enough energy can be transferred to the struck atom to displace it from its normal position in the lattice to some interstitial site, leaving a vacancy in the lattice. If the recoil energy of the struck atom is greater than the atomic displacement energy for the lattice, it will undergo interactions with other atoms in the lattice producing secondary and ternary knock-ons resulting in a cascade effect. The vacancies produced by this process diffuse away from the impact site until they are trapped by a chemical impurity or a lattice defect. The interstitial atoms also consititute a lattice defect. There are several types of lattice defects that can be formed from the interactions of the interstitials and vacancies with the lattice. The exact mechanisms of defect formation are not well understood at this time; however, a general dependence on incident particle type and energy, type and amount of impurities present, type of semiconductor material, and temperature has been observed. The threshold particle energy for displacements, E_T, (i.e., the minimum incident particle energy required to produce an atomic displacement) varies with the semiconductor material, the type of incident particle, and the direction of the incident particle relative to the crystal axis. Minimum values of E_T for protons and electrons in silicon and germanium are tabulated in Table 4-1.

Table 4-1. Minimum Values of E_T

E_T	Particle	Material
0.145 Mev	Electrons	Silicon
0.680 Mev	Electrons	Germanium
98 ev	Protons	Silicon
270 ev	Protons	Germanium

A 1 Mev proton is capable of producing an average of 9000 displacements per centimeter in silicon. For an electron of the same energy, the number of displacements/centimeter is reduced to 5.6. This decrease in effectiveness is due mainly to the fact that the proton is approximately 1800 times more massive than an electron resulting in a higher cross-section for a primary collision and the transfer of more energy per primary collision, creating more secondary displacements. The same considerations also apply to neutrons which cause displacements by hard-sphere collisions producing an average of 500 displacements/centimeter for fast neutrons (Reference 1). The decreased effectiveness of neutrons relative to protons is due to the absence of charge on the neutron. As a result, the neutron must interact with the shorter range nuclear force field and is not affected by the coulomb force seen by the proton. Consequently, the cross-section for a neutron collision is lower.

Each type of radiation induced defect will produce a discrete allowed electronic energy level within the forbidden energy gap of the semiconductor material and this will be similar in action to the introduction of chemical impurities. James and Lark - Horovitz have proposed that each vacancy gives rise to two acceptor levels corresponding to the

presence of one or two electrons near each vacancy. Two donor energy levels are also associated with each interstitial atom corresponding to the first and second ionization potentials. Thus, the interstitial vacancy pairs produce two donor and two acceptor energy levels in the forbidden gap. In an unirradiated semiconductor, the carrier concentration is normally governed by the donor and acceptor levels produced by added impurities. Therefore, the introduction of these radiation induced energy levels alters the carrier concentration and hence, the conductivity. The efficiency of these levels in accepting or donating an electron depends upon the position of the defect level with respect to the Fermi level. Since the position of these levels depends on the type of defect formed, it can be seen that bulk damage effects cannot be accurately predicted just from a determination of the number of displaced atoms alone. As a result, one cannot confidently determine the relative effectiveness of different types of particles or particles of different energy in damage production simply by making a ratio of the number of displacements/centimeter produced by each without knowing the nature of the defects that are formed.

4.1.1 EFFECTS ON CONDUCTIVITY AND LIFETIME

The two properties of a semiconductor that are most significantly affected by displacement production are the conductivity and the lifetime.

4.1.1.1 CONDUCTIVITY

The conductivity of a semiconductor is related to the carrier concentration and mobility by

$$\sigma = n e \mu_n + p e \mu_p \qquad (1)$$

where

- n - electron concentration in the conduction band
- p - hole concentration in the valence band
- e - electronic charge
- μ_n - electron mobility
- μ_p - hole mobility

The relative importance of each of the radiation induced donor and acceptor levels varies with the type of material, whether it is n or p type, and the initial conductivity. In n-type germanium, the acceptor levels (electron traps) play a dominant role. The conductivity initially decreases with dose as more and more electrons are removed from the conduction band to the acceptor levels. As the dose is further increased, the conductivity falls to a minimum at which point, a redistribution of the trapped electrons

to vacant states of lower energy occurs. After this redistribution occurs, the vacancies left in the low lying states begin to act as acceptors, removing electrons from the valence band causing the material to become P-type and for additional bombardment, the conductivity will increase. In initially P-type germanium, the behavior of the conductivity is dependent upon its initial value and hence, the Fermi level. For an initial conductivity of less than about 20 mhos/cm, the acceptor levels remove electrons from the valence band and create holes. The conductivity will, therefore, increase with dose, asymptotically approaching a value of 20 mhos/cm. If the initial conductivity is greater than 20 mhos/cm, the positions of the Fermi level relative to the defect levels will be such that hole trapping occurs and the conductivity will asymptotically decrease to 20 mhos/cm. The changes in conductivity in germanium under neutron bombardment are shown in Figure 4-1.

For both n and p-type silicon, the conductivity exhibits a more uniform behavior than for germanium. In n-type silicon, the acceptor levels dominate and remove electrons from the conduction band resulting in a conductivity decrease with dose which asymptotically approaches the intrinsic value (i.e., the value corresponding to pure silicon). In p-type material, the donor levels dominate, removing holes from the valence band, and also resulting in a conductivity decrease with dose which again asymptotically approaches the intrinsic value. The behavior of the conductivity with dose for silicon is depicted in Figure 4-2.

Based on fast neutron damage experiments, a model has been proposed (Reference 2) which for low doses ($<10^{14}$ nvt) assumes a linear variation of conductivity with dose so that

$$\sigma = \sigma_o \pm \xi \varphi \tag{2}$$

where

σ_o is the initial conductivity

ξ is the conductivity damage constant

φ is the neutron dose

The choice of sign depends upon the initial conductivity and the type of material. In germanium it is negative for n-type, positive for p-type if σ_o is less than 20 mhos/cm, and negative for p-type if σ_o is greater than 20 mhos/cm. In silicon the sign is always negative.

4.1.1.2 LIFETIME EFFECTS

The disruption of the lattice periodicity by radiation induced defects also serves to catalyze the recombination of holes and electrons thereby reducing the minority carrier

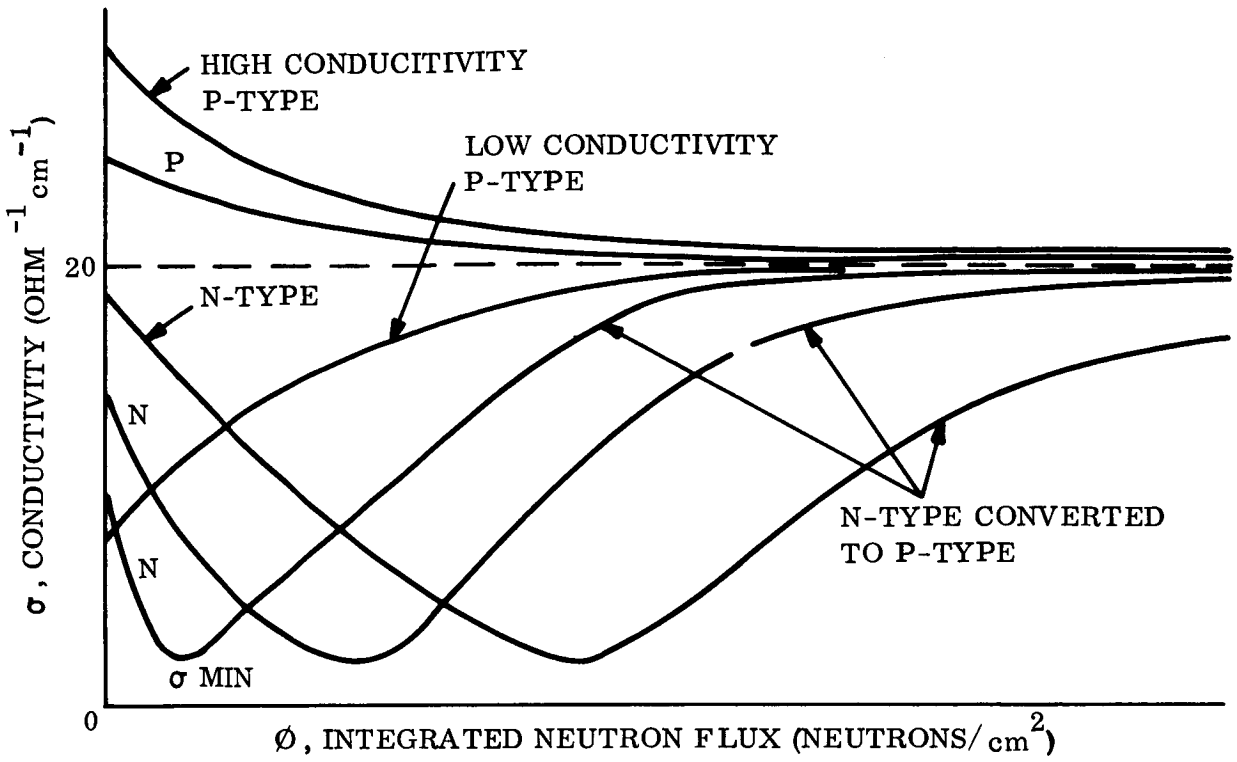

Figure 4-1. The Effect of Neutron Irradiation on the Conductivity of Germanium

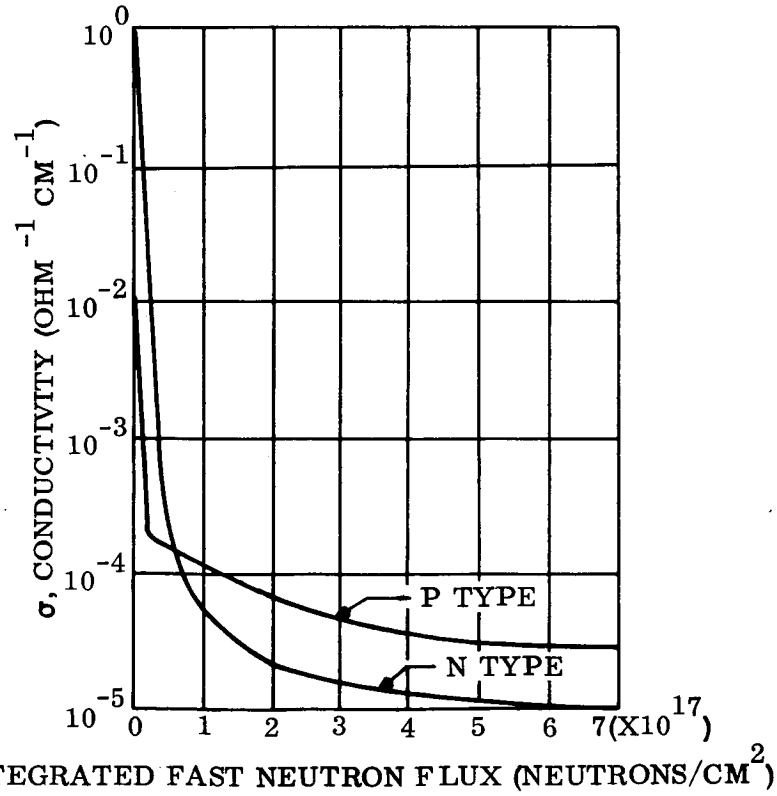

Figure 4-2. The Effect of Neutron Irradiation on the Conductivity of Silicon

lifetime. This is the major source of device degradation from bulk effects. In agreement with theory, the minority carrier lifetime has been found to decrease according to (Reference 3)

$$\frac{1}{\tau} = \frac{1}{\tau_o} + \frac{\varphi}{K} \tag{3}$$

where φ is the time integrated particle flux and K is a constant hereafter referred to as the lifetime damage constant. The damage constant is essentially the link between the type and number of defects produced and their effect on the lifetime and therefore depends on such factors as: type and energy of the bombarding particle; type of semiconductor (germanium or silicon, n or p-type, etc.); equilibrium conductivity; temperature; and amount and type of impurities present. Due to the lack of knowledge concerning the interaction of all of these variables, the damage constant can be determined only by experiment. Values of K in germanium are usually about one order of magnitude higher than in silicon indicating that germanium is a more damage resistant material. This is in agreement with simple displacement theory predictions since the germanium atom is heavier and therefore exhibits a lower cross-section for displacement production. Values for K for fast fission neutrons have been determined by several experimenters (References 3, 4, 5, 6). Average values for various materials are shown in Table 4-2.

Table 4-2. K Values for Fast Fission Neutrons

Material	K
n - type Ge	$5.0 \pm 2.0 \times 10^7$ nvt - sec
p - type Ge	$2.4 \pm 0.4 \times 10^7$ nvt - sec
n - type Si	$2.8 \pm 0.8 \times 10^6$ nvt - sec
p - type Si	$3.2 \pm 1.1 \times 10^6$ nvt - sec

4.1.2 SPECIFIC APPLICATION TO TRANSISTOR AND DIODE PARAMETERS

4.1.2.1 TRANSISTORS

In transistors, the most significant effect of displacement damage is a reduction in the current gain due to effects on the conductivity and the minority carrier lifetime. The basic mechanism of transistor operation depends upon the diffusion of minority carriers, injected at the emitter, across the base region to the collector junction. The percentage of these carriers which recombine in the base before reaching the collector determine the current gain. A radiation induced reduction in the lifetime therefore lowers the current gain. Since carrier lifetime becomes less important as the width of the base region decreases, one would expect narrow base, high frequency

transistors to be less sensitive to this type of damage. Also, since less atomic displacements are produced in germanium, germanium transistors exhibit a greater resistance to this effect. Changes in the base conductivity are responsible for two additional effects which ultimately affect the current gain. They are a reduction in emitter efficiency and depletion layer widening of the collector region (i.e., a decrease in the base width). In general then, one can see that the damage sensitivity of a transistor varies with the alpha cut-off frequency, the base conductivity, junction structure (abrupt, graded, etc.), and the semiconductor material from which it is made. The behavior of conductivity and lifetime with dose has been previously described. Elementary device theory analytically relates these parameters to the current gain (Reference 7). For a PNP unit, the common emitter current gain may be expressed as,

$$\frac{1}{\beta} = \frac{S\,A_S\,W}{D_p\,A_e} + \frac{\sigma_b W}{\sigma_e L_e} + \frac{W^2}{2\,L_p^{\,2}} \tag{4}$$

where

β - common emitter current gain

S - surface recombination velocity

W - effective base width

A_S - effective surface recombination area around the emitter

A_e - area of the emitter junction

D_p - diffusion constant for holes

σ_b - base conductivity

σ_e - emitter conductivity

L_e - diffusion length for electrons in the emitter

L_p - diffusion length for holes in the base

For a base of uniform resistivity, the width of the collector depletion region is given by

$$W_b = \left(\frac{2\,\epsilon\,\mu\,V_c}{\sigma_b}\right)^{1/2} \tag{5}$$

The effective base width is given by

$$W = W^1 - W_b = W^1 - \left(\frac{2\,\epsilon\mu V_c}{\sigma_b}\right)^{1/2} \tag{6}$$

where:

W^1 - geometrical width of the base region

ϵ - dielectric constant

μ - majority carrier mobility

V_c - collector voltage

The first term on the right hand side of equation (4) is the surface recombination term and remains essentially unaltered by bulk damage. The effect of ionizing radiation on the surface of a semiconductor will be discussed in Section 3.2. The second term represents the emitter efficiency. Use of equations (2) and (3) yields

$$\frac{\sigma_b W}{\sigma_e L_e} = \frac{(\sigma_{bo} \pm \xi\varphi)\,W}{(\sigma_{eo} \pm \xi\varphi)\,D^{1/2}} \left(\frac{1}{\tau_{eo}} + \frac{\varphi}{K}\right)^{1/2} \tag{7}$$

where

$$L_e^2 = D_e \tau_e$$

Whether the signs in equation (7) are positive or negative depends whether the material is silicon or germanium, the initial conductivity, and the structure, i.e., npn or pnp. For typical germanium pnp's, the signs become negative and the emitter efficiency will tend to decrease. In the npn case, the sign in the numerator becomes positive while the one in the denominator goes negative causing an increase in emitter efficiency. For silicon npn and pnp transistors, both signs are negative with a resulting decrease in emitter efficiency. Changes in the emitter efficiency term become significant only at higher doses ($\sim 10^{14}$ nvt) and usually are not important when compared to the effects on the volume recombination which is represented by the third term in equation (4). The effect on the volume recombination term can be attributed to permanent changes in the minority carrier lifetime. Making use of the relation

$$L_p^2 = D_p \tau_p \tag{8}$$

and substituting in the lifetime degradation, equation (3), the volume recombination term can be written as

$$\frac{1}{2}\left(\frac{W}{L_p}\right)^2 = \frac{1}{2}\frac{W^2}{D_p}\left(\frac{1}{\tau_o} + \frac{\varphi}{K}\right) \tag{9}$$

The volume recombination term is also subject to degradation induced by conductivity changes since the base width is related to σ_b by equation (6). However, for npn germanium and all silicon transistors, the lifetime changes at a much faster rate than the base conductivity. Therefore, this effect may be ignored and a constant base width may be assumed. If the effects on the emitter efficiency term are ignored and if β_o is the preirradiation current gain then

$$\frac{1}{\beta} - \frac{1}{\beta_o} = \frac{1}{2}\frac{W^2 \varphi}{D_p K} \tag{10}$$

Assuming a uniform base, the base width may be related to the alpha cutoff frequency, $f_{\alpha o}$,

$$W^2 = \frac{1.22}{\pi}\frac{D_p}{f_{\alpha o}} \tag{11}$$

Substituting this into (10) and normalizing

$$\frac{\beta}{\beta_o} = \frac{1}{1 + \frac{.194\,\varphi\,\beta_o}{K f_{\alpha o}}} \tag{12}$$

The damage constants to be used in equation (12) are listed in Table 4-2 and depend on the transistor material and type. Specifically, the value of K selected depends only on the base material since the damage is due to minority carrier lifetime degradation in the base. For example, for a silicon npn transistor the damage constant for p-type silicon would be selected. Inserting the appropriate values for K into equation (12) the degradation equation becomes

$$\text{for silicon npn } \frac{\beta}{\beta_o} = \frac{1}{1 + \frac{6.06 \times 10^{-8}\,\varphi\,\beta_o}{f_{\alpha o}}} \tag{13}$$

$$\text{for silicon pnp } \frac{\beta}{\beta_o} = \frac{1}{1 + \frac{6.93 \times 10^{-8}\,\varphi\,\beta_o}{f_{\alpha o}}} \tag{14}$$

for germanium npn $$\frac{\beta}{\beta_o} = \frac{1}{1 + \frac{8.1 \times 10^{-9} \varphi \beta_o}{f_{\alpha o}}} \qquad (15)$$

For the purposes of comparison, the degradation functions for 1 mc and 50 mc silicon npn and germanium npn transistors are plotted in Figure 4-3. From these curves one can see the relative improvement in resistance to bulk damage gained by using higher frequency devices. The greater vulnerability of silicon as opposed to germanium is also evident. In pnp germanium transistors, the constant base width assumption will not always hold. For alpha cutoff frequencies above 5 mc, the effective base width becomes smaller and significant changes in the base conductivity will occur before the lifetime decay can appreciably reduce the current gain. Since the base is n-type germanium, the conductivity will decrease producing a decrease in the effective base width due to depletion layer widening as per equation (5) thus changing $f_{\alpha o}$. This will actually cause β to increase since the recombination effects will be reduced. This base width reduction will continue to occur until either the base material is converted to p-type, or punch-through occurs, at which point β will rapidly fall to zero. Neglecting any

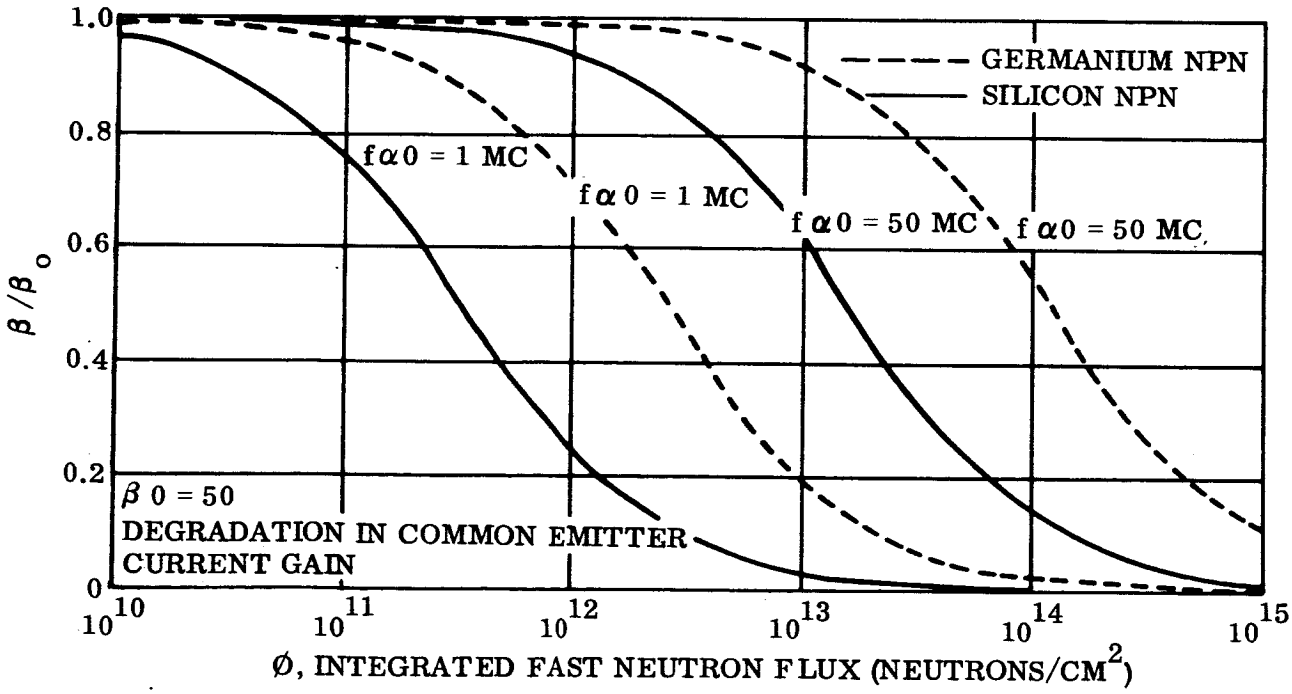

Figure 4-3. Gain Degradation Due to Bulk Damage for Typical NPN Transistors

effects of emitter efficiency from equation (4), for a non-constant base width (alpha cutoff frequency), the gain degradation becomes

$$\frac{1}{\beta} - \frac{1}{\beta_o} = \frac{1}{2}\left(\frac{W}{L_p}\right)^2 - \frac{1}{2}\left(\frac{W_o}{L_p}\right)^2 \tag{16}$$

where

W_o represents the initial effective base width.

Using $L_p^2 = \tau_p D_p$ and the lifetime degradation equation results in

$$\frac{1}{\beta} - \frac{1}{\beta_o} = \frac{1}{2 D_p}\left[\frac{W_o^2}{\tau_o}\left(\frac{W^2}{W_o^2} - 1\right) + \frac{W^2 \varphi}{K}\right] \tag{17}$$

By assuming an emitter efficiency of unity, and neglecting the surface recombination term, then

$$\beta_o \approx \frac{W_o^2}{2 D_p \tau_o} \tag{18}$$

Substituting this into (17) and rearranging terms yields

$$\frac{1}{\beta} = \left(\frac{1}{\beta_o} + \frac{W_o^2 \varphi}{2 D_p K}\right)\left(\frac{W}{W_o}\right)^2 \tag{19}$$

Normalizing to β_o the degradation equation becomes

$$\frac{\beta}{\beta_o} = \frac{(W_o/W)^2}{1 + \frac{W_o^2 \varphi \beta_o}{2 D_p K}} \tag{20}$$

In terms of the alpha cutoff frequency, the equation, for a uniform base, is

$$\frac{\beta}{\beta_o} = \left(\frac{f_\alpha}{f_{\alpha o}}\right)\left(\frac{1}{1 + \frac{.194 \varphi \beta_o}{K f_{\alpha o}}}\right) \tag{21}$$

Therefore, to correct for a varying base width the normal degradation equation (12) must be multiplied by the ratio of the cutoff frequency to its initial value. Substituting the proper value for the damage constant, the degradation function for germanium pnp transistors becomes

$$\frac{\beta}{\beta_o} = \left(\frac{f_\alpha}{f_{\alpha o}}\right) \left(\frac{1}{1 + \frac{3.88 \times 10^{-9} \phi \beta_o}{f_{\alpha o}}}\right) \tag{22}$$

The damage function for 1.2 ohm-cm initial base resistivity germanium pnp devices (10) with initial alpha cutoff frequency as a parameter is shown in Figure 4-4. For lower frequency units corresponding to larger base widths, lifetime degradation effects dominate and the curves for these transistors exhibit a similar behavior to that observed for the other device types. Higher frequency units with smaller base widths exhibit an initial slow decay in gain (due to lifetime effects) to a minimum value corresponding to where the conductivity changes begin to dominate. Under further bombardment, depletion layer widening continues, causing a decrease in the base width which actually increases the current gain. The gradual increase in β will continue until a sudden rapid drop occurs corresponding to the occurrence of punch-through or conversion of the base to p-type material and transistor operation ceases.

4.1.2.2 EFFECTS ON DIODES

Changes in lifetime and conductivity induced by displacement damage produce the following effects in diodes. In the forward direction at low currents, the current for a constant voltage increases and dynamic resistance decreases. At higher currents, the effect will reverse and a decrease in current will be observed. In the reverse direction, both the current at constant voltage and the breakdown voltage increase. These changes can be explained by examining the diode equation.

$$I = I_s \left[e^{\frac{q\,Vo}{k\,T}} - 1 \right] \tag{23}$$

where

I - the diode current

I_s - the reverse saturation current

V_D - the potential difference across the junction

T - the junction temperature

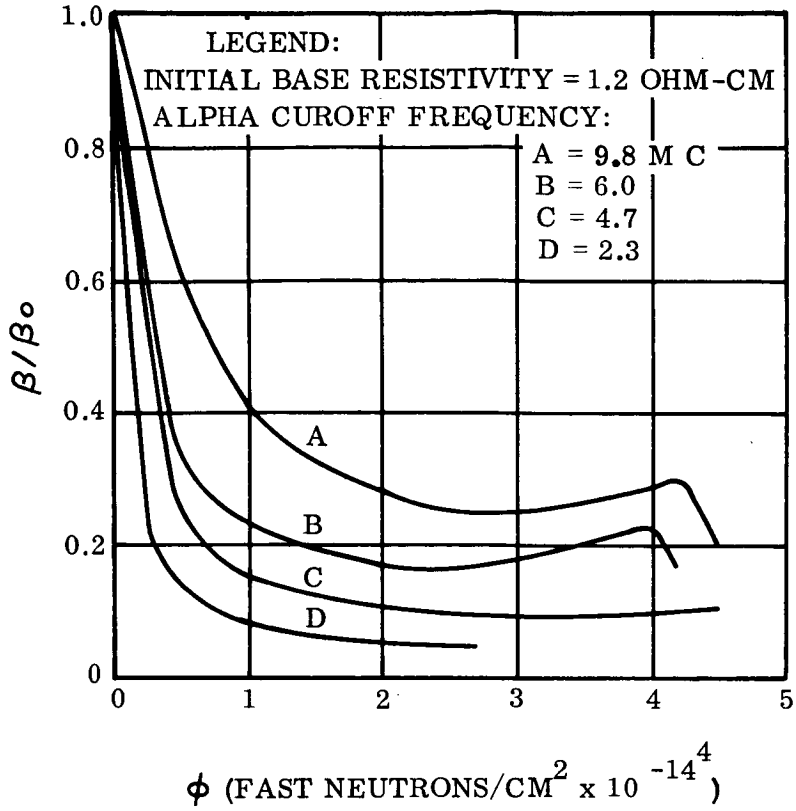

Figure 4-4. Typical Current Gain Degradation on Germanium PNP Transistors Under Neutron Bombardment

k - Boltzman's constant

q - electronic charge

Elementary device theory indicates the dependence of I_s on minority carrier lifetime as

$$I_s = A\left(\frac{1}{\tau}\right)^{1/2} \tag{24}$$

where A is a constant determined by material parameters. Consequently, the reduction in minority carrier lifetime from displacement damage will cause an increase in I_s with a subsequent increase in diode current. At higher currents, however, this behavior changes as conductivity effects become dominant. The voltage applied at the diode terminals, V_A, and the junction potential, V_D, differ by

$$V_D = V_A - V_B \tag{25}$$

where V_B is the voltage drop due to the material conductivity. In general, for most material and doping levels used in diode manufacture, conductivity decreases will occur under bombardment. At higher current levels, V_B will become increasingly

significant, lowering the junction potential which, according to the diode equation, will reduce the current. The typical behavior of the semiconductor diode characteristic after successive exposures is shown in Figure 4-5.

4.1.3 CALCULATIONAL PROCEDURE FOR ESTIMATING BULK EFFECTS FOR THE VOYAGER INTERNAL ENVIRONMENT

The discussion of the bulk damage mechanisms has shown that the damage constant must be experimentally determined by irradiation in the laboratory. It is obviously impossible to simulate the complex space radiation environment in the laboratory, so the damage constants are determined for monoenergetic beams of electrons and protons in accelerators or fast fission neutrons in reactors. To estimate the effects produced by the complex Voyager internal radiation environment, it is necessary to develop a procedure which will reduce the spectrally distributed electrons and protons to an equivalent particle flux which can be produced in a reactor or accelerator. The first step then requires the selection of the most convenient equivalent flux, one which will allow the fullest use of existing data. Because of economy and availability, almost all of the transistor radiation effects experiments have been performed under reactor irradiation resulting in a scarcity of proton and especially electron data. For this reason, the incident proton and electron spectrums are reduced to an equivalent fast (average energy $\sim$1 MEV) fission spectrum neutron flux (Figure 4-6). The criteria for equivalence was chosen to be equal damage production. Therefore, the object of the following calculations will be to reduce the internal environment given in Section 1 to an equally damaging fast neutron flux. Specifically, the approach will involve these three steps:

a. Reduction of the internal electron and proton spectrums to equivalent monoenergetic fluxes by simple displacement theory.

b. Conversion of these monoenergetic fluxes to an equivalent fast neutron flux by the application of experimentally determined proton-neutron and electron-neutron damage equivalence factors.

c. Application of damage constants measured under neutrons and the equivalent fast neutron flux determined in steps b and c to predict the degradation in transistor and diode paramerters.

4.1.3.1 DETERMINATION OF THE EQUIVALENT MONOENERGETIC FLUX

If it is assumed that the type of defects formed are independent of particle energy and vary only with the type of particle (whether it is proton, neutron, electron, etc.), then it follows that the damage produced by particles of different energy (but of the same type) will be proportional to the number of atomic displacements produced by each. For example, the relative effectiveness of 1 MEV protons to 10 MEV protons would depend on the ratio of the number of atomic displacements produced at 1 MEV to those produced at 10 MEV and if the 1 MEV particle produces one hundred times as many displacements per unit track length, then one 1 MEV proton can be assumed

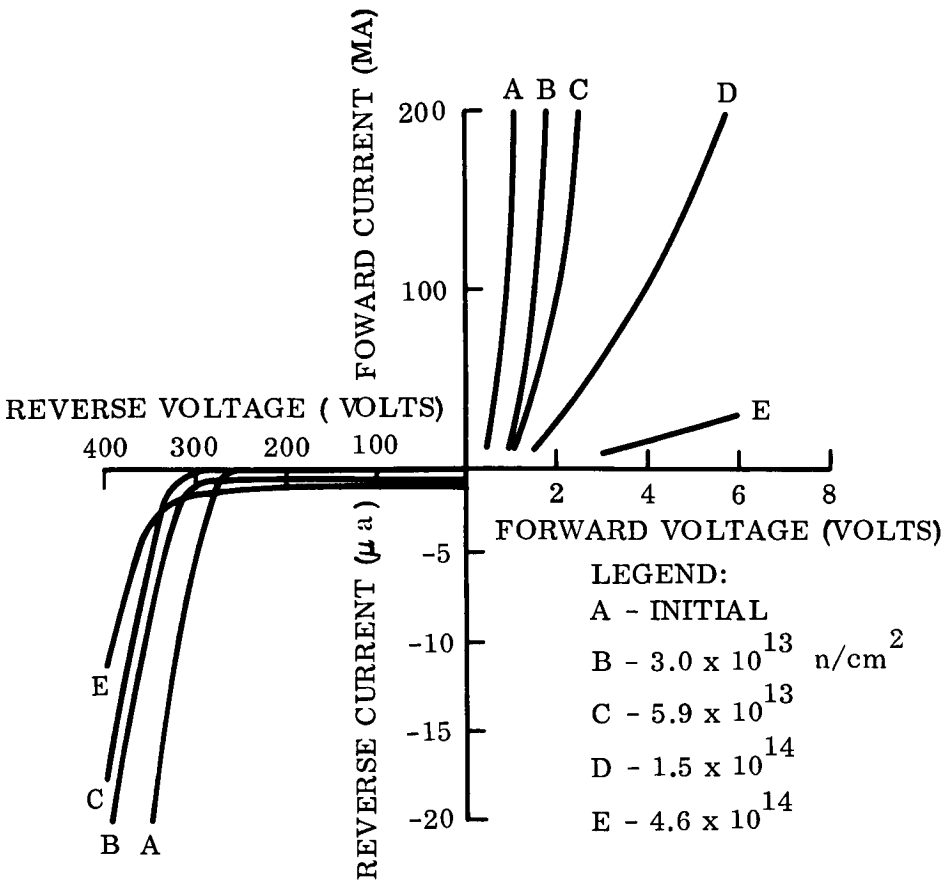

Figure 4-5. Typical Diode Characteristics After Successive Irradiations

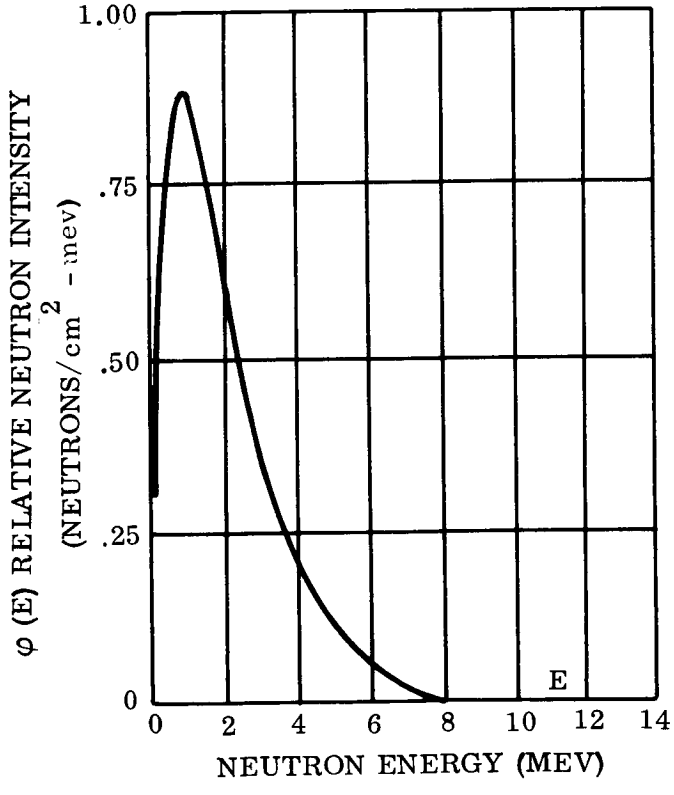

Figure 4-6. Typical Differential Energy Spectrum of Fast Fission Neutrons

to be equivalent to one hundred times as many displacements per unit track length, and one 1 MEV proton can be assumed to be equivalent to one hundred 10 MEV protons. For the most part, these assumptions are not strictly true. For example, in most cases, a high energy particle will cause a different type of defect (i.e. how it behaves electrically) than a low energy particle. This effect of defect type as a function of particle energy will be briefly discussed later. For the moment, however, assume that equal atomic displacement densities will produce equal damage. Now, if the particle energy loss in the material is small compared to the incident energy, the number of atomic displacements/cm^3 produced by a spectrum of particles may be obtained by weighting the differential spectrum φ (E) with an energy dependent displacement function, η_D (E) and integrating over all energies. Therefore,

$$\eta_{DT} = \int_{-\infty}^{+\infty} \eta_D (E) \, \varphi (E) \, dE \tag{26}$$

where

η_{DT} - total number of displacements/cm^3 produced

$\eta_D(E)$ - number of displacements/cm produced by a particle of energy E.

φ (E) - differential flux (particles/cm^2 - MEV)

Now if the total number of displacements/cm^3 produced by the monoenergetic particle flux, F (E_1), of energy E_1, is given by

$$\eta_{DT} = F (E_1) \, \eta_D \, (E_1) \tag{27}$$

then the monoenergetic flux, F (E_1), required to produce the same damage as the spectrum defined by φ (E) may be obtained by equating the displacement densities produced by each. Therefore,

$$F (E_1) = \frac{1}{\eta_D (E_1)} \int_{-\infty}^{+\infty} \eta_D (E) \, \varphi(E) \, dE \tag{28}$$

At present, there is no transistor data which can confirm this premise, however, solar cell data does tend to verify these assumptions for protons in the 10 - 500 MEV range (Reference 4). Outside this range, the data shows departures from this simple behavior indicating a change in the type of defect being formed. However, a look at the internal proton spectrum, Figure 2-6, shows that most of the particles lie in the 10 - 500 MEV energy range. Therefore, the error resulting from using simple displacement theory will be small compared to other errors.

Similarly, for electrons, insufficient transistor data forces the use of solar cell data to investigate the correctness of simple displacement theory. In the range of 0.5 - 2 MEV, observed damage correlates well with displacement theory prediction. For energies above this, experimenters (Reference 8) have found that electrons are much more damaging than the theory indicates with 5.6 MEV electrons ~ 10 - 20 times more effective. Again, this is probably due to the formation of a defect, possibly a divacancy, that is a much more efficient trapping center than those formed by less energetic particles. For energies less than 0.5 Mev experimental data (Reference 12) tends to show less damage than predicted. Simple displacement theory uses a minimum value for the atomic threshold displacement energy, E_D, and does not correct for variations in incident particle direction within the crystal (i.e., straggling). This is somewhat unrealistic at particle enrgies (<0.5 Mev) where the transferred energy (recoil energy) is comparable to E_D with the result that a greater number of atomic displacements are predicted than actually occur, since E_D can increase significantly above the minimum value along other crystal axes. Therefore, lower energy particles appear to be more damaging than observed. The internal electron environment is such that the bulk of the spectrum lies within the .5 - 2 MEV range so that these high and low energy effects will not cause a significant error. Also, since displacement theory is optimistic at higher energies and pessimistic at lower energies, there is a degree of error compensation present. Therefore, the application of simple displacement theory should be suitable for this analysis and will enable the conversion of the internal spectra to equivalent monoenergetic fluxes. To evaluate equation (28), it is necessary to determine the displacement function $\eta_D(E)$. Since $\eta_D(E)$ depends on particle type and material it must be evaluated for both electrons and protons in both silicon and germanium.

4.1.3.1.1 PROTONS

The dominant class of collisions for atomic displacements for protons of energy less than 500 MEV is Rutherford scattering in which the coulomb fields of the proton and the nuclei interact to permit the exchange of momentum and energy. Above 500 MEV, significant nuclear disintegrations begin to occur which give rise to neutrons, protons, alpha particles, etc. of just about the right energy (5-20 MEV) to produce a large number of secondary displacements. At present, a good model of this process is not available. However, this is not a serious consequence for the present analysis since most of the protons are below 500 MEV. Simple displacement theory states that the mean number of displaced atoms/cm produced by an incident particle of energy E is given by

$$\eta_D(E) = N_A \sigma_o \overline{\nu} \tag{29}$$

where

σ_o - the displacement cross section

$\overline{\nu}$ - the mean number of secondary displacements per primary recoil

N_A - atomic density of the lattice (atoms/cm^3)

For protons, the application of classical collision theory yeields the following relation for the displacement cross section from Rutherford scattering:

$$\sigma_D = \frac{4 \pi a_o^2 Z^2 E_R^2}{E E_D M} \tag{30}$$

where

- E - atomic number of the lattice atoms
- M - atomic weight of the lattice atoms
- E_D - Threshold energy for displacement of the lattice atom*
- E_R - the Rydberg energy (13.6 ev)
- a_o - Bohr radius of hydrogen (5.29×10^{-9} cm)
- E - proton energy

The mean number of secondary displacements is given by

$$\bar{\nu} = 0.107 + 0.561 \ln \frac{Tm}{E_D} \qquad \left(\frac{Tm}{E_D}\right) >> 1 \tag{31}$$

where

$$Tm = \frac{4 M E}{(M+1)^2} \tag{32}$$

Substituting equations (30) and (31) into (29), the mean number of displaced atoms/cm produced by an incident proton of energy E becomes,

$$\eta_D (E) = \frac{4 \pi N_A a_o^2 E_R^2 Z^2}{E E_D M} \left(0.107 + 0.561 \ln \left(\frac{Tm}{E_D}\right)\right) \tag{33}$$

*It is assumed that each lattice atom is bound to its normal site in a square potential well of depth E_D.

The minimum energy, E_D, for displacement is dependent upon the material, temperature, and the direction of recoil with respect to the crystal axes. Experimental measurements indicates minimum values for E_D of 13 ev in silicon and 31 ev in germanium. Substituting appropriate values for the constants, the proton displacement functions become in silicon

$$\eta_D (E) = \frac{964}{E} (9.43 + \ln E) \tag{34}$$

and in germanium

$$\eta_D (E) = \frac{735}{E} (7.66 + \ln E) \tag{35}$$

4.1.3.1.2 ELECTRONS

Similarly, for electrons in the 0.1 to 10 MEV energy range, the dominant mechanism is also Rutherford scattering caused by interaction between the electron and the nuclear charge. However, the determination of the displacement cross section is more complicated since, because of its smaller mass, an electron must move at relativistic speeds to produce atomic displacements. The displacement cross section for relativistic Rutherford scattering for an electron of energy E is given by

$$\sigma_o = \frac{\pi b^2}{4} \left[\left(\frac{T_M}{E_D} - 1 \right) - \beta^2 \ln \left(\frac{T_M}{E_D} \right) + \pi \alpha \beta \left\{ 2 \left[\left(\frac{T_M}{E_D} \right)^{1/2} - 1 \right] - \ln \left[\frac{T_M}{E_D} \right] \right\} \right] \tag{36}$$

where

$$\frac{\pi b^2}{4} = \frac{2.5 \times 10^{-25} Z^2}{\beta^4 \gamma^2} \qquad \beta = \frac{V}{c} ; \quad \alpha = \frac{Z}{137}$$

$$T_M = \frac{560.8}{M} \left(\frac{E}{.511} \right) \left(\frac{E}{.511} + 2 \right)$$

V = electron velocity (cm./sec.)

c = speed of light (cm./sec.)

E = electron energy (MEV)

the mean number of secondary displacements per primary collision is given by

$$\overline{\nu} = \left[0.107 + 0.561 \ln \frac{T_M}{E_D} \right] \frac{T_M}{T_M - E_D} \qquad \frac{T_M}{E_D} > 2 \tag{37}$$

$$\overline{\nu} = 1 \qquad \frac{T_M}{E_D} < 2$$

The mean number of displacements/cm. can then be computed from

$$\eta_D(E) = N_A \, \sigma_D(E) \, \overline{\nu}(E) \tag{38}$$

The equations above have been evaluated for silicon and germanium and the displacement functions are plotted in Figure 4-7. The functions for protons are also shown and one can see that the curves illustrate the much greater effectiveness of protons over electrons in displacement production. The relative improvement of germanium vs. silicon is also evident. Since the best particle correlation data available was found to be between 1 MEV electrons and fast neutrons and 30 MEV protons and fast

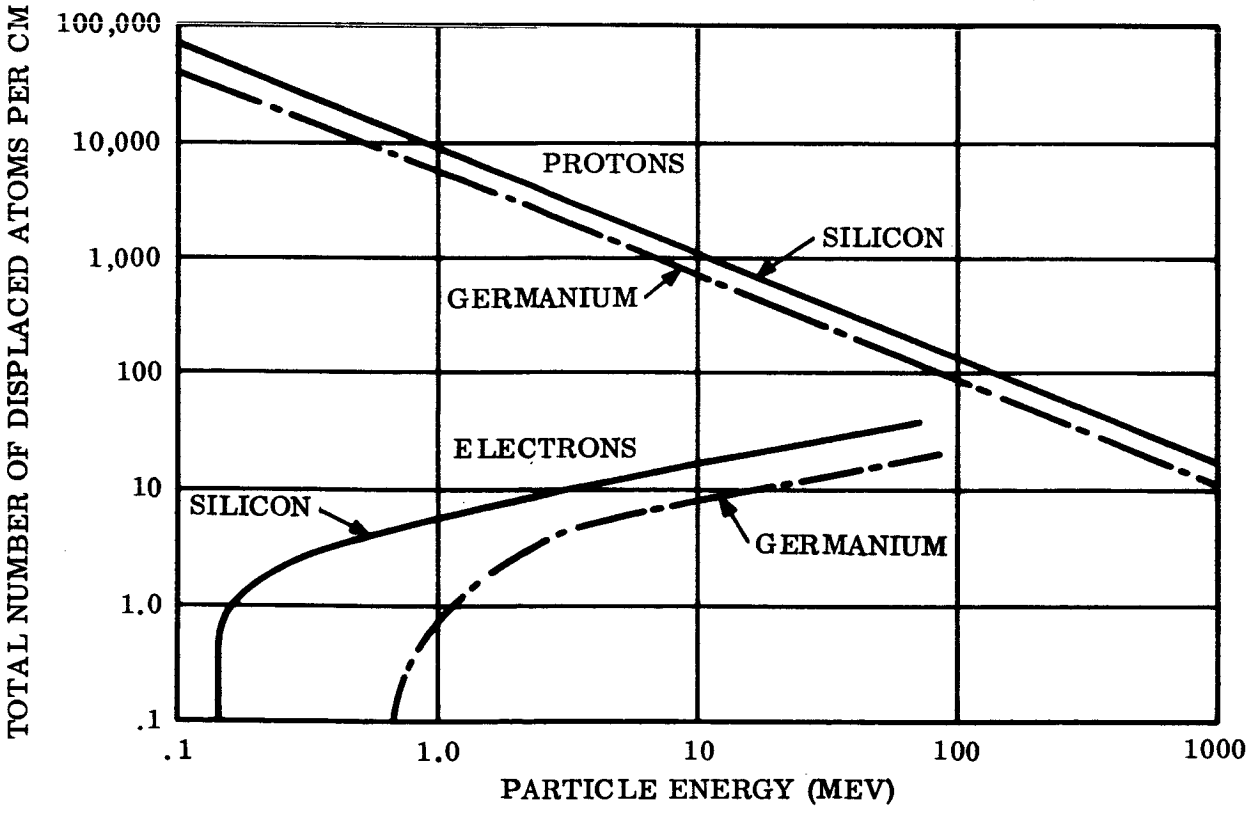

Figure 4-7. Displacement Functions for Electrons and Protons

neutrons, the electron spectrum will be reduced to an equivalent 1 MEV electron flux and the proton spectrum will be reduced to an equivalent 30 MEV proton flux. For a 30 MEV equivalent proton flux, equation (28) becomes

in silicon

$$F_P(30) = \frac{1}{420} \int_{-\infty}^{+\infty} \eta_D(E)\ \varphi_P(E)\ dE \tag{39}$$

in germanium

$$F_P(30) = \frac{1}{270} \int_{-\infty}^{+\infty} \eta_D(E)\ \varphi_P(E)\ dE \tag{40}$$

where

$$\varphi_P(E) = \text{protons/cm}^2 - \text{MEV}$$

The equivalent 1 MEV electron flux is given by

in silicon

$$F_e(1) = \frac{1}{5.6} \int_{-\infty}^{+\infty} \eta_D(E)\ \varphi_e(E)\ dE \tag{41}$$

in germanium

$$F_e(1) = \frac{1}{0.7} \int_{-\infty}^{+\infty} \eta_D(E)\ \varphi_e(E)\ dE \tag{42}$$

where

$$\varphi_e(E) = \text{electrons/cm}^2 - \text{MEV}$$

A 7090 computer program has been coded to evaluate equations (39), (40), (41), and (42). Essentially, the program numerically integrates the appropriate displacement function over the internal electron and proton spectrums computed in Section 1.

4.1.3.2 CONVERSION OF THE EQUIVALENT MONOENERGETIC FLUXES TO AN EQUIVALENT FAST NEUTON FLUX

The final step in the determination of the equivalent fast neutron flux requires the selection of appropriate damage equivalence factors between neutrons, protons, and electrons. The monoenergetic fluxes computed in Section 3.1.3 (a) can thus be converted to equivalent fast neutron fluxes. The effects of the proton and electron spectra will then be reduced to a common denominator and the total equivalent fast neutron flux will be equal to the sum of the equivalent neutron flux for protons and the equivalent flux for the electrons. Unfortunately, determining an equivalence between particles of different types is not easily done. Here the equal damage for equal displacements assumption does not hold since the type of defects produced are no longer the same. Therefore, direct experimental data rather than simple displacement theory must be relied on to determine the damage equivalence. Equal damage correlations have been performed between various proton energies (References 3, 5, 10) and fast fission neutrons. Similarly, correlations have been performed between various electron energies (5, 10) and neutrons. In what follows, the damage equivalence factor, Δ, of a particle is defined to be the ratio of the fast neutron flux to the particle flux required to produce equal damage. Damage equivalence factors determined from the correlations listed above are displayed in Figure 4-8 for protons and in Figure 4-9 for electrons. One can see that an extremely wide spread exists

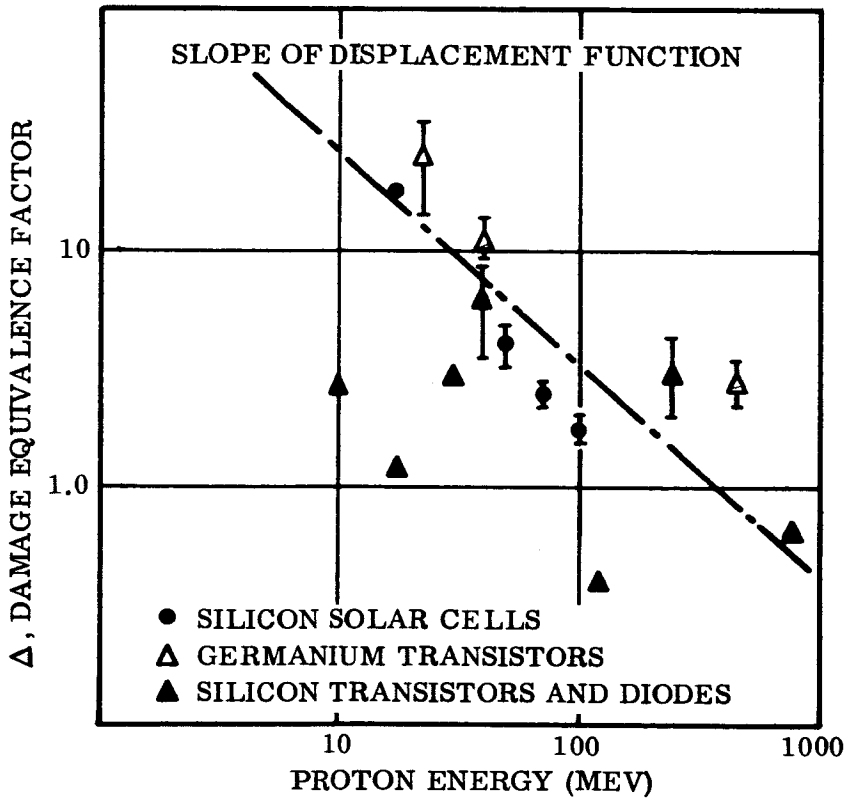

Figure 4-8. Proton - Neutron Damage Equivalence Factors

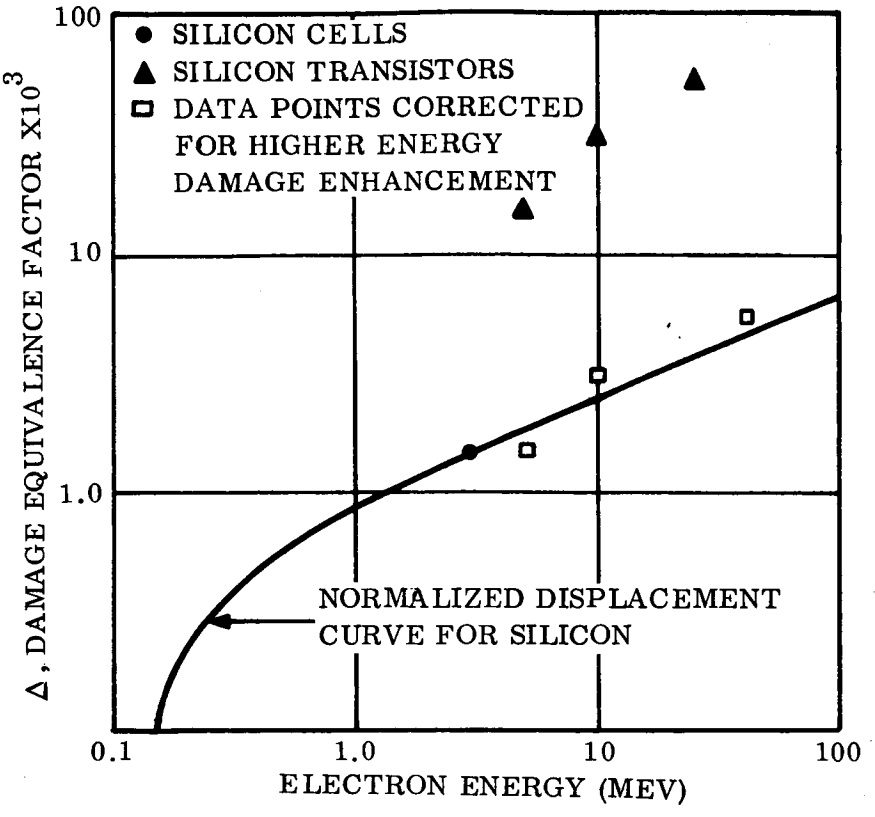

Figure 4-9. Electron - Neutron Damage Equivalence Factors

in the data. This is because most of the data points represent measurements made on differenct types of devices (solar cells vs. transistors), poor sample sizes, different semiconductor materials, etc. An average value for Δ for 30 Mev protons was determined for use with the 30 Mev monoenergetic flux computed in part 3.13 (a). A data point at energy E was referred to 30 Mev by correction for the number of displacements produced relative to those at 30 Mev, i.e.

$$\Delta(30) = \frac{\eta_D(30)}{\eta_D(E)} \Delta(E) \tag{43}$$

All values thus obtained were averaged giving a mean value of $\bar{\Delta}$ (30) $\approx$ 10, at 30 Mev. Because of the wide spread in the data, the damage equivalence factor was taken to be the same in silicon and germanium. The determination of an average value for Δ for 1 Mev electrons is a more difficult problem. A glance at Figure 4-9 will show that all but one of the data points lie above 2 Mev. These higher energy points cannot be easily referred back to 1 Mev since, as previously pointed out, simple displacement theory does not apply to these higher energies. The 1 Mev data point represents an average of p/n and n/p, 1 ohm-cm., solar cell data (Reference 10). Cross correlations with available data (Reference 3) give a fair degree of confidence in this point. To provide an additional check, the displacement function for electrons in silicon was normalized to the 1 Mev data point and plotted as shown in Figure 4-9.

Data presented in Reference 11 shows the average of N/P and P/N solar cell damage constants at 3 Mev to be 4.6 times the 1 Mev value. The point is plotted in Figure 4-9. Other solar cell data (Reference 8) on high energy electrons indicates that 5.6 Mev particles are approximately ten times as damaging as displacement theory indicates. The points for 5 Mev and above represent data from Reference 12 for silicon npn transistors. These points were reduced by a factor of ten in accordance with the results from Reference 8 and are plotted as squares. It can be seen that by correcting the high energy data to account for the change in the type of defect formed reasonable good agreement is obtained with the normalized displacement curve. Since the curve was normalized to the 1 Mev Δ, this exercise provides additional confidence in the validity of the data. Accordingly, $\bar{\Delta}$ (1) = 8.3×10^{-4} is used as the damage equivalence factor for electrons.

Now if φ_{np} is defined as the equivalent neutron dose for protons, then

$$\varphi_{np} = \bar{\Delta}\,(30)\,F_p\,(30) = 10\,F_p\,(30) \tag{44}$$

Similarly, if φ_{ne} is the equivalent neutron dose for electrons, then

$$\varphi_{ne} = \bar{\Delta}\,(1)\,F_e\,(1) = 8.3 \times 10^{-4}\,F_e\,(1) \tag{45}$$

the total equivalent neutron dose, φ_{nT} is then

$$\varphi_{nT} = \varphi_{ne} + \varphi_{np} \tag{46}$$

By utilizing these calculational techniques and the internal particle spectra derived in Section 1.3, the equivalent neutron dose as a function of shield thickness can be obtained. These results are shown in Figure 4-10 for various assumptions on the Martian belt intensity and represent the total accumulated equivalent neutron dose in both silicon and gemanium for the entire 1971 mission for each assumption.

From a consideration of the spacecraft structure, packaging, etc., it appears that a shielding of at least 1.0 gms/cm^2 ($\sim$ 0.5 cm of equivalent aluminum) will exist for all internal components. Considerably more shielding will be afforded many of the components. However, taking 1.0 gm/cm^2 as the minimum shielding and comparing the equivalent neutron doses of Figure 4-10 with the gain degradation of Figure 4-3, the following observations on bulk damage can be made:

a. For a Martian radiation belt intensity up to 100 times the Earth's belt intensity, the total mission dose, including solar flares, will be on the order of 10^{11} equivalent neutrons/cm^2 for the minimum shielding case. This does not constitute a serious radiation dose, except for some possible high gain, low frequency ($f_{\alpha o}$ < 1.0 mc) silicon power transistors.

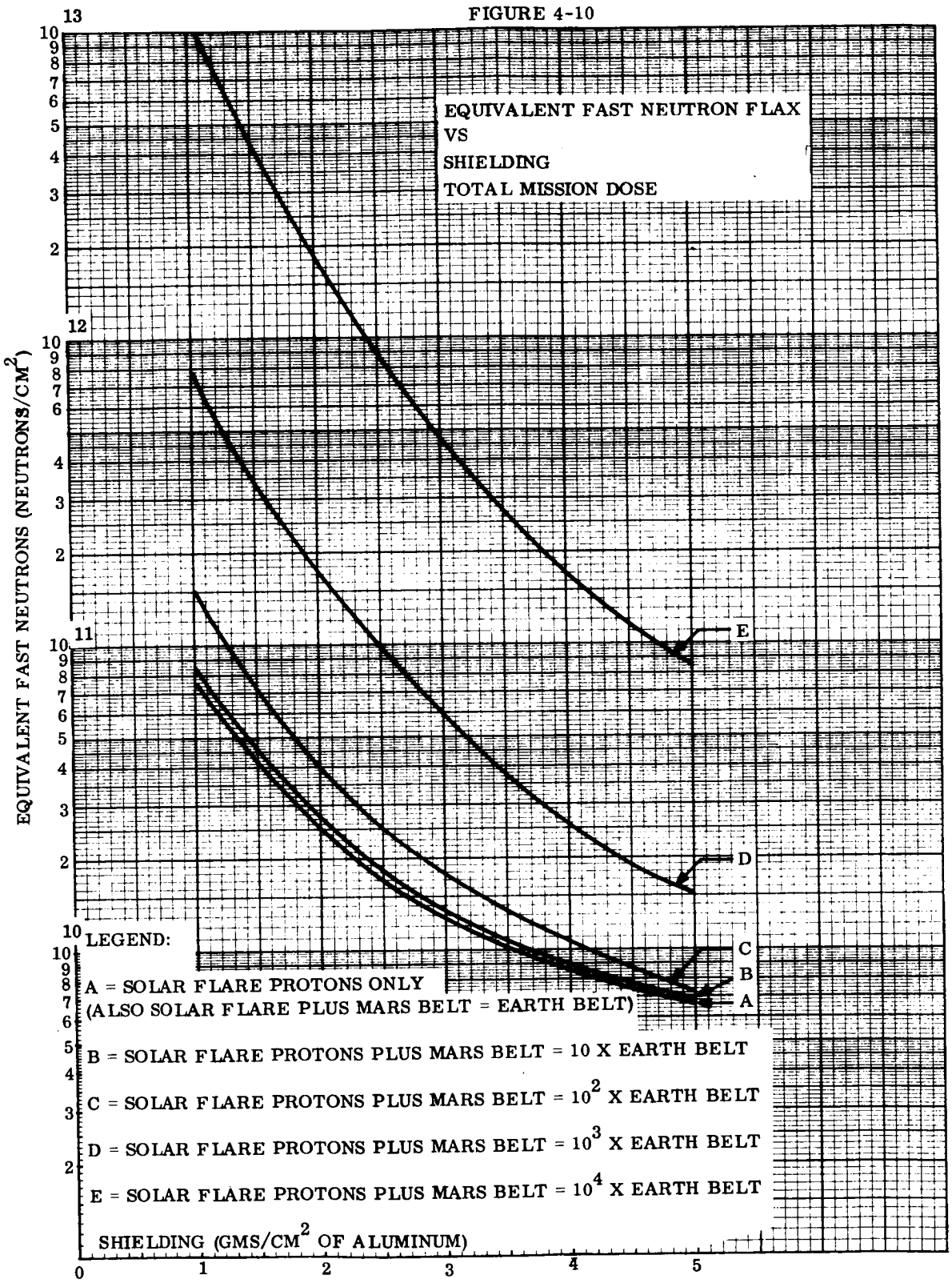

Figure 4-10. Equivalent Fast Neutron Flux Versus Shielding, Total Mission Dose

b. For a Martian radiation belt 1000 times as intense as the Earth's belt, the equivalent neutron dose with 1.0 gm/cm^2 shielding will be nearly 10^{12} neutrons/cm^2 for the entire mission. This dose does not pose a serious threat to the high frequency ($f_{\alpha o}$> 100 mc) signal devices. However, derating requirements would have to be imposed on most high gain, medium frequency ($f_{\alpha o}$ < 50 mc) signal transistors such as the 2N2432, 2N930 and 2N2453 devices. Also derating and/or shielding would have to be imposed on the power electronics.

c. The assumed "worst-case" environment for the Martian radiation belts that is 10^4 times as intense as the Earth's belt would pose some very serious design problems. The equivalent neutron dose would be 10^{13} neutrons/cm^2 behind 1.0 gm/cm^2 shielding. This would require derating of all transistors including the high frequency units. Also, additional shielding would probably be required for the medium frequency devices. The power electronics would definitely require shielding. The required shielding for the power transistors would be approximately 5 gms/cm^2 (about 2 cm of aluminum) in order to reduce the dose to about 10^{11} neutrons/cm^2. Judicious placement within the spacecraft of particularly sensitive components in order to benefit from the shielding afforded by less sensitive components could help appreciably in achieving the required shielding without increasing weight. This "worst-case" environment would not pose a serious threat to most diodes, although some derating may be required in specific applications. Also this dose is not considered to pose a serious threat to microelectronic circuits, since most of the transistors in these circuits have a frequency capability on the order of 1000 megacycles.

4.2 SURFACE EFFECTS

In contrast to the reasonably well understood and controllable effects due to bulk damage in transistors, the radiation induced surface effects are not nearly as well understood or controllable. Basically, the effect is thought to arise from the interaction of the gas, which is encapsulated in the transistor can, and the semiconductor surface. One of the main reasons for the encapsulating gas, usually dry nitrogen, is to control surface contaminants and to maintain a controlled atmosphere surrounding the semiconductor surface. Normally this results in very stable surface characteristics. However when the transistor is under the influence of an ionizing radiation, a wholly different situation can exist. First the encapsulating gas becomes ionized and maintains a certain state of ionization as long as it is exposed to a radiation field. The ionized gas can, as a consequence of its ionized state, more readily interact with the semiconductor surface. Moreover, the ionized gas is essentially a plasma and as such will be influenced by the electric fields that surround the semiconductor junctions which depend upon the biasing conditions on the device. The degree to which the gas interacts with the semiconductor surface depends very strongly on the nature of the surface itself. For example, mesa nonpassivated, devices have the bare semiconductor junctions exposed directly to the ionized gas as compared to a planar passivated device which has a thin insulating layer of silicon dioxide covering the semiconductor

junctions. The result is that non-passivated devices are, in general, much more sensitive to induced surface phenomena than passivated devices. The problem is further complicated by the fact that surface impurities also play a dominant role in the effect. These impurities can contribute to the effect in basically two ways. First, they can be directly ionized by the incident radiation. Second, they can play an intermediate role and act as efficient charge exchangers with the ionized gas and the semiconductor surface.

Further insight into this phenomenon can be obtained by considering the mesa type NPN transistor shown in Figure 4-11(a). The exposed junctions produce a fringing electric field between the collector and base junction. For a reverse-biased collector the direction of the field lines are such as to cause ionization-produced electrons to deposit on the collector side while positive gas ions are attracted to the base, resulting in the production of inversion layers on the surface (Figure 4-11(b). This process is often referred to as the channeling effect. The presence of the inversion layer results in an increase in the effective area of the collector-base junction causing an increase in the reverse collector saturation current. In addition, the reverse resistance is lowered since the inversion layers also act as conducting paths. The total result can be large increases in I_{cbo}, the collector-base leakage current. Similar channeling effects can occur at the emitter junction and will act to increase the injection of holes from the base to the emitter. These will add to the total emitter current but will make no contribution to the collector current. Thus, this process acts to diminish the emitter efficiency, thereby lowering the current gain. It has also been found that if the collector is electrically connected to the transistor can, the resulting electric field will increase the ion collection efficiency thereby magnifying the effect.

Identical phenomena can, of course, take place in a planar passivated device, except they will be modified by the presence of the passivation layer as can be seen by considering the schematic of Figure 4-12. Theoretically, a silicon planar transistor would be less sensitive to the surface effect since it has a passivated layer of silicon dioxide on its surface to provide insulation of the semiconductor surface and junctions from the ambient environment. This process of surface passivation has greatly reduced the variability of device characteristics as far as device manufacturing is concerned. Theoretically, it should also improve the stability of the device when operating in an ionizing radiation environment since the passivated layer would tend to reduce the fringing field thereby reducing the collection efficiency of the ions that are produced in the gas by the radiation. Although some ions still can collect on the passivated surface, their effectiveness in inducing channeling is reduced since they are physically separated from the charges in the semiconductor material by the thickness of the passivated layer, resulting in a square law attenuation of the force between the charges. In practice, however, the improvement is not as significant as might be expected. Apparently, this is due to the non-uniformity in the passivated layer, and that it is not physically thick enough to appreciably reduce the fringing field and the channeling effect caused by surface collection of the ionized gas. Experiments have shown that the effect is primarily dependent on the total dose rather than dose rate (Reference 13). Since the effect is produced mostly by the ionization of the encapsulating gas, it is essentially

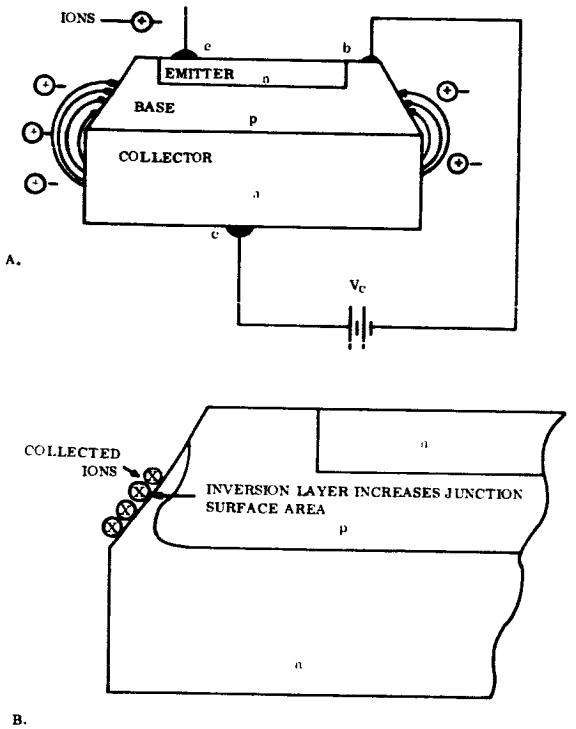

Figure 4-11. The Surface Effect in the Mesa Transistor

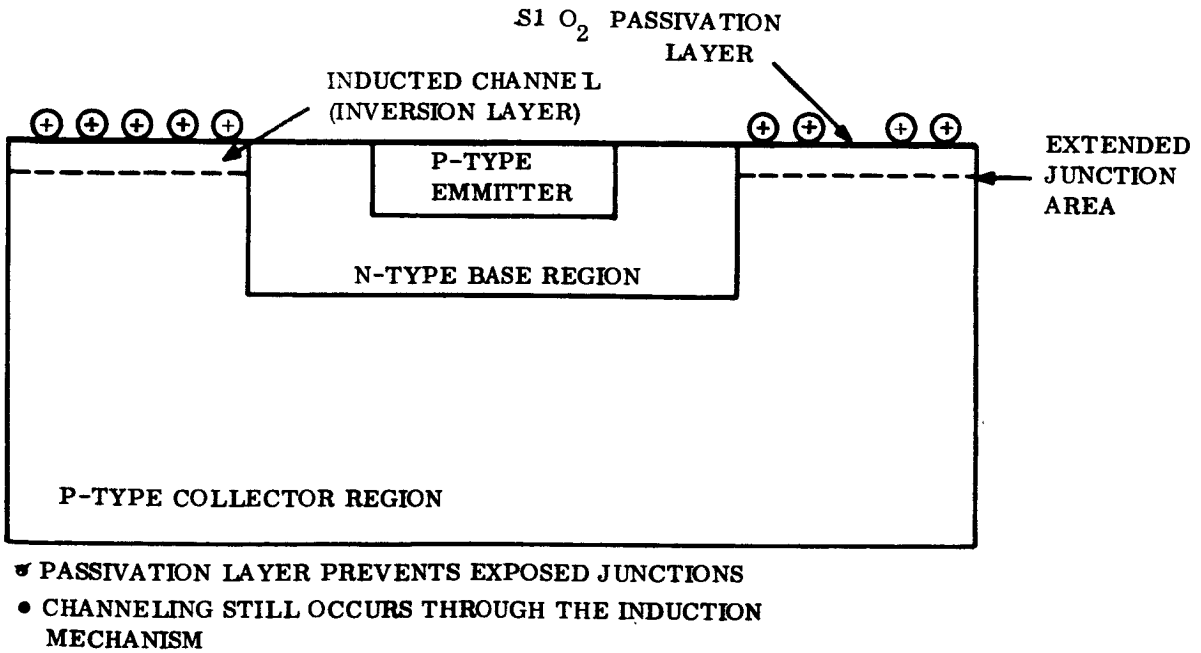

Figure 4-12. Planar Transistor Structure

independent of the type of incident ionizing particle and depends only on the particle energy loss in the gas. Also there does not appear to be any strong correlation between alpha cutoff frequency ($f_{\alpha o}$) and degradation as exists for bulk effects. High frequency transistors appear to be affected just as readily as low frequency units. The Spacecraft Department of the General Electric Company has been conducting a company funded experimental radiation program to further investigate this problem for the past year. The radiation experiments that have been carried out under this program have utilized low energy X-rays (50 Kev) as the ionizing radiation source. As such, all the effects seen are thus due to surface phenomena only, since 50 Kev X-Rays are incapable of causing bulk damage. Much of the data presented below has been obtained under this program.

4.2.1 EFFECTS ON TRANSISTOR PARAMETERS

Two of the most sensitive transistor parameters to surface effects in both passivated and non-passivated devices are the collector-base leakage current, I_{CBO}, and the current gain, β.

4.2.1.1 EFFECTS ON I_{CBO}

In general, non-passivated devices are much more sensitive to I_{CBO} variations than passivated devices. Figure 4-13 shows an example of I_{CBO} variations in 2N335A non-passivated devices as a function of radiation dose. As can be seen, the increases can be quite severe and varied. This sort of behavior is somewhat typical for non-passivated devices. In general, a threshold for large I_{CBO} increases for non-passivated devices appears to be between 10^3 and 10^4 Rads (Air), although there is a large variability about this threshold for many devices.

It is much more difficult to make generalizations about I_{CBO} increases on passivated devices. For example, Figures 4-14 and 4-15 show I_{CBO} variations for 2N1893 and 2N2432 devices respectively. Each type was made by a different manufacturer. As can be seen, large variations are again present, with a threshold between 10^4 and 10^5 Rads (Air). On the other hand, this past year, the GE Spacecraft Department has tested hundreds of passivated 2N708, 2N914, 2N930, and 2N2453 devices made by a still different manufacturer; none of these devices showed any significant I_{CBO} increases up to doses of approximately 10^6 Rads (Air), the maximum dose for these experiments. Thus it appears that the quality of the passivation on the collector-base junction is a controlling factor here. This implies that in order to ensure stable collector-base junction characteristics for doses exceeding 10^4 Rads (Air), sample monitoring of a manufacturer's production line would have to be maintained.

4.2.1.2 EFFECTS ON β

As was pointed out in the previous section, many devices can be made very stable in their collector-base leakage characteristics by proper passivation of the collector-base junction. Unfortunately this improvement does not follow through for the

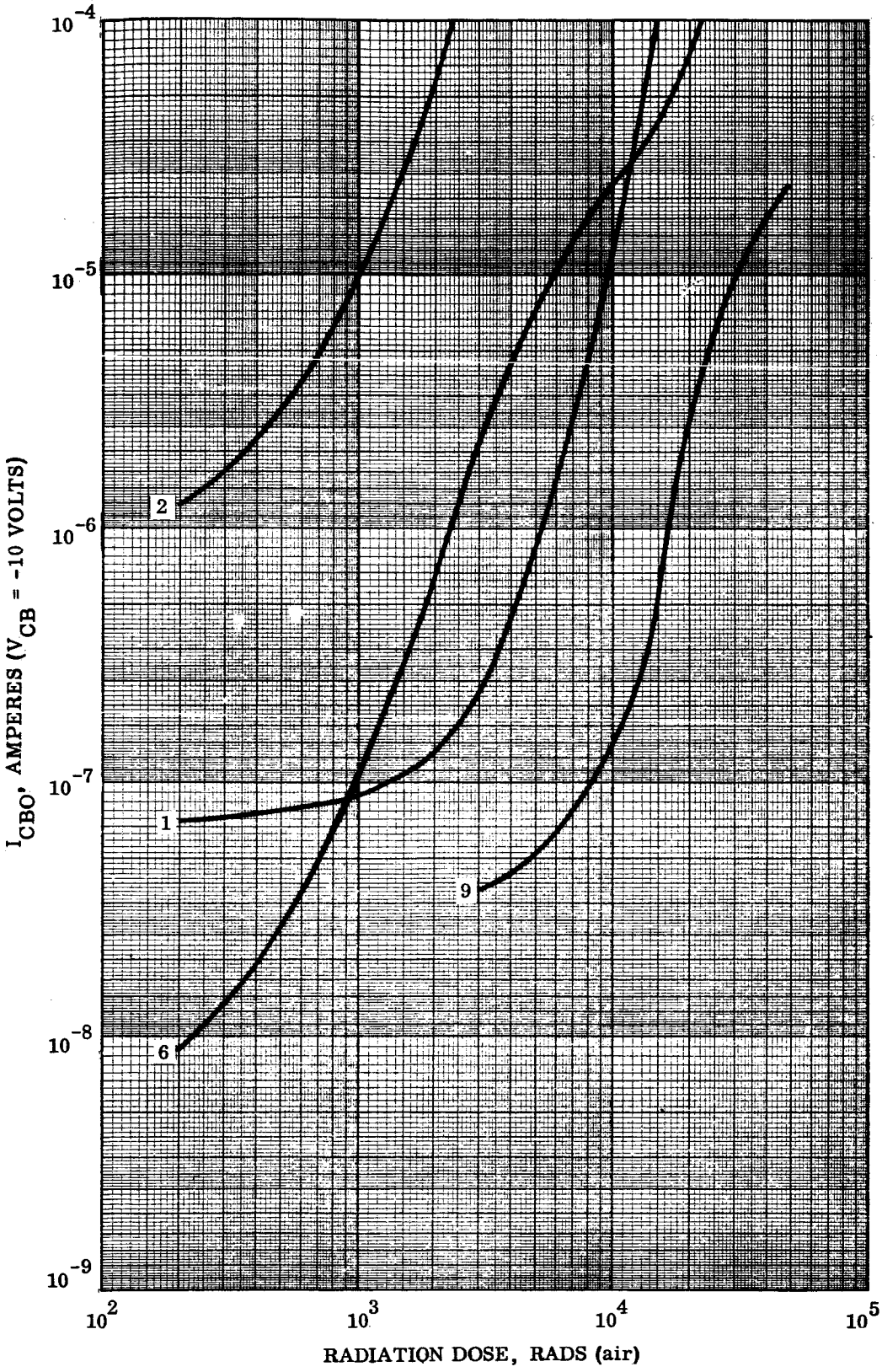

Figure 4-13. I_{CBO} Versus Radiation Dose, 2N335A

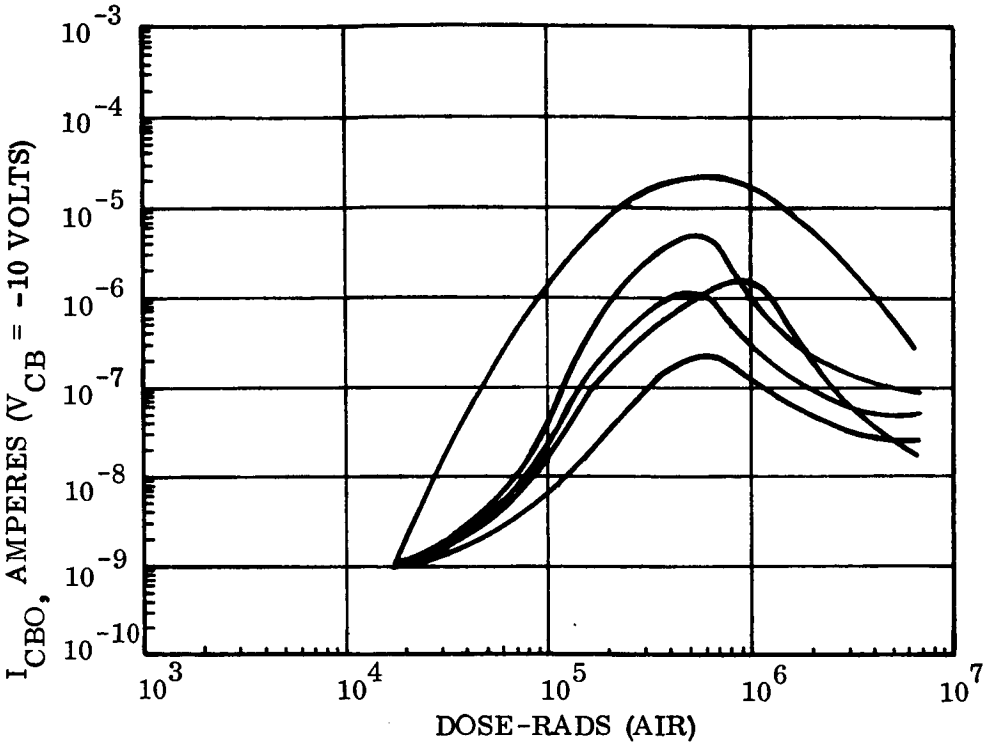

Figure 4-14. I_{CBO} Variation With Dose, 2N1893

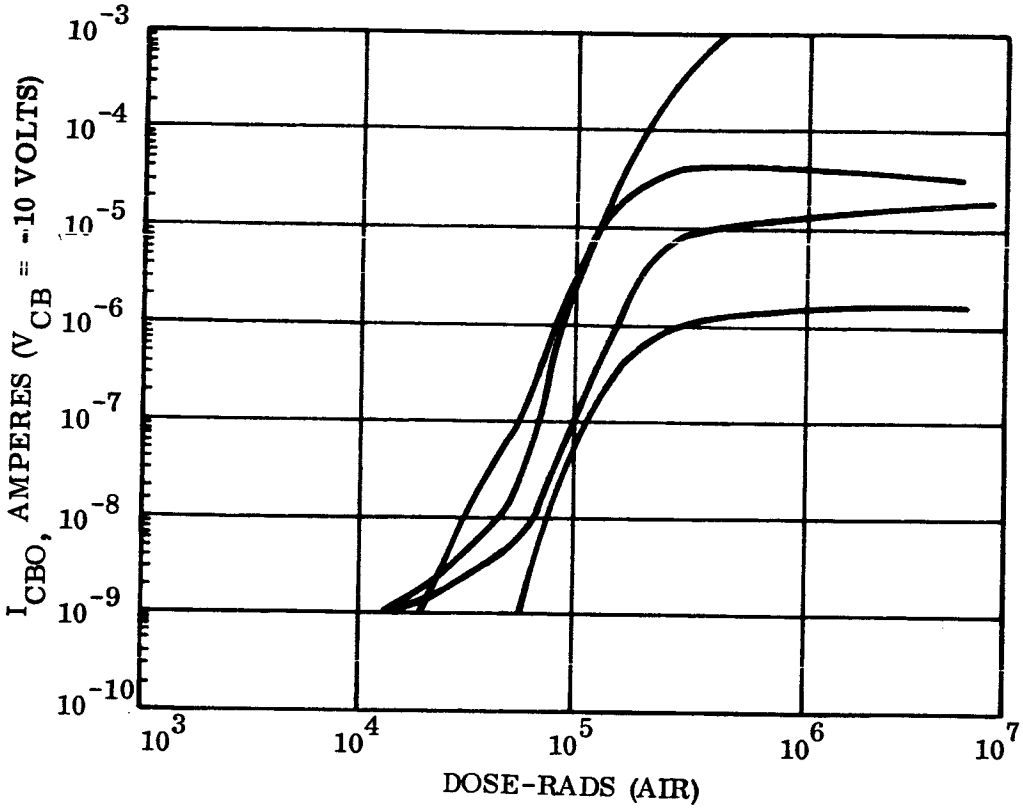

Figure 4-15. I_{CBO} Variation With Dose, 2N2432

base-emitter junction, quite possibly because the passivation in this region is more difficult to control. As a result, the transistor gains for both passivated and non-passivated devices are still very much affected by induced surface effects. An example of this is shown in Figure 4-16 for 2N708 devices. The data shown is the average of 30 units. None of these units showed much sensitivity to I_{CBO} changes. However, as can be seen, large gain changes were observed. Similar results have been obtained on previous experiments using Cobalt-60 gamma rays (Reference 14). The data shown in Figure 4-16 is the average gain degradation for different current levels in the devices. As can be seen, the degradation is much more severe for the lighter current levels. These results are typical of those seen on hundreds of these devices tested to date.

Figure 4-17 shows a similar set of data for 2N914 devices. These particular 2N914 devices were obtained from the same silicon wafer as the thirty 2N708 devices shown in Figure 4-16. That is, these two types of units were made at the same time, on the same piece of silicon, with identical masks, etc.

Silicon power transistors appear to be as sensitive to induced surface effects as the signal devices. An example of this is shown in Figure 4-18 for some 2N2658, five ampere silicon units. The current level at which data was taken was only 10 ma however.

Germanium power devices, on the other hand, appear to be much less sensitive to surface effects than silicon units. Figure 4-19 shows the variation in I_{CEX} on several 2N1358 and Honeywell, Inc. MHT2305 power devices. As can be seen, little variation is noted in I_{CEX}. Somewhat surprising results have been seen on the gain variation of these germanium units. These results are shown in Figure 4-20, where the gains are seen to actually increase significantly. No reasonable explanation has been found for this behavior.

It is interesting to note that all of the above effects on current gain are essentially of a permanent nature, at least at room temperature. The I_{CBO} variations, on the other hand, generally, show a quick recovery once they are removed from the radiation. The gain degradations can be removed rather easily, however, by maintaining the devices at moderately high annealing temperatures for short periods of time (10 minutes at 300°C.).

4.2.1.3 EFFECTS OF BIAS

As was mentioned previously, the magnitude of the induced surface effects is strongly influenced by the biasing conditions of the transistor. One example of this is shown in Figure 4-21, which shows the gain degradation of the 2N708 device as a function of radiation dose for several different current levels in the device. The device was initially held in a reverse biased state with 10 volts reverse bias on the base-emitter junction. As can be seen the gains decreased in the usual fashion, as seen before. At point "A" however, the reverse bias conditions were removed and the radiation continued. As can be seen, a large amount of recovery takes place with the bias removed

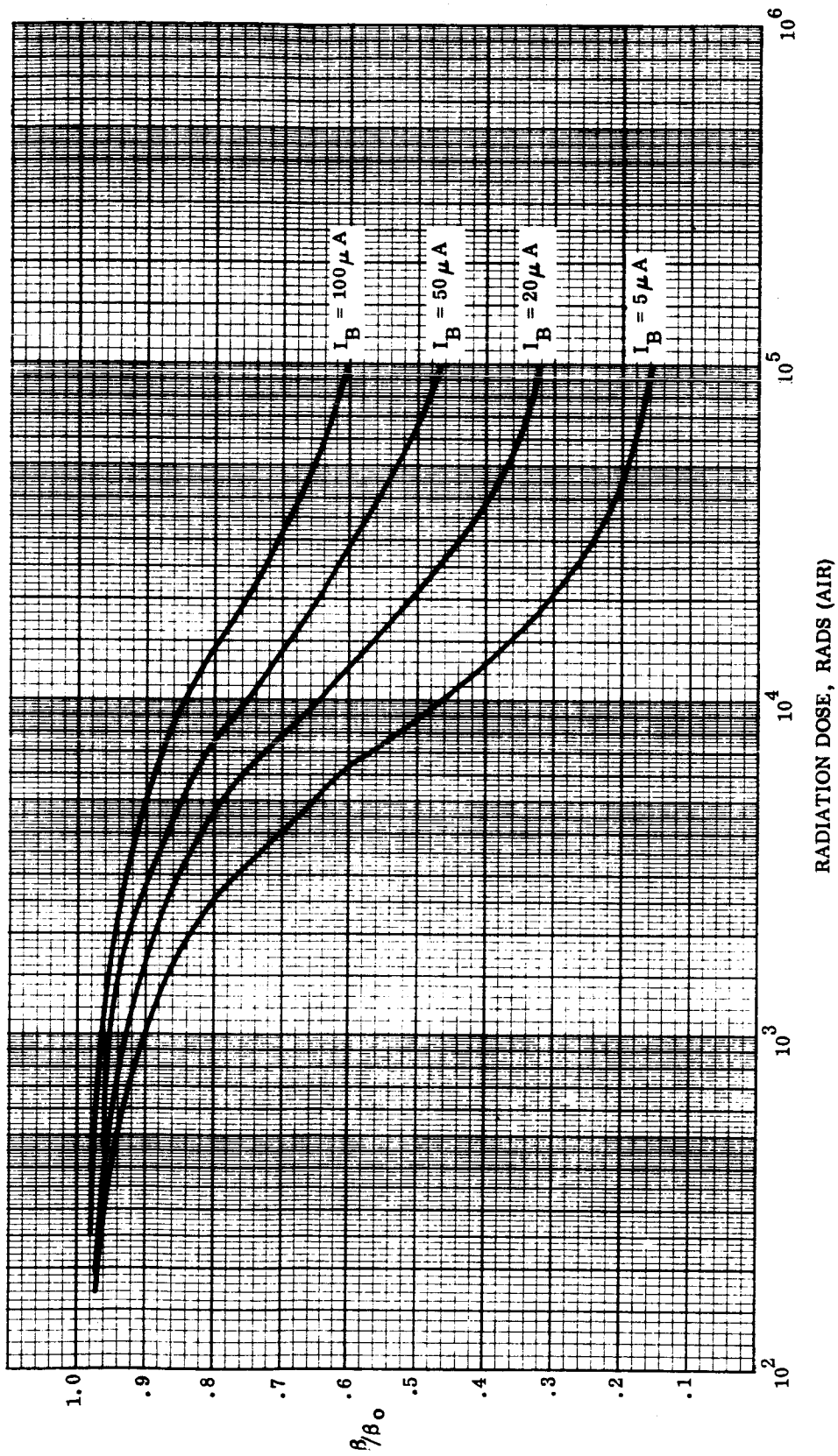

Figure 4-16. Gain Degradation of 2N708

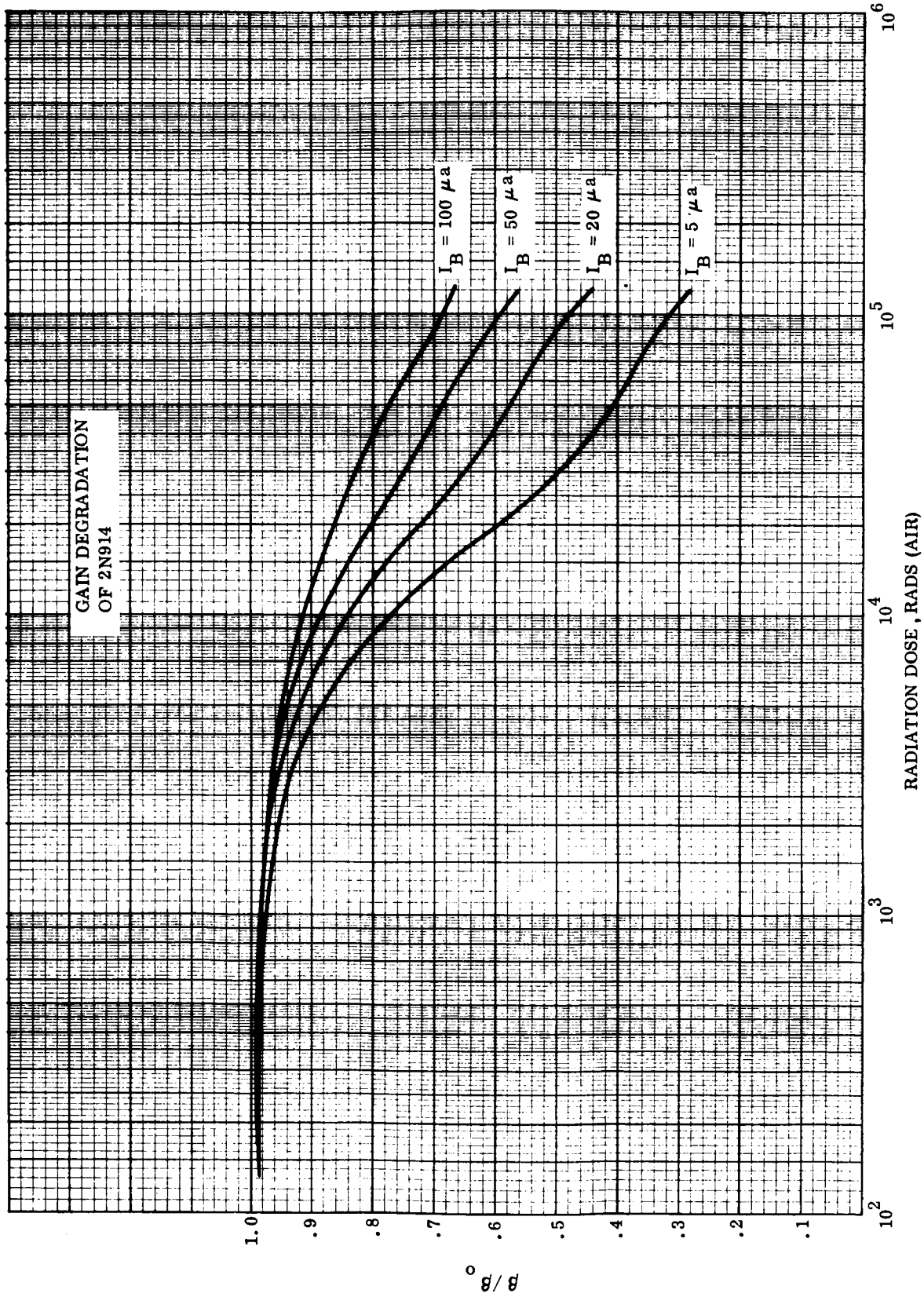

Figure 4-17. Gain Degradation of 2N914

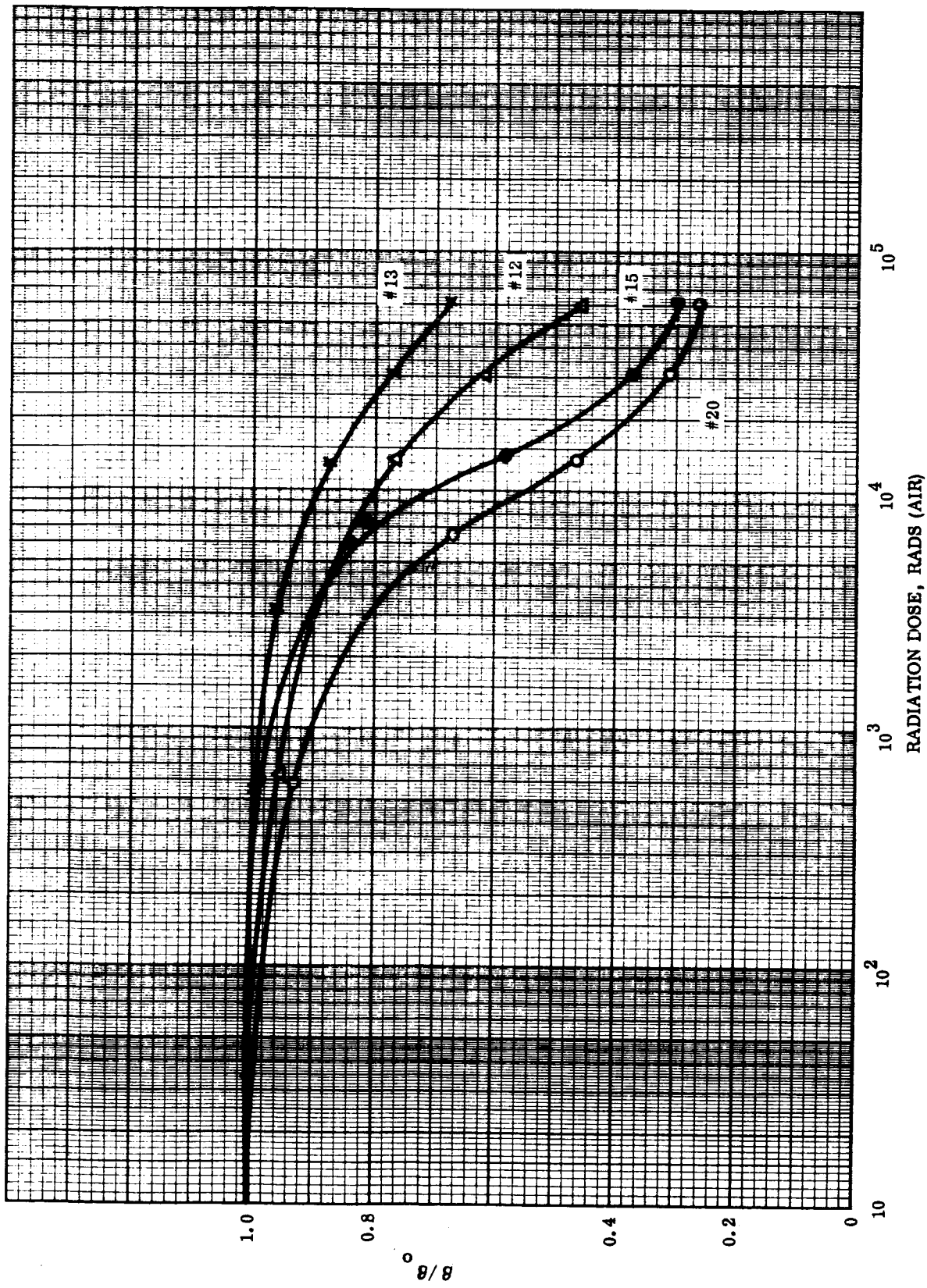

Figure 4-18. Gain Degradation for Several 2N2653, Silicon Power Transistors, I_{COLL} = 40 ma.

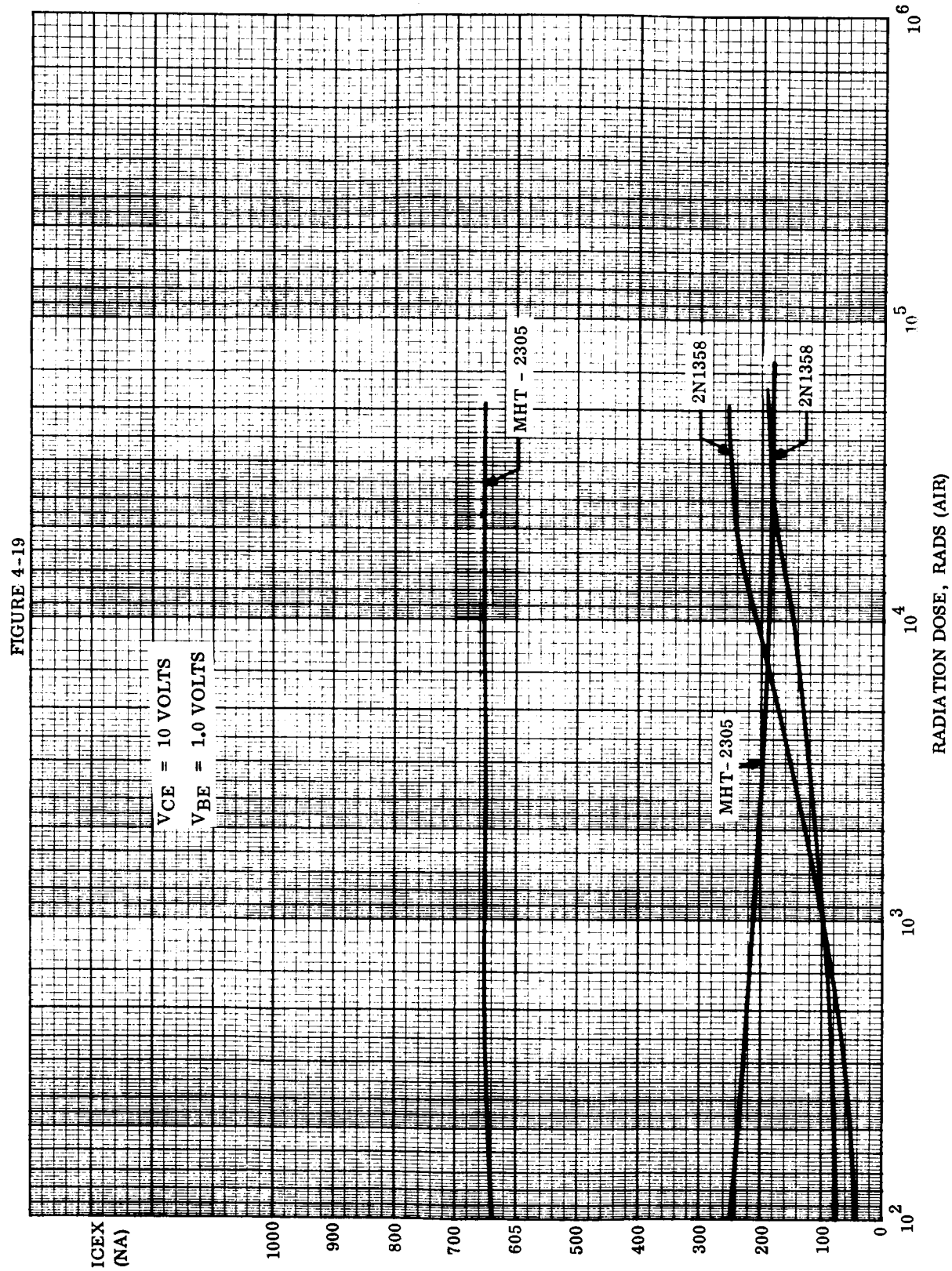

Figure 4-19. I_{CEX} Versus Radiation Dose, Germanium Transistors

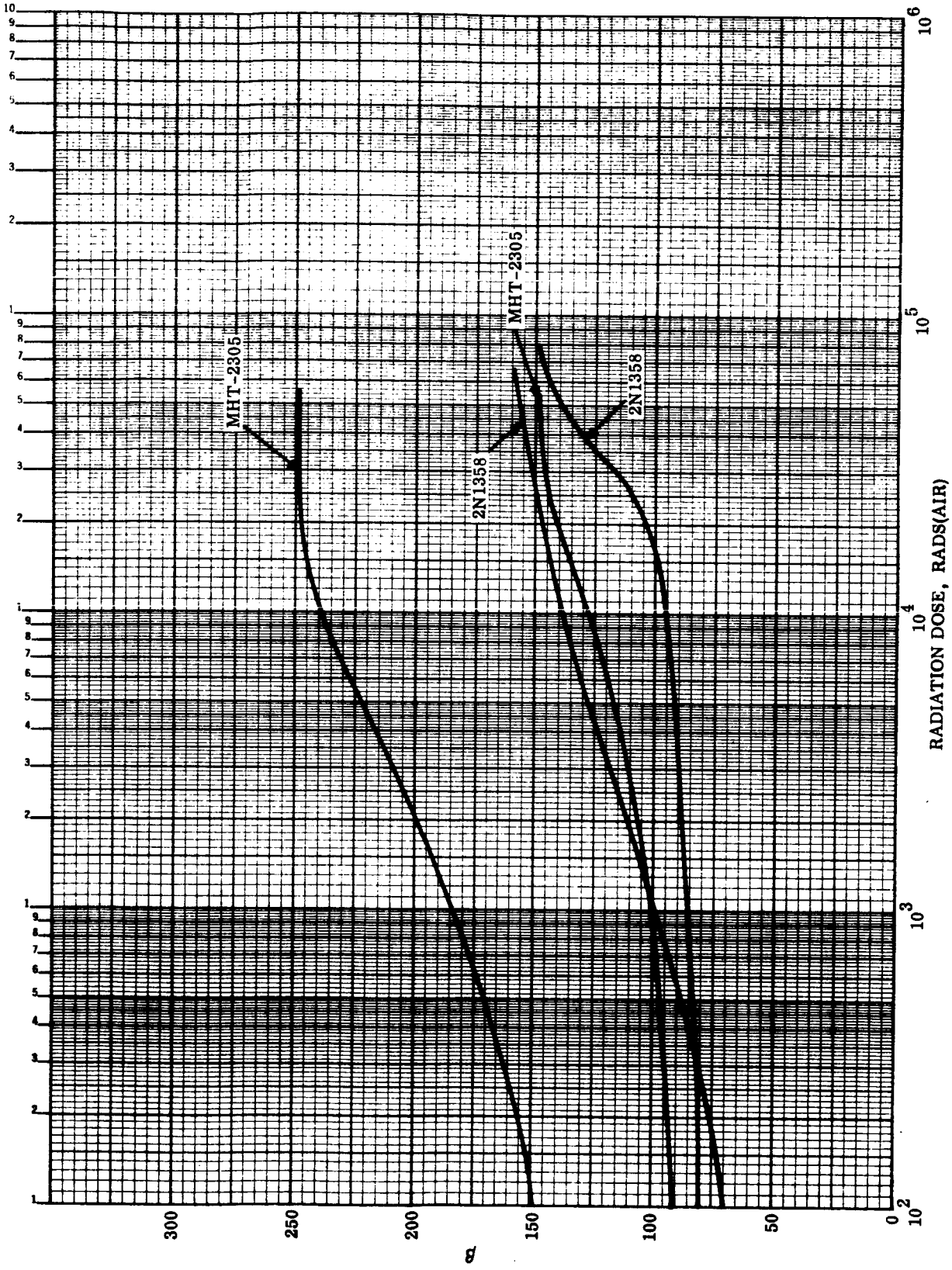

Figure 4-20. Gain Variation for Germanium Transistors

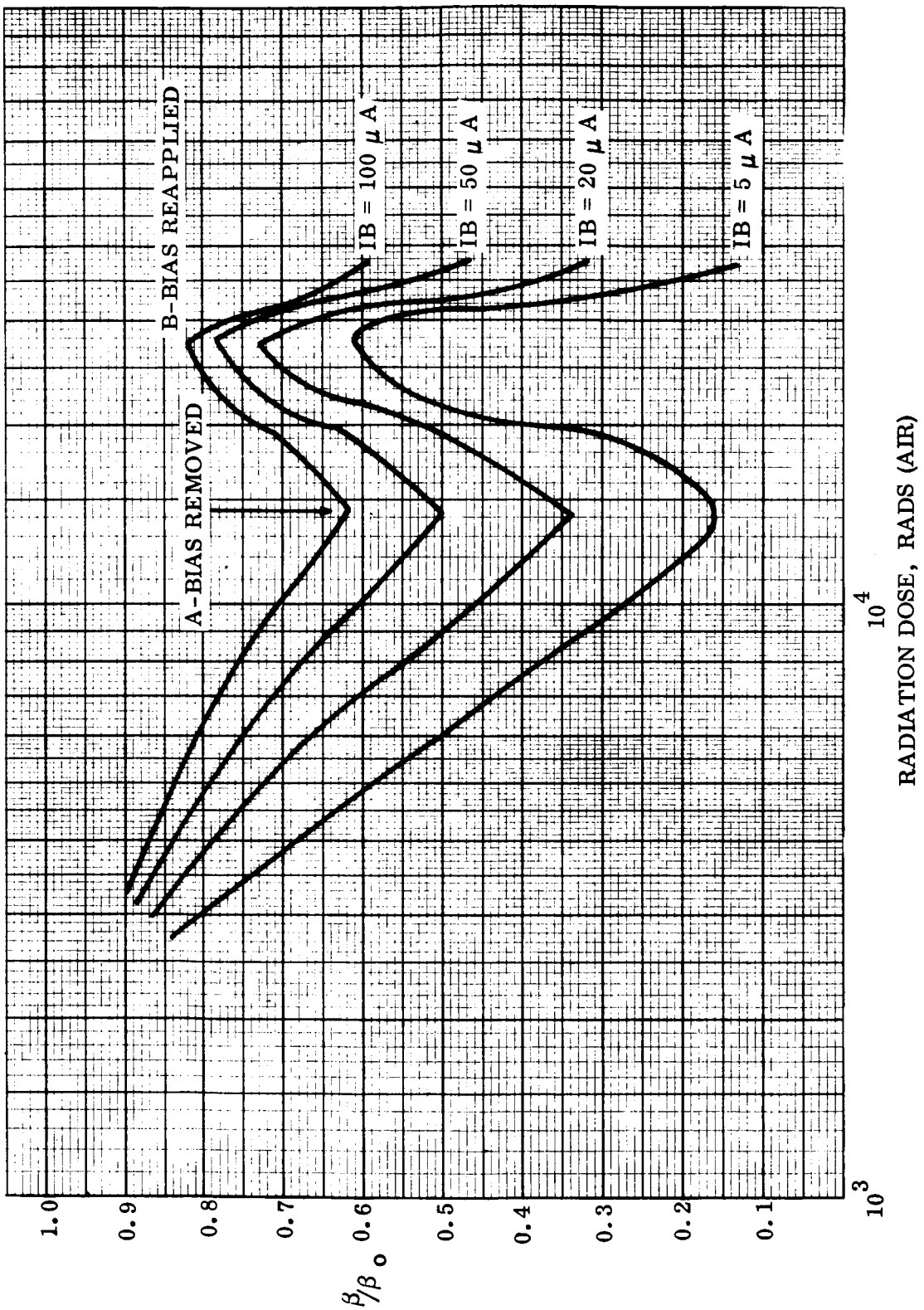

Figure 4-21. Gain Variation With Radiation and Bias, 2N708

and with the device maintained in the radiation environment. Very little recovery would have been seen if the radiation had also been removed at the same time the bias was removed. At point "B" the reverse bias was reapplied and the radiation continued. Once again the gains show a rapid decrease.

Figure 4-22 shows the gain variation with radiation for a 2N708 device when there was no initial application of bias. Even here, some degree of degradation is seen without any bias applied. At point "A", a reverse bias on the collector and emitter junctions is applied and a very rapid degradation is once again seen.

The variation of gain with still a different set of bias conditions is shown in Figure 4-23. Here the device was held in a common emitter circuit configuration with the collector current equal to 10 milliamperes during the initial part of the irradiation. It is seen that the gain decreases in a manner similar to the situation where both junctions are reverse biased. Of course, in the common emitter configuration, the collector junction is also reverse biased. For the circuit configuration used, this reverse bias was 7 volts. At point "A" in Figure 4-23, the circuit configuration is changed from a common emitter configuration to one where both junctions are reverse biased. Very little change is seen to take place in the degradation characteristics due to this change in biasing conditions.

4.2.1.4 EFFECTS OF GAS PRESSURE

As was stated before, the presence of the encapsulating gas is a major factor governing the magnitude of the induced surface effects. Direct evidence of this is seen in Figure 4-24. Here are shown the results of experiments performed in a radiation-vacuum chamber. The transistors were held in a reverse biased mode with a reverse bias on both of the junctions. The lower curve shows the average gain degradation of nine 2N708 transistors with their normal gas encapsulate. The middle curve, marked 10^{-2} mm of Hg, shows the average gain degradation of nine 2N708 transistors which were irradiated in the vacuum chamber with the transistor cans punctured and a vacuum of 10^{-2} mm of Hg in the chamber. The top curve is again the average gain degradation of nine 2N708 transistors irradiated in the vacuum chamber with the transistor cans punctured and with the chamber vacuum at 10^{-4} mm of Hg.

As can be seen, the greater the vacuum, the smaller the degradation. The results are somewhat surprising in that even at a vacuum of 10^{-4} mm of Hg a fairly large amount of degradation is seen. Apparently, it takes only a very small percentage of the ionized gas atoms to participate in reactions with the surface to produce these large changes, and/or the ionizable surface impurities also play a very dominant role.

4.2.2 SURFACE EFFECTS IN MICROELECTRONICS

As far as available experimental evidence indicates, radiation induced surface effects in microelectronic circuits appear to be much reduced from that seen in discrete parts. Figure 4-25 shows the variation in isolation region leakage current for a

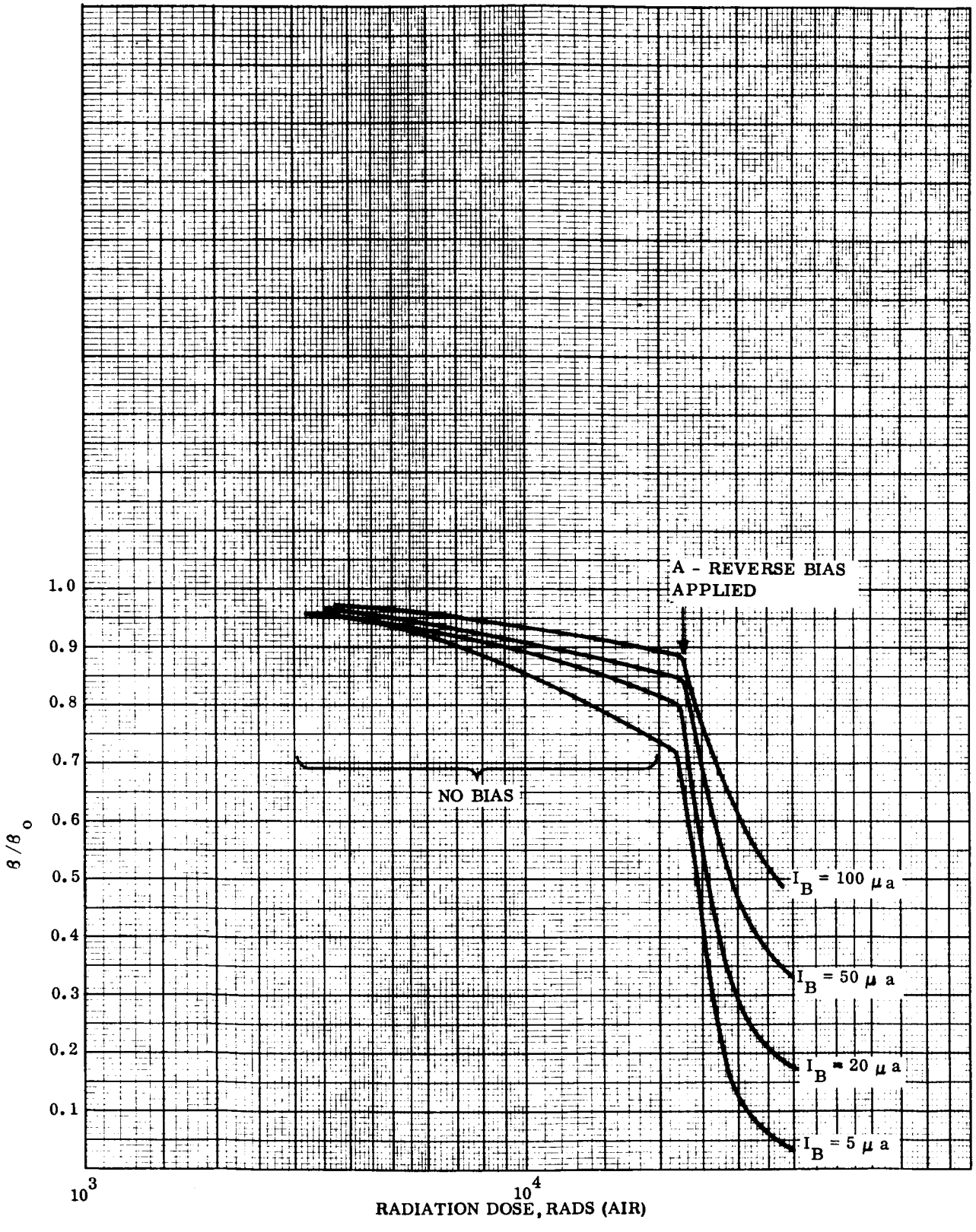

Figure 4-22. Gain Variation with Radiation and Bias, 2N708

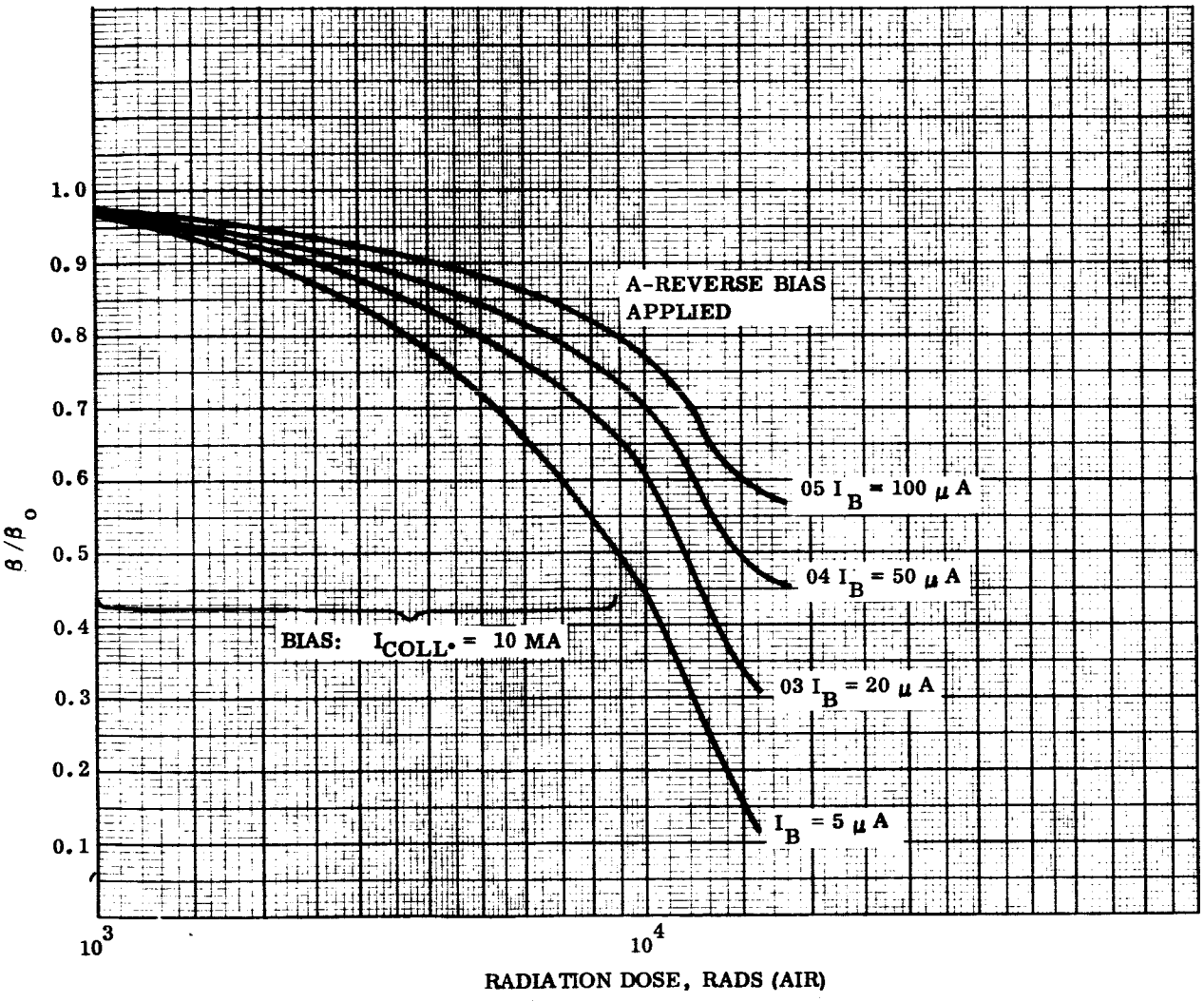

Figure 4-23. Gain Variation with Radiation and Bias, 2N708

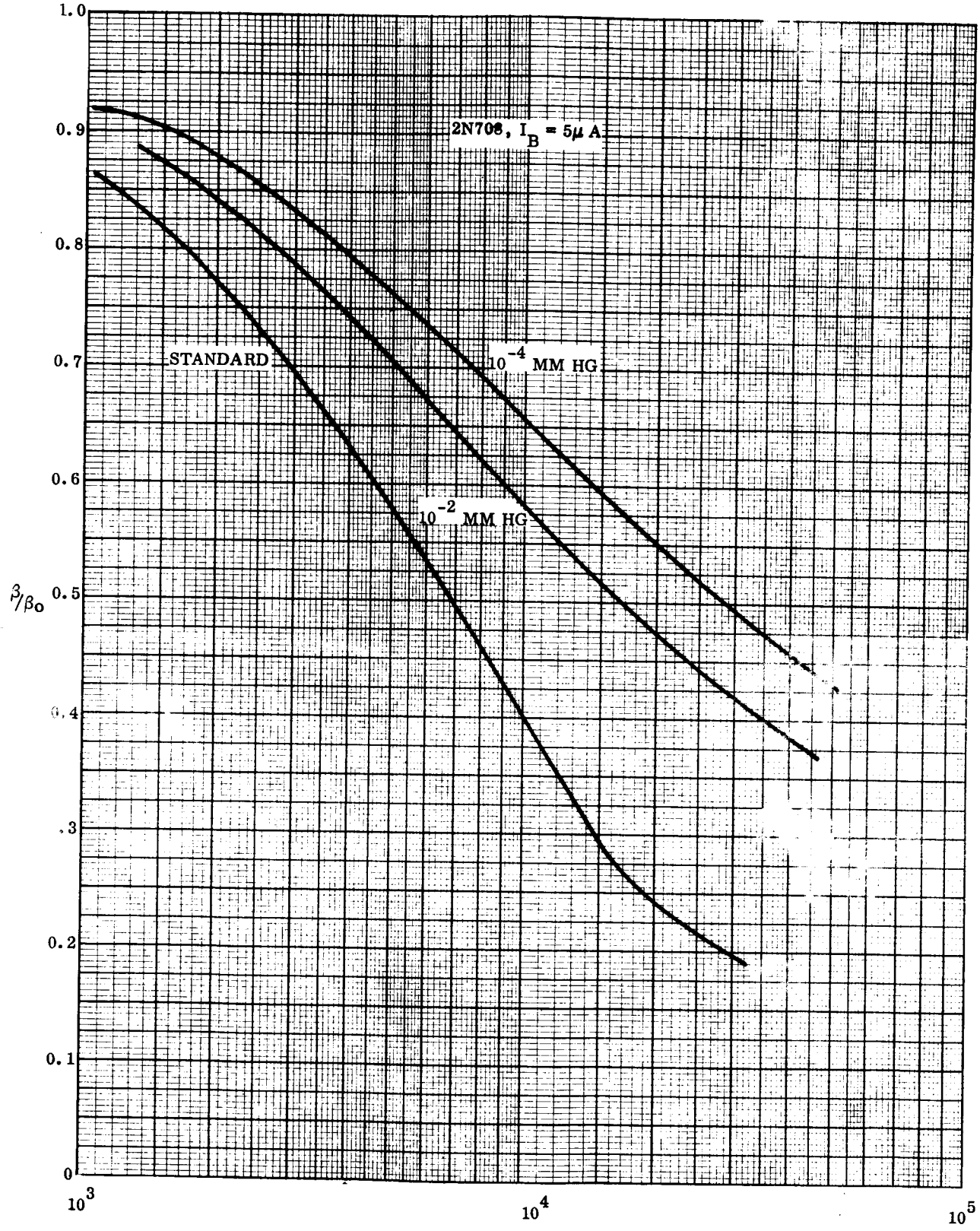

Figure 4-24. Gain Variation with Radiation and Vacuum, 2N708

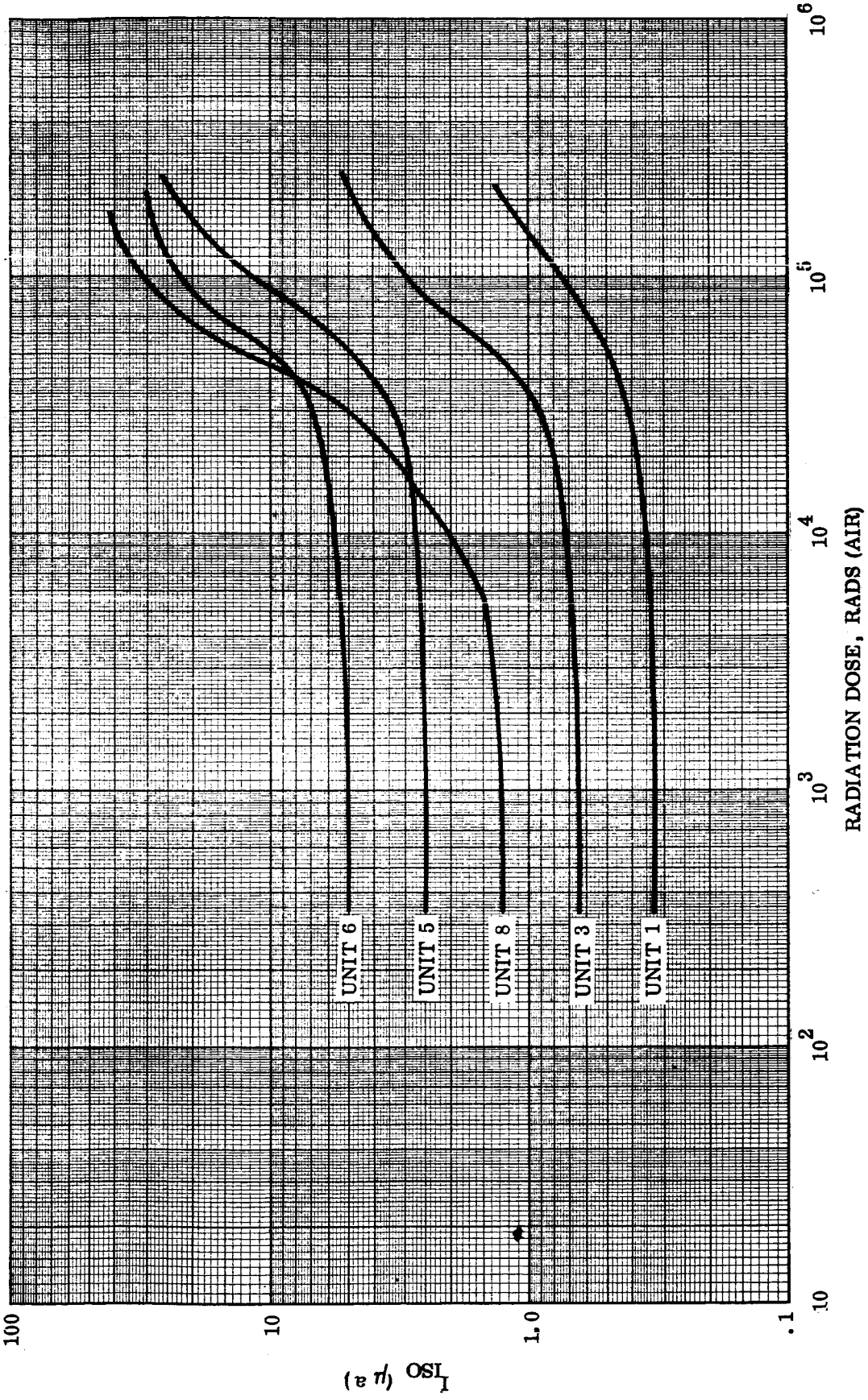

Figure 4-25. Microcircuits, Isolation Leakage Current

number of microelectronic logic circuits, NAND gates and majority gates, as a function of radiation dose. About an order of magnitude increase is seen to take place in the leakage current in these units. However, no corresponding change was seen in the output characteristics of these devices. Similar results on microcircuits have also been obtained at other laboratories (Reference 15). Several possible reasons may be postulated for this apparent resistance to surface effects for microcircuits. First, the passivation techniques for microcircuits may possibly be better than for discrete parts. Also, since microcircuits have a network of metal conductors deposited on their surface, these networks may influence the surface electric fields, in such a way as to mininimize the collection of surface ions and thus act as a sort protective "guard ring." The results of experiments recently conducted by General Electric with discrete transistors which have such "guard rings" deposited on the collector and emitter junctions indicate that the induced surface effects can be controlled to a large degree by such "guard rings."

4.2.3 ASSESSMENT OF SEMICONDUCTOR SURFACE EFFECTS ON VOYAGER

From a consideration of the data presented in the preceding section, it would appear that for mission doses on the order of 10^3 Rads (Air), induced surface effects would be of little consequence. Comparing this to the mission doses of Figure 2-4, it is seen that for Martian radiation belt intensities up to ten times the Earth belt intensity, induced surface effects would not be considered a serious problem.

For the assumption of a Martian belt intensity 100 times as intense as the Earth belt, the maximum mission dose would be 10^4 Rads (Air). Induced surface effects would begin to take on a serious nature at this point. Some consideration of shielding and device operating current levels would have to be taken into account.

A Martian belt 1000 times as intense as the Earth belt would result in a maximum mission dose of 10^5 Rads (Air). Here very definite considerations on shielding, device operating current levels, and device derating would be required.

For the "worst case" condition of a Martian belt 10^4 times the Earth belt, the radiation induced surface effects on all semiconductor components would become a very serious problem. Specialized shielding, restrictions on device operating current levels, device derating, parts screening and/or device manufacturing process line monitoring would have to be imposed on the spacecraft design to ensure a reliable system.

5.0 REFERENCES

1. V.A.J. vanLint, E.G.Wilkner, "Correlation of Radiation Types with Radiation Effects," I.E.E.E. Trans. on Nuc. Science, Vol. NS-10, No. 1, Jan., 1963.

2. J.J. Loferski, "Analysis of the Effect of Nuclear Radiation on Transistors," J. Appl. Phys. 29, 1 (1958), p. 35.

CII - VB220AA101

ALTERNATE SYSTEM PHILOSOPHIES AND SYSTEM MECHANIZATIONS CONSIDERED

TRAJECTORY SELECTION

Index

1	Introduction
2	Applicable Documents
3	Orbit Requirements
4	Guidelines for Orbit Selection
5	Capsule Trajectory
6	Choice of Design Trajectories for 1971 Mission
7	Arrival Date Separation
8	Engineering Design Parameters
9	Altitude Dispersions of Aerocentric Orbit
10	1973 Mission Trajectories
11	References

1.0 INTRODUCTION

The 1971 Voyager mission consists of the launching of two identical spacecraft. The overall Flight Spacecraft consists of a Flight Spacecraft and a Flight Capsule. The capsule is separated from the orbiter about one day from encounter with Mars and impacts at a predetermined site while the orbiter proceeds to encounter and injects itself into a predetermined orbit about Mars.

The trajectory can be divided into several phases:

Launch Trajectory
Coasting Orbit
Departure Hyperbola
Heliocentric Transfer Orbit
Approach Hyperbola
Impact Hyperbola
Aerocentric Orbit

The phases are all related; that is, each is dependent on the other. Of special interest are the relationships between the last four phases. Assuming Sun-Canopus oriented spacecraft, the general approach to selecting a design orbit was to first investigate the effects of each of the specifications on the heliocentric transfer trajectory. Next, within the region of allowable trajectories, six transfer trajectories were chosen for further analysis. After selecting aerocentric orbit altitudes which comply with the lifetime requirement, orbits about the planet for three different orbit inclinations using each transfer trajectory as a starting point were investigated for compliance with the specifications and guidelines.

References 1, 2, and 3 were used as the primary sources of constraints on the heliocentric transfer, capsule impacting, and aerocentric orbits for the 1971 and 1973 Voyager missions. The constraints from Reference 1 are specifications and therefore cannot be violated. References 2 and 3 gave helpful guidelines. In addition, several constraints have been imposed by the design of the spacecraft.

2.0 APPLICABLE DOCUMENTS

VB211SR101	Mission Objectives and Design Criteria
VB211SR102	Guidance Philosophy
VB220SR101	Design Characteristics
VB220SR102	Design Restraints
VB220FD101	Standard Trajectories

3.0 ORBIT REQUIREMENTS

3.1 SPECIFICATIONS

Reference 1 defines the orbit specifications listed below.

a. Only Type I trajectories are applicable.

b. The departure injection energy, C_3, must be less than 18 km^2/sec^2.

c. The approach velocity (V_∞) to Mars must be less than 5 km/sec.

d. The absolute value of the declination of the departure asymptote (DLA) must be between five and 33 degrees.

e. The inclination (I) of the heliocentric transfer ellipse must be greater than .1 degree.

f. The launch window must be at least two hours per day for 45 to 60 days.

g. Coast times in the near Earth parking orbit must range from two to 25 minutes.

h. Capability for launching two identical spacecraft a minimum of two days apart must exist with arrival at Mars separated by a minimum of 10 days.

i. The orbiter injection into the aerocentric orbit must take place in view of Goldstone.

j. The probability of contaminating Mars with the orbiter for 50 years after arrival must be less than 1×10^{-4}.

k. Occultation of the Sun by Mars must be avoided for at least the first month after arrival and should be delayed for as long as possible with the maximum occultation per orbit being less than 10 to 15 percent of the orbital period.

l. Loss of the orbiter roll reference on every orbit due to occultation by Mars is not allowed.

m. Capsule entry, descent, and impact must take place in view of Goldstone.

n. The capsule impact parameter must be 1,000 km less than the impact parameter which yields a grazing trajectory.

The shaded areas of Figure 3-1 indicate the heliocentric transfer trajectories eliminated by the first five specifications. Specifications a, d, f, and g are related and are met by allowing northeast launches.

3.2 ARRIVAL DATE

The constraint of having Goldstone view capsule entry, descent and impact, and orbiter injection constrains the time of arrival and the landing site to be on the Earth side of Mars at encounter. If the landing site is not selected, any arrival date is allowable; only the time of day at encounter need be controlled. If, however, a landing site is selected, a restriction on arrival date results. For example, if Syrtis Major (latitude 10 degress north, longitude +290 degrees) is chosen as a landing site, the arrival dates are limited to those shown in Figure 3-2.

The unshaded areas of Figure 3-1 indicate that a launch window of 60 days is possible if only the restrictions noted on the figure are applied. There is also a wide choice of possibilities for launching the second spacecraft and meeting the 10 day separation at arrival constraint. If, however, a landing site is selected, the launch window could be reduced to a minimum of 45 days due to a restriction on arrival date.

3.3 CONTAMINATION RESTRAINT

The restraint of highest priority is the contamination restraint which limits the minimum altitude of the orbit about Mars. When considering this restraint, the midcourse and injection guidance errors must be considered. Figure 3-3 was taken from Reference 2 except for the addition of the 50 year lifetimes curves. Figure 3-4 presents the injection velocity increments for various orbits if the approach velocity is 3.5 km/sec. Superimposed on this curve is the lifetime limit for two ballistic coefficients and a 6,100 ft/sec limit on the injection velocity. This limit was obtained from the propulsion design and represents the maximum velocity increment available within the weight restraint. Considering a 350 km (3 σ) uncertainty in the periapsis of the approach hyperbolic trajectory, the lowest orbits possible would be those whose periapsis is at least 440 km (3.77 σ) to the right of the drag limit. The 3.777 σ limit is adequate to give 10^{-4} probability of contamination since errors which raise the periapsis also raise the apoapsis, both of which tend to increase the time till the orbit decays. Only the navigation uncertainty is considered since the effects of the execution errors are small compared to those caused by the navigational error. Radiation pressure and gravity effects were also found to be negligible.

The drag area of the spacecraft as viewed from the spacecraft roll axis is 325 square feet; 45.8 square feet as viewed normal to the roll axis. The spacecraft weight including unused fuel is 2844 pounds as follows:

Spacecraft bus weight		2000 lb
Propulsion hardware weight		677 lb
Propulsion fuel		
Unuseable fuel	81 lb	
Unused fuel	86 lb	167 lb
Total		2844 lb

Using a drag coefficient of 2.1, the ballistic coefficients (m/C_DA) as viewed along the roll axis and normal to the roll axis are 0.129 and 0.918 slug/ft^2 respectively.

Combining the two values of the coefficient per the method shown in JPL Document EPD250, "Mariner Mars 1969 Orbiter Technical Feasibility" study yields:

$$(m/C_dA)_{cff} = \frac{\pi}{2}\left[\frac{2}{\pi}\left(\frac{1}{.129} + \frac{1}{.918}\right) + \frac{1}{.918}\right]^{-1}$$

$$= 0.234 \text{ slugs/ft}^2$$

If it is assumed that after the first six months, the spacecraft tumbles in a random fashion, the ballistic coefficient can be calculated by using the method of Sterne, An Introduction to Celestial Mechanics. For this method, the spacecraft total superficial area is 700 square feet. The effective area is taken as one quarter of the superficial area for a body with a convex area; the ballistic coefficient is 0.234 slug/ft^2.

Referring to Figure 3-4, it is seen that taking the conservative approach of using the lower ballistic coefficient of 0.129 slug/ft^2 still allows the choice of a desirable orbit from a scientific viewpoint: orbits of reasonably low periapsis altitude and orbit periods of less than the Mars spin period. Minimum allowable periapsis and apoapsis altitudes for various approach velocities, a velocity change of 5750 fps and an m/C_DA of .22 slugs/ft^2 are shown in Figure 3-5. The minimum altitudes for an m/C_DA of 0.129 are even higher. From Figure 3-5, the conclusion is drawn that approach velocities greater than 3.5 km/sec result in orbits of high apoapsis altitude and long orbit periods if the orbit injection velocity change is limited to a constant value of the order of 6000 fps. Thus, an orbit of 3000 km periopsis altitude, 25,000 km apoapsis altitudes, and 19.3 hours orbit period is chosen for design purposes.

The choice of a conservative satellite orbit has the additional advantage of allowing flexibility in trajectory and propulsion design. If a solid propellant propulsion system were used, either a constant approach velocity over the launch period must be used or an inefficient orbit injection propulsion operation must be accepted for launches over part of the launch period. If the latter approach is selected, an error in time of arrival could result in a lower apoapsis altitude and a shorter decay life. The conservative approach to the satellite orbit selection allows for the inefficient orbit injection and arrival time error if the higher value of the spacecraft m/C_DA is accepted.

3.4 AEROCENTRIC ORBIT OCCULATION CHARACTERISTICS

In order to investigate the occultation times for the Sun, Earth, and Canopus, several heliocentric transfer trajectories in the acceptable region of Figure 3-1 were selected for further analysis. The trajectories were chosen in pairs of constant arrival dates or constant approach velocity so as to cover the launch period. Only orbit injections on the Sun side of Mars were considered; injection occurs at periapsis and for scientific purposes the periapsis should be in the sunlight.

The surface area of Mars of greatest scientific interest lies between 10 degrees north and 40 degrees south latitude according to Reference 2. This requires that the inclination of the orbit to the Mars equatorial plane be at least 40 degrees in order to ensure full coverage of this region. A southern hemisphere injection ensures that the periapsis will lie over the region of interest if the orbit inclination is greater than or equal to 40 degrees. The southern injection also decreases the possibility of Canopus occultation since the periapsis is in the same hemisphere as the star for this case.

Table 3-1 is a list of the selected trajectories and their parameters which most influence the aerocentric orbit properties. For each of these trajectories three aerocentric orbits were investigated; all at the same altitudes (3000 km periapsis-25000 km apoapsis) but with 40, 50, and 60 degree inclinations to the planet. Table 3-2 gives the aim point required to achieve the indicated aerocentric orbits for each of the selected trajectories. Figure 3-6 defines the aim point in terms of the approach asymptote and impact parameter plane.

In this discussion, occultation is defined as shown by Figure 3-7. If the body-orbiter-near limb angle (β) becomes less than zero, the body is considered occulted. The atmosphere is not considered in the radius of Mars for this calculation. Table 3-3 indicates the occultation times for the Sun and Earth for each of the selected trajectories and for different days after encounter. It is evident from the table that avoiding Sun occultations for the first month in the band of allowable trajectories, orbit inclinations and altitudes is not a problem. Canopus occultation times are not included in Table 3-3 because no occultations occured. Table 3-4, however, indicates the minimum Canopus-Orbiter-near limb angles for each orbit on various days after arrival. This angle is never less than 35 degrees for the orbits considered.

4.0 GUIDELINES FOR ORBIT SELECTION

4.1 GUIDELINES DEFINITION

Reference 2 defines several guidelines to be followed when choosing the trajectories for various phases of the mission. These include orbit dependent conditions desirable for the conduction of the scientific experiments listed.

a. A fixed amount of retropropellant should be used for both spacecraft throughout the launch window.

b. The approach velocity should be held constant over the entire launch window.

c. The flight times and communication distances should be kept as short as possible.

d. The arrival dates and geometry should be held as constant as possible over the launch window.

e. Sun occultation should be avoided for as long as possible after arrival.

Table 3-1. Heliocentric Transfer Trajectories to Mars 1971 (Type I)

Launch Date	(Calendar) (Julian)	May 4, 1971 244 1074.5	June 23, 1971 244 1125.5	May 9, 1971 244 1080.5	June 24, 1971 244 1126.5	May 11, 1971 244 1082.5	June 28, 1971 244 1130.5
Trip Time	(days)	182	143	200	154	222	174
Arrival Date	(Calendar) (Julian)	November 2, 1971 244 1257.5	November 13, 1971 244 1268.5	November 25, 1971 244 1280.5	November 25, 1971 244 1280.5	December 19, 1971 244 1304.5	December 19, 1971 244 1304.5
C3 x 10^{-8}	(m^2/sec^2)	0.10 Class I	.18 Class I	.09 Class II	.18 Class I	.09 Class II	.18 Class I
Declination of Geocentric Asymptote	(deg)	-30.5	-25.5	-29	-25	-27	-20
Approach Velocity	(km/sec)	3.5	3.5	2.9	3.25	2.83	3.1
Mars Orbit Plane-Approach Asymptote Angle	(deg)	1.	-9.	2.5	-9.5	-.5	-12
Sun — Mars — Approach Asymptote Angle	(deg)	128	124	97	108	82	86

Table 3-2. Aim Points For Selected Trajectories

1971 Mars Orbits

Altitude 3000 – 25000 KM

Launch Date	Arrival Date	Incli-nation	Approach Asymptote S_x	S_y	S_z	V_∞ (km/sec)	B (km)	θ (deg.)	ΔV (km/sec)
May 4, 1971	Nov 2, 1971	40	0.709	-.705	0.006	3.5	9260	18.58	1.76
		50						29.95	
		60						40.90	
June 23, 1971	Nov 13, 1971	40	0.677	-.714	-0.177	3.5	9260	22.32	1.76
		50						32.58	
		60						42.77	
May 9, 1971	Nov 25, 1971	40	0.549	-.836	-0.010	2.9	10300	17.11	1.36
		50						27.85	
		60						38.38	
June 24, 1971	Nov 25, 1971	40	0.629	-.752	-0.194	3.3	9550	21.57	1.62
		50						31.72	
		60						41.84	
May 11, 1971	Dec 19, 1971	40	0.457	-.888	-0.032	2.85	10410	16.86	1.33
		50						27.26	
		60						37.56	
June 28, 1971	Dec 19, 1971	40	0.514	-.827	-0.229	3.1	9910	19.76	1.48
		50						29.77	
		60						39.79	

S_x, S_y, S_z - Direction Cosines of Approach Asymptote in Ecliptic Coordinates (x, y, z)

V_∞ - Approach Velocity

B - Impact Parameter Magnitude

θ - Direction of Impact Parameter

ΔV - Injection Velocity, Aerocentric Orbit

Table 3-3. Occultation Times Per Orbit For Example Trajectories

Launch Date	Arrival Date	Incli-nation (deg)	Vs Days From Encounter: Sun Occultation Time - Minutes, Days After Encounter 0	30	60	90	120	150	180	1971 Mars Orbits: Earth Occultation Time - Minutes, Days After Encounter 0	30	60	90	120	150	180
May 4, 1971	Nov 2, 1971	40	0	0	0	0	0	130.00	108.33	43.33	46.67	0	0	0	0	138.33
		50	0	0	0	0	0	0	106.67	40.00	0	0	0	0	0	0
		60	0	0	0	0	0	0	66.67	40.00	0	0	0	0	0	0
June 23, 1971	Nov 13, 1971	40	0	0	0	0	0	0	91.67	63.33	46.67	0	0	0	0	0
		50	0	0	0	0	0	0	70.00	53.33	16.67	0	0	0	0	0
		60	0	0	0	0	0	0	44.67	56.33	0	0	0	0	0	0
May 9, 1971	Nov 25, 1971	40	0	0	0	0	125.00	106.67	63.33	0	0	0	0	0	116.67	116.67
		50	0	0	0	0	51.67	106.67	66.67	0	0	0	0	0	0	115.00
		60	0	0	0	0	0	89.17	71.67	0	0	0	0	0	0	80.00
June 24, 1971	Nov 25, 1971	40	0	0	0	0	0	46.67	91.67	66.33	56.33	0	0	0	0	0
		50	0	0	0	0	0	0	81.67	59.83	0	0	0	0	0	0
		60	0	0	0	0	0	0	68.33	45.17	0	0	0	0	0	0
May 11, 1971	Dec 19, 1971	40	0	0	0	110.00	103.33	72.50	45.83	0	0	0	0	98.33	119.17	70.00
		50	0	0	0	0	100.83	70.00	25.00	0	0	0	0	0	105.00	71.67
		60	0	0	0	0	86.67	71.67	25.00	0	0	0	0	0	74.17	74.17
June 28, 1971	Dec 19, 1971	40	0	0	0	0	0	83.33	75.00	61.67	0	0	0	0	0	85.00
		50	0	0	0	0	0	8.33	6.67	0	0	0	0	0	0	15.83
		60	0	0	0	0	0	66.67	60.83	0	0	0	0	0	0	66.67

Table 3-4. Minimum Canopus-Orbiter-Near Limb Angles

Apoapsis Altitude – 25000 KM
Periapsis Altitude – 3000 KM

Launch Date	Arrival Date	Inclination (Deg.)	Canopus-Orbiter-Near Limb Angle (Deg.) Days After Encounter						
			0	30	60	90	120	150	180
May 4, 1971	Nov 2, 1971	40	54.34	52.67	51.02	49.38	47.77	46.15	44.56
		50	50.99	50.01	49.05	48.11	47.13	46.31	44.48
		60	43.50	43.23	42.82	42.42	42.01	41.60	41.18
June 23, 1971	Nov 13, 1971	40	63.41	61.83	60.89	58.41	56.71	55.04	53.38
		50	55.31	54.87	54.30	53.56	52.80	51.92	50.87
		60	45.67	45.63	45.53	45.43	45.22	44.99	44.76
May 9, 1971	Nov 25, 1971	40	52.95	51.25	49.57	47.85	46.17	44.52	42.92
		50	49.25	48.24	47.26	46.00	44.64	43.29	41.94
		60	42.07	41.60	41.12	40.63	40.14	39.50	38.84
June 24, 1971	Nov 25, 1971	40	63.54	61.94	60.21	58.50	56.79	55.10	53.43
		50	55.37	54.87	54.28	53.48	52.70	51.75	50.69
		60	45.78	45.67	45.54	45.38	45.13	44.89	44.61
May 11, 1971	Dec 19, 1971	40	53.60	51.77	49.35	48.15	46.38	44.63	42.92
		50	49.55	48.31	47.12	45.81	44.61	43.37	42.11
		60	42.11	42.01	41.08	40.55	40.01	39.37	38.68
June 28, 1971	Dec 19, 1971	40	64.19	62.60	60.84	59.07	57.30	55.52	53.74
		50	55.68	55.11	54.44	53.60	52.74	51.71	50.64
		60	41.03	45.27	45.70	45.40	45.10	44.80	44.41

f. The following combination of conditions should not hold for more than one to two hours per orbit.

clock angles of the bright limb of Mars ± 35°

cone angles of the bright limb of Mars 90 ± 60°

g. The wave of darkening is of interest and arrival dates should be adjusted accordingly.

h. The aerocentric orbit plane should not be perpendicular to the Earth-Mars line.

i. The orbit rate should not be zero with respect to the Earth-Mars line.

j. Scientific Constraints

1. Topographic TV Experiment

(a) The area of interest on the planet is between 10° north and 40° south latitude.

(b) The local vertical cone angle must be between 100 and 140°.

(c) The altitude should be as low as possible without causing image motion compensation problems.

2. Color TV Experiment

(a) The area of interest on the planet is between 10° north and 40° south latitude.

(b) The local vertical cone angle should be as close to 180 degrees as possible.

(c) The altitude should be as low as possible without causing image motion compensation problems.

3. Mars Scanner Experiment

(a) The orbital altitude and velocity should be kept constant.

(b) The local vertical cone angle should be greater than 80 degrees.

4. Ultraviolet Spectrometer

(a) The altitude should be kept as low as possible.

(b) The inclination to the ecliptic should be 30 degrees.

5. Dual Frequency Occultation Receiver

After the first few days after arrival the Earth should be occulted during every orbit for less than a month and then not again.

The experiments listed are considered to be typical for a Mars orbiter mission. The selection of a typical set of experiments was made in order to determine the effect of various scientific instrument requirements on the trajectory selection and does not mean that these particular experiments are being proposed for the mission. In the case of the TV and Scanner experiments, it is desirable to have the ground traces to repeat once every one to three months. The swath widths should be evenly spaced and the period should not exceed the orbital period of Mars.

4.2 APPROACH CHARACTERISTICS

Trajectories allowing the use of a fixed amount of orbit injection propellant simplifies the design of the retropropulsion subsystem. This can be achieved in either of three ways: keeping the approach velocity constant and performing an in-plane injection into the same altitude orbit for all trajectories; changing the altitude of the orbit to match the injection velocity requirements; or keeping the altitude constant but performing and out-of-plane or non-periapsis injection to waste propellant. A constant approach velocity philosophy is most desirable to meet this condition. This philosophy is also suggested in the guidelines of Reference 2.

Figure 3-1 indicates early arrival dates tend to keep the flight times as short as possible. Figure 4-1 indicates early arrivals also tend to provide lower communication distances.

The arrival date and approach geometry cannot both be held constant over the launch window. The approach geometry itself cannot be held constant since it is defined by two angles, the Sun-Mars approach asymptote angle, (ZAP) and the angle between the Mars orbit plane and the approach asymptote (γp). The two angles vary in a different manner with launch date. Figures 4-2, 4-3, 4-4 and 4-5 indicate the variation of three of the four parameters if the fourth is held constant. For example, if the approach velocity is held constant at 3.5 km/sec for all launch dates, Figures 4-3, 4-4, and 4-5 indicate the variation of the arrival date, ZAP angle, and γ_p angle respectively. In this case the variations are not too extreme. Figures 4-2, 4-4 and 4-5 also indicate the variations in approach velocity, ZAP angle and angle for two boundaries on which the arrival dates are held constant, November 25, 1971 and December 20, 1971. In these cases the variation in approach velocity may become a problem if solid propellant orbit injection engines are used. For liquid propellant engines, however, complications would not necessarily result since propellant could conceivably be off loaded.

4.3 OCCULTATION

The orbit inclination to the ecliptic plane should be as high as possible in order to minimize the Sun occultation. However, to minimize Canopus occultation the orbit

plane should be nearly parallel to the ecliptic. Thus, a compromise inclination is indicated in which the inclination is as high as possible without causing Canopus occultations and choosing other parameters to minimize Sun occultation.

The approach geometry also effects the time till Sun occultation. By comparing Tables 3-1 and 3-3, it is evident that if the Sun-Mars-approach asymptote angle (ZAP) is large, the time till Sun occultation increases. This is true because the larger ZAP angle increases the angle between the line-of-nodes of the aerocentric orbit plane and the Mars-Sun line in such a direction as to require the plane to rotate further with respect to the Sun before occultation occurs. Apparent motion of the line of nodes due to seasonal progression tends to initially decrease the angle between the line of nodes and the sun line. Since both the motion of Mars around the Sun and the nodal regression tend to move the orbit plane in the same direction with respect to the Sun line, increasing the altitude and inclination and thereby reducing the nodal regression rate delays the Sun occultation. However, if the ZAP angle is made too large, Sun occultation occurs in the first orbit after arrival.

Canopus occultation and the minimum angle between the limb of Mars and the direction to Canopus has already been discussed in Section 3. In the case of the selected trajectories, Table 3-4 indicates that this guideline (f) has not been violated.

The γ_p angle effects the initial periapsis position. The periapsis is initially further from the ascending node for lower angles and a constant approach velocity and inclination. The periapsis in all cases was less than 90° of true anomaly from the ascending node. Keeping the periapsis as far as possible from the ascending node but less than 90° increases the altitude of the orbit when the spacecraft passes the terminator thereby reducing the occultation possibility; this condition holds for the 1971 trajectories defined by Figure 3-1.

4.4 MARS SEASONAL CHARACTERISTICS

Figure 4-6 indicates when during the Martian year the waves of darkening occur. Also indicated are the range of arrival dates and the time the spacecraft is expected to return useful data (180 days after encounter). In order to see as much of the wave as possible, late arrivals (December 20, 1971) are desirable. This allows viewing of about 70% of the travel of the wave sweeping from North to South assuming 180 days orbiter lifetime. For early arrival only one third of the waves travel is visible. However, with the uncertainty in the nature of the waves and considering that some positions of the waves will be viewed during the orbit phase for all arrival dates, the trajectories should not be further restricted for the purpose of obtaining better viewing of the wave.

4.5 TRACKING CONSTRAINTS

The doppler tracking and orbit determination characteristics (guidelines h and i) were not investigated in any detail, but preliminary investigation indicates that the

aerocentric orbit plane is not perpendicular to the Earth-Mars line for any appreciable time and the orbit rate is never zero with respect to this line.

4.6 SCIENTIFIC EXPERIMENT COMPATIBILITY

The five experiments listed in Reference 2 included two TV experiments, a Mars scanner experiment, an ultraviolet spectrometer and a dual frequency occultation experiment. The one TV experiment consists of taking black and white TV pictures of the Mars terrain at lighting angles which produce shadows that indicate the variation in elevation of the terrain. The other TV experiment employs a color TV. These pictures are to be analyzed to determine the color contrast for various locations on the planet and various seasons of the year. The Mars scanner data is used to determine water vapor content on the planet and temperature profiles while the ultraviolet spectrometer performs a spectral analysis of the atmosphere. The occultation experiment provides a means of studying the height and density of the Martian atmosphere. As previous noted, these experiments were assumed to be typical for purposes of trajectory analysis.

The local vertical cone angle or Sun-Orbiter planet angle is a measure of the incident angle of the sunlight on the planet at the subsatellite point. This angle is extremely important for the TV experiments. For color TV, high intensity direct lighting is preferred while for topographic TV a large incident angle for the sunlight is desired so that elevated portions of the terrain will cast visible shadows. Figures 4-7a through 4-7r and 4-8a through 4-8r indicate the lighting angles versus latitude and altitude respectively for the selected trajectories. Figures 4-9a through 4-9f indicate the latitude and the longitude from the Sunline of the periapsis for each trajectory. The latitude of the sub-solar point is also presented in these figures.

The area of interest on the surface of the planet for the typical experiments lies between 10° north latitude to 40° south latitude. In order to maximize the instrument resolution, the periapsis should be located in this region and the orbit inclination should be close to 40°. The TV experiment requires as low an altitude as possible but consistant with camera characteristics and blurring of the image. The TV pictures should be taken at or within two times the periapsis altitude if possible.

Tables 4-1a through 4-1d are a summary of the curves shown in Figures 4-7a through r, Figures 4-8a through r, and Figures 4-9a through f and indicate the minimum and maximum altitudes and latitudes in the regions where the Sun-Orbiter-Mars angle is between 100 and 140°. This angular range yields the optimum topographic resolution due to the shadowing. The region of desired cone angle occurs twice per orbit; once just after the spacecraft passes the morning and again before the spacecraft reaches the evening terminator.

During the initial orbiting phase, the conditions for topographic TV are best near the evening terminator. That is the altitudes, in which the subsatellite points are over the area of interest (10°N to 40°S latitude) for a 40° inclined orbit, are lower than for the morning terminator region. For the most part, the 50 and 60 degree

Table 4-1a. Conditions for Topographic TV at Day Zero

Cone Angle 100°-140°

Launch Date	Arrival Date	Inclination (deg)	Morning Terminator Region					Evening Terminator Region				
			Altitude		Latitude			Altitude		Latitude		
			min	max	in	out	max	min	max	in	out	max
May 4, 1971	Nov 2, 1971	40	7600	16100	-3	-28	-28	3000	3300	-33	-10	-33
		50	7200	16800	+2	-32	-32	3000	3400	-47	-19	-47
		60	6800	17600	+8	-37	-37	3000	3700	-60	-28	-60
June 23, 1971	Nov 13, 1971	40	6600	13800	+2	-24	-24	3000	3400	-36	-15	-36
		50	6300	14100	+5	-29	-29	3000	3500	-48	-22	-48
		60	5800	14500	+9	-38	-38	3000	4000	-60	-30	-60
May 9, 1971	Nov 25, 1971	40	5600	11000	-15	-36	-36	3000	3800	-24	+2	-24
		50	4800	11000	-15	-46	-46	3000	3700	-37	-3	-37
		60	4100	11100	-15	-59	-59	3000	3500	-56	-7	-56
June 24, 1971	Nov 25, 1971	40	5600	11700	-3	-29	-29	3000	3600	-34	-11	-34
		50	5100	11700	-2	-38	-38	3000	3500	-46	-15	-46
		60	4600	12000	0	-50	-50	3000	3600	-60	-21	-60
May 11, 1971	Dec 19, 1971	40	4300	7800	-24	-39	-39	3100	4800	-26	+12	-26
		50	3800	7500	-28	-49	-49	3100	4700	-25	+11	-25
		60	3300	7100	-33	-58	-60	3000	4800	-40	+12	-40
June 28, 1971	Dec 19, 1971	40	4200	8000	-13	-36	-36	3100	4600	-27	0	-27
		50	3800	7800	-16	-47	-47	3000	4600	-38	-2	-38
		60	3000	7500	-20	-3	-40	--	--	--	--	--

Table 4-1b. Conditions for Topographic TV at Day 60
Cone Angle 140°-100°

Launch Date	Arrival Date	Incli-nation (deg)	Morning Terminator Region					Evening Terminator Region				
			Altitude		Latitude			Altitude		Latitude		
			min	max	in	out	max	min	max	in	out	max
May 4, 1971	Nov 2, 1971	40	4500	8600	-25	-40	-40	3000	4400	-10	+17	+17
		50	4000	8000	-30	-50	-50	3000	4500	-22	+15	-22
		60	3400	7600	-34	-55	-60	3000	4500	-45	+12	-45
June 23, 1971	Nov 13, 1971	40	3900	7400	-22	-39	-39	3100	4800	-17	+11	-17
		50	3500	6800	-28	-50	-50	3100	5000	-28	+11	-28
		60	3000	6300	-33	+10	-60	--	--	--	--	--
May 9, 1971	Nov 25, 1971	40	3600	6200	-35	-37	-40	3500	5700	+1	+26	+26
		50	3500	5700	-42	-47	-50	3600	6000	-4	+30	+30
		60	3100	5300	-50	-51	-60	3400	6400	-12	+33	+33
June 24, 1971	Nov 25, 1971	40	3600	6400	-28	-40	-40	3300	5500	-12	+16	+16
		50	3300	5900	-34	-39	-50	3100	5500	-22	+18	-22
		60	3000	5300	-41	-45	-60	3000	6200	-45	+19	-45
May 11, 1971	Dec 19, 1971	40	3200	4800	-39	-35	-40	4200	7800	+10	+32	+32
		50	3100	4500	-48	-42	-50	4400	8300	+10	+39	+39
		60	3000	4200	-57	-46	-60	3300	7100	+8	+45	+45
June 28, 1971	Dec 19, 1971	40	3100	4800	-34	-38	-40	4000	7700	-2	+24	+24
		50	3000	4300	-43	-45	-50	4100	8300	-5	+30	+30
		60	3000	4000	-53	-45	-60	4000	9200	-10	+37	+37

Table 4-1c. Conditions for Topographic TV at Day 120

Cone Angle 100°-140°

Launch Date	Arrival Date	Inclination (deg)	Morning Terminator Region					Evening Terminator Region				
			Altitude		Latitude			Altitude		Latitude		
			min	max	in	out	max	min	max	in	out	max
May 4, 1971	Nov 2, 1971	40	3100	5500	-39	-32	-40	4000	6700	+15	+35	+35
		50	3100	4800	-49	-41	-50	4000	7500	+11	+40	+40
		60	3000	4300	-58	-44	-60	4200	8400	+6	+46	+46
June 23, 1971	Nov 13, 1971	40	3100	4700	-39	-34	-40	4300	8000	+9	+32	+32
		50	3000	4200	-48	-40	-50	4400	9000	+7	+39	+39
		60	3000	3800	-58	-41	-60	4600	10400	+4	+46	+46
May 9, 1971	Nov 25, 1971	40	3100	4300	-39	-25	-39	4800	9100	+24	+39	+39
		50	3000	4000	-50	-32	-50	5200	10000	+25	+47	+47
		60	3000	3700	-60	-32	-60	5600	11300	+26	+55	+55
June 24, 1971	Nov 25, 1971	40	3000	4200	-39	-32	-40	4700	9100	+16	+35	+35
		50	3000	3900	-50	-37	-50	5100	10400	+14	+42	+42
		60	3000	3400	-59	-39	-60	5400	12000	+15	+50	+50
May 11, 1971	Dec 19, 1971	40	3000	3600	-37	-19	-37	6200	12300	+30	+40	+40
		50	3000	3500	-47	-25	-47	6700	13300	+33	+50	+50
		60	3000	3300	-57	-31	-57	7200	14600	+36	+50	+50
June 28, 1971	Dec 19, 1971	40	3000	3500	-40	-26	-40	6300	12600	+21	+38	+38
		50	3000	3400	-49	-31	-49	6900	14200	+25	+48	+48
		60	3000	3200	-59	-34	-59	7700	16100	+30	+57	+57

Table 4-1d. Conditions For Topographic TV at Day 180

Cone Angle 100°0140°

Launch Date	Arrival Date	Incli-nation (deg)	Morning Terminator Region					Evening Terminator Region				
			Altitude		Latitude			Altitude		Latitude		
			min	max	in	out	max	min	max	in	out	max
May 4, 1971	Nov 2, 1971	40	3100	3800	-35	-15	-35	5400	10600	+32	+40	+40
		50	3000	3700	-46	-23	-46	6100	11900	+35	+50	+50
		60	3000	3500	-57	-29	-57	6700	13800	+37	+59	+59
June 23, 1971	Nov 13, 1971	40	3000	3500	-38	-19	-38	6300	12700	+29	+40	+40
		50	3000	3200	-47	-25	-47	6300	14100	+33	+50	+50
		60	3000	3200	-57	-29	-57	8200	17000	+36	+60	+60
May 9, 1971	Nov 25, 1971	40	3000	3400	-29	-6	-29	6900	14100	+37	+37	+40
		50	3000	3200	-40	-12	-40	7600	15500	+43	+48	+50
		60	3000	3200	-50	-19	-50	8400	17200	+46	+59	+60
June 24, 1971	Nov 25, 1971	40	3000	3400	-35	-16	-35	7000	14300	+32	+40	+40
		50	3000	3300	-45	-21	-45	8100	16500	+36	+50	+50
		60	3000	3200	-55	-25	-55	9300	18700	+41	+60	+60
May 11, 1971	Dec 19, 1971	40	3000	3300	-23	+2	-23	9000	18500	+39	+33	+40
		50	3000	3500	-33	-3	-33	9100	20000	+47	+44	+50
		60	3000	3600	-42	-8	-42	10400	20100	+52	+56	+60
June 28, 1971	Dec 19, 1971	40	3000	3300	-31	-9	-31	9500	18900	+36	+36	+40
		50	3000	3500	-40	-12	-40	10700	20800	+43	+48	+50
		60	3000	3700	-48	-17	-48	14300	22400	+49	+58	+60

inclined orbits have subsatellite points outside the area of interest during the optimum lighting and altitude periods. A brief look at the subsatellite points during other days of the mission indicates a 40° inclined orbit is more desirable than either a 50° or 60° inclined orbit.

On day zero, the May 4 launch, November 2 arrival transfer trajectory results in orbits which have the lowest altitudes, best lighting, and cover the area of interest in the evening terminator region. The June 23-November 13 orbit is second in desirability to the May 4-November 2 trajectory. However, none of the trajectories yield unacceptable orbits when considering only a 40° inclined orbit.

As the mission progresses, the altitudes in the morning terminator region decrease while the altitudes in the evening terminator region increase. By day 180, conditions have shifted so the altitudes over the morning terminator region are optimum. For the latter part of the orbit phase, the May 11 - December 19 and June 28 - December 19 orbits are slightly better, but all the orbits are acceptable.

The optimum lighting angle for color TV is obtained when the Sun-Orbiter-Planet angle is close to 180 degrees. Table 4-2 indicates the maximum cone angle for each of the selected trajectories at 60 day intervals. Also indicated are the altitude and latitude at which the maximum cone angle occurs. The following conclusions can be drawn from Table 4-2:

a. In order to achieve good color TV pictures early in the orbit phase over the region of interest (10°N to 40°S latitude), inclinations of 40 degrees must be chosen.

b. The early arrival dates are favored near the end of the mission when color TV lighting conditions are best since the subsatellite points of the later arrivals are out of the latitude regions of interest and the altitude is generally higher.

c. The later arrivals have slightly better altitude characteristics.

d. The best altitude condition occurs in the middle phase of the mission.

e. The early launch dates are desirable since the cone angles are slightly higher.

f. None of the launch or arrival dates analyzed are far superior to any other.

The Mars Scanner experiment has about the same lighting requirements as the sum of the two TV experiments. However, the requirement for constant altitude and velocity is not met by the sample trajectories. The injection velocity increment eliminates circular or near circular orbits as indicated in Figure 3-5.

Table 4-2. Conditions For Color TV Experiment 1971 Example Mars Orbits

Launch Date	Arrival Date	Incli-nation	Day 0			Day 60			Day 120			Day 180		
			Cone <	Alt	Lat	Cone <	Alt	Lat	Cone <	Alt	Lat	Cone <	Alt	Lat
May 4, 1971	Nov 2, 1971	40	164	4400	-39	163	3100	-31	172	3200	-10	177	3450	10
		50	155	4800	-48	152	3250	-41	162	3200	-16	177	3400	6
		60	147	4600	-53	141	3200	-50	153	3300	-20	173	3900	5
June 23, 1971	Nov 13, 1971	40	165	4200	-39	154	3200	-35	160	3250	-15	174	4000	6
		50	156	3900	-47	148	3200	-43	158	3350	-19	172	4100	2
		60	147	4400	-54	132	3300	-52	150	3600	-20	169	4700	3
May 9, 1971	Nov 25, 1971	40	162	4200	-39	166	3050	-23	178	3300	-1	171	4300	19
		50	150	3800	-49	158	3050	-30	171	3500	-5	172	4350	17
		60	142	3700	-59	148	3050	-35	165	3650	-6	174	4600	9
June 24, 1971	Nov 25, 1971	40	161	3600	-39	155	3100	-31	161	3350	-12	177	3950	9
		50	153	3200	-49	146	3050	-40	157	3600	-14	175	3450	4
		60	145	3800	-58	140	3100	-45	154	3750	-15	173	5000	5
May 11, 1971	Dec 19, 1971	40	163	3100	-34	170	3150	-15	173	3750	7	168	5000	25
		50	152	3100	-43	162	3250	-18	174	3850	5	167	5100	25
		60	143	3100	-50	156	3300	-20	175	4100	4	165	5750	25
June 28, 1971	Dec 19, 1971	40	159	3150	-39	160	3100	-25	169	3950	-3	175	5150	16
		50	149	3200	-49	153	3300	-28	167	4100	-3	175	5500	17
		60	139	3200	-58	145	3400	-30	164	4500	-3	175	7100	17

Table 4-1a through 4-1d, which give topographic TV conditions, gives a good measure of the conditions for the scanner. The maximum altitudes will be larger in the case of the scanner but as far as orbit selection, all violate the constant altitude and velocity constraint equally.

The ultraviolet spectrometer experiment also requires a low altitude which of course is not fully satisfied. The inclination to the ecliptic varies during the 180 days in orbit. Initially the inclination to the ecliptic is between 17 and 22 degrees for all the selected trajectories. The inclination then decreases slightly and finally increases to inclinations greater than the 30° which is required.

The dual frequency occultation experiment requires Earth occultation. It is desirable to carry out this experiment as early as possible in the mission in case of spacecraft malfunction. However, Earth occultation disrupts the transmission of data back to Earth. The Earth occultations should be as short as possible in order to minimize the loss of data transmission time. Table 3-3 indicates that most of the sample trajectories yield the desired characteristics.

5.0 CAPSULE TRAJECTORY

For an approach velocity of 3.5 km/sec, the spacecraft velocity at the separation distance of 300,000 is 3.54 km/sec. The component of the separation Δ V normal to the path which is required to achieve the desired capsule aim point is given by:

$$\Delta V_N = \frac{\Delta B \times Vs}{R_s} = \frac{7730 \times 3.54}{3 \times 10^5} = .0912 \text{ km/sec}$$

The component of ΔV_N in the plane of the orbiter trajectory is 0.79 km/sec and the out-of-plane component is 0.046 km/sec.

If the separation Δ V is perpendicular to the spacecraft path (i.e., no tangential component), capsule entry occurs about 17 minutes prior to the time of periapsis passage of the orbiter. If a 40 mb atmosphere is assumed with parachute deployment at Mach 1, the time from entry to impact is about 15 minutes. Therefore, at the time of impact, the orbiter is only two minutes from periapsis. However, line-of-sight from orbiter to capsule is lost before impact since the orbiter will disappear below the horizon before capsule impact. Since there is a requirement that the capsule-orbiter communication link be maintained up to impact, the capsule must be given a tangential Δ V at separation in order to increase its velocity and make entry occur sooner. If a tangential Δ V is imparted to the capsule such that entry occurs 12 minutes earlier than would be the case with no tangential ΔV, or 29 minutes before orbiter periapsis, then the line-of-sight from capsule to orbiter at impact, (again assuming a descent time of 15 minutes) is 10° above the horizon. The tangential ΔV required is 0.0315 km/sec, giving a total ΔV of 0.0965 km/sec. With these conditions

the capsule angle of attack at entry is about 70°, assuming that the capsule attitude remains unchanged from separation until entry. The direction cosines of the ΔV direction in ecliptic coordinates are

$$\Delta V = \begin{pmatrix} 0.671 \\ 0.210 \\ 0.710 \end{pmatrix}$$

corresponding to a cone angle of 133° and a clock angle of 202°.

The cone angle is defined as the Sun-vehicle-ΔV angle while the clock angle is the angle between the projections of Canopus and the ΔV onto the plane perpendicular to the Sun-vehicle vector measured from the Canopus projection in a clockwise sense when looking from behind the spacecraft toward the Sun. Figure 5-1 defines the vehicle coordinate system as well as the cone and clock angles for a Sun-Canopus oriented coordinate system. This system is centered at the spacecraft.

If $\bar{S}c^1$ is the unit vector representing the capsule approach asymptote direction:

$$\overline{S_c'} = \overline{S'} + \frac{\Delta V}{V_\infty} \overline{\Delta V'}$$

The change in direction as compared to the spacecraft approach asymptote is about 1.5°. A recalculation of the capsule impact parameter and the separation ΔV, using the improved values for the direction of the capsule asymptote, produces no substantial change in the results given above, indicating that the original assumption that the capsule approach asymptote is the same as the orbiter asymptote is valid.

The time of visibility of the capsule from Goldstone after impact can be made longer than two hours, which is the limiting value for the capsule trajectory described above, by landing nearer the morning terminator. Since the change in aim point is larger requiring a larger normal ΔV component, a larger separation ΔV is required. Also the capsule must be speeded up even more in order to maintain capsule - orbiter line-of-sight, requiring a larger tangential ΔV component.

The separation ΔV can be reduced considerably if a landing site in the southern hemisphere is selected. For a landing site in the plane of the orbiter trajectory and the same entry angle (42°) as for the previous trajectory, the required ΔV is only 0.054 km/sec and no tangential velocity component is required. The latitude of the landing would be about 40°S and visibility from Goldstone is maintained for more than two hours after entry. The choice of Syrtis Major as a landing site may be too harsh a constraint on the Voyager system indicating a change to a southern hemisphere landing site.

6.0 CHOICE OF DESIGN TRAJECTORIES FOR 1971 MISSION

The design landing site for the capsule was chosen to be Syrtis Major since this site placed the most severe restrictions on the design of the spacecraft and trajectories. That is, the range to the capsule from the orbiter is greater during the approach phase since the orbiter is in the southern hemisphere during approach and the capsule is in the northern hemisphere. The time Goldstone can see the landing site is slightly reduced. More important is that loss of line of sight between the capsule and orbiter before capsule impact is more likely, which means the capsule must be given a time of flight velocity adjustment.

Choosing a specific landing sight restricts the allowable arrival dates since entry and impact must take place in view of Goldstone. The time of arrival during the day is also restricted but this is true even if a landing site is not chosen. The arrival dates due to the Goldstone constraint were presented in Figure 3-2. There is an additional restriction however. If dates after November 12 are chosen, the capsule must land too far toward the morning termination thus causing a loss of capsule-orbiter line of sight. This is true even assuming that the capsule is given a tangential velocity increase of reasonable magnitude. The same restriction decreases the second period shown by Figure 3-2 to those dates before December 16.

Examining Figure 3-1 indicates the constant approach velocity boundary of 3.5 km/sec provides arrival dates in the allowable region as far as the Goldstone view constraint as well as the orbit specification. The two sample trajectories which are located on this boundary are acceptable from the standpoint of all the specification and guidelines. Therefore, these two trajectories are chosen as the design trajectories.

7.0 ARRIVAL DATE SEPARATION

The problem of launching the second spacecraft on a mission similar to that of the first spacecraft is not a small one, due to the ten day separation in arrival date requirement. Examining Figures 3-1 and 3-2 indicates that two choices exist. If the first spacecraft is launched in the beginning of the launch window and arrives near November 2, the second spacecraft can be launched such as to arrive near November 12. If however, the first spacecraft is not launched during the early part of the window (before May 28) the second spacecraft must be set to arrive in the period between December 6 and 16 for a Syrtis Major capsule impact area. The disadvantage to the latter choice is the different approach velocity and geometry.

Going to the later arrival dates may also result in the dual frequency occultation experiment being postponed till the end of the orbit phase and Sun occultations will occur sooner. A late launch will tend to maintain the approach geometry and velocity more similar to the first spacecraft for the December arrival date.

8.0 ENGINEERING DESIGN PARAMETERS

8.1 HELIOCENTRIC AND AEROCENTRIC ORBIT

Several trajectory dependent parameters are required for design of various subsystems of the spacecraft, such as the antenna pointing, communications, power, experiment pointing and approach guidance sensors. Three heliocentric transfer trajectories were chosen to bracket the range of parameters. Table 8-1 indicates the parameters of interest as well as their use. Also indicated are the figures on which they are presented.

Figure 5-1 defines the vehicle coordinate system assuming a Sun-Canopus attitude reference system. The system has its center at the spacecraft. Direction from the spacecraft to various bodies are specified by cone and clock angles. The cone angle is defined as the Sun-vehicle-body angle while the clock angle is the angle between the projections of Canopus and the body onto the plane perpendicular to the Sun-vehicle vector measured from the Canopus projection in a clockwise sense when looking from behind the spacecraft toward the sun.

Table 8-1. Design Parameters

Parameter	Use	Figure No.
Distance to Sun	Solar Array Design	8A
Communication Distance	Telecommunication System Design	8B
Earth Clock Angle Versus Time	Design of gimbal and gimbal drives	8C
Earth Cone Angle versus Time		8D
Earth Cone versus Clock Angle	Design of beamwidth for antennas	8E
Canopus Cone Angle	Design of gimbal freedom in Canopus Sensor and sensor placement	8F
Distance to Planet versus Time	Approach Guidance Sensor design	8G
Mars Cone Angle Versus Time	Design of beamwidth and gimbal freedom of Approach Guidance Sensors	8H
Mars Clock Angle Versus Time		8I

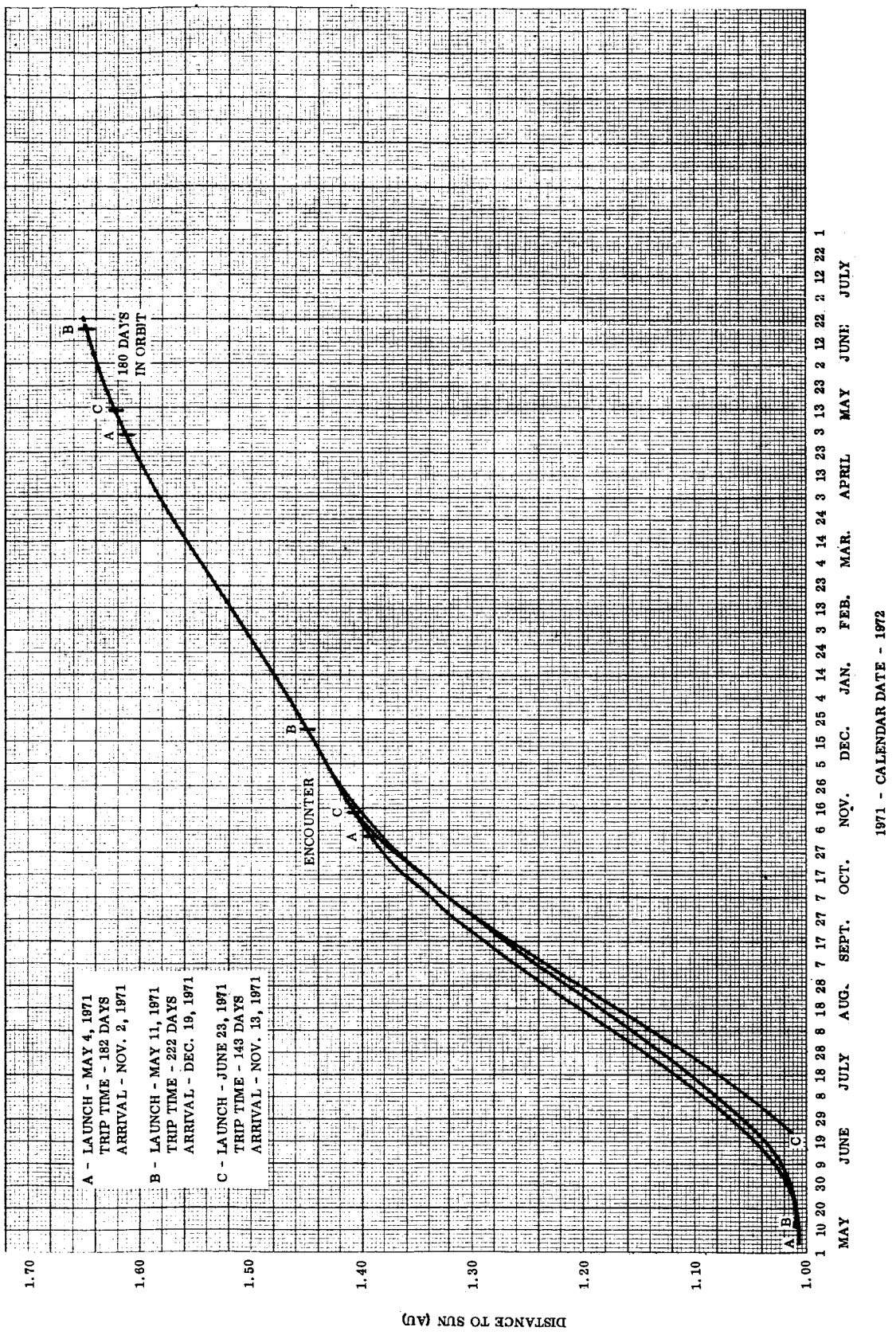

Figure 8A. Distance to Sun

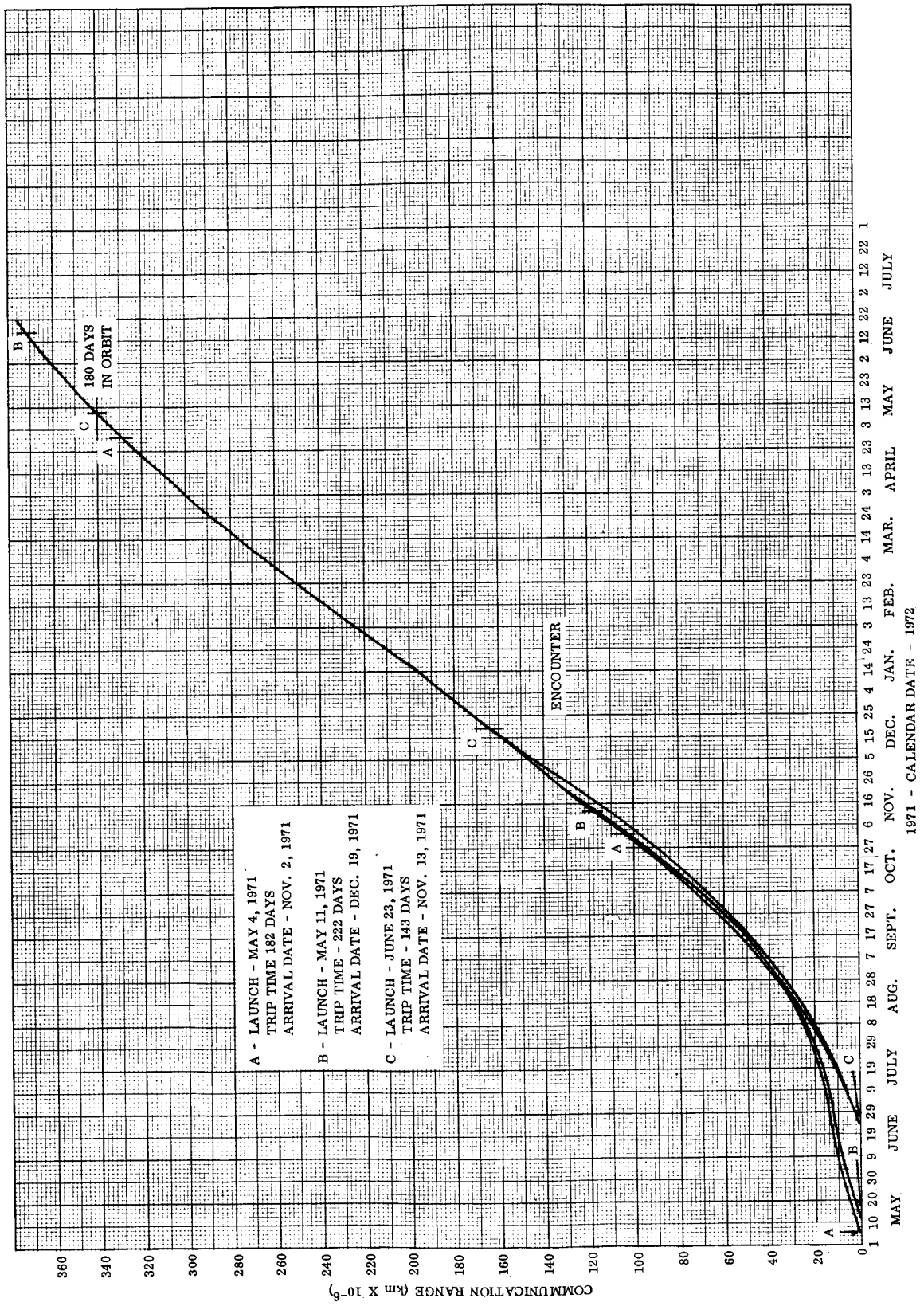

Figure 8B. Communication

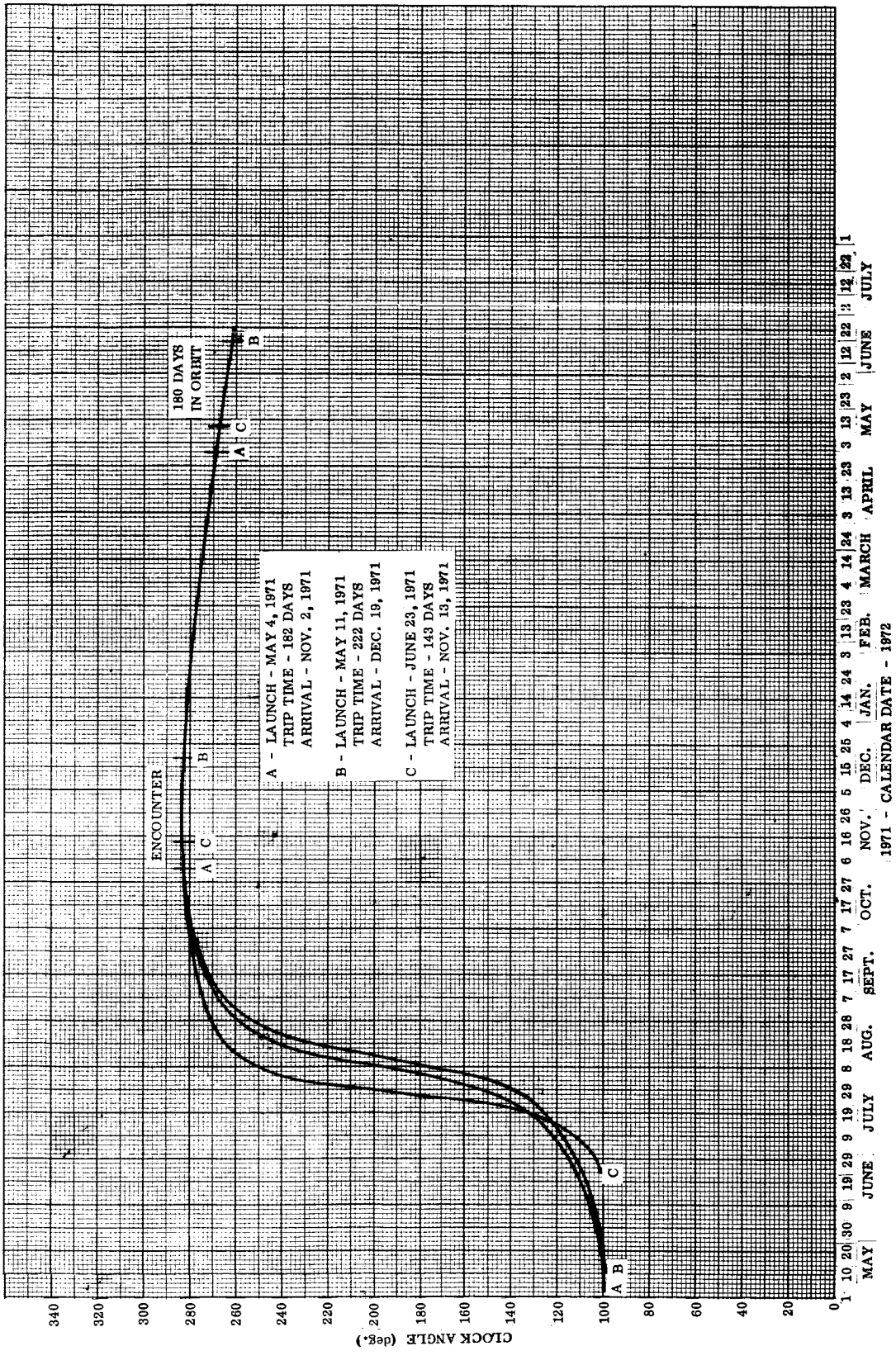

Figure 8C. Earth Clock Angle

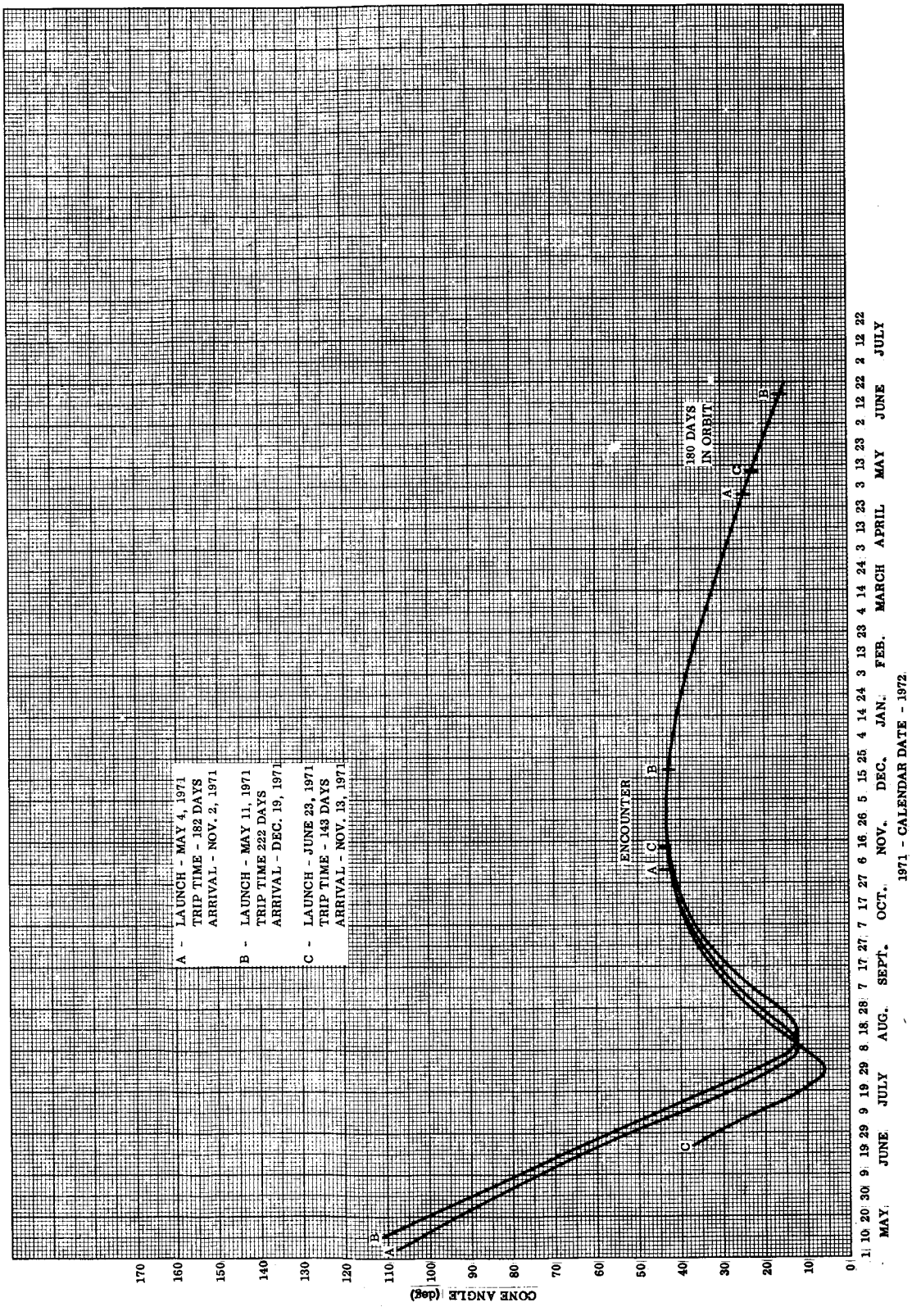

Figure 8D. Earth Cone Angle

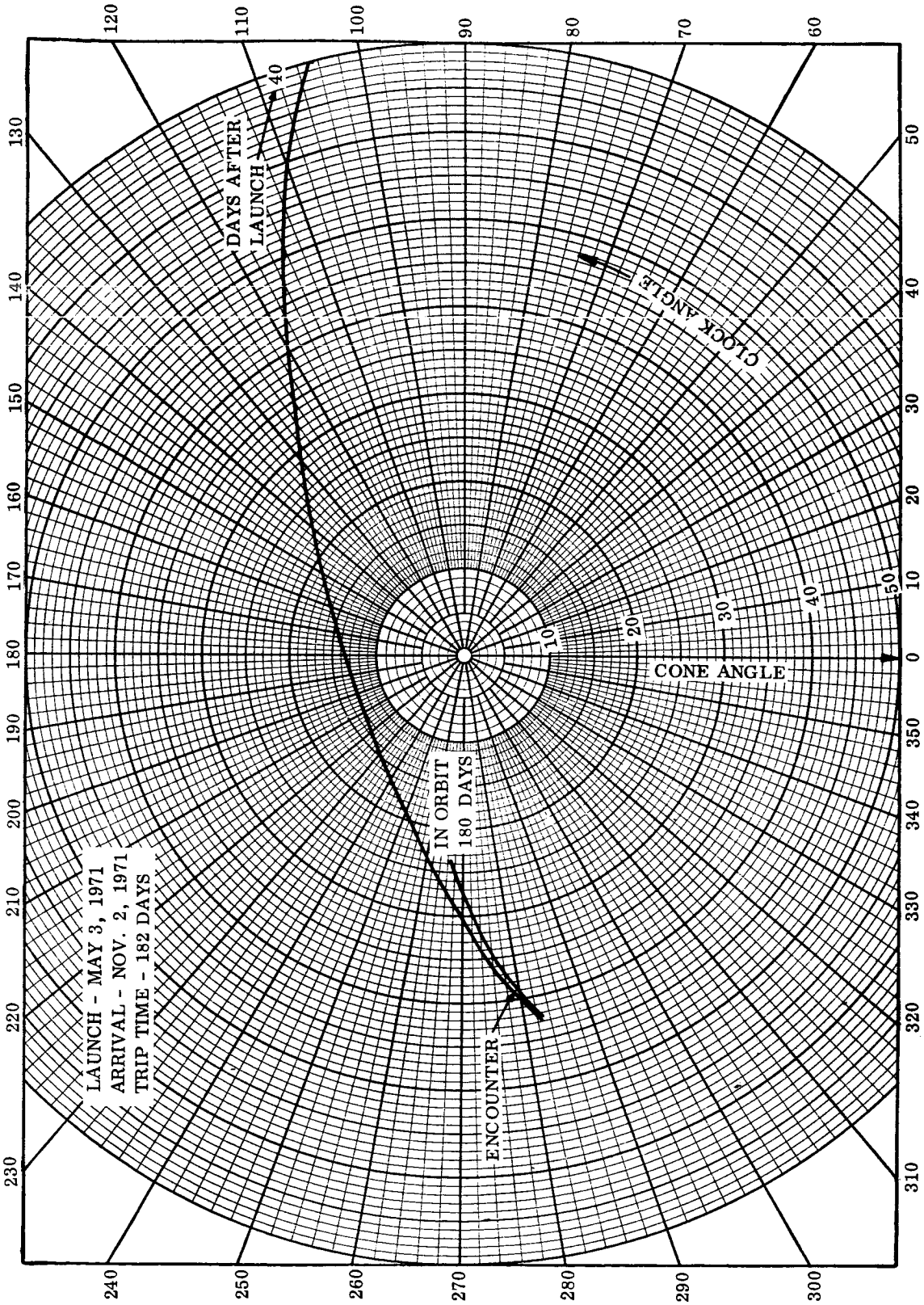

Figure 8E-1. Earth Cone and Clock Angles

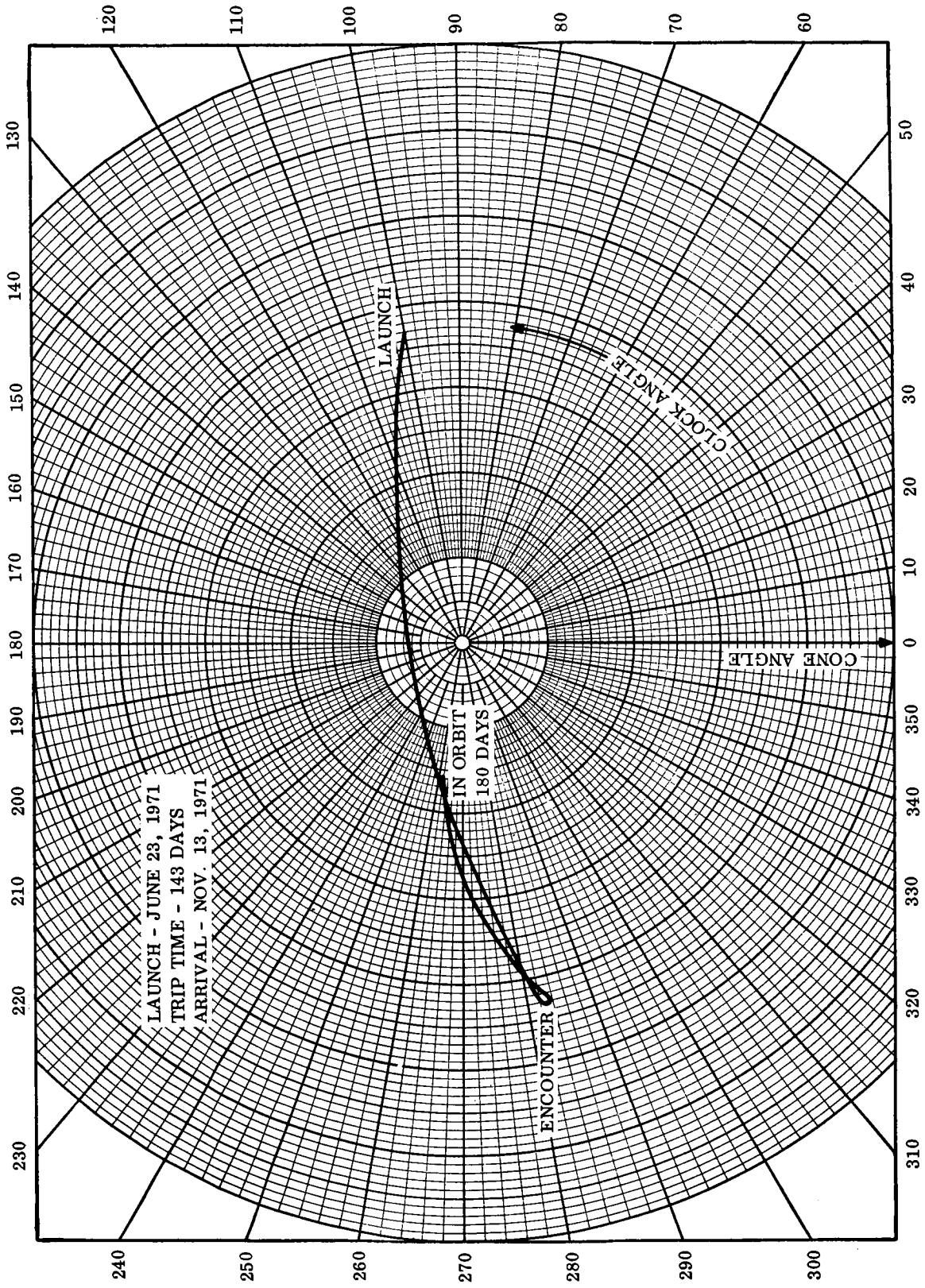

Figure 8E-2. Earth Cone and Clock Angles

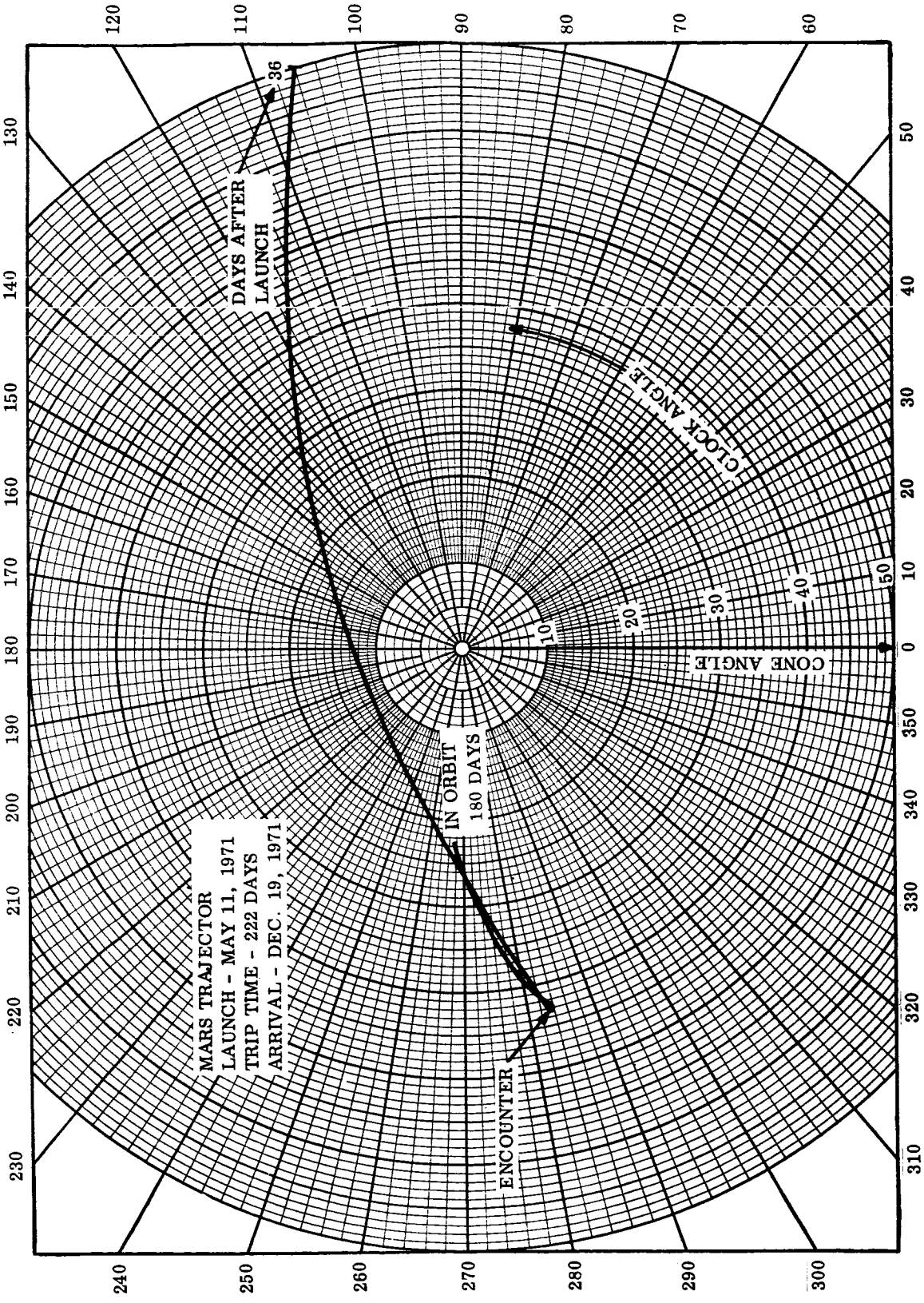

Figure 8E-3. Earth Cone and Clock Angles

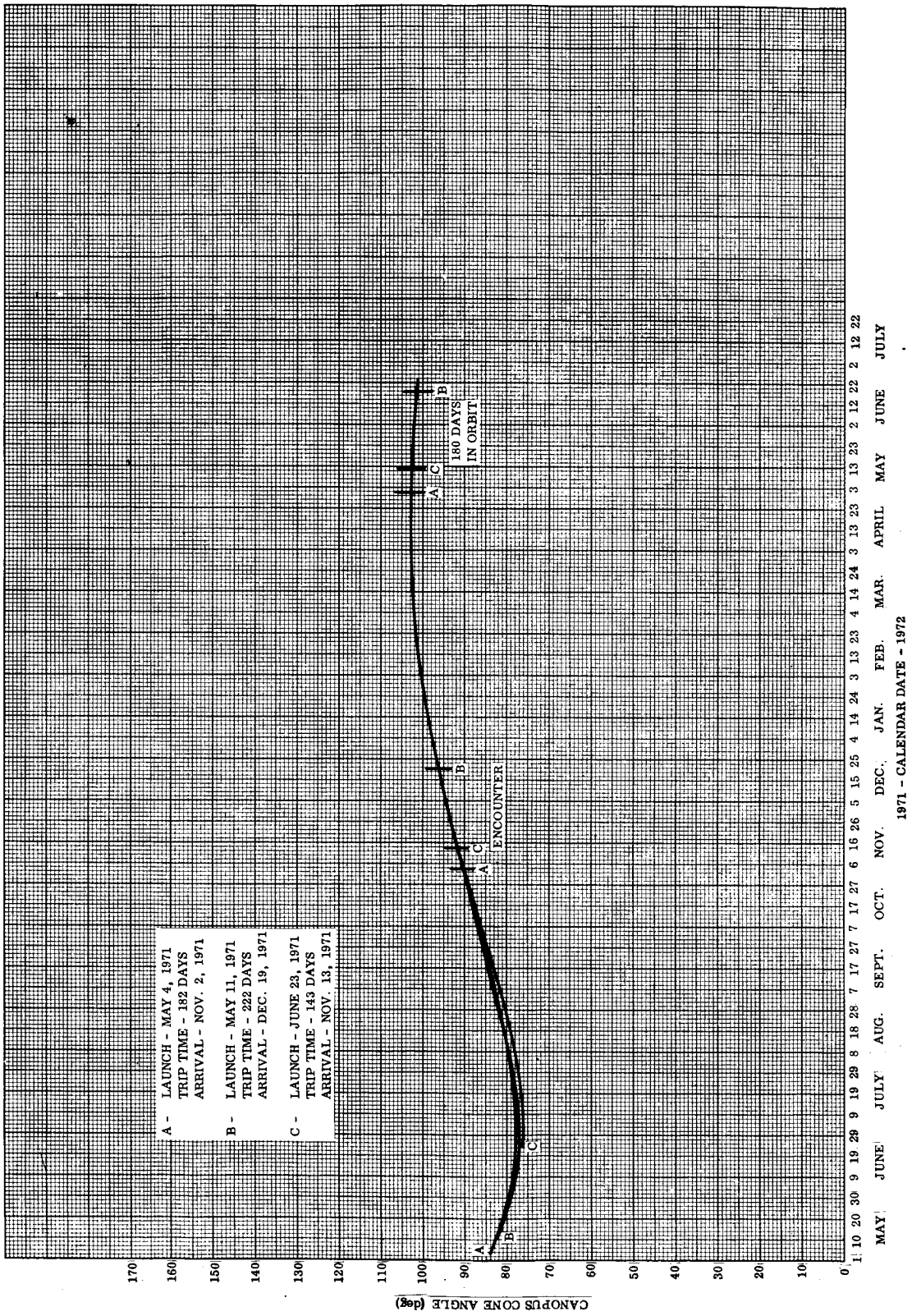

Figure 8F. Canopus Cone Angle

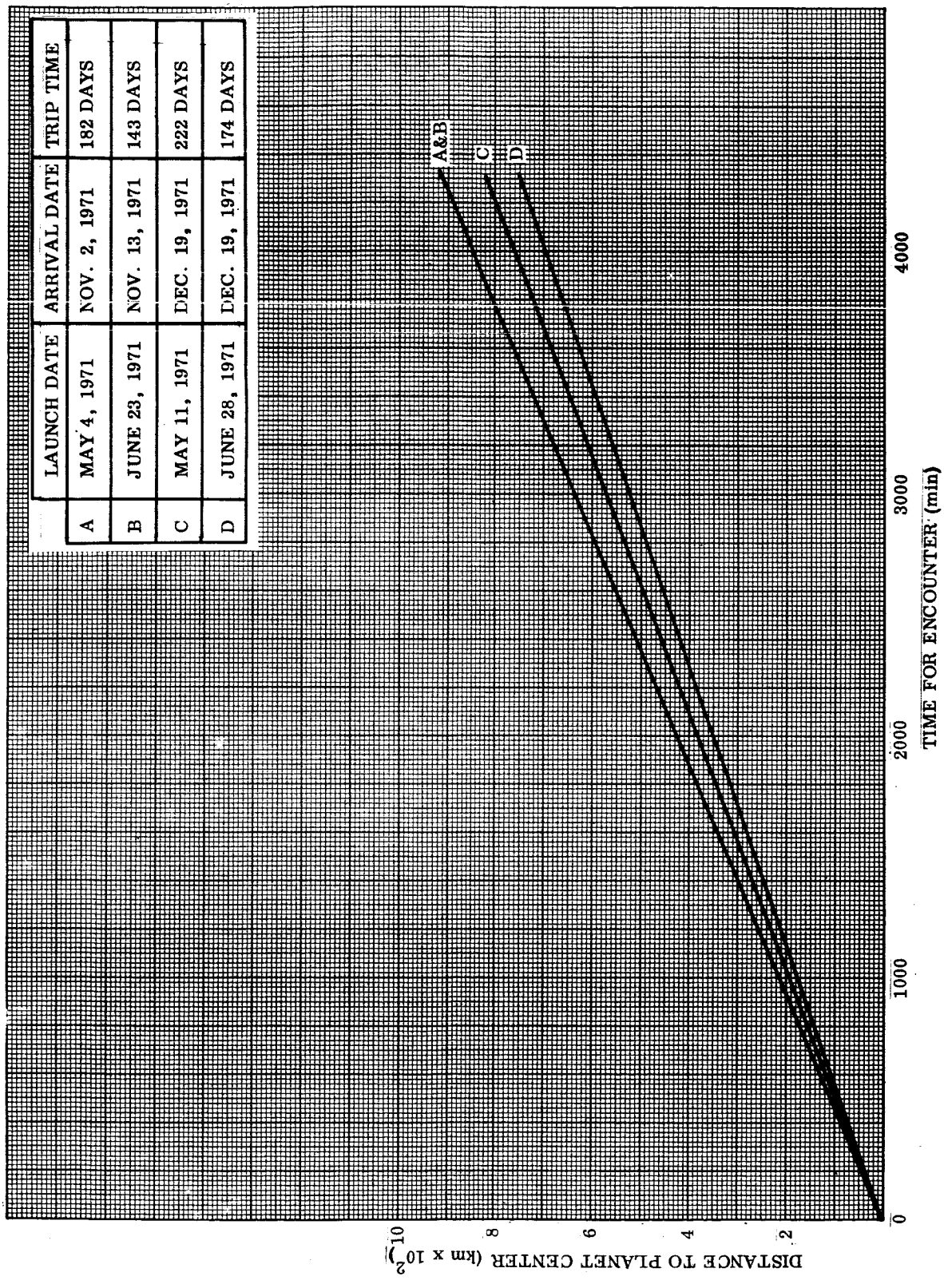

	LAUNCH DATE	ARRIVAL DATE	TRIP TIME
A	MAY 4, 1971	NOV. 2, 1971	182 DAYS
B	JUNE 23, 1971	NOV. 13, 1971	143 DAYS
C	MAY 11, 1971	DEC. 19, 1971	222 DAYS
D	JUNE 28, 1971	DEC. 19, 1971	174 DAYS

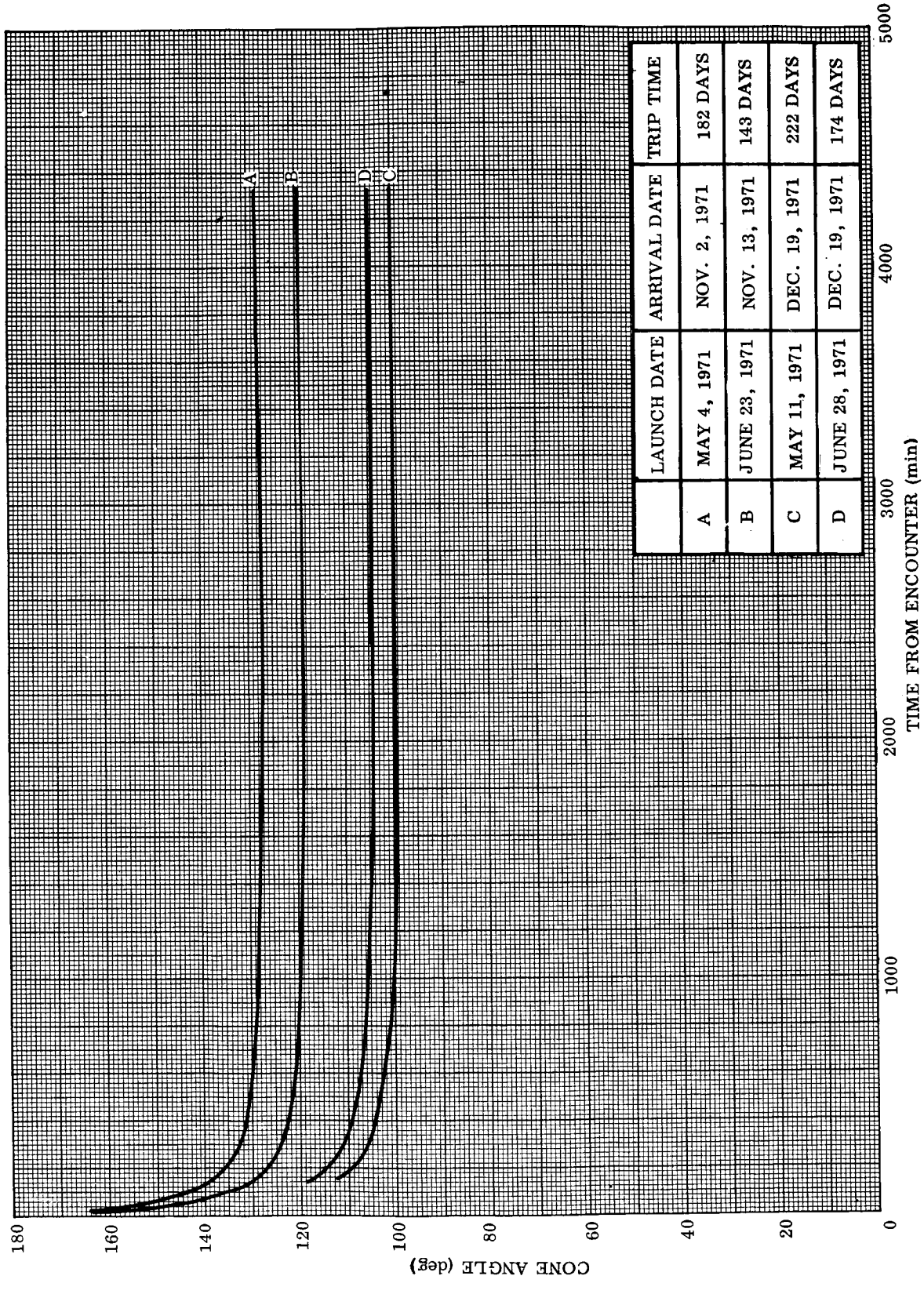

	LAUNCH DATE	ARRIVAL DATE	TRIP TIME
A	MAY 4, 1971	NOV. 2, 1971	182 DAYS
B	JUNE 23, 1971	NOV. 13, 1971	143 DAYS
C	MAY 11, 1971	DEC. 19, 1971	222 DAYS
D	JUNE 28, 1971	DEC. 19, 1971	174 DAYS

Figure 8H. Mars Cone Angle Approach Phase

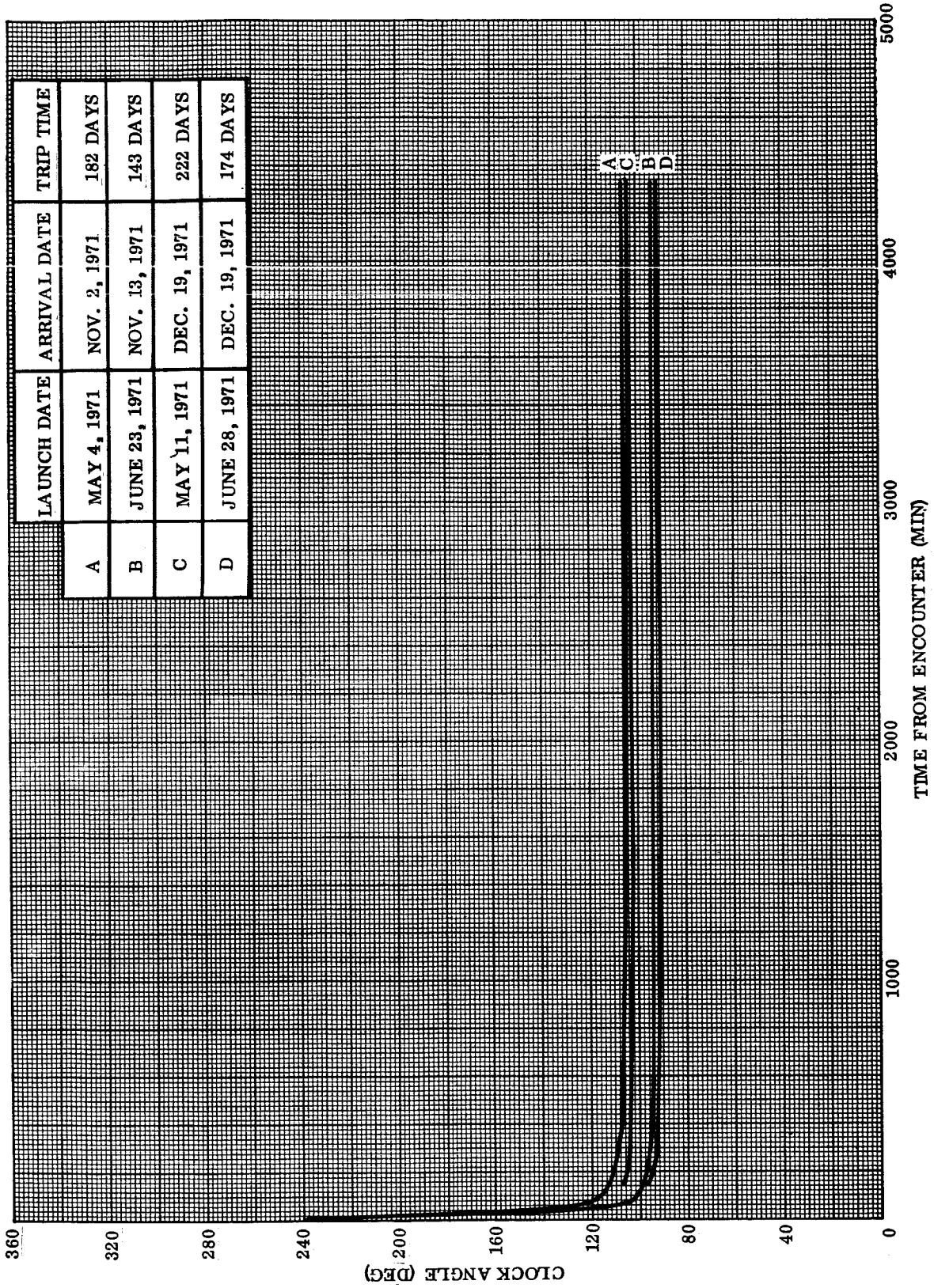

	LAUNCH DATE	ARRIVAL DATE	TRIP TIME
A	MAY 4, 1971	NOV. 2, 1971	182 DAYS
B	JUNE 23, 1971	NOV. 13, 1971	143 DAYS
C	MAY 11, 1971	DEC. 19, 1971	222 DAYS
D	JUNE 28, 1971	DEC. 19, 1971	174 DAYS

Figure 8I. Mars Clock Angle Approach Phase

8.2 NEAR EARTH TRAJECTORY CHARACTERISTICS

The near Earth tracking geometry is of interest for designing the communication equipment. Tracking data for three radar stations are presented in Figures 8-1, 8-2 and 8-3. The data consists of range, range rate, azimuth and elevation as functions of time. The azimuth is measured from north and the elevation from the geodetic local horizontal. Six tracking stations were considered as shown in the following table of coordinates.

Station	Latitude (deg)	Longitude (deg)	Altitude (ft)
Cape Kennedy	28.4468	-80.57	8.58
Johannesburg	-25.8874	27.6848	4491.
Woomera	-31.1026	136.7882	525
Camberra	-35.40111	148.98027	-
Madrid	40.27	-3.42	-
Goldstone	35.3895	243.1518	3460

The trajectory considered in this case is typical for 1971.

Launch Date	May 11, 1971
Launch Azimuth	75°
Launch Site	Cape Kennedy
Parking Orbit	
Inc.	33°
Altitude	185 km
Transfer Injection Point	
Latitude	23.44
Longitude	9°W
Departure Asymptote	

Declination	31.2°
Right Ascension	339°
Trip Time	191 days
Arrival Date	November 18, 1971
C_3	-0.088

For the trajectory chosen only three stations are in view for the initial portion of the departure trajectory which was considered out to a radius of 64,000 km from the earth. They are Johannesburg, Woomera and Camberra. The ground trace of the departure trajectory is shown in Figure 8-4.

8.3 SPACECRAFT - CAPSULE LINE OF SIGHT

Of prime importance for the design of the capsule - orbiter - Earth relay link are the time histories of orbiter-lander range, range rate, clock angle and cone angle for the time interval starting at lander separation and ending at lander impact. Corresponding velocity increment requirements are also specified.

The following is a summary of the trajectory and encounter parameters:

Launch date - May 4, 1971

Arrival date - November 2, 1971

Trip time - 182 days

Arrival velocity - 3.5 km/sec

ZAP angle - 124 degrees

Orbiter periapsis altitude -3000 km

Inclination of orbiter plane - 40 degrees

Lander separation distance - 300,000 km

Martian atmosphere - 40 mb

Parachute deployment - Mach 1

Entry altitude - 304.8 km

$W/C_D A = 3.22\ lb/ft^2$

Touchdown velocity = 3353 m/sec

Time from entry to touchdown with parachute - 1094 seconds

Two touchdown points were selected for this study. The first landing site (Syrtis Major) is located at 10 degrees north latitude and at 359.4 degrees east longitude. Longitude is measured from the meridian containing the Mars-Sun line. The details of this trajectory including velocity requirements and parameters for the Capsule - Orbiter - Earth relay radio link are given in VS 220 FD 101. The trajectory for the second landing site, an in-plane site, is described in Section 5 of this document.

The time histories of trajectory related communication parameters for the in-plane landing site are given in Figures 8-5 through 8-10. As for the out of plane landing site, Syrtis Major, the cone and clock angles remain essentially constant until the time that the orbiter assumes its retro-thrust attitude. For this landing site, the maximum range is about 4800 km. The range rate extremes vary from -1.6 km/sec to +2.5 km/sec. The maximum rate of change of range rate is 62 m/sec^2 for a short period of time just after the time of entry. Average rate of change of range rate during most of the remaining entry period is 5.2 m/sec^2.

The results reported in this section are based on the dense 40 mb Martian atmosphere which accentuates the problem of maintaining line-of-sight between the orbiter and the capsule until capsule touchdown. However, it should be noted that the light 10 mb atmosphere and lower scale height is the more severe case when considering the rates of change of range rate during entry. The maximum rate of change of range rate during entry for the case of the 10 mb atmosphere is estimated to be 500 m/sec^2 for the 10° N latitude landing site.

9.0 ALTITUDE DISPERSION OF AEROCENTRIC ORBIT

Due to navigation and guidance errors discussed in VB 220AA102 other than nominal orbits may be achieved. The inclination dispersion effects can be neglected since this deviation is small; the effects have already been noted (see Section 4). The altitude dispersions are appreciable and must be investigated. For the following nominal trajectory and orbit

Launch Date	June 23, 1971
Trip Time	143 days
Arrival Date	November 13, 1971
Approach Velocity	3.5 km/sec
C3	0.18 $(km/sec)^2$

Inclination	40°
Periapsis Altitude	3000 km
Apoapsis Altitude	25000 km

two dispersion orbits were investigated. The altitudes were 2500-21000 km and 3500-32000 km. They were chosen by allowing the periapsis altitude to vary by 500 km and using the velocity increment for the nominal orbit. This procedure results in dispersions larger than are expected thus the analysis is very pessimistic. The expected dispersions of the periapsis altitude are only ±350 km.

Table 9-1 indicates a slight change in the occultation times for the Sun and Earth; the higher orbit having less occultation and the lower orbit having more as would be expected. There is no significant change however. Canopus is not occulted and Table 9-2 indicates the Canopus sensor will not see the planet since the minimum angle to the limb is greater than 35 degrees.

Except for changes in altitude, the color TV and topographic TV conditions are not seriously changed although the lower altitudes are preferable as indicated in Tables 9-3 and 9-4. These tables are derived from Figures 9-1a and b and 9-2A and 9-2B. Figure 9-3 indicates the effect on the position of the periapsis.

The above indicates the general conclusion that even for pessimistic altitude dispersion estimates, the scientific and engineering characteristics of the orbit are not appreciably changed.

10.0 1973 MISSION TRAJECTORIES

Applying the same specifications to the 1973 trajectories as were imposed on the 1971 trajectories eliminates a large number of trajectories as indicated in Figure 10-1. As for 1971, the 3.5 km/sec approach velocity line has been superimposed on Figure 10-1. Two example trajectories at either end of the launch period on this boundary were selected because of the similarity with the 1971 design trajectories. The approach velocities are identical while the approach geometry is only slightly different (slightly higher ZAP angles). The time of the year of arrival for the 1973 trajectories is approximately two months later than that for 1971. The 3.5 km/sec boundary for 1973 extends over almost the entire launch period possible, which is approximately 36 days.

The Syrtis Major viewing times for the range of 1973 arrival dates are shown in Figure 10-2. The 3.5 km/sec approach velocity boundary is now satisfactory since the arrival dates occur during the period that Syrtis Major is not in view of Goldstone for a minimum of two hours at any time during the first two days after encounter. A later arrival and lower approach velocity must be used if Syrtis Major is to be the landing site and Goldstone is to view the impact.

Table 9-1. Occultation Times per Orbit for Dispersion Orbits

Altitude (km)	Sun Occultation Time - Minutes							Earth Occultation Time - Minutes						
	Days After Encounter							Days After Encounter						
	0	30	60	90	120	150	180	0	30	60	90	120	150	180
2500 - 21000	0	0	0	0	0	88.33	105.	53.33	56.67	0	0	0	0	86.67
3000 - 25000 (N)	0	0	0	0	0	0	91.67	63.33	46.67	0	0	0	0	0
3500 - 32000	0	0	0	0	0	0	0	61.67	63.33	0	0	0	0	0

Nominal Orbit

Launch	June 23, 1971
Arrival	Nov. 13, 1971
Inclination	40°

Table 9-2. Minimum Canopus-Orbiter-Near Limb Angles for Dispersion Orbits vs Days

Altitudes (km)	Canopus-Orbiter-Near Lime Angle (DE6)						
	0	30	60	90	120	150	180
2500 - 21000	61.24	58.62	55.91	53.17	50.43	47.72	45.04
3000 - 25000	63.41	61.83	60.89	58.41	56.71	55.04	53.38
3500 - 32000	65.33	64.45	63.52	62.54	61.53	60.50	59.46

Table 9-3. Conditions for Topographic TV Dispersion Orbits

Launch	June 28, 1971
Arrival	November 13, 1971
Inclination	40°
Norminal Altitude	3000 - 25000 km

Cone Angle 100° - 140°

Day	Altitude (km)	Morning Terminator Region					Evening Terminator Region				
		Altitude		Latitude			Altitude		Latitude		
		Min.	Max.	In	Out	Max.	Min.	Max.	In	Out	Max.
0	2500 - 21000	6800	12200	+ 2	-24	-24	2500	2800	-36	-15	-36
	3000 - 25000 (N)	6600	13800	+ 2	-24	-24	3400	3400	-36	-15	-36
	3500 - 32000	7500	17700	+ 2	-24	-24	3500	4000	-36	-15	-36
60	2500 - 21000	4900	6700	-25	-40	-40	2700	4100	-16	+13	-16
	3000 - 25000	3900	7400	-22	-39	-39	3100	4800	-17	+11	-17
	3500 - 32000	4500	8300	-23	-39	-39	3700	5800	-19	+10	-19
120	2500 - 21000	2700	4200	-39	-32	-40	3500	6600	+12	+34	+34
	3000 - 25000 (N)	3100	4700	-39	-34	-40	4300	8000	+ 7	+39	+39
	3500 - 32000	3600	5200	-38	-35	-40	5100	9800	+ 6	+31	+31
180	2500 - 21000	2500	3100	-36	-26	-36	5100	10100	+32	+40	+40
	3000 - 25000 (N)	3000	3500	-38	-19	-38	6300	12700	+29	+40	+40
	3500 - 32000	3500	3900	-36	-21	-36	7800	16300	+26	+40	+40

Table 9-4. Conditions For Color TV - Dispersion Orbits

Altitude (km)	Day 0			Day 60			Day 120			Day 180		
	Cone <	Alt.	Lat.	Cone <	Alt.	Lat.	Cone <	Alt.	Lat.	Cone <	Alt.	Lat.
2500 - 21000	164	3400	-39	159	2600	-34	167	2600	-13	180	3000	10
3000 - 25000 (N)	165	4200	-39	154	3200	-35	160	3250	-15	174	4000	6
3500 - 32000	164	4600	-39	158	3500	-35	161	3600	-17	171	4500	-2

The significant spacecraft parameters for the 1973 mission have been presented in VB220FD101.

11.0 REFERENCES

1. Preliminary Voyager 1971 Mission Specification, JPL Project Document No. 45, V-MA-004-001-14-03, May 1, 1965.

2. Voyager 1971 Mission Guidelines, JPL Project Document No. 46, V-MA-004-002-14-03, May 1, 1965.

3. Mariner, Mars 1969 Orbiter Technical Feasibility Study, JPL, EDP-250, 16 November 1964.

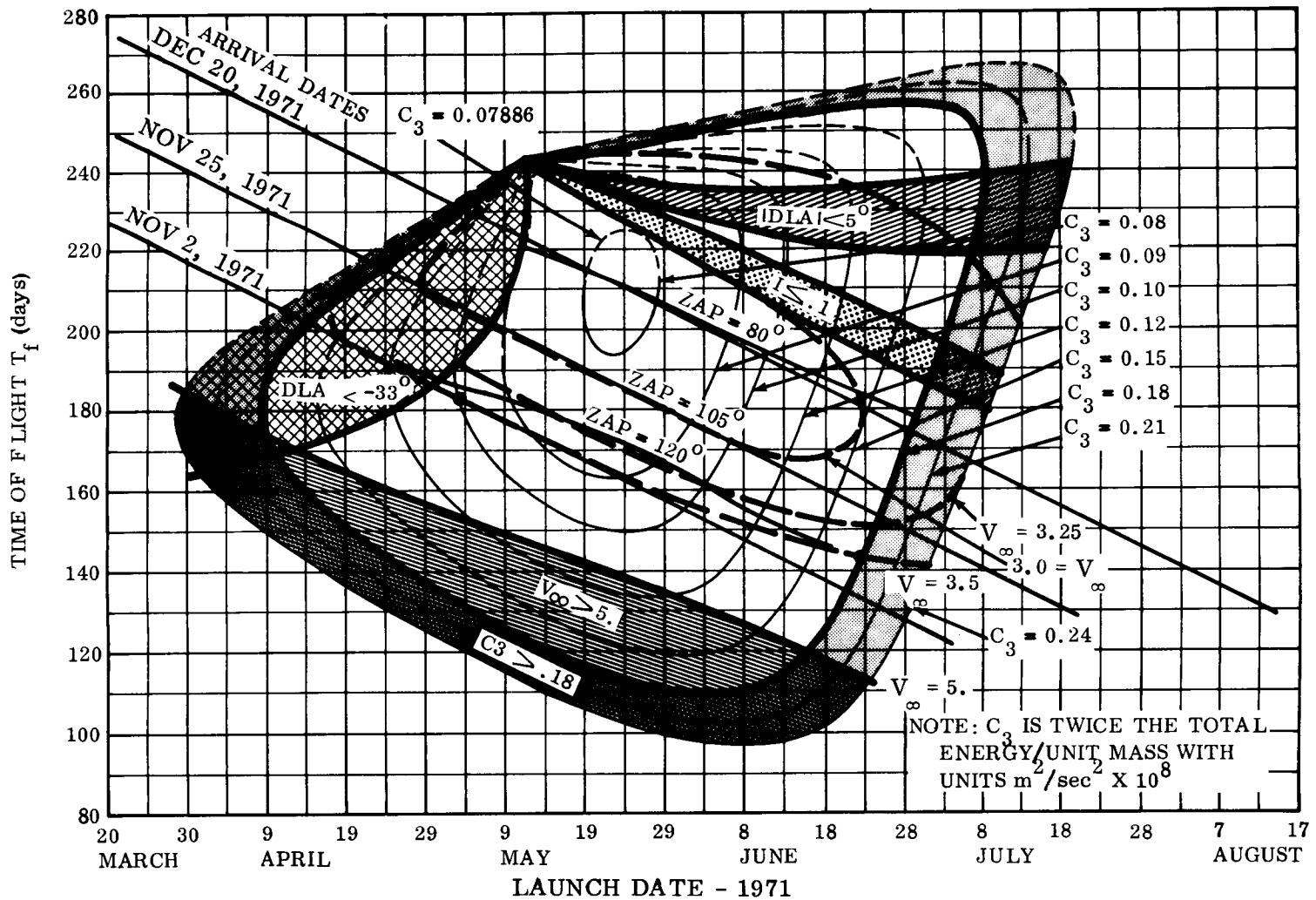

● = DESIGN TRAJECTORIES
ZAP = SUN-MARS APPROACH ASYMPTOTE ANGLE
DLA = DECLIMATION OF DEPARTURE ASYMPTOTE
I = INCLINATION TO THE ECLIPTIC
V_∞ = APPROACH VELOCITY < KM/SEC

Figure 3-1. Mars 1971: Time of Flight vs. Launch Date

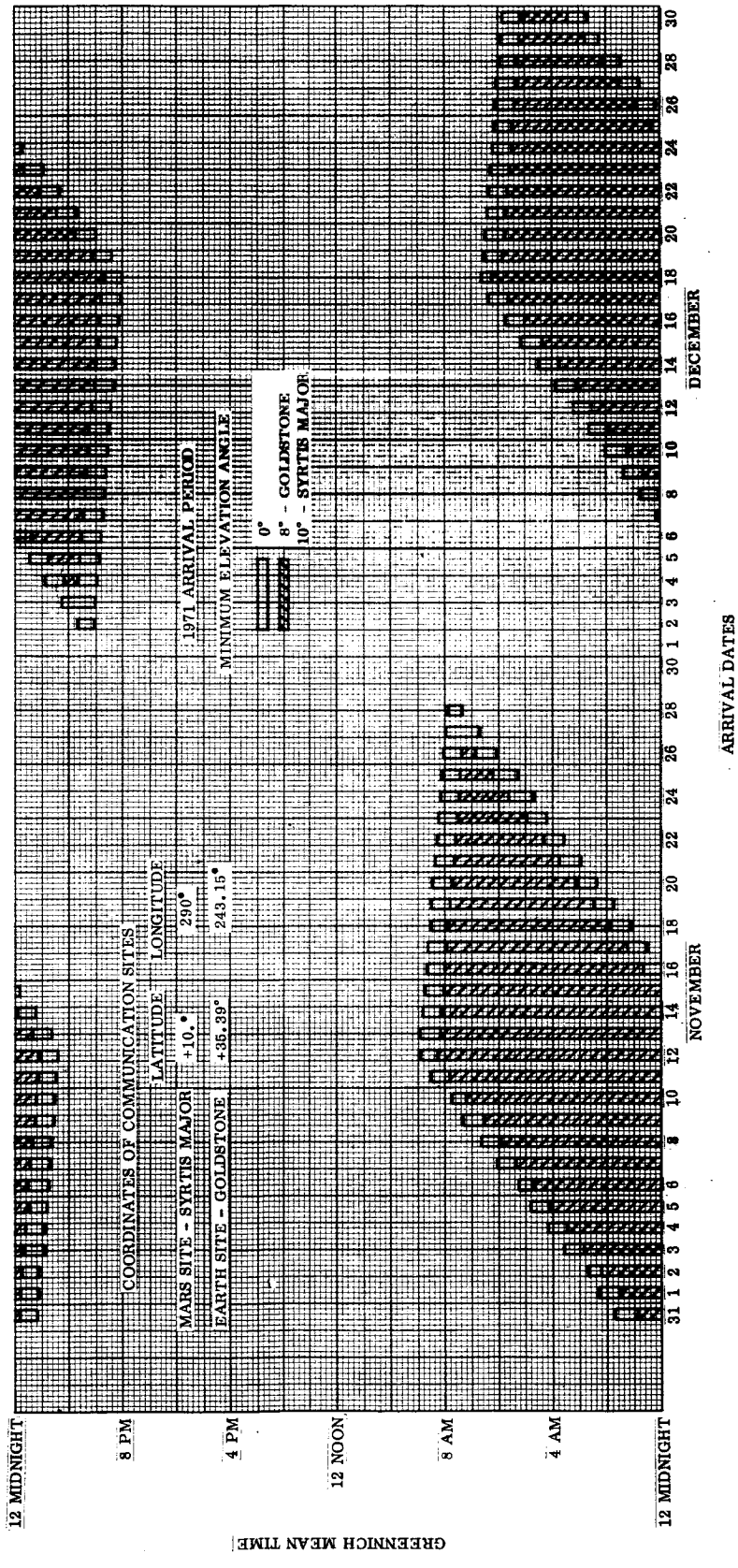

Figure 3-2. Periods of Time When Goldstone Can View Syrtis Major

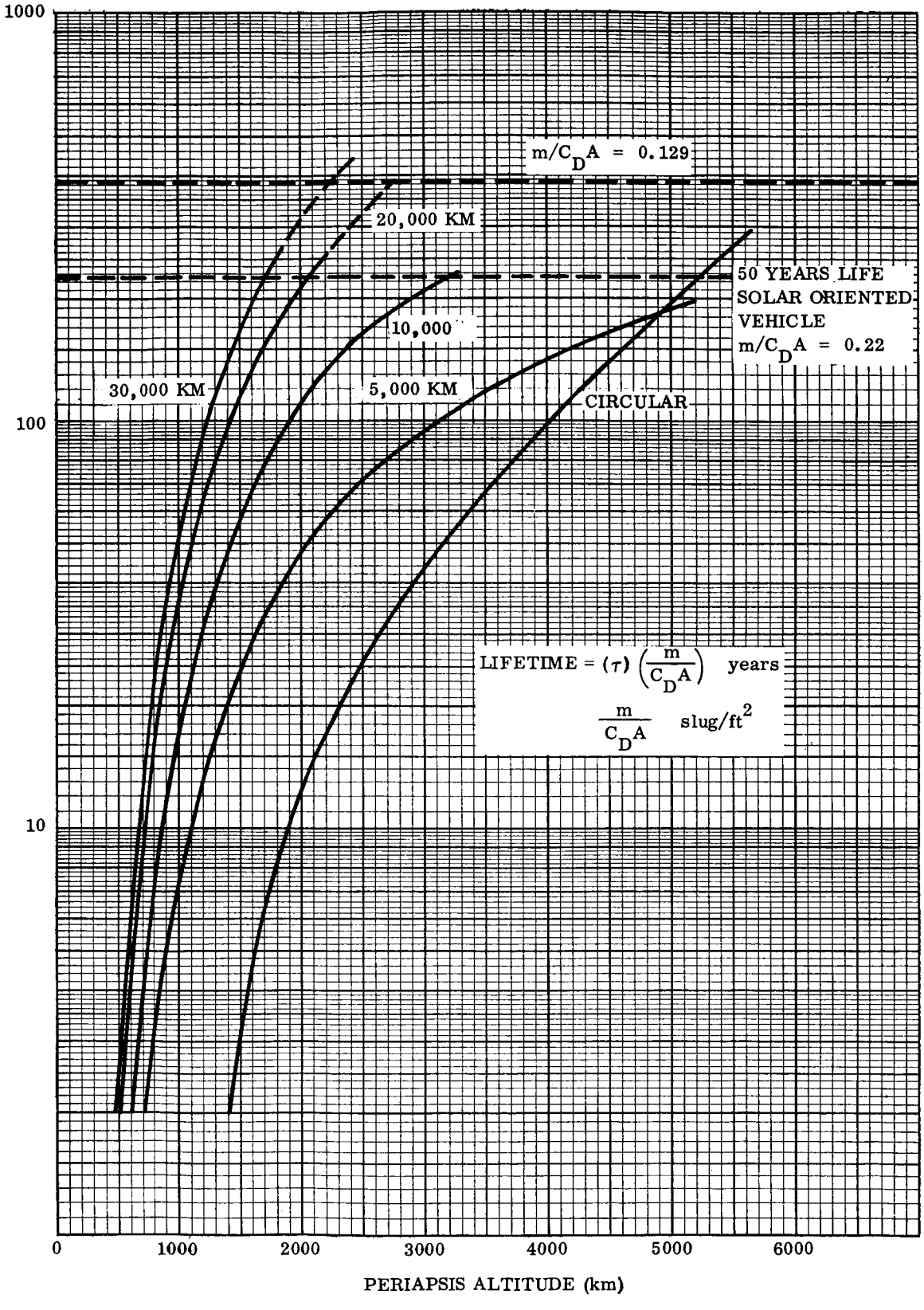

Figure 3-3. Mars Satellite Orbit Lifetime in Presence of Atmospheric Drag (Conservative Density Profile)

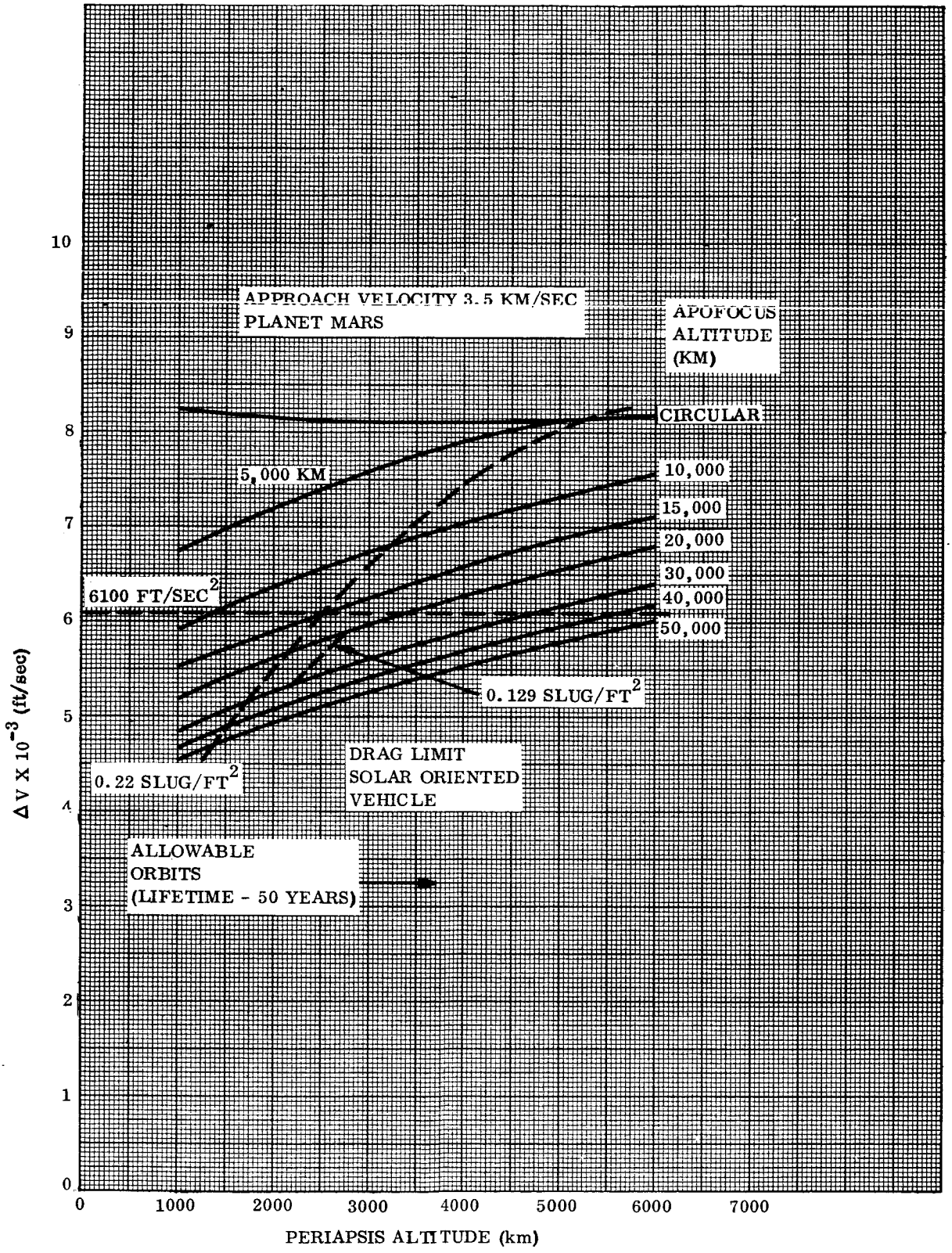

Figure 3-4. Injection Velocity, Approach Velocity 3.5 km/sec., Planet Mars

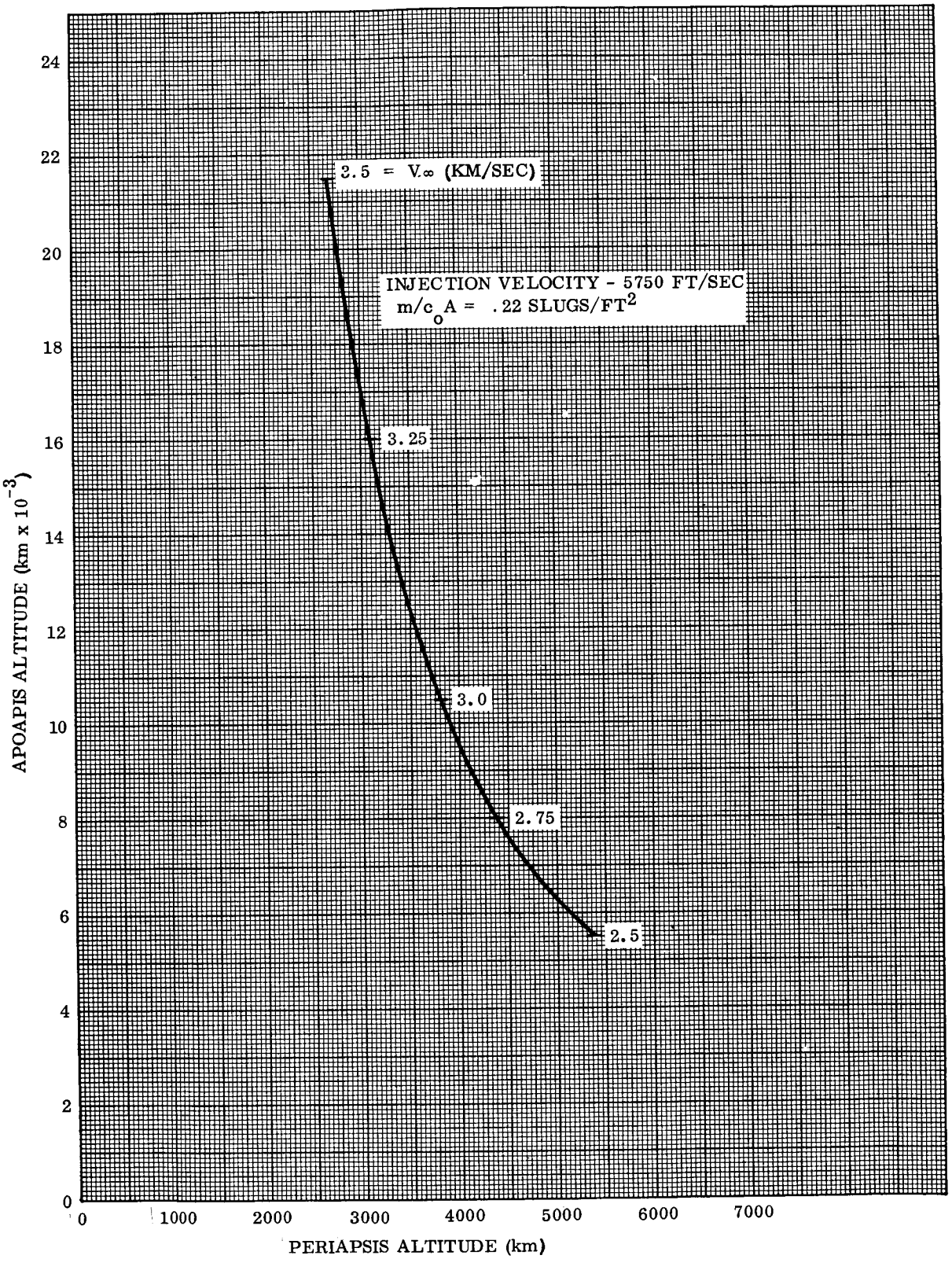

Figure 3-5. Minimum Altitude for a 50-Year Lifetime Mars Orbit

THE AIM POINT IS DEFINED BY

1. IMPACT PARAMETER = $\overline{B}$
2. DIRECTION OF IMPACT PARAMETER = θ

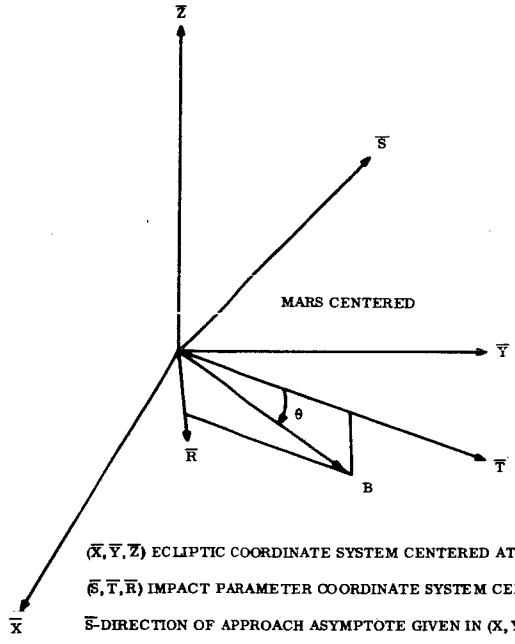

$(\overline{X}, \overline{Y}, \overline{Z})$ ECLIPTIC COORDINATE SYSTEM CENTERED AT MARS

$(\overline{S}, \overline{T}, \overline{R})$ IMPACT PARAMETER COORDINATE SYSTEM CENTERED AT MARS

$\overline{S}$-DIRECTION OF APPROACH ASYMPTOTE GIVEN IN (X, Y, Z) SYSTEM

$\overline{T} = \overline{S} \times \overline{Z}$

$\overline{R} = \overline{S} \times \overline{T}$

Figure 3-6. Aim Point Definition

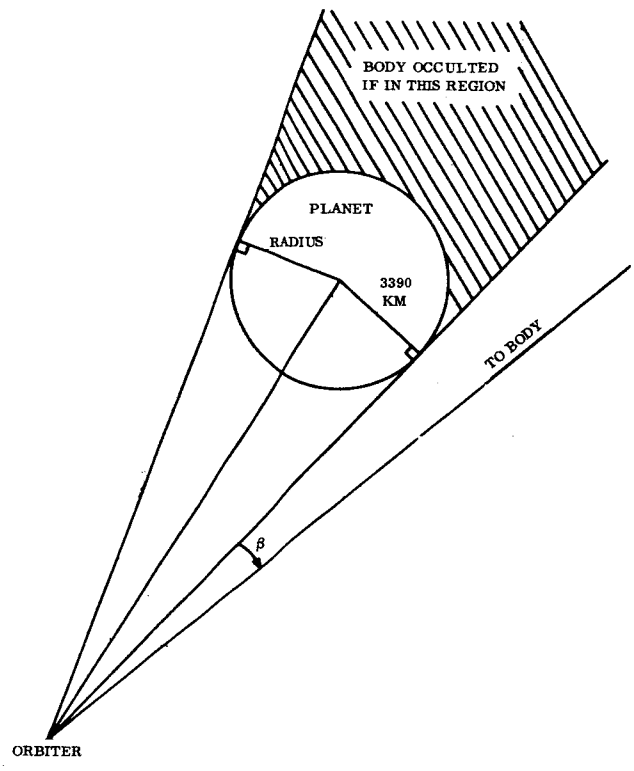

Figure 3-7. Occulation Geometry

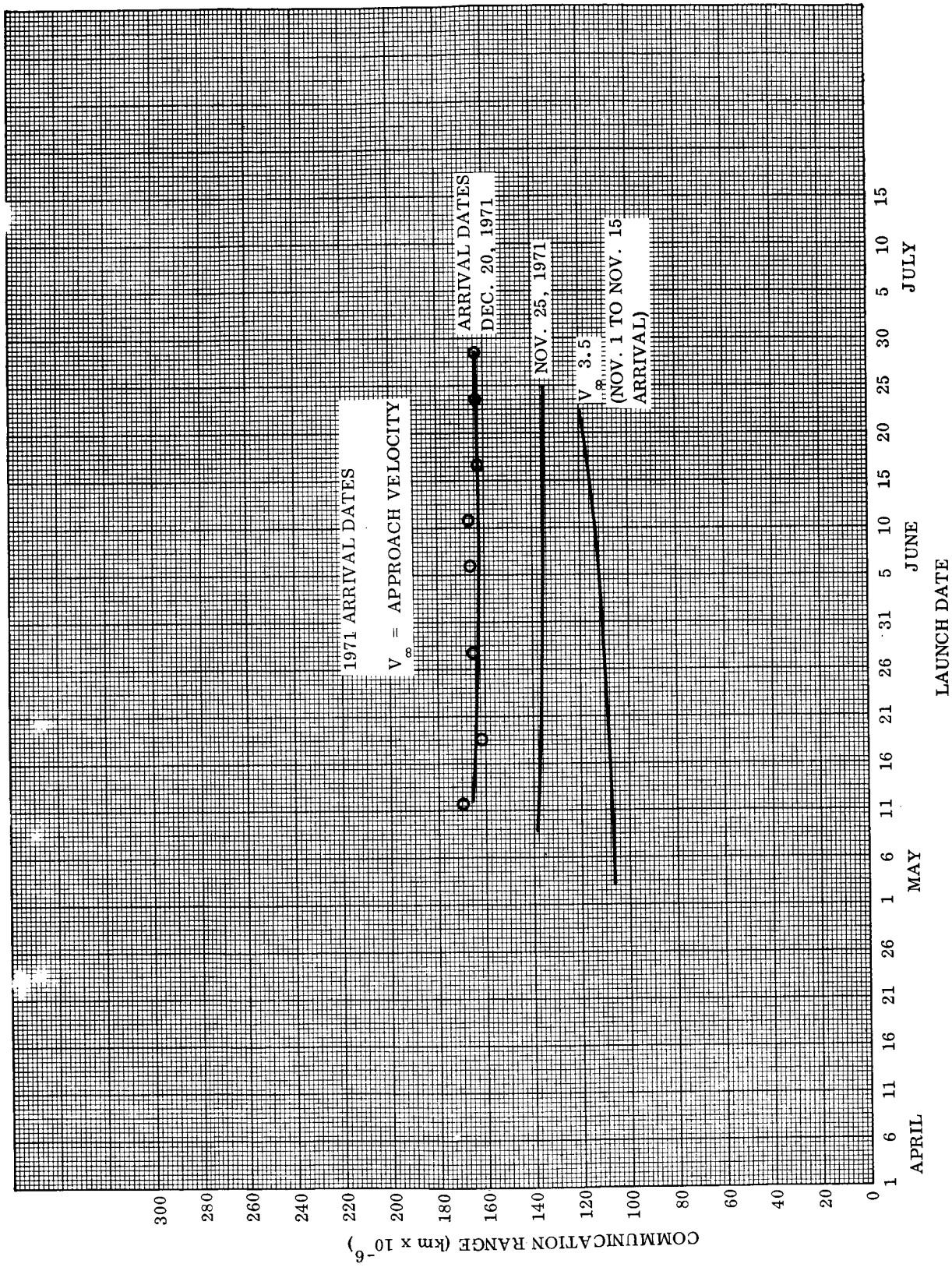

Figure 4-1. Variations in Mars Communication Range at Encounter

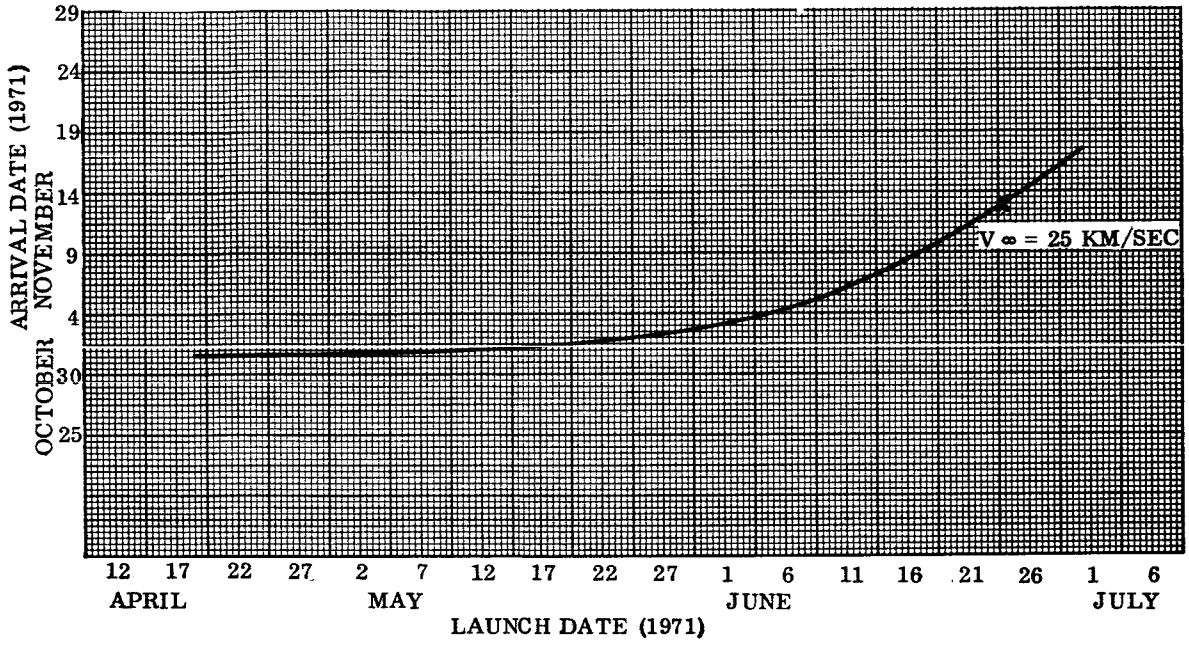

Figure 4-2. Variations in Approach Velocity (v_∞) over Launch Period (1971 Mars Trajectories)

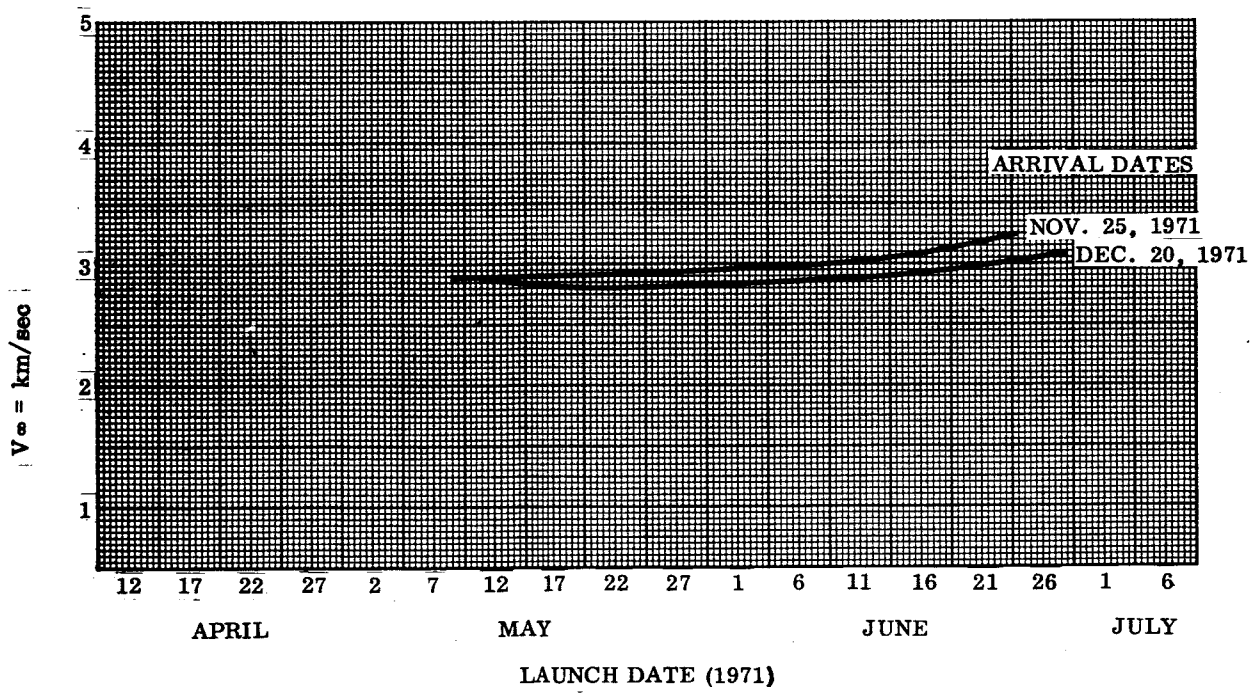

Figure 4-3. Variation of Arrival Date for Constant Approach Velocity (1971 Mars Trajectories)

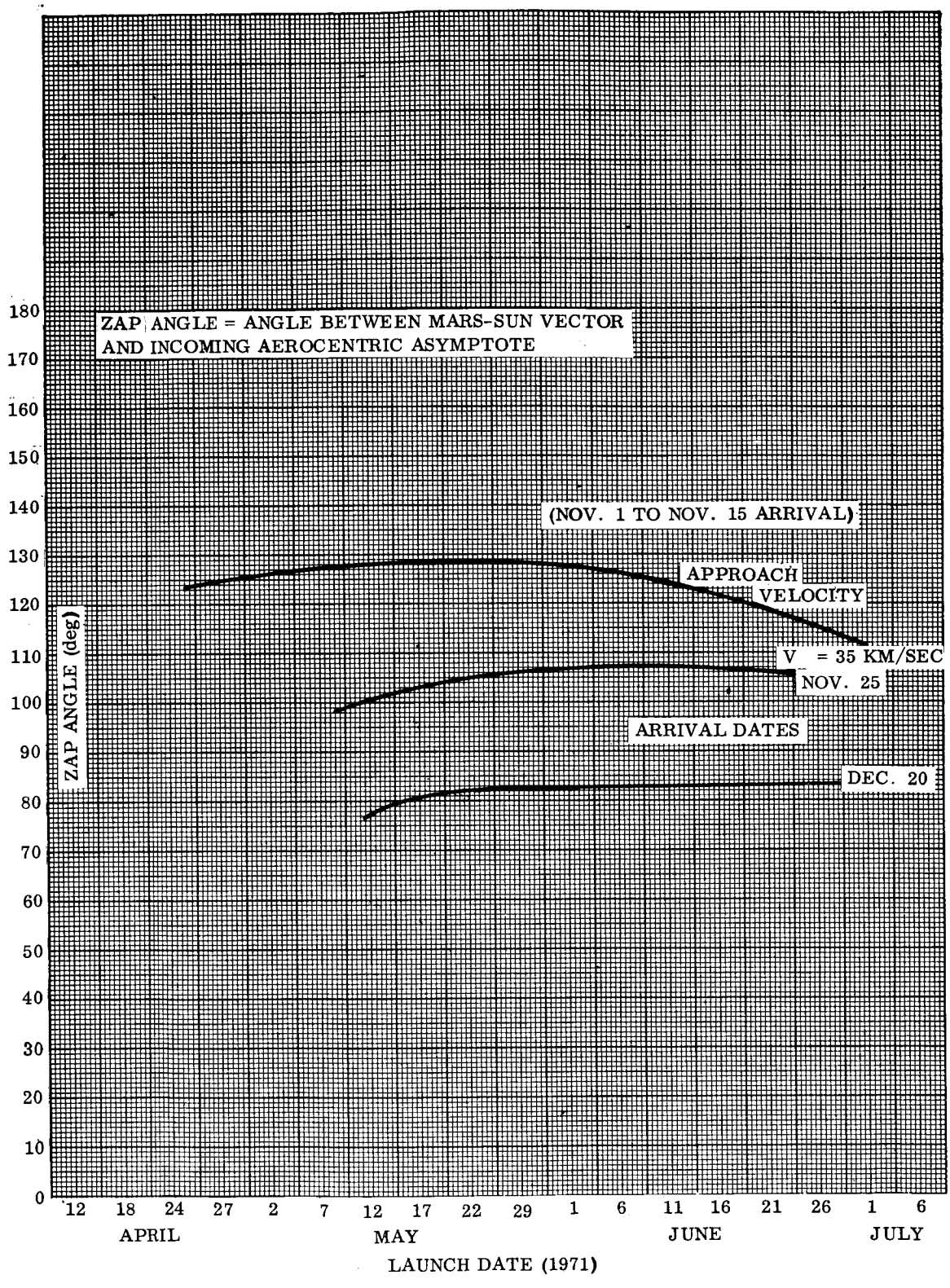

Figure 4-4. Variation in ZAP Angle over Arrival Boundaries Considered (1971 Mars Trajectories)

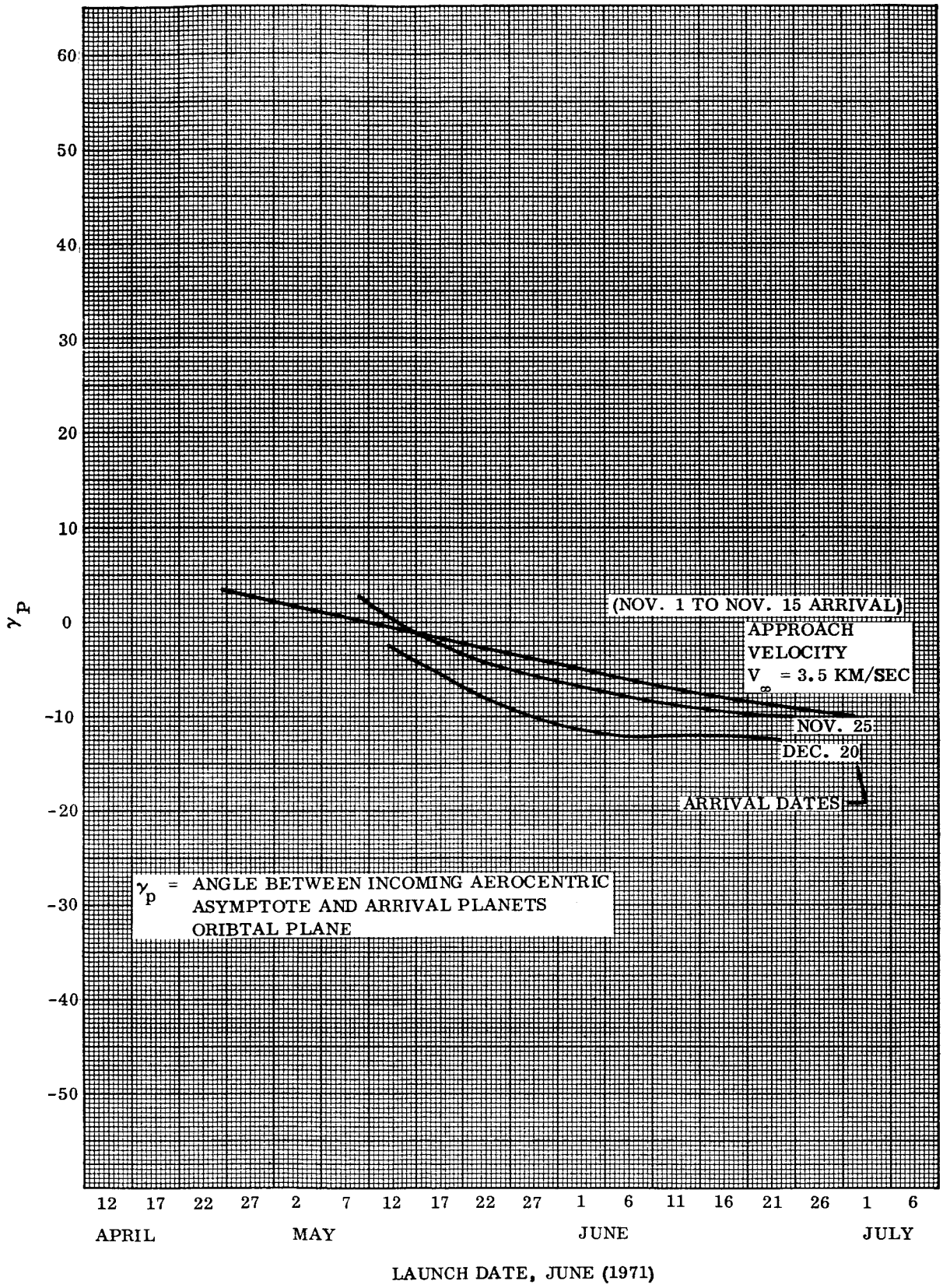

Figure 4-5. Variation in γ_p Angle over Arrival Boundaries Considered (1971 Mars Trajectories)

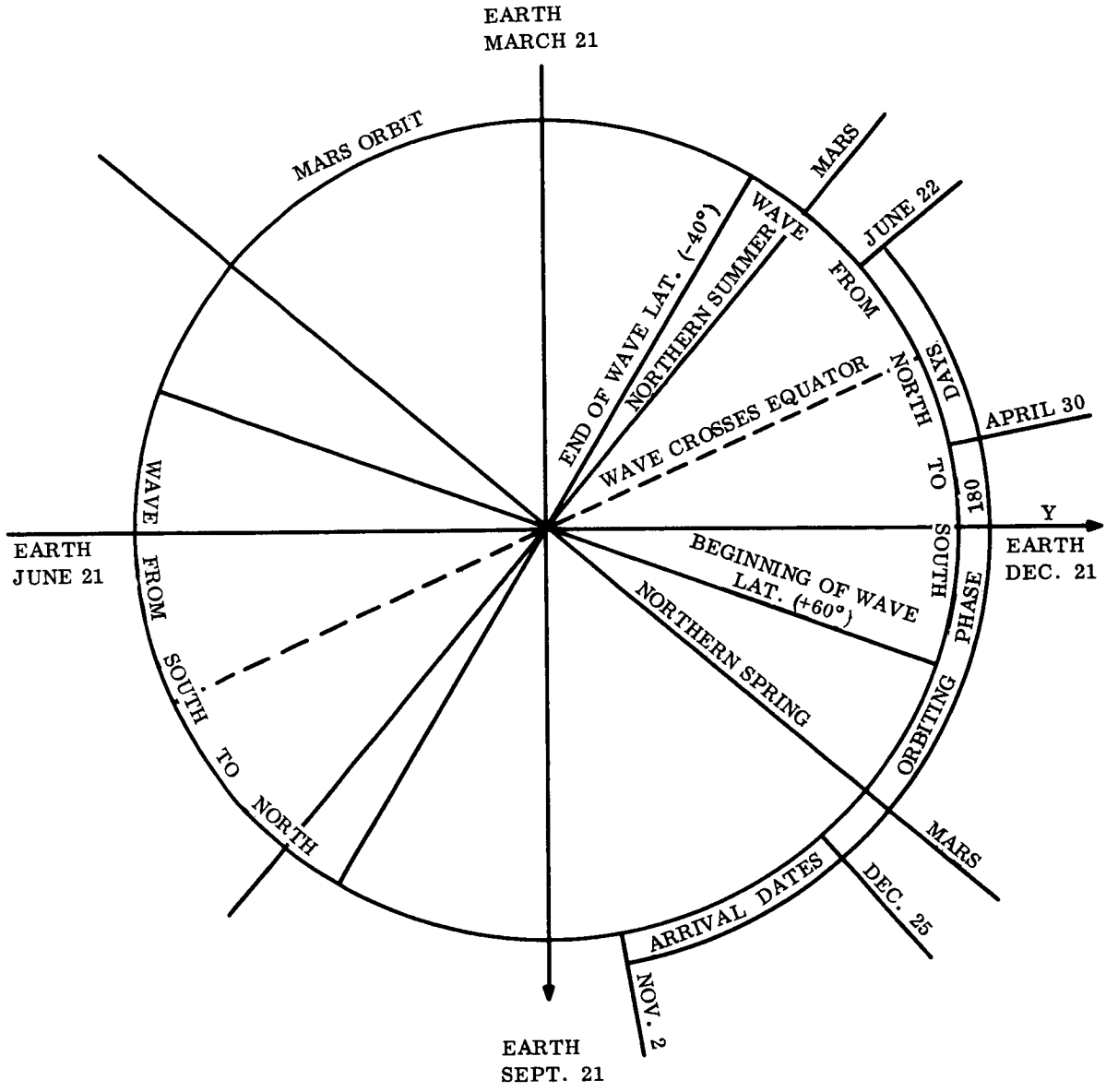

Figure 4-6. Ecliptic Plane Projection (Mars Orbit)

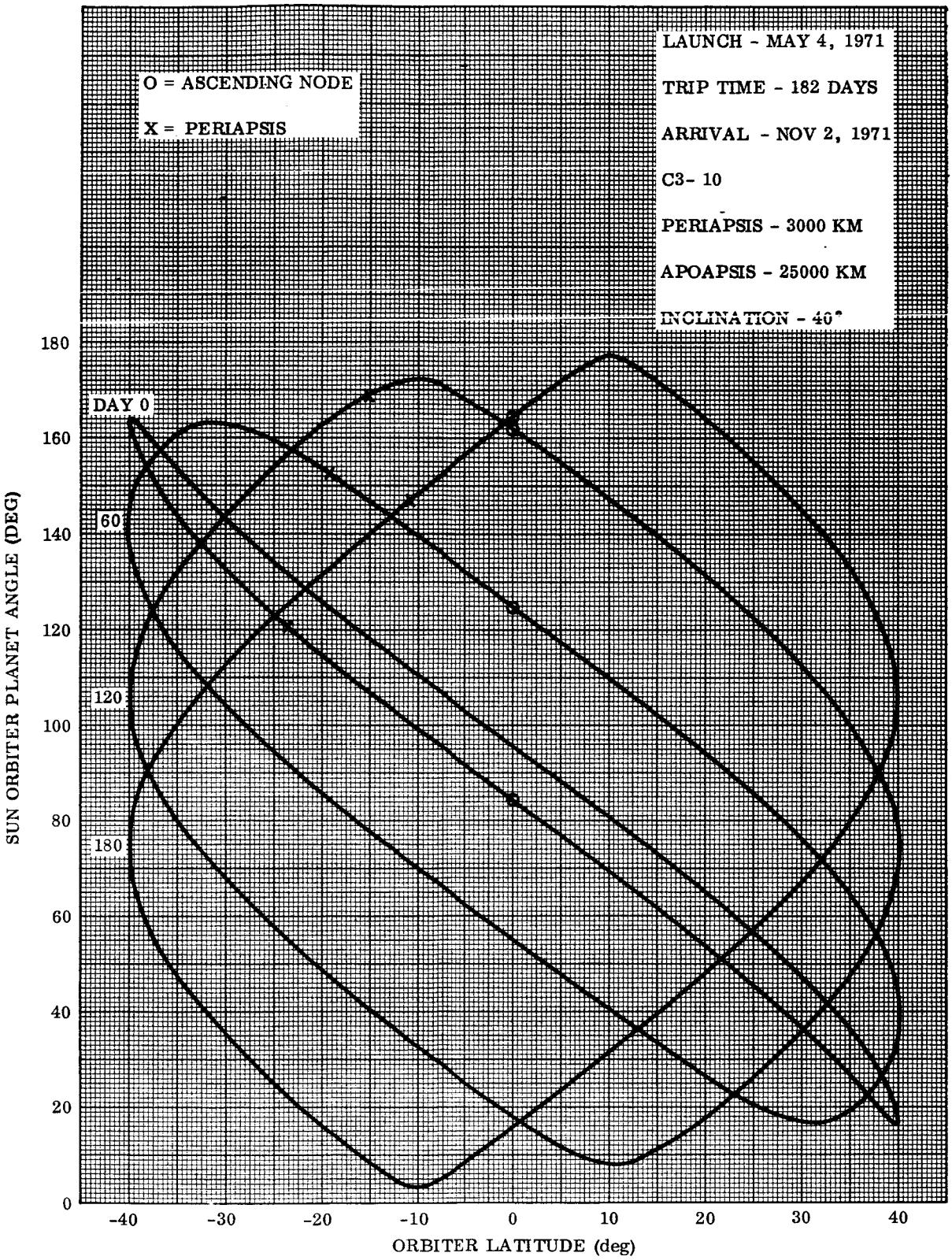

Figure 4-7a. Sun-Orbiter-Planet Angle vs. Latitude

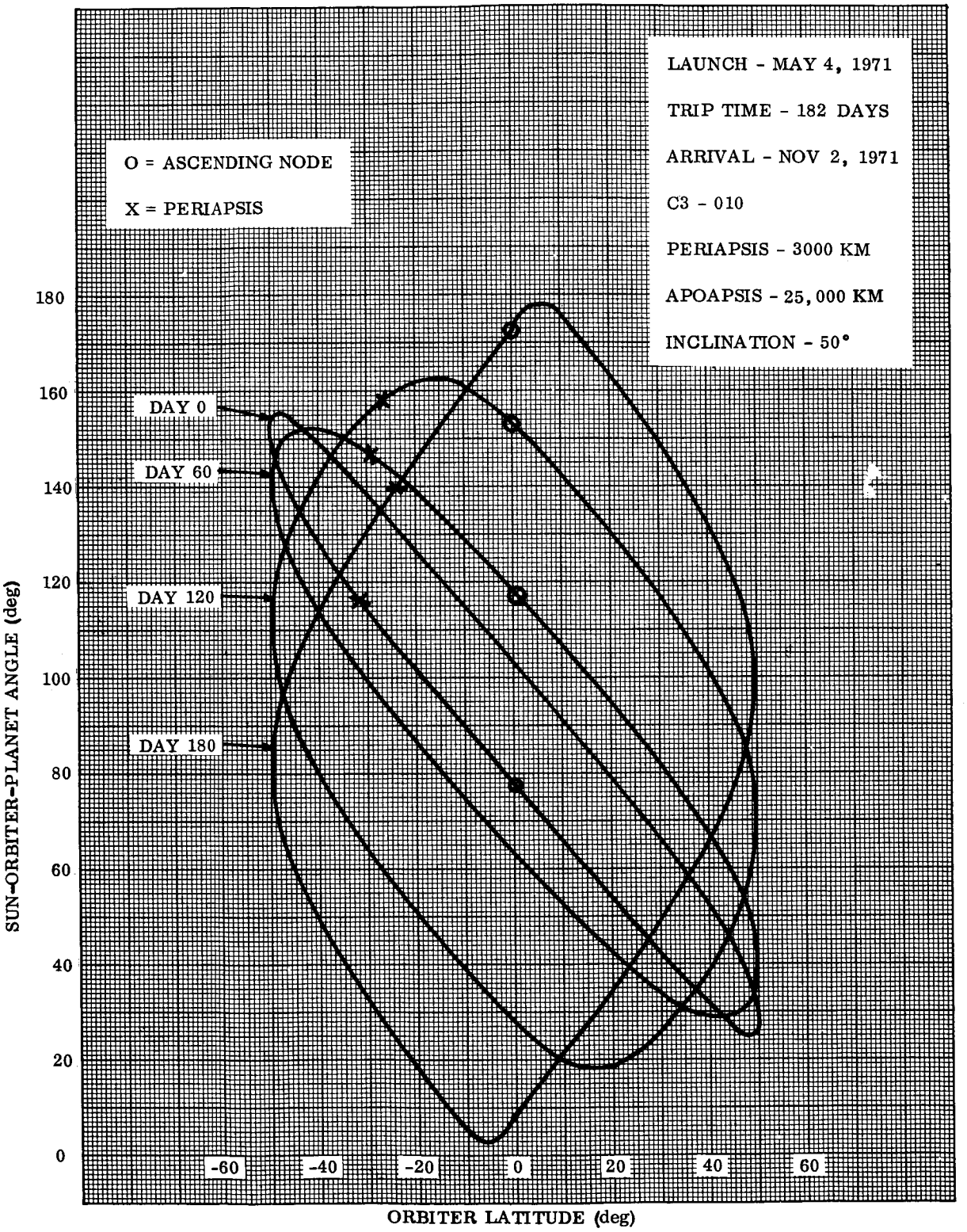

Figure 4-7b. Sun-Orbiter-Planet Angle vs. Latitude

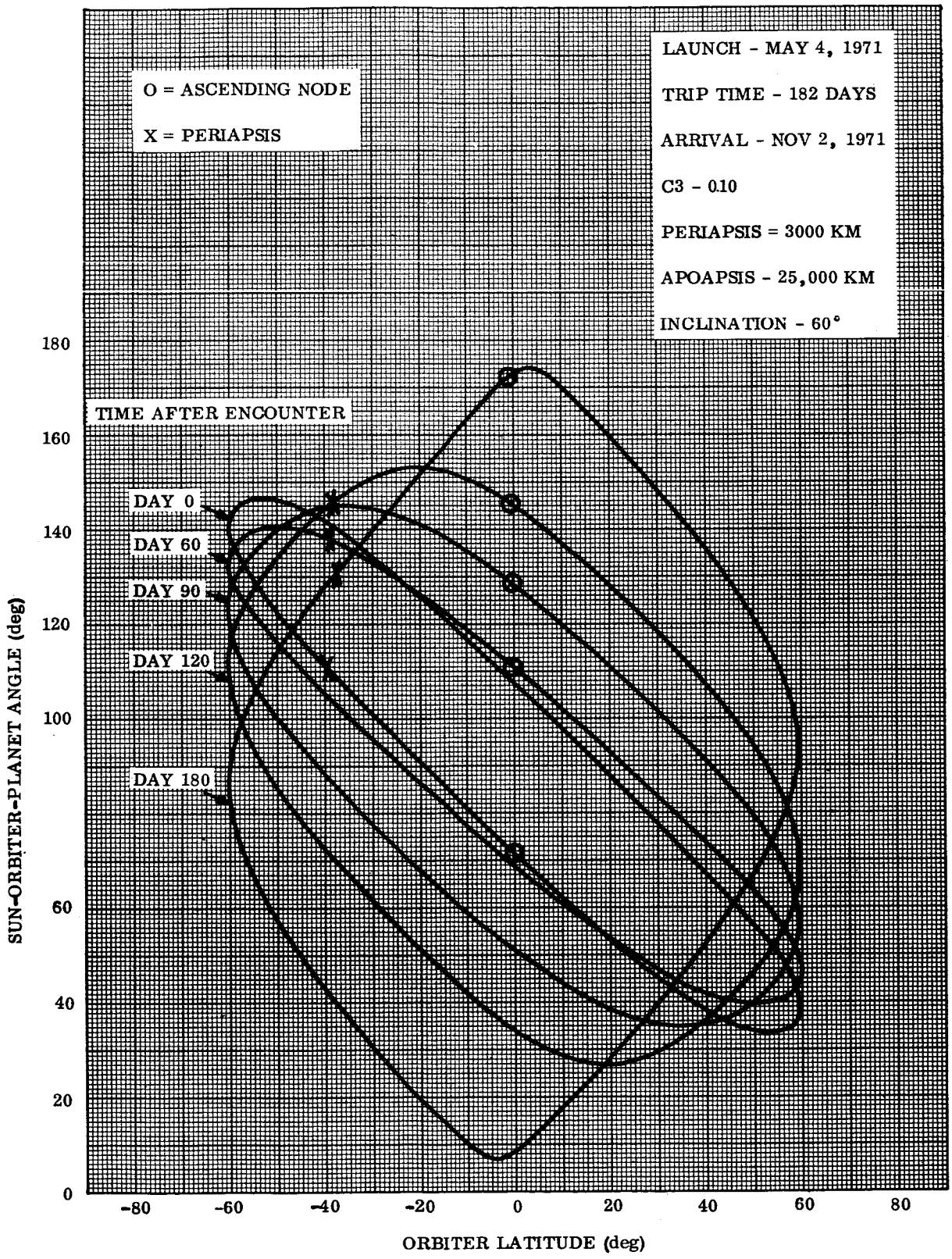

Figure 4-7c. Sun-Orbiter-Planet Angle vs. Latitude

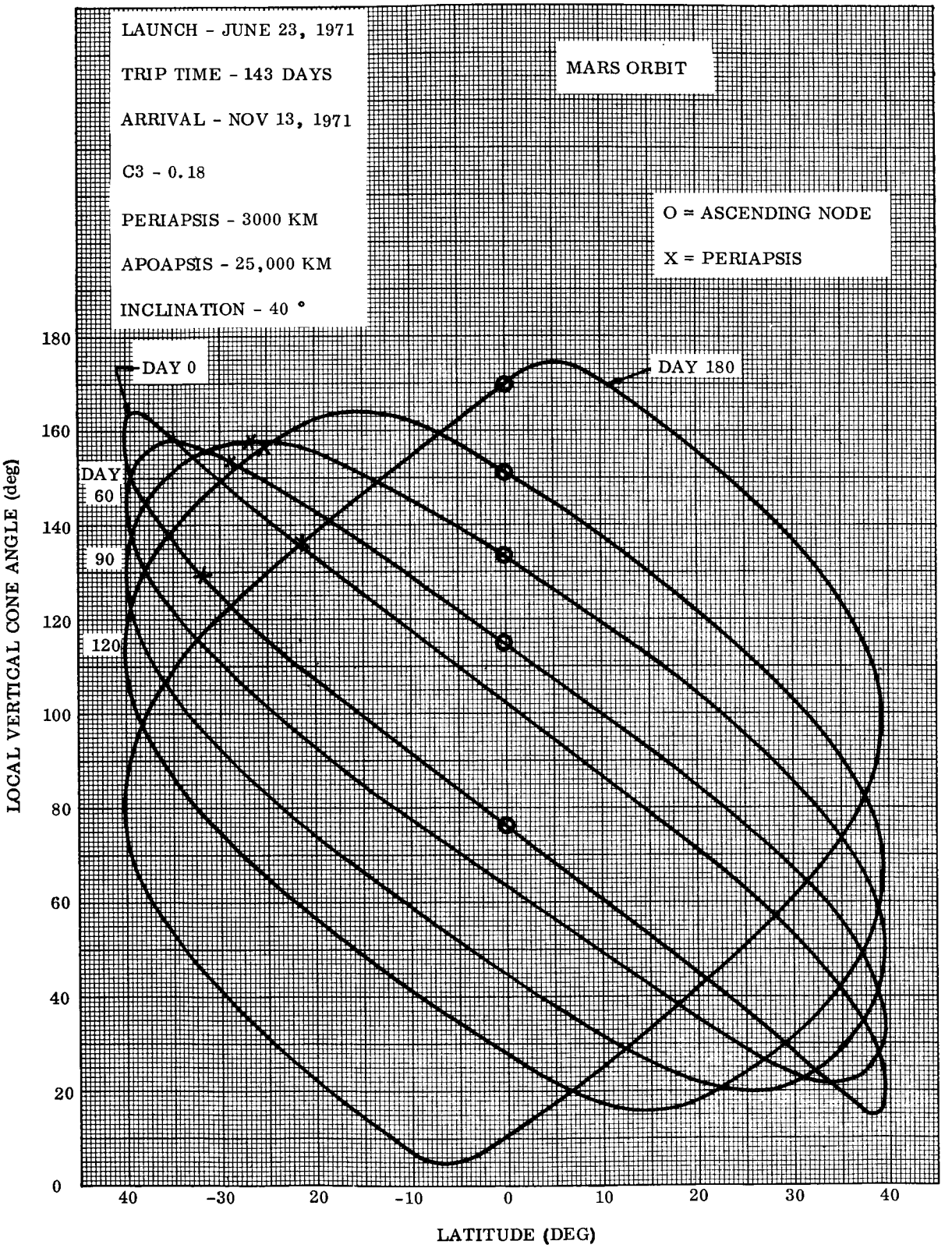

Figure 4-7d. Sun-Orbiter-Planet Angle vs. Latitude

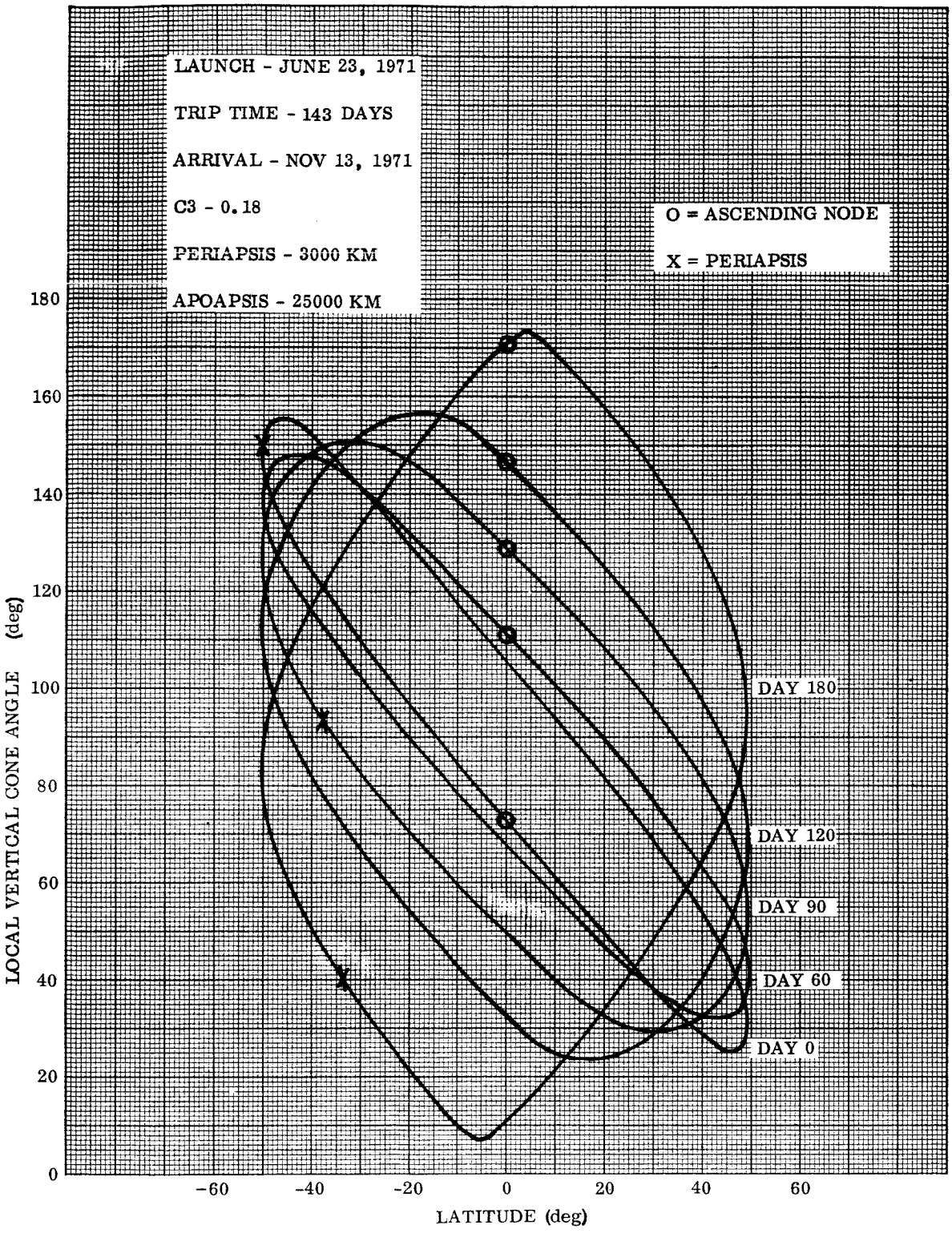

Figure 4-7e. Sun-Orbiter-Planet Angle vs. Latitude

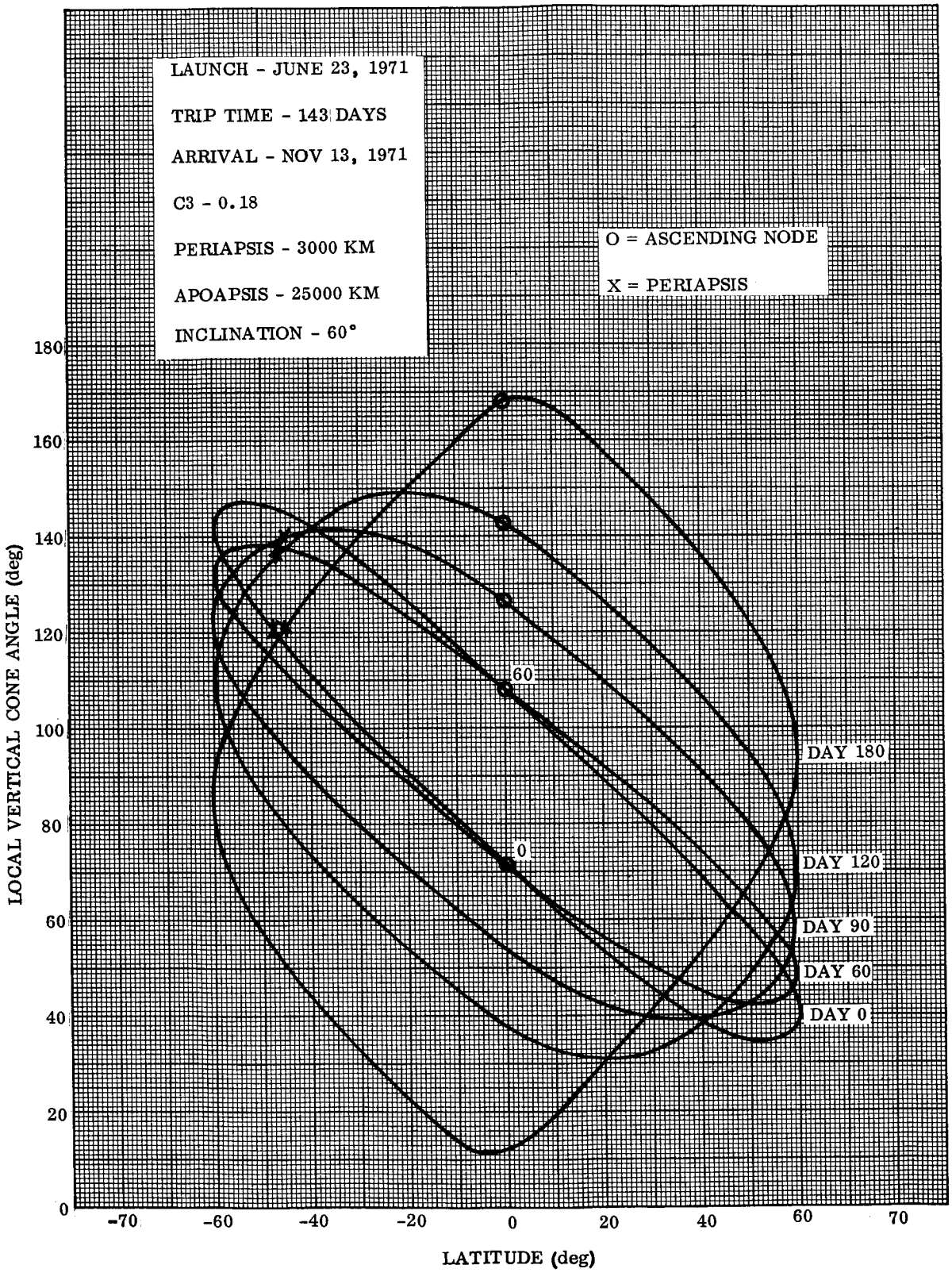

Figure 4-7f. Sun-Orbiter-Planet Angle vs. Latitude

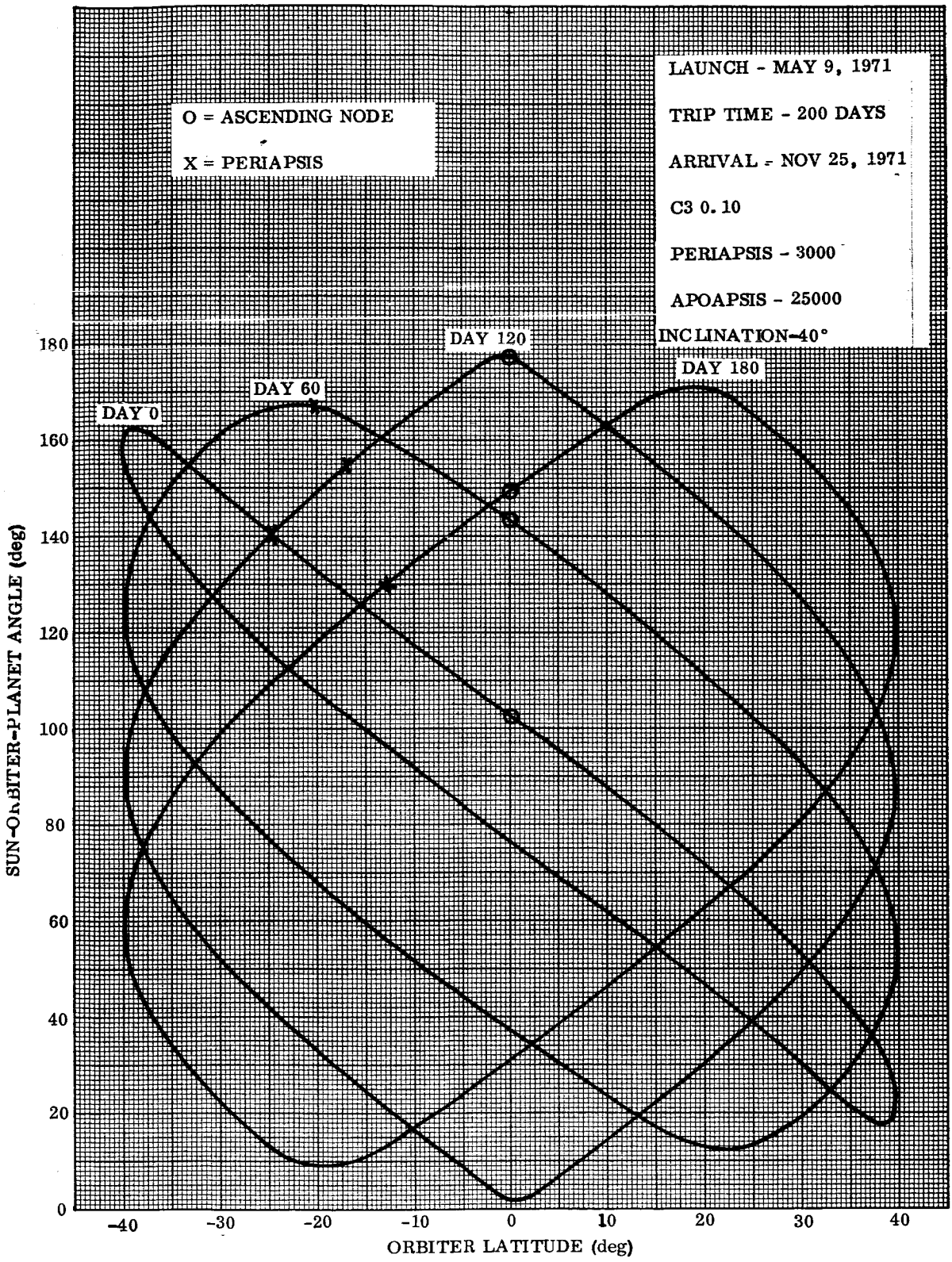

Figure 4-7g. Sun-Orbiter-Planet Angle vs. Latitude

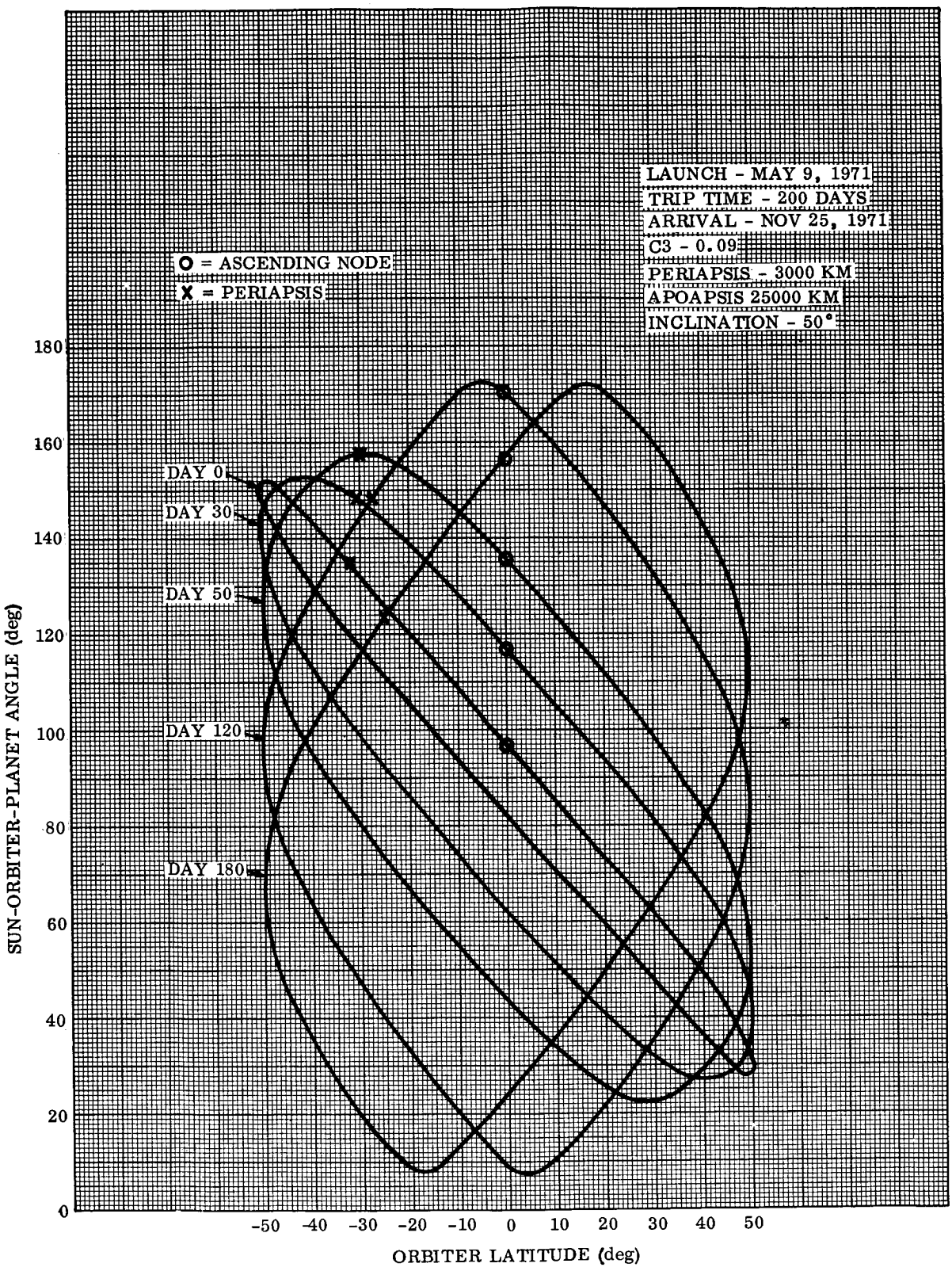

Figure 4-7h. Sun-Orbiter-Planet Angle vs. Latitude

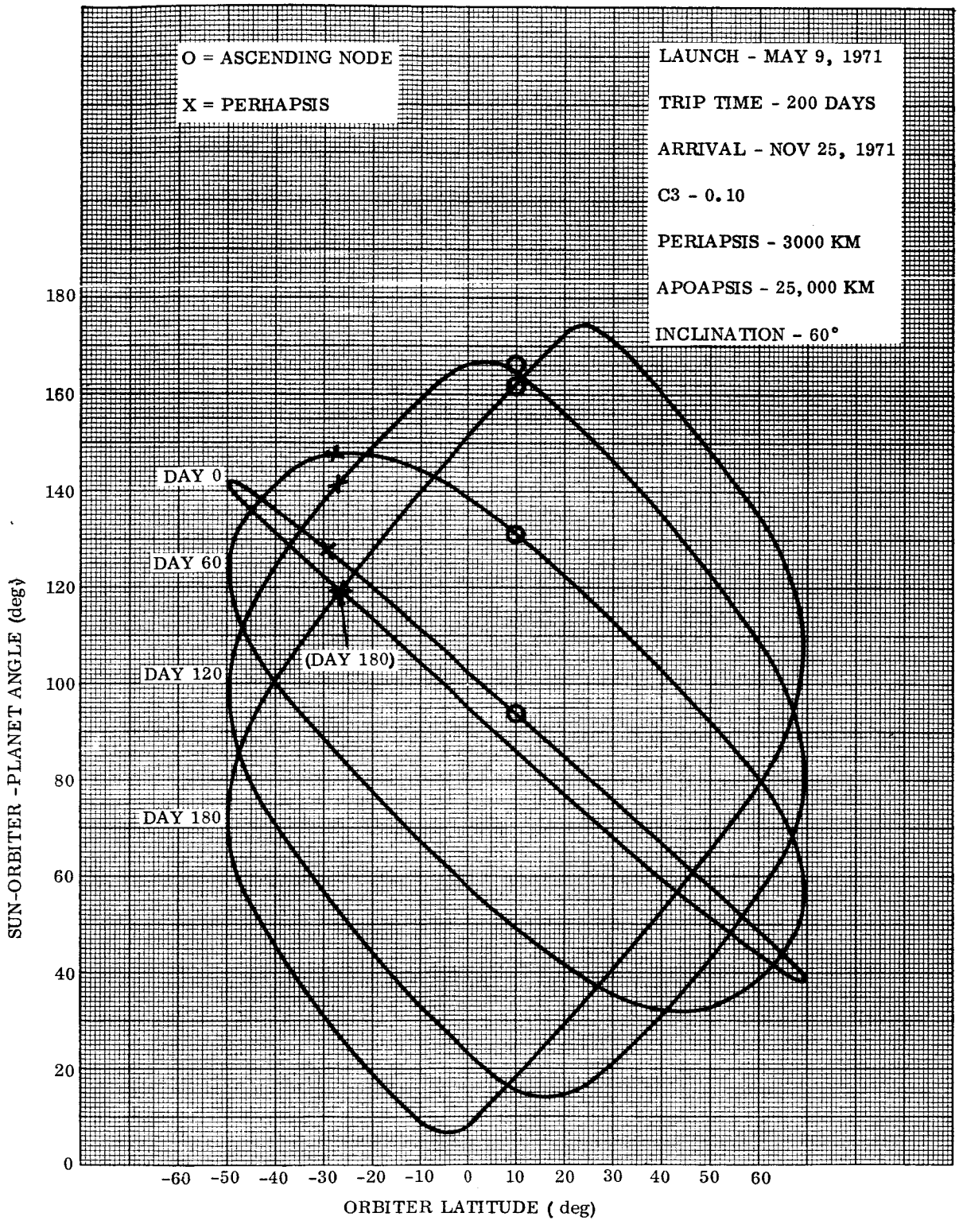

Figure 4-7i. Sun-Orbiter-Planet Angle vs. Latitude

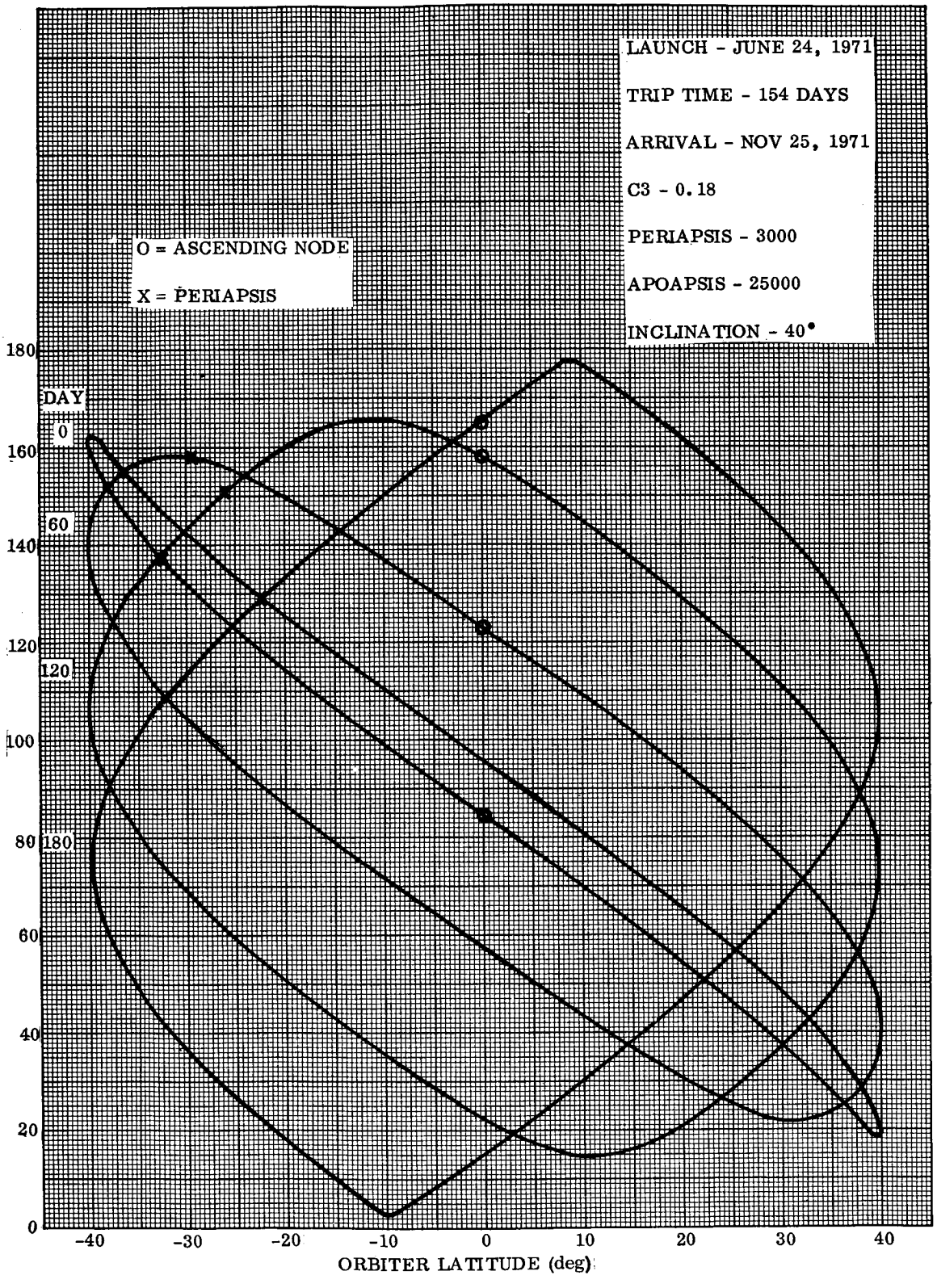

Figure 4-7j. Sun-Orbiter-Planet Angle vs. Latitude

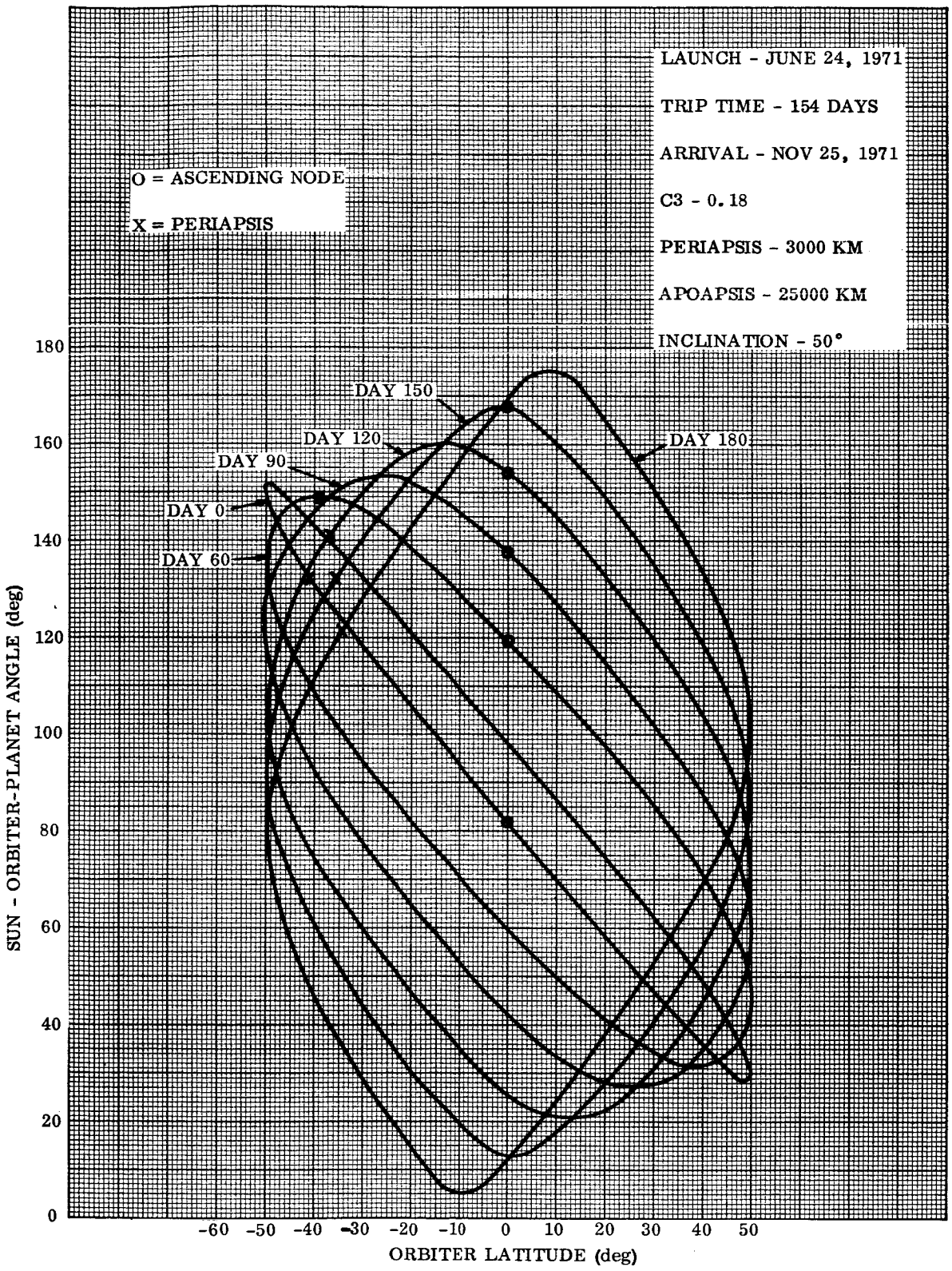

Figure 4-7k. Sun-Orbiter-Planet Angle vs. Latitude

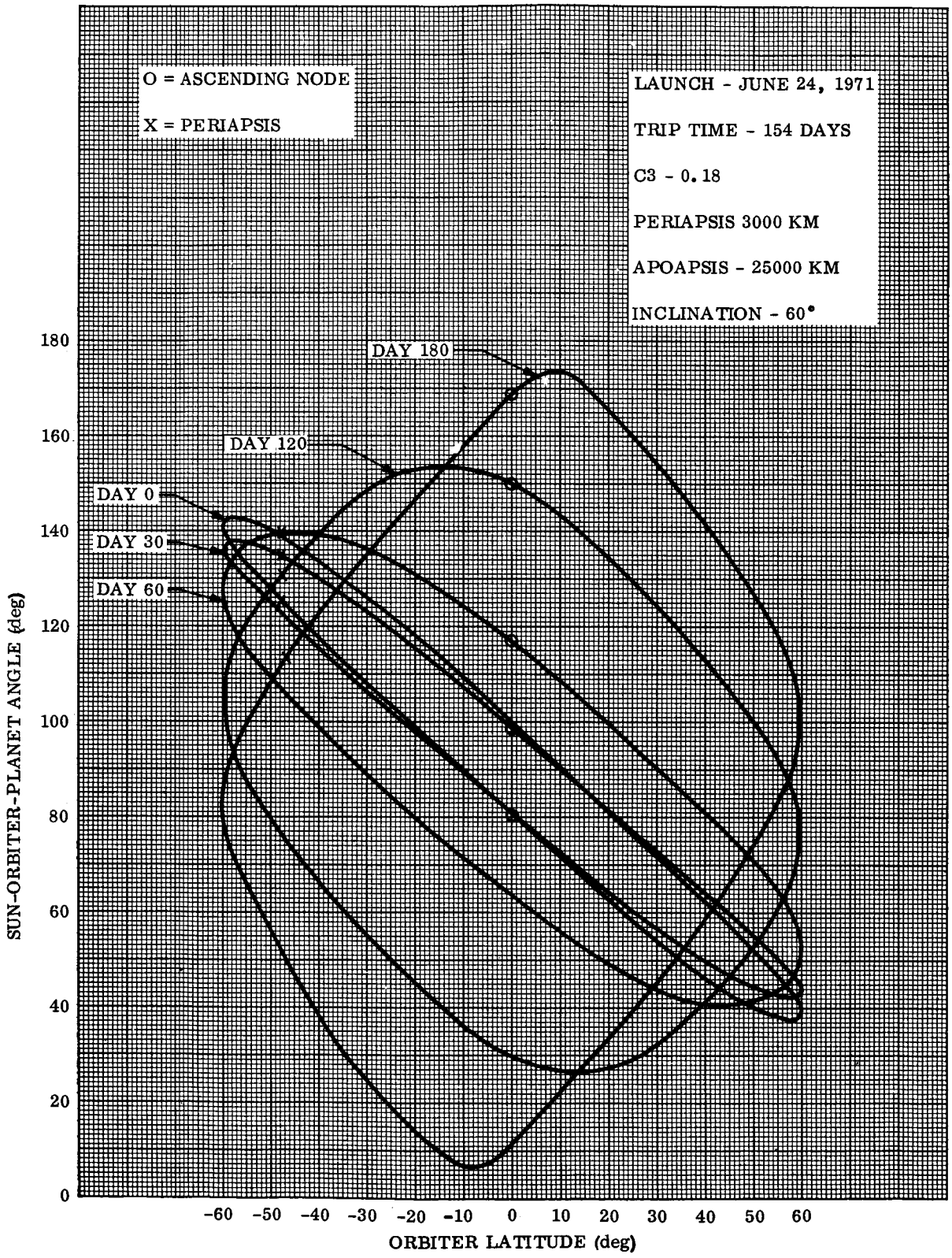

Figure 4-71. Sun-Orbiter-Planet Angle vs. Latitude

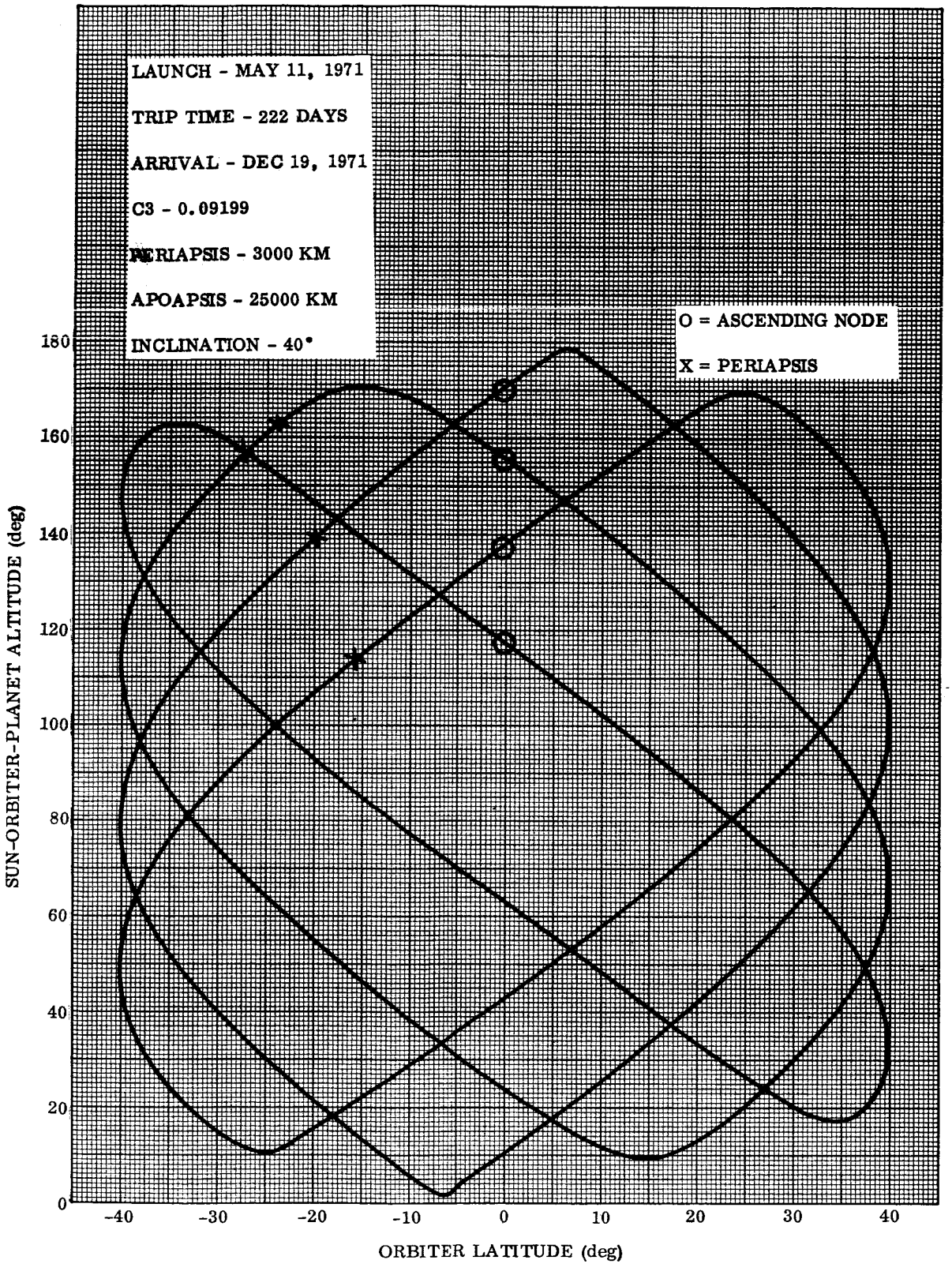

Figure 4-7m. Sun-Orbiter-Planet Angle vs. Latitude

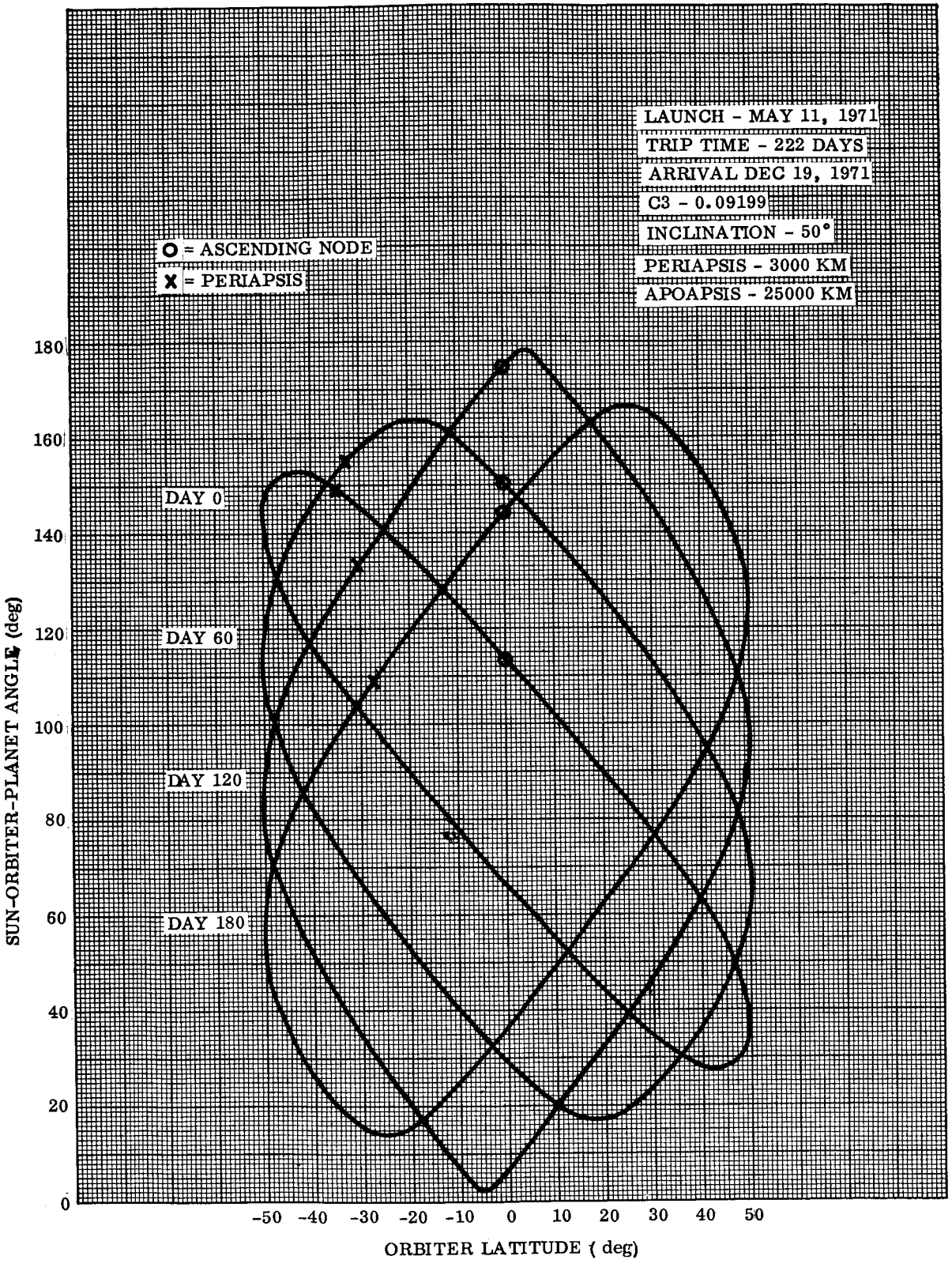

Figure 4-7n. Sun-Orbiter-Planet Angle vs. Latitude

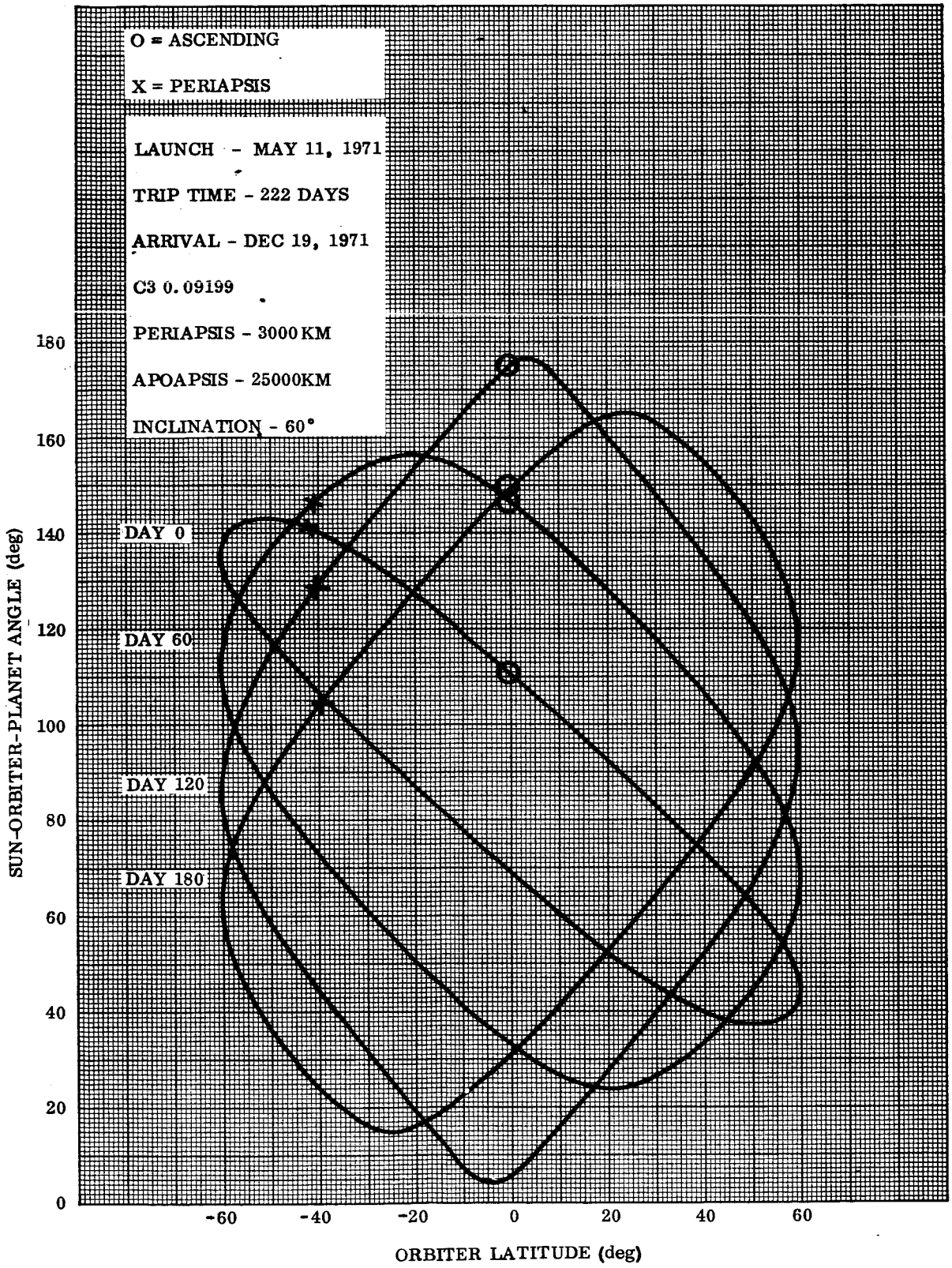

Figure 4-7o. Sun-Orbiter-Planet Angle vs. Latitude

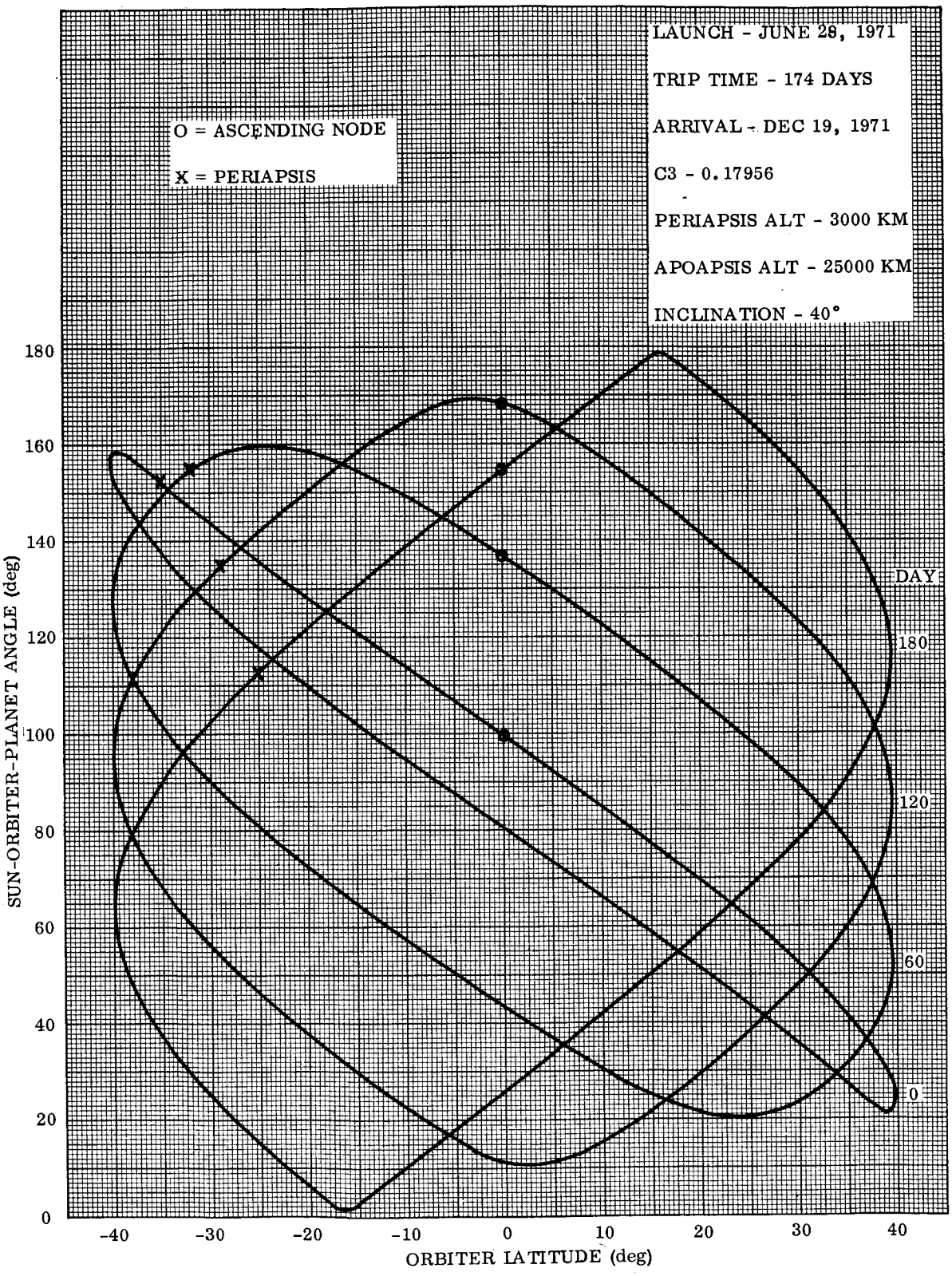

Figure 4-7p. Sun-Orbiter-Planet Angle vs. Latitude

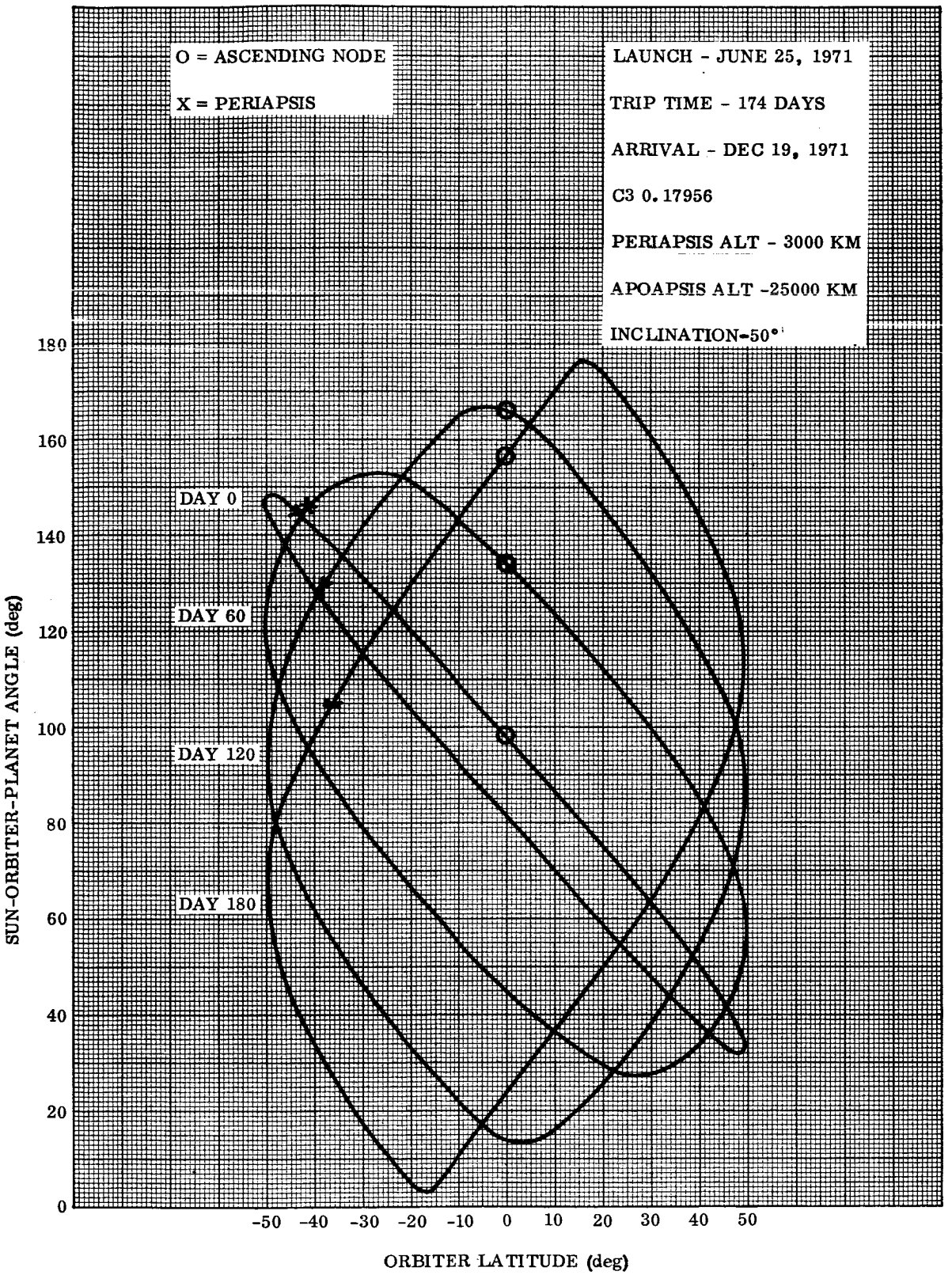

Figure 4-7q. Sun-Orbiter-Planet Angle vs. Latitude

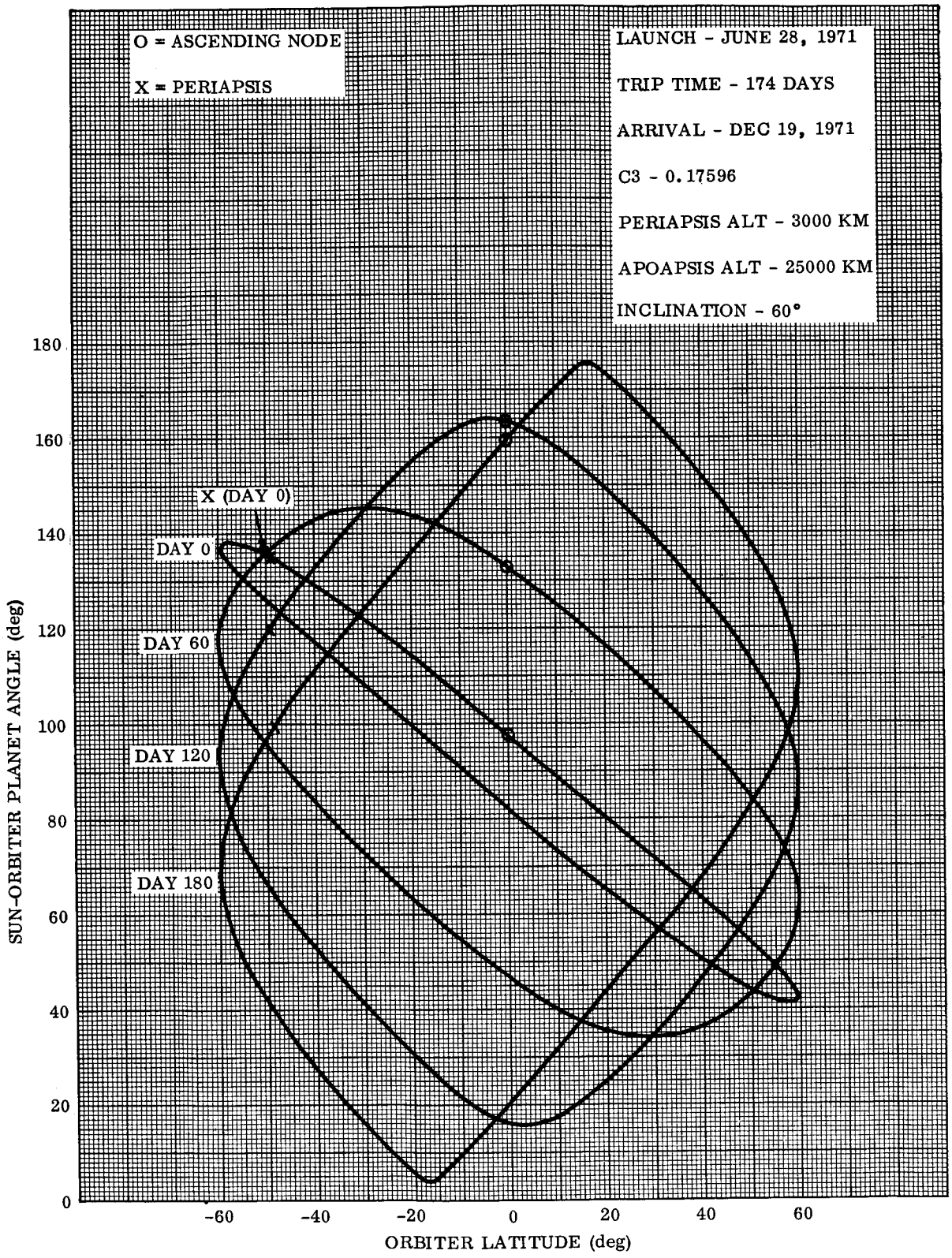

Figure 4-7r. Sun-Orbiter-Planet Angle vs. Latitude

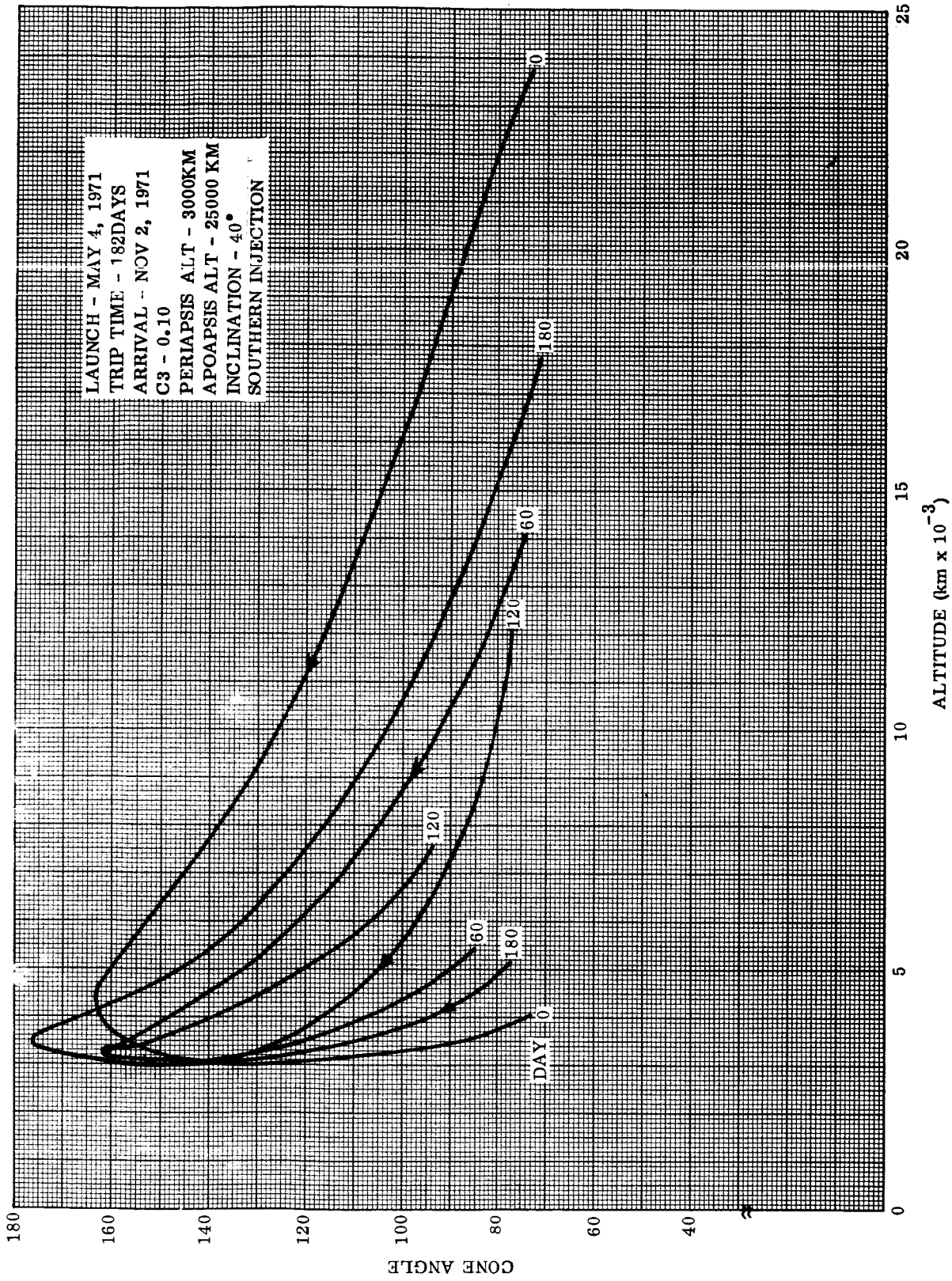

Figure 4-8a. Sun-Orbiter-Planet Angle vs. Altitude

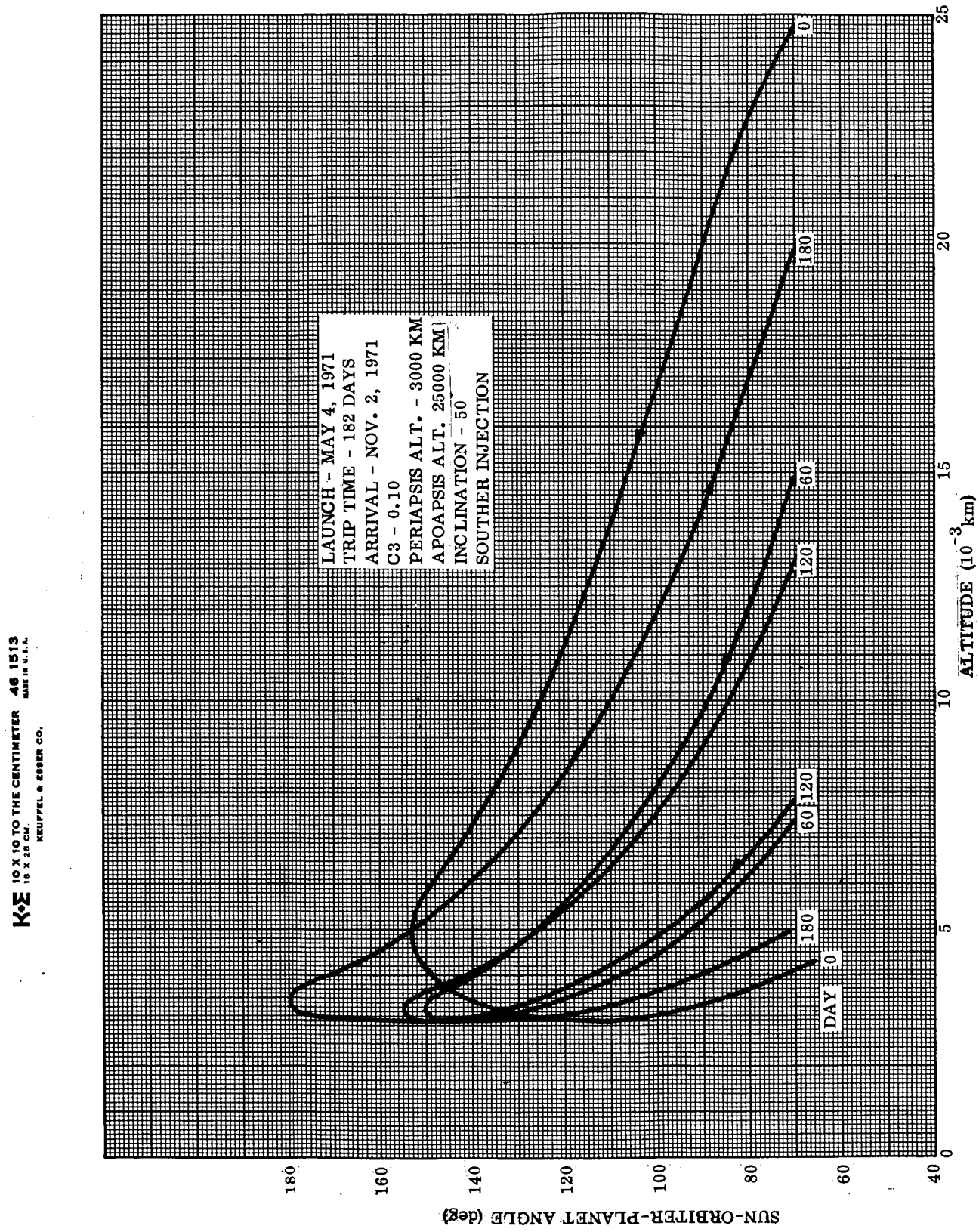

K+E 10 X 10 TO THE CENTIMETER 46 1513
18 X 25 CM. MADE IN U.S.A.
KEUFFEL & ESSER CO.

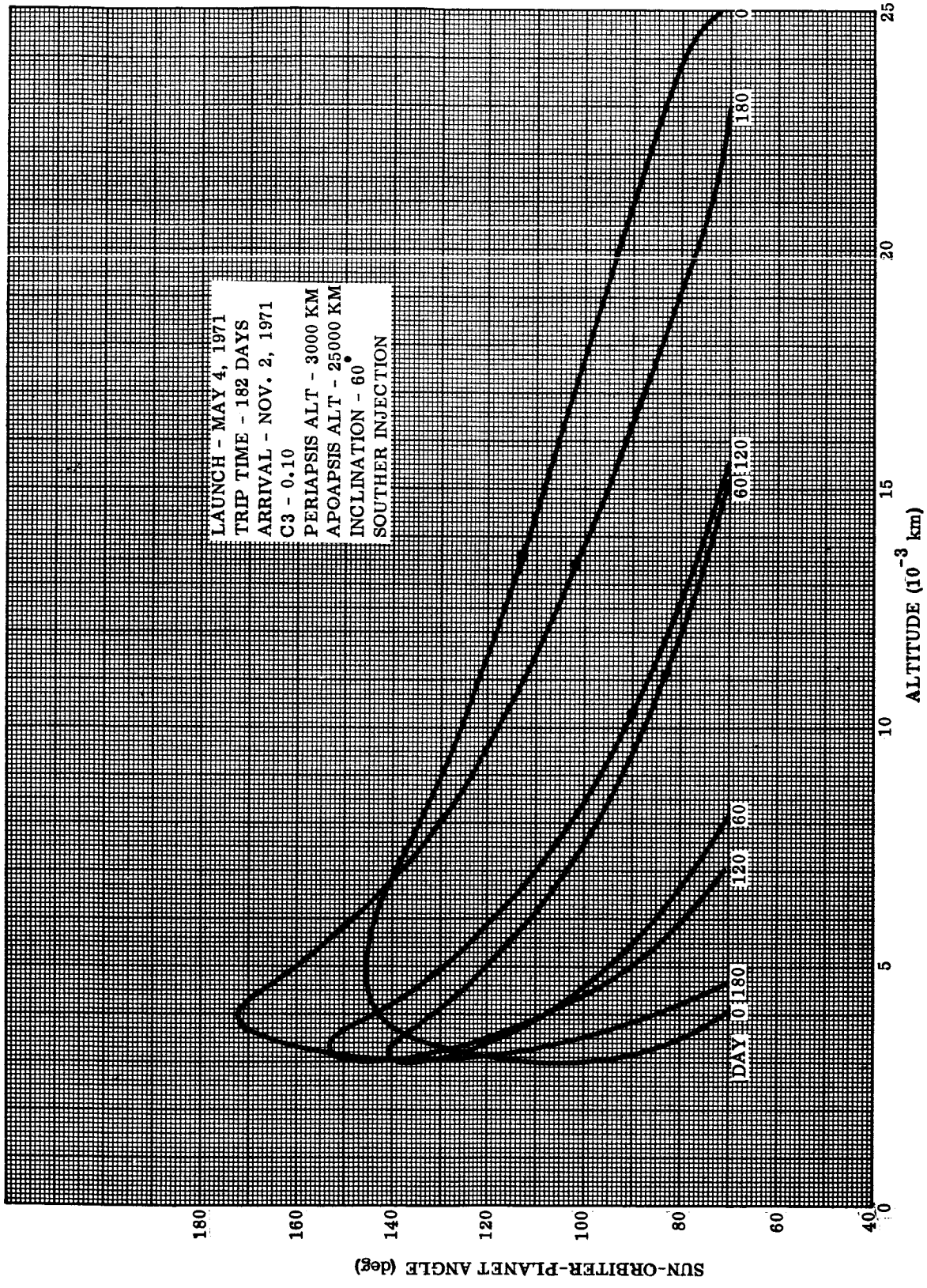

Figure 4-8c. Sun-Orbiter-Planet Angle vs. Altitude

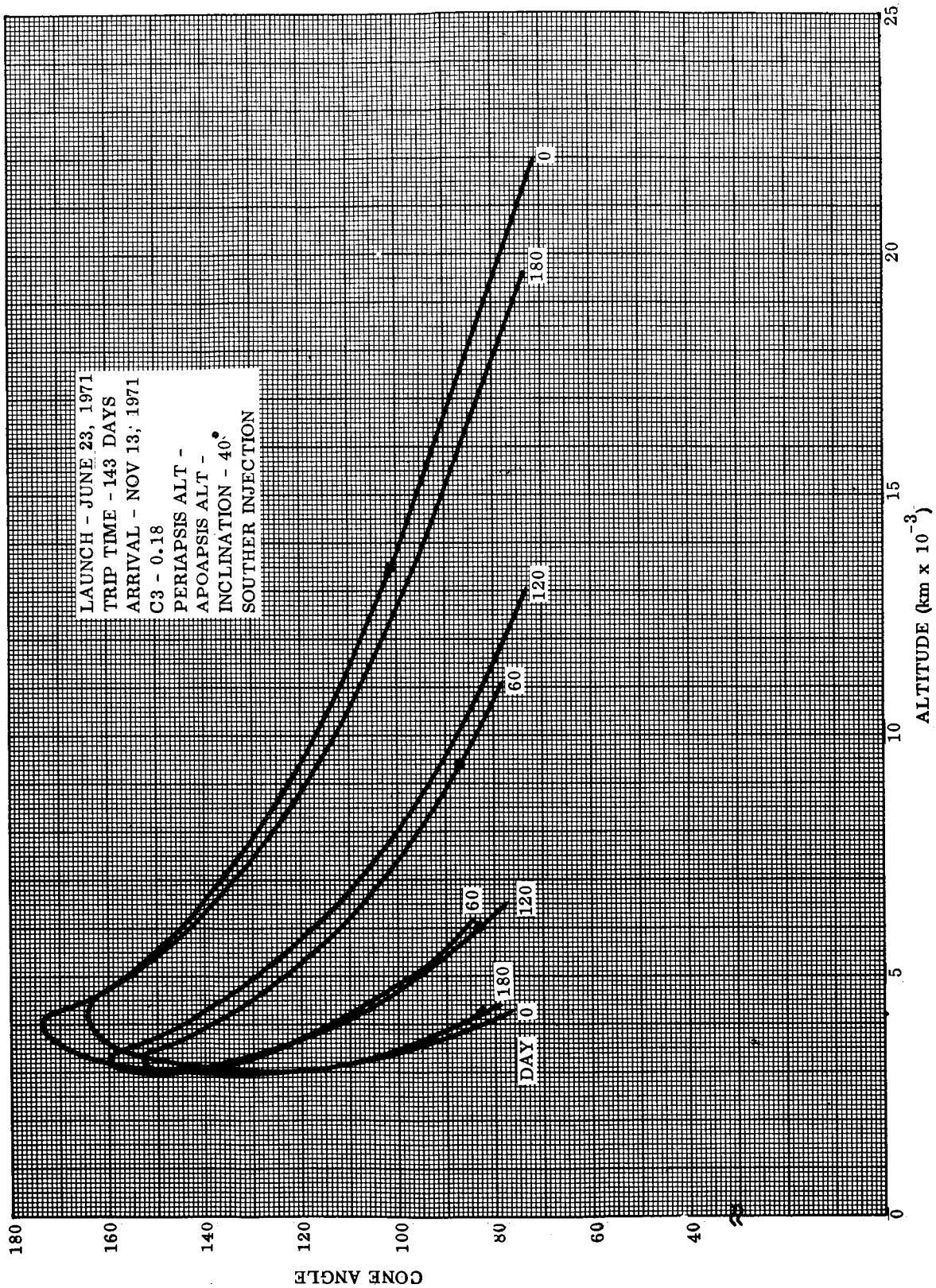

Figure 4-8d. Sun-Orbiter-Planet Angle vs. Altitude

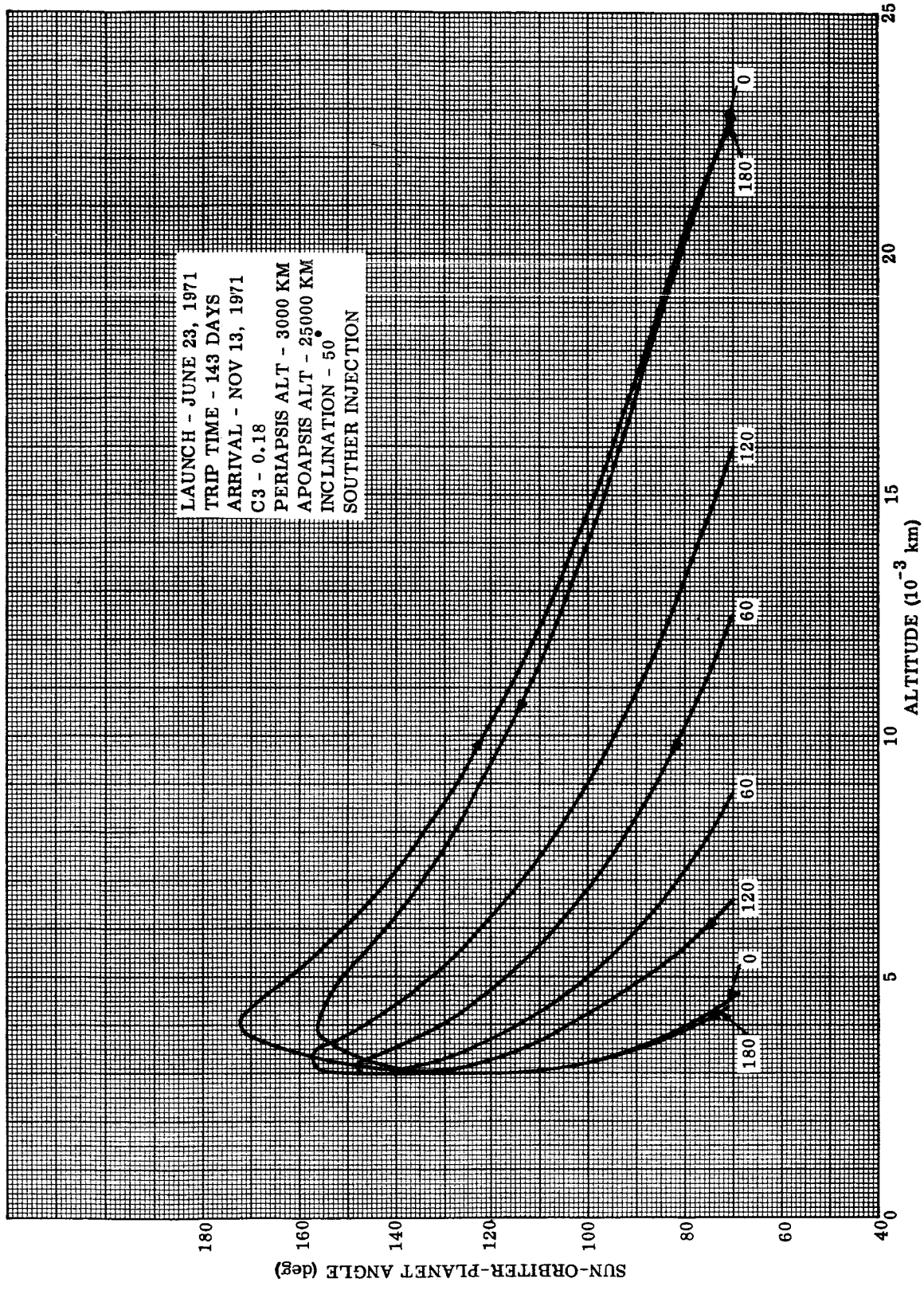

Figure 4-8e. Sun-Orbiter-Angle vs. Altitude

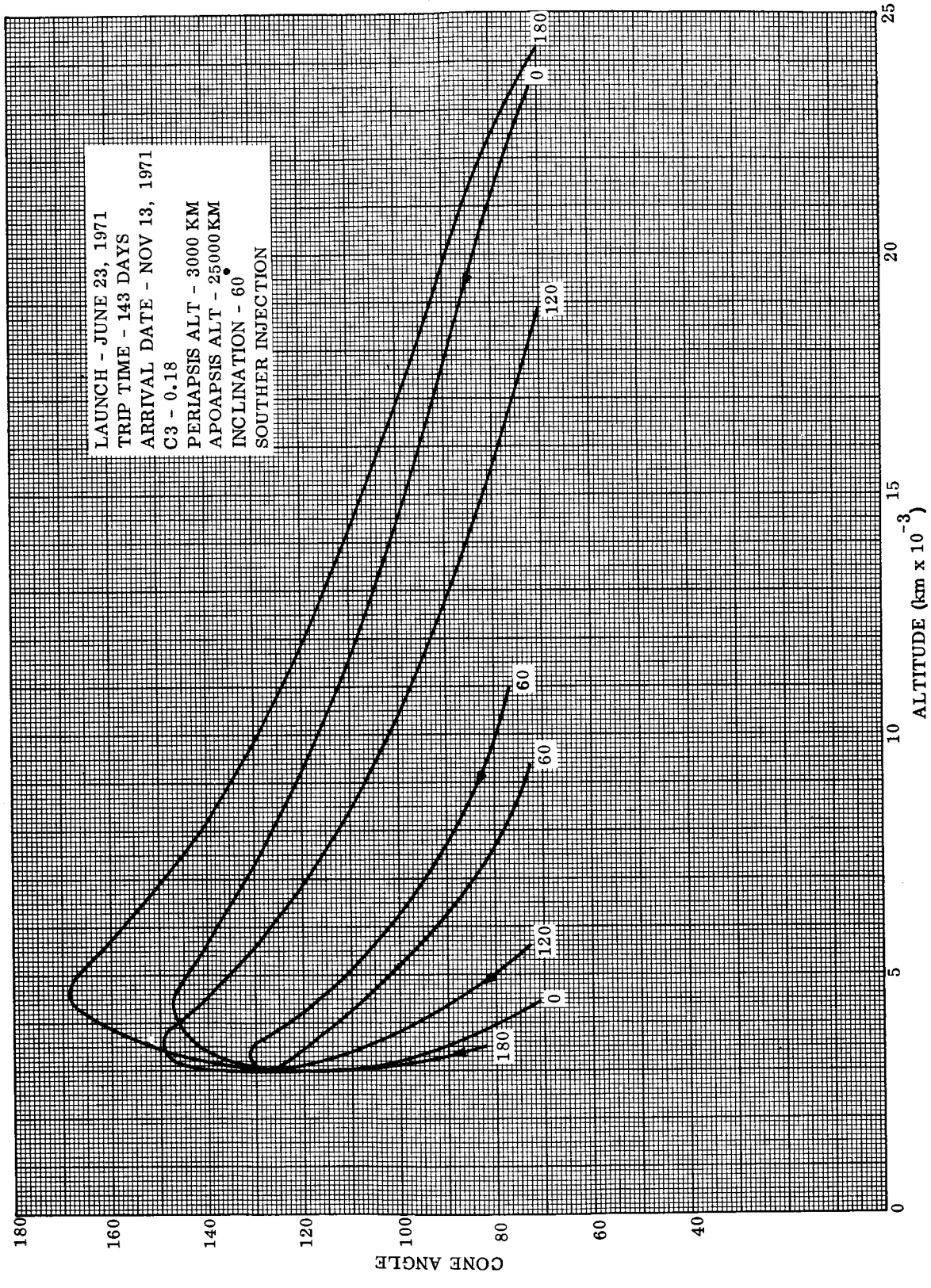

Figure 4-8f. Sun-Orbiter-Planet Angle vs. Altitude

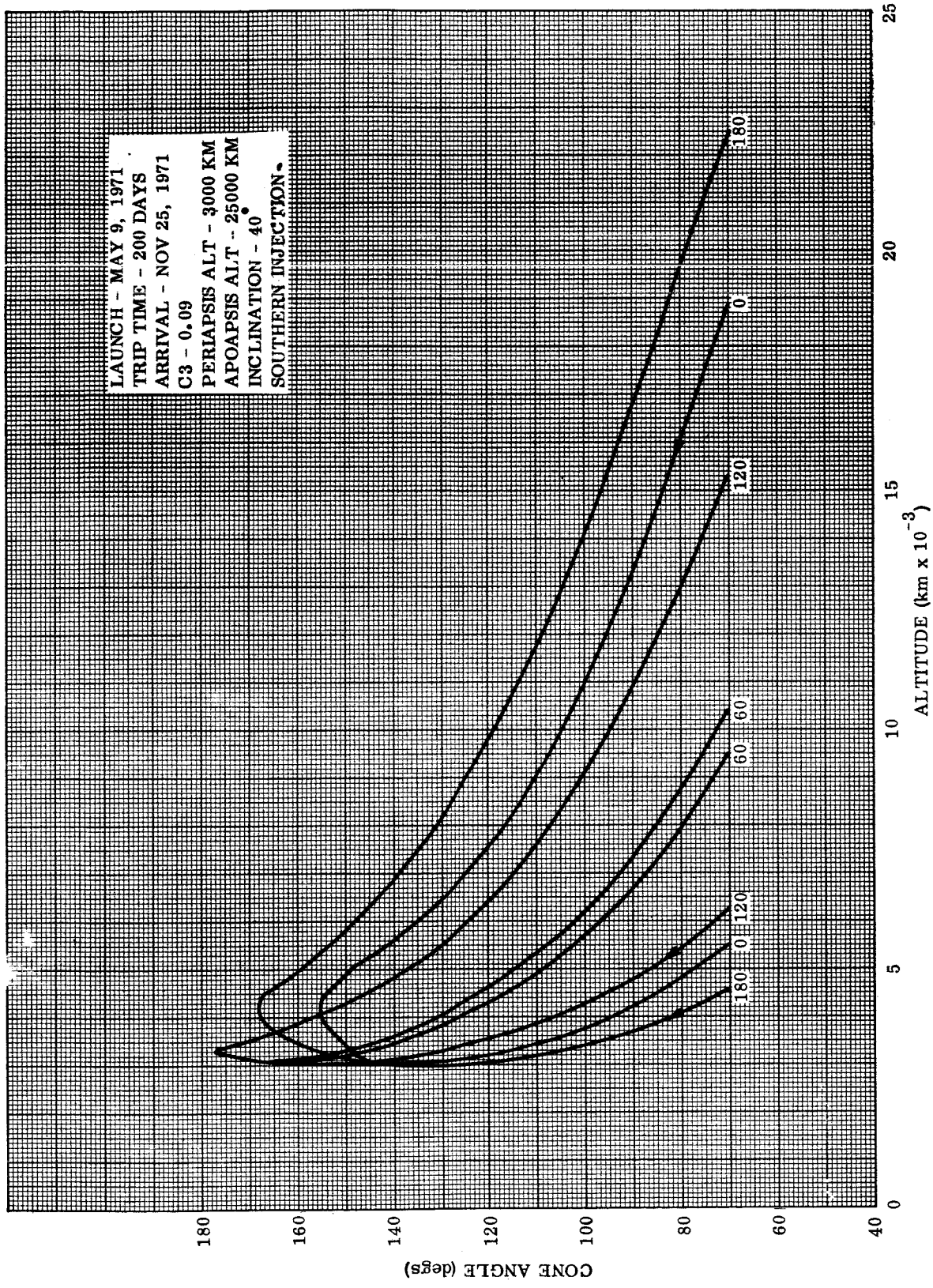

Figure 4-8g. Sun-Orbiter-Planet Angle vs. Altitude

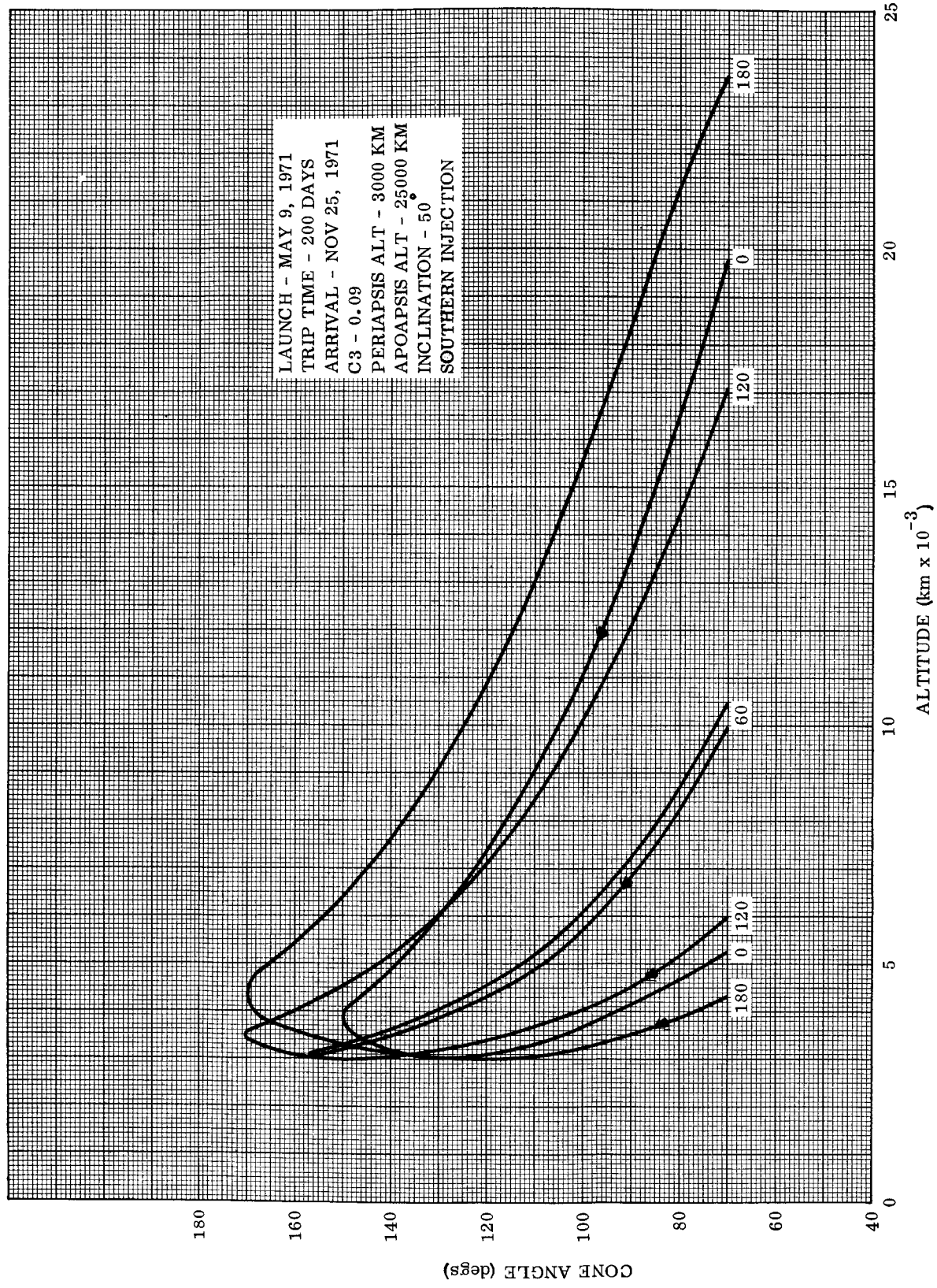

Figure 4-8h. Sun-Orbiter-Planet Angle vs. Altitude

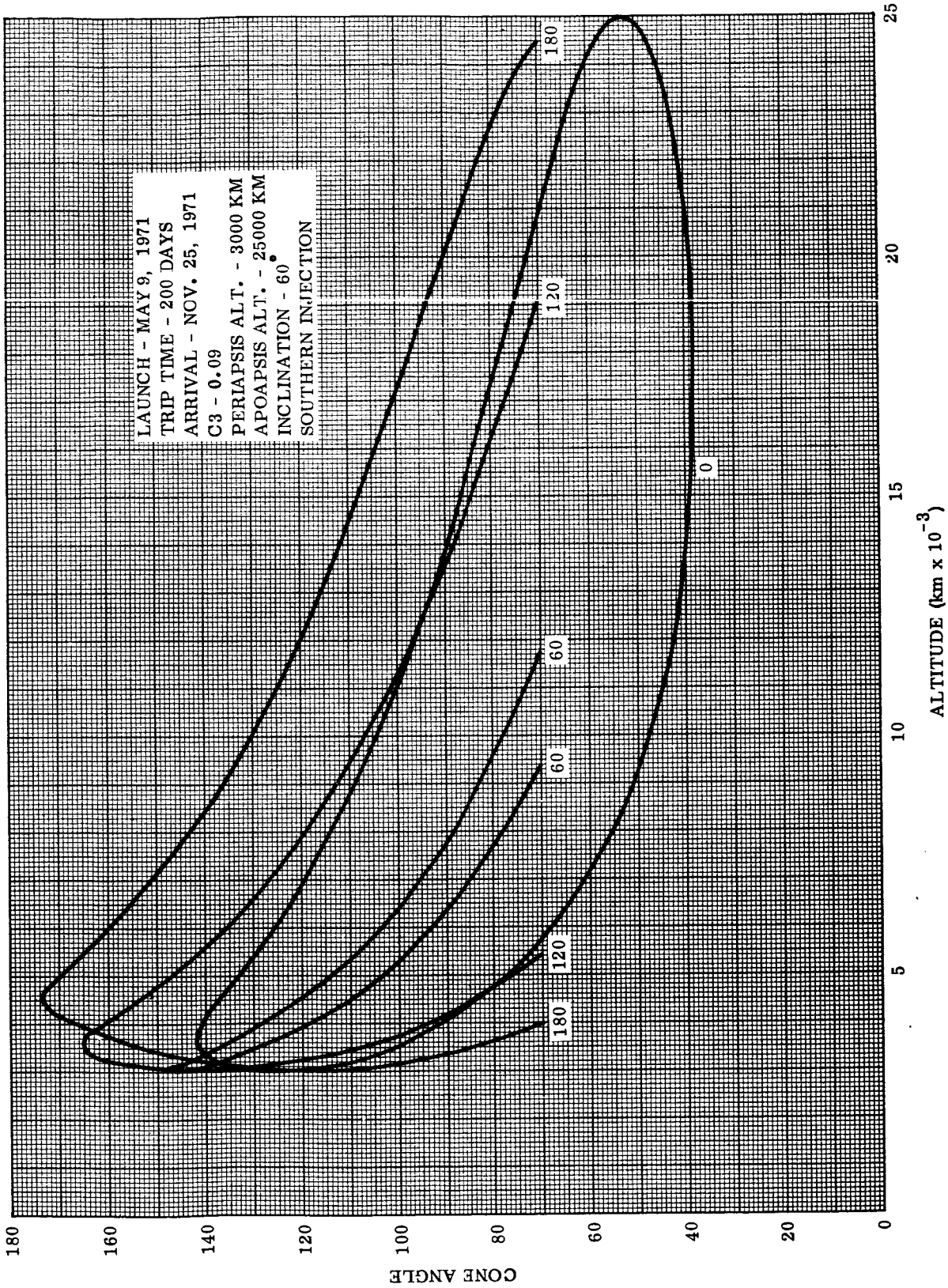

Figure 4-8i. Sun-Orbiter-Planet Angle vs. Altitude

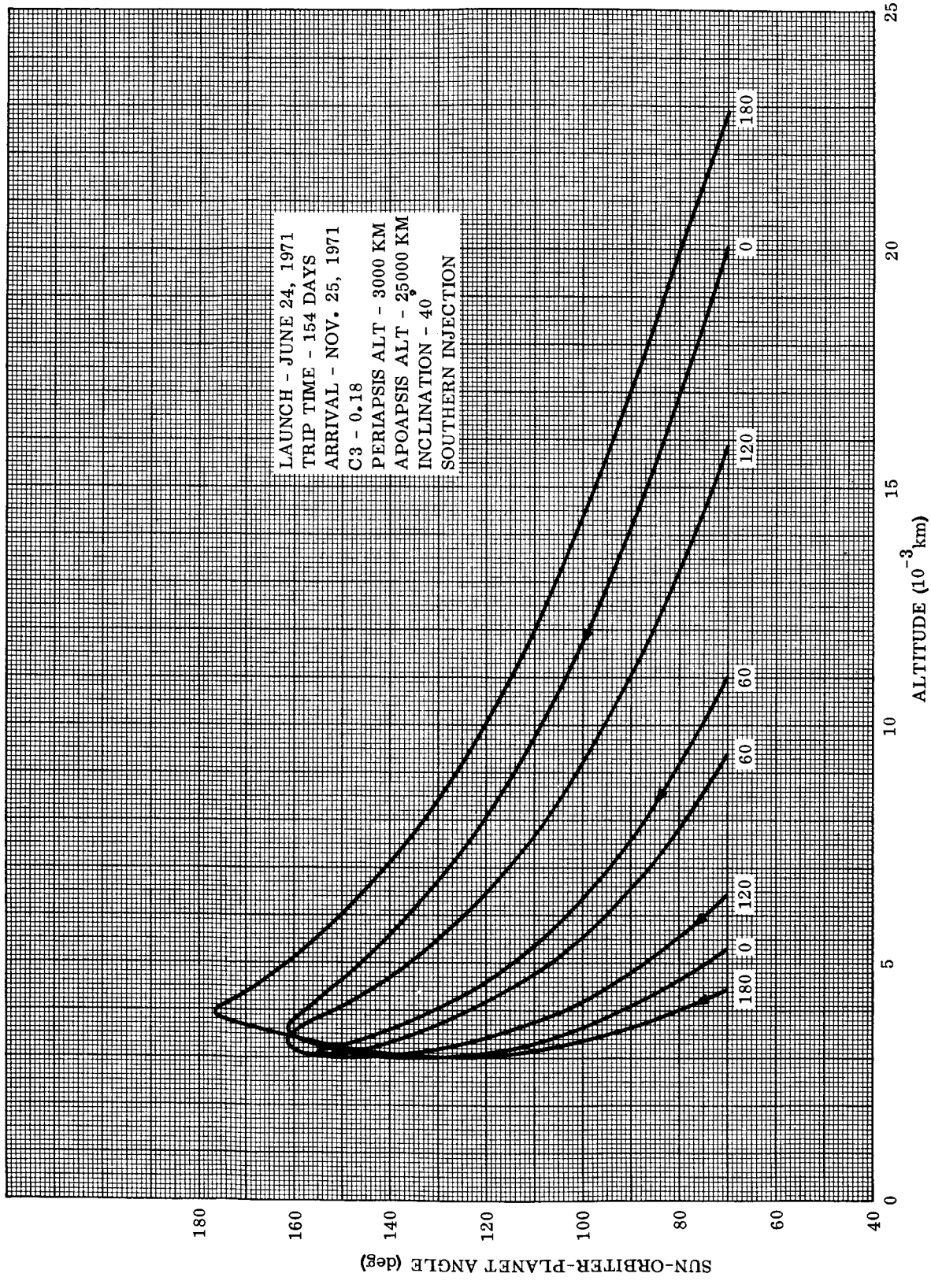

Figure 4-8j. Sun-Orbiter-Planet Angle vs. Altitude

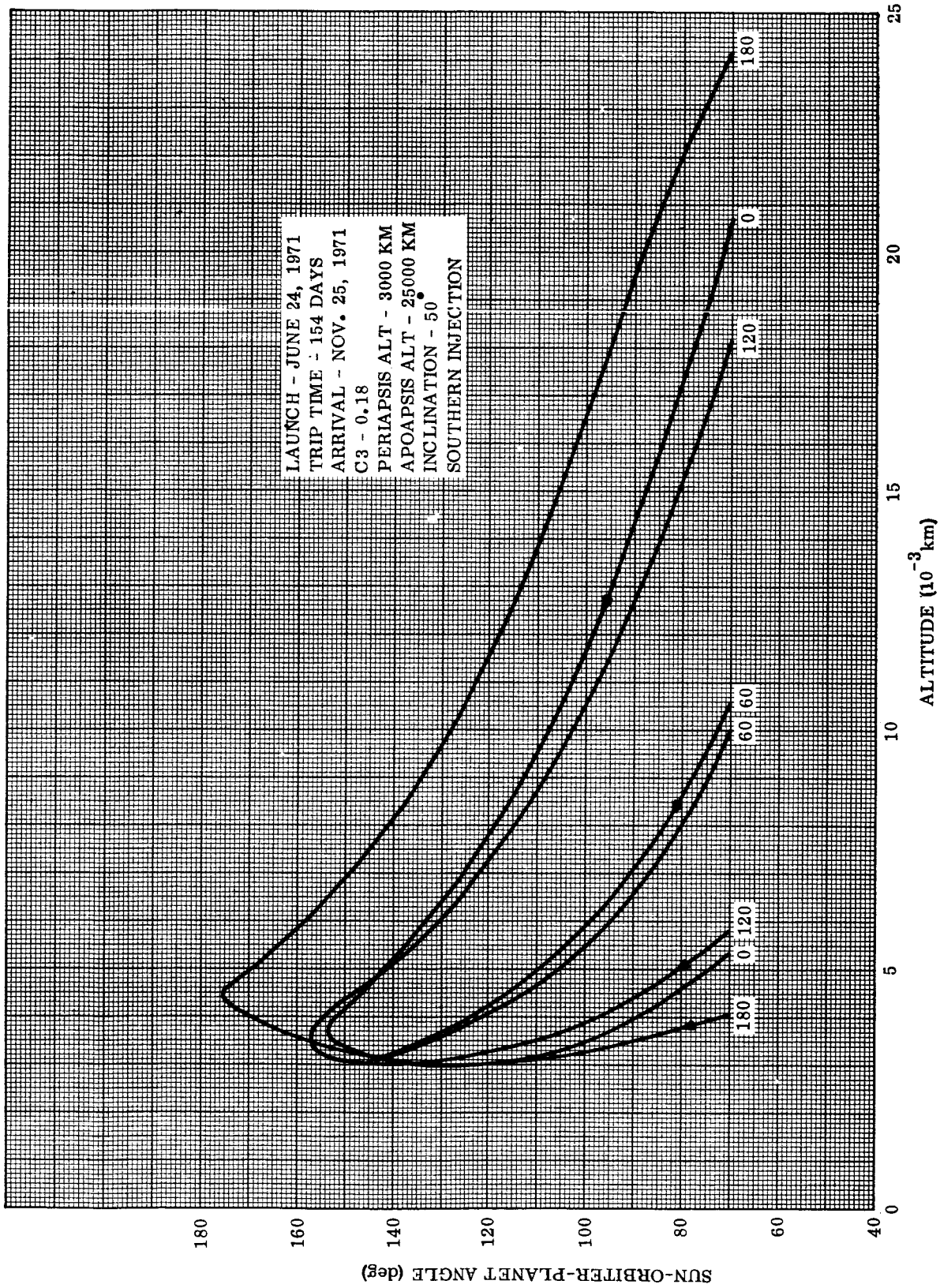

Figure 4-8k. Sun-Orbiter-Planet Angle vs. Altitude

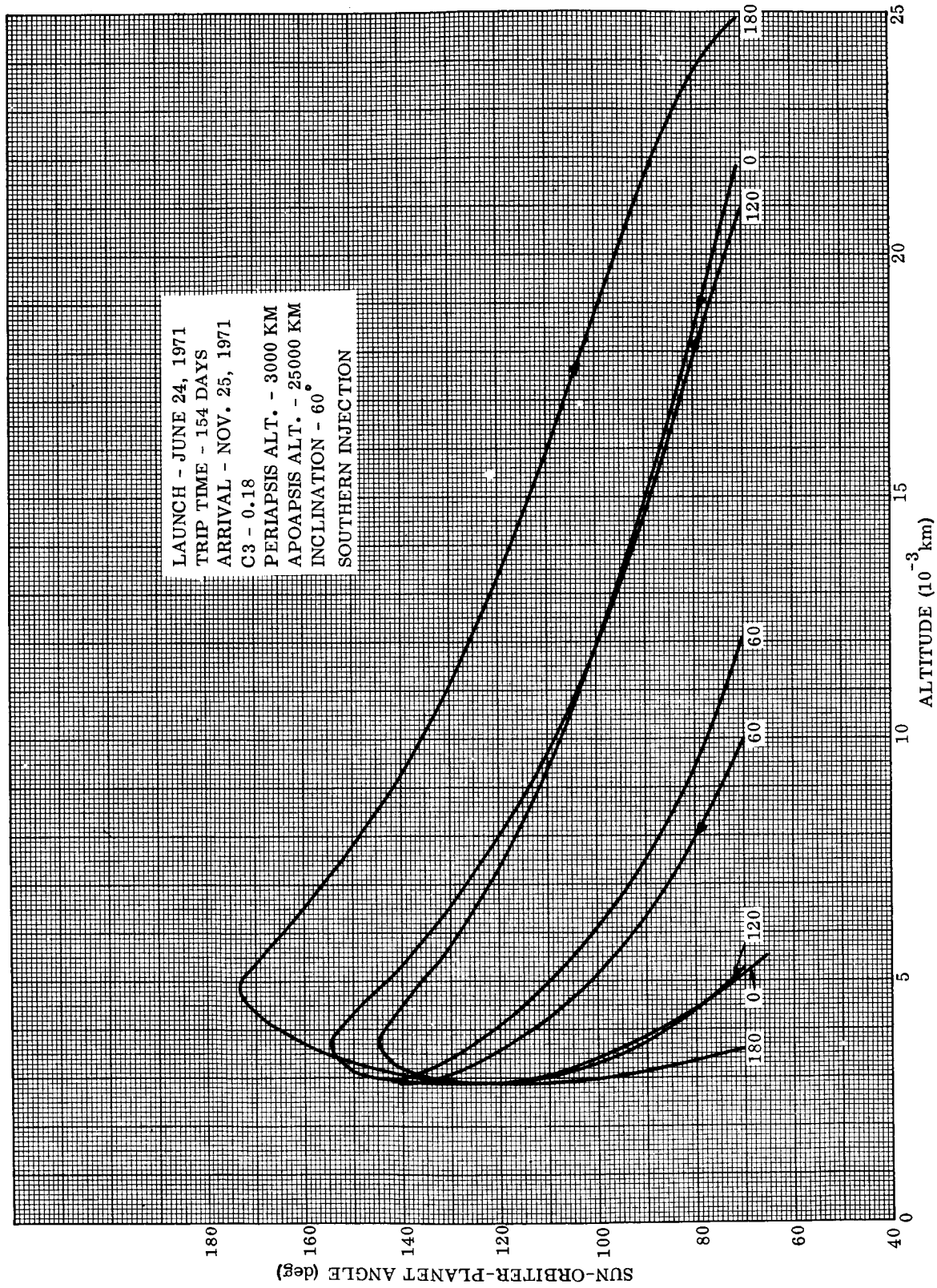

Figure 4-81. Sun-Orbiter-Planet Angle vs. Altitude

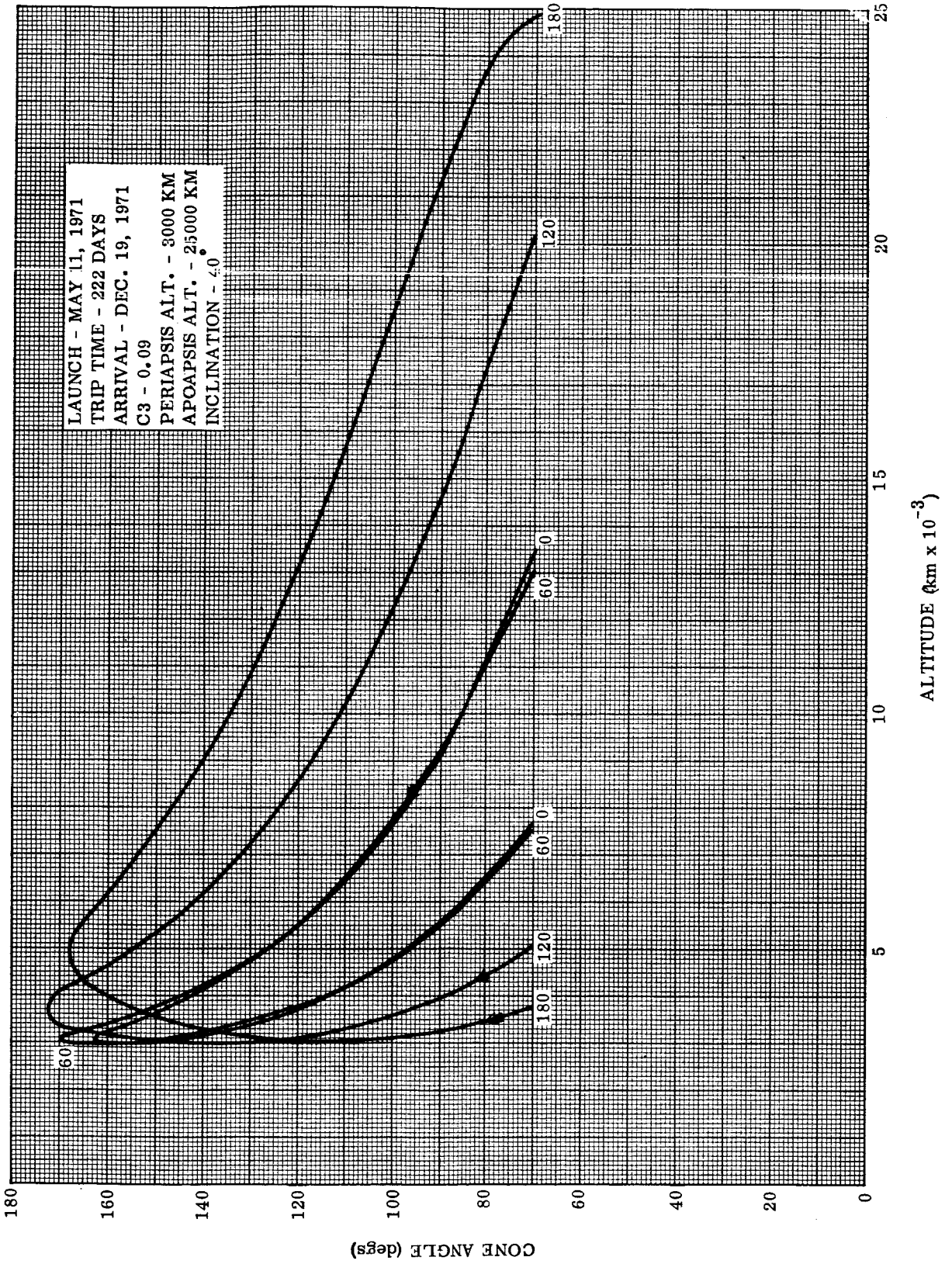

Figure 4-8m. Sun-Orbiter-Planet Angle vs. Altitude

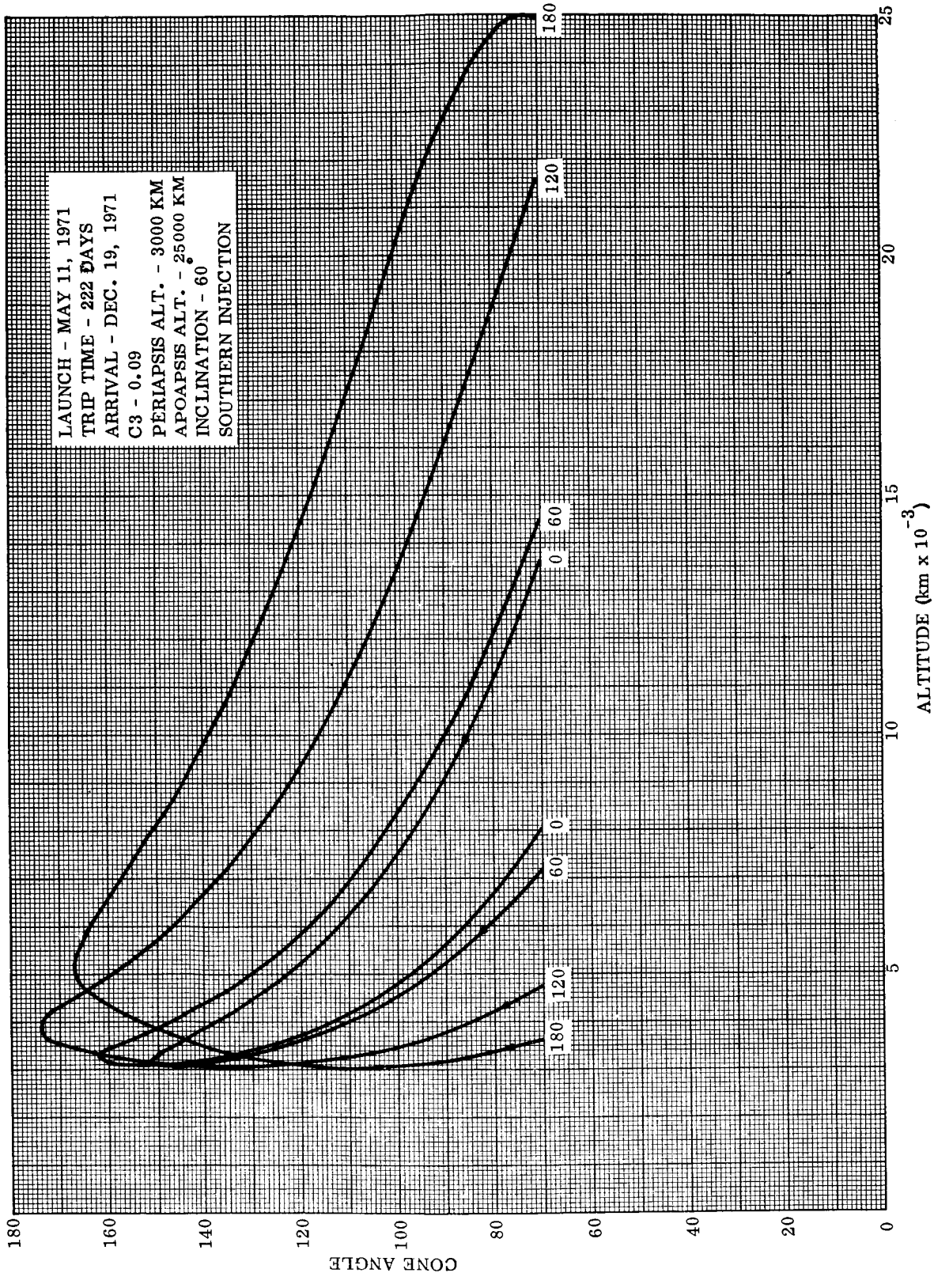

Figure 4-8n. Sun-Orbiter-Planet Angle vs. Altitude

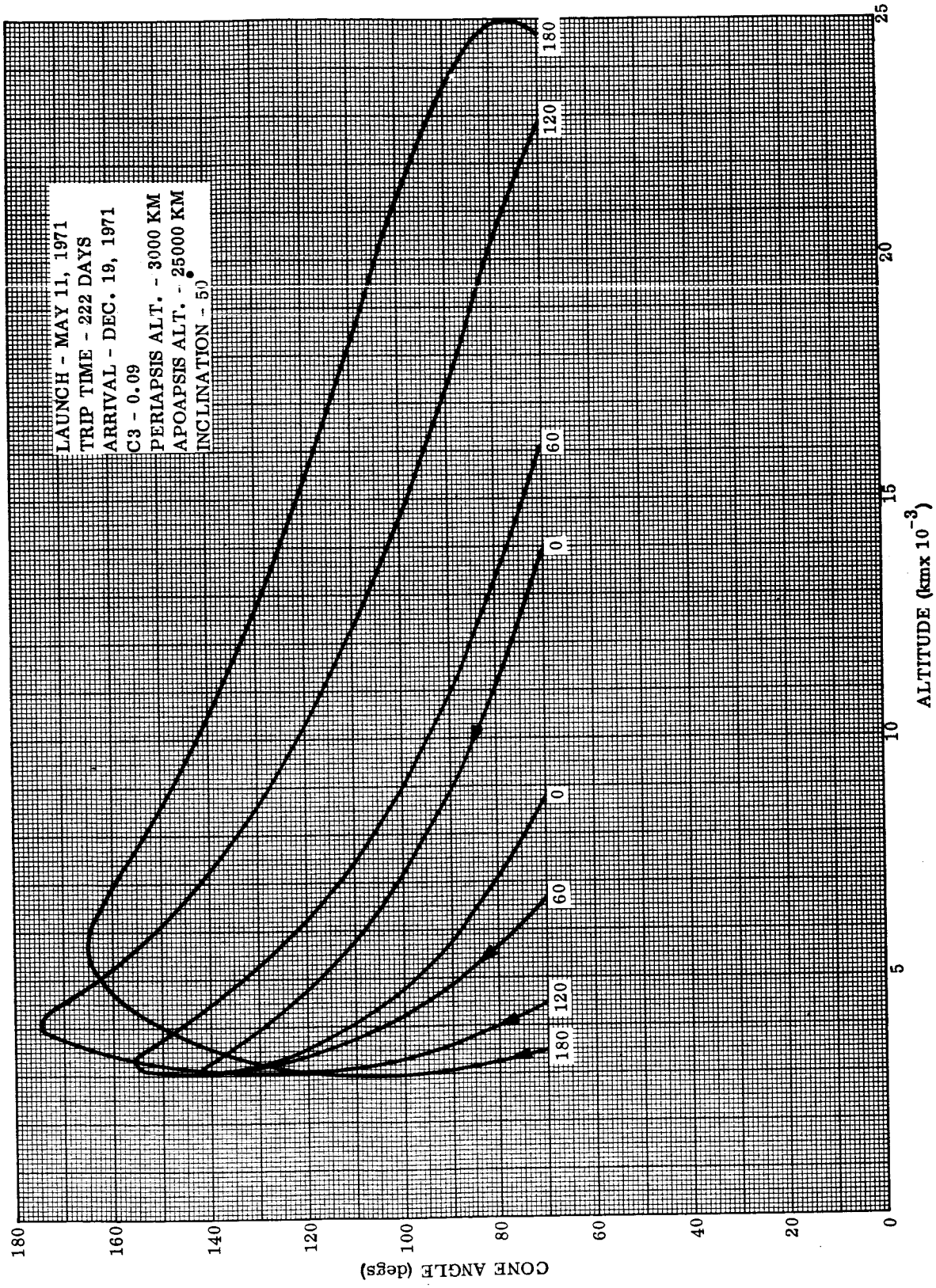

Figure 4-8o. Sun-Orbiter-Planet Angle vs. Altitude

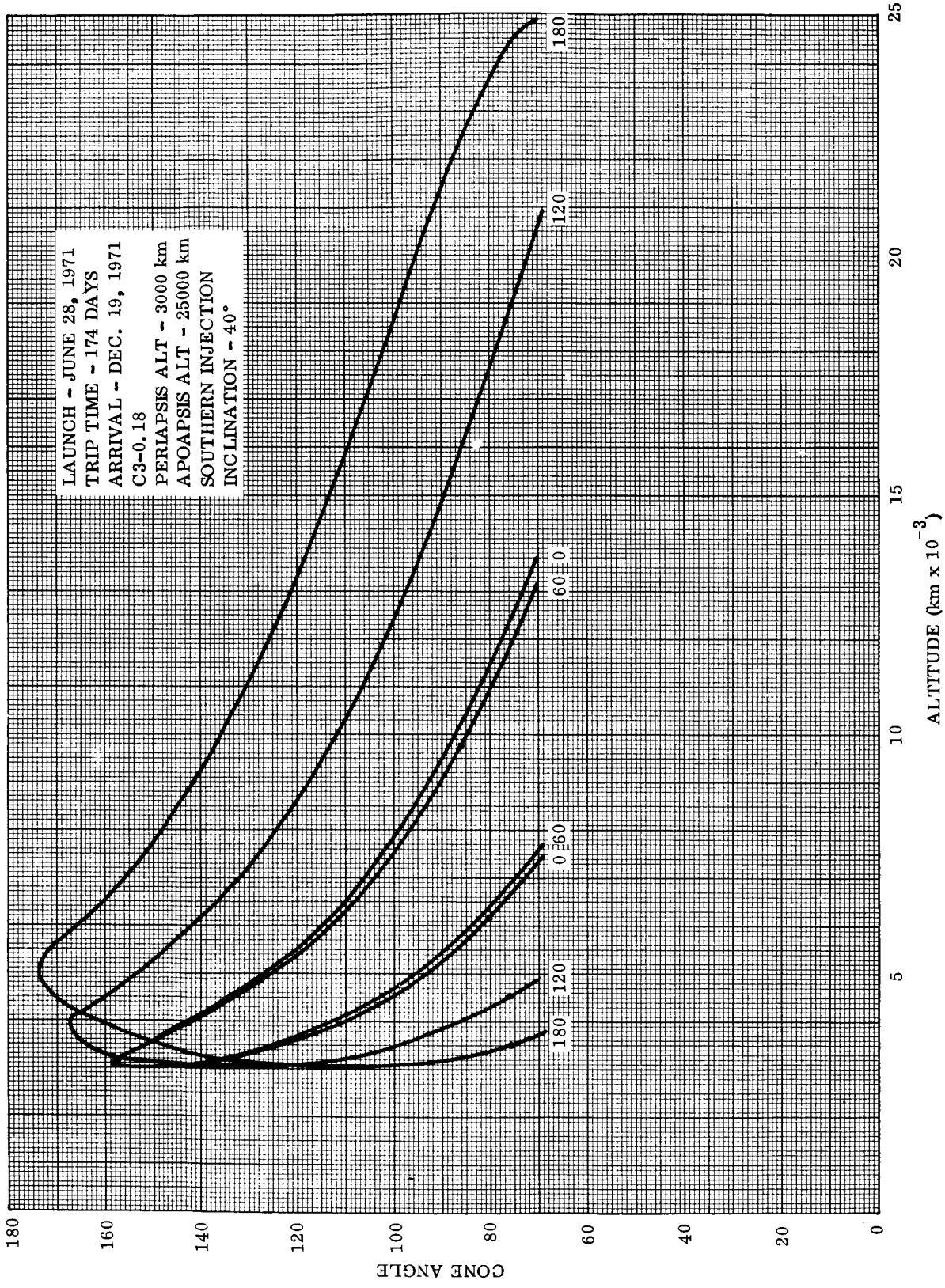

Figure 4-8p. Sun-Orbiter-Planet Angle vs. Altitude

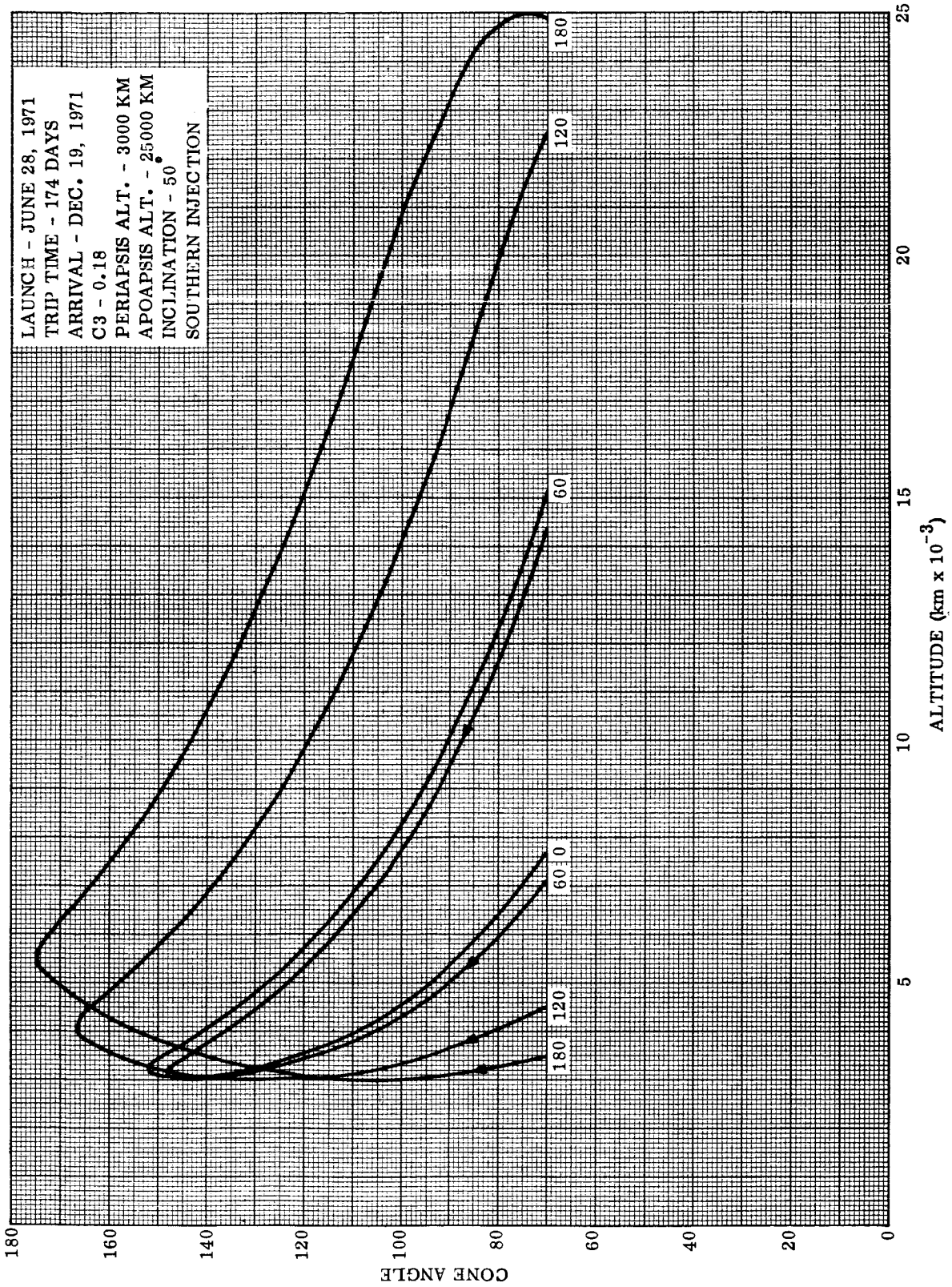

Figure 4-8 q. Sun Orbiter Planet Angle vs. Altitude

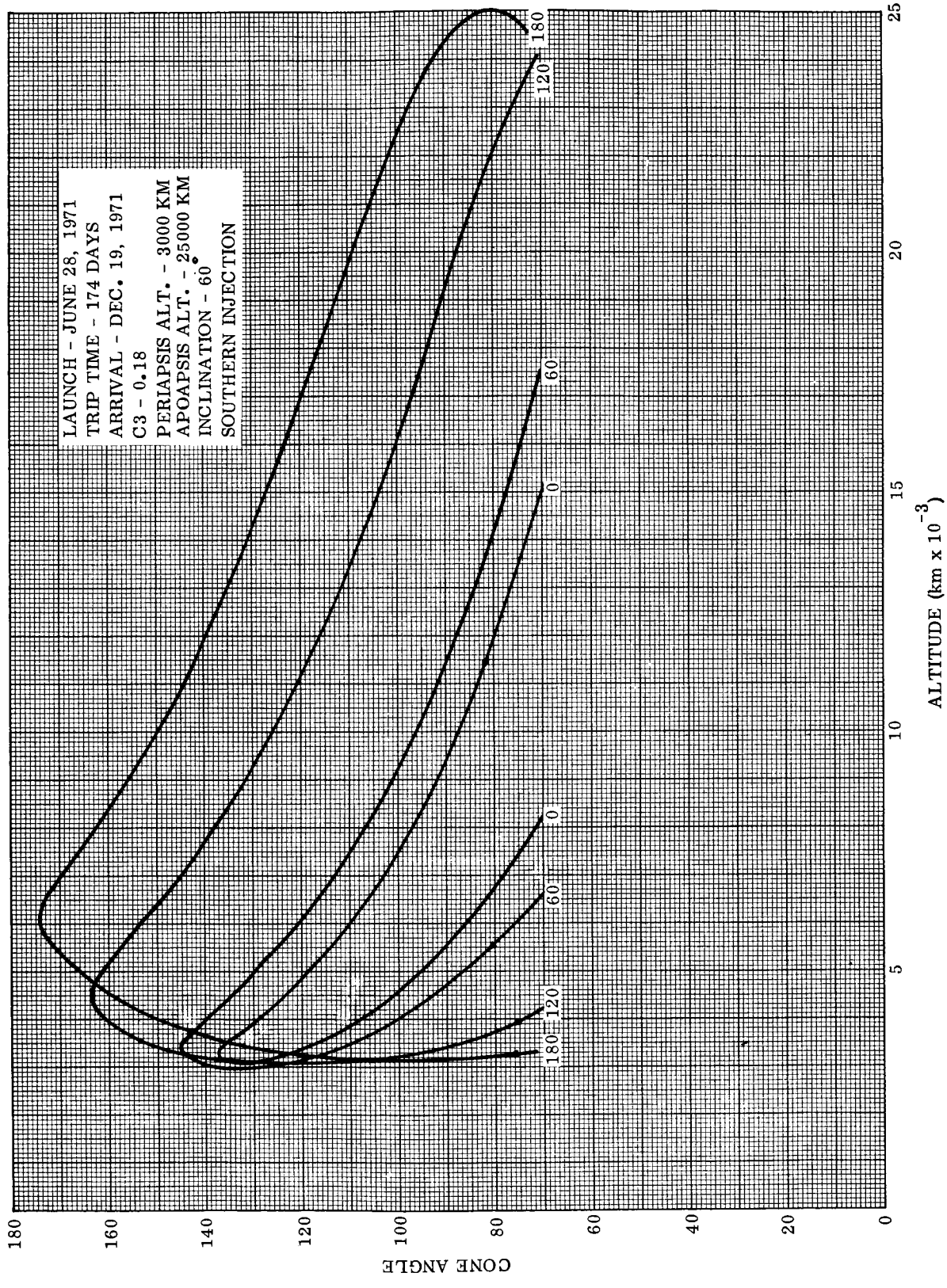

Figure 4-8 r. Sun Orbiter Planet Angle vs Altitude

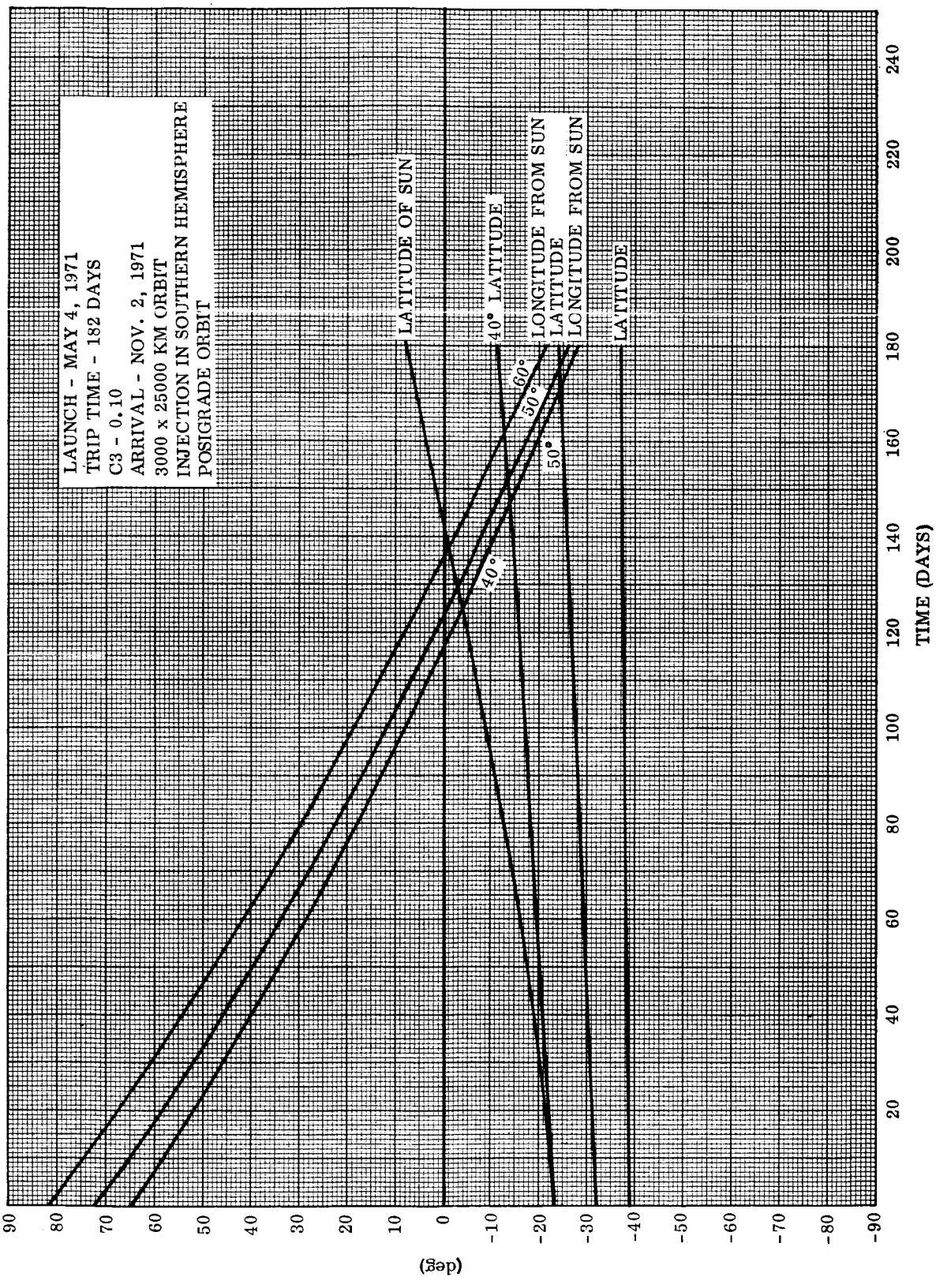

Figure 4-9 a. Position of Periapsis

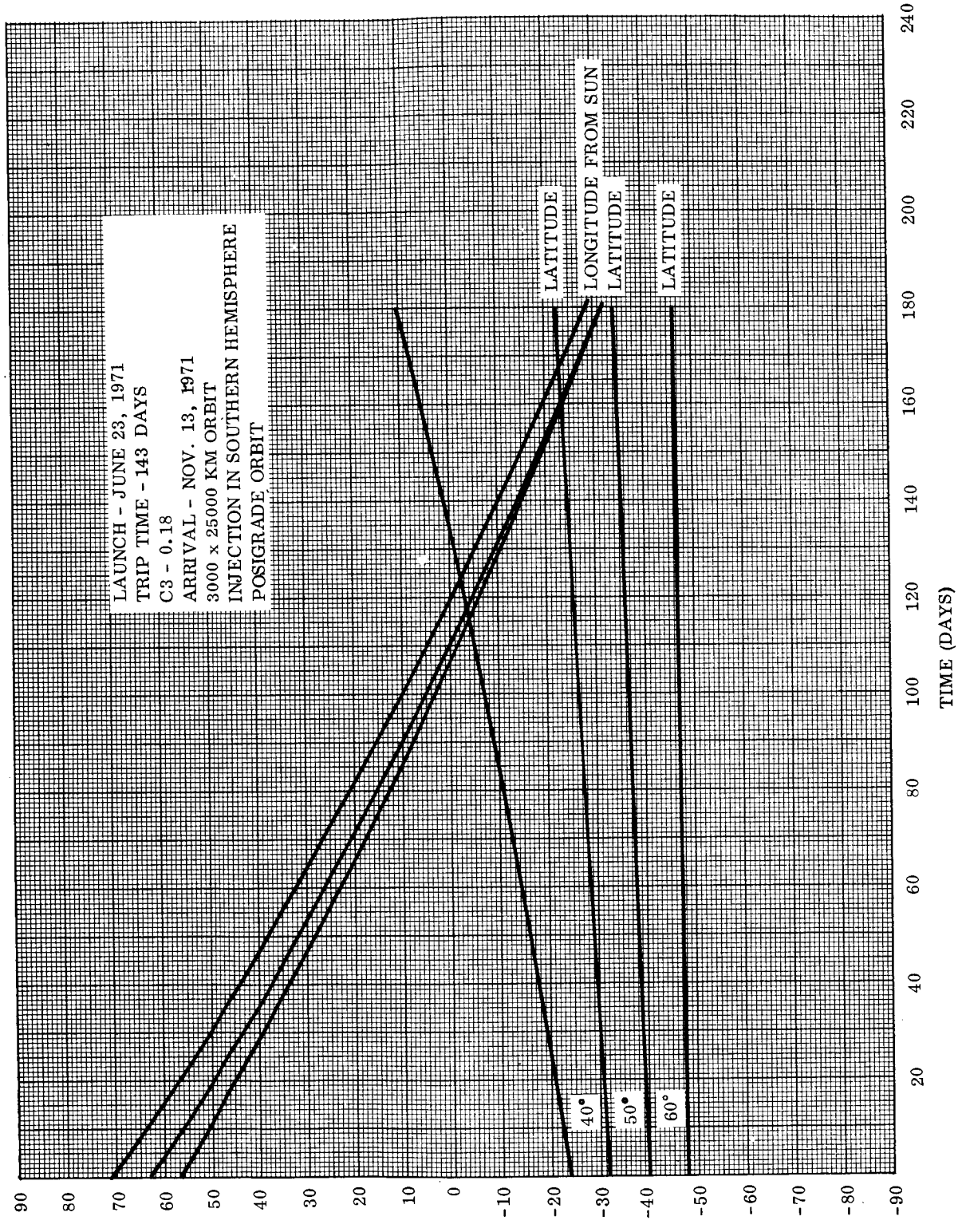

Figure 4-9 b. Position of Periapsis

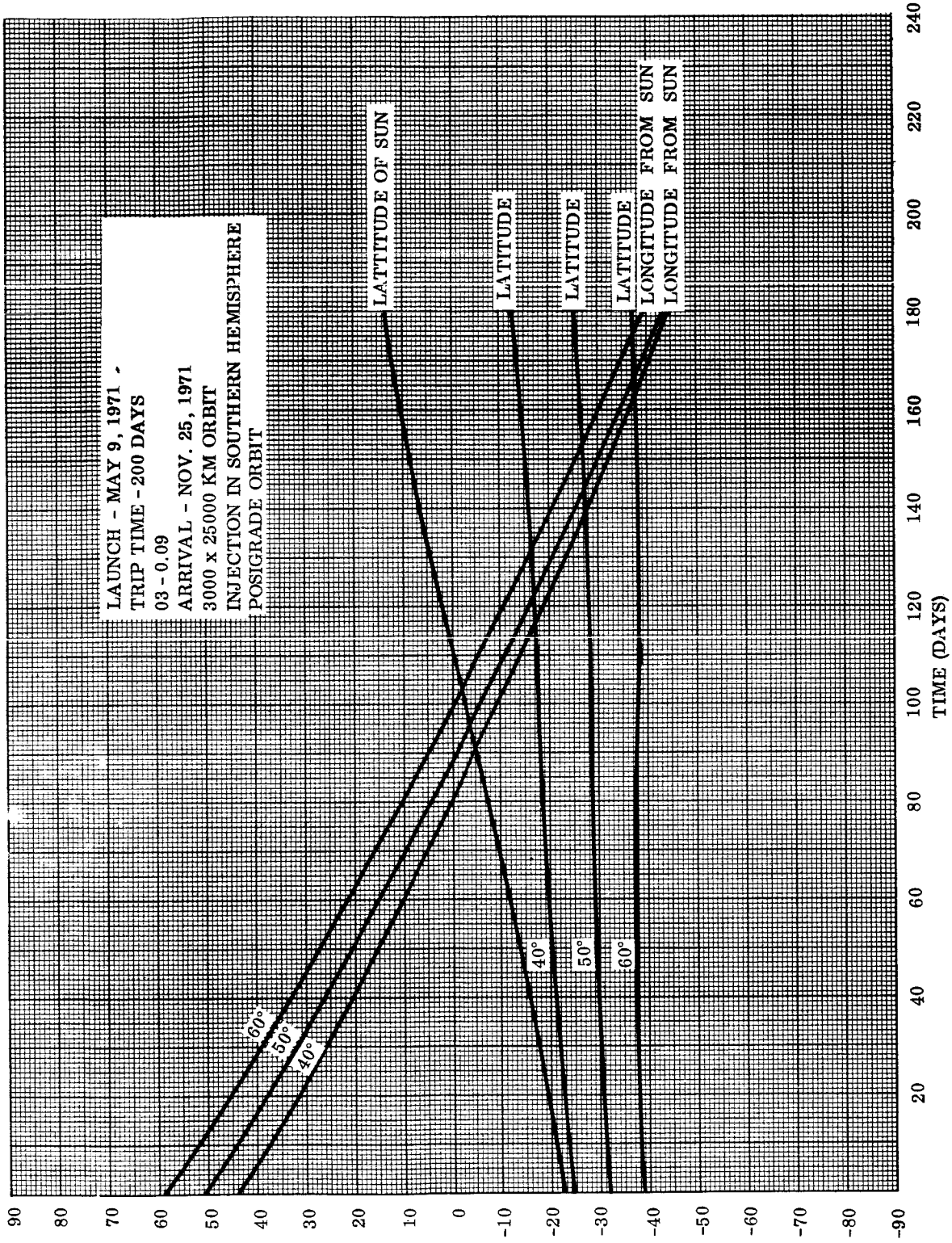

Figure 4-9 c. Position of Periapsis

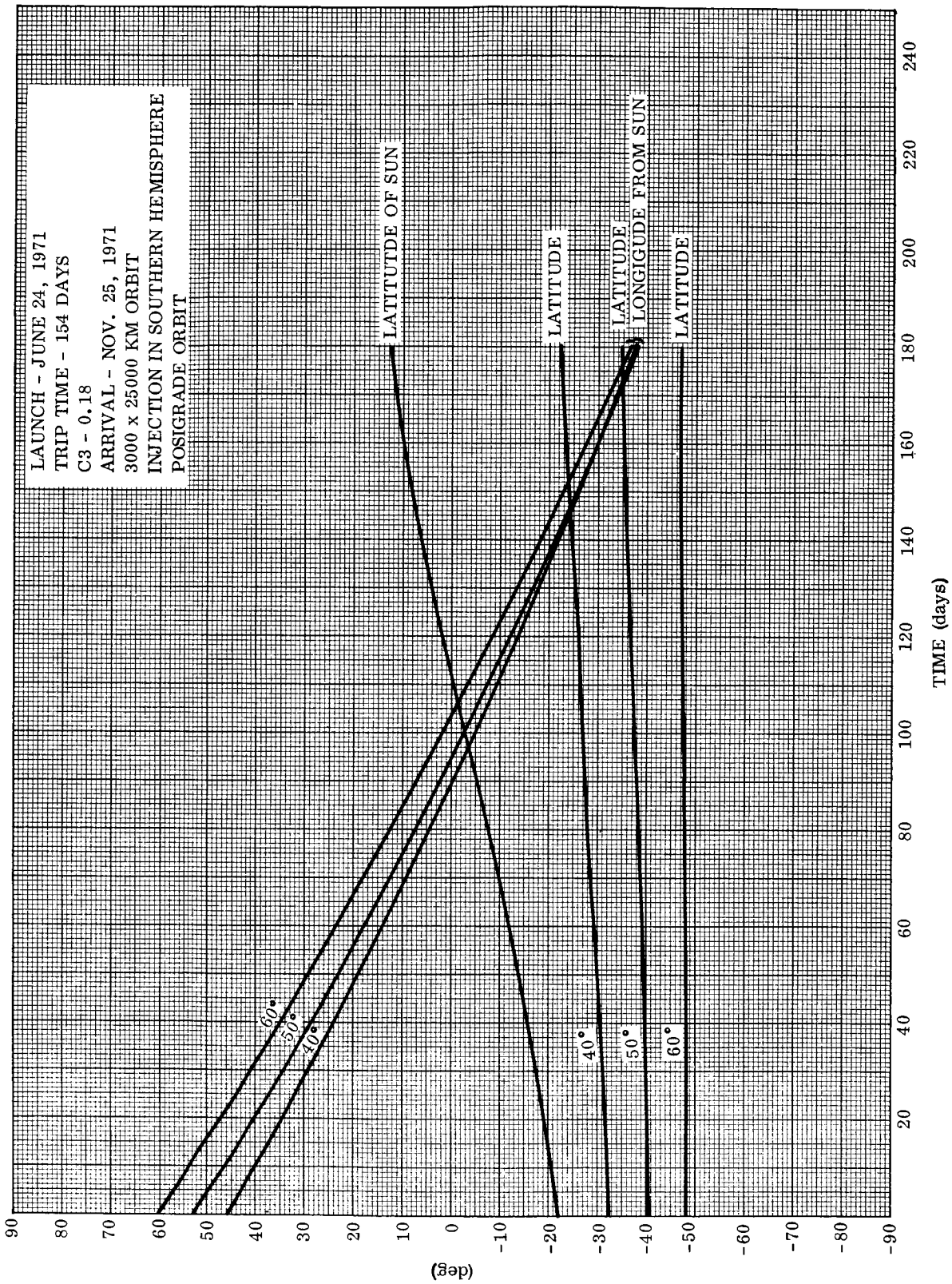

Figure 4-9 d. Position of Periapsis

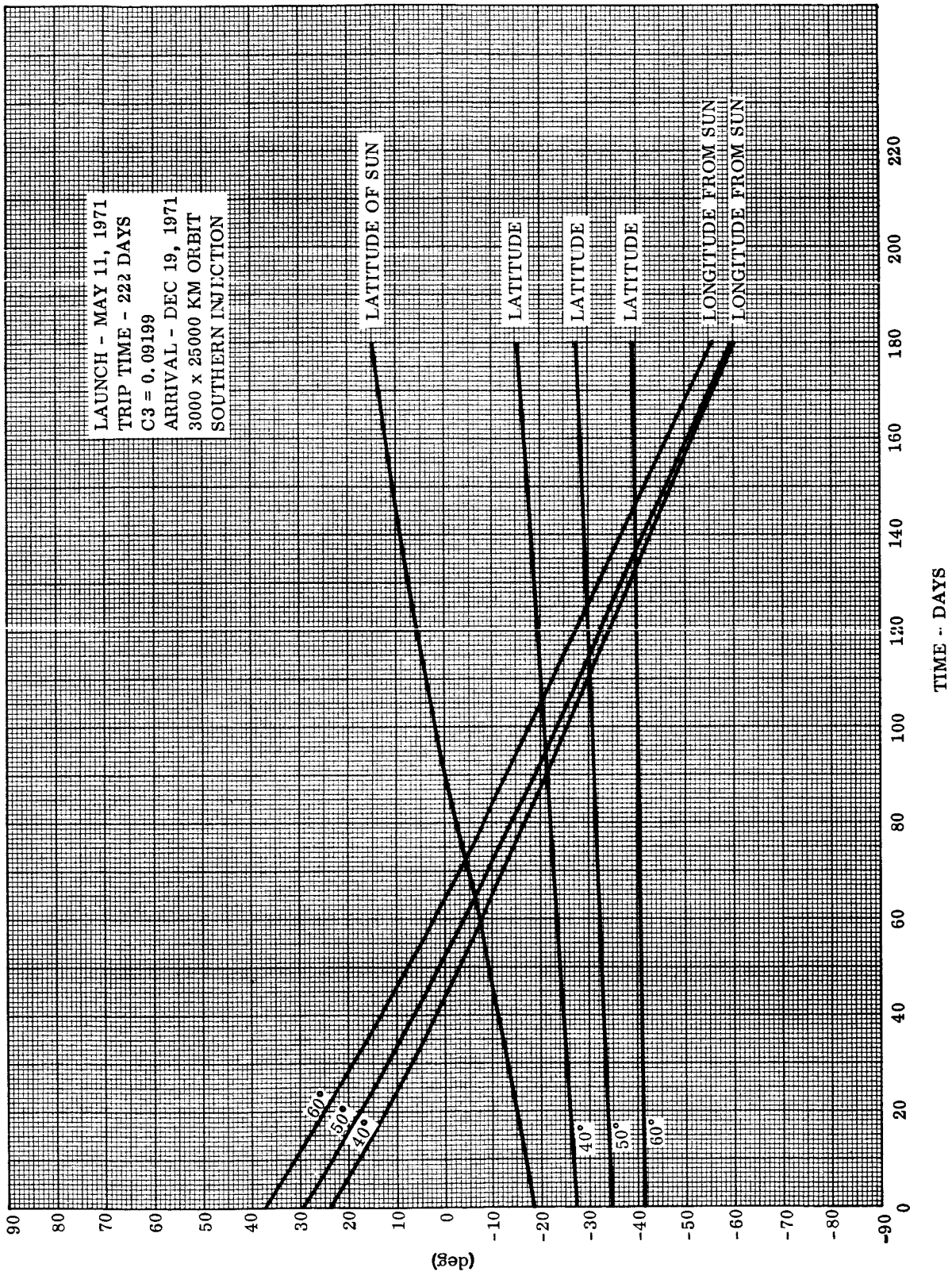

Figure 4-9 e. Position of Periapsis

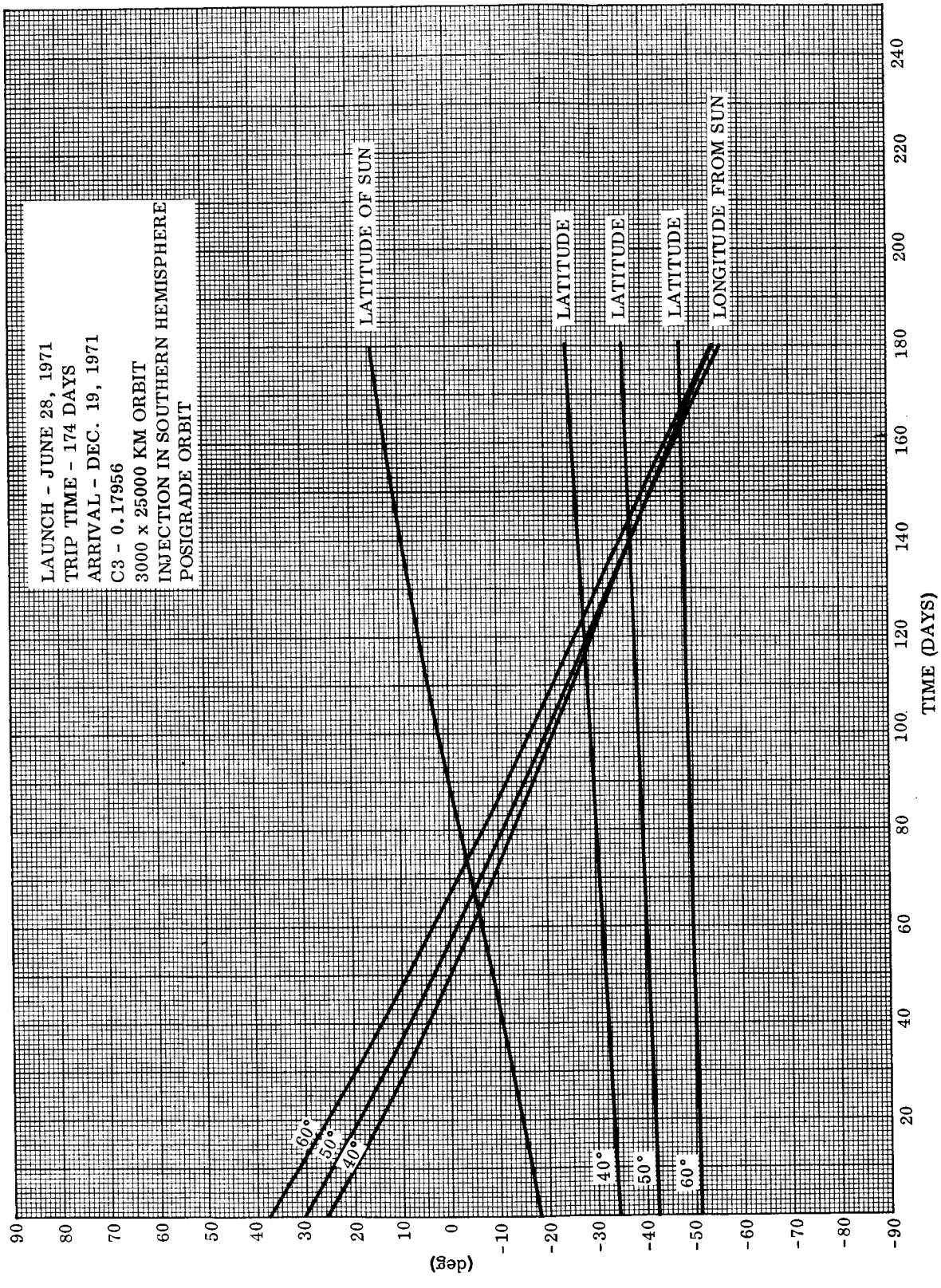

Figure 4-9 f. Position of Periapsis

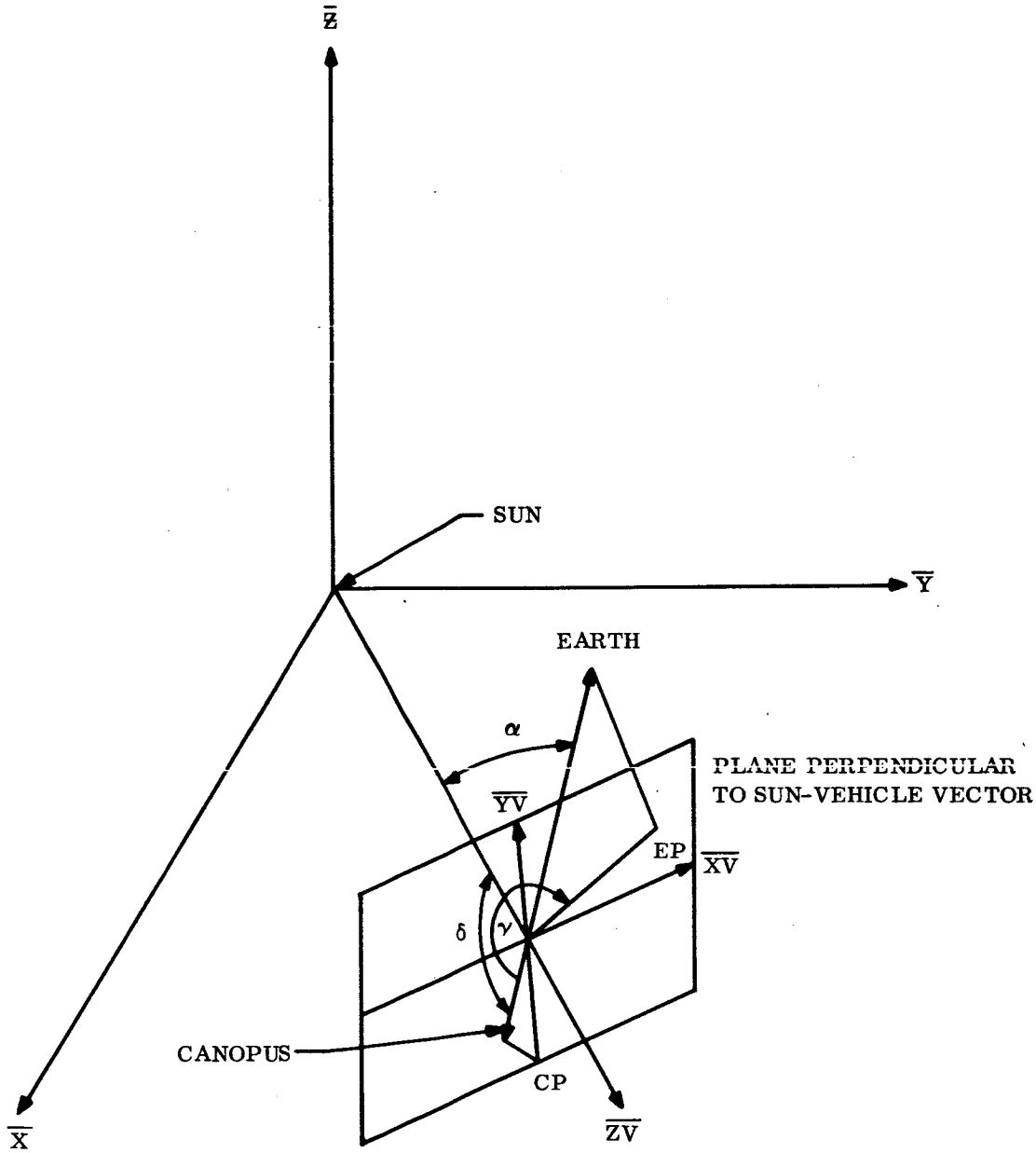

($\overline{XV}$, $\overline{YV}$, $\overline{ZV}$) VEHICLE COORDINATE SYSTEM

$\overline{ZV}$ = SUN-VEHICLE VECTOR

$-\overline{YV} = C_p$ = PROJECTION OF CANOPUS VECTOR ON THE PLANE PERPENDICULAR TO TO THE SPACECRAFT - SUN LINE

$\overline{XV}$ = $\overline{YV} \times \overline{ZV}$

E_p = PROJECTION OF EARTH LINE-OF-SIGHT VECTOR ON THE PLANE PERPENDICULAR TO THE SPACECRAFT SUN LINE

α = EARTH CONE ANGLE

γ = EARTH CLOCK ANGLE

δ = CANOPUS CONE ANGLE

Figure 5-1. Sun-Canopus-Vehicle Coordinate System

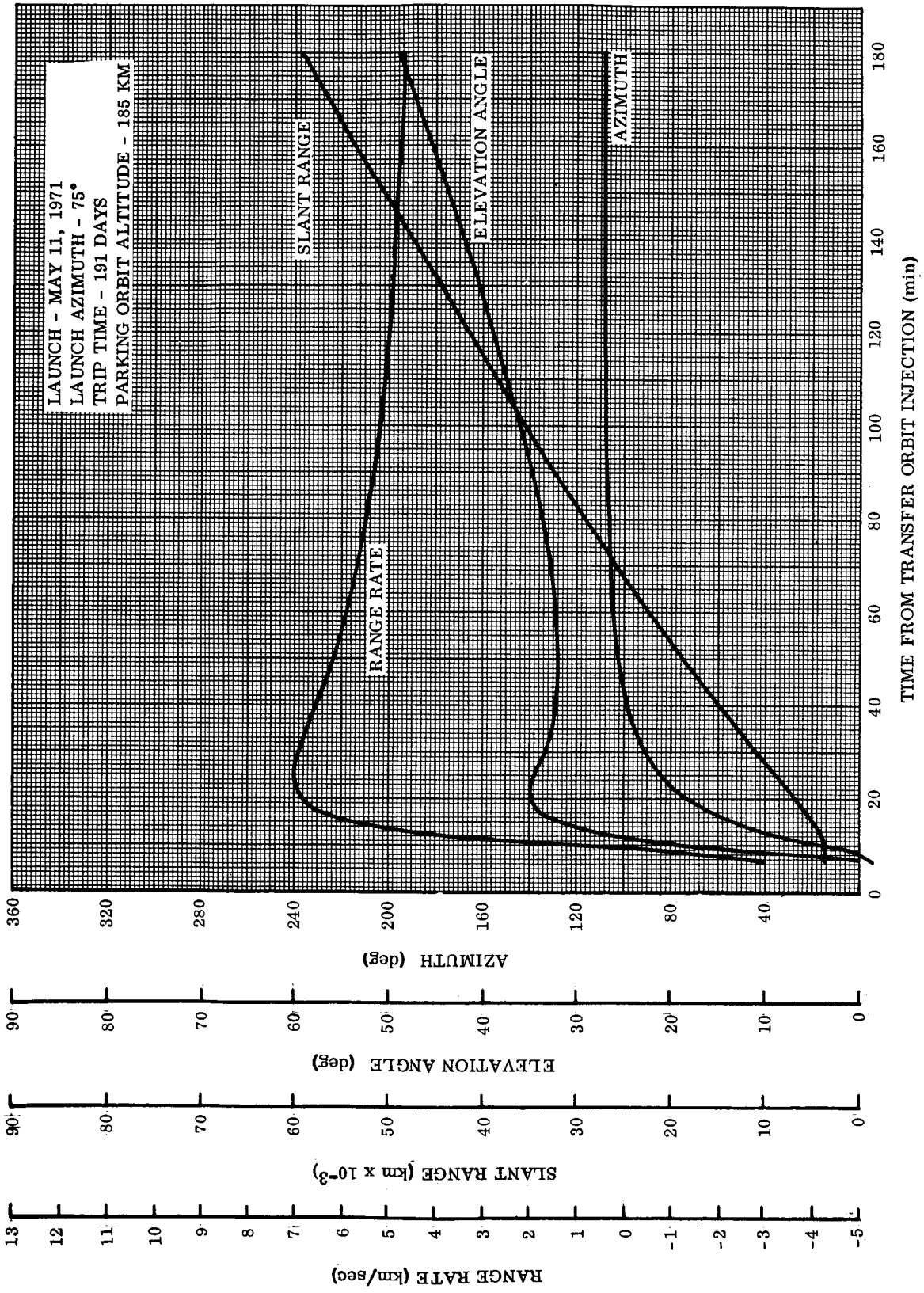

Figure 8-1. Near Earth Tracking Geometry-Johannesburg

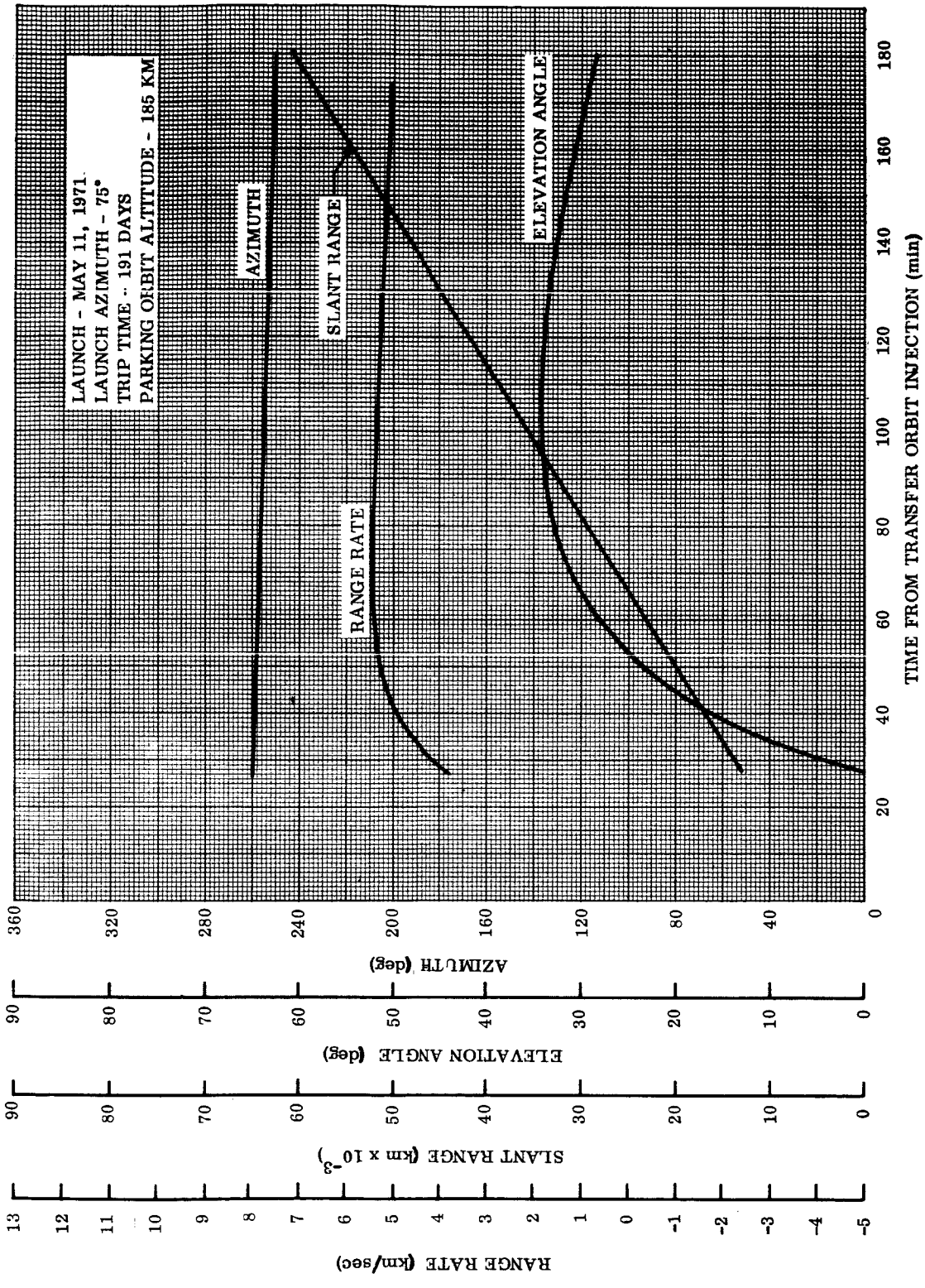

Figure 8-2. Near Earth Tracking Geometry-Woomera

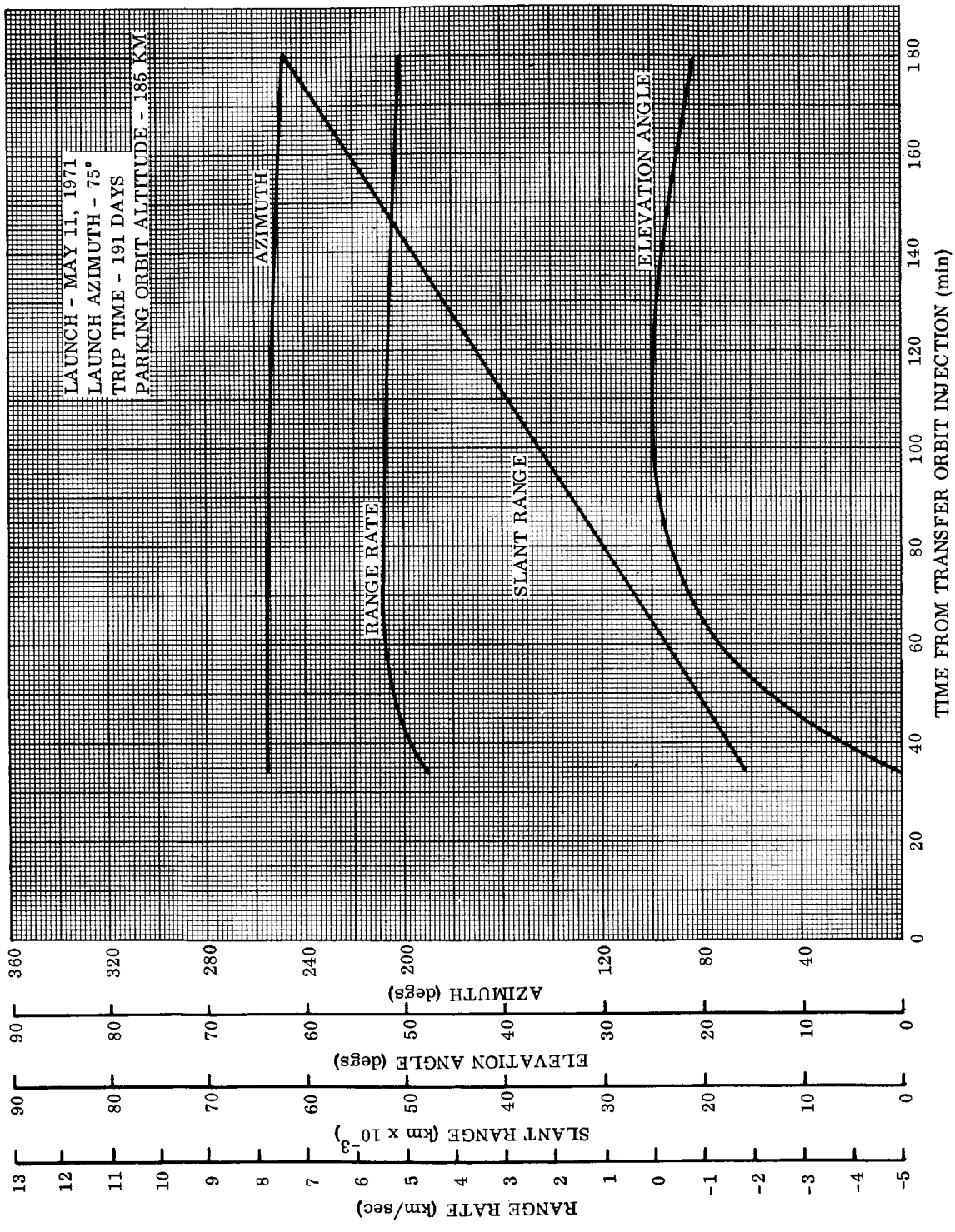

Figure 8-3. Near Earth Tracking Geometry-Camberra

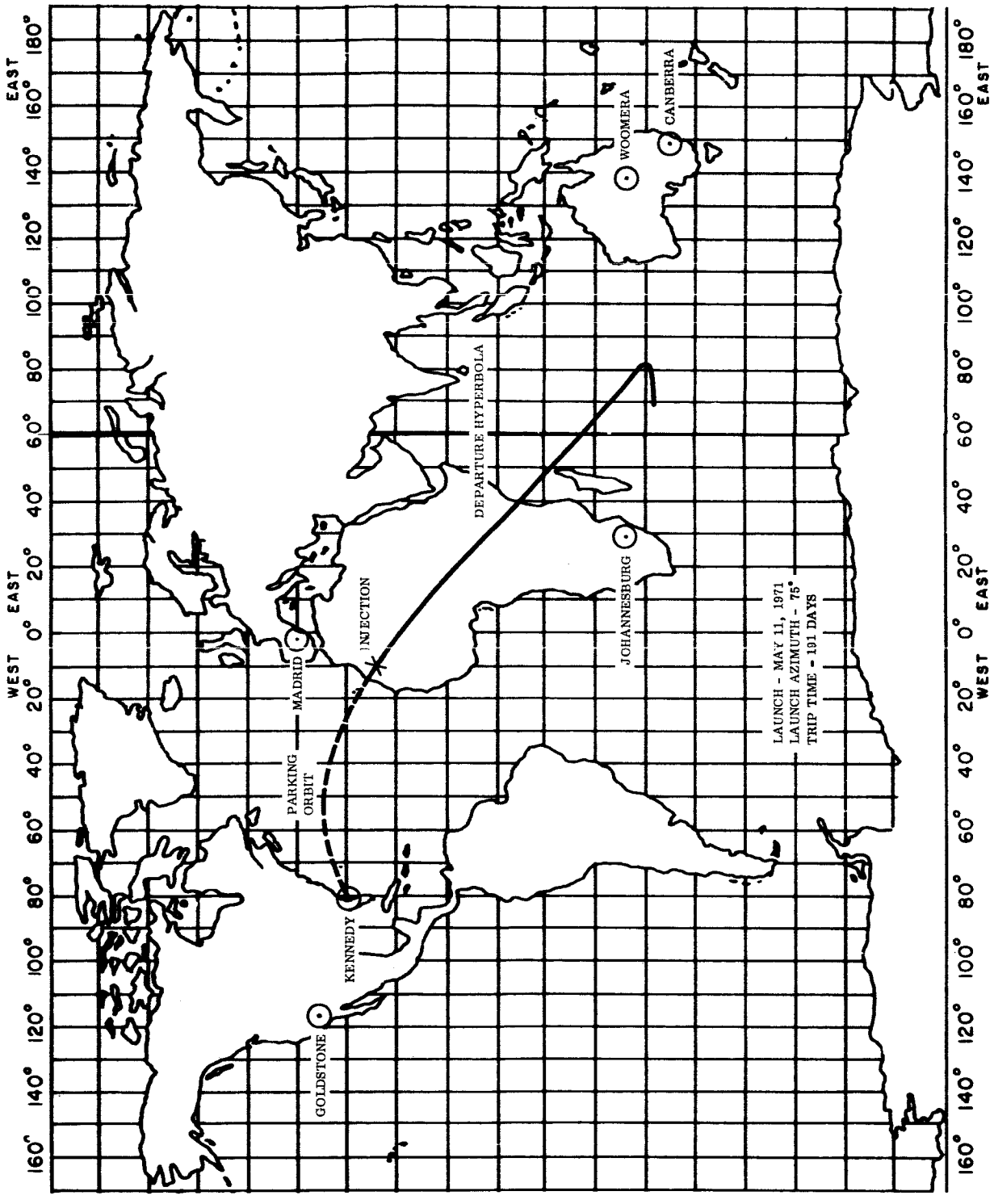

Figure 8-4. Departure Trajectory

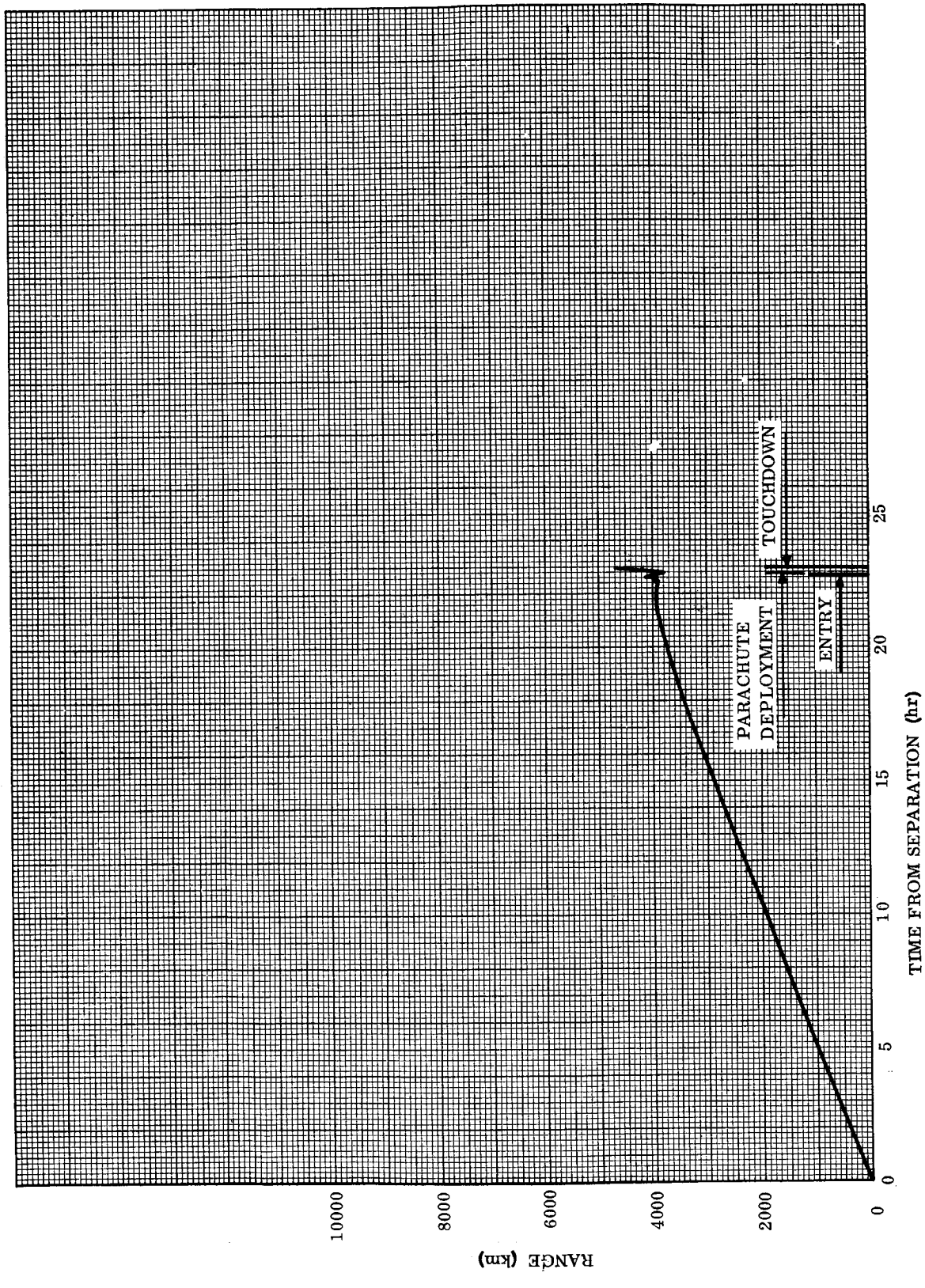

Figure 8-5. Orbiter Capsule Range vs. Time from Separation

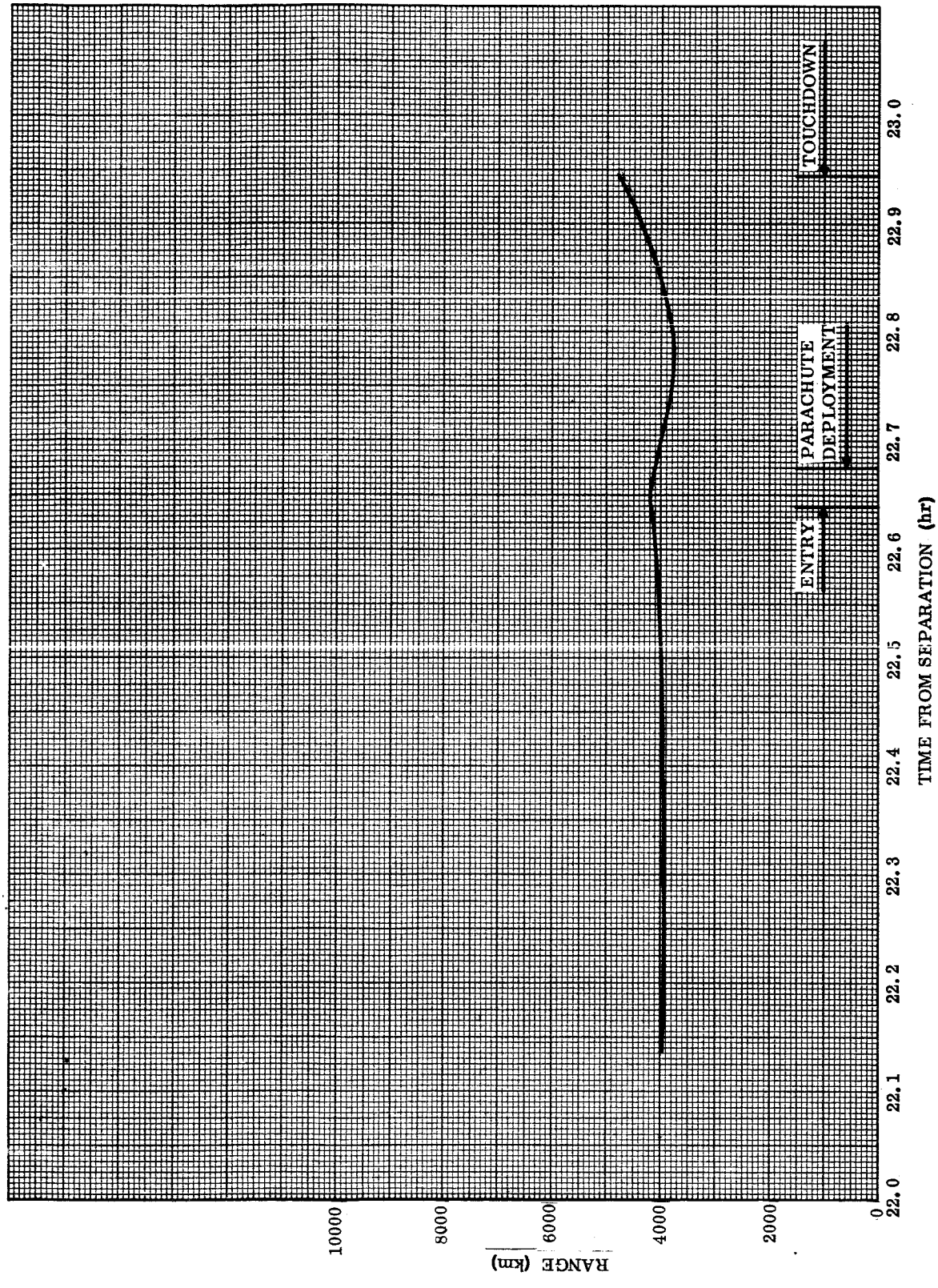

Figure 8-6. Orbiter Capsule Range vs. Time from Separation

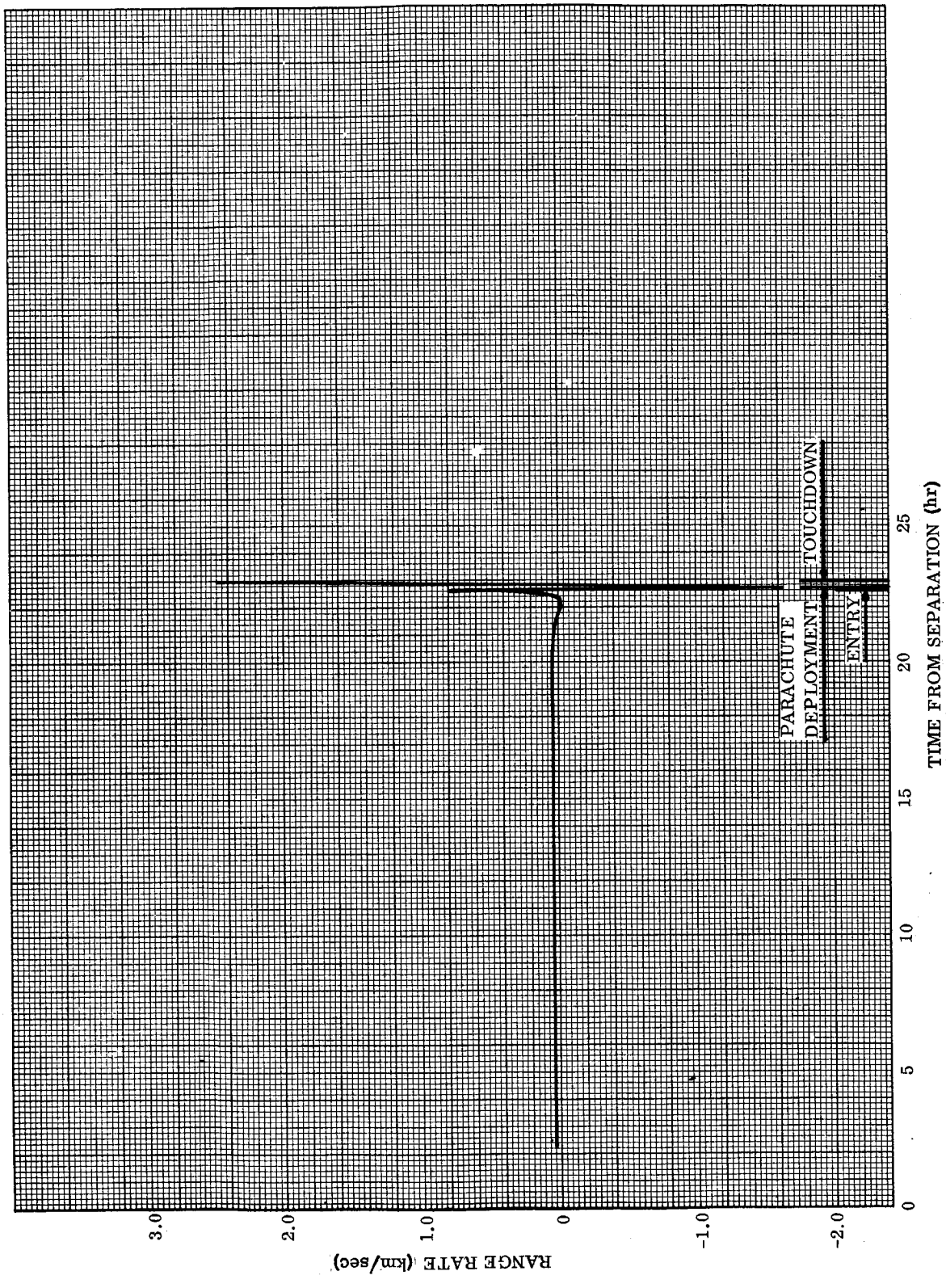

Figure 8-7. Orbiter Capsule Range Rate vs. Time from Separation

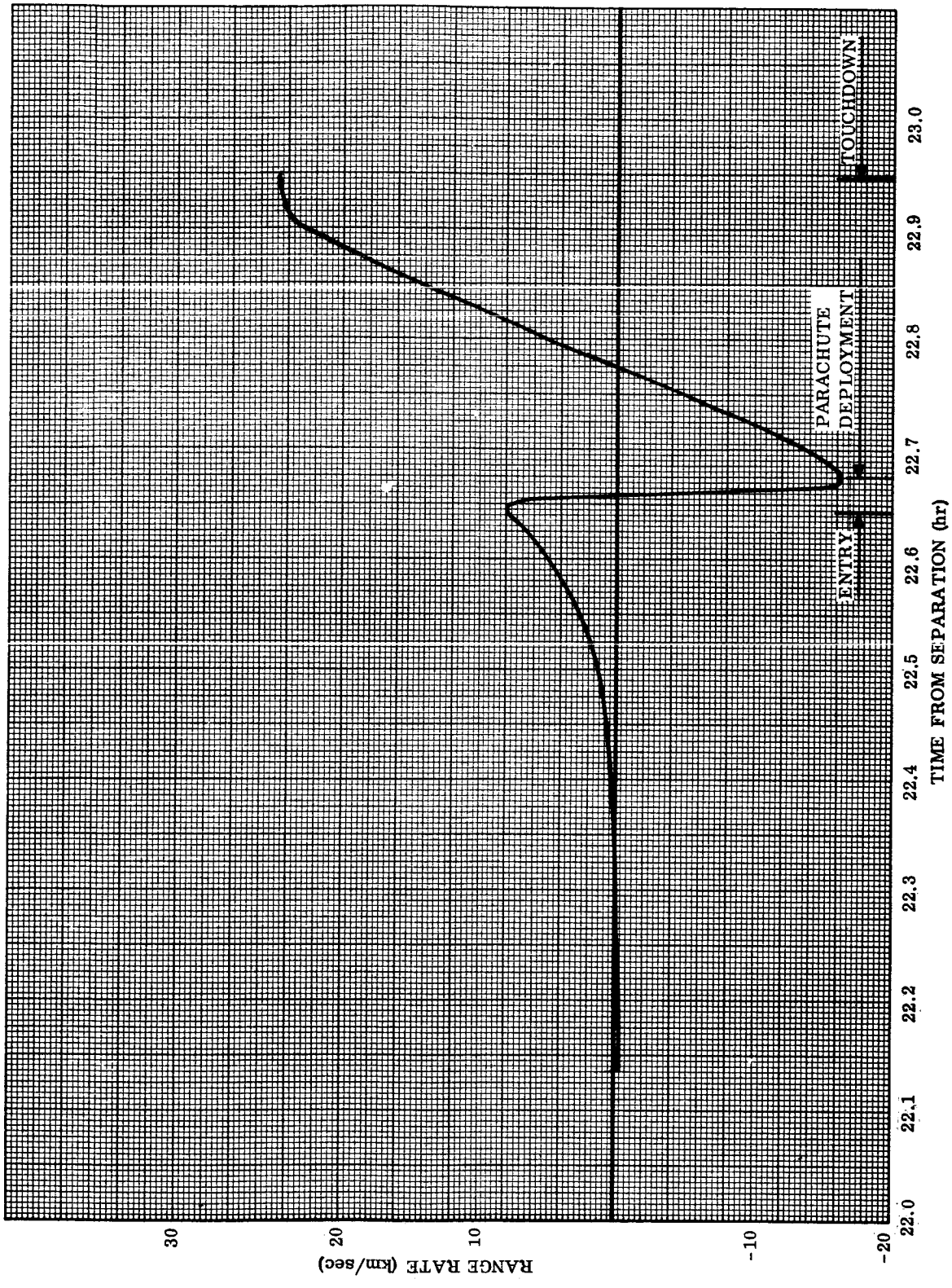

Figure 8-8. Orbiter Capsule Range Rate vs. Time from Separation

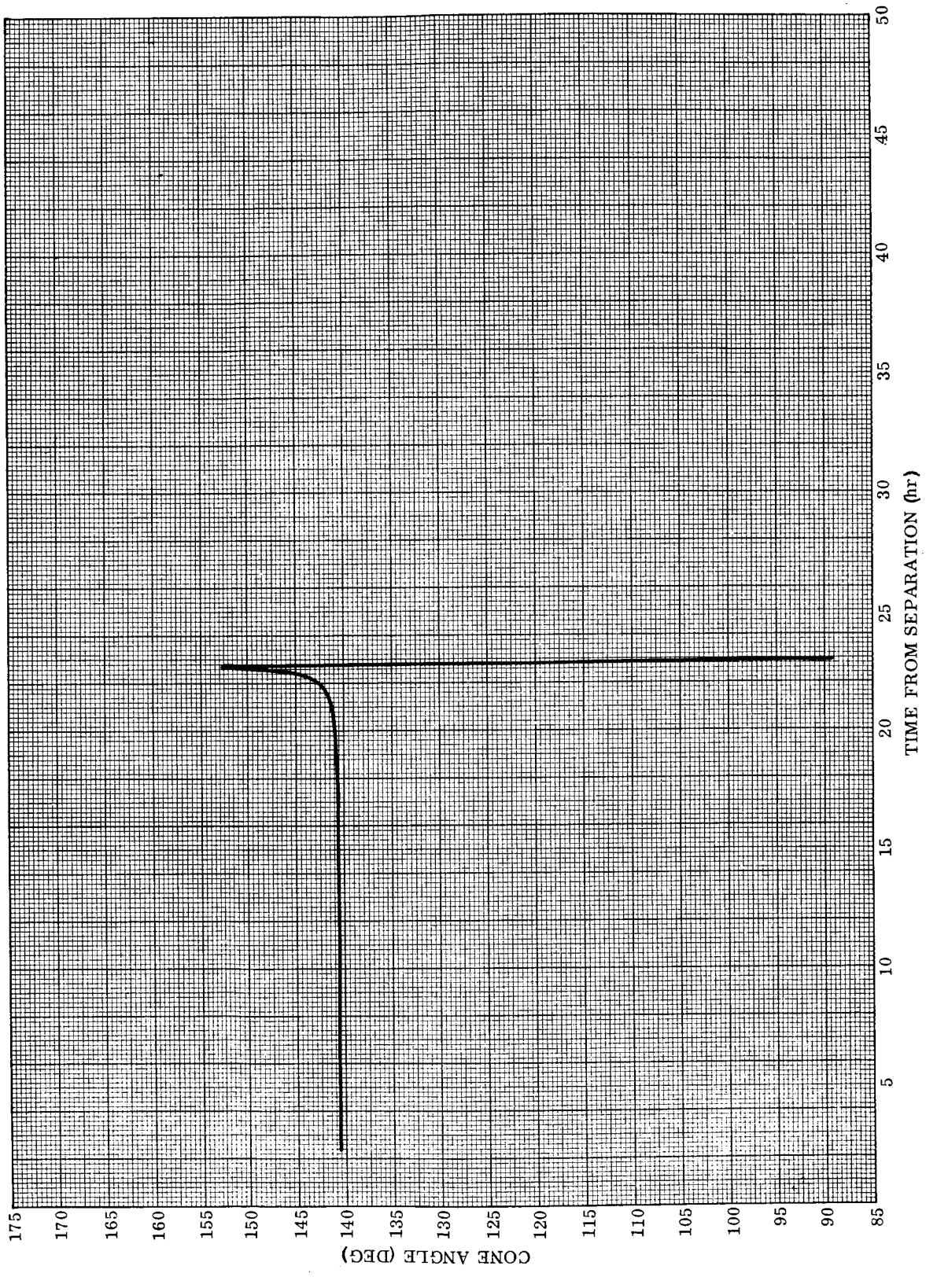

Figure 8-9. Orbiter Capsule Cone Angle

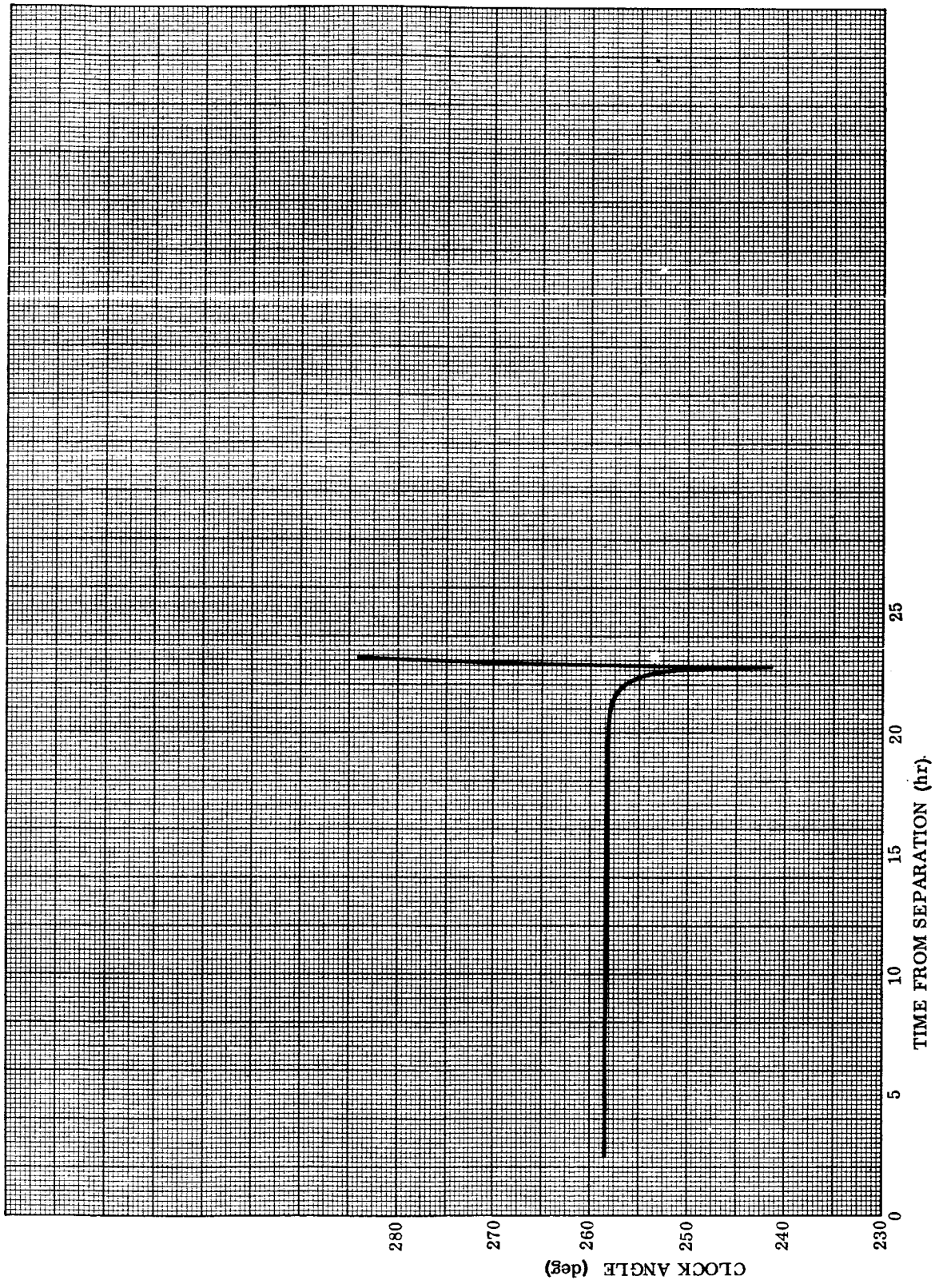

Figure 8-10. Orbiter-Capsule Clock Angle vs Time from Separation

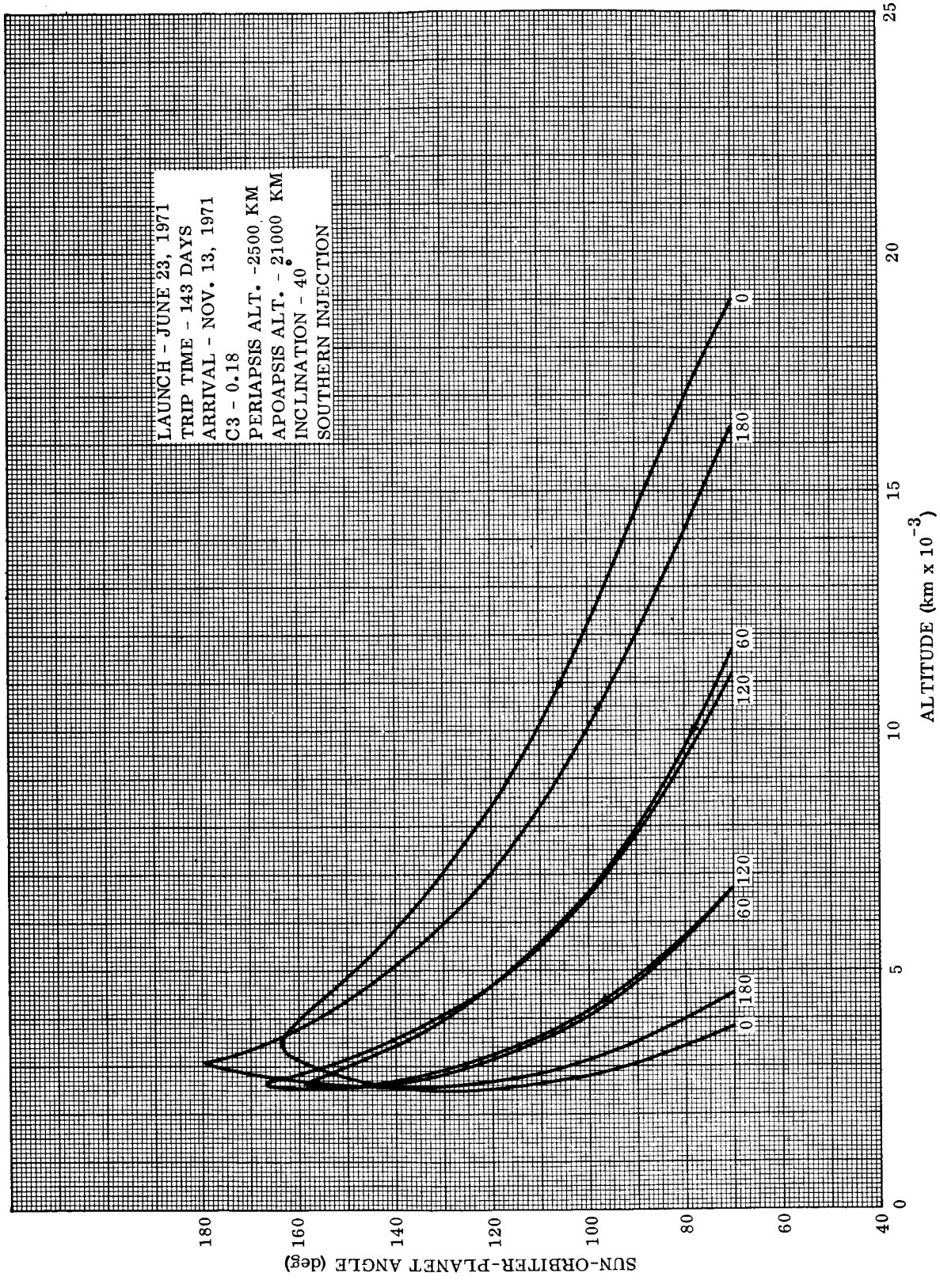

Figure 9-1 a. Sun-Orbiter-Planet Angle vs. Altitude (Mars Orbit)

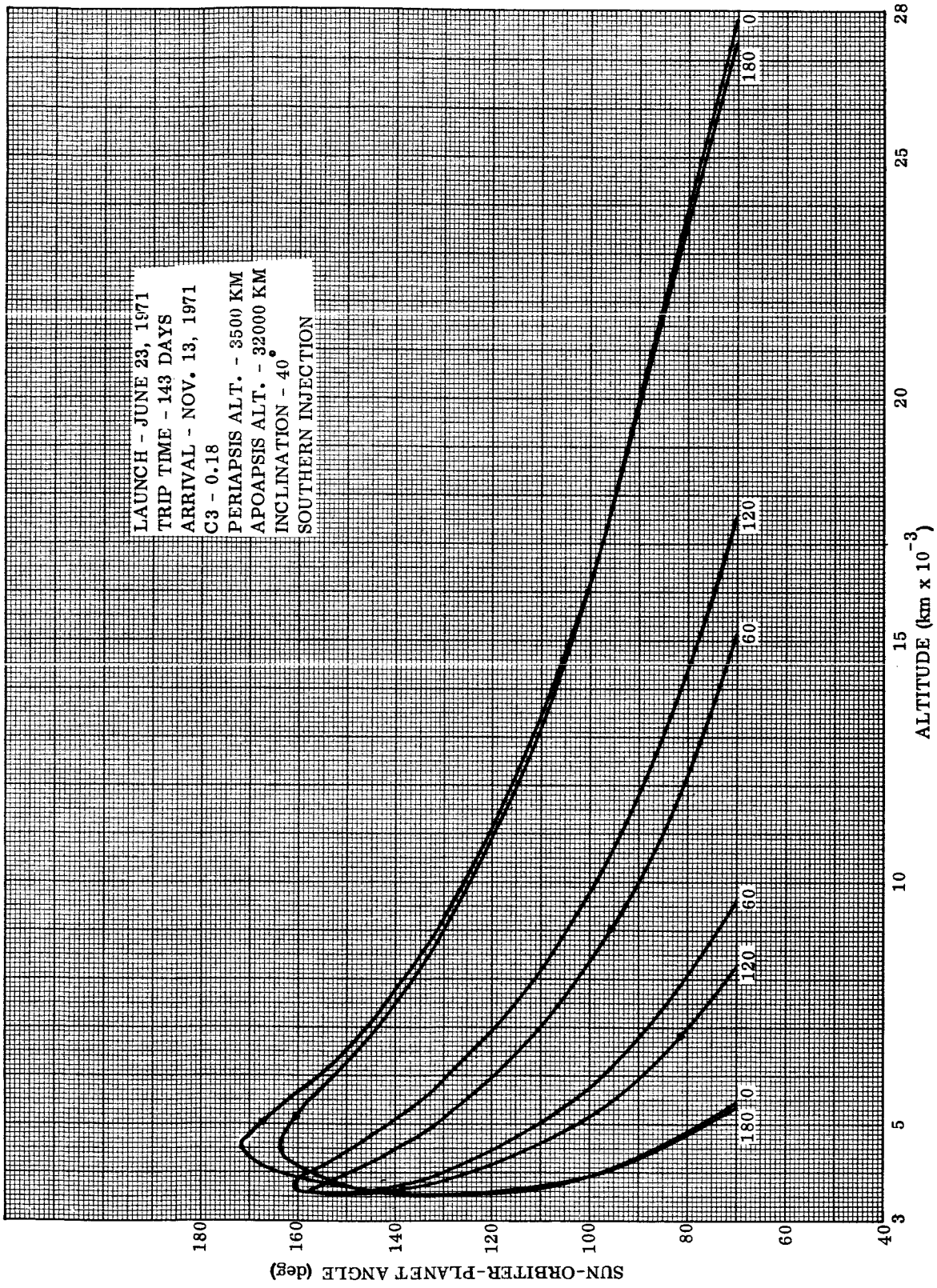

Figure 9-1 b. Sun-Orbiter-Planet Angle vs. Altitude (Mars Orbit)

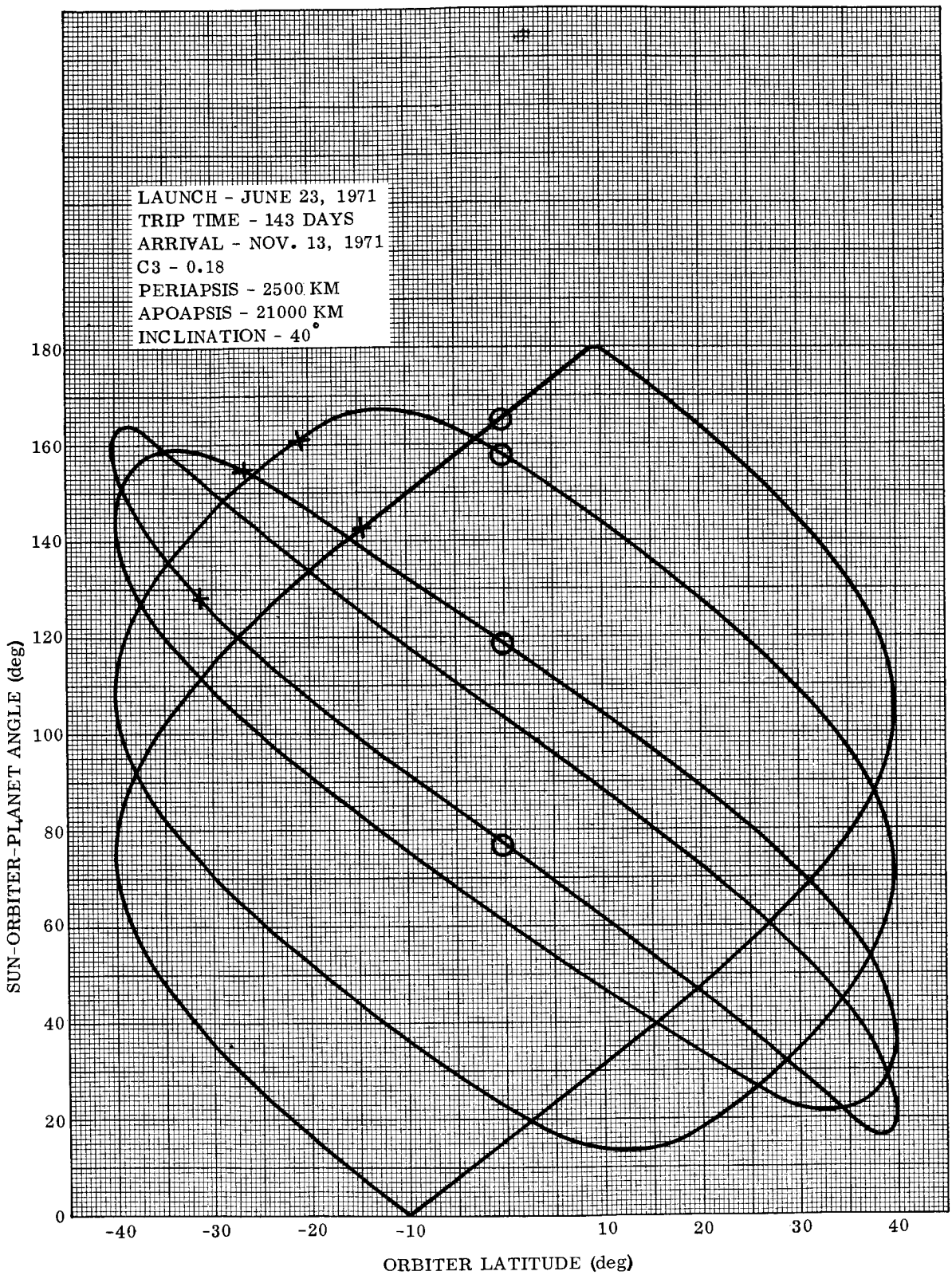

Figure 9-2 a. Sun-Orbiter-Planet Angle vs. Latitude during single orbit at 0, 60, 120, and 180 days

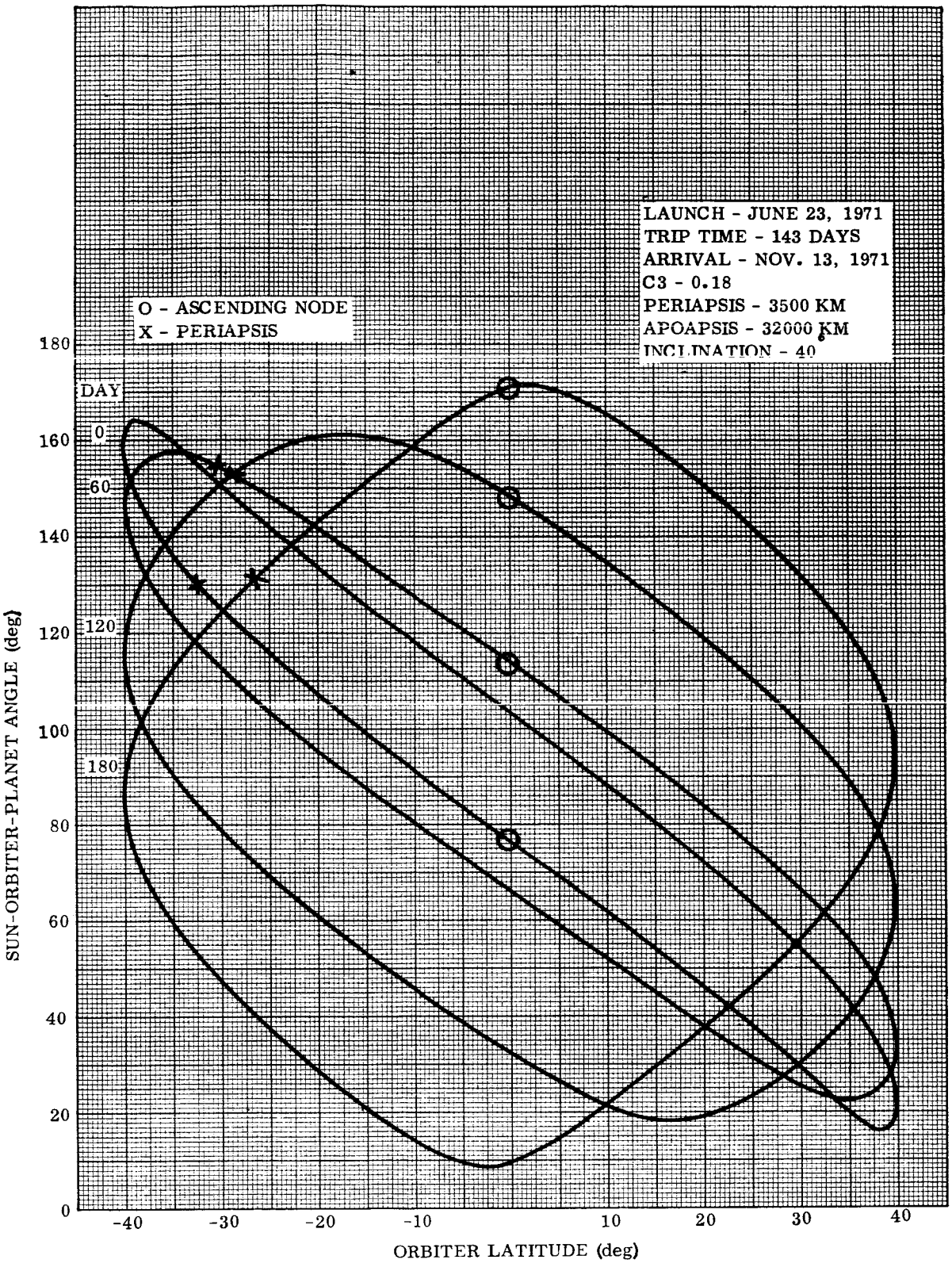

Figure 9-2 b. Sun-Orbiter-Planet Angle vs. Latitude during single orbit at 0, 60, 120, and 180 days

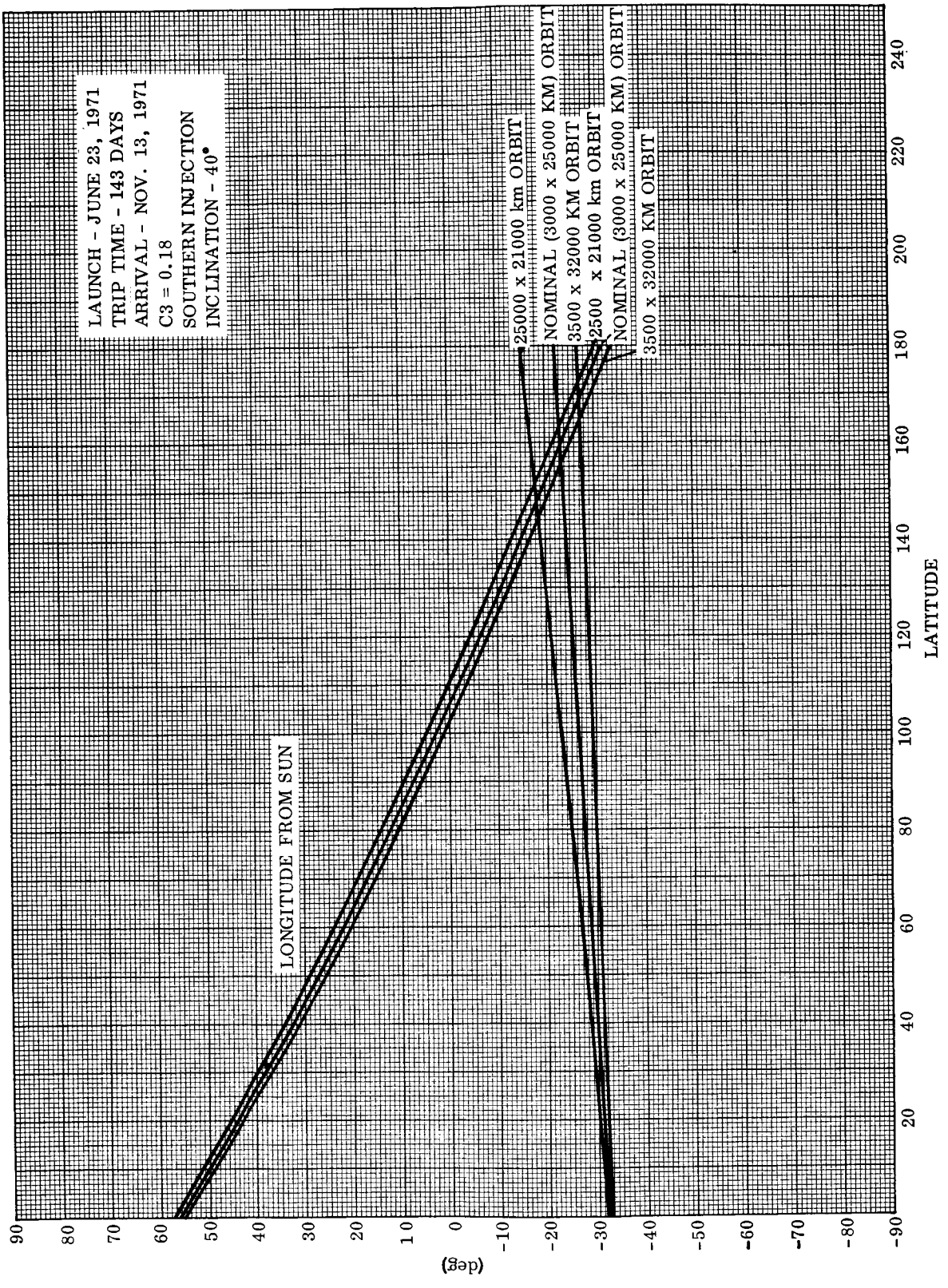

Figure 9-3. Position of Periapsis (Mars Orbit)

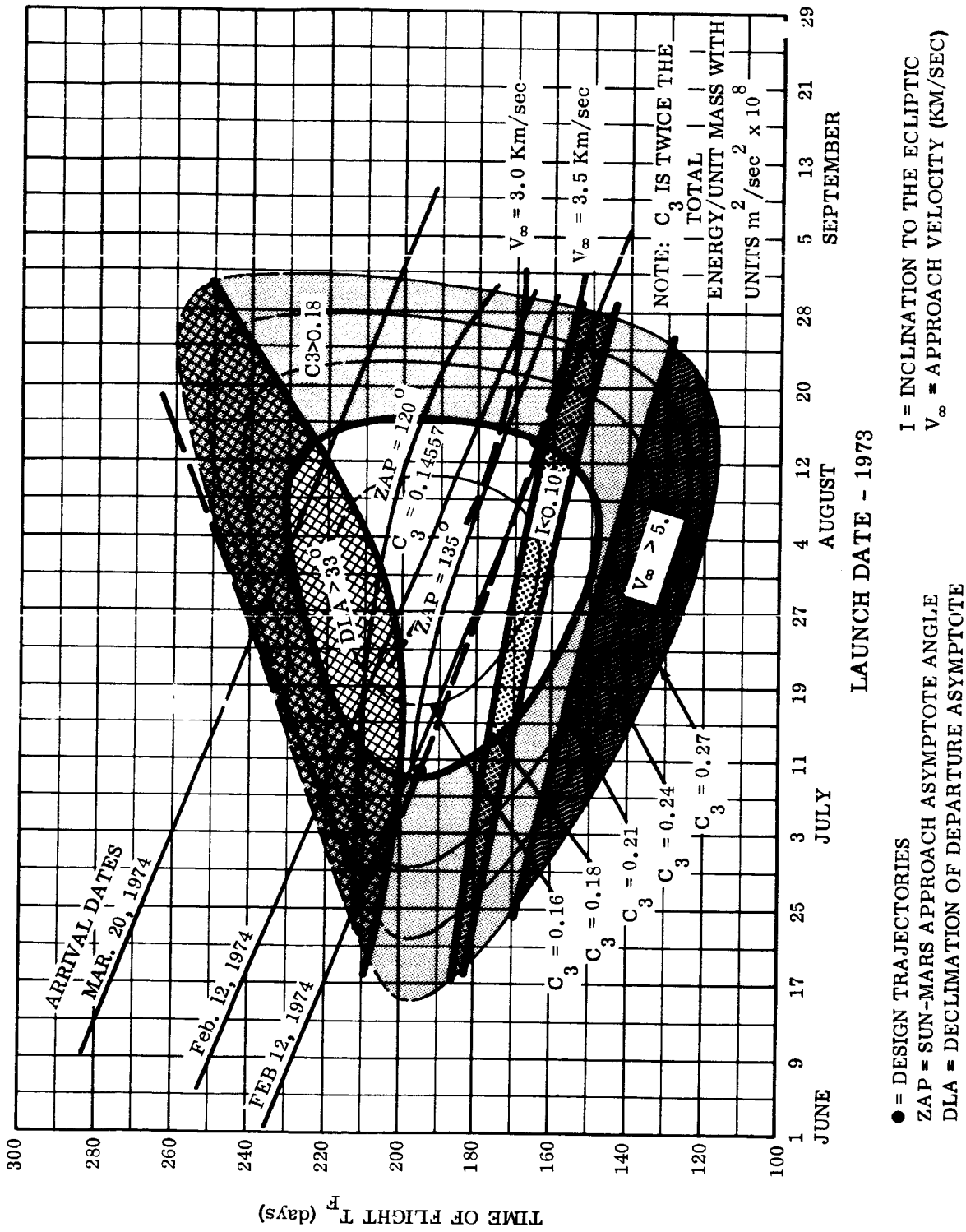

● = DESIGN TRAJECTORIES
ZAP = SUN-MARS APPROACH ASYMPTOTE ANGLE
DLA = DECLIMATION OF DEPARTURE ASYMPTOTE

I = INCLINATION TO THE ECLIPTIC
V_∞ = APPROACH VELOCITY (KM/SEC)

Figure 10-1. Mars 1973: Time of Flight vs. Launch Date

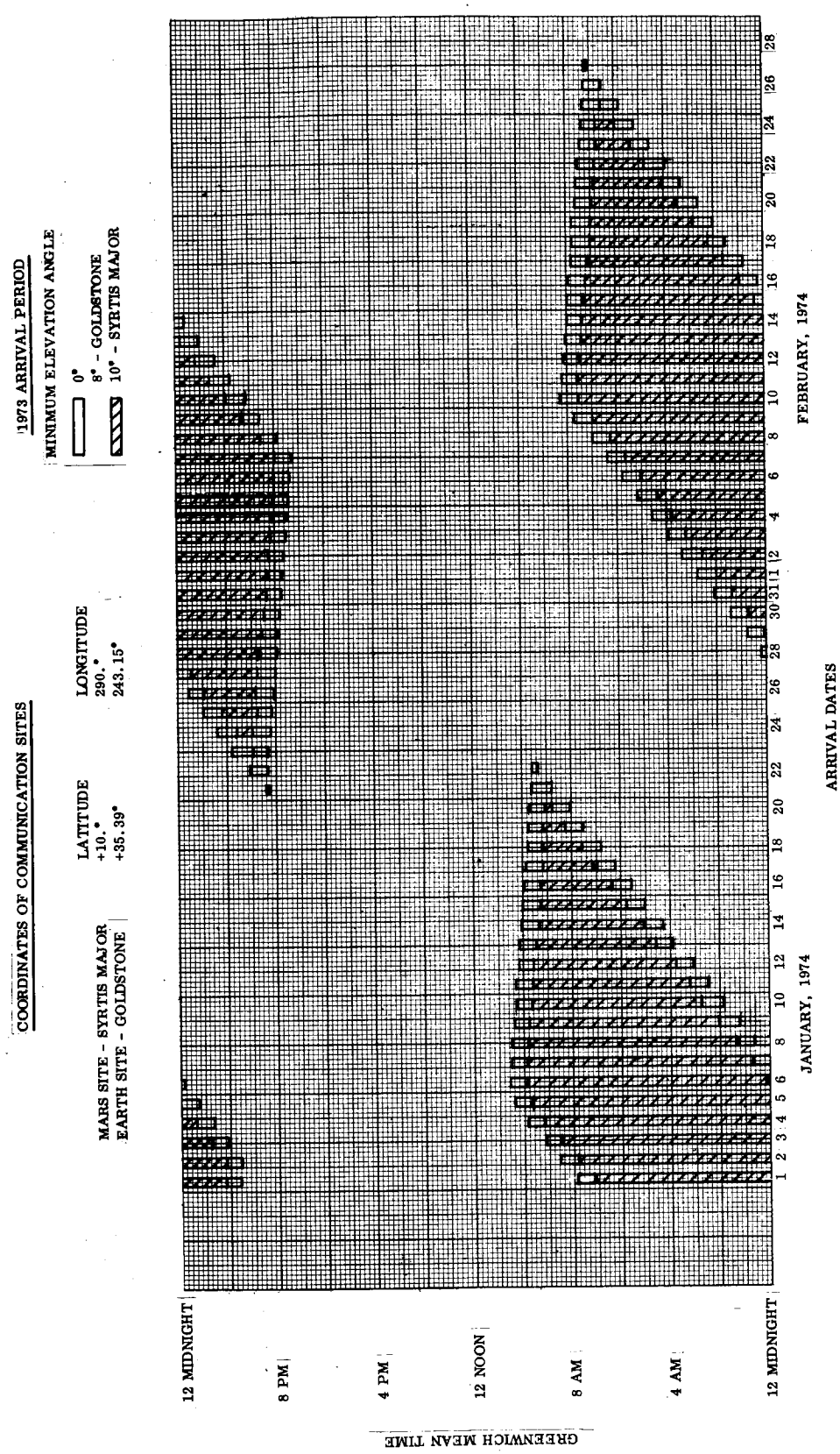

Figure 10-2. Periods of Time During Which Goldston Can View-Syrtis Major

CII - VB220AA102

ALTERNATE SYSTEM PHILOSOPHIES AND SYSTEM MECHANIZATIONS CONSIDERED

GUIDANCE PHILOSOPHY

Index

1 Introduction
2 Summary
3 Midcourse Guidance Sequence
4 Capsule Guidance
5 Orbit Insertion

1.0 INTRODUCTION

Guidance is concerned with various maneuvers from the time of initial injection to the point where the capsule is separated and the flight spacecraft is in orbit. Overall guidance of the capsule after separation is not a subject of this study. Nevertheless, references are inferred from the flight spacecraft prior to capsule separation, so that spacecraft guidance is a significant factor in determination of capsule impact site.

Three major phases are considered; the midcourse correction sequence, the capsule deflection maneuver, and the Flight Spacecraft orbit insertion. During each phase the major sources of error are divided between DSIF or navigation error and execution error caused by velocity vector increment errors. All maneuvers of the Flight Spacecraft and the Overall Flight Spacecraft must be made subject to the overall contamination probability limit of 10^{-4}.

2.0 SUMMARY

2.1 MIDCOURSE CORRECTION SEQUENCE

The pre-mission analysis presented here indicates that at least three midcourse corrections are definitely needed. It does not conclusively show that three are sufficient, but strongly indicates it. With the provision for one more correction for back-up, the conclusion is that capability for four midcourse corrections should be provided.

The amount of fuel allocated for midcourse corrections should be on the order of 75 meters per second where the fuel source is essentially for midcourse corrections. If the source is from the main orbit insertion supply, 50 meters per second appears adequate.

A minimum velocity increment capability of 0.1 meter per second with 0.01 meter per second accuracy is adequate to meet the target accuracy goal. A larger value of 1 meter per second with 0.1 meter per second error may be adequate, but is marginal. More precise analysis would be needed to definitely show whether or not the target accuracy goal could be met.

An execution accuracy for the midcourse correction of 1% (1 σ) in either magnitude or direction is definitely adequate. A value double this could likely be tolerated, but at the possible expense of an additional midcourse correction.

2.2 CAPSULE DISPERSION

Dispersions for an in-plane and out-of-plane landing site were obtained. They are 9.3° downrange and 4.5° cross range for the out-of-plane case. For the in-plane case, the corresponding dispersions are 7.4° and 4.4° respectively. These dispersions

assumed a 2% (3 σ) velocity increment error, an error in spacecraft orientation at separation about each axis of 0.024 radians (3 σ) and additional orientation error during thrusting of 0.027 radians (3 σ).

2.3 ORBIT INSERTION

a. A guidance law for orbit insertion requiring that the thrusting direction remain fixed with respect to inertial space is recommended since it is the easiest to implement and the fuel weight penalty is insignificant.

b. An accelerometer should be used to signal the termination of thrusting since this greatly reduces the dispersion of the orbital elements. Thrust termination based on time should be used as a back-up.

c. The selected nominal orbit has a periapsis altitude of 3000 km, an apoapsis altitude of 25,000 km and an inclination of 40°. The corresponding three sigma dispersions in these orbital elements are 460 km and 4560 km, and 3.7 degrees, respectively. The corresponding three sigma dispersion in period is 4.2 hours and the three sigma dispersion in in-plane orbit rotation is 5.5 degrees. The worst case combination of these errors will not prevent capture of the orbiter by Mars. Based on present estimates of the Martian atmosphere, atmospheric entry of the orbiter will not occur during the 50-hear period following orbit insertion for the worst case orbit.

3.0 MIDCOURSE GUIDANCE SEQUENCE

3.1 INTRODUCTION TO MIDCOURSE GUIDANCE POLICY

The Guidance Sequence analysis must be concerned with analysis, decisions, and executions to be made both during the progress of a flight and pre-mission analysis to ensure adequate design capability to properly handle a sufficient percentage of possible real flight situations.

Factors which must be considered in the pre-mission analysis include the following:

a. The number of necessary midcourse maneuvers.

b. The timing of the execution of the maneuvers.

c. The acceptable bounds for the midcourse execution errors.

d. The degree of accuracy that can be expected at the target (capsule impact and orbiter insertion).

e. The DSIF orbit redetermination strength after each maneuver.

f. Biasing to meet the quarantine requirement.

g. Mapping of errors at a point on the heliocentric orbit into potential target errors.

h. Expected booster injection errors.

i. Propellant requirement.

Pre-mission analysis is decidedly non-Gaussian for several reasons. First, even in the very simple case where the first midcourse correction tends to leave a residual error which is Gaussian for a particular size correction, the total distribution is not Gaussian since the size correction to be made may itself be Gaussian. Second; The execution error is a combination of magnitude and direction errors and the various components of the residual error after execution map into target errors in the RST space in different manners which vary along the trajectory. Third, The biasing required during any execution maneuver depends on the size of the maneuver. Finally, and particularly for the later midcourse correction, there are non-proportional execution errors due to the small size of ΔV to be applied.

Because of these factors and perhaps others, a pre-mission analysis of the midcourse sequence would have to utilize some complex technique such as Monte Carlo or a method which can put reasonable bounds on the probability distribution. The latter course will be used here.

The approach taken was to attempt to analyze the problem as if a real flight was in progress. In this case then, a particular potential maneuver becomes fixed in size and direction as the DSIF orbit determination accuracy converges sufficiently. This helps to take out some of the non-Gaussian aspects of the problem. Other assumptions necessary to allow the use of Gaussian distributions will be discussed later.

With the use of these assumptions, a pessimistic, intermediate, and optimistic analysis was made. The use of pessimistic and optimistic here refers to the analysis, and not to the component accuracies anticipated. There was a chance, before starting, that this approach would give widely different answers for both the number of midcourse corrections and fuel required, in which case, the results would be worthless. However, the results came suprisingly close together.

Using a target accuracy goal of ± 500 km (3 σ) in the impact parameter space and an execution accuracy of 1% (1 σ) in each of three directions, the results indicated that three midcourse corrections, even using the pessimistic case, were sufficient and that 2 were just barely sufficient using the optimistic case. Going to a 2% (1 σ)

execution error value, changed these to four and three executions required respectively. The difference in the fule required for the two cases was negligible. The intermediate case gave three required corrections for either 1% or 2% execution error.

3.2 MAJOR ASSUMPTIONS MADE IN BOUNDING THE PROBLEM

A very important consideration is the timing of a potential correction. Subsequent to injection or a correction, orbit knowledge will tend to increase with time. Initially the error in knowledge may even exceed the indicated correction. As time passes, the error will decrease to a fraction of the indicated correction required (except possibly for the very last correction). Again, except possibly for the last correction, the execution error will essentially be proportional to the magnitude of the correction. For the following reasons, the proper timing of the correction, except possibly the final one, would appear to be when the orbit determination error and the execution error are equal. Delaying past this point wastes valuable time for any future orbit determination, and can only reduce the potential residual error by 1.4 to 1. Performing the correction before the errors become equal may have some merit in that it saves valuable time for later orbit redetermination. However it has the bad effects of increasing the bias required for quarantine, and otherwise leaving larger residual error after the correction, thus slowing the convergence of the correction series.

At any correction point, it will be assumed that one of the three velocity error components is more critical or effective in producing impact parameter space error than the other two. Further, it is assumed that the bias direction will lie along the Mars center-aiming point line although this could be the subject of further effort.

In fact, after the completion of the present analysis, it was pointed out that this may well be a bad way to use the bias concept. Contamination by capture due to probabilistic guidance errors was covered here as well as considering that subsequent corrections have a probability of not being accomplished. However, the chance of the engines not cutting off at the proper time was not covered. Philosophically it appears that this type of failure could easily violate the contamination restraint, especially for radial biasing. Figures 3-1 and 3-2 show pictorially the guidance sequence corrections, errors, and biases both for radial bias and bias tending to be normal to the Mars center final aim point line. In the latter case, each correction will tend to decrease the bias of the aim point without pointing the correction vector so as to intersect the capture circle.

The execution error in the critical direction will be taken as 1% (1 σ) and 2% (1 σ) to see the effect on the number of midcourse corrections and fuel required. At injection, the potential target error due to a velocity error in the critical direction will be taken as 3 $\Delta V(T)$ for the pessimistic case, where T is time to go. This rule of thumb formula has analytical backing and appears to be in agreement with JPL trajectories. The multiplying factor of three is a maximum, but in some cases can be as small as unity.

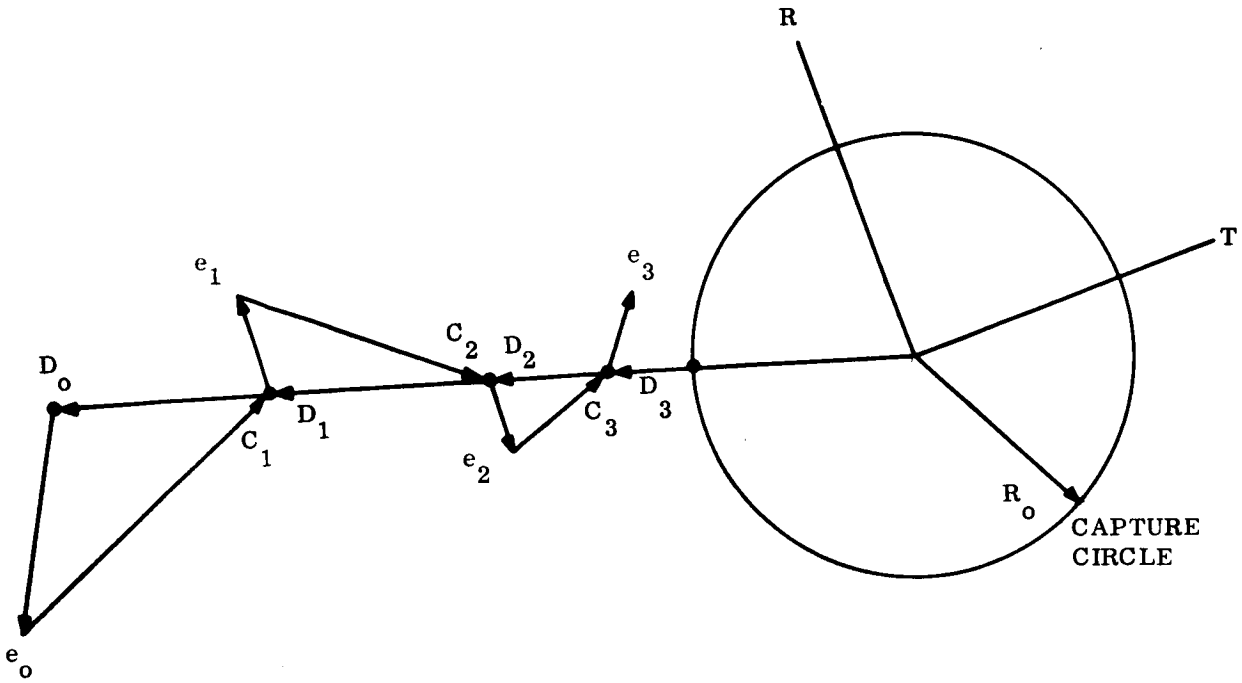

Figure 3-1. Midcourse Guidance - Correction Sequence Radial Biasing

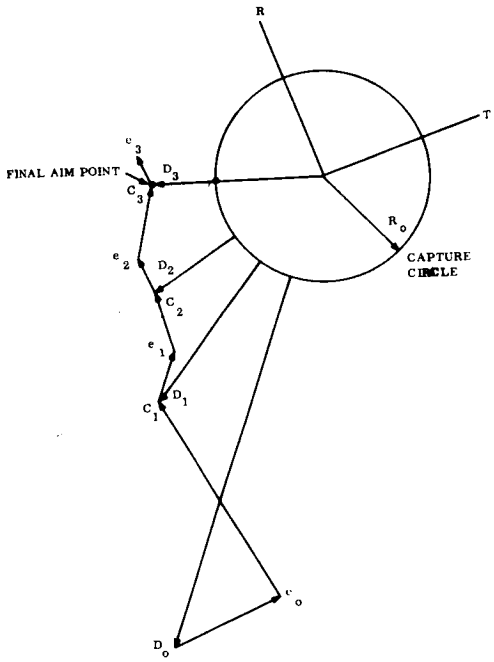

Figure 3-2. Midcourse Guidance - Correction Sequence Biases Arranged to Reduce Capture Probability

Non-proportional execution errors will be disregarded when the proportional error is large, but will be considered for the last correction if necessary.

It is difficult to assign different values to the booster, spacecraft, capsule and flight spacecraft as far as planetary quarantine is concerned. During an actual flight, it would seem that a quite involved setup to aid in each decision as to biasing and correction would be required. For the pre-mission analysis, the following approach was taken. For one maneuver, the bias needed, to avoid capture with 10^{-4} probability was found as a function of guidance error. The results are as shown in Figures 3-3 and 3-4. R_o is the capture radius for Mars or 6500 km for a V_∞ of 3 km/sec, σ is the guidance error in each direction and D is the bias required measured from the capture circle to the aim point.

The initial injection error, equivalent to an error in ΔV of 15 m/sec at 2 to 10 days after injection maps into a target error on the order of 540,000 km for a flight time of 12,000,000 seconds. Then σ/R_0 is 83. Thus, as shown by curve $\overline{2}$, of Figure 3-4, (or a similar curve for probability less then 10^{-4}) it would appear that the booster would not be a major factor in the quarantine requirement even without retro capability.

However, dropping the multiplying factor of three in obtaining the potential target error gives trouble. In this case the potential target error becomes 180,000Km (1 σ) or about 28 capture radii. By Figure 3-4, this requires a bias of 52 capture radii or 340,000 km. In this case retro capability is definitely needed for the Centaur or considerably more bias than 340,000 km would be required for the boost aim point. From this point on, Centaur retro will be assumed in order to eliminate any significant contribution by it to the total contamination probability.

Suppose now that both the capsule and spacecraft were each assigned half the 10^{-4} probability of contamination. Further suppose that each of three midcourse corrections, orbiter injection and initial injection were assigned 1/5 the total of $0.5(10)^{-4}$ for them combined or $0.1(10)^{-4}$ each. If there is an 0.8 chance that a subsequent midcourse can undo an error which potentially will produce contamination, then each midcourse correction or boost injection can be allowed $0.5\ (10)^{-4}$ chance of producing contamination by itself assuming no subsequent correction. The orbit injection maneuitself would have to meet the figure of $0.1\ (10)^{-4}$ in the absence of any way to achieve a subsequent correction to avoid atmospheric capture.

Figures 3-3 and 3-4 could be redone for a probability of $0.5\ (10)^{-4}$ instead of 10^{-4}, but the numerical results would change only slightly. For instance, the initial slope of curve 3 of Figure 3-3 would go to 3.86 instead of 3.73.

To help in summarizing to this point, Figure 3-1 may be useful. Actually a three-dimensional figure in the RST space would be more realistic, but perhaps more confusing. So what is to follow should be thought of in 3 dimensions.

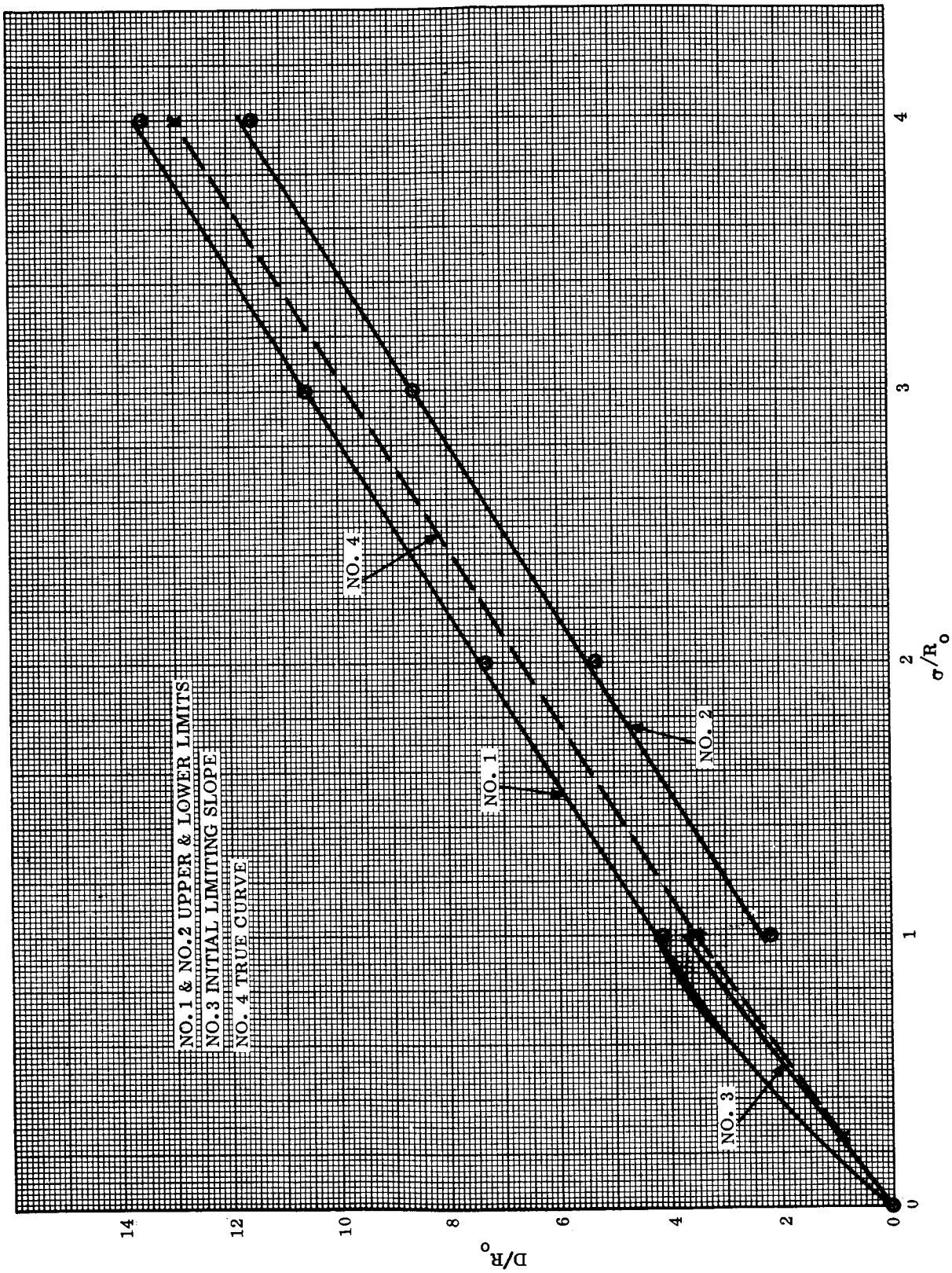

Figure 3-3. Aim Point Bias as Function of Guidance Error

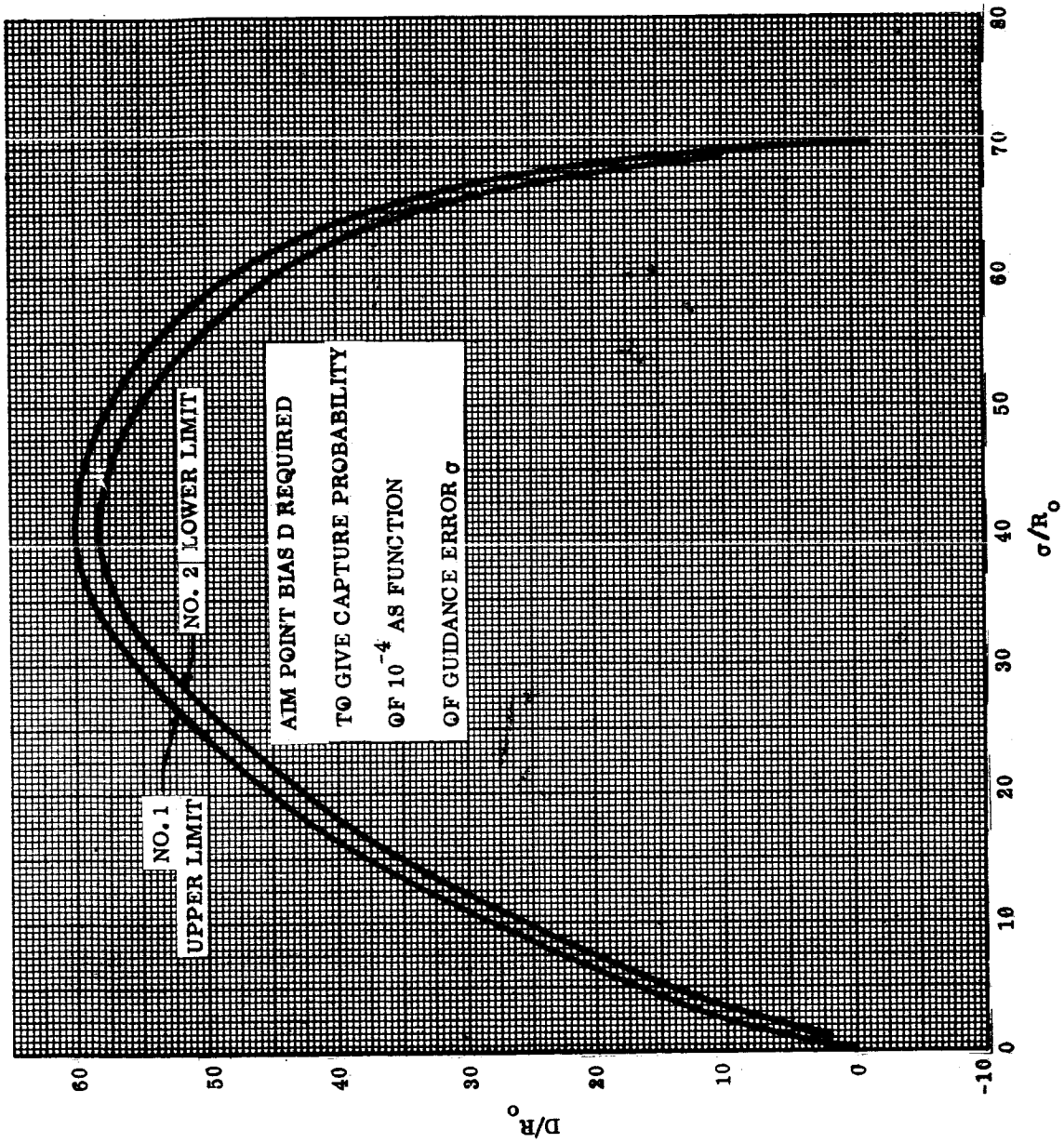

Figure 3-4. Aim Point Bias D

The initial aim point of the booster is designated by point 0 with an attendant injection error e. The first correction, C_1, is so sized to give a bias D_1 with an attendant 1st midcourse error e_1 resulting. Similar conditions exist for possible second and third corrections or even a fourth in some situations. The final correction bias (D_3 in the figure) will be chosen to give the desired aim point (but must be at least great enough to satisfy the quarantine requirement).

As discussed earlier, and also in EPD-250, a probability analysis of the situation depicted in Figure 3-1 or 3-2 becomes very complex and very non-Gaussian. Inherent assumptions made in getting the situation to the point of Figure 3-1 are that only errors in the RT plane will be considered and each midcourse aim point will lie along the line connecting Mars center and the final aim point.

Further assumptions mentioned earlier as they relate to Figure 3-1 are depicted in Figures 3-5 and 3-6 for the pessimistic and optimistic cases.

Each midcourse correction error except the last will be taken as $\sqrt{2}$ times the execution error by the previous assumption that the correction will be made when the orbit determination and execution errors are equal. An additional choice exists for the final correction. If the final error by the above assumption is on the borderline of meeting the 500 km goal and considerable tracking time remains, the correction could be delayed achieving some improvement in accuracy, or the decision to make one additional correction will be made. In this case, the final error would depend mainly on the orbit determination ultimate accuracy subject to the non-porportional execution limitation.

This seems to be more a subject for in-flight analysis. To simplify the pre-mission analysis, the final error will be taken as $\sqrt{2}$ times the execution error. Whenever this starts to dip very far below the 500 km goal, the final error will depend more on the DSIF capability and execution non-proportional error than on the size of the correction.

Each midcourse bias (within limits) depends on the size correction to be made and the size correction to be made depends partly on the bias required. Figures 3-3 and 3-4 will be used to determine the bias required in terms of a midcourse 1 σ error. It is noted that the bias required has a maximum value of 3.7 σ for very accurate guidance, going to 3.5 σ when the guidance 1σ is 1 capture radius and 3.2 σ when the 1σ guidance error is 4 capture radii.

3.2.1 PESSIMISTIC CASE

As given in the mission specification, the error e. will be equivalent to 15 m/sec (1 σ). Using the empirical formula of 3 TΔV for potential final target error, this becomes, for a 12,000,000 second flight, 1,620,000 km (3 σ) at the target. By

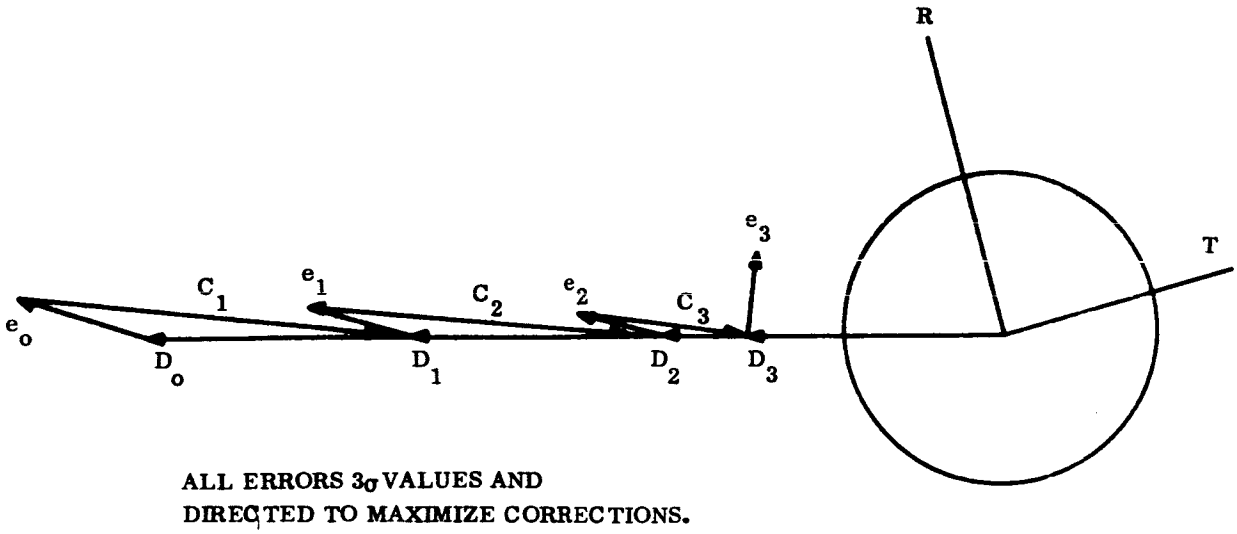

Figure 3-5. Pessimistic Case

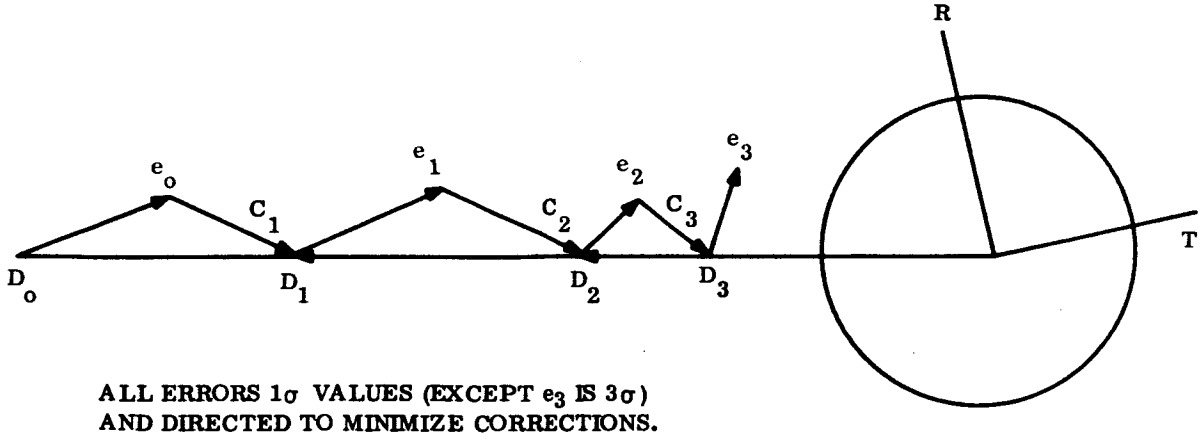

Figure 3-6. Optimistic Case

Figure 3-4, this would indicate that no bias is needed for the injection aim point. However, as indicated earlier, bias is needed if the amplification factor of 3 used in the preceding is dropped. Since this case is to be taken pessimistically, assume an initial bias Do of 600,000 km.

From Figure 3-5

$$D_1 + C_1 = Do + e_o = 600,000 + 1,620,000 = 2,220,000 \text{ km}$$

For the moment assume that the first midcourse bias D_1 will be about 5% of C_1. Then

$$C_1 = 2,110,000 \text{ km}$$

$$D_1 = 110,000 \text{ km}$$

The execution error $\frac{e_1}{3}$ (1 σ) will be 1.4% of C_1 or 29500 km.

$$e_1 = 88,500 \text{ km.}$$

By Figure 3-4 the 1σ guidance error $\frac{e_1}{3}$ of 29, 500 km (4.5 capture radii) requires a bias D_1 of 15 capture radii or 97,500 km. Then the preceding assumption of 110,000 km for D_1 is adequate but not large enough to require recomputing the preceding values for C_1 and e_1.

Again from Figure 3-5

$$D_2 + C_2 = D_1 + e_1 = 110,000 + 88,500 = 198,500 \text{ Km.}$$

Assume D_2 to be about 5% of C_2 so that

$$C_2 = 188,500 \text{ km}$$

$$D_2 = 10,000 \text{ km}$$

The second midcourse execution error $\frac{e_2}{3}$ (1 σ) will be 1.4% of C_2 or

$$\frac{e_2}{3} = 2640 \text{ km.}$$

$$e_2 = 7920 \text{ km.}$$

By Figure 3-3 the 1 σ guidance error $\frac{e_2}{3}$ of 2640 km (less than 1 capture radii) requires a bias D_2 3.73 times the 1σ error or 9,900 km.

For a periapsis altitude of 3000 km, the aim point must be about 10,000 km from Mars center or 3500 km beyond the capture circle. Then letting D_3 equal 3,500 km and from Figure 3-5.

$$D_3 + C_3 = D_2 + e_2$$

or

$$C_3 = 10,000 + 7920 - 3500 = 14420 \text{ km}$$

$$e_{3/3} = 0.014\ C_2 = 200 \text{ km}$$

$$e_3 = 600 \text{ km}$$

Thus with all the pessimism involved in the preceding, the final error after three midcourse corrections was brought very close to the goal of 500 km (3 σ).

3.2.2 OPTIMISTIC CASE

The situation to be analyzed here is shown in Figure 3-6. The initial error e_o will be taken as T ΔV (instead of 3 T ΔV) or 180,000 km (1 σ). This is 28 capture radii requiring a bias Do of 52 radii or 340,000 km by Figure 3-4.

From Figure 3-6.

$$D_1 + C_1 = Do - e_o = 340,000 - 180,000 = 160,000 \text{ km.}$$

Let D_1 be about 5% of C_1 so that

$$C_1 = 152,000 \text{ km}$$

$$D_1 = 8,000 \quad \text{km}$$

The guidance error e_1 will be 1.4% of C_1 or

$$e_1 = 2,130 \text{ km}$$

The assumed bias of 8,000 km is adequate.

Now $D_2 + C_2 = D_1 - e_1$

Let D_2 be the final aim point bias of 3,500 km. Then

$$C_2 = 8,000 - 2,130 - 3,500 = 2,370 \text{ km.}$$

The guidance error of 1.4% of this is

$$e_2 = 33 \text{ km } (1\ \sigma) \text{ or } 100 \text{ km } (3\ \sigma).$$

Of course, the actual final accuracy in this case becomes more dependent on the ultimate DSIF accuracy as well as non-proportional execution errors. The conclusion is that certainly two midcourse corrections are needed even for this very optimistic analysis, and for the very pessimistic case, three corrections just barely fail to meet the goal of 500 km (3 σ). The preceding will be repeated with the execution error doubled to 2% (total guidance error of 2.8% (1 σ)). Also for the poorer execution accuracy, a case will be studied intermediate between the pessimistic and optimistic cases.

The question arises about the effect of the non-Gaussian nature produced when Gaussian errors are pyramided by multiplication. The following two simple numerical results may be helpful in giving some insight.

The situation is taken where a final error is the result of an initial normal error e_1 with a normalized standard deviation σ_1 equal to 1, and a correction proportional to e_1 with a normalized standard deviation σ_2 equal to one. For the normal curve, 26/10,000 of the errors are larger than 3 σ. For the resulting non-Gaussian error, let us define "3 σ" as meaning that 26/10,000 cases are larger than "3 σ" rather than 3 σ is 3 times σ. Now $\sqrt{\frac{26}{10,000}}$ is roughly equal to 0.051. On the normal curve 0.051 of the original possibilities the percent of cases lie at errors larger than 1.96 σ. Then for the series case considered here, 26/10,000 occur at errors at least larger than $(1.96)^2$ or 3.84. That is 0.051 of the original possibilities has an error of 1.96 σ or greater. And of these 0.051 percentage has an error of 1.96 σ or greater for the correction error. Of course, there are actually more than 26/10,000 cases at $(1.96)^2$ or greater due to combinations of larger initial and smaller correction errors and vice versa. Therefore, the actual value on the normal curve to give a composite value is somewhat larger than 1.96 σ.

JPL EPD 250 indicates that the answer to this problem is a Bessel function. Any extensive work with this composite result should make use of this. A simple brute force numerical case was computed. The result was that at least (but not many more) 40/10,000 cases lay at a composite error of $(2\ \sigma)^2$ or more. Thus, it seems certain that the true values for the initial and correction error to give a composite "3 σ" can not exceed 2 σ by very much. Thus the preceding value of 1.96 σ obtained very simply gives a very good approximation to the true value.

The preceding can be extended to four errors in series. The fourth root of 26/10,000 is 0.227. On the normal curve 0.227 percentage of cases are 1.21 σ or larger. Take 1.4 σ as the value which will yield a composite "3 σ" for four series Gaussian errors. This value will be used along with the 1 σ and 3 σ values used in the preceding analysis of the midcourse sequence.

3.2.3 EXECUTION ERROR OF TWO PERCENT (1 σ) - PESSIMISTIC CASE

Again assume 1,620,000 km (3 σ) for the injection potential target error as well as an initial bias D_0 of 600,000 km. Doubling the values obtained previously for 1 percent guidance error gives

$$D_1 = 220,000 \text{ km}$$

$$e_{1/3} = 59,000 \text{ km}$$

$$e_1 = 177,000 \text{ km}$$

By Figure 3-4 the error $e_{1/3}$ of 59,000 km requires a bias of 165,000 km. Therefore, the assumed value of 220,000 was adequate but reducing it to 165,000 will not appreciably change the value of e_1.

As before

$$D_2 + C_2 = D_1 + e_1 = 220,000 + 177,000 = 400,000 \text{ km.}$$

Assume $D_2 = 40,000$ km

and then $C_2 = 360,000$ km

$$e_{2/3} = 0.028\ (360,000) = 10,000 \text{ km}$$

$$e_2 = 30,000 \text{ km.}$$

The assumed value for D_2 of 40,000 Km is adequate. As before

$$D_3 + C_3 = D_2 + e_2 = 40,000 + 30,000 = 70,000 \text{ km}$$

Let $D_3 = 7,000$ km

$$C_3 = 63,000 \text{ km}$$

Then $e_{3/3} = (0.028)\ (63,000) = 1760$ km

$$e_3 = 5300 \text{ km}$$

The assumed value of 7,000 km for D_3 is adequate.

Now

$$D_4 + C_4 = D_3 + e_3$$

Let $D_4 = 3,500$ km (the final desired aim bias)

Then $C_4 = 7,000 + 5,300 - 3,500 = 8,800$ km

$$e_{4/3} = 0.028\ (8,800) = 246 \text{ km}$$

$$e_4 = 740 \text{ km.}$$

3.2.4 OPTIMISTIC CASE - EXECUTION ERROR TWO PER CENT (1 σ)

Taking the figures from the one percent case and doubling D_1 and e_1 gives

$$C_1 = 152,000 \text{ km}$$

$$D_1 = 16,000 \text{ km}$$

$$e_1 = 4,260 \text{ km}$$

As before

$$C_2 + D_2 = D_1 - e_1 = 11,740 \text{ km}$$

Let $D_2 = 3,500$ km (final aim point)

Then $C_2 = 8,240$

$$e_2 = 0.028\ (8,240) = 230 \text{ km } (1\ \sigma)$$

and the 3 σ error after 2 corrections is 690 km.

Thus going to 2% execution error instead of 1% pushed the number of executions required from 2 optimistic and 3+ pessimistic to 2+ optimistic and 4+ pessimistic.

3.2.5 1.4 σ ERRORS PYRAMIDED - TWO PERCENT (1 σ) EXECUTION ERROR

Take the 15 m/sec injection error as 540,000 km 1 σ equivalent target error. This is somewhat on the pessimistic side. The injection biases used previously were 600,000 km and 340,000 km for the pessimistic and optimistic cases respectively. These could perhaps be averaged for this intermediate case. However, to keep the results slightly pessimistic, use 600,000 km as the injection bias.

Utilizing Figure 3-5

$$D_1 + C_1 = e_o + D_o = (540,000)\ (1.4) + 600,000 = 1,360,000 \text{ km.}$$

Assuming D_1 temporarily to be about 10% of C_1 gives

$$C_1 = 1,224,000 \text{ km}$$

$$D_1 = 136,000 \text{ km}$$

And $\frac{e_1}{1.4} = 0.028\ C_1 = 35,700$ km (1 σ 1st correction error)

$$e_1 = 50,000 \text{ km.}$$

The assumed value for D_1 of 136,000 km is seen to be adequate. Again

$$D_2 + C_2 = e_1 + D_1 = 50,000 + 136,000 = 186,000 \text{ km.}$$

Letting D_2 be about 10% of C_2 yields

$$C_2 = 167,000 \text{ km}$$

$$D_2 = 18,600 \text{ km}$$

$$e_{2/1.4} = 0.028\, C_2 = 4,800 \text{ km.}$$

$$e_2 = 6,800 \text{ km.}$$

Similarly

$$D_3 + C_3 = e_2 + D_2 = 25,400 \text{ km.}$$

Let D_3 = 3,500 km or the final desired aim point.

C_3 = 22,000 km

$e_{3/1.4} = 0.028\ C_3 = 620$

e_3 = 870 km.

The assumed value of 3500 km for D_3 was sufficient. In this case three midcourse corrections do not quite meet the goal of 500 km (3 σ). While the analysis was not really pessimistic as far as pyramiding 3 σ errors, there were four areas of pessimism. The initial potential target error of 540,000 km, due to a 15 m/sec injection error, was three times what it would be on a straight line basis. For this reason, the bias of 600,000 km used at injection was larger than probably needed. The execution error of 2% was larger than actually anticipated. The 1 σ velocity error of 15 m/sec was taken as if it existed in the most critical direction rather than spherically distributed as specified. On an RMS or 1σ basis it can be shown that a spherically distributed error of 15 meter/sec. corresponds to 9 m/sec in each of three directions. On the other hand, the radial error needed so that the sphere will enclose 3σ (0.9974) cases is about 3.8 times the one sigma error in one direction or in this case (9) (3.8) or 34 meters per second. This is about 0.8 of (3) (15) so that not too much pessimism was involved in treating the 15 m/sec (1σ) error as if it existed in the most critical direction.

It would appear from the preceding that the capability for three to four midcourse corrections almost certainly is needed (not counting a backup), though in some lucky cases only two might be performed. Actually for the better execution error of 0.01 in magnitude and direction, only 3 are indicated even for the pessimistic case studied. Using the 1.4σ values in series also indicated 3 midcourses required even for the poorer 0.02 execution error case, but it was more marginal.

The question arises as to the difference in penalties involved between providing for a possible correction, and its actual use. It seems very possible that little unreliability is incurred by providing for an extra midcourse correction as compared to its actual use. If this is true, it would seem that the present analysis, with perhaps some added refinement, is adequate to ensure enough on-board capability. The actual in-flight analysis would handle the situation as the flight proceeded. On the other hand, if the addition of a 4th midcourse correction capability forced a design change, this conceivably could lead to a reliability degradation even though the 4th correction was never used. If such a situation is indicated, a more involved analysis would be called for to try to show that 3 is definitely, or definitely not, adequate.

The present results indicate that an execution error of 2% rather than 1% does not necessarily greatly degrade the final accuracy. However, it is not implied that the execution error should be allowed to go to 2% directly. Rather it should be kept as close to 1% (1 σ) as possible, but if reaching that goal complicates the system or introduces unreliability, then relaxing it to perhaps 2% is possibly indicated.

3.2.6 NON-PROPORTIONAL EXECUTION ERRORS

The preceding analysis more or less neglected the fact that execution errors will tend to reach an irreducible minimum as the size correction required becomes small. This minimum, of course, depends strongly on the engine size and the time to go at the point of final correction.

At 500,000 seconds before encounter (about 6 days), a 1 m/sec correction with 0.1 m/sec non-proportional error will produce an impact parameter space error of about 50 km. On the other hand, a 10 m/sec correction with 1 m/sec non-proportional error would produce 500 km error at encounter. Delaying the final execution can increase the size of correction needed rather inversely proportional to the time to go, thus tending to reduce the effect of the non-proportional errors. However, several factors can act to prevent waiting too long for the final midcourse correction. At 500,000 seconds before injection the capsule may require on the order of 20 m/sec ΔV. Cutting the time in half approximately doubles this ΔV requirement.

The complete sequence of events from final correction to orbiter injection can put a lower limit on the time involved. For instance, recharging of batteries after final correction, and before capsule separation could be a factor. Maintaining communications between capsule, orbiter and Goldstone during the landing phase must also be considered.

It appears from the foregoing that an execution error on the order of 0.1 m/sec is tolerable for small corrections.

3.2.7 FINAL MIDCOURSE CORRECTION

The question may arise as to why the final indicated midcourse correction should not be included in the capsule and orbit injection ΔV's. It would appear that it could be for the capsule with capsule impact latitude and longitude being controlled by vernier timing and pointing of the deflection velocity increment. However, for the Flight Spacecraft, the final correction must be done prior to the injection maneuver in order to maintain the proper periapsis altitude.

Then it would appear that a choice exists for the final midcourse correction. It could be performed prior to capsule separation putting both the Capsule and Flight Spacecraft on proper course. Or it could be incorporated into the Capsule deflection maneuver with the Flight Spacecraft receiving the final correction after capsule separation.

In the absence of approach guidance, there does not seem to be much point in delaying the final midcourse correction until capsule separation. The effect of execution error does not tend to vary with time, and the orbit determination error will tend to converge to a final level at least several days prior to encounter.

Where approach guidance is to be used to further refine the accuracy beyond 500 km, the preceding appears to still apply for the last DSIF determined correction. But the final correction, based on approach guidance measurements, must be delayed to the order of one day before encounter to obtain its full benefit. There does not appear to be a strong reason for choosing between the two possible choices. They are doing the correction prior to separation, or incorporating the correction into the deflection maneuver and then applying the Flight Spacecraft correction. The latter choice appears to add slightly to capsule ejection reliability by not requiring another trajectory correction maneuver prior to the separation maneuver.

3.2.8 MIDCOURSE FUEL

Factors to be considered in the ΔV capability provided include:

a. The amount needed for the 1st maneuver (EPD 250 indicates providing 5σ instead of 3σ).

b. The convergence of successive midcourse correction.

c. Whether or not the fuel comes from a separate source or one which has other purposes and therefore safety factor for other reasons.

d. Delay of a known needed correction increases the ΔV required approximately inversely as time to encounter (in general not an important effect).

Item b tends to be of little importance. Each successive midcourse correction tends to be on the order of 1/10 the preceding one or even less depending on the execution error. The amount needed for the 1st correction tends to be the important consideration, and tempered by item c as to whether the source is separate or not. The mission specifications gives 15 m/sec as the 1σ injection error to be allowed for. Then the ΔV required is 45 or 75 m/sec depending upon whether 3σ or 5σ is used. Philosophically it sounds reasonable to allocate 75 m/sec for a separate source system and 50 for a system drawing on a larger supply in place for other reasons.

4.0 CAPSULE IMPACT DISPERSION

4.1 INTRODUCTION

The accuracy with which the capsule can achieve impact at the desired landing site depends on the navigation uncertainties at the time of separation and the execution errors incurred in the separation process. Approximate values for the capsule impact point dispersion can be found by first combining navigation errors and execution errors (assumed independent) into in-plane and out-of-plane errors in capsule aiming point. The landing site dispersions can then be found by multiplying by sensitivity coefficients relating aiming point errors to landing site dispersions. These sensitivities are shown in Figures 4-1 and 4-2 as functions of entry angle and approach velocity. The in-plane sensitivity coefficients give down-range dispersions due to aim point errors in the plane of the capsule trajectory (b errors), and the out-of-plane coefficients give cross range dispersions due to out-of-plane aim point errors (Θ errors).

The curves show that, for entry angles less than about 50°, in-plane errors are magnified at impact, whereas out-of-plane errors are reduced due to gravitational focusing. These curves neglect the effect of atmospheric retardation; however, for entry angles larger than 40°, these effects are usually negligible.

4.2 AIMING POINT ERRORS

It will be assumed that the error in the knowledge of the actual spacecraft aiming point at the time of separation is 350 km in any direction (3σ). Misdirection of the capsule due to alignment error relative to the spacecraft and spacecraft orientation errors at separation is taken as 24 milliradians (3σ). Assuming a comparable additional error of 27 milliradians (3σ) incurred during capsule thrusting gives a total thrust misdirection of 36 milliradians (3σ). A 2% (3σ) error in the magnitude of the separation ΔV is assumed.

Two types of separation were examined; one with the landing site out of the plane of the spacecraft approach trajectory (Syrtis Major) and one with an in-plane landing site. In each case the approach velocity is 3.5 km/sec, the spacecraft aiming point is given by b = 9260 km and $\theta = 18°$, and the capsule entry angle is 42°. Separation distance is 300,000 km. The out-of-plane case is shown in Figure 4-3. The total ΔV magnitude is 0.0966 km/sec which includes a forward tangential component of 0.0314 km/sec. The ΔV direction therefore makes an angle of 19° with the plane normal to the approach velocity direction. It can be seen from the figure that the direction of the change in aiming point (and therefore the direction of the normal component of the separation ΔV) is almost at right angles to the capsule trajectory plane. Errors in thrust direction therefore result in in-plane capsule aim point errors equal to $0.036 \times \frac{\Delta V}{V_s} = R_s$.

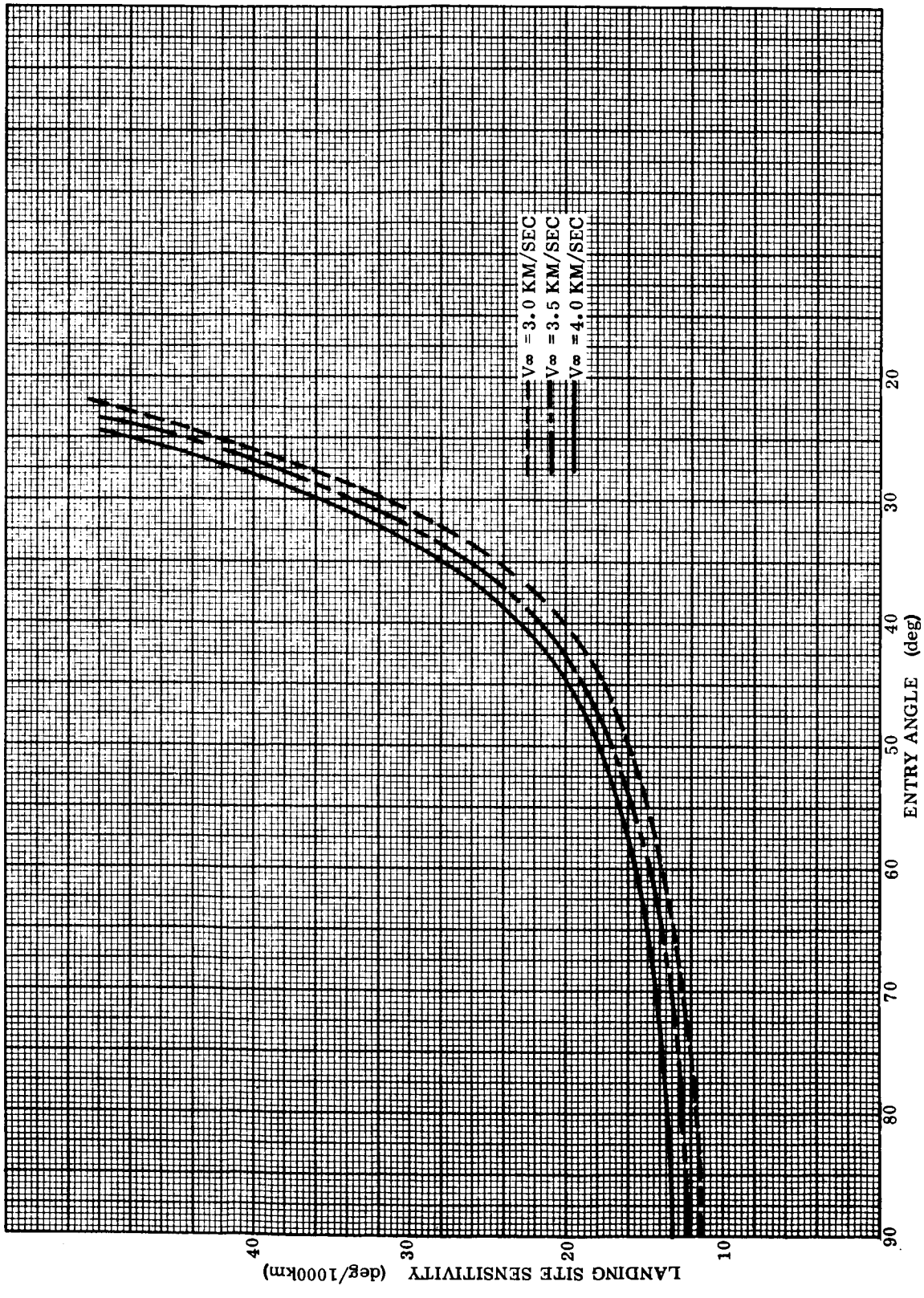

Figure 4-1. In-Plane Landing Site Sensitivity (With Respect To Impact Parameter) vs Entry Angle

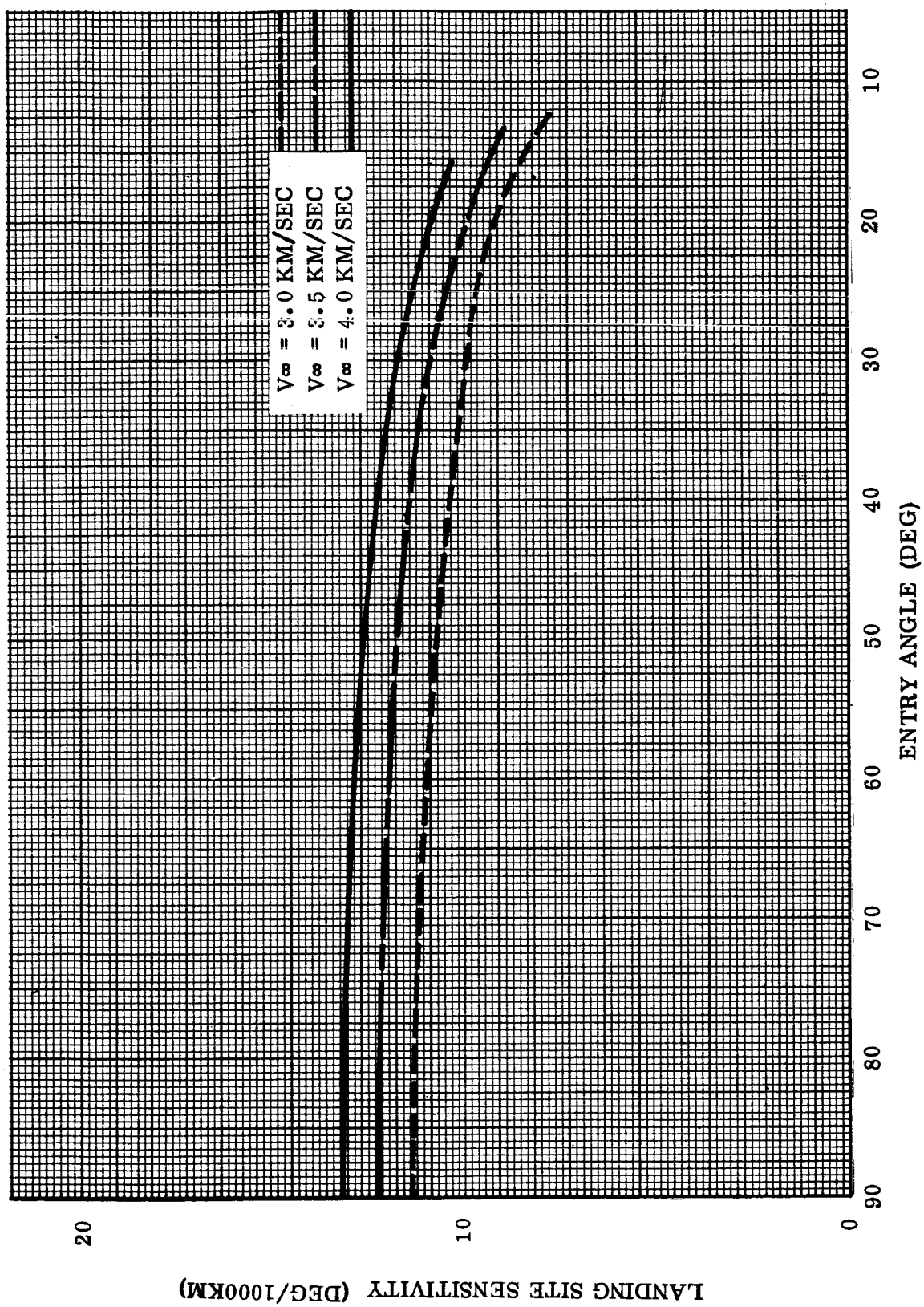

Figure 4-2. Out-Plane Landing Site Sensitivity (With Respect To Impact Parameter) vs Entry Angle

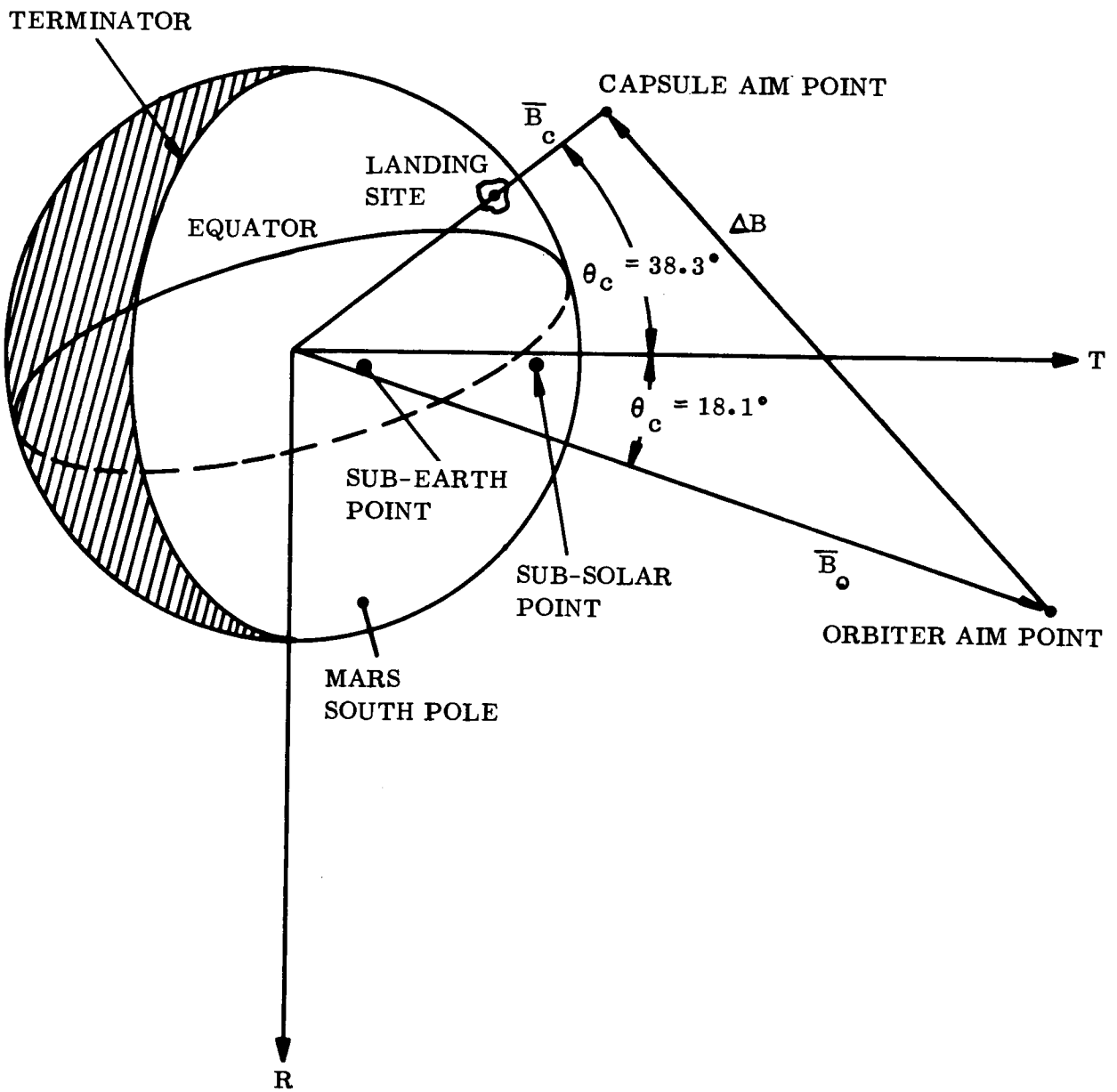

Figure 4-3. Impact Parameter Plane

where

R_s = 300,000 km = separation distance

V_s = 3.54 km/sec = spacecraft velocity at separation

ΔV = 0.0966 km/sec = magnitude of separation impulse

The in-plane error due to thrust direction error is

$$0.036 \times \frac{0.0966}{3.54} \times 300{,}000 = 294 \text{ km}$$

and the out-of-plane error is:

$$294 \times \sin 19° = 95 \text{ km}$$

The component of thrust direction error normal to the impact parameter plane causes only a small change in the magnitude of the capsule approach velocity, which has a negligible effect on the landing site dispersion.

The 2% error in ΔV magnitude causes an out-of-plane error of:

$$0.02 \times \frac{0.0966}{3.54} \times 300{,}000 \times \cos 19° = 155 \text{ km}$$

The total out-of-plane error due to capsule separation is then:

$$\sqrt{155^2 + 95^2} = 182 \text{ km.}$$

When these execution errors are combined with the navigation errors of 350 km the result is:

$$\text{in-plane error} = \sqrt{350^2 + 294^2} = 457 \text{ km}$$

$$\text{out-of-plane error} = \sqrt{350^2 + 182^2} = 394 \text{ km}$$

From Figures 4-1 and 4-2, the landing site sensitivities for an approach velocity of 3.5 km/sec and an entry angle of 42° are 20.4 degrees/1000 km for in-plane errors and 11.4 degrees/1000 km for out-of-plane errors. The 3σ landing site dispersions are, therefore 9.3 degrees down range and 4.5 degrees cross range.

For a landing site in the spacecraft trajectory plane and a 42 degree entry angle, the required ΔV is 0.054 km/sec with no tangential component. In this case, the effects of separation errors are the reverse of the previous case; i.e., a thrust

direction error causes an out-of-plane aiming point error and a thrust magnitude error causes an in-plane aiming point error. The aiming point errors resulting from the separation maneuver are:

$$\text{in plane error} = 0.02 \times \frac{0.054}{3.54} \times 300{,}000 = 92 \text{ km}$$

$$\text{out-of-plane error} = 0.036 \times \frac{0.054}{3.54} \times 300{,}000 = 166 \text{ km}$$

The total aiming point errors, including the 350 km navigation errors are:

$$\text{in plane error} = \sqrt{350^2 + 92^2} = 361 \text{ km}$$

$$\text{out-of-plane error} = \sqrt{350^2 + 166^2} = 387 \text{ km}$$

These errors result in landing site dispersions of 7.4 degree down range and 4.4 degree cross range.

In both of these cases, the navigation errors are the predominant error source. If these errors are increased from 350 km to 500 km, the landing site dispersions are increased almost proportionately.

It can be seen that the dispersion errors for the in-plane landing site are less than those for the out-of-plane site, due to the lower separation ΔV, and also because the major execution error is out-of-plane and subject to gravitational focusing.

5.0 ORBIT INSERTION ERROR ANALYSIS

5.1 INTRODUCTION

The Voyager spacecraft must be placed in an appropriate orbit about Mars in order that mission objectives can be accomplished. Thus, when the spacecraft reaches the vicinity of the point of closest approach to Mars, the propulsion subsystems will be used to change the velocity of the vehicle in order to transfer the spacecraft from its hyperbolic approach trajectory to an orbit about Mars. The orbit achieved will differ from the desired nominal orbit because of errors resulting from the insertion process and because of navigation and guidance errors. It is the purpose of this study to first, investigate the effects which various error sources have on the orbit, and second, to obtain a statistical description of the resulting orbit.

The results of the first part of this study were obtained using a powered flight digital computer program for integrating the equations of motion of the spacecraft moving in an inverse square law central force field, while acted upon by thrusting forces. Since the effects of errors on the in-plane orbital parameters were of primary interest, the

study is confined to motion within a single plane for purposes of simplification. The study includes the effects of non-impulsive thrusting (non-zero burn time) although a comparison is made with results computed on the basis of impulsive thrusting.

Two nominal orbits about Mars have been selected which are intended to bracket the orbit requirements. Error sources associated with the orbit injection process, as well as navigation and guidance errors, are considered. In this study the direction of thrust is fixed with respect to inertial space, this being the simplest system to implement. The propulsion fuel penalty incurred as a result of this selection is small when comparison is made with fuel requirements based on the more efficient gravity turn or the theoretically minimum fuel requirements computed on the basis of impulsive thrusting.

The results of the second part of the study were obtained using a Monte Carlo approach for investigating the combined effects of orbiter insertion errors. A description of the computer program simulation model is given.

5.2 EFFECTS OF INDIVIDUAL ERROR SOURCES

5.2.1 NOMINAL ORBITS

The following two nominal orbits were selected for this investigation:

a. A circular orbit with an altitude of 4,000 km (4 x 4 orbit)

b. An elliptical orbit with a periapsis altitude of 3000 km and an apoapsis altitude of 30,000 km (3 x 30 orbit)

These orbits were selected on the assumption that they would bracket the final selection for the recommended orbit. The recommended orbit, with a periapsis altitude of 3000 km and an apoapsis altitude of 25,000 km (3 x 25 orbit), is very close to the 3 x 30 orbit studied in this investigation.

The hyperbolic excess velocity for the approaching spacecraft was assumed to be 3.0 km/sec. The final selection for the interplanetary trajectory results in a hyperbolic excess velocity of 3.5 km/sec. The approach trajectory and the orbit about Mars are constrained to lie in the same plane in this study.

5.2.2 PROPULSION SYSTEM

The propulsion system selected for the study of non-impulsive thrusting provides 1066 pounds of thrust. This is lower than the final selection of thrust level which is approximately 2360 pounds. Therefore, the results obtained for non-impulsive thrusting and impulsive thrusting bracket the final selection of the thrust level. The specific impulse for the fuel was assumed to be 300 lb sec/lb. The dry weight of the spacecraft was assumed to be 1945 pounds. This figure includes the orbit injection propulsion

system but excludes the weight of the fuel. This is lower than the final dry weight figure of 2682 pounds.

5.2.3 GUIDANCE LAW CONSIDERATIONS

Since this study includes the effects of non-impulsive thrusting, it is necessary to determine a satisfactory nominal thrusting maneuver for the accomplishment of orbit insertion. The following considerations, which result from analyses based on impulsive thrusting, apply also to the case of non-impulsive thrusting.

a. Fuel requirements are reduced when insertion occurs in the vicinity of periapsis on the hyperbolic approach trajectory.

b. Fuel requirements are reduced when the direction of thrust coincides with the direction of the velocity vector.

c. Fuel requirements are reduced when the periapsis radius of the approach hyperbolic trajectory is approximately equal to the desired periapsis radius for the elliptical orbit.

d. Fuel requirements are reduced when the desired elliptical orbit lies in the same plane as does the approach hyperbolic trajectory.

The minimization of the fuel requirement is not the only criterion upon which to judge a nominal injection maneuver. It is also important to make use of an injection guidance law which is easy to mechanize. The simplest insertion maneuver to mechanize would require that the thrust orientation remain fixed with respect to inertial space throughout the entire thrusting period and that the thrusting magnitude remain constant during the period of thrusting. Since the orientation of the velocity vector changes as the vehicle moves along the hyperbolic approach trajectory, this guidance law would not meet the second requirement for reducing fuel requirements as well as would the "gravity turn." However, the implementation of the "gravity turn" introduces added complication since the thrust direction must coincide with the velocity vector direction and this direction, of course, must be known instantaneously.

In order to satisfy the simplicity of implementation requirement, an injection maneuver was tested which requires that the thrust orientation remain fixed in inertial space in a direction perpendicular to the periapsis radius vector of the nominal elliptical orbit. Table 5-1 shows the fuel weight penalty incurred with the use of this method by comparing the percent increase in fuel required by this maneuver and the "gravity turn" with that required for the impulsive periapsis to periapsis transfer which gives the theoretically minimum fuel requirements. The results for the 3 x 30 orbit are given for injection at periapsis on the elliptical orbit and for injection on the elliptical orbit at a point corresponding to a true anomaly of +4°. Table 5-1 shows that the fuel weight penalty incurred is greater for the 4 x 4 orbit than for the 3 x 30 orbit, and is, therefore, dependent upon the thrusting time. More importantly, the results given in the Table show that the additional fuel required for the constant inertial thrusting direction

Table 5-1. Fuel Penalties Resulting from the Combined Effects of Finite Thrusting Time and Type of Injection Maneuver

Orbit	True Anomaly on Ellipse at Injection (deg)	Fuel Penalty (%)	
		Fixed Inertial Thrusting	Gravity Turn
3 x 30	0	0.27	0.14
3 x 30	+4	0.10	0.07
4 x 4		0.48	0.17

injection maneuver in the worst case (4 x 4 orbit) amounts to a 0.31% increase when compared with the "gravity turn" requirement, and to a 0.48% increase when compared with the theoretically minimum requirement based on impulsive thrusting. Thus, the injection maneuver selected incorporates both of the features which are most desirable, simplicity in implementation and negligible fuel weight penalty.

5.3 INVESTIGATION OF INDIVIDUAL ERROR SOURCES

Since the error sources which must be considered in an error analysis depend upon the implementation of the process, the orbit injection process which has been assumed for the purposes of this study will now be described. The approach trajectory of the spacecraft is determined by means of the Earth-based DSIF. Based on the tracking data, appropriate commands will be computed by Earth-based computers and transmitted to the spacecraft. Prior to the time of injection, the spacecraft will be commanded to assume its retro-thrust attitude. The retro-thrust attitude remains fixed with respect to inertial space throughout the entire period of thrusting. At a computed time, thrusting is initiated in order to accomplish the required orbit transfer. The thrust level is assumed to remain constant during the thrusting period. The thrusting is terminated by means of a signal which is based on either a velocity increment measurement made with an accelerometer or a time increment measurement made with a timer. These measured values are compared on-board with the computed values which have been transmitted to the spacecraft, and the signal for thrust termination is given when the measured value equals the commanded value.

A description of the method used to obtain the non-impulsive thrusting results of this study will next be briefly described. The nominal injection maneuver was first obtained by using a powered flight digital computer program for integrating the equations of motion of the spacecraft moving in an inverse square law central force field while acted upon by thrusting forces. The initial conditions for position and velocity were determined for the periapsis point on the nominal orbit about Mars. The fixed direction for the thrust vector was taken normal to the radius vector of the periapsis point. The initial weight (injection weight) was taken as 2,000 pounds and thus includes an allowance of 55 pounds for spare fuel requirements. The program was then run backwards in time until the position

and velocity corresponded to the appropriate energy per unit mass for the assumed hyperbolic approach trajectory. These end conditions thus become the initial conditions for the injection maneuvers when the program is run forward in time.

The error sources considered in this study are as follows:

a. . DSIF timing error - this corresponds to a translation along the nominal approach trajectory (time of flight error).

b. DSIF impact parameter error - this corresponds to a translation in the plane of the trajectory which is normal to the nominal approach asymptote. This error results in an off-nominal approach trajectory which also affects time of periapsis passage (hyperbolic trajectory) as well as producing correlated position and velocity errors.

c. Thrust orientation error - the attitude control system is the major contributor to this error.

d. Thrust duration error - this is a timing error which results when thrust is terminated by a timer signal.

e. Velocity increment error - this is an error which results from accelerometer measurement errors when thrust is terminated by an accelerometer signal. Accelerometer bias, scale factor, and alignment errors contribute to errors in the measurement of the velocity increment.

f. Fuel flow rate error - this error affects the change in vehicle weight as well as thrust level.

g. Specific impulse error - this error affects the thrust level.

h. Error in initial vehicle weight.

The approach velocity can be determined very accurately; therefore the effect of this error source has not been considered. The error in the knowledge of the gravitational constant of Mars has also been neglected since the present uncertainty in this quantity should be greatly reduced by 1971.

Computer runs were made in order to determine the separate effects of these error sources on the selected nominal orbits about Mars. Since this study is restricted to a single plane, the terminal conditions at injection are related to the following in-plane orbital parameters:

a. Periapsis altitude

b. Apoapsis altitude

c. Rotation of the line of apsides for the elliptical orbit, measured from the line of apsides of the nominal orbit, the positive direction corresponding to the direction of motion of the spacecraft.

d. Orbital period

The effect of each error source was determined separately by introducing only a single source of error into each computer run. The program was run forward in time from the appropriate initial conditions. The position and velocity data at the time of thrust termination were then used to compute the four in-plane orbital parameters. The results obtained are given in Figures 5-1 through 5-43. Where appropriate, the results obtained using non-impulsive thrusting are compared with the results obtained using impulsive thrusting. In Figures 5-15 through 5-21 and in Figures 5-35 through 5-43, ΔT refers to the time duration of thrusting and ΔV refers to the magnitude of the velocity increment.

Some comments on the results obtained are in order at this point. The question of capture by Mars is seen to be not critical for either of the two orbits selected for this study. On the other hand, the use of an accelerometer for the control of thrust termination greatly reduces the errors in the orbital parameters which result from propulsion system errors, the associated error in vehicle weight, and timer errors. DSIF timing errors and errors in the direction of thrusting are the major errors sources which contribute to orbit rotation. The periapsis altitude is not appreciably changed by any of the error sources in the case of the 3 x 30 elliptical orbit except for errors in the impact parameter. However, all of the error sources are capable of producing relatively large changes in apoapsis altitude in the case of the 3 x 30 orbit and these changes result in corresponding changes in the period of the resulting orbit.

5.4 COMMENTS ON THE COMBINED EFFECTS OF ERROR SOURCES

As has been previously noted, the use of an accelerometer for thrust termination greatly reduces the errors in the orbit parameters which result from propulsion system errors, errors in vehicle weight, and timer errors. On the assumption that an accelerometer will be used to determine the time of thrust termination, only the remaining four error sources (DSIF timing error, impact parameter error, ΔV error, and thrust orientation error) contribute significantly toward making the resulting orbit different from the desired nominal orbit. Since it is desired to obtain an estimate of the statistical distribution of the orbit errors, the effects of these four error sources must be combined. It should be noted, however, that the apoapsis altitude error curves resulting from these four error sources are nonlinear so that an error analysis based on the assumption of linearity would not be valid. For this reason, the Monte Carlo technique described in the next section was used in order to obtain a statistical description of the resulting orbit and to determine maximum deviations in the statistical distributions for the resulting orbit errors.

In order to reduce the computation requirements in the Monte Carlo simulation it would be desirable to use impulsive thrusting in computing the resulting errors in the orbital elements if this could be done without the introduction of significant errors.

Since the final orbit selection has been made, it is desirable to obtain results based on this selection. The orbit which has been selected is the 3 x 25 km orbit with an approach velocity of 3.5 km/sec. This is reasonably close to the 3 x 30 km orbit investigated in this study. Therefore, the results obtained in this study for the 3 x 30 km orbit can be used as a guide when considering the errors in the orbital parameters which would be associated with the 3 x 25 km orbit. An examination of Figures 5-1 through 5-6 and Figures 5-9 through 5-14 indicates that the results obtained for the orbital parameters using the impulsive thrusting model are in good agreement with the non-impulsive thrusting model results with the exception of the apoapsis altitude results corresponding to errors in thrust orientation and DSIF timing error (refer to Figures 5-2 and 5-10). However, when considering realistic three sigma dispersions of 35.2 m/sec in velocity increment, 500 km in impact parameter, 3° in thrust orientation and 300 seconds in DSIF timing, it is seen that the two error sources which show the greatest differences in apoapsis altitude due to model differences (DSIF timing error and thrust orientation error) also contribute much less to the resulting total dispersion in apoapsis altitude resulting from the combined effects of all four error sources. Therefore, the impulsive thrusting model was used initially in generating the errors in the Monte Carlo program.

5-5. MONTE CARLO ERROR ANALYSIS FOR ORBITER INSERTION

5.5.1 INTRODUCTION

A Monte Carlo approach for investigating the combined effects of orbiter insertion errors was initiated in order to account for non-linear sensitivities and to determine maximum deviations (e.g., in periapsis altitude) in the statistical distributions for the resulting orbit errors. This section gives a description of a computer program simulation model and presents some results obtained to date for a representative case. Future work will investigate the effects of biases and correlations in the source errors.

5.5.2 ERROR MODELING

Nominal orbital transfer is assumed to be an impulsive transfer to periapsis of the nominal orbit at periapsis of the nominal approach hyperbola. As a model for error analysis studies this is a reasonable approximation to that of non-impulsive thrusting. Both the approach hyperbola and the final orbit are assumed coplanar. The sources of error include those in impact parameter, time of flight (time to periapsis passage), and magnitude and direction of the impulsive velocity increment. The resulting orbit errors considered are those in periapsis altitude, apoapsis altitude, period, and orbit rotation (deviation from nominal line of apsides). Fixed biases in the error

sources will allow investigations for impulsive transfer at points other than periapsis.

5.5.3 SIMULATION PROGRAM

Using analytic expressions for the described error model a computer program was developed for performing very rapid multiple sampling of the resulting orbit errors. Generated source errors can include both bias errors and random gaussian errors. In addition, correlations can be simulated between the impact parameter and time of flight random errors. The resulting orbit errors are statistically analyzed by computing the first four moments of the sampled distributions. These moments determine the sample means and standard deviations, and coefficients for measures of skewness and kurtosis. Also, frequency distribution histograms are obtained.

5.5.4 RESULTS

To date a limited investigation has been performed using the Monte Carlo stimulation program. These results are presented in the following tables and figures. The representative case studied had the nominal values:

Hyperbolic Excess Speed = 3.5 km/sec

Orbit Periapsis Alt. = 3,000 km

Orbit Apoapsis Alt. = 25,000 km

(Period = 19.3 hour)

with the following transfer source errors:

	3σ (gaussian, no bias)
Impact Parameter	500 km
Time of Flight	300 sec
Delta Velocity Magnitude	2%
Delta Velocity Direction	3 deg

Table 5-2 indicates the resulting orbit errors due to the combined source errors for a sample size of 1,000. The standard error values in parentheses refer to the errors in the sample mean and standard deviation. Figures 5-44 through 5-47 are the frequency distribution histograms for the errors indicated in Table 5-2. The dashed histograms are for theoretical normal distributions having the sample means and standard deviations. This comparison shows that the resulting orbit errors distributions are approximately normal. However, the apoapsis altitude and period errors are slightly skewed. (These observations are verified by the values of the coefficients

Table 5-2. Orbit Errors for Combined Source Errors (Sample Size = 1000)

	Sample Mean	Stand. Error	Sample Stand. Dev.	Stand. Error	Max. Value	Min. Value
Periapsis Alt. (km)	-12	(5)	154	(3)	-507	451
Apoapsis Alt. (km)	265	(57)	1815	(41)	-4410	5855
Period (hr)	0.24	(0.05)	1.62	(0.04)	-3.96	5.49
Orbit Rotation (deg)	0.04	(0.09)	2.76	(0.06)	-7.89	8.06

for skewness and kurtosis). These orbit error frequency histograms give the following empirical probabilities:

	Limits	Probability
Periapsis Alt.	± 450 km	0.996
Apoapsis Alt.	± 5500 km	0.994
Period	± 5 hr	0.994
Orbit Rotation	± 8°	0.998

Table 5-3 indicates the resulting orbit errors due to the individual source errors. Table 5-4 indicates the effects of combined source errors for a sample size of 10,000. Referring to Tables 5-3 and 5-4, the biases in the apoapsis altitude and period errors are due to the non-linear effects of the source errors (primarily the time of flight error).

Referring to Table 5-2, it should be pointed out that a more precise model of the non-impulsive thrusting will change the standard deviation values by a few percent. Further parametric investigations are planned, especially to determine the effects of correlations between the impact parameter and time of flight errors.

5.6 RESULTS

a. A guidance law for orbit injection requiring that the thrusting direction remain fixed with respect to inertial space is recommended since it is the easiest to implement and the fuel weight penalty is insignificant.

b. An accelerometer should be used to signal the termination of thrusting as this greatly reduces the dispersion of the orbital elements. Thrust termination based on time should be used as a backup.

Table 5-3. Orbit Errors for Individual Source Errors (Sample Size = 1000)

	Impact Parameter	Time of Flight	Delta Vel. Magnitude	Delta Vel. Direction
Periapsis Alt. (km)				
Mean	-8	-3	0	-1
Standard Deviation	154	5	0	1
Apoapsis Alt. (km)				
Mean	-21	210	38	38
Standard Deviation	1419	291	1060	50
Period (hr)				
Mean	-0.01	0.18	0.04	0.03
Standard Deviation	1.31	0.24	0.89	0.04
Orbit Rotation (deg)				
Mean	0.02	0.01	0	0.03
Standard Deviation	0.41	2.41	0	1.34

Table 5-4. Orbit Errors for Combined Source Errors (Sample Size = 10,000)

	Sample Mean	Stand. Error	Sample Stand. Dev.	Stand. Error	Max. Value	Min. Value
Periapsis Alt. (km)	-4	(2)	155	(1)	-507	506
Apoapsis Alt. (km)	352	(18)	1840	(13)	-5331	8598
Period (hr)	0.31	(0.02)	1.65	(0.01)	-4.58	7.83
Orbit Rotation (deg.)	-0.03	(0.03)	2.78	(0.02)	-9.05	9.49

c. The purpose of the Voyager orbit insertion guidance system is to transfer the spacecraft from the approach hyperbolic trajectory (V_∞ = 3.5 km/sec) to an orbit about Mars which has the following orbital elements:

(1) periapsis altitude = 3,000 ±500 km (3σ)

(2) apoapsis altitude = 25,000 km (nominal)

(3) inclination = 40 ± 5 degrees (3σ)

Thus, no tight restrictions have been placed on the orbital elements of the resulting orbit about Mars. However, atmospheric capture of the orbiter must not occur for at least fifty years after orbit insertion.

Four errors sources can have significant effects on the in-plane orbital elements of the resulting orbit. These error sources, along with their anticipated three sigma dispersion limits, are as follows:

a. DSIF timing error (time-of-flight error) = 150 seconds

b. Impact parameter error = 500 km

c. Error in thrust orientation = 3 degrees

d. Error in measurement of velocity increment = 1% of ΔV, max. or 17.6 m/sec.

On the basis of these estimates, three sigma dispersions in periapsis altitude and apoapsis altitude are 460 km and 4560 km, respectively, with a corresponding dispersion in period of 4.2 hours. The three sigma dispersion in in-plane orbit rotation is 5.5 degrees. These results are obtained by scaling the results given in Table 5-3 for the corresponding changes in the dispersion limits for DSIF timing error and error in the measurement of ΔV. The worst case combination of these errors will not prevent capture of the orbiter by Mars. Based on present estimates of the Martian atmosphere, atmospheric capture of the orbiter will not occur during the fifty year period following orbit insertion for the worst case orbit. The three sigma dispersion in orbit inclination has been calculated to be 3.7 degrees.

These general conclusions have also been substantiated in a similar investigation which is reported in the Jet Propulsion Laboratory document entitled, "Mariner Mars 1969 Orbiter Technical Feasibility Study", EPD-250, Section VIII-E, dated 16 November 1964.

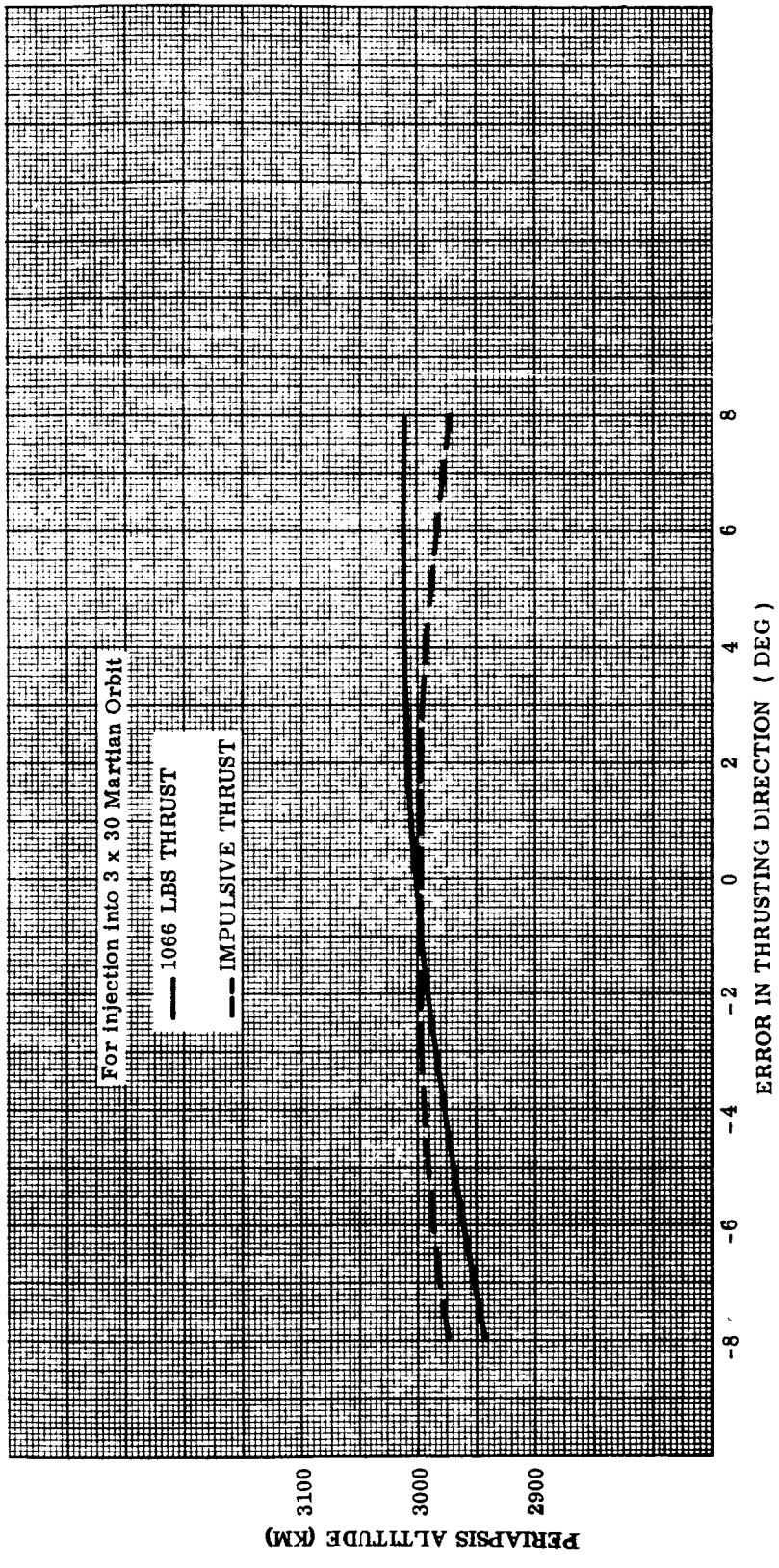

Figure 5-1. Periapsis Altitude vs Error in Thrusting Direction

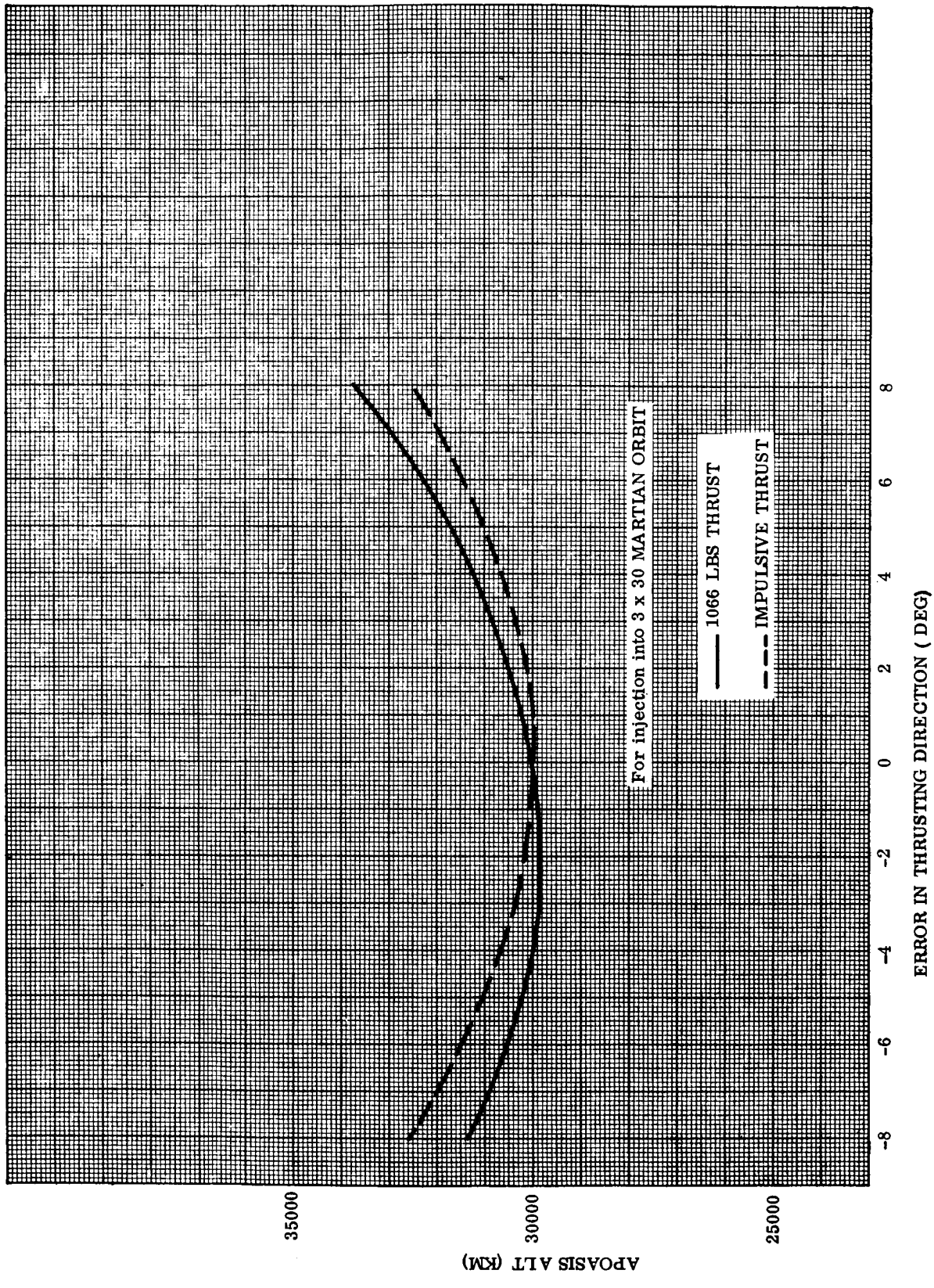

Figure 5-2. Apoapsis Altitude vs Error in Thrusting Direction

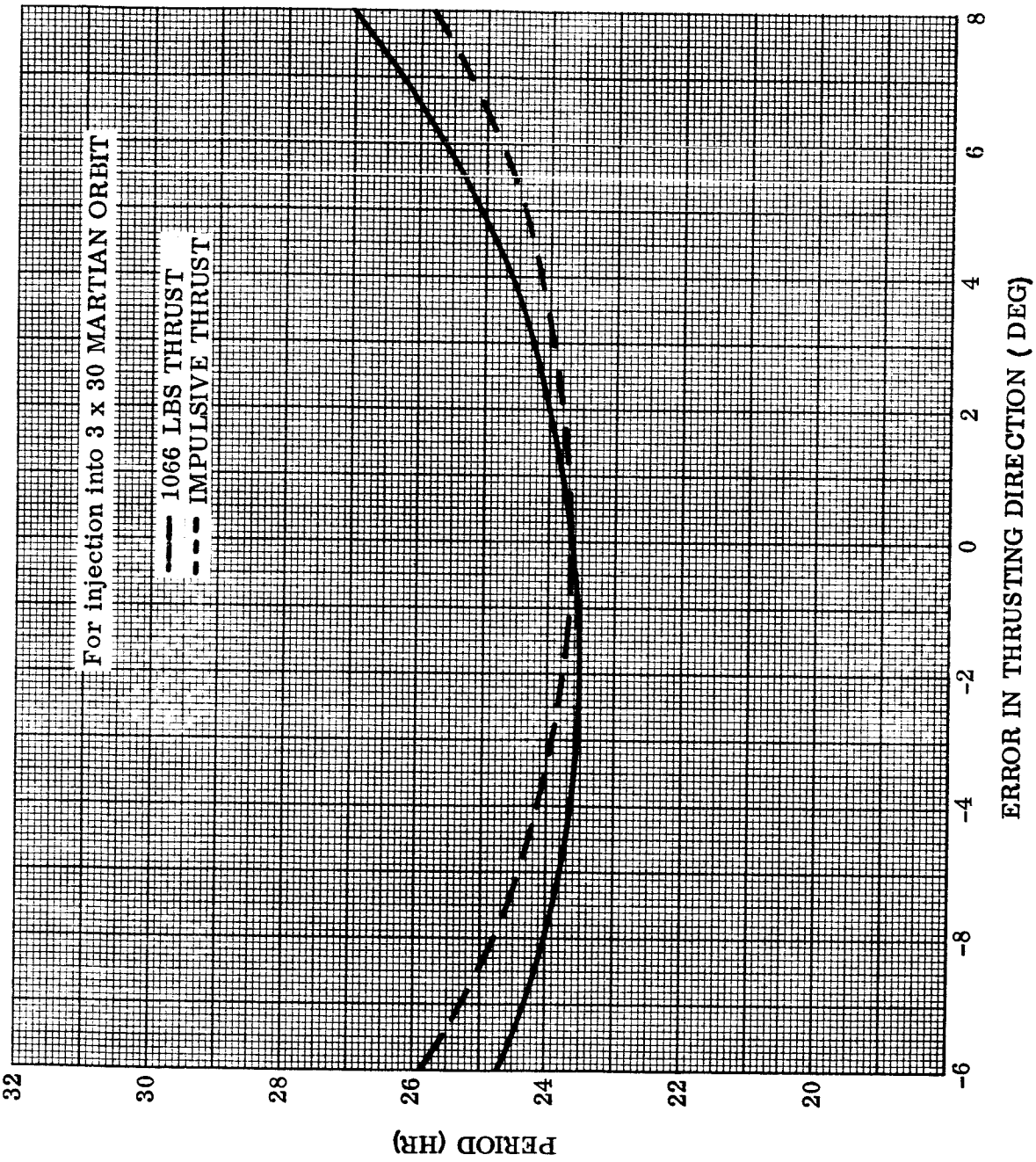

Figure 5-3. Period vs Error in Thrusting Direction

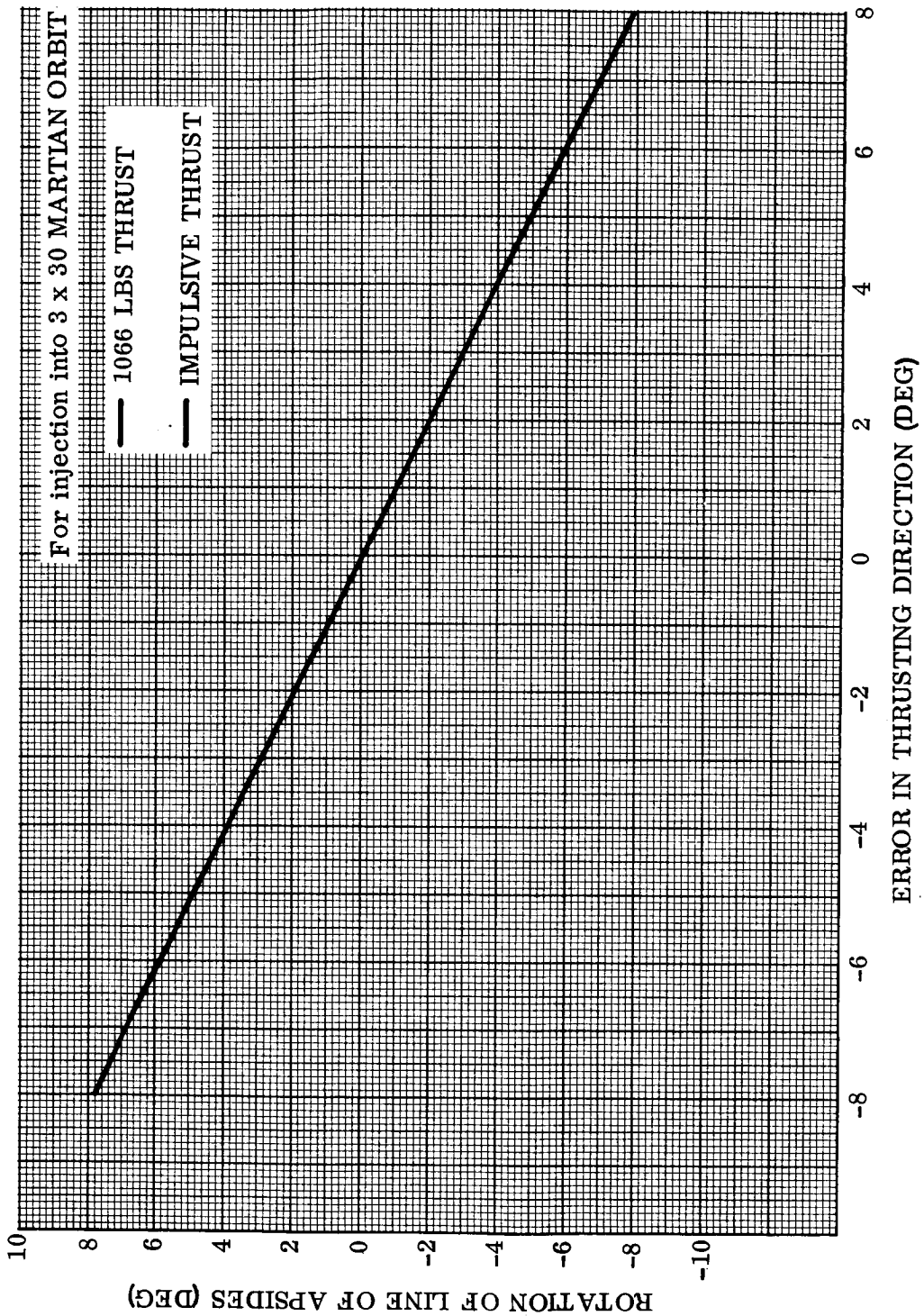

Figure 5-4. Rotation of Line of Apsides vs Error in Thrusting Direction

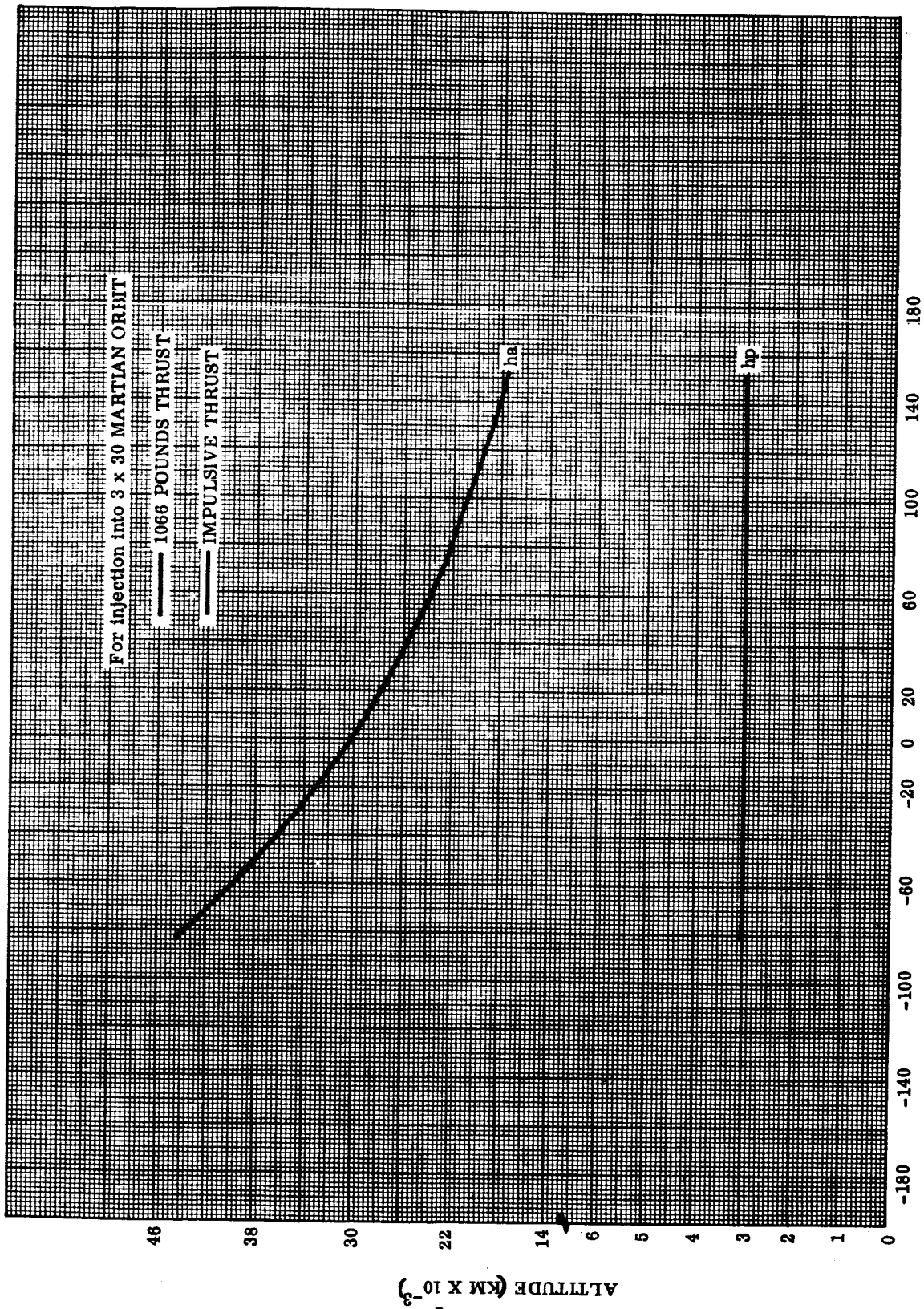

Figure 5-5. Apoapsis Altitude, h_a, and Periapsis Altitude, h_p, vs Error in Velocity Increment Measurement

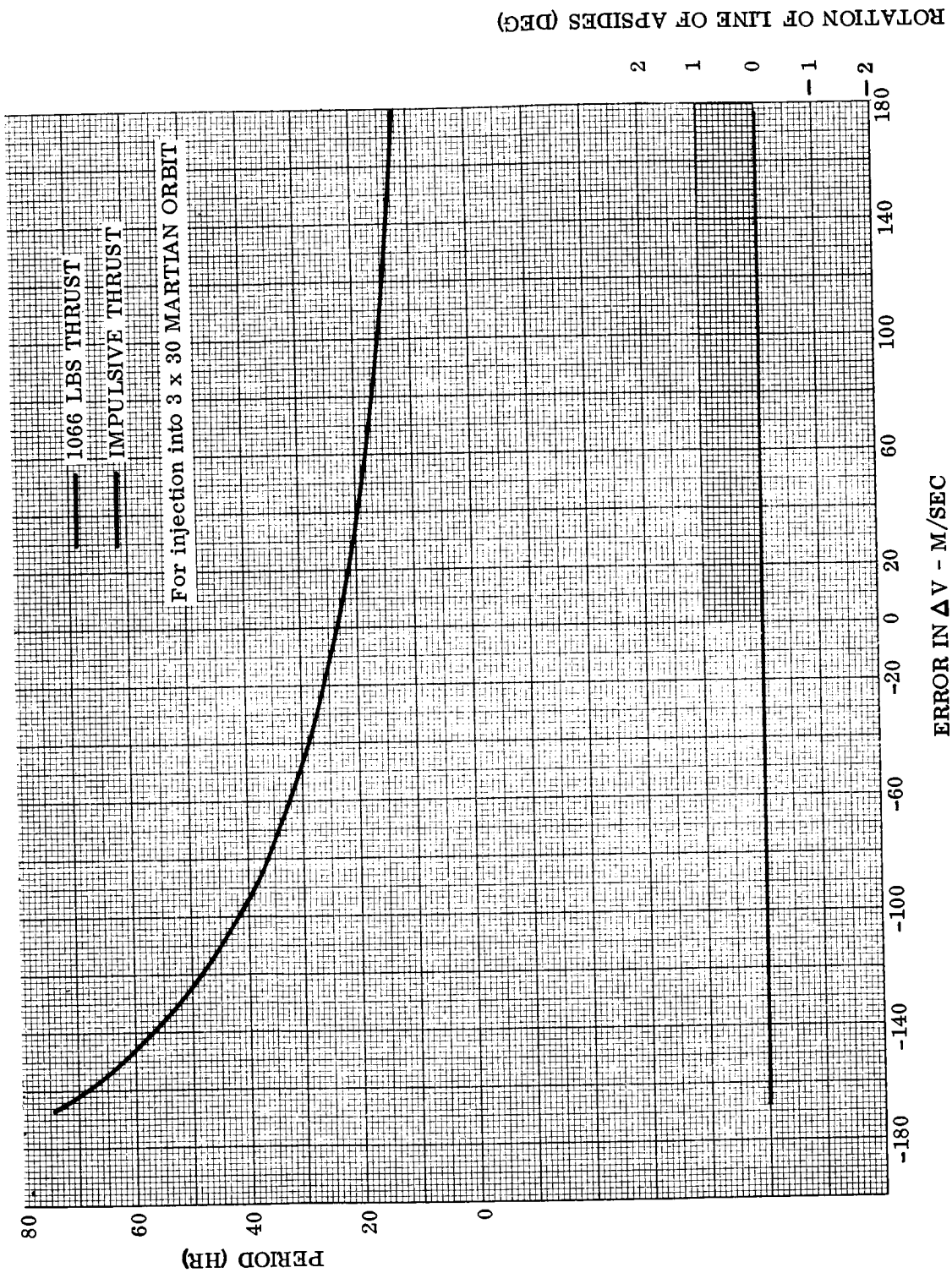

Figure 5-6. Period and Rotation of the Line of Apsides vs Error in Velocity Increment Measurement

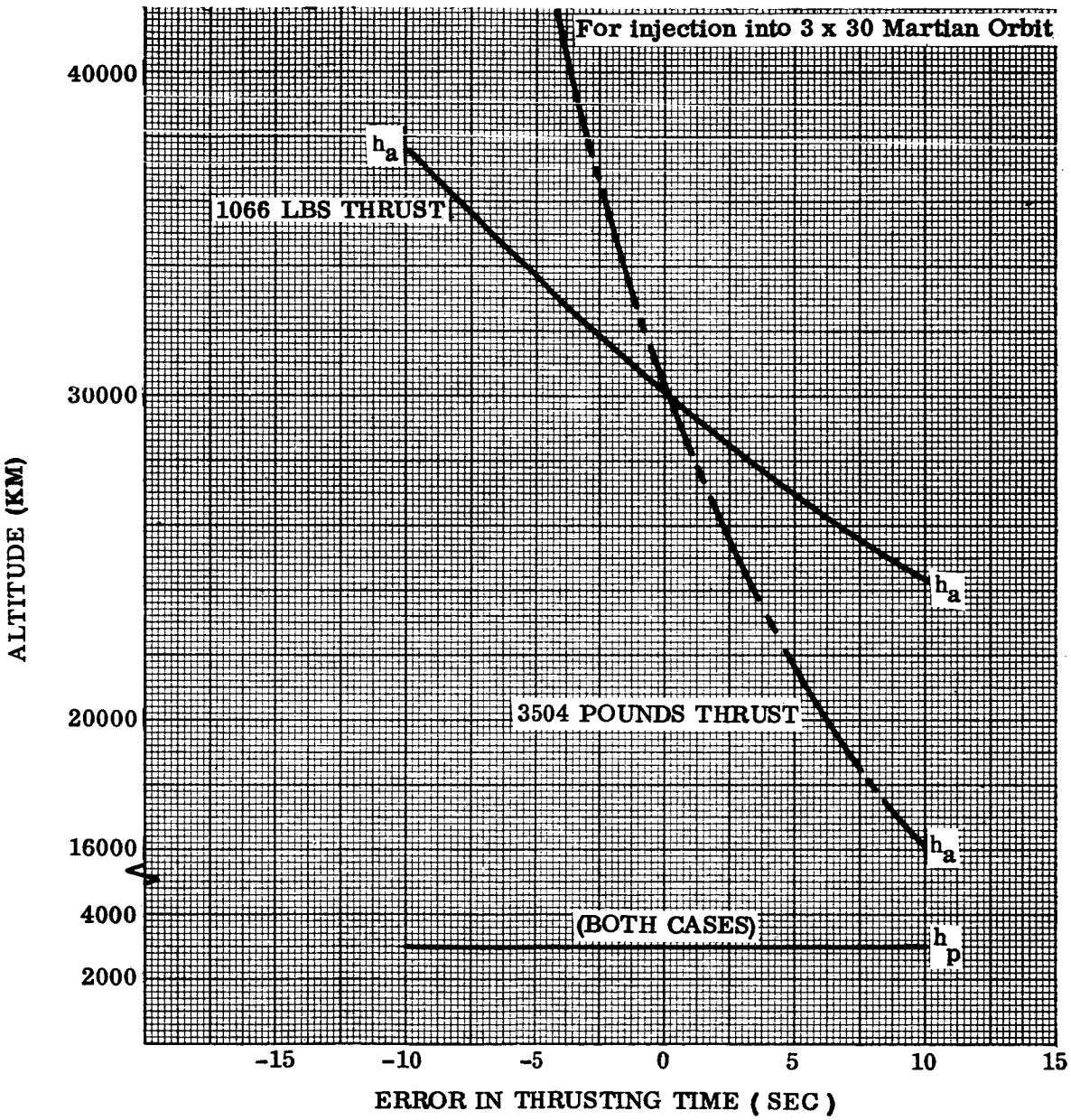

Figure 5-7. Apoapsis Altitude, h_a, and Periapsis Altitude, h_p, vs Error in Thrusting Time

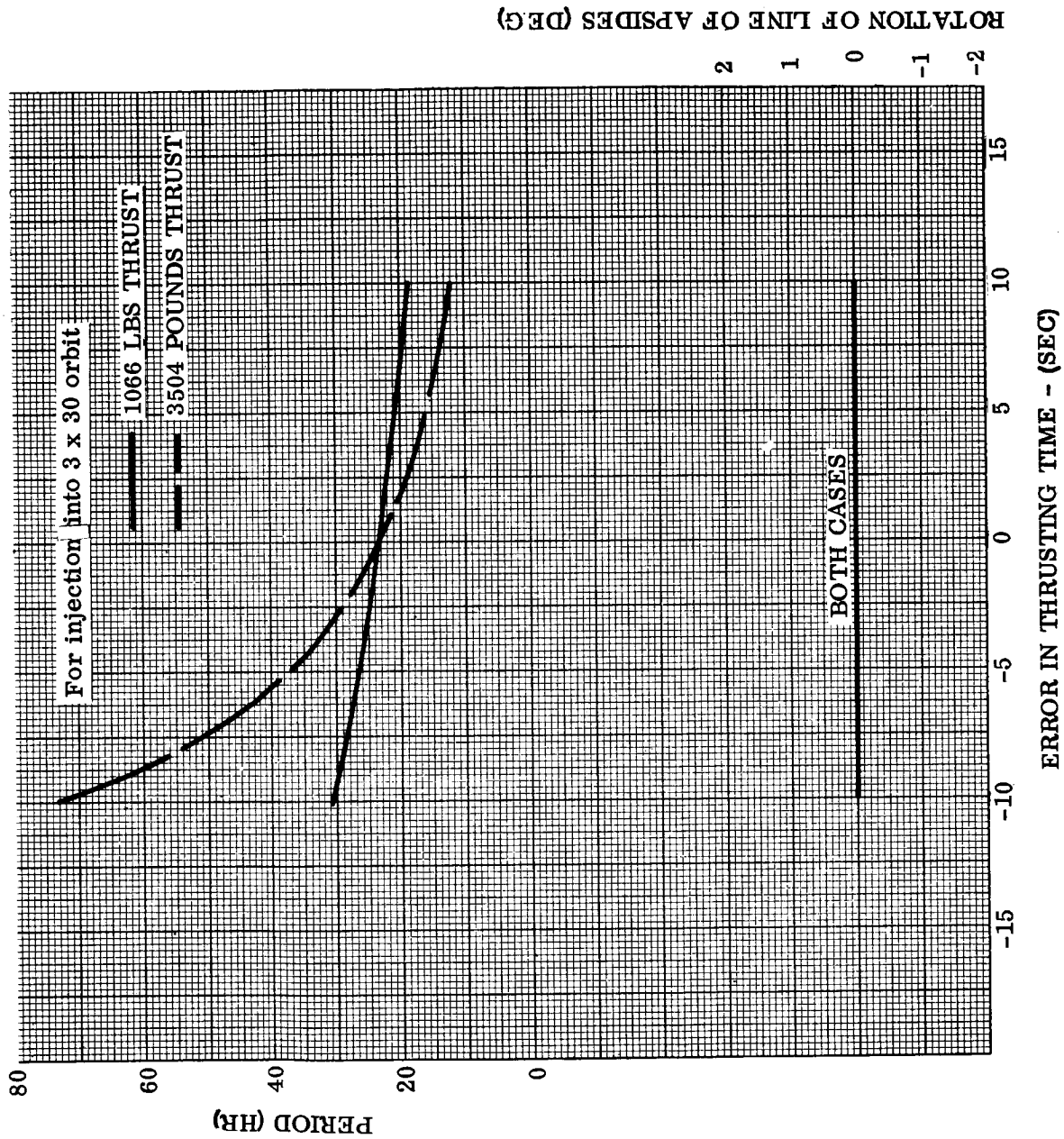

Figure 5-8. Period and Rotation of the Line of Apsides vs Error in Thrusting Time

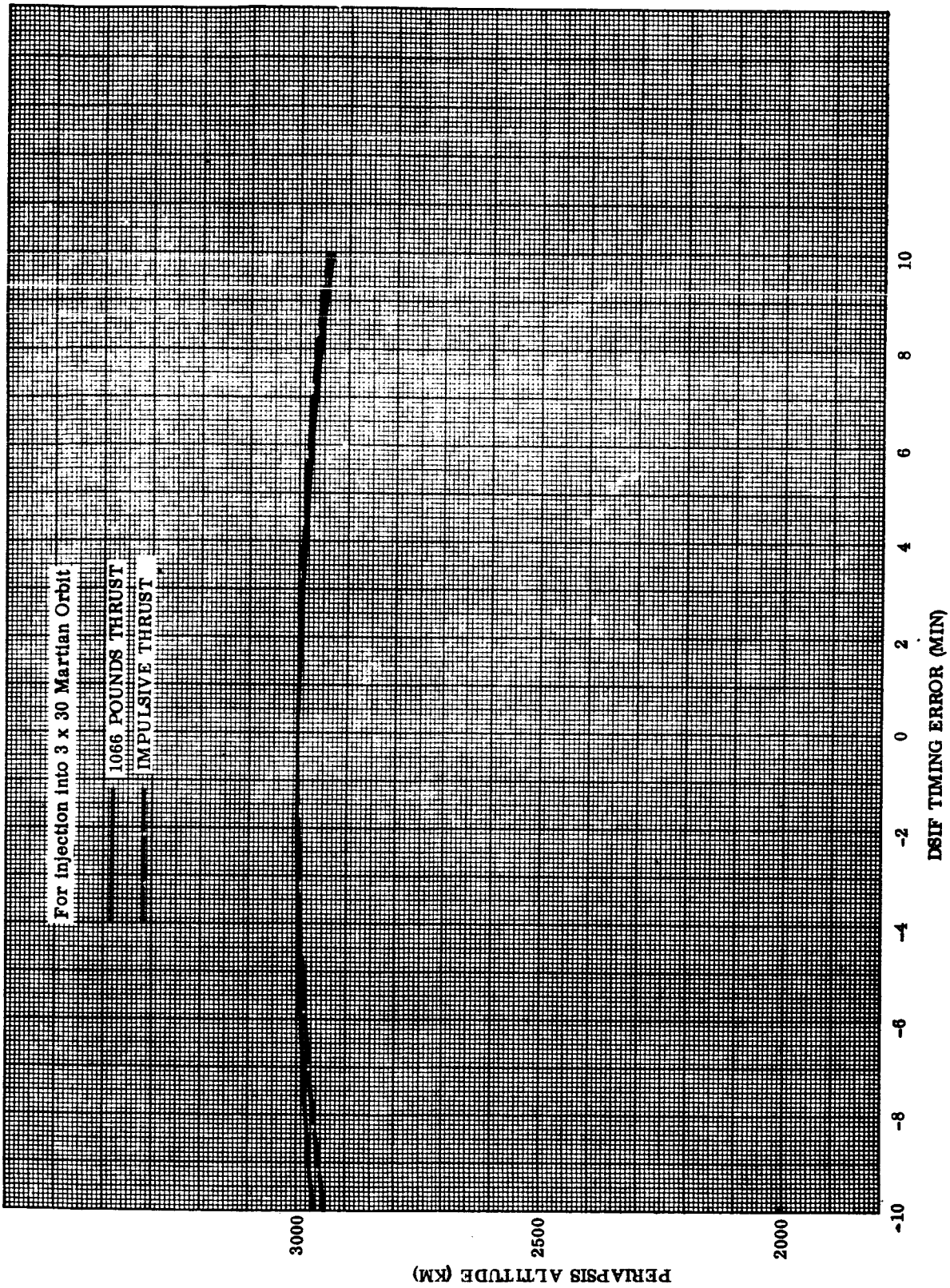

Figure 5-9. Periapsis Altitude vs DSIF Timing Error

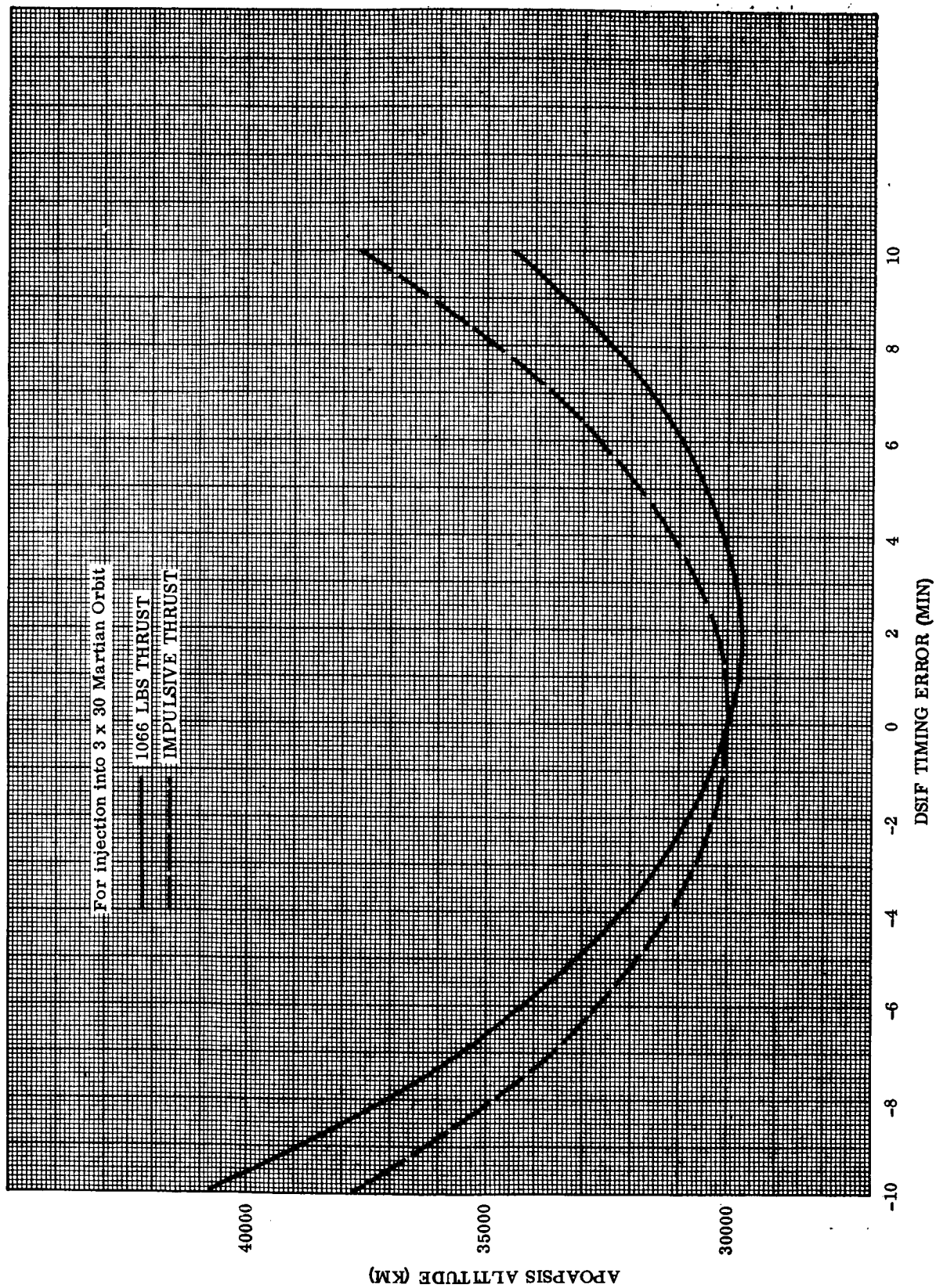

Figure 5-10. Apoapsis Altitude vs DSIF Timing Error

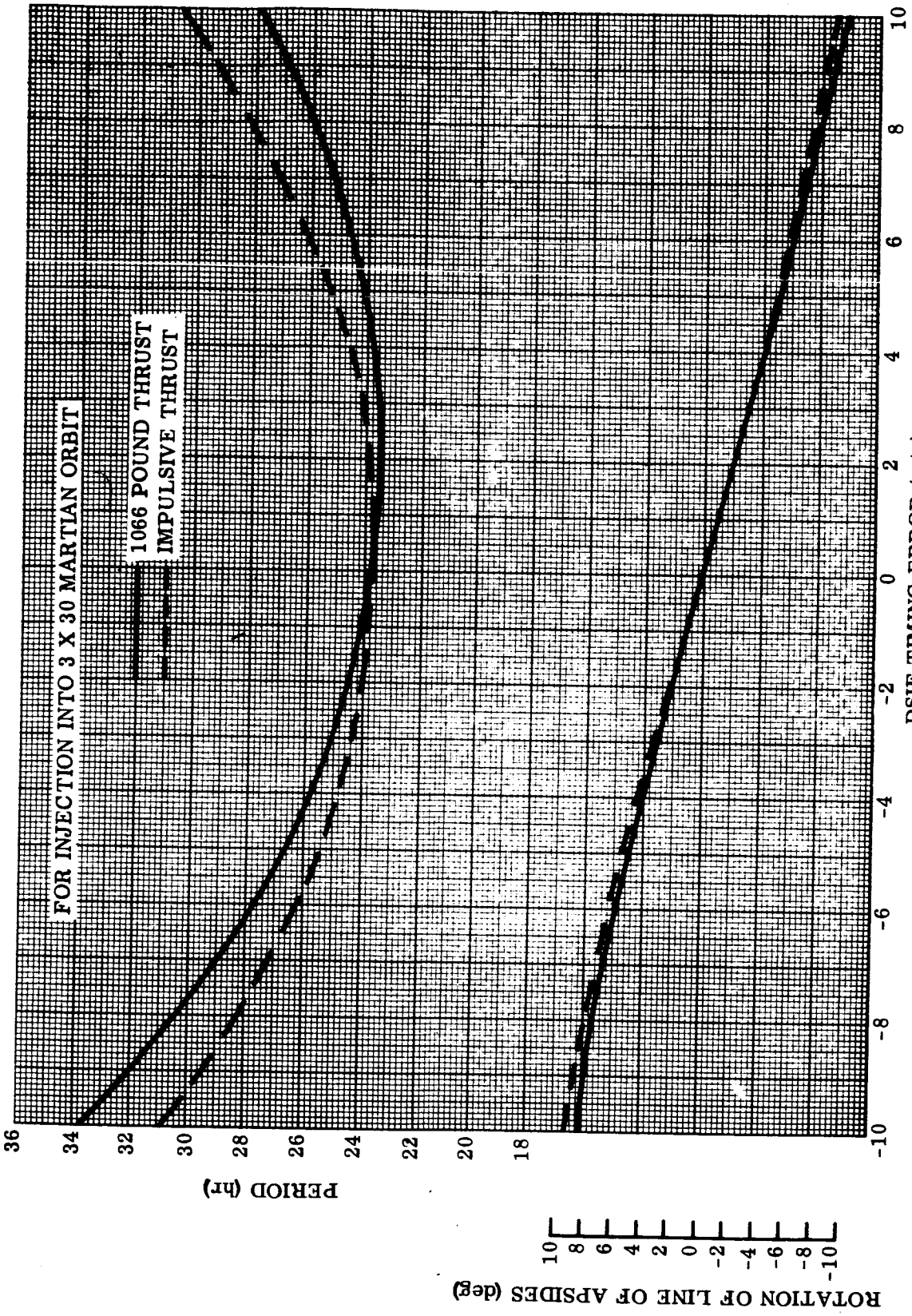

Figure 5-11. Period and Rotation of the Line of Apsides vs DSIF Timing Error

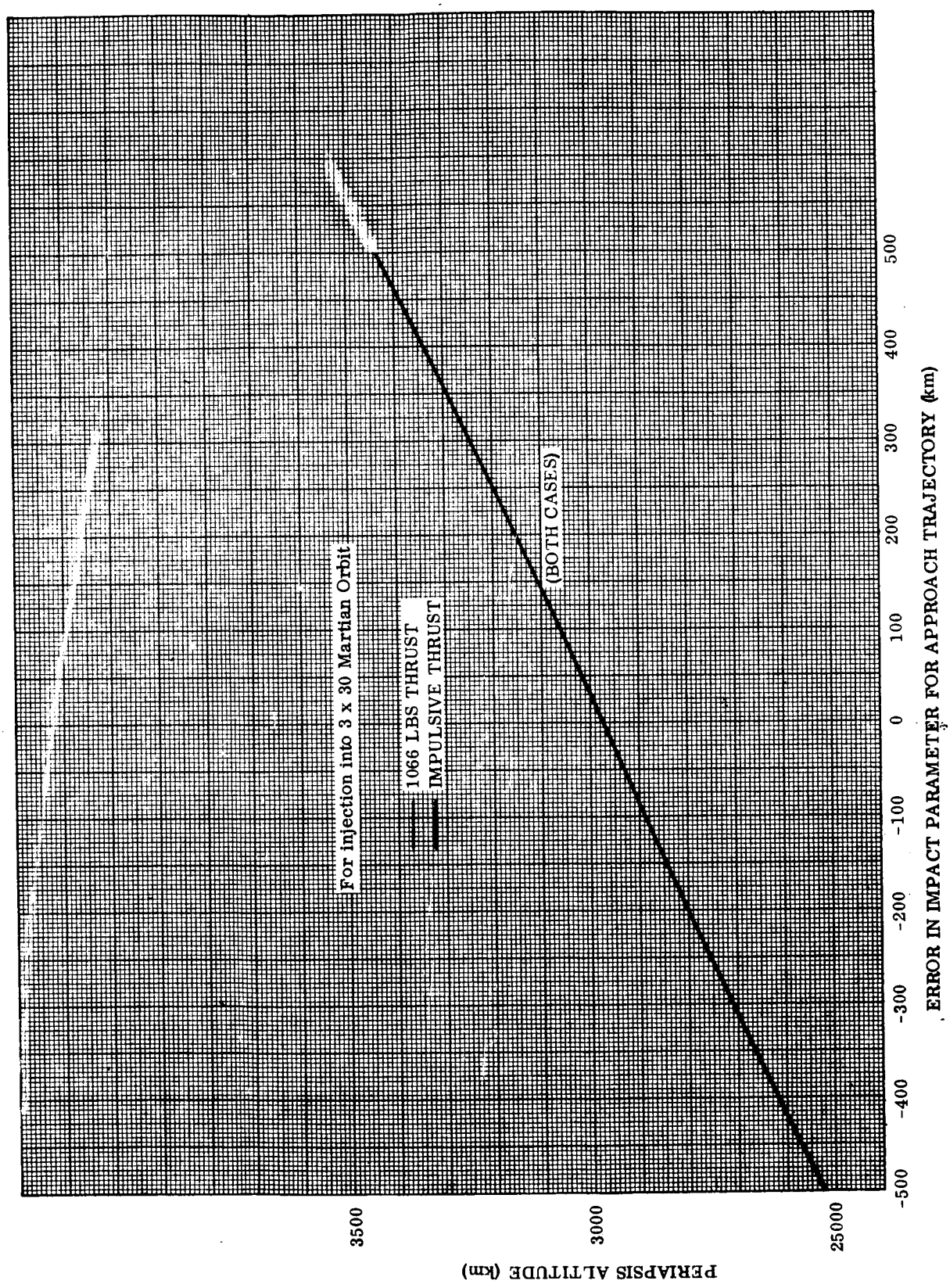

Figure 5-12. Periapsis Altitude vs Error in Impact Parameter

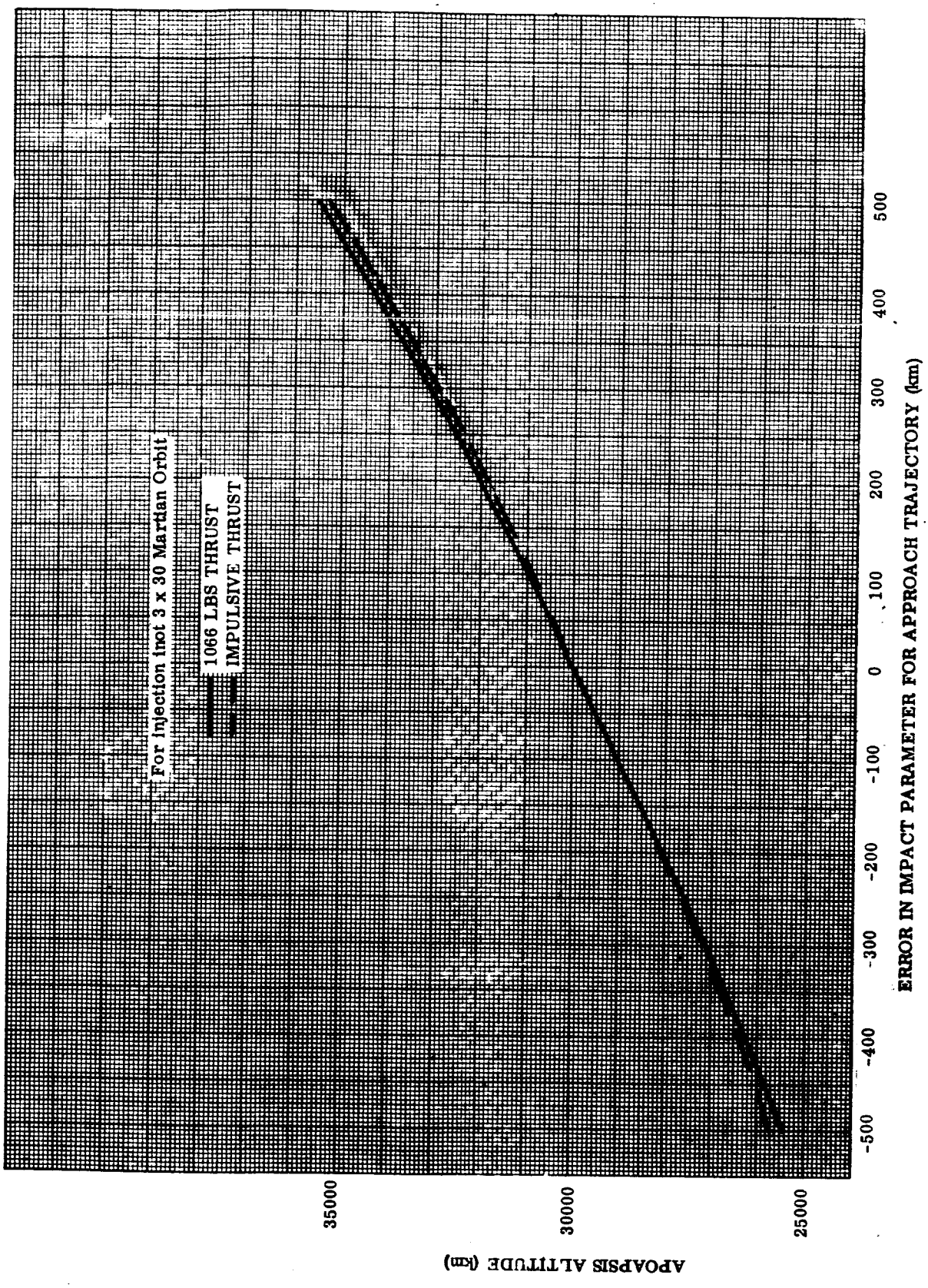

Figure 5-13. Apoapsis Altitude vs Error in Impact Parameter

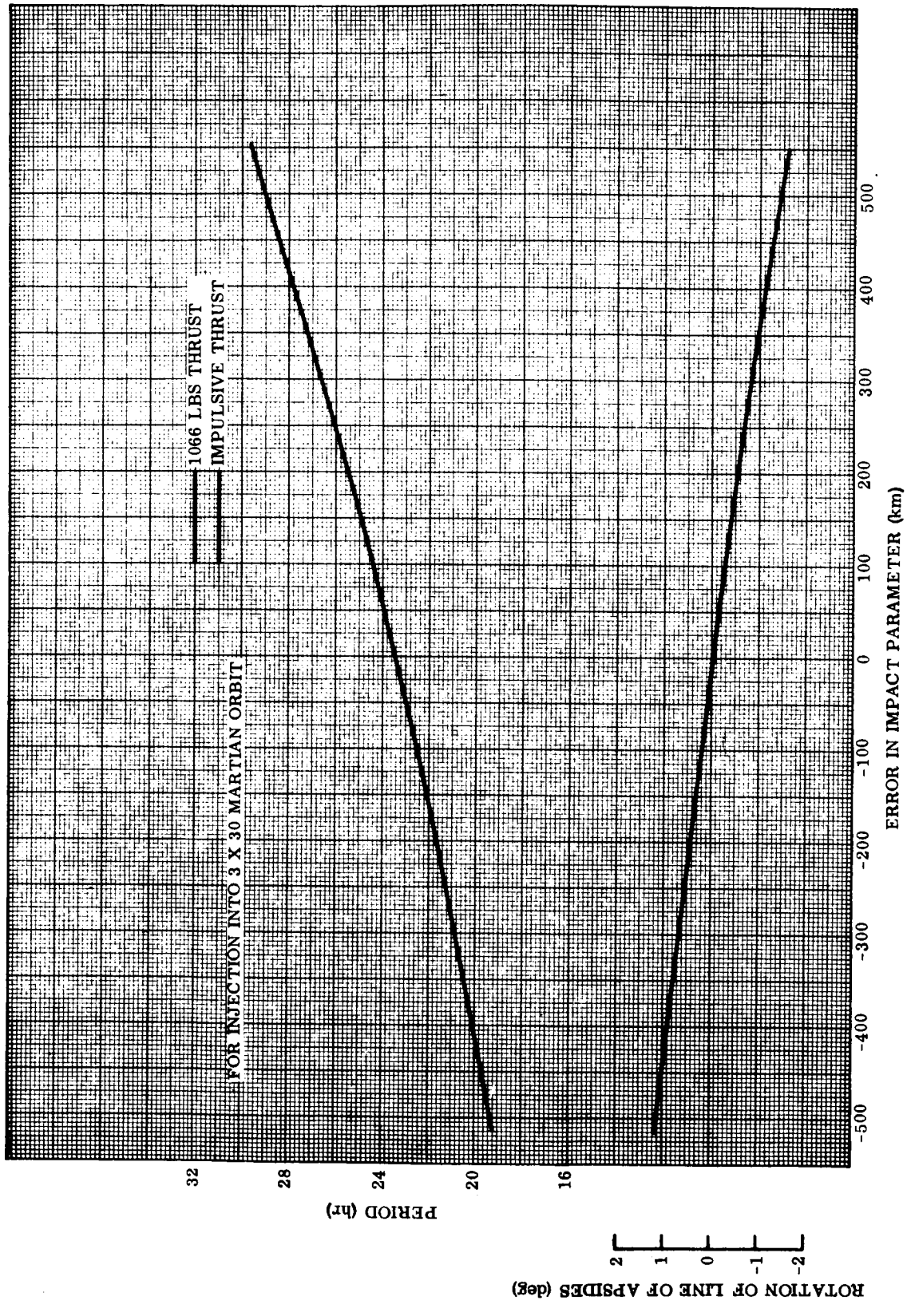

Figure 5-14. Period and Rotation of the Line of Apsides vs Error in Impact Parameter

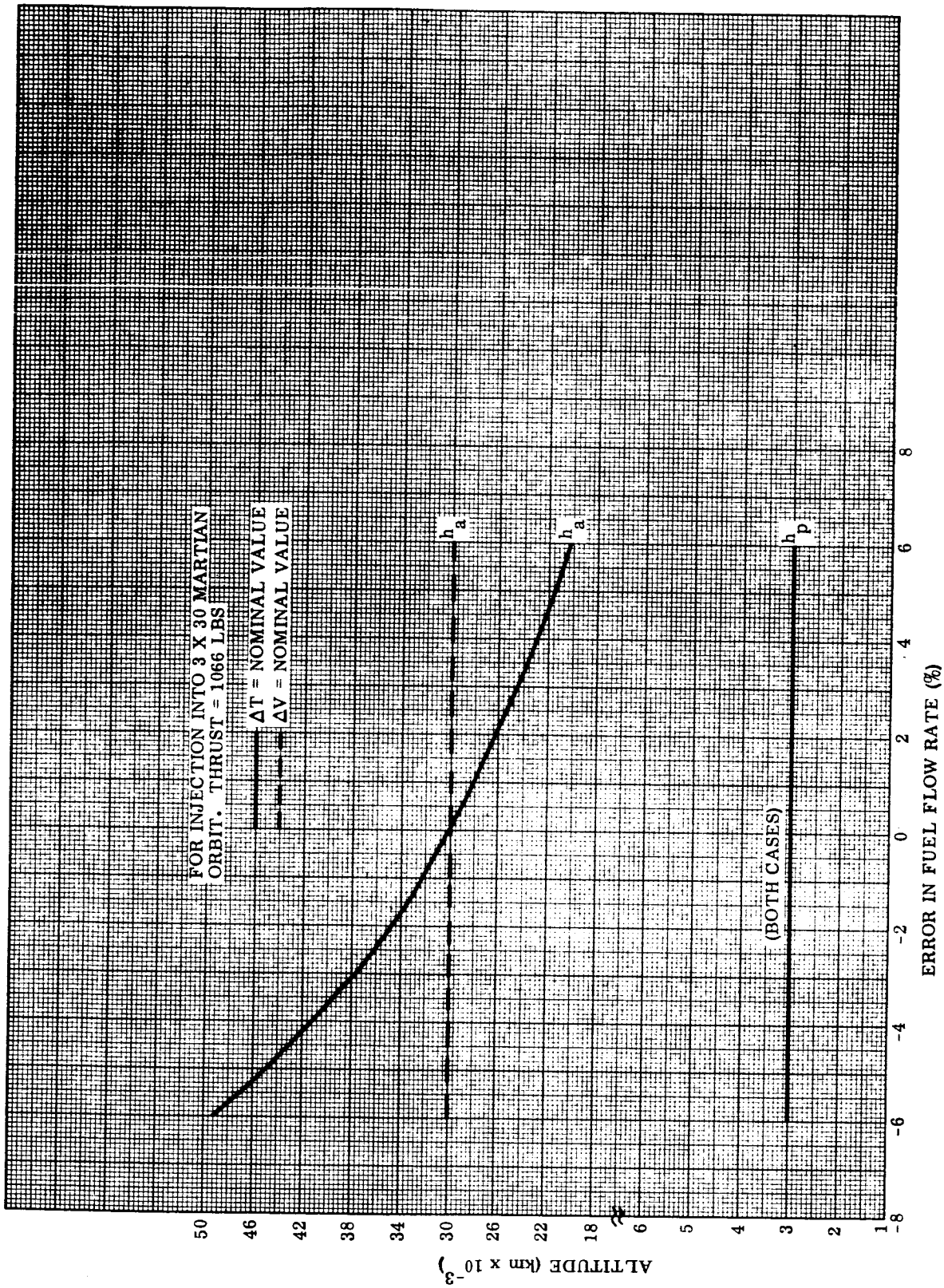

Figure 5-15. Apoapsis Altitude, h_a, and Periapsis Altitude, h_p, vs Error in Fuel Flow Rate

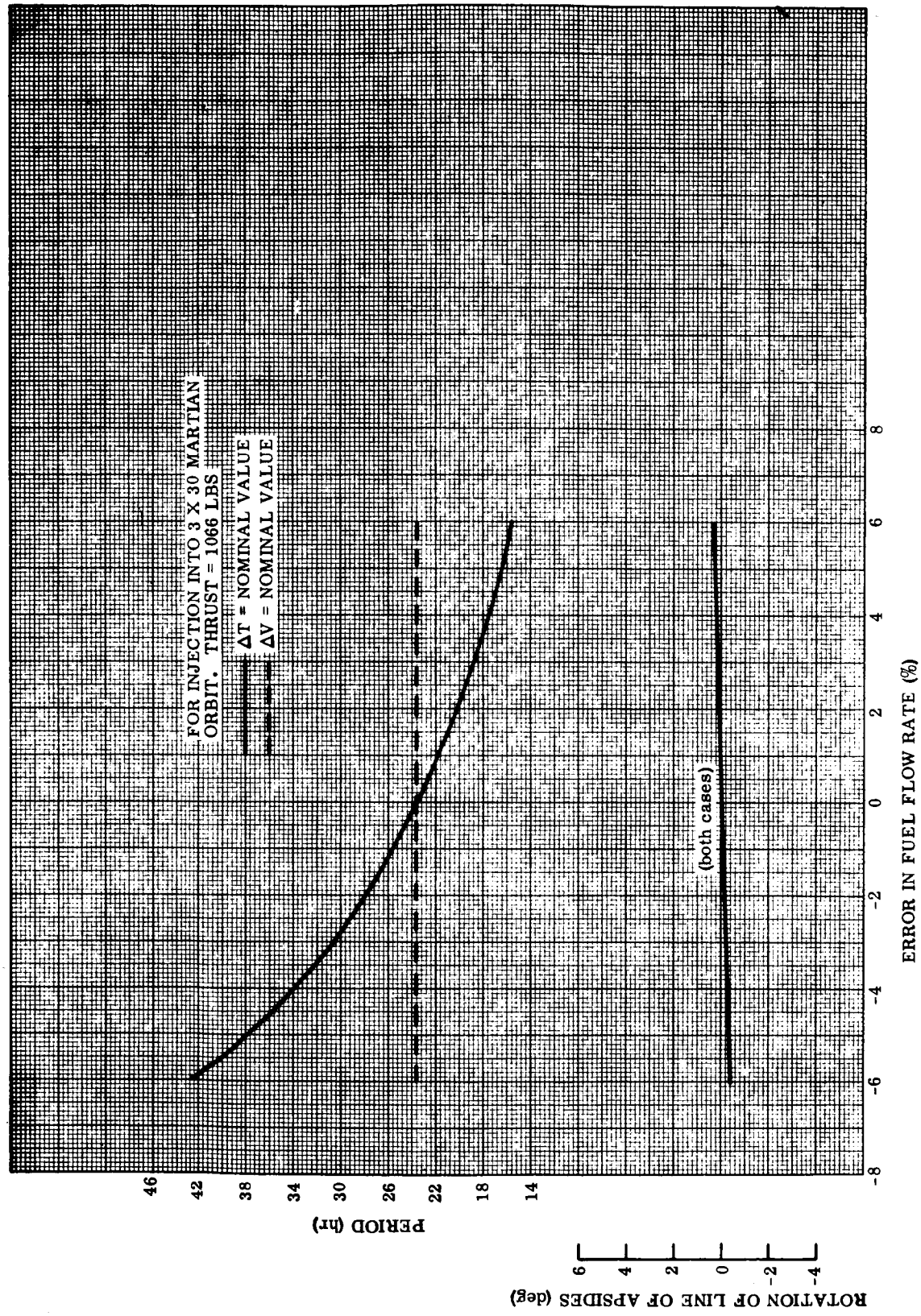

Figure 5-16. Period and Rotation of the Line of Apsides vs Error in Fuel Flow Rate

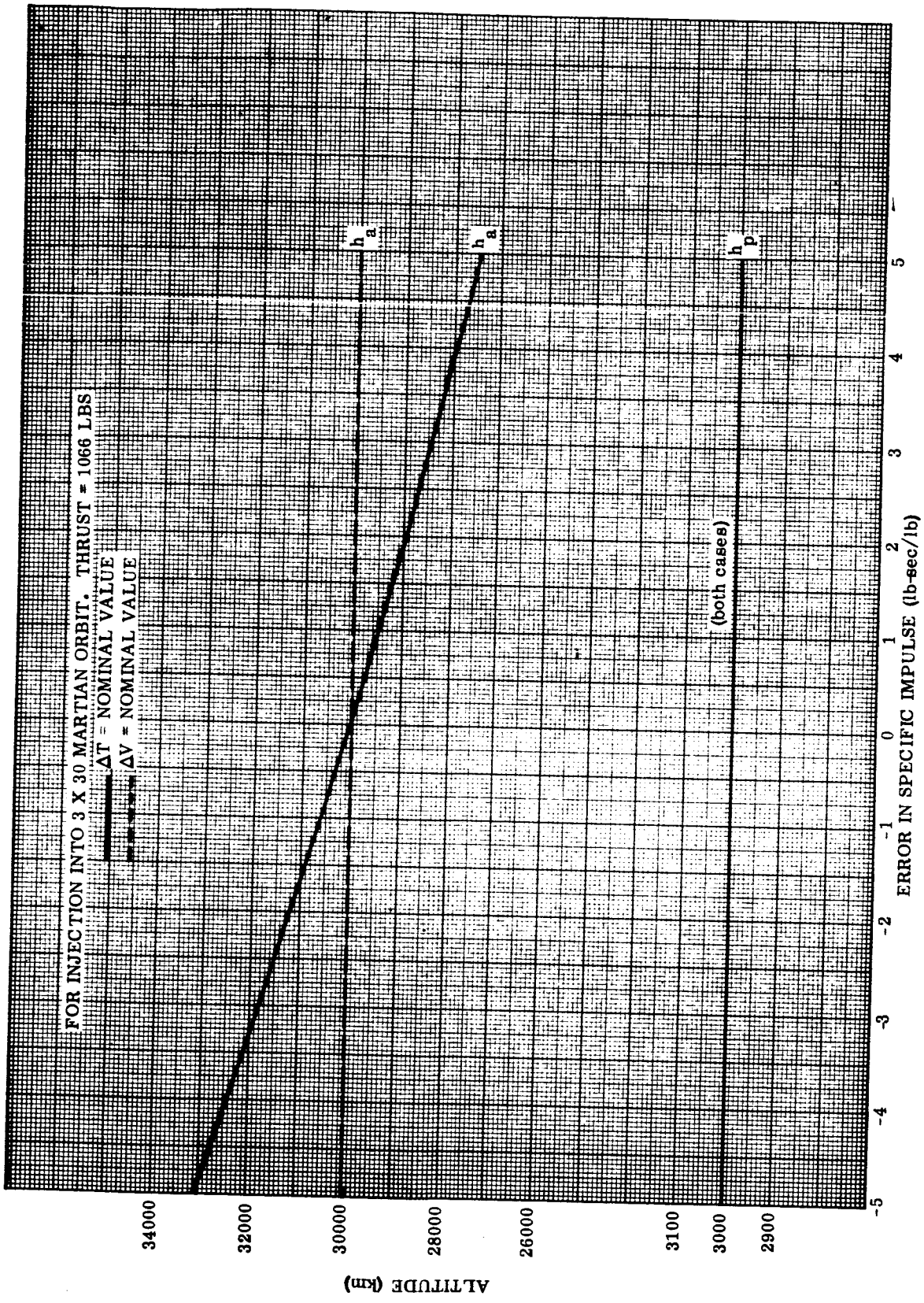

Figure 5-17. Apoapsis Altitude, h_a, and Periapsis Altitude, h_p, vs Error in Specific Impulse

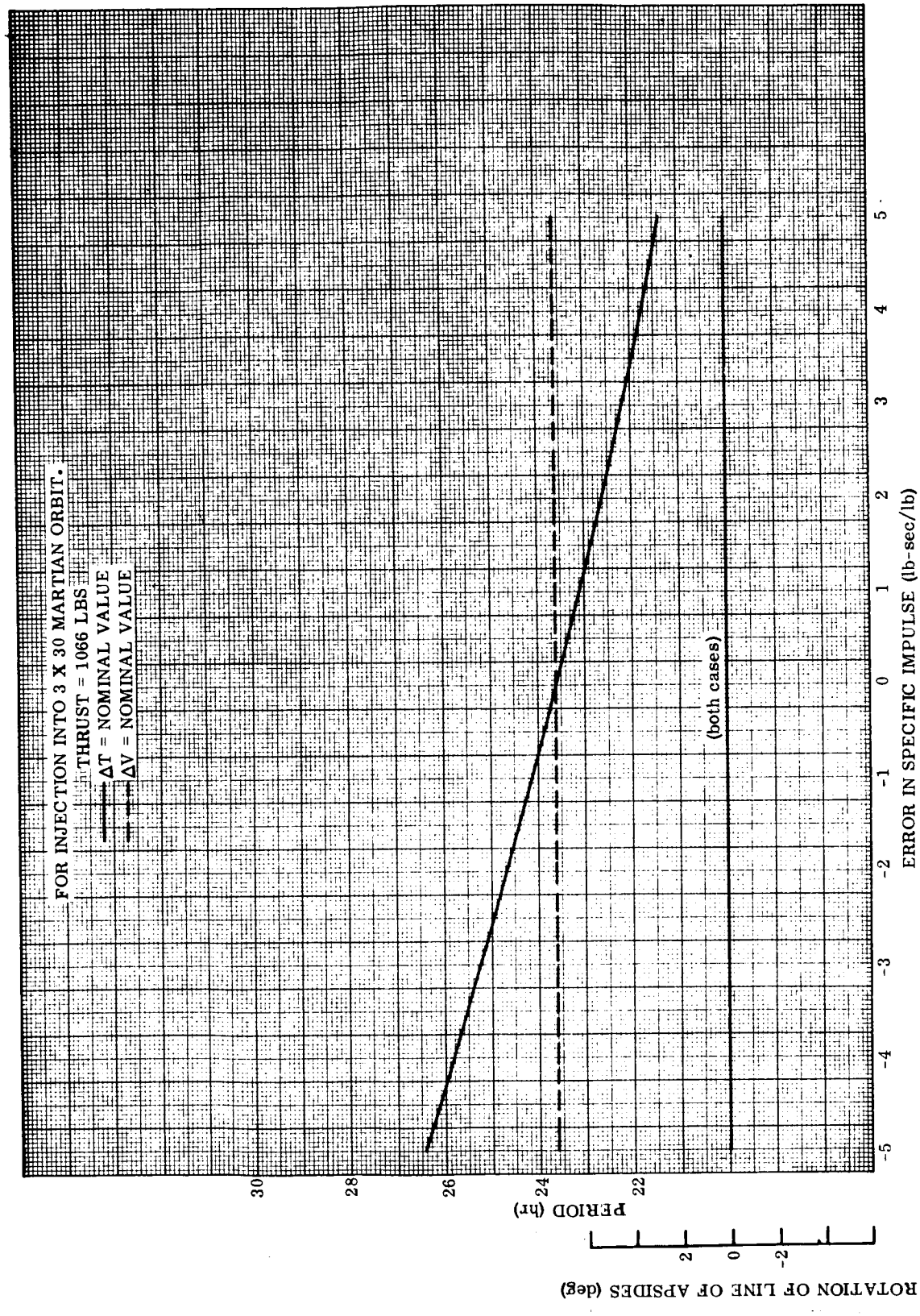

Figure 5-18. Period and Rotation of the Line of Apsides vs Error in Specific Impulse

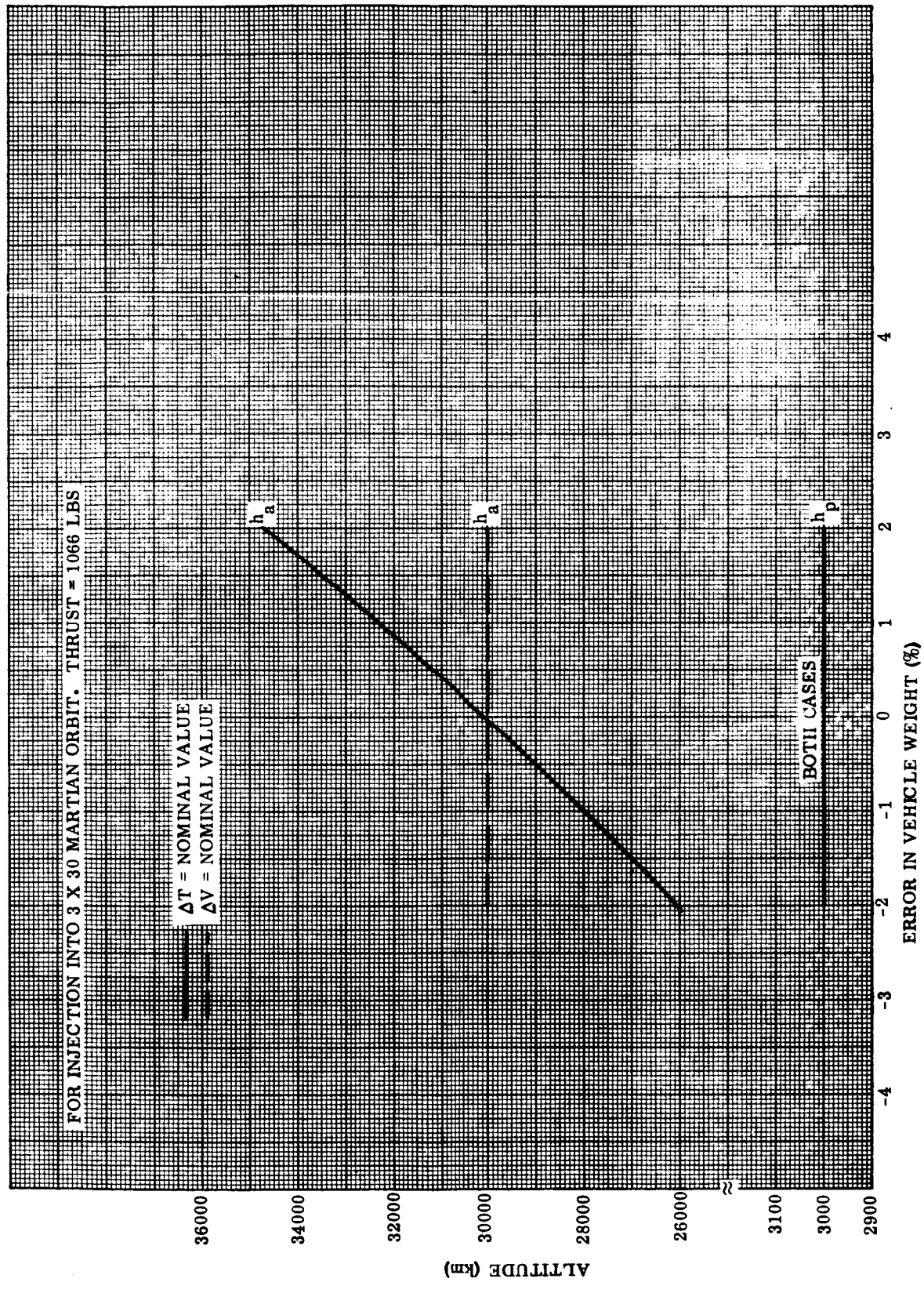

Figure 5-19/20. Apoapsis Altitude, h_a, and Periapsis Altitude, h_p, vs Error in Vehicle Weight

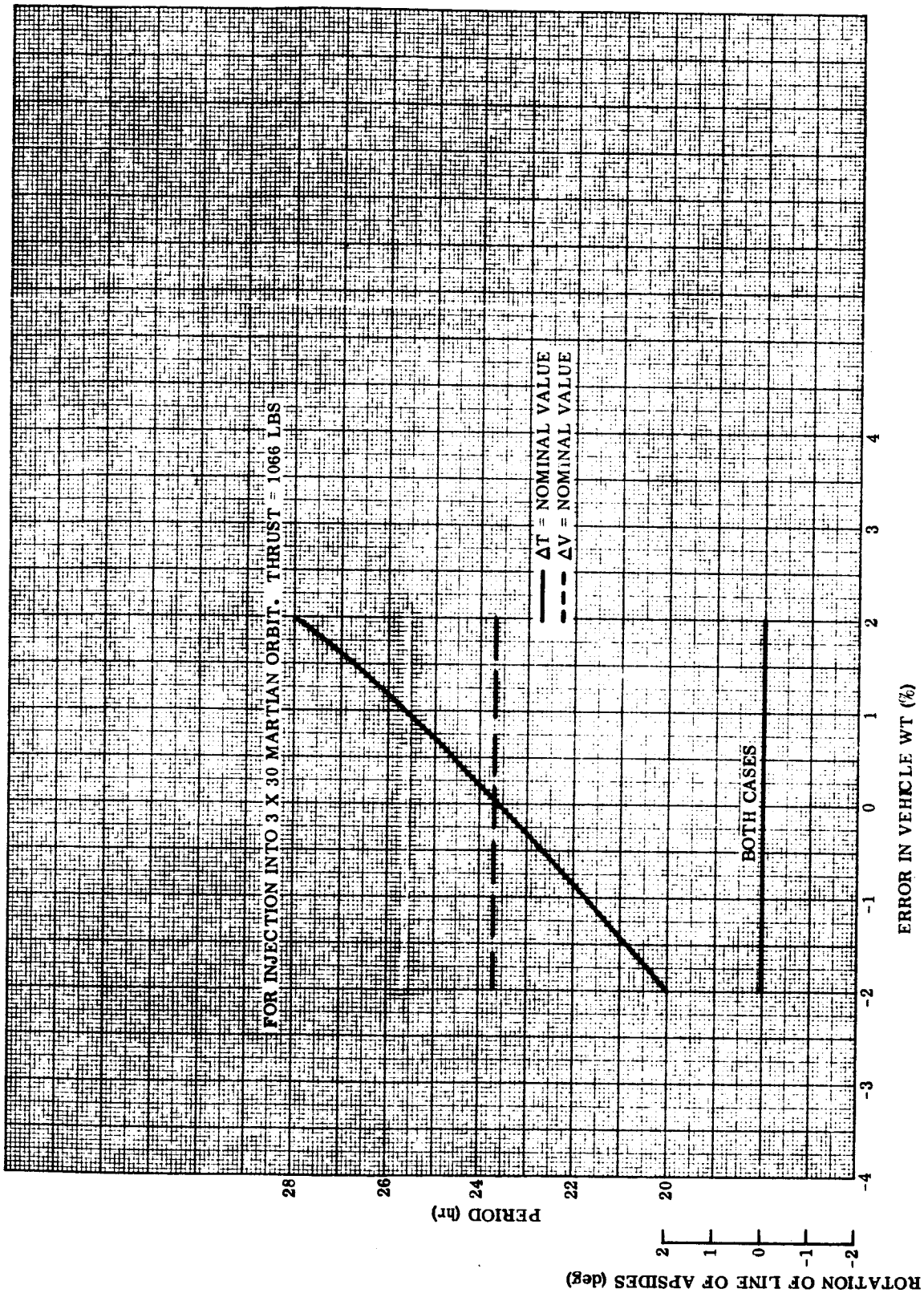

Figure 5-21. Period and Rotation of the Line of Apsides vs Error in Vehicle Weight

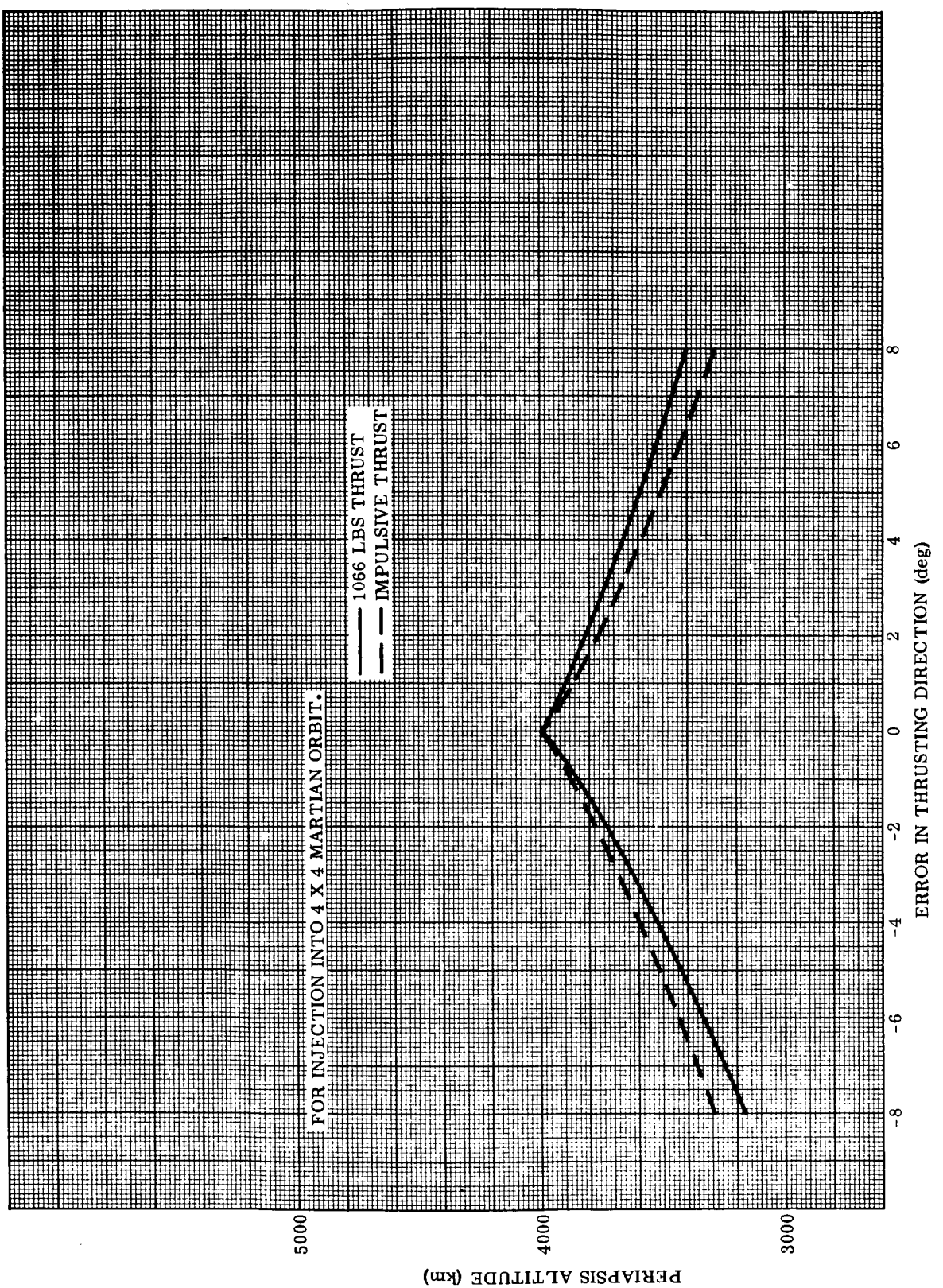

Figure 5-22. Periapsis Altitude vs Error in Thrusting Direction

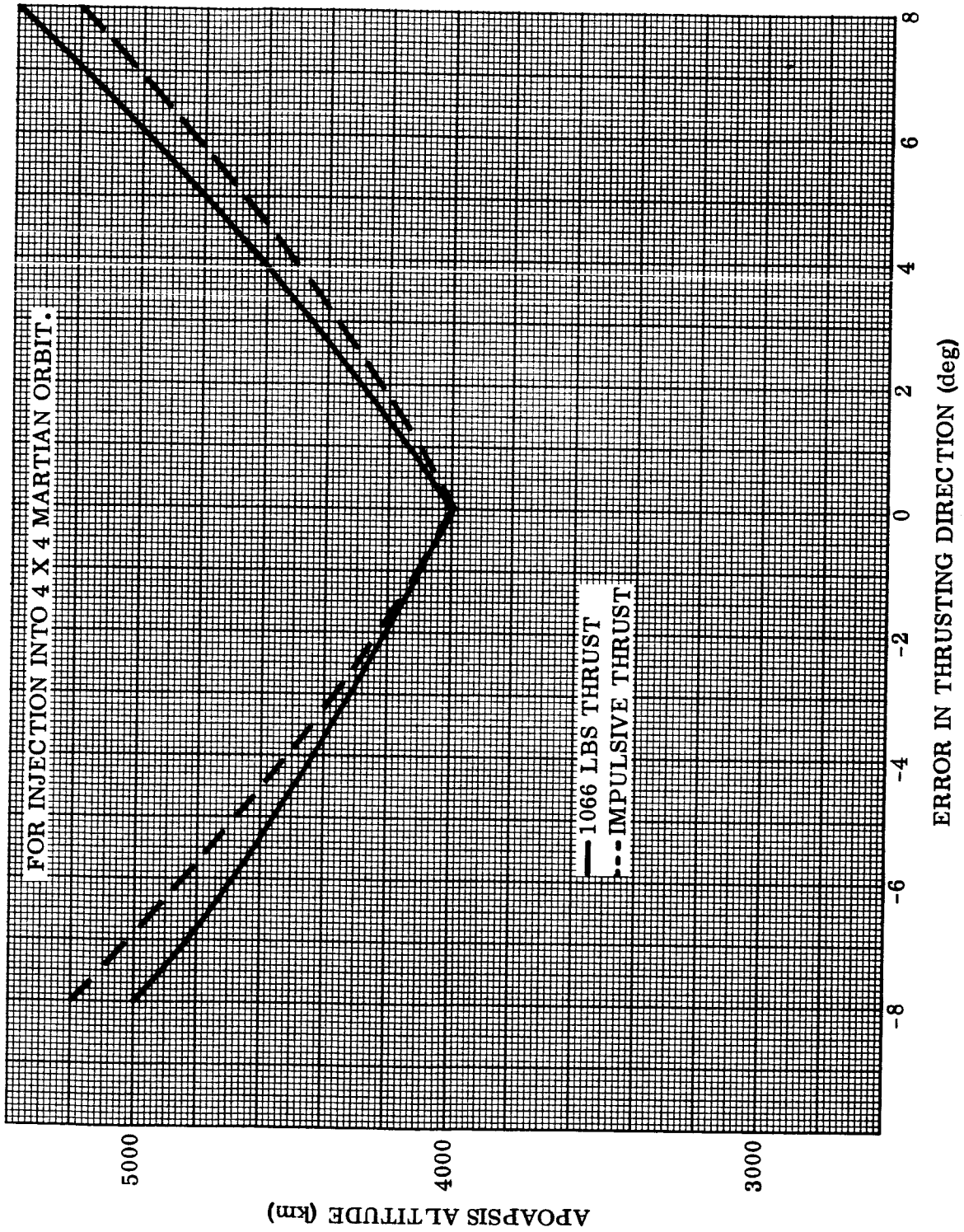

Figure 5-23. Apoapsis Altitude vs Error in Thrusting Direction

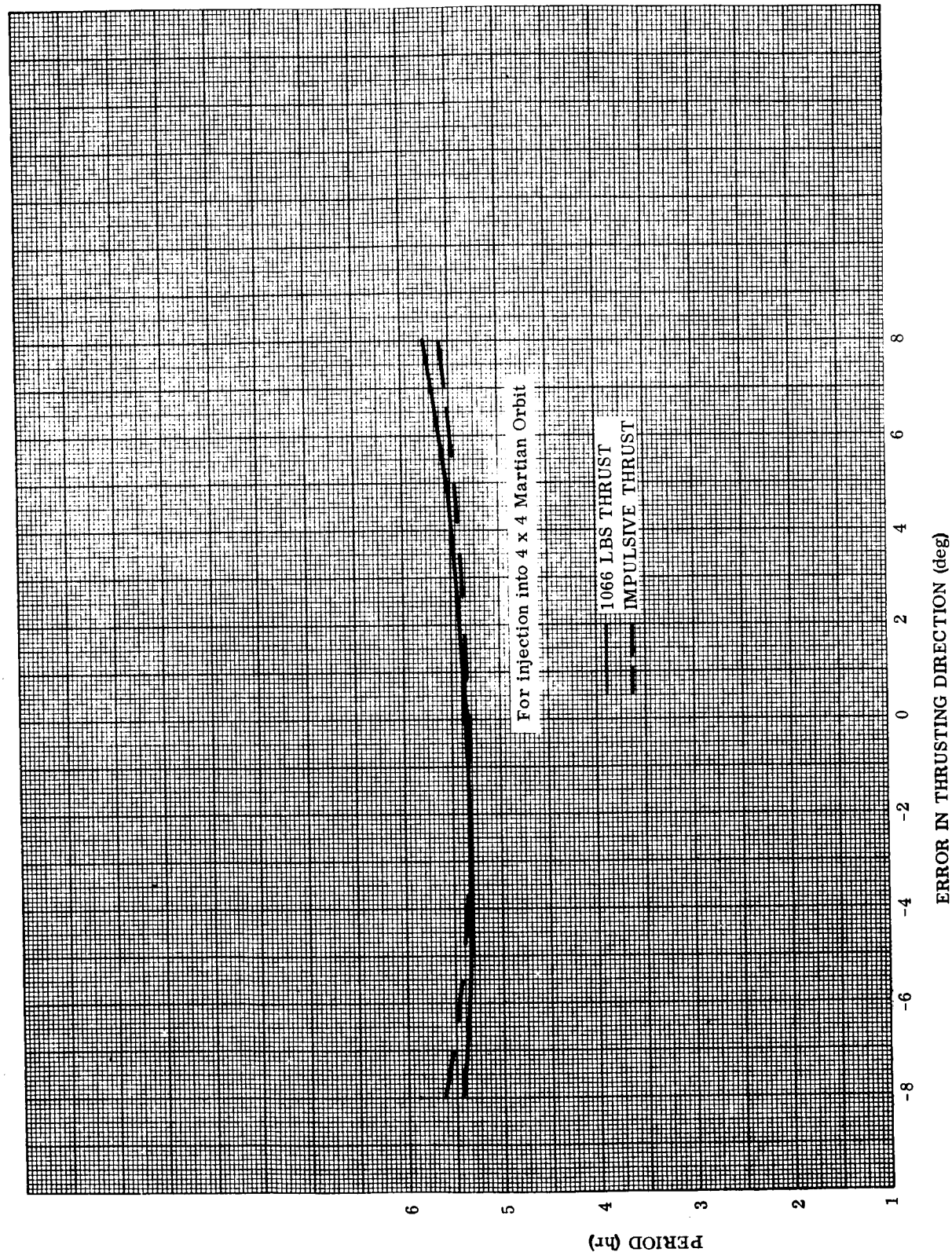

Figure 5- 24. Period vs Error in Thrusting Direction

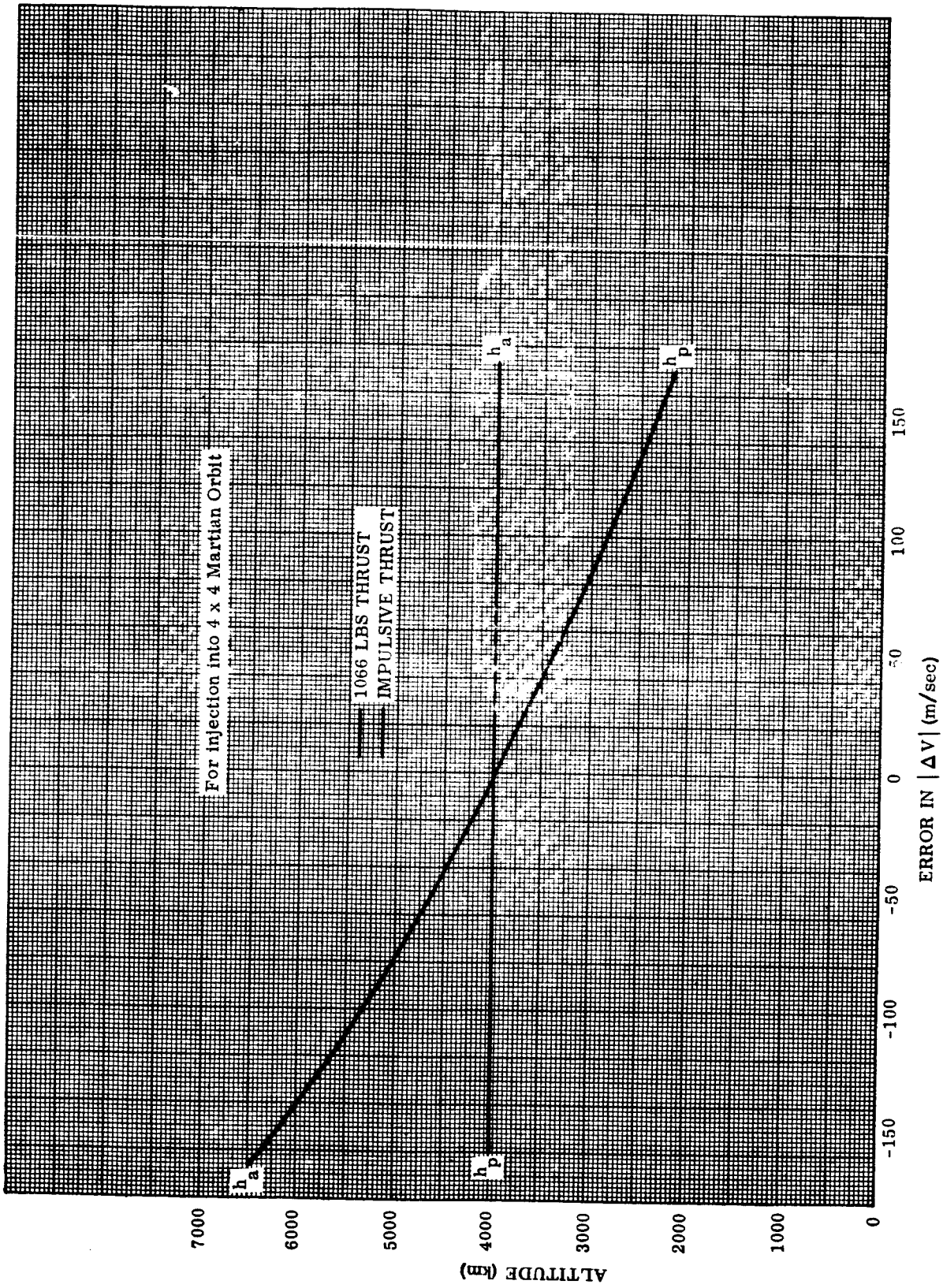

Figure 5-25. Apoapsis Altitude, h_a, and Periapsis Altitude, h_p, vs Error in Velocity Increment Measurement

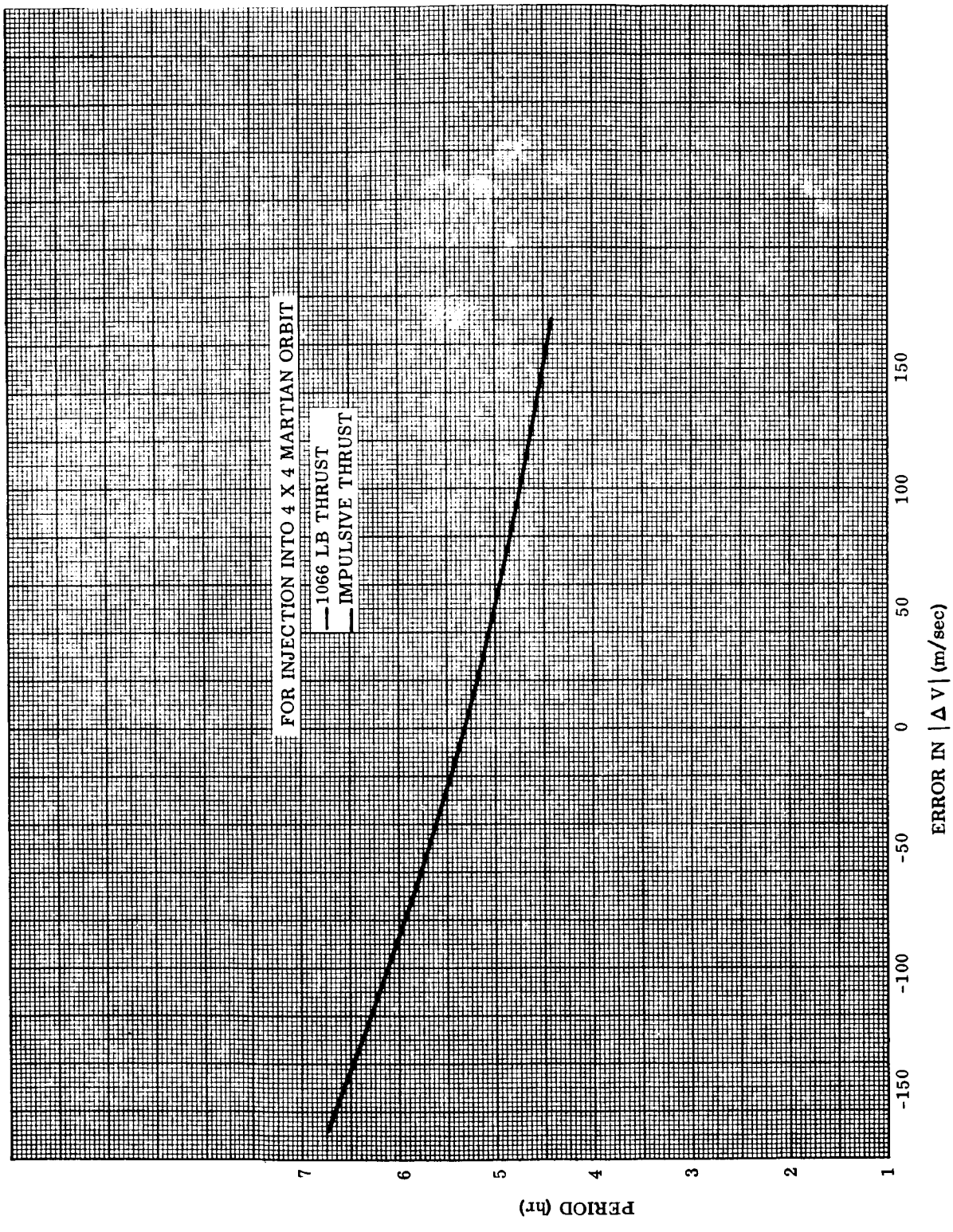

Figure 5-26. Period vs Error in Velocity Increment Measurement

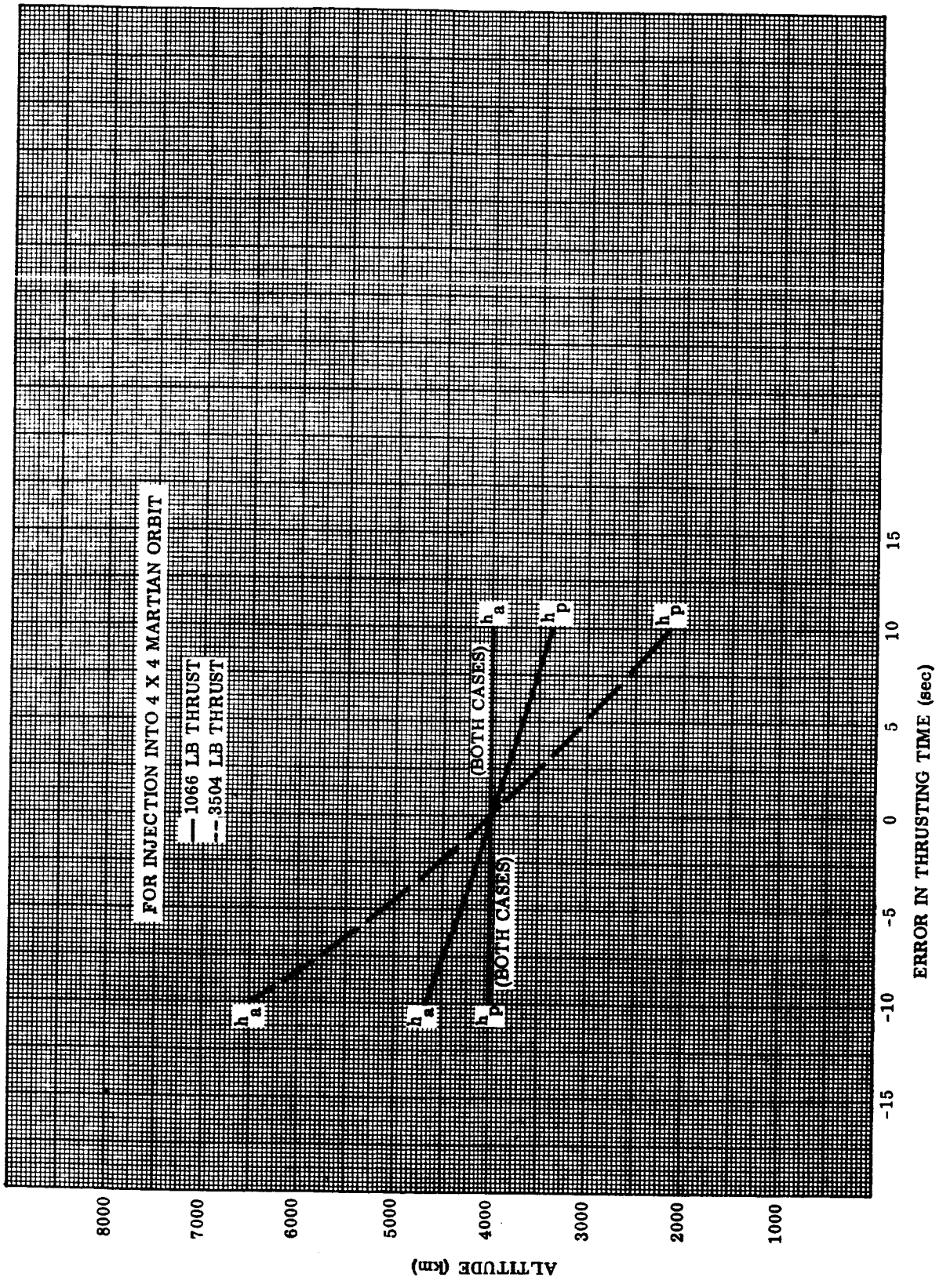

Figure 5-27. Apoapsis Altitude, h_a, and Periapsis Altitude, h_p, vs Error in Thrusting Time

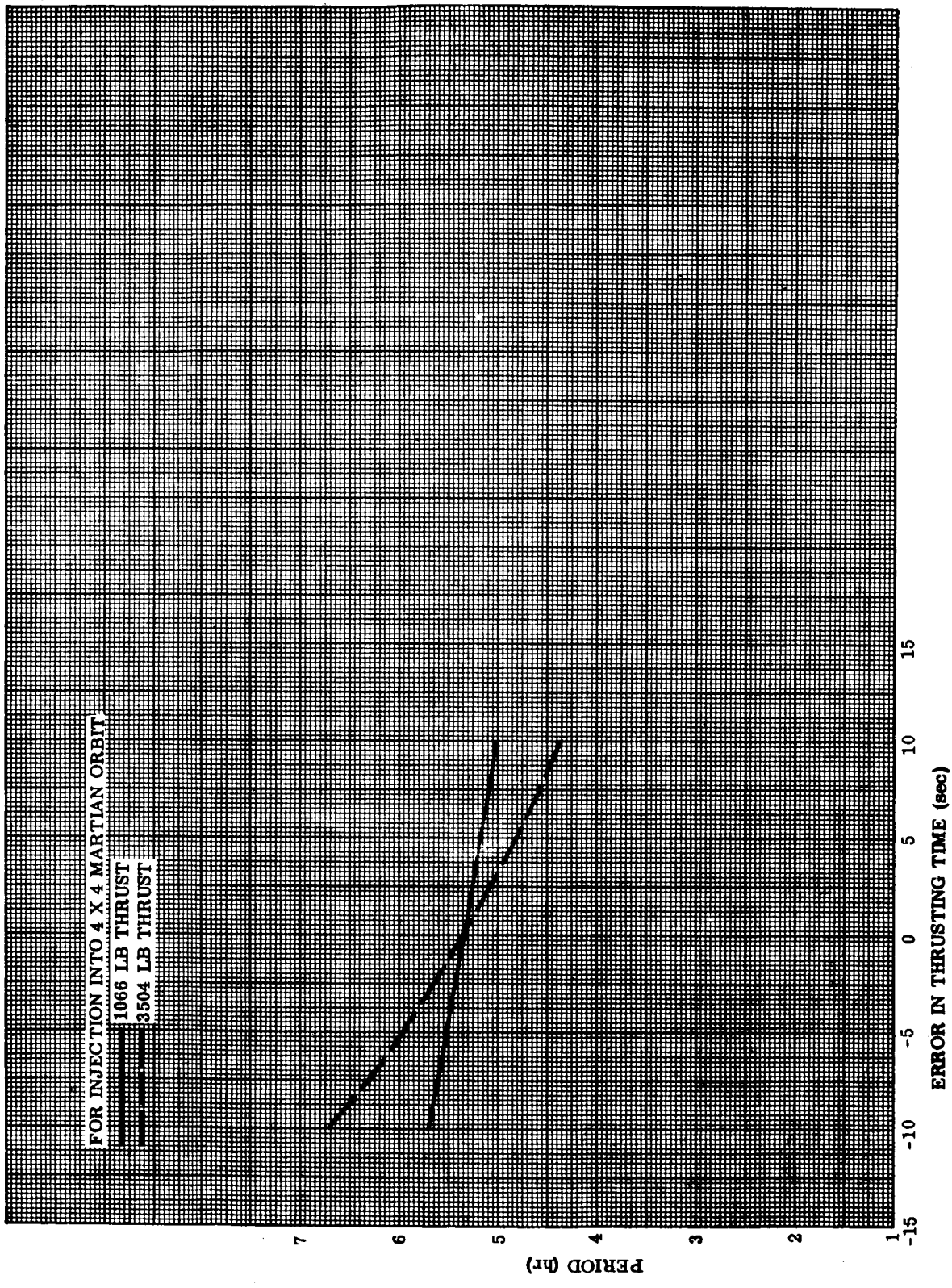

Figure 5-28. Period vs Error in Thrusting Time

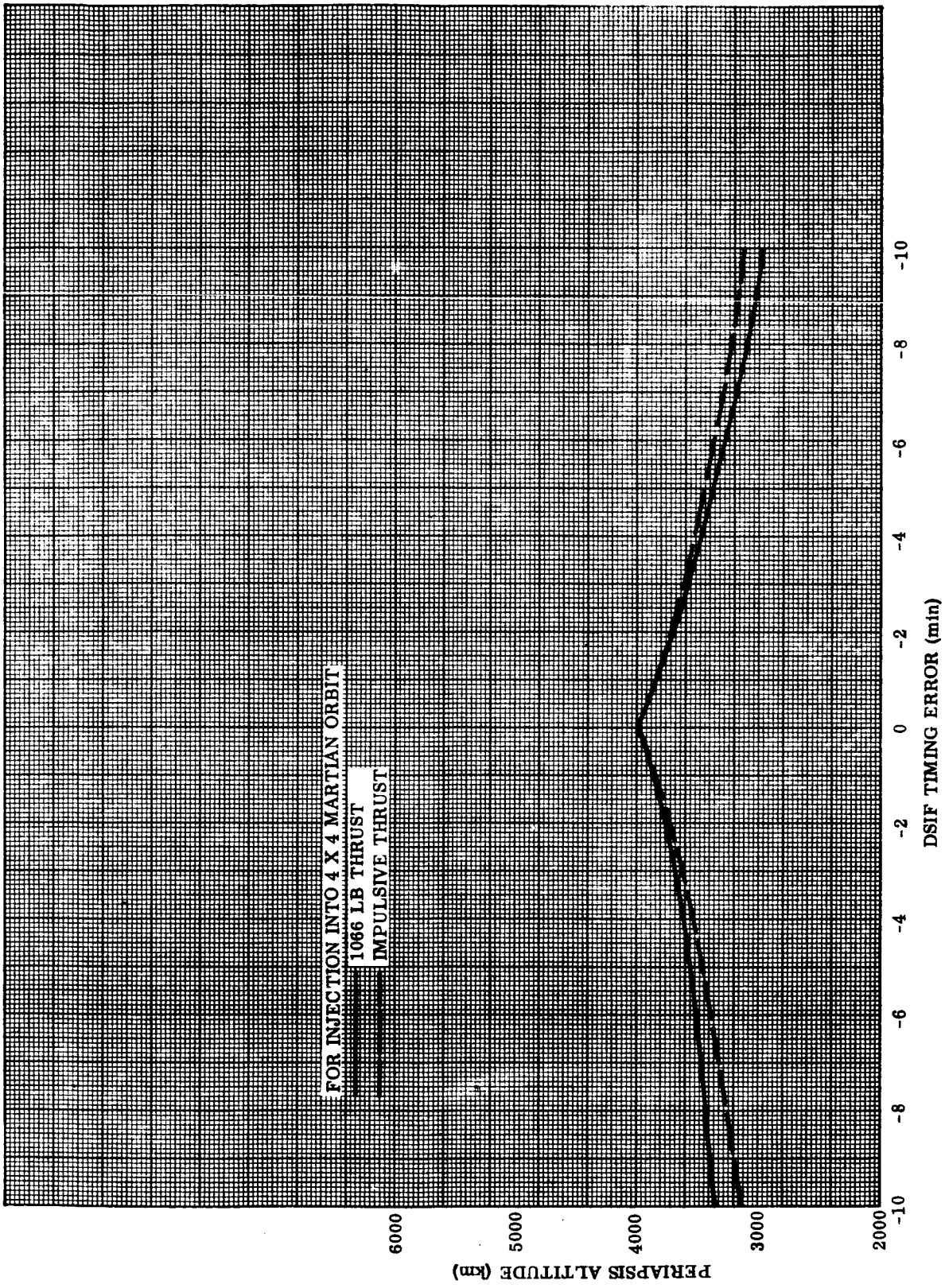

Figure 5-29. Periapsis Altitude vs DSIF Timing Error

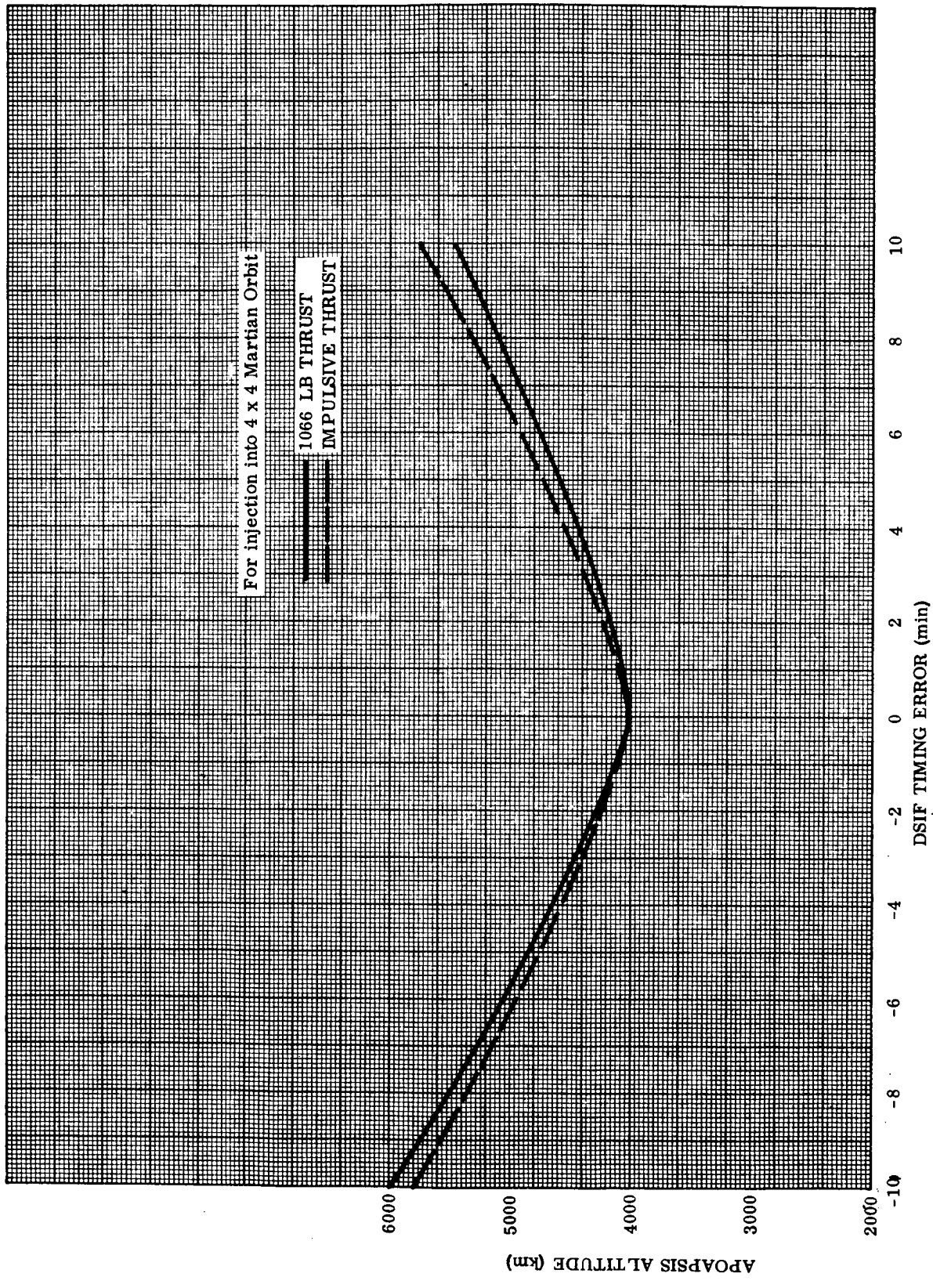

Figure 5-30. Apoapsis Altitude vs DSIF Timing Error

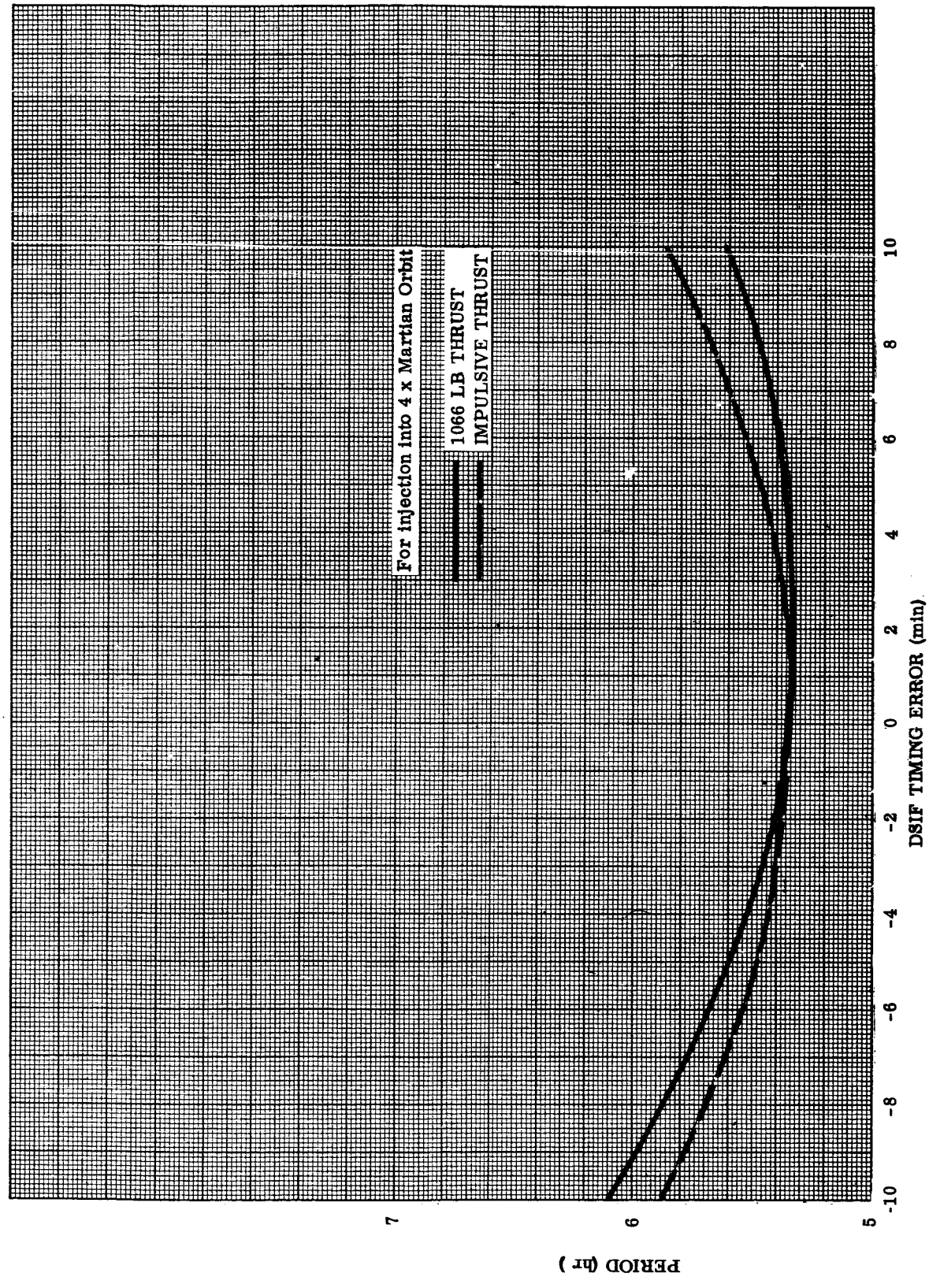

Figure 5-31. Period vs DSIF Timing Error

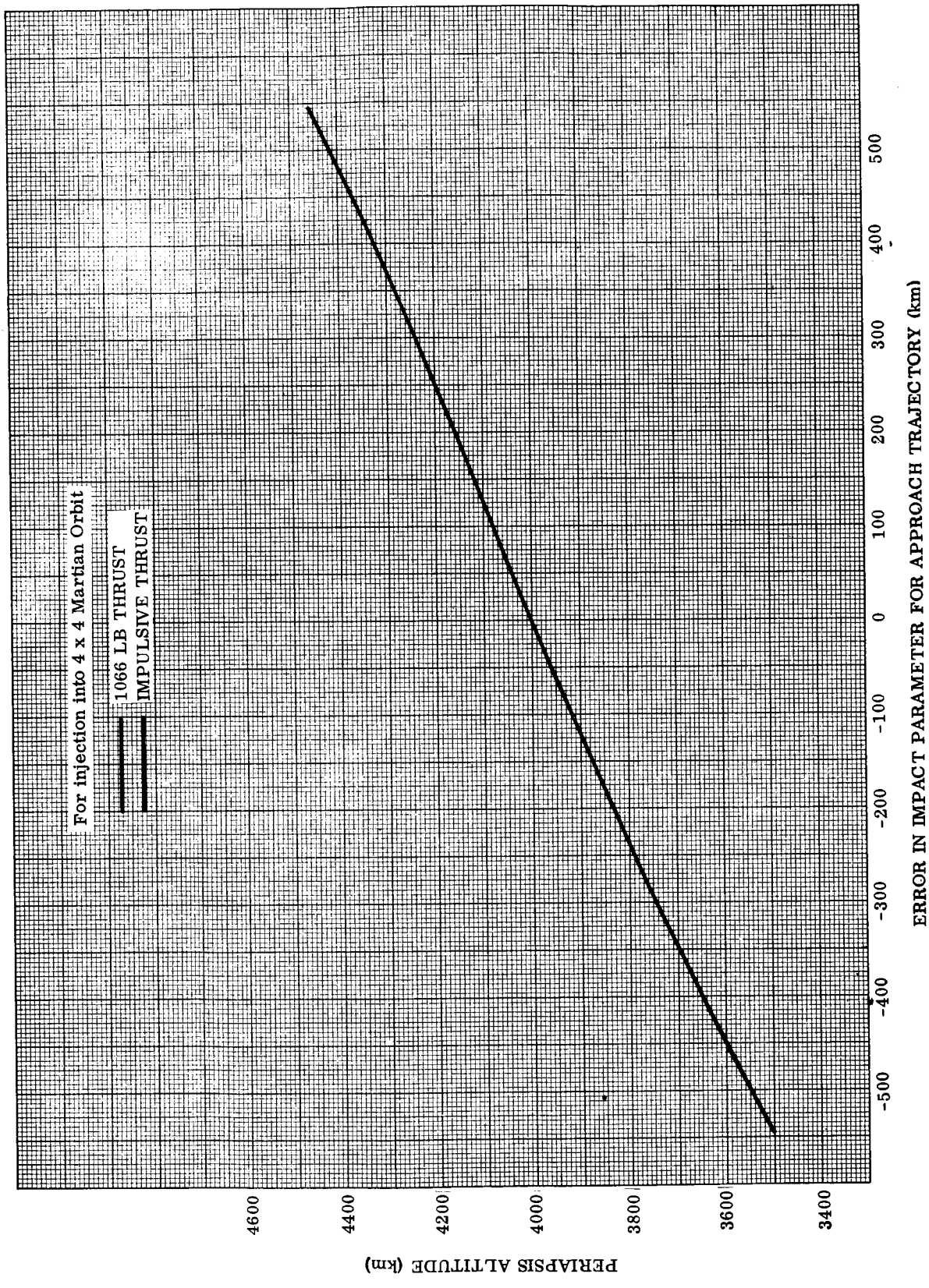

Figure 5-32. Periapsis Altitude vs Error in Impact Parameter

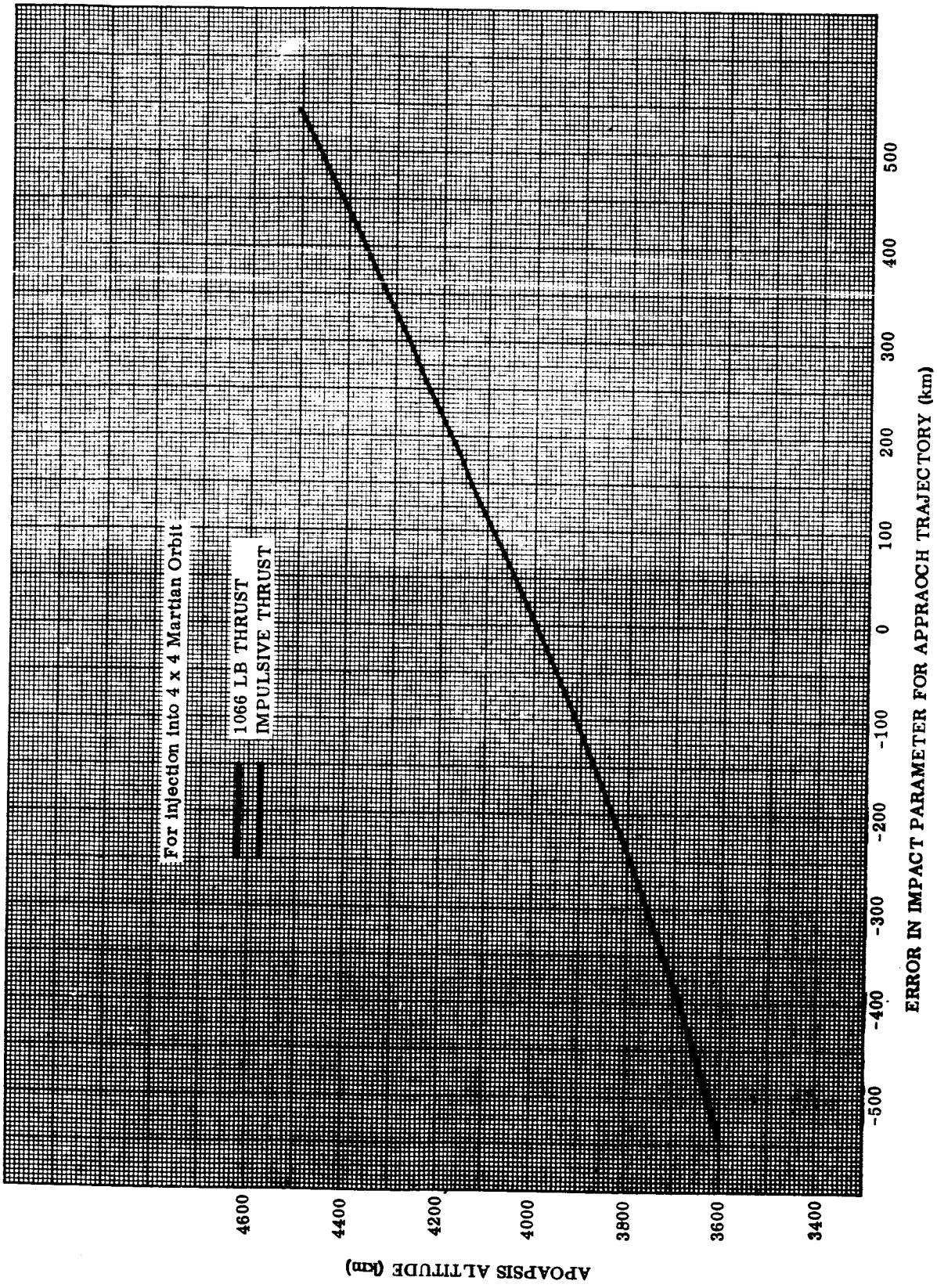

Figure 5-33. Apoapsis Altitude vs Error in Impact Parameter

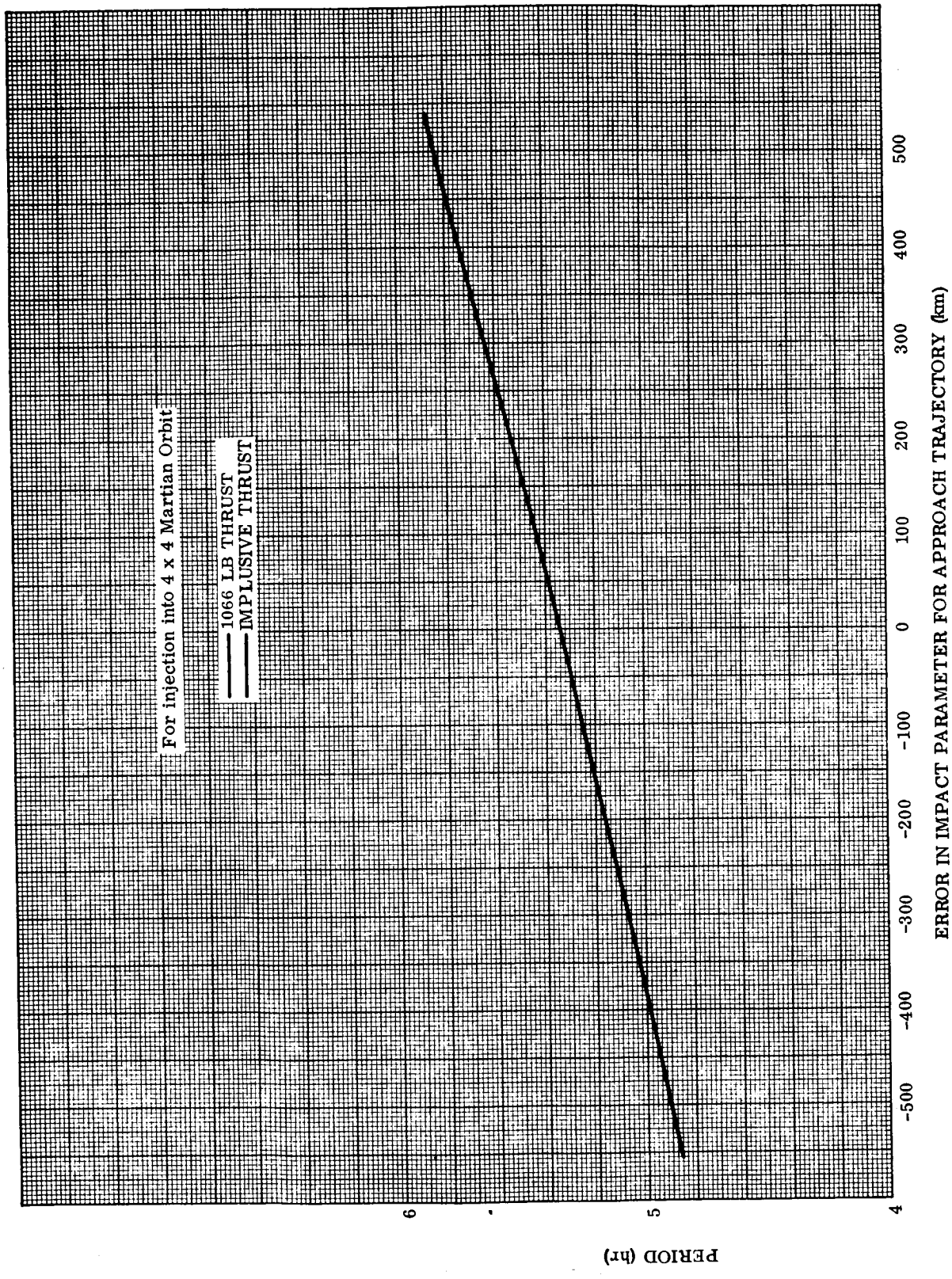

Figure 5-34. Period vs Error in Impact Parameter

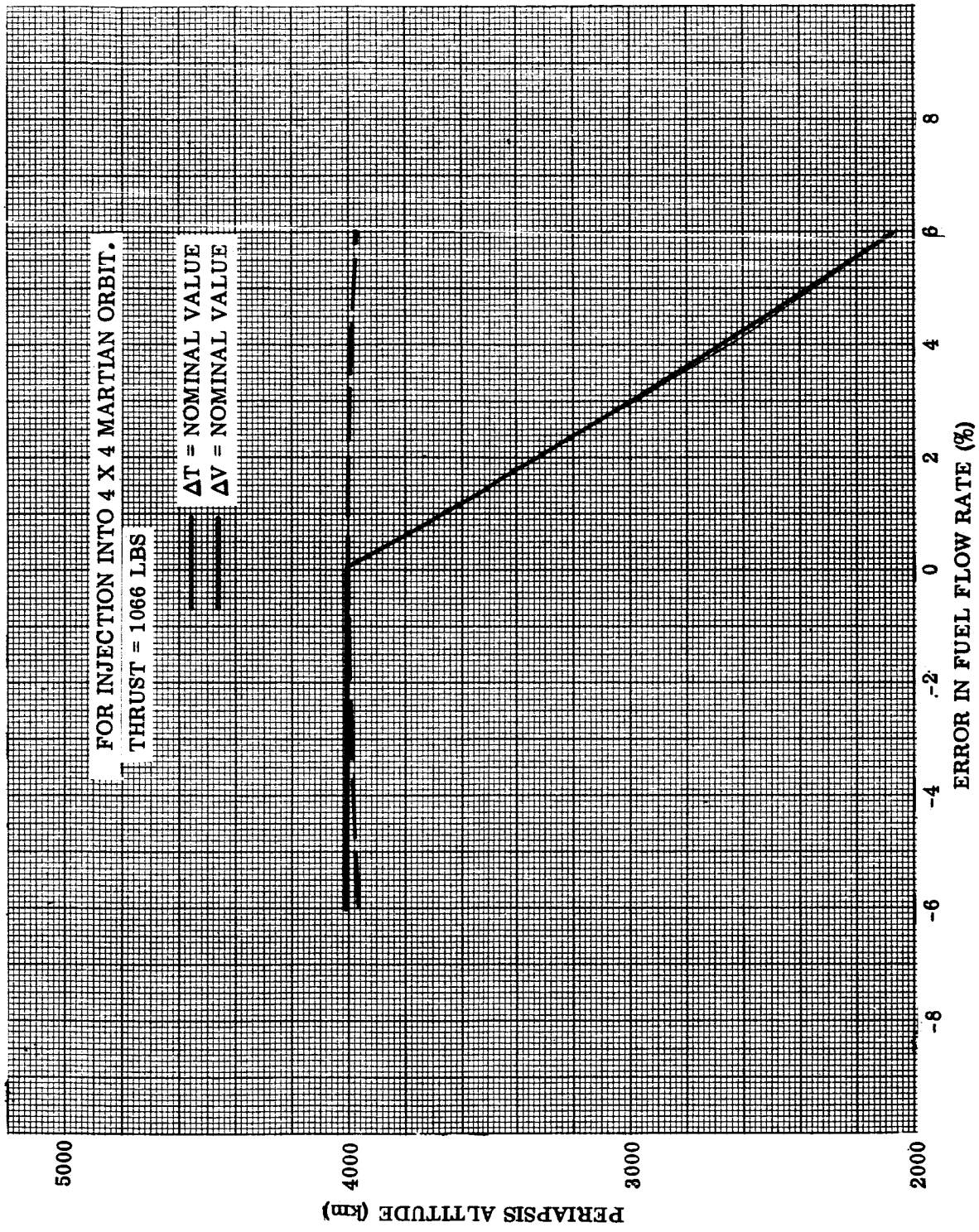

Figure 5-35. Periapsis Altitude vs Error in Fuel Flow Rate

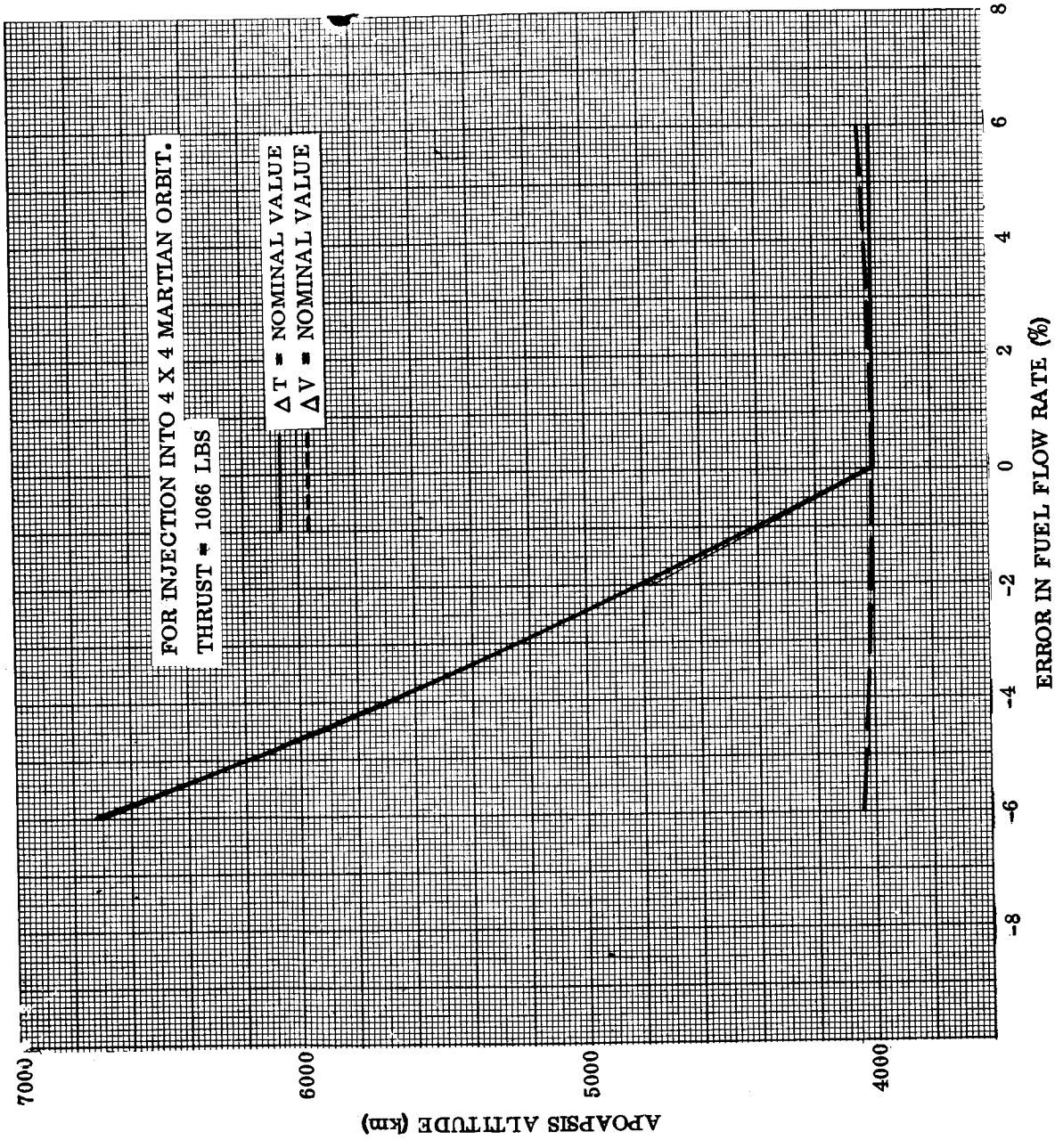

Figure 5-36. Apoapsis Altitude vs Error in Fuel Flow Rate

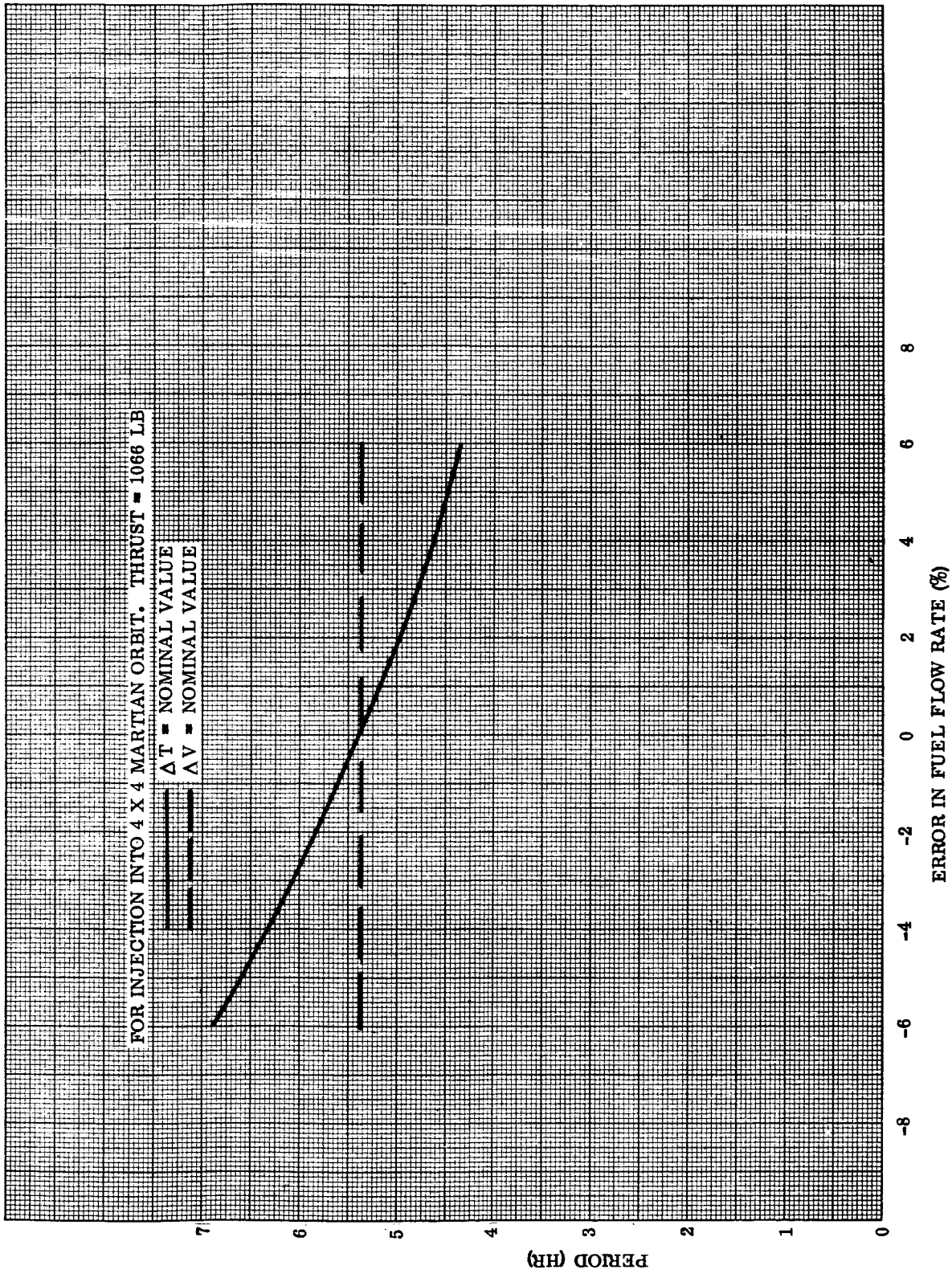

Figure 5-37. Period vs Error in Fuel Flow Rate

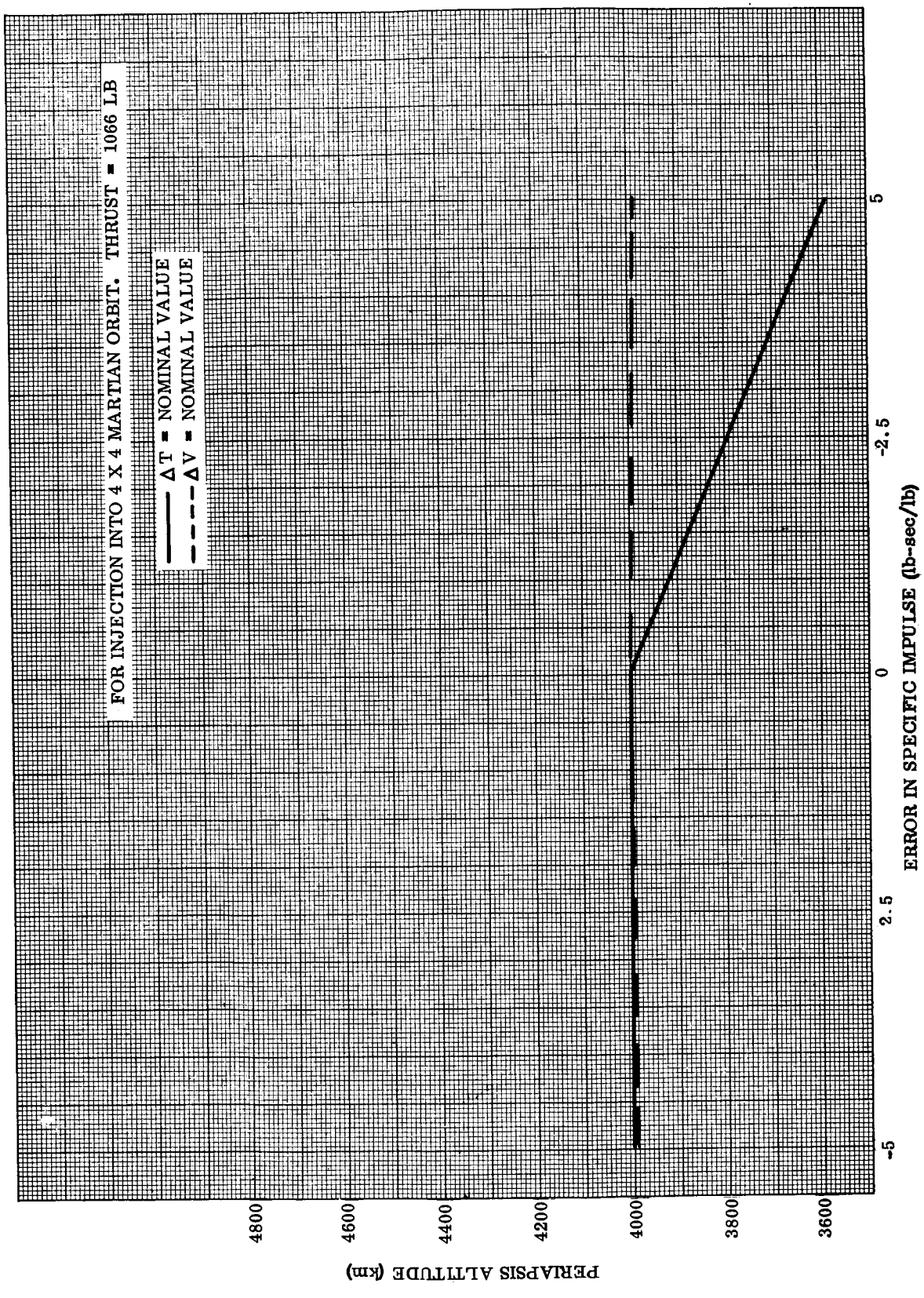

Figure 5-38. Periapsis Altitude vs Error in Specific Impulse

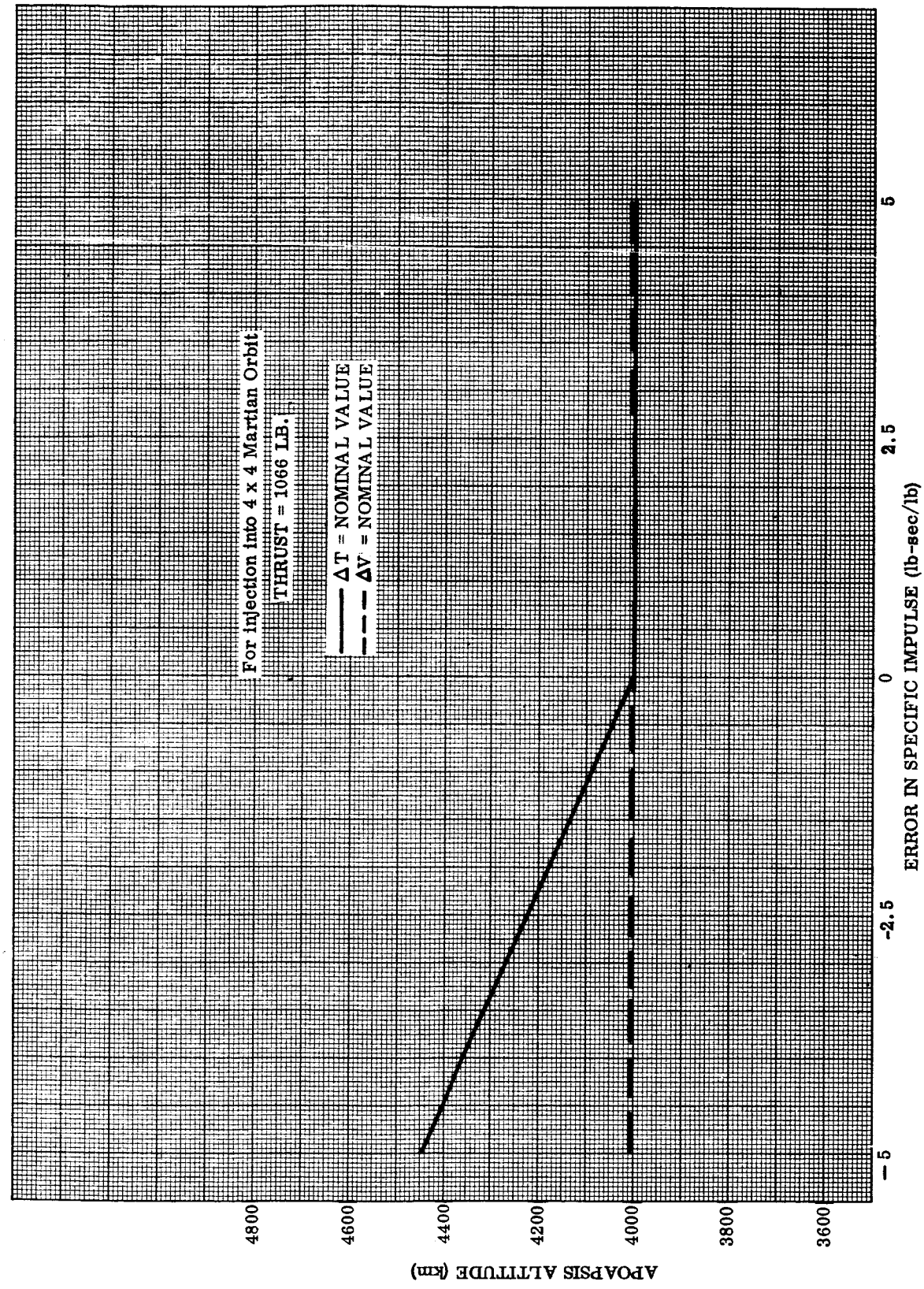

Figure 5-39. Apoapsis Altitude vs Error in Specific Impulse

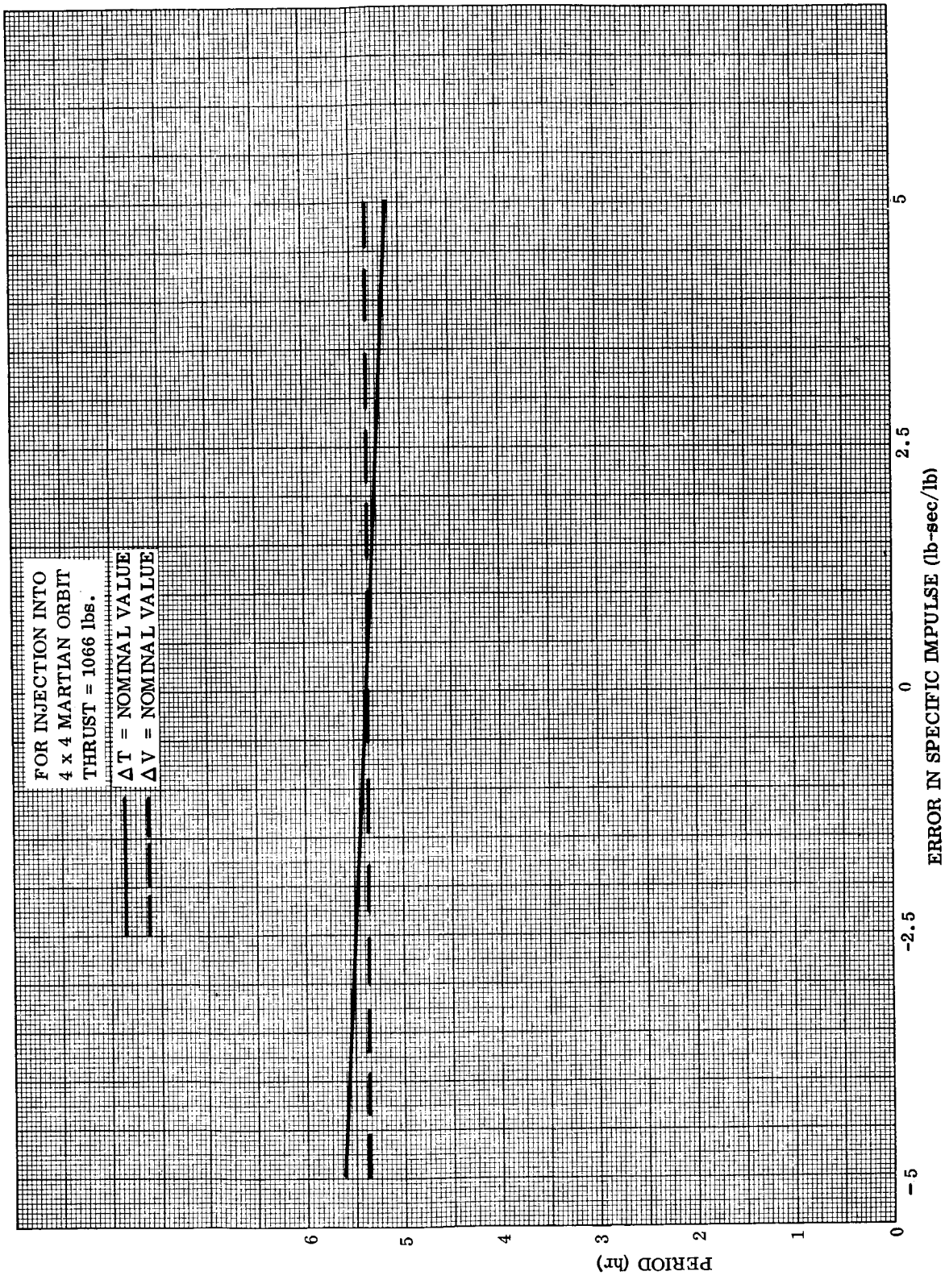

Figure 5-40. Period vs Error in Specific Impulse

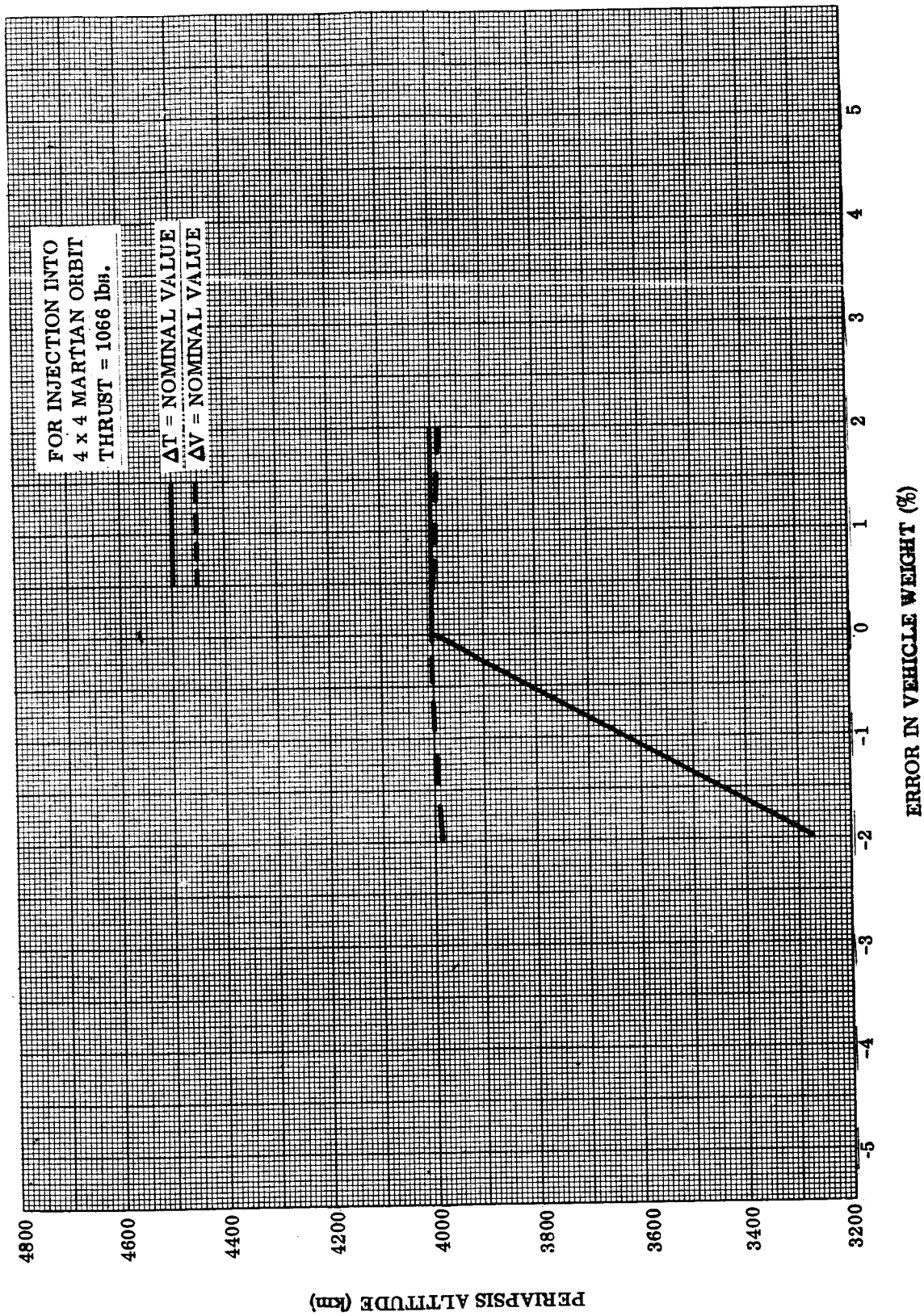

Figure 5-41. Periapsis Altitude vs Error in Vehicle Weight

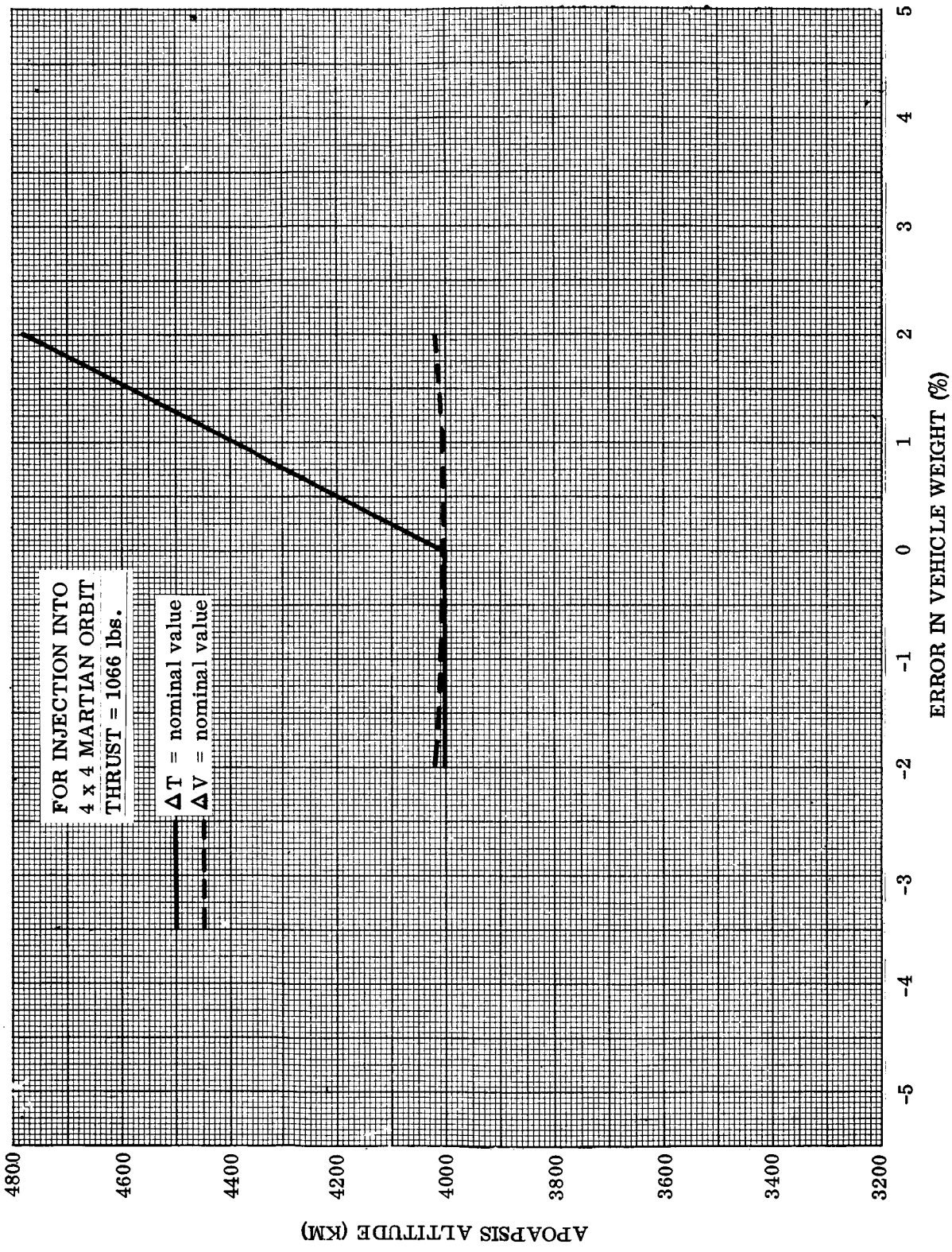

Figure 5-42. Apoapsis Altitude vs Error in Vehicle Weight

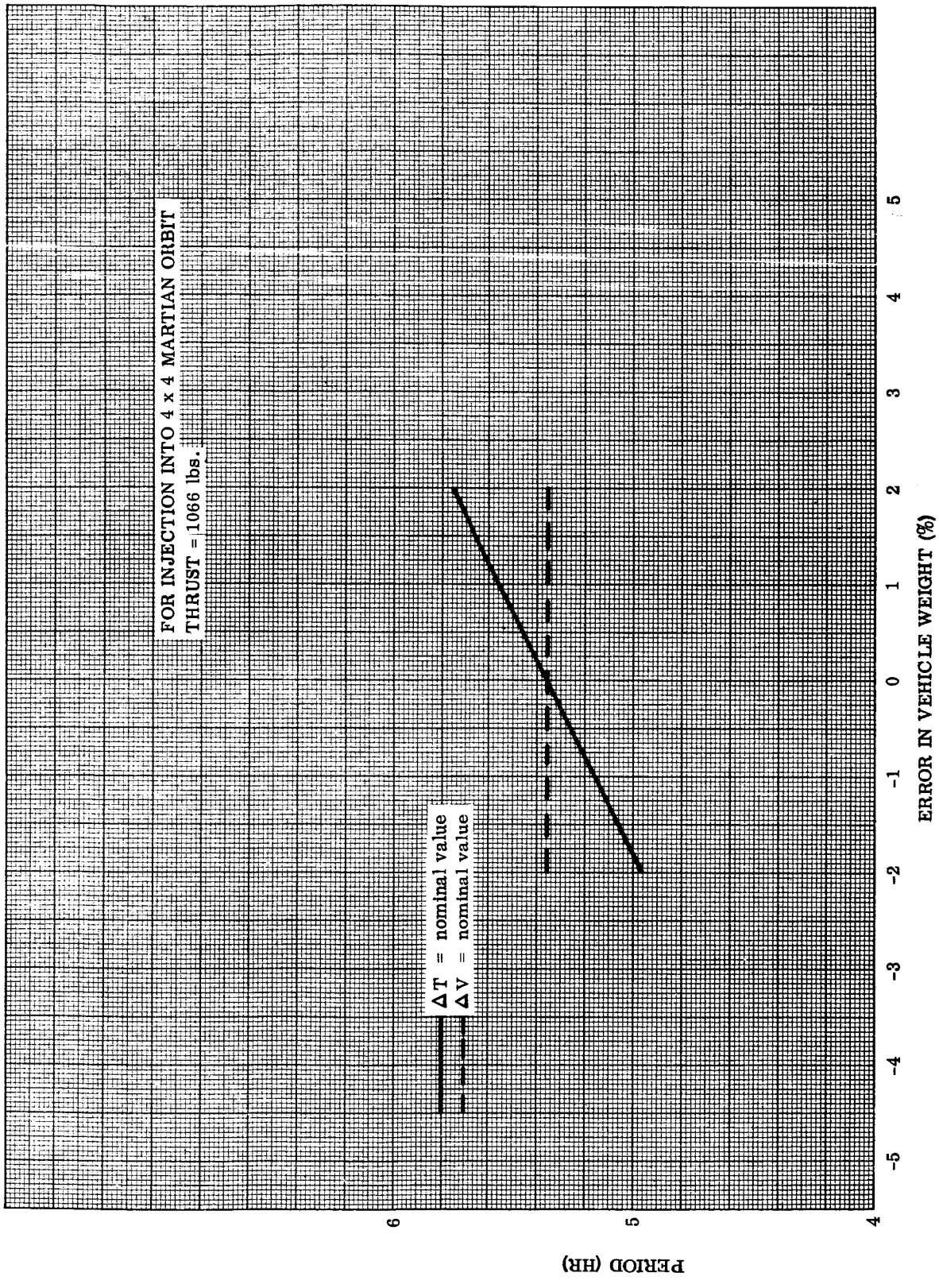

Figure 5-43. Period vs Error in Vehicle Weight

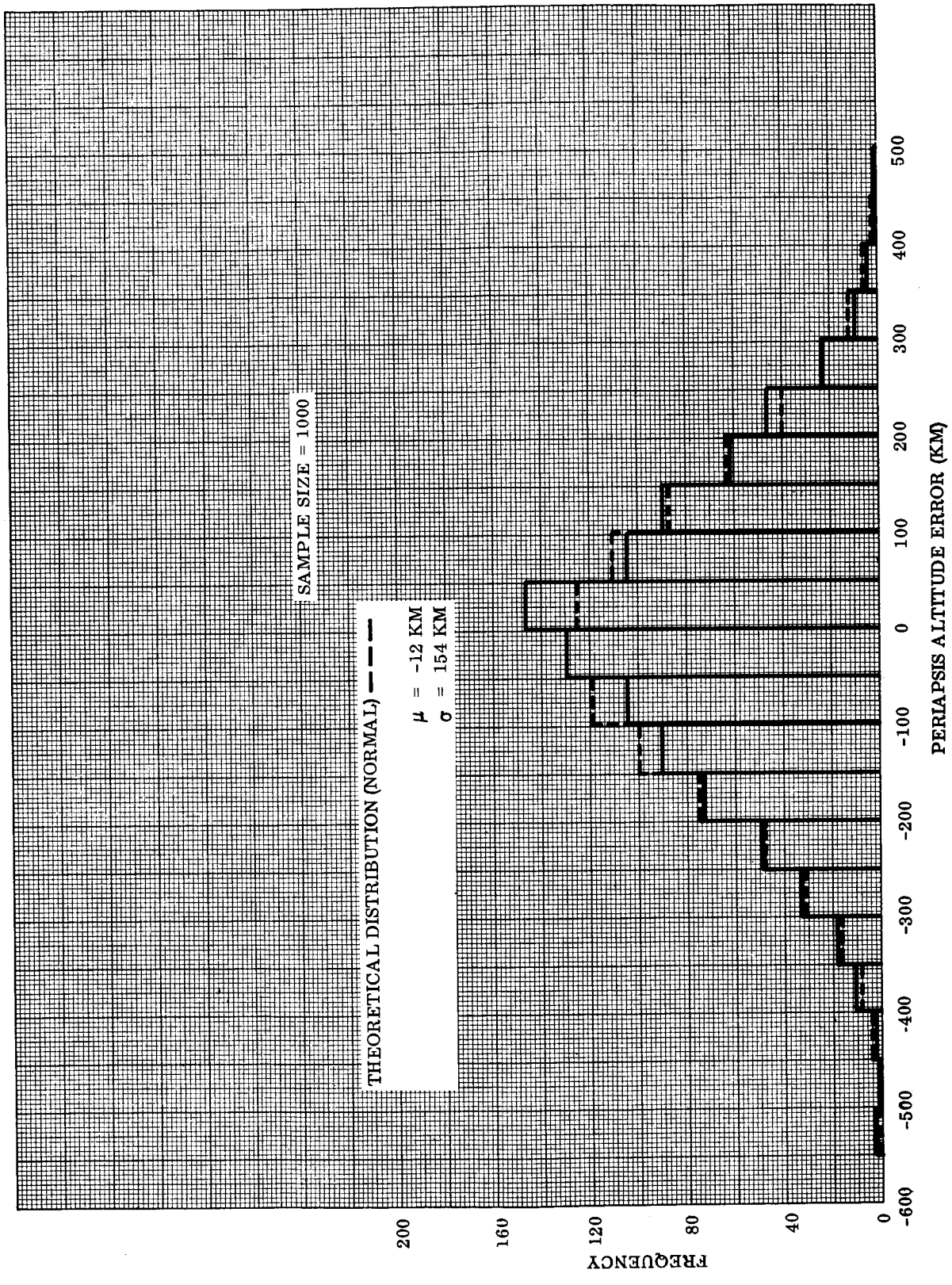

Figure 5-44. Monte Carlo Error Analysis - Frequency vs Periapsis Altitude Error

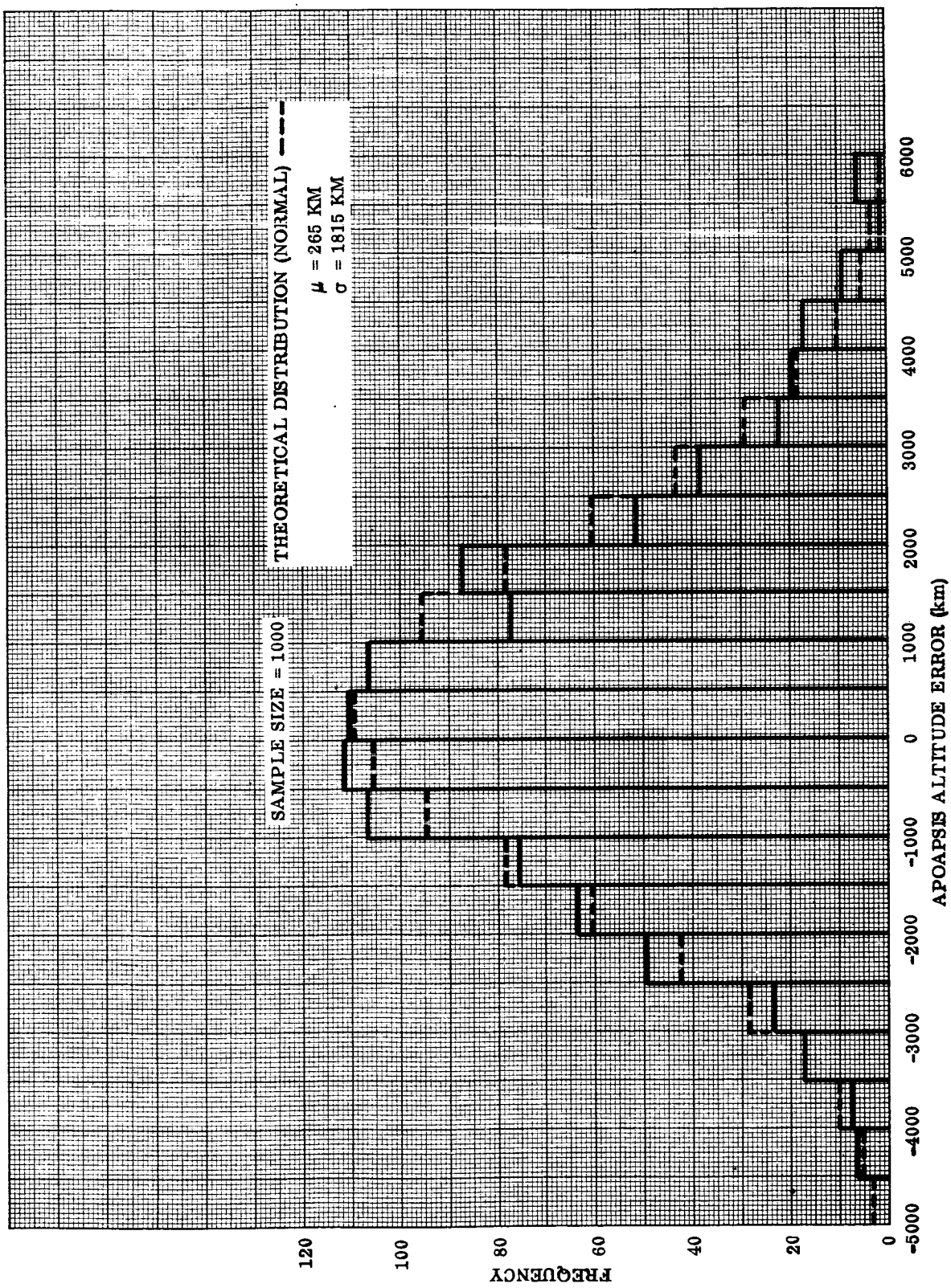

Figure 5-45. Monte Carlo Error Analysis - Frequency vs Apoapsis Altitude Error

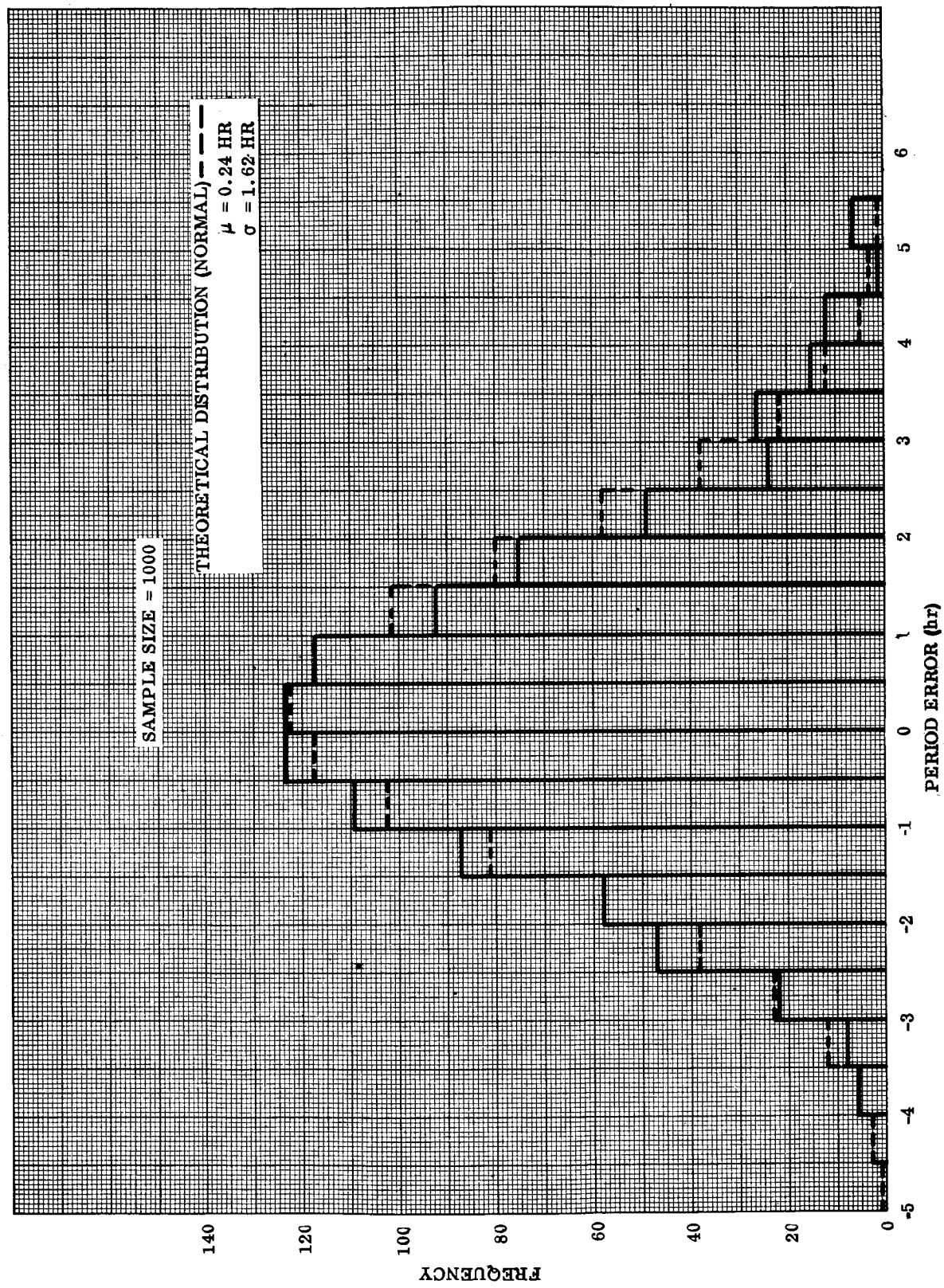

Figure 5-46. Monte Carlo Error Analysis - Frequency vs Period Error

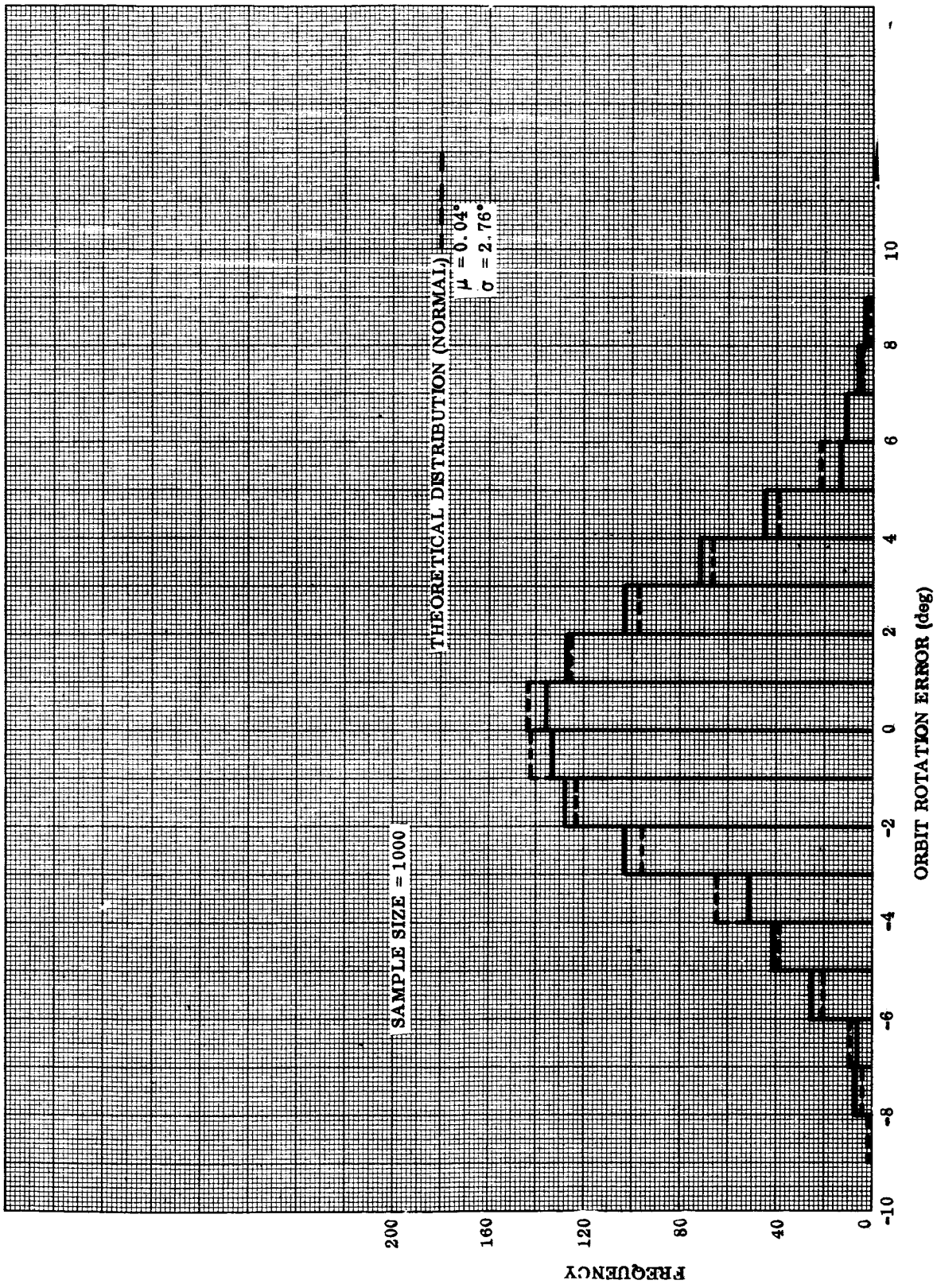

Figure 5-47. Monte Carlo Error Analysis - Frequency vs Orbit Rotation Error

CII - VB220AA112

ALTERNATE SYSTEM PHILOSOPHIES AND SYSTEM MECHANIZATIONS CONSIDERED

ALTERNATE MISSION SEQUENCES

Index

1 Introduction
2 Capsule Separation and Final Guidance Correction Timing
3 Time of Arrival Separation Between Capsule and Spacecraft
4 Capsule-Spacecraft Separation

1.0 INTRODUCTION

Several major alternatives were considered in arriving at the mission sequence of events described in Volume A. This section discusses the rationale used in arriving at the recommended approach for:

a. Time of capsule separation and final spacecraft guidance correction.

b. Separation between capsule and spacecraft at time of arrival.

c. Sequence of events at capsule separation.

2.0 CAPSULE SEPARATION AND FINAL GUIDANCE CORRECTION TIMING

The constraint that capsule separation as well as capsule impact and orbit insertion occur within view of Goldstone, requires that Capsule separation occur approximately an integral number of days from the planet.

The question of appropriate timing for capsule separation and final spacecraft guidance correction is intimately tied to the question of the use of approach guidance measurements relative to the planet. If approach guidance is not employed, capsule separation can be accomplished several days from the planet with no degradation in guidance accuracy. The effect of execution error does not tend to vary with time, and the orbit determination error will tend to converge to a final level several days prior to encounter. A vernier guidance correction is available by adjusting the capsule release point. Early capsule release has the following considerations:

a. Weight of the capsule retro-rocket fuel varies linearly with the inverse of time to the planet at separation.

b. Execution errors in the capsule deflection maneuver are insignificant compared to the navigation uncertainty of 350 KM.

c. Capsule internal power and length of timing sequences are increased for separations far from the planet.

In the preferred design, an approach guidance system which measures the direction in inertial space of the spacecraft-Mars line is recommended. Several of these measurements, over a period of time, can reduce the navigation error from 350 KM to 90 KM at separation as discussed in VB234AA106. With this system, however, the accuracy obtained is a strong function of the time over which it is used. It is extremely desirable to make measurements up to one day before encounter to realize the maximum decrease in orbit uncertainty (refer to VB234FD106). Thus the spacecraft design has been established to provide a capability for capsule separation and a

final spacecraft trajectory correction one day prior to encounter. The implications of this decision on the design are as follows:

a. Capsule power requirements are minimized since separation to impact time is minimized.

b. A "busy" operational period exists due to the requirement within an approximate 24 hour period for capsule separation, final guidance correction, and orbit insertion. This requirement is alleviated somewhat by providing capability to pre-load commands into the controller and sequencer. However, up-dating of these commands based on approach guidance measurements is still required.

c. For the nominal spacecraft periapsis altitude of 3000 KM, a capsule velocity increment of 54 meters/second normal to the pre-separation velocity vector is required to produce an in-plane impact with an entry angle of 42 degrees and no time of flight separation. For the nominal spacecraft trajectory described in Volume A, a Syrtis Major capsule landing site requires 96.5 meters/sec. to achieve the necessary out of plane component plus a small time of arrival separation to allow spacecraft-capsule line of sight viewing to impact. This increment appears reasonable but could be reduced substantially for an earlier separation at the expense of navigation accuracy.

d. The requirement for three maneuvers within a 24 hour period imposes a heavy requirement on the spacecraft batteries. However, analysis has shown that design for a 3 hour occultation in orbit is still the limiting case, provided the time between the final trajectory correction and orbit insertion is at least 12 hours to insure batteries are fully charged prior to initiation of the orbit insertion maneuver (refer to VB236FD101).

In the sequence described in VB220FD112, the final spacecraft trajectory correction is accomplished immediately after capsule separation without intervening return to Sun and Canopus reference. This minimizes the total time required for the two maneuvers at a small penalty in pointing accuracy so that time to recharge batteries before orbit insertion is maximized. The design is not critically dependent on this specific sequence and Sun and Canopus re-acquisition can precede the final trajectory correction if desired. The only firm requirement is that adequate time for battery recharging be allowed prior to start of the orbit injection maneuver.

3.0 TIME OF ARRIVAL SEPARATION BETWEEN CAPSULE AND SPACECRAFT

During first capsule entry into the Martian atmosphere, entry measurements can provide data of great scientific value as well as engineering usefulness in the design of future capsules. Reliability of returning this data to earth is enhanced if the high gain antenna is in use during entry. This provides direct relaying of data rather than relying solely on storage in the spacecraft with subsequent playback. This can be accomplished if the spacecraft is in the cruise attitude throughout entry, or if the

retro-attitude is assumed prior to start of entry. In moving from one attitude to another, however, the high gain antenna cannot be used. Additionally, design of the spacecraft relay antenna to view the capsule while moving from the cruise to retro-attitude may be difficult. Viewing, when in either of these two attitudes, can be accomplished.

Apart from relay considerations, the question exists as to when should the retro attitude be assumed prior to point of closest approach. Considering that the antenna pointing and spacecraft orientation time may require 37 minutes, confirmation of proper orientation requires 30 minutes, and transmitting a command to enable retro-fire requires 10 minutes; the maneuver sequence must be initiated at least 77 minutes prior to point of closest approach. The question arises as to what provisions should be made for reaction to possible spacecraft malfunctions during this period. To assume retro-attitude sufficiently early to allow re-acquisition of Sun and Canopus and a second maneuver attempt should the first be unsuccessful, is not feasible without a significant increase in battery capacity and/or a decrease in time required for Sun/Canopus acquisition, both of which are undesirable.

Short of a second maneuver attempt, there may well be useful alternates that could be attempted such as a fly-by sequence should a failure occur during the retro-maneuver. These could include activation of body mounted instruments and possibly deployment of the scan platform for fly-by observation of the planet. Thus, it would appear wise to start the retro sequence an hour earlier than the minimum to provide time for ground analysis plus time for the spacecraft to respond to subsequent commands in the event of a malfunction.

Therefore, if the capsule entry is to be viewed from cruise attitude, time of flight separation between spacecraft and capsule of approximately 2 hours is required.

Achieving a time of arrival separation of this magnitude, for capsule separation one day from encounter requires a velocity differential between capsule and spacecraft along the flight path of approximately 300 meters/sec. An increment of this magnitude is undesirable this late in the trajectory whether it be supplied by the capsule or the spacecraft or partially by each. Supplying the velocity increment with the capsule deflection rocket has the following disadvantages:

a. The weight of the capsule propulsion system is increased substantially. Compared to the nominal Syrtis Major impact described in Volume A, the required velocity increment is increased by approximately a factor of three.

b. The execution error associated with capsule separation is increased. Compared to a nominal in-plane separation, the errors in landing site location are larger, both because the velocity errors are larger and because pointing errors produce more severe down range errors when the separation is not normal to the flight path.

Achieving the velocity differential by retarding the spacecraft (relative to Mars) has the following considerations:

a. The weight penalty is less severe than in the capsule case since some portion of the velocity increment is recovered in the orbit injection maneuver.

b. A correction of this magnitude with its associated execution error causes a relatively large uncertainty in the spacecraft trajectory. The orbit determination is corrupted and accurate re-establishment of the trajectory knowledge is not possible prior to orbit insertion.

The penalties for achieving time of flight separation are less if the spacecraft rather than the capsule provides the correction. However, both are undesirable and there appears to be no significant penalty paid for putting the spacecraft in the orbit insertion attitude and establishing the high gain communication link prior to start of entry. Thus, this approach has been selected for the preferred design.

4.0 CAPSULE-SPACECRAFT SEPARATION

The design described in Volume A assumes a number of things relative to the capsule such as:

a. The capsule deflection rocket is mounted on the opposite end of the vehicle from the heat shield.

b. The bio-barrier separation occurs circumferentially at the maximum diameter.

The separation sequence described in Volume A, and major reasons for it, are:

a. The separation velocity and direction must be such that no possibility exists for entry of the barrier. With a separation rate of a few feet per second, at one day from encounter, any direction is allowable.

b. Separation should be in a direction such that subsequent confusion of the Canopus sensor or the approach guidance planet sensor will not occur.

c. Separation should be as late as possible to minimize the probability of capsule contamination from the spacecraft.

d. With the capsule deflection rocket mounted opposite the spacecraft, and with separation occuring along the capsule thrust axis, collision between the spacecraft and capsule can occur when the deflection rocket fires if positive steps are not taken to prevent it. In the preferred design, this is accomplished by exhausting a small cold gas bottle to give the spacecraft a small velocity increment, 0.06 meters/second, normal to the line of separation. Firing of the capsule deflection rocket is delayed to insure no collision under worst case capsule pointing errors. This time delay

also insures the capsule rocket will be spent prior to crossing the spacecraft trajectory so that no plume impingement on the spacecraft is possible.

Other means to avoid a possible collision appear undesirable. Separation of the capsule in a direction other than along its thrust axis appears to pose a complex problem for the separation system. Similarly, assuming a spin stabilized capsule, imparting a velocity to it normal to its thrust axis after separation is impractical.

If the capsule deflection rocket were mounted on the heat shield, as in the Mercury vehicle, the collision avoidance maneuver could possibly be eliminated. The deflection rocket firing would have to be delayed to avoid plume impingement, and assurance given that no damaging objects, such as igniters are ejected upon engine ignition. Other implications of re-locating this deflection rocket are:

a. The conical portion of the bio-barrier must be separated in other than the capsule separation attitude.

b. A smaller spacecraft maneuver is required to go from cruise attitude to capsule separation attitude.

One problem area involved in capsule separation is the avoidance of capsule contamination from the spacecraft attitude control gas. When the aft portion of the bio-barrier is separated, for example, the disturbance imparted to the spacecraft will cause gas to be expelled to maintain attitude. Some of this gas will almost certainly impinge on the capsule and hence it must be biologically clean. This can probably be achieved by having sterile tanks, tubing, etc., loading the tanks with non-contaminated gas, and perhaps treating exposed nozzles with ethylene-oxide prior to launch. This will require further analysis and perhaps experimentation to provide the necessary assurance that no contamination will result.

There appears to be no simple way to avoid this problem completely. Small inertia wheels could be used to reorient the spacecraft during the separation maneuver, but the additional complexity introduced into the attitude control subsystem is undesirable. Separating the capsule in its bio-barrier, spinning the entire unit, and subsequently separating the barrier before firing the deflection rocket appears to be a difficult design to implement.

CII - VB220AA113

ALTERNATE SYSTEM PHILOSOPHIES AND SYSTEM MECHANIZATIONS CONSIDERED

SPACECRAFT CONFIGURATION

Index

1 Scope
2 Discussion

1.0 SCOPE

This section is to discuss the trade-off studies made in the integration of the final selected subsystems into the 1971 Preferred Spacecraft Configuration. The major constraints that must be satisfied are discussed and justification presented for the final selected configuration.

2.0 DISCUSSION

Summary tables of the constraints to configuration design along with their effects on the configuration are presented here, and a discussion of the more important factors follows. The major constraints are listed in Table 2-1, and secondary constraints are listed in Table 2-2.

2.1 MAJOR CONFIGURATION ELEMENTS

A study was conducted to determine the major configuration-influencing factors and the alternate approaches thereof so that all possible configurations could be examined. These alternate approaches have been developed within the constraints of the following subsystem definitions:

a. Retropropulsion system: A single nozzle bi-propellant liquid rocket engine using hypergolic propellants. The fuel (Aerozine 50-50) and oxidizer (N_2O_4) are used with a mixture ratio of fuel-to-oxidizer of 1.6:1, so that the volumes of each are approximately equal. The thrust level is 2200 pounds and the length of nozzle and thrust chamber is 56 inches for an expansion ratio of 100:1.

b. A circular parabolic dish antenna of variable size (7-1/2 - 9-1/2 feet in diameter) with f/d in the range of 0.30-0.35. The antenna's deployed position and required rotations are as shown in the preferred design (reference VB220FD113).

c. The sun line is along the Z axis with the spacecraft being on the sun side with respect to the Flight Capsule.

d. Solar array area required of more than 200 square feet.

With the above ground rules the major configuration element alternates are as shown in Figure 2-1.

With the above alternates to each of the three major configuration constraints there could be a total of 16 different possible configurations. However, inspection of the above alternates show some definite advantages and disadvantages that reduce the number of desirable combinations as follows:

Antenna storage position A_4 is similar to A_3 but the available dimension would decrease the maximum diameter from A_3 and the problem of snubbing the antenna down during boost is made more complex; therefore A_4 is omitted.

Table 2-1. Major Configuration Constraints

Constraints	Effect on Configuration
1. Geometry envelope 2. Photovoltaic power supply system and array area requirements thereof 3. Preference for a fixed solar array 4. Sun - Canopus orientation	These factors combine to orient the solar array, and consequently the sun line, since the requirement for a fixed solar array of >200 ft^2 can best be accomplished with the array surface in a station plane. (The requirement for this area exists during transit and therefore the array cannot encroach upon the capsule envelope.)
5. Flight Capsule Interface Diameter 6. Boost Adapter Interface Diameter 7. Structural Weight Minimization	These factors combine to make the most efficient structure be a conical shell from the Flight Capsule interface to the Launch Vehicle interface (59 inches long, 80 inch diameter at forward end and 120 inch diameter at aft end). The constraint of antenna size/storage problem and propulsion module size does not restrict this, although other factors do (which are discussed later).
8. Orientation of the propulsion thrust vector along Z-axis or sun-line. 9. Modularity of propulsion system 10. Minimization of roll inertia	Combine to locate the propulsion module as a compact system located as close as possible to the Z-axis, and symmetrically arranged about it. The thrust levels and total impulse requirements size a system compatible with the volume available.
11. Thermal control requirements for radiation view area. 12. Separation joint shock impulse 13. Desire for maximum area of solar array 14. Stability under solar pressure	Constraints 11 and 13 desire the solar array to be located as far down as possible while 12 and 14 desire to have it located up. The existing location at Station 8 is a compromise in favor of 11 and 13.

Table 2-2. Secondary Configuration Constraints

Constraints	Effect on Configuration
1. Field-of-view requirements, plume size, and radio transmission paths.	There are 15 optical sensors on 8 sensor assemblies (exclusive of the science instruments but including the horizon scanner on the science platform), 6 antennas, 13 cold gas nozzles and 5 hot gas nozzles that are positioned so that operating efficiencies of the associated components remain within acceptable limits and there is no impingement damage on adjacent components. The major constraints influencing configuration are the high-gain antenna and the science package requirements.
2. Compatibility of 1971 S/C with the 1969 Atlas-Centaur mission.	Shroud diameter limitation limits the diameter of the E/M and thus requires vertical sides for the internal packaging volume requirements. The choice of vertical sides affects manufacturing and thermal shutter efficiency favorably while imposing a structural weight penalty.
3. 1966 State-of-the-art and reliability a. Solar panel, conventional cells vs. roll-out arrays, thin film solar cells, etc. b. Circular parabolic dish antenna (nonfoldable) vs. foldable antennas, array antennas, etc. c. Conventional pressure-fed rocket engines vs. pump-fed, ring nozzles, retractable nozzles, thrust-plate engines, etc. d. Conventional materials vs. beryllium-aluminum alloy.	a. Limits design configurations and flexibility of stowing, deploying, etc. b. Affects stowage provisions during boost mainly on basis of size, and also affects unobstructed view area requirements. c. Affects performance and thus weight and packaging volume requirements and also affects supporting structure requirements. d. Affects structural weight and natural frequency.
4. Severe load environment and requirement to design 1971 S/C for the 1975 Flight Capsule.	Imposes penalty on structural weight.
5. Solar-pressure balance and field-of-view requirements.	These combine to yield a wire-mesh antenna design and one (1) balancing vane rather than a solid antenna and 10 times the balance vane area (which would present possible obstruction to the planet scanner).

Table 2-2. Secondary Configuration Constraints (Continued)

Constraints	Effect on Configuration
6. Integration of electronic package structure with primary structure and provision of high natural frequency for electronic components support structure.	The present design incorporating the attachment of each electronic box to the longeron severely limits accessibility to the electronic packages.
7. The meteoroid-flux, desired probability of puncture, and method of penetration analysis.	Combine to develop requirement for double-wall meteoroid bumper over the entire lower end of the propulsion module.
8. Magnetic field requirements.	Requirements for usage of non-magnetic materials impose constraints on material selection, manufacturing techniques, and joint design as follows: 1) material selection requires titanium fasteners rather than steel and selection of non-magnetic stainless steel for rocket nozzle extension shield. Basic structure is aluminum and is unaffected, 2) manufacturing techniques will require a process to remove surface particles from steel cutting tools (probably chemical etch process), and 3) joint design is affected by desire to have an insulator at joints for minimization of electrical loops, the desire to have a conductor at joints for thermal heat transfer, and the desire for no joint separation of any type from structural reasons.
9. C.G. envelope, inertia minimization, and principal axes location with respect to control axes.	These are not significant restraints on the configuration but are factored into the design by general principles such as symmetry of design about Z-axis, assignment of bay areas to subsystems, location of retropropulsion tanks on X-and Y-axes, mass density concentrated closely to Z-axis, and stationwise C.G. plane.

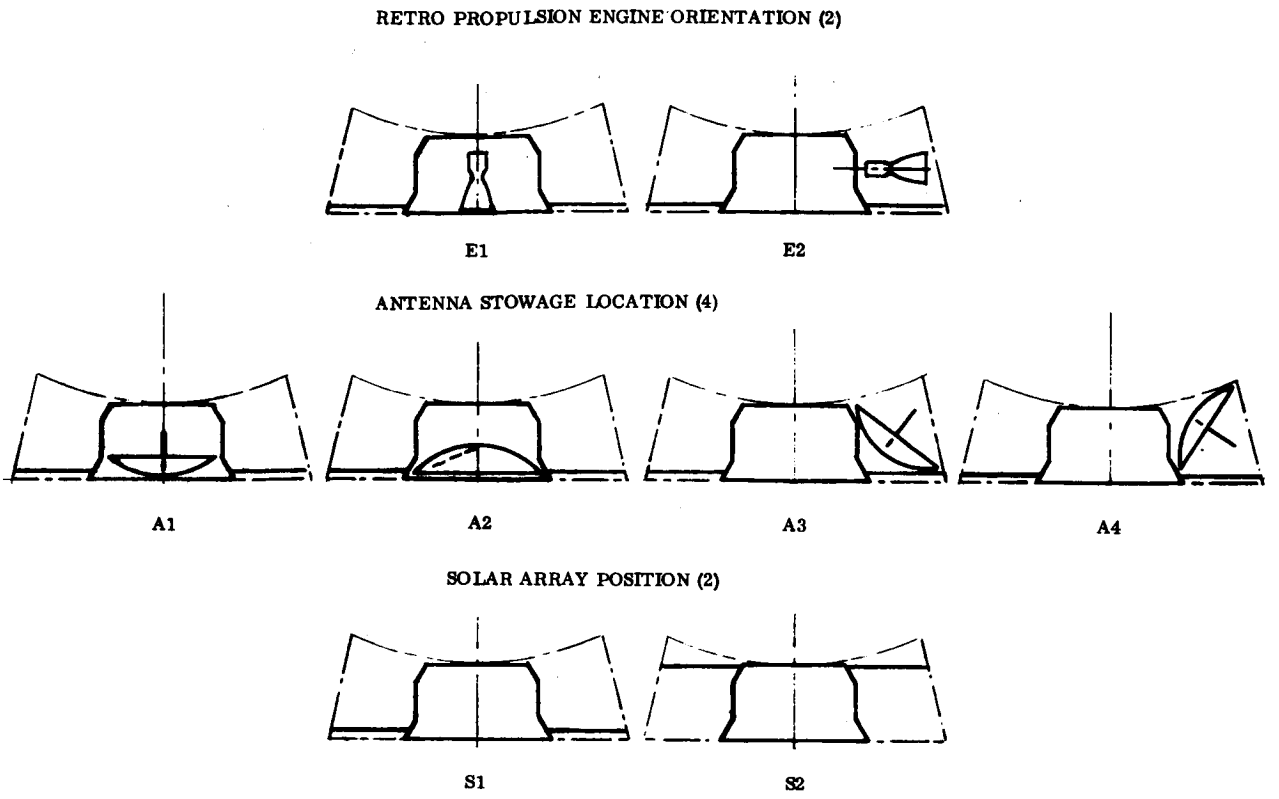

Figure 2-1. Alternate Configuration Elements

Antenna position A_2 requires a folded feed which is detrimental to reliable performance and since it has no real advantage over A_1, it can be omitted.

The solar array position S_2 can be considered less desirable than S_1 because of decrease of cross-sectional area going up, Flight Capsule structure obstructing back-face radiation from the solar array, no shading of the equipment module, and more likelihood of obstruction by the spacecraft body of sensing or transmitting elements mounted on the array.

Consequently the possible combinations of configurations immediately is reduced to two (2) engine orientation positions, E_1 & E_2, and two (2) antenna storage positions A_1 and A_3 for a total of four (4) configurations defined as follows:

Configuration / Variable	A	B	C	D
Engine location	E1	E1	E2	E2
Antenna storage position	A3	A1	A3	A1

Table 2-3. Advantages of Final Alternate Configuring Elements

Method	Advantages
Engine Positions #1 - Engine thrust axis on Z-axis. E1	1. Compatible with 1969 Atlas-Centaur shroud diameter of 10 feet. 2. Lower roll inertia 3. Pitch and yaw inertia are more equal. 4. General symmetry about thrust axis. 5. Less travel of high-gain antenna required. 6. Less plume impingement problem. 7. Permits possible accomplishment of mid-course function and retro fire function with single engine or use of mid-course engines for thrust vector control of main retro engine. 8. Modularity is more easily effected. 9. No blockage of radiation surfaces of equipment submodules. 10. Does not encroach upon packaging volume (E2 removes 1 or 2 bays). 11. With multiple midcourse engines aligned parallel to the Z-axis longitudinal C.G. location can have large limits, thus providing greater packaging flexibility.
#2 - Engine thrust axis off to side. E2	1. Two propellant tanks in place of four and subsequent advantages: a. More usable propellant. b. Less tank weight. c. Less support weight. d. Less surface area and greater tank thickness, consequently less meteoroid bumper weight required. 2. Better alignment of propellant with thrust vector, and subsequent less steady-state and oscillatory motion of C.G. during engine burning. 3. Engine gimbal position can be farther away from C.G., thus giving longer control arm and a better situation for engine stability.
Antenna Storage Positions #1 - Antenna outside shell. A_3	1. Less interference with accessibility to components within basic shell. 2. Greater packaging volume within shell. 3. No interference with engine operation.

Table 2-3. Advantages of Final Alternate Configuring Elements (Continued)

Method	Advantages
#1 - Antenna outside shell.	4. No interference with spacecraft booster separation joint (Position 2 would restrict choice of separation systems). 5. Does not require stowage of antenna feed in engine nozzle.
#2 - Antenna inside shell. A_1	1. Larger antenna size possible. (9 1/2 feet vs. 7 1/2 feet diameter). 2. Two (2) antenna gimbals rather than three (3). 3. Better support arrangement for boost loads. 4. No interference with thermal control during ascent. 5. Greater packaging volume outside of shell.

The exact station location of the solar array was still a variable but this was only a matter of several inches motion.

The advantages of each of these four alternate approaches is listed in Table 2-3.

The above table listings do not show many significant differences in the alternates that tend to selection of one over another, and the engine orientation decision was originally made to provide capability of using a single engine to perform both midcourse and orbit injection. This desire coupled with the large longitudinal motion of the C.G. from the Transit to the Orbit Injection configuration (and requirement for either very large gimbal angles or a two-position motor for a sidemounted engine) led to the selection of the engine aligned along the Z-axis. It also makes possible the use of midcourse engines to provide thrust vector control during orbit injection.

The antenna storage location is not as significant as the engine orientation and the preferred design location of the #1 position (stowed outside the shell on the back of the solar array support structure) is not a clear-cut decision. However there are several factors which led to this selection: (1) the accessibility requirement (although with the requirement for a meteoroid bumper the problem here is only a matter of degree, (2) the transmission data rate appears to be sufficient with the smaller 7-1/2 foot diameter antenna, and (3) the desire for a circumferential severance device (encapsulated MDF) for the spacecraft booster separation is complicated by the presence of an antenna deployment arm. Consequently the preferred design is configuration A, shown here as Figure 2-2.

A layout of configuration B, which was the closest contender, is shown here as Figure 2-3.

Configuration C is not a particularly desirable combination for several reasons. The chief reason is the encroachment of both the engine and the antenna, which have large volume requirements, upon the packaging volume outside the shell, and the possible interference with the various sensors and other antennas. Consequently this configuration was not developed further.

One configuration D approach is presented as a preliminary layout in Figure 2-4.

2.2 VARIATION TO MAJOR CONSTRAINTS

2.2.1 SOLID PROPELLANT CONFIGURATIONS

An alternate configuration to the preferred 1971 design which uses a solid propellant rocket motor in place of a liquid rocket engine for the retro propulsion unit is shown as Figure 2-5. This design has no major configuration problems other than those listed in VB238AA which enumerates the basic trade-offs of a liquid propellant system vs. a solid propellant system. A solid propellant alternate to configuration D is shown as a preliminary layout in Figure 2-6.

2.2.2 ARRAY ANTENNA ALTERNATE

A promising configuration from a growth standpoint is that shown in Figure 2-7 which is configuration D using a flat array antenna and additional fixed solar array in the inside of the 120-inch diameter of the Bus. Of course, this configuration does not have the advantages of configuration A and in addition it possesses the complexity of designing a reliable flat array antenna.

2.3 SECONDARY CONFIGURATION CONSIDERATIONS

This section evaluates alternate approaches to some more detailed configuration problems and presents justification for the final design selection.

2.3.1 SIZE AND GEOMETRY OF EQUIPMENT MODULE

This is a fairly straightforward trade-off study, once the basic study ground rules have been evolved. The following constraints were imposed on this design selection:

a. Thermal radiation area of 38 square feet required with a reliable thermal control system.

b. Internal volume requirements for efficient packaging of the propulsion system, which is about 20 ft^3 of oxidizer, 20 ft^3 of fuel, a conical frustrum envelope (56 inches long, 32 inches diameter lower, and 11 inches diameter upper) for the rocket engine, and pressurant. (These requirements develop a requirement for an 80-inch diameter envelope.)

c. Electronic equipment packaging volume (net) of 43200 in^3 total, with standardize packaging approach and integration of electronic subassembly structure with the primary structure.

d. The desire to maintain a maximum external diameter for any point of the E/M, with thermal shutters in the open position, of 110 inches, as determined from the 1969 Atlas-Centaur internal shroud diameter. This limitation is desirable to avoid the necessity for extensive redesign of the Centaur structure, since the alternate approach of increasing the shroud diameter beyond 120 inches would require a bulbous, or "hammerhead," nose shape. This shape could result in bending moments due to buffeting which would be beyond the allowable load capability of the as-designed Centaur booster; however, it should be noted here that the effect of shape on buffeting is a very difficult analytical problem and most present methods tend towards conservatism.

e. Maximum handling weight per electronic equipment sub-assembly of about 90 lbs.

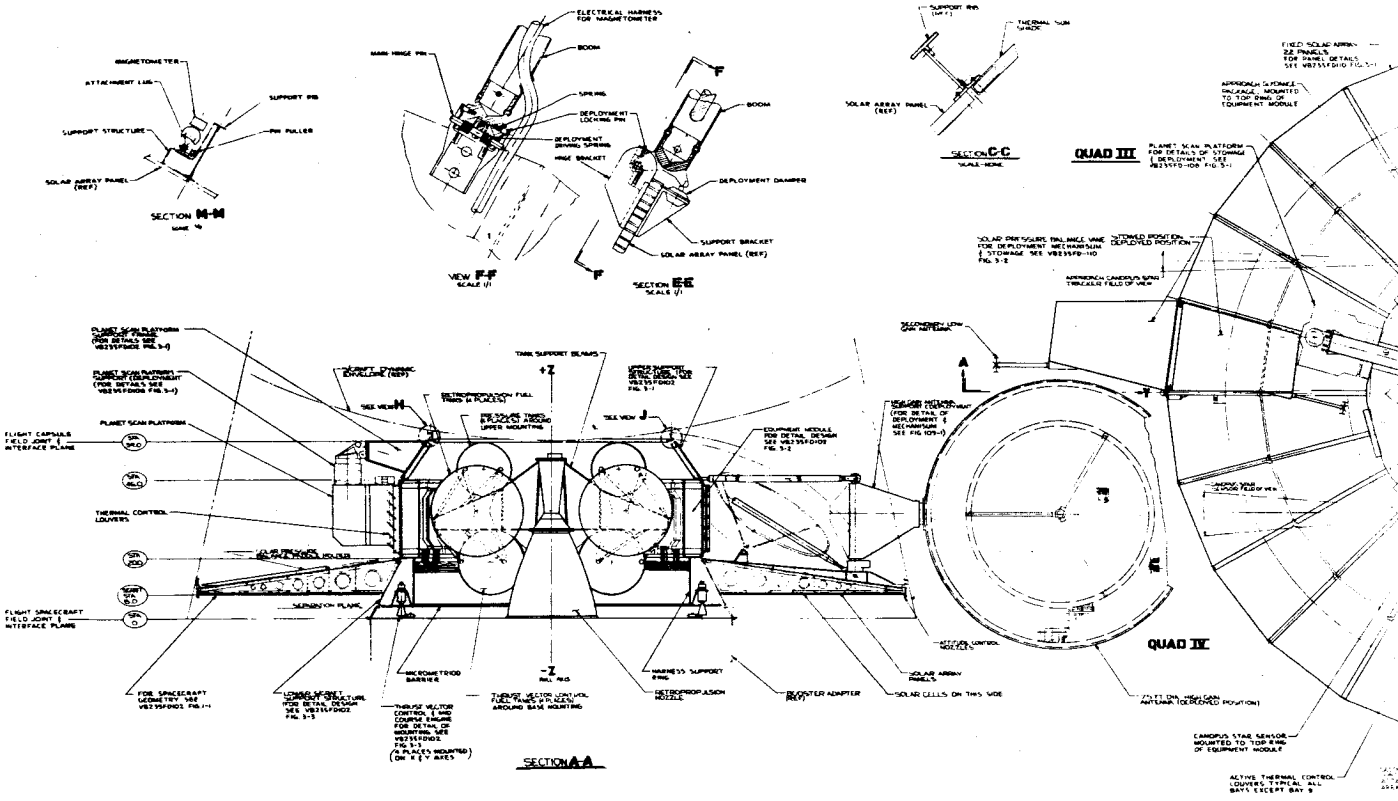

[redacted]

11 of 30

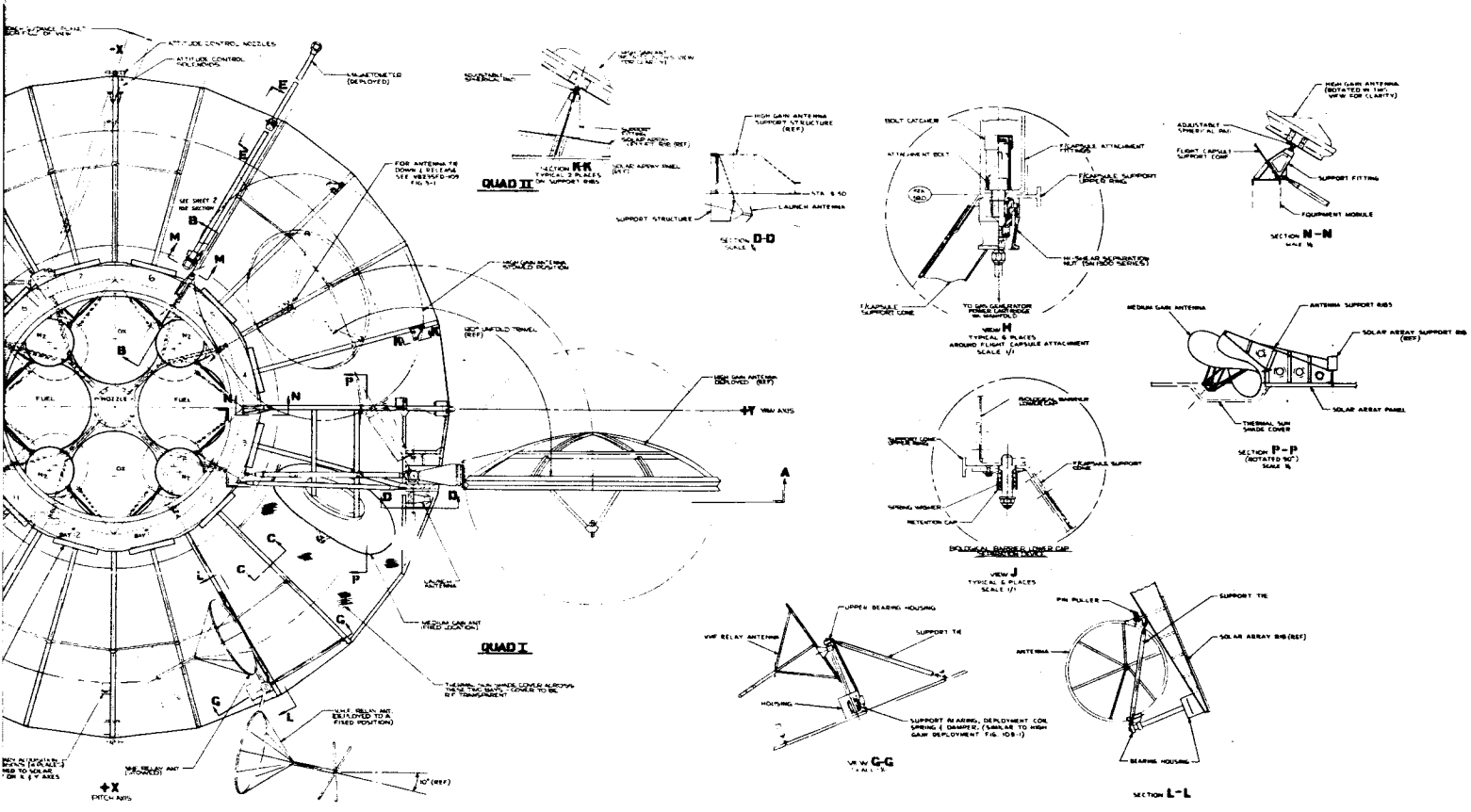

Figure 2-2. Spacecraft Structure General Arrangement

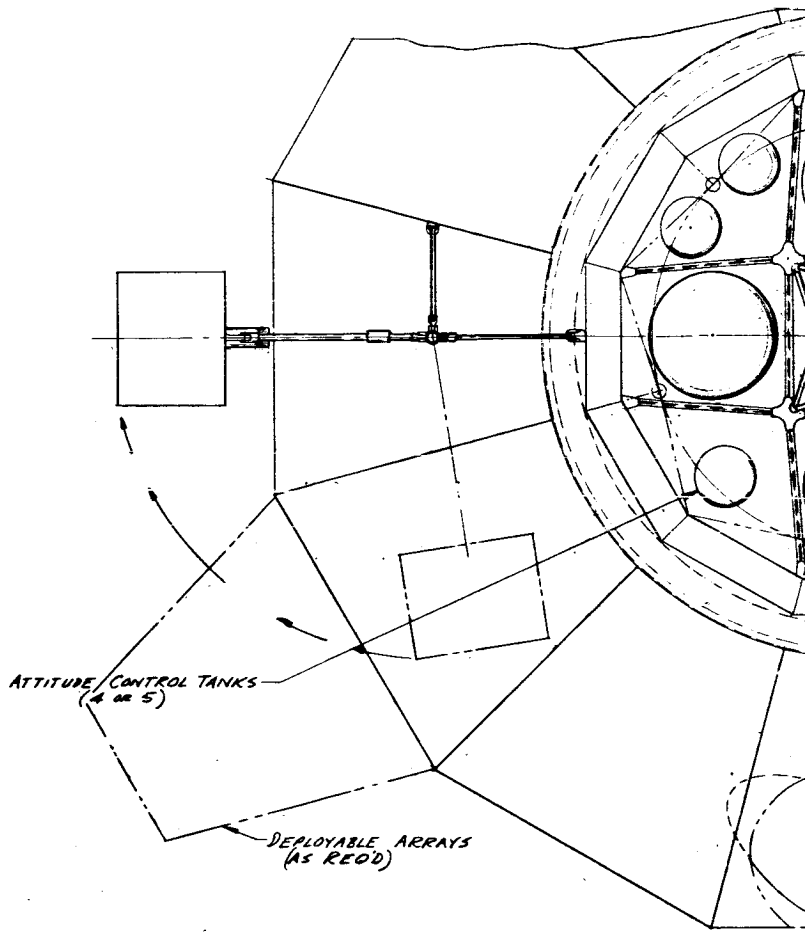
ATTITUDE CONTROL TANKS
(4 or 5)
DEPLOYABLE ARRAYS
(AS REQ'D)

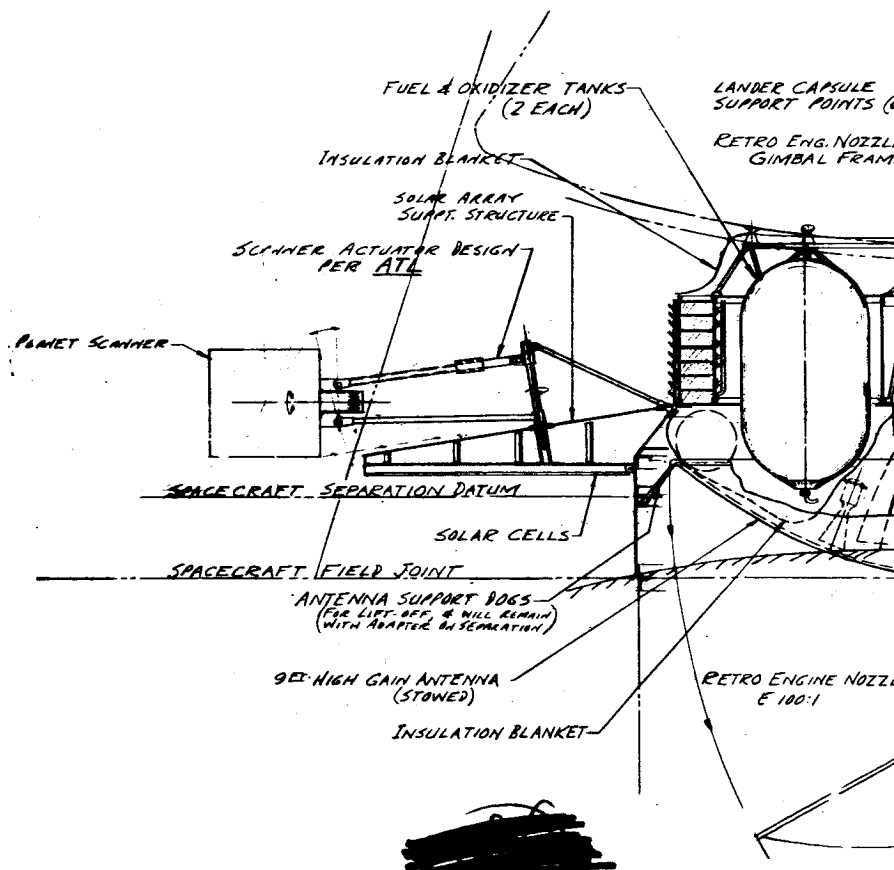
FUEL & OXIDIZER TANKS
(2 EACH)
LANDER CAPSULE
SUPPORT POINTS
RETRO ENG. NOZZL
GIMBAL FRAM
INSULATION BLANKET
SOLAR ARRAY
SUPPT. STRUCTURE
SCANNER ACTUATOR DESIGN
PER ATL
PLANET SCANNER
SPACECRAFT SEPARATION DATUM
SOLAR CELLS
SPACECRAFT FIELD JOINT
ANTENNA SUPPORT DOGS
(FOR LIFT-OFF, & WILL REMAIN
WITH ADAPTER ON SEPARATION)
9ft HIGH GAIN ANTENNA
(STOWED)
RETRO ENGINE NOZZL
E 100:1
INSULATION BLANKET

[redacted]

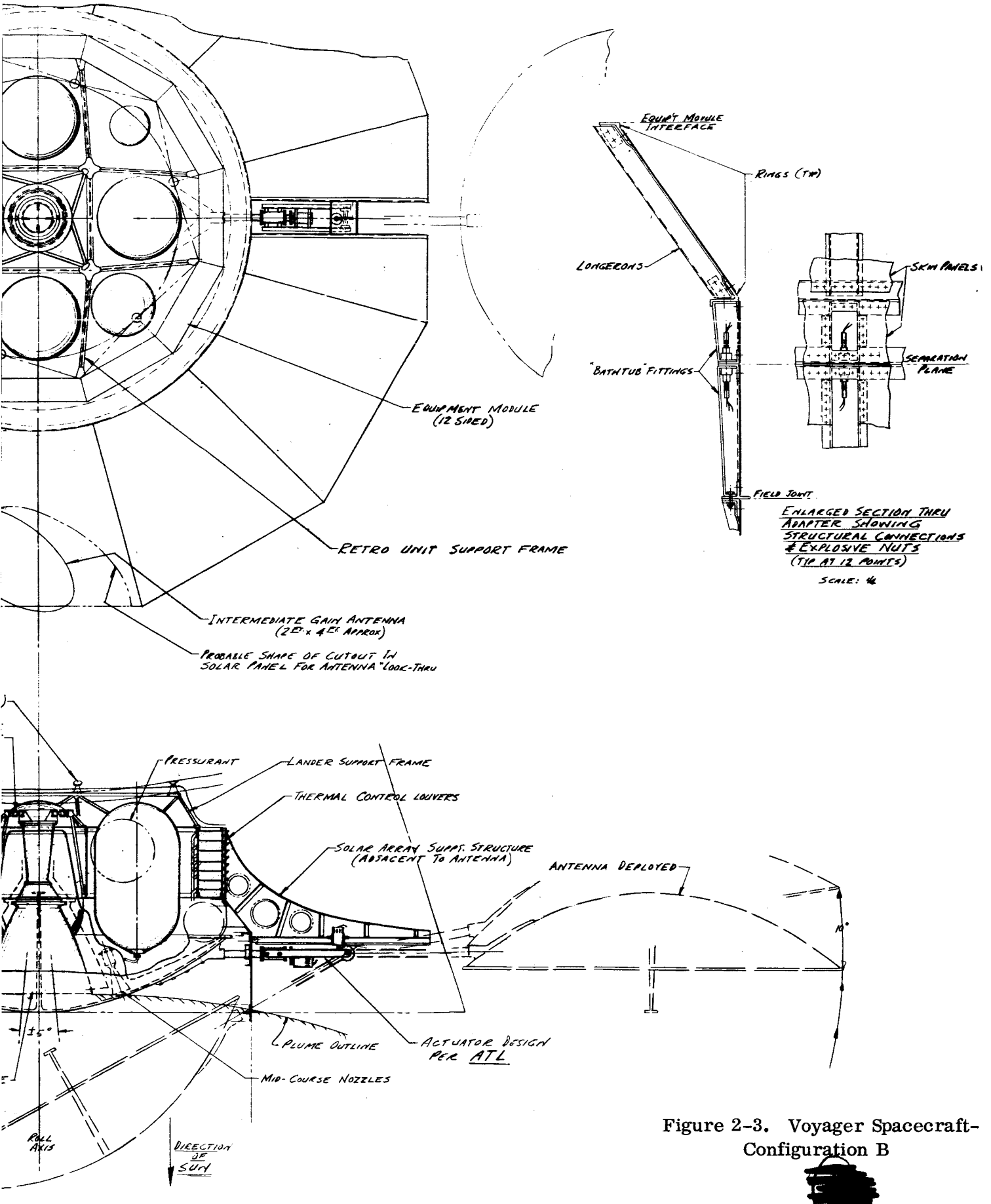

Figure 2-3. Voyager Spacecraft-Configuration B

[redacted]

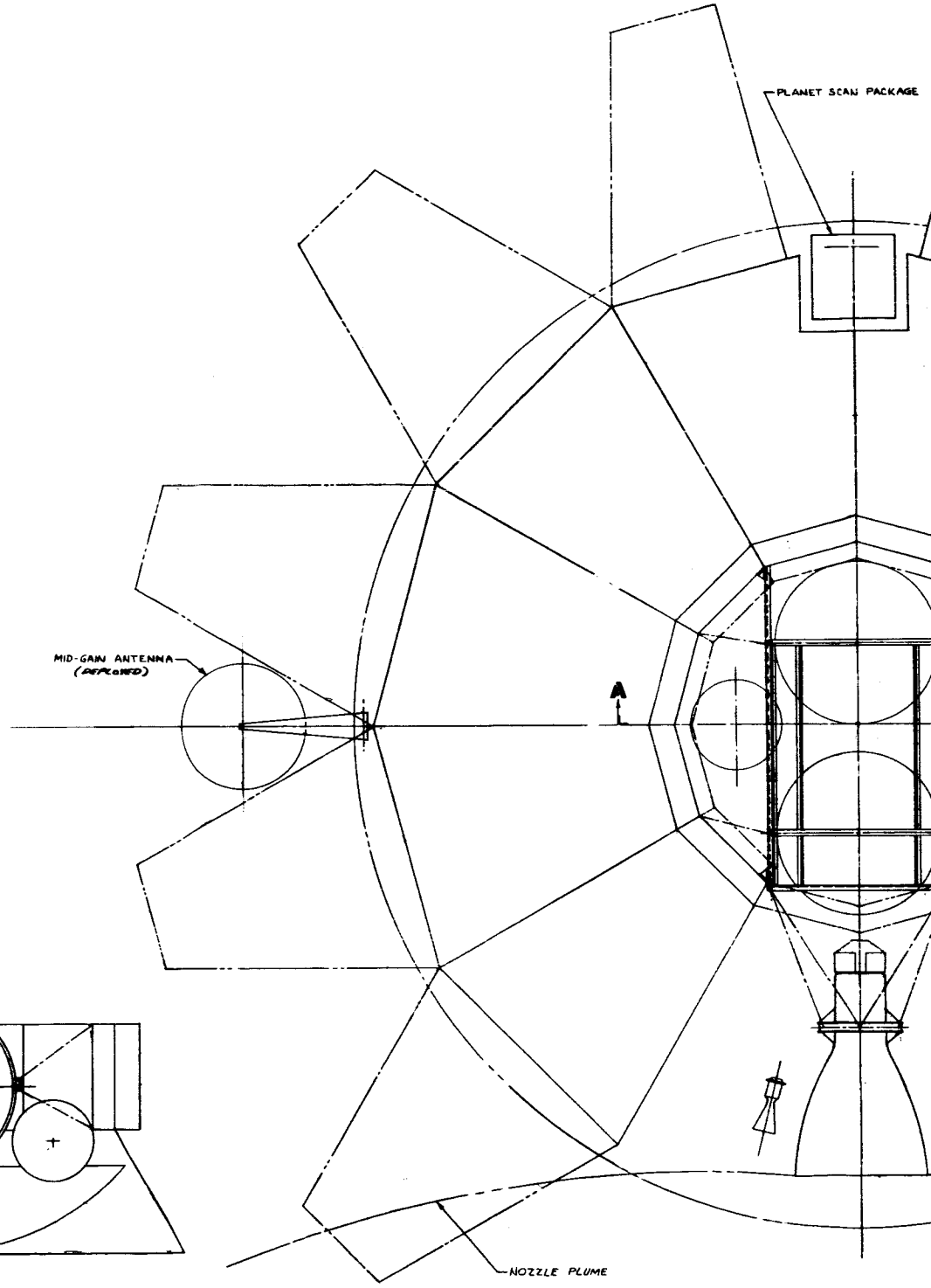

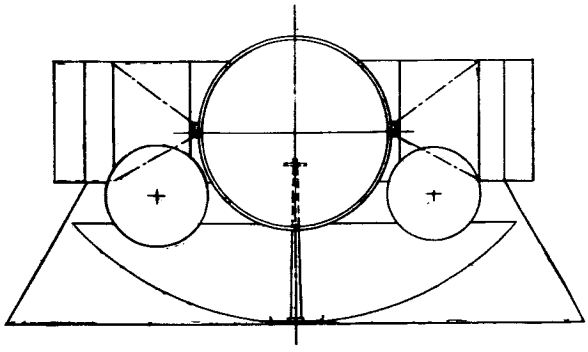

SECTION A-A

[redacted]

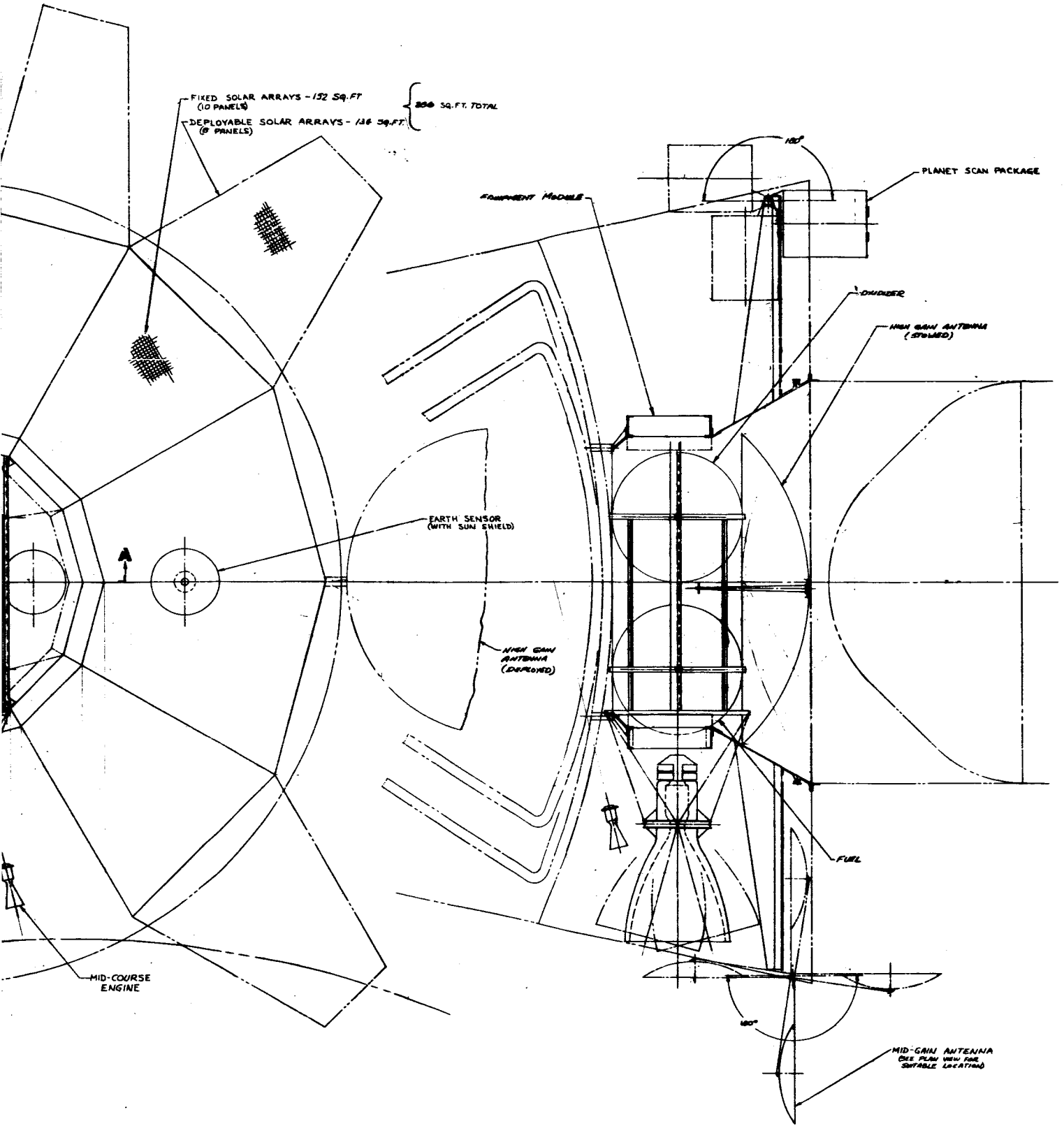

Figure 2-4. Liquid Engine-Side Mounted

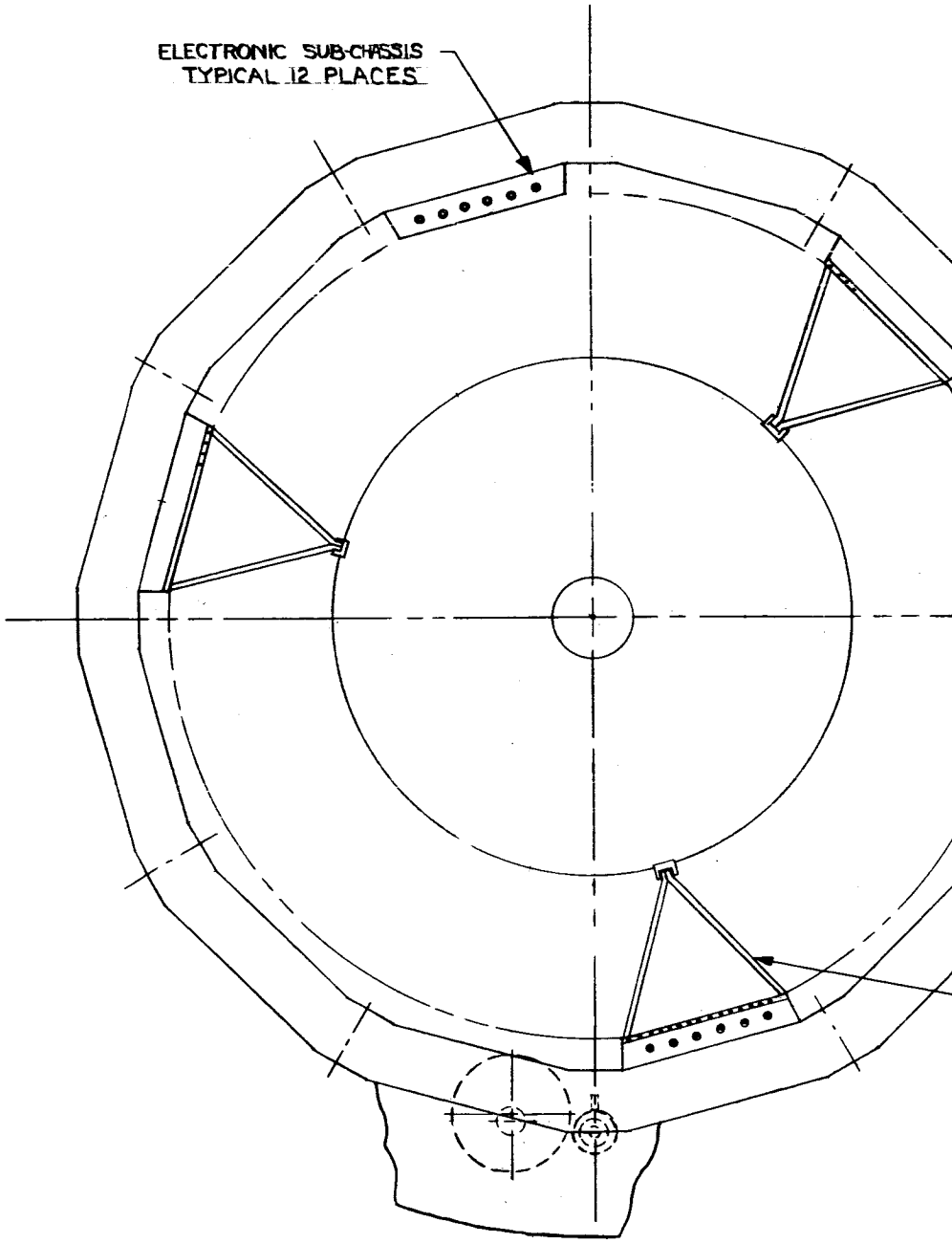

[redacted]

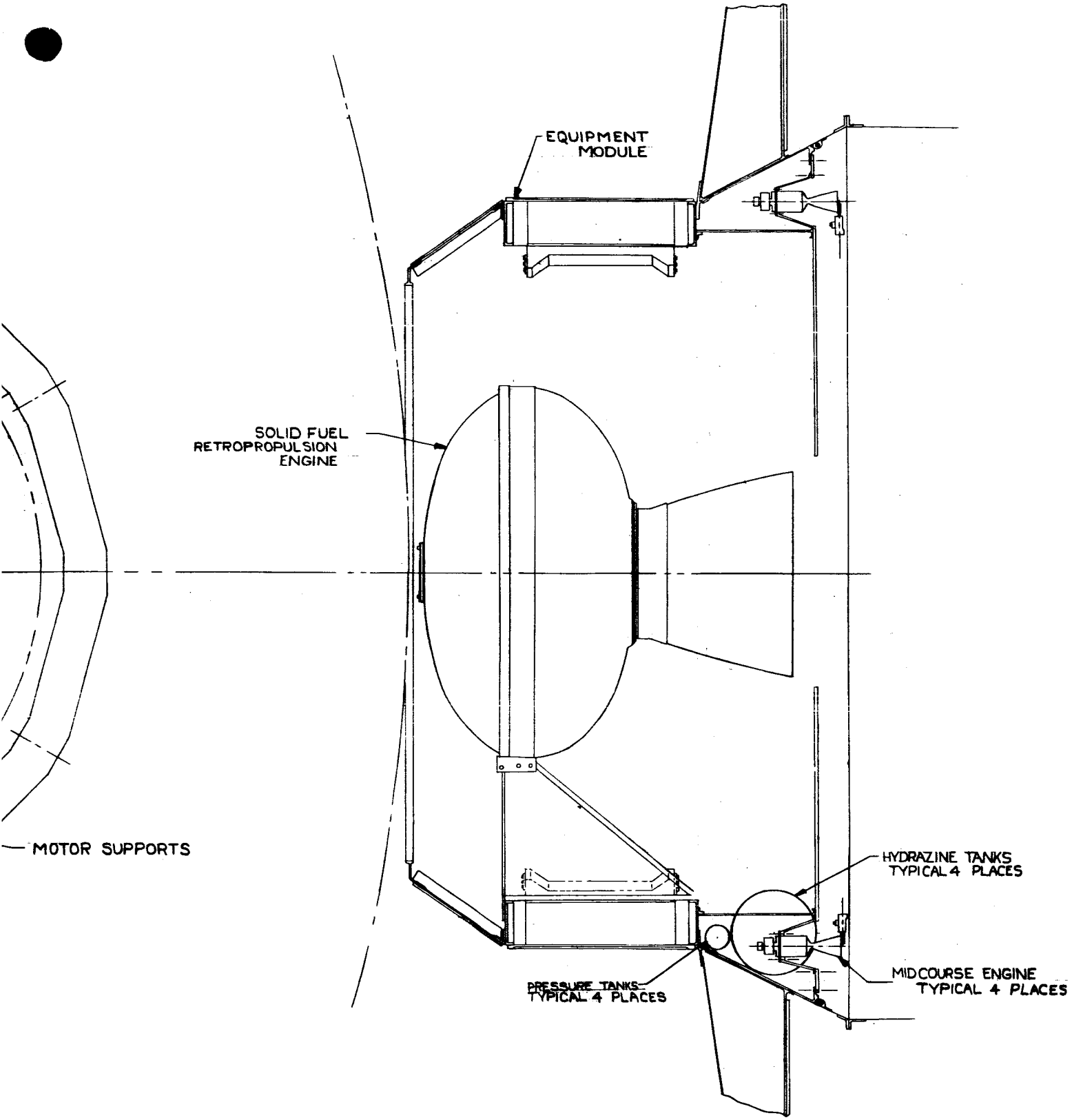

Figure 2-5. Voyager Solid Fuel Retropropulsion Configuration

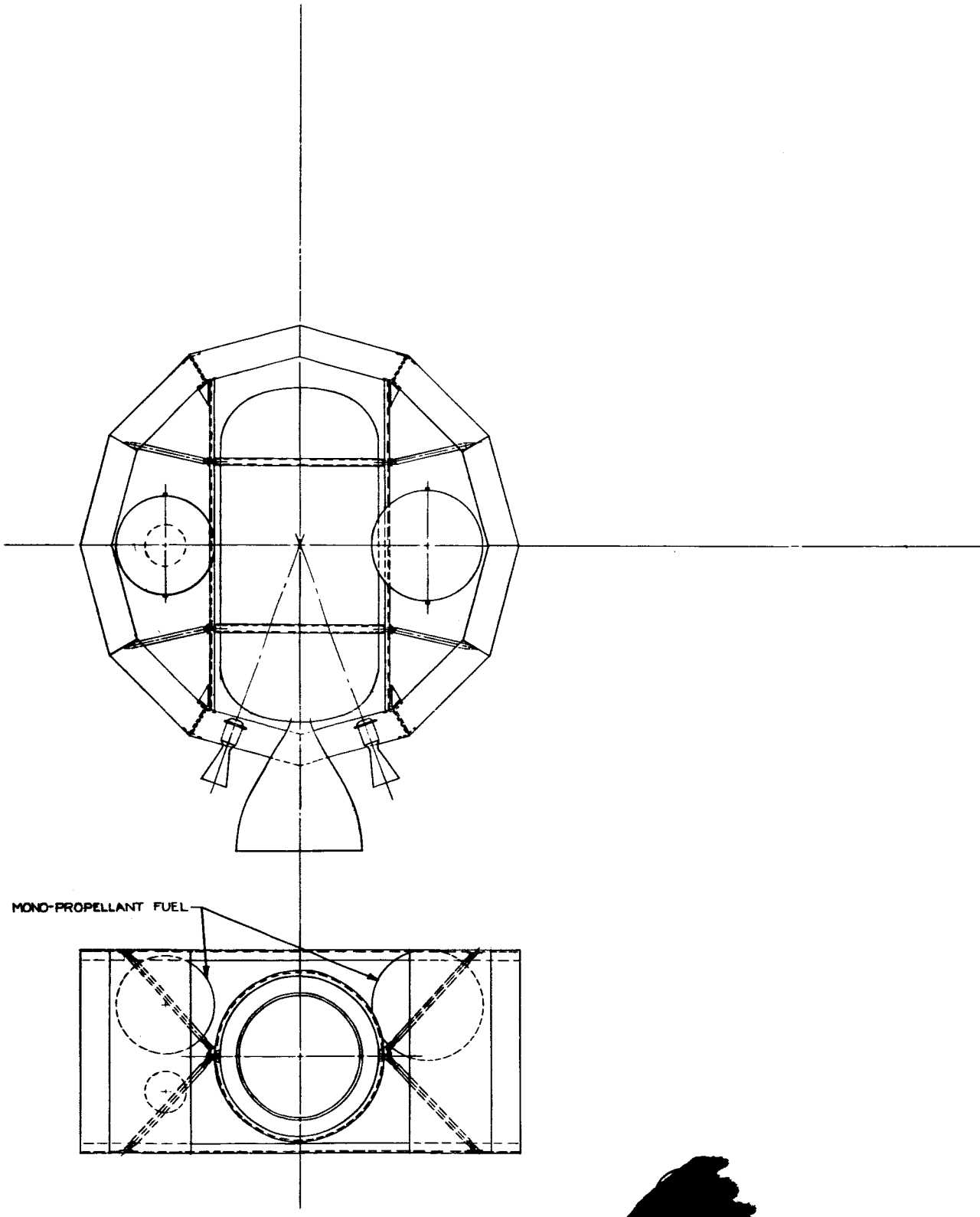

[redacted]

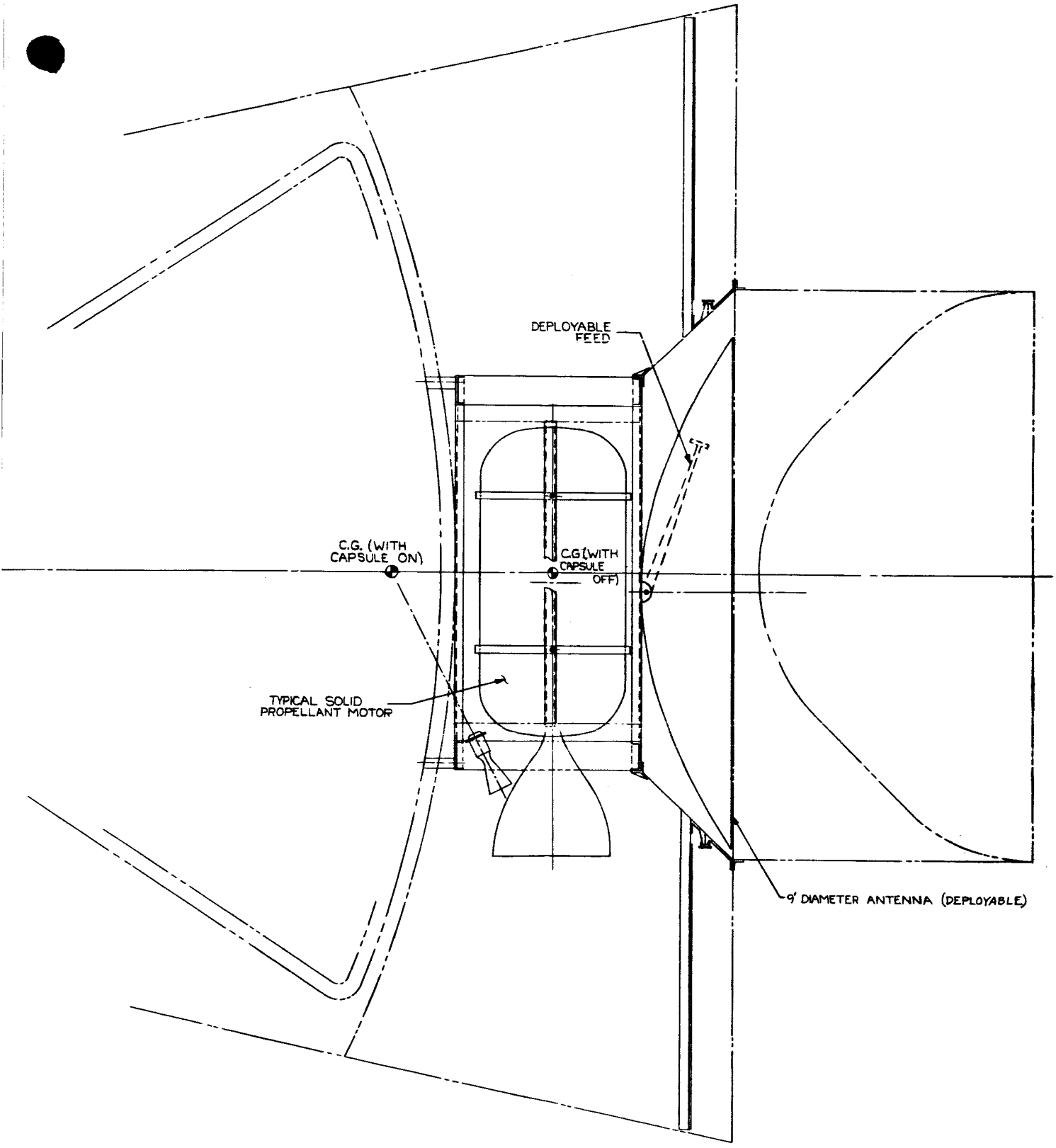

Figure 2-6. Study-Solid Engine-Side Mounted-Spacecraft [redacted]

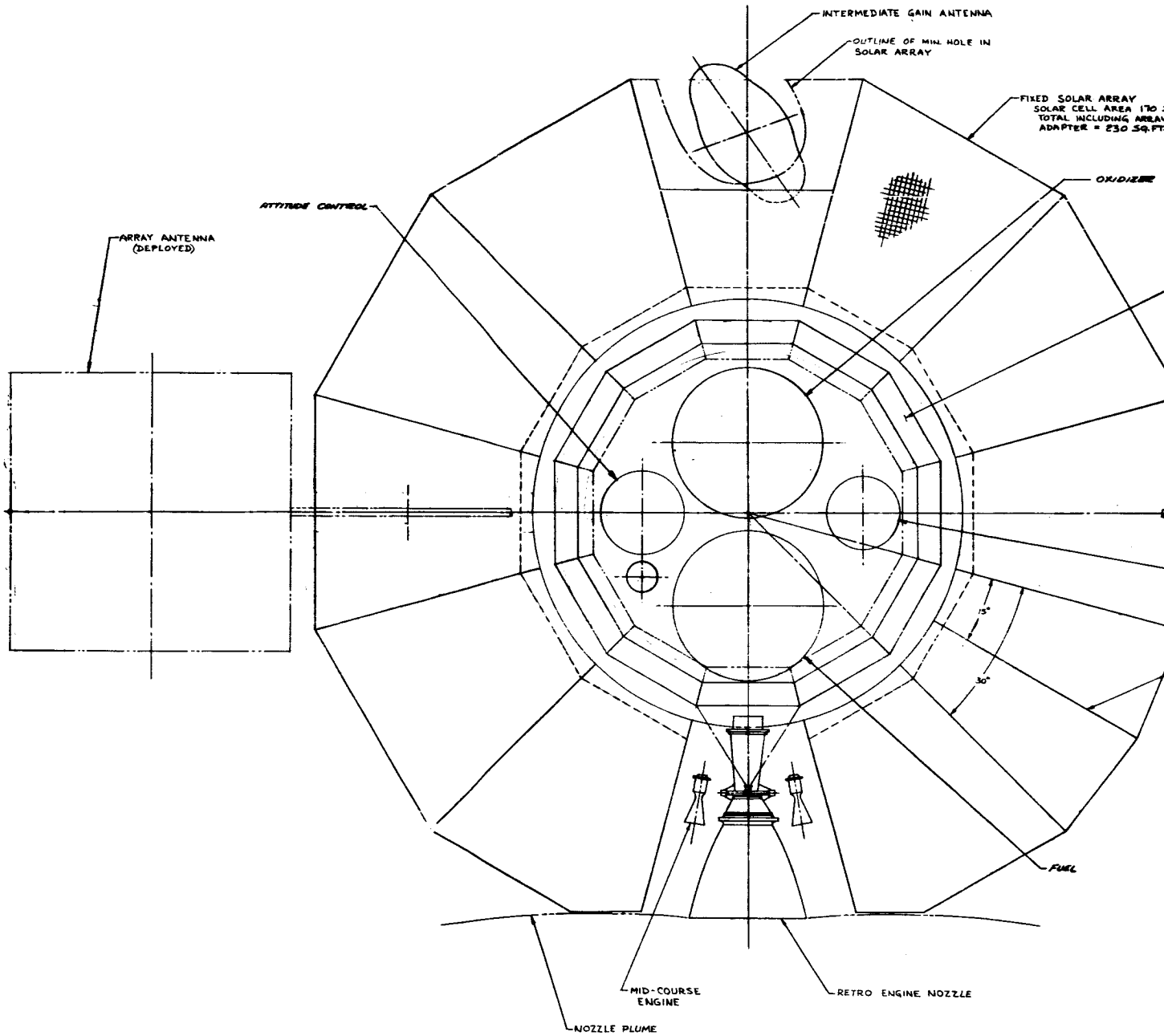
INTERMEDIATE GAIN ANTENNA
OUTLINE OF MIN. HOLE IN SOLAR ARRAY
FIXED SOLAR ARRAY
SOLAR CELL AREA 170
TOTAL INCLUDING ARRAY
ADAPTER = 230 SQ.FT.
OXIDIZER
ATTITUDE CONTROL
ARRAY ANTENNA (DEPLOYED)
15°
30°
FUEL
MID-COURSE ENGINE
RETRO ENGINE NOZZLE
NOZZLE PLUME

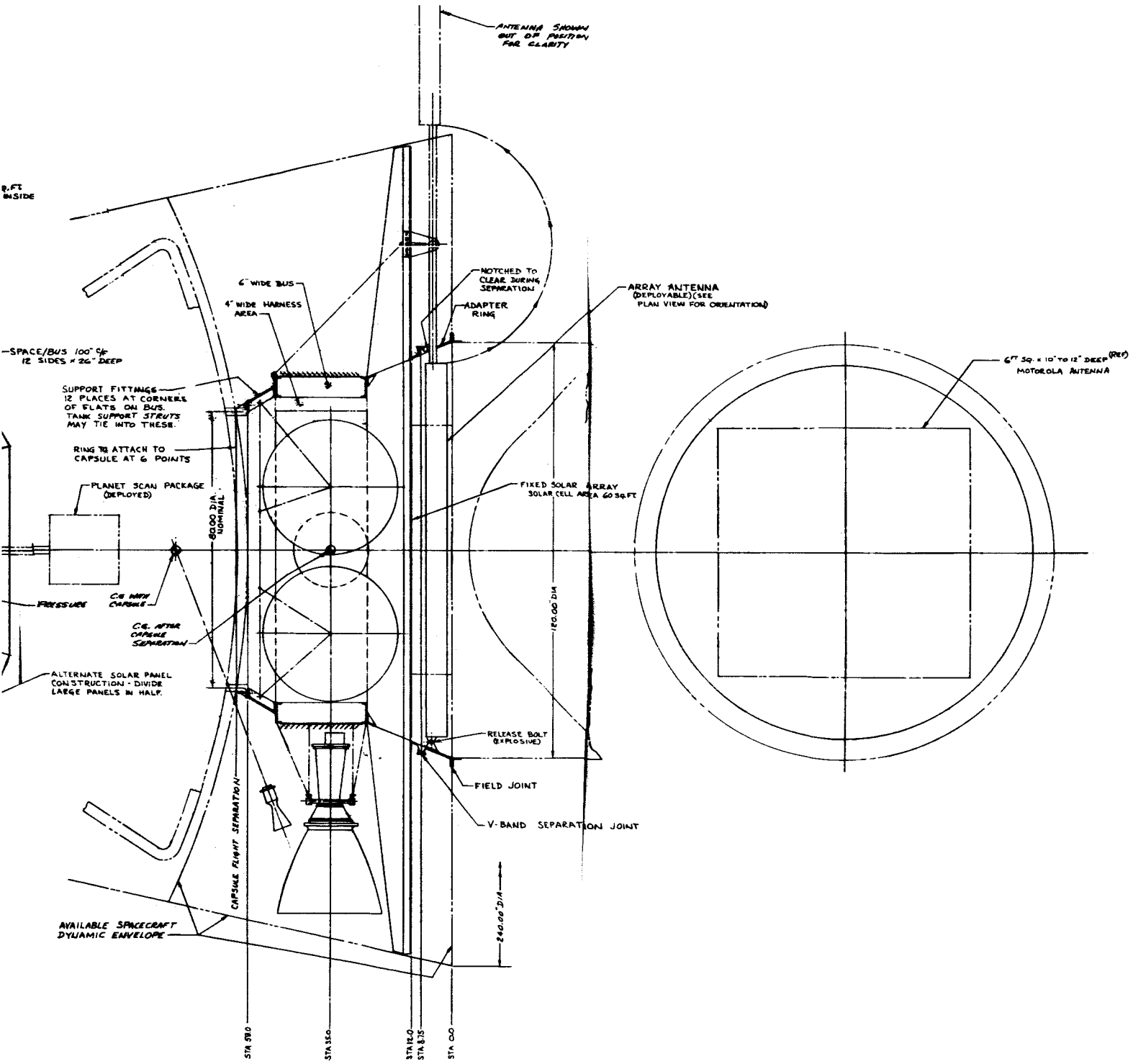

Figure 2-7. Study-Side Mounted Engine-Spacecraft Array Antenna

[redacted]

[redacted]

22 of 30

f. Compatibility with primary structural load path requirements and minimization of weight.

g. Compatibility with subsystem packaging and harnessing requirements.

The primary decision to be made here was the selection of diameter and slope of the surface of the E/M, and the influencing constraints here were letters a, b, c, d, and f. The desire to integrate the electronic package structure with the primary structure tends to align the electronic subassembly along a cone of direct load path for minimum weight (f). However, the electronic subassembly should be about six (6) inches deep for standardized packaging efficiency, thus tending to design a similar depth primary structural framework in the area of the E/M. This is not compatible with structural load requirements, except for the necessity to have structure extending inwards to pick-up the propulsion module. The desire to use 4 spherical tanks in a concentric arrangement around the engine tends to fix the propulsion module envelope at an 80-inch external diameter.

The interaction of a sloping sided E/M with the other packaging volume requirements is shown by a plot of equipment packaging volume (integrated from upper end since full utilization of the upper portion of the E/M gives minimum dimension compatible with constraint d) presented as Figure 2-8. Also presented is the area of external cover surface and the radius vs station location. These are presented for a circular cross-section as differentiated from the flat sided shape of the final design. Inspection of the curve shows that the inner radius of 40 inches occurs at station 40 and outer radius of 55 inches occurs at station 36.7 and the volume enclosed between these two stations is only $\approx$ 4300 in ^{3}; therefore, the sloping sided system is incompatible with a constraint such as this. Actually these constraints are rather severe and the requirements could be changed to accomodate the sloping sides but other considerations enter here also. Reliable thermal control of the spacecraft is a high priority item and the thermal louvers have been selected to be a parallel acting system for reasons of simplicity and reliability. The paralled acting louvers require the hinge line to be on the lower edge to avoid viewing the back surface of the solar array. Blockage by the capsule structure for partially open louvers is thus decreased by vertical sides, and would be reduced further if the E/M had a reverse slope from that being discussed.

Therefore the conclusion here is that the only significant reason for having a slope-sided E/M would be the structural weight penalty involved with load path discontinuities. The oversize framework (with thicknesses determined by minimum machining gages) necessary for the electronic subassemblies provides rings sufficient to withstand the "kick" loads, and the weight penalty for vertical sided E/M is therefore small. It should be noted here that (1) the entire design concept of integration of these electronic subassemblies should be the subject of further optimization studies, (2) with a double-acting louver system the thermal control system would desire the sloping sided E/M; (3) removal of some packaging conservatism or more flexibility in packaging

ground rules could result in significantly different design, (4) relaxation of the maximum 1969 Atlas-Centaur payload envelope could affect diameter, and (5) longitudinal C. G. location has not been considered due to use of multiple midcourse engines.

The conclusion here is that with the decision for a vertical-sided E/M based upon thermal control considerations, structual requirements, and manufacturing advantages (not previously mentioned), the diameter can also be made compatible with both the propulsion module requirement of 80 inches diameter and the 110-inch diameter of the Centaur shroud.

The above considerations were the basis for the size and shape of the E/M, and one other design feature is now discussed - the choice of the number of bays, to be twelve (12). The considerations here are general handling size and weight and the subsystem packaging requirements of the electronic subassemblies, and the effect on the structural load path. Flat sided panels are a constraint initially imposed for standardized packaging techniques, but this is a separate effect on structural weight that is not discussed here. Results of present study show that with 750 lbs. of electronic equipment and 40% maximum variation among bays the panel weight vs. bay number is tabulated as follows:

Number of bays	Maximum weight/bay
8	131.0
12	87.5
16	65.5

The breakdown of subsystems requires less than 12 bays since it is seen that several subsystems have equipment on two or three bays.

Packaging volume requirements tend to desire more bays so that the volume can be better distributed to a circular ring shape, thus reducing the volume cut out by the flats, and the handling weight requirements makes twelve bays essentially a minimum due to limitations of handling and installation (however, special handling fixtures could be designed to accommodate this requirement).

With the assumed usage of a separation nut system on the flight capsule (Ref. VB220FD106) the desire for minimization of number of tie-down points is obvious from a reliability standpoint. However, the severe loading environment of the 1971 Voyager mission specifications (Ref. VB235FD103) a larger number of load introduction points is desirable at the flight capsule interface. A compromise of six (6) attachment points was effected, leading to a 6 longeron structure in the capsule support and 12 longerons (and thus 12 bays) in the E/M. It should be noted that a more uniform distribution at the interface would be structurally more desirable.

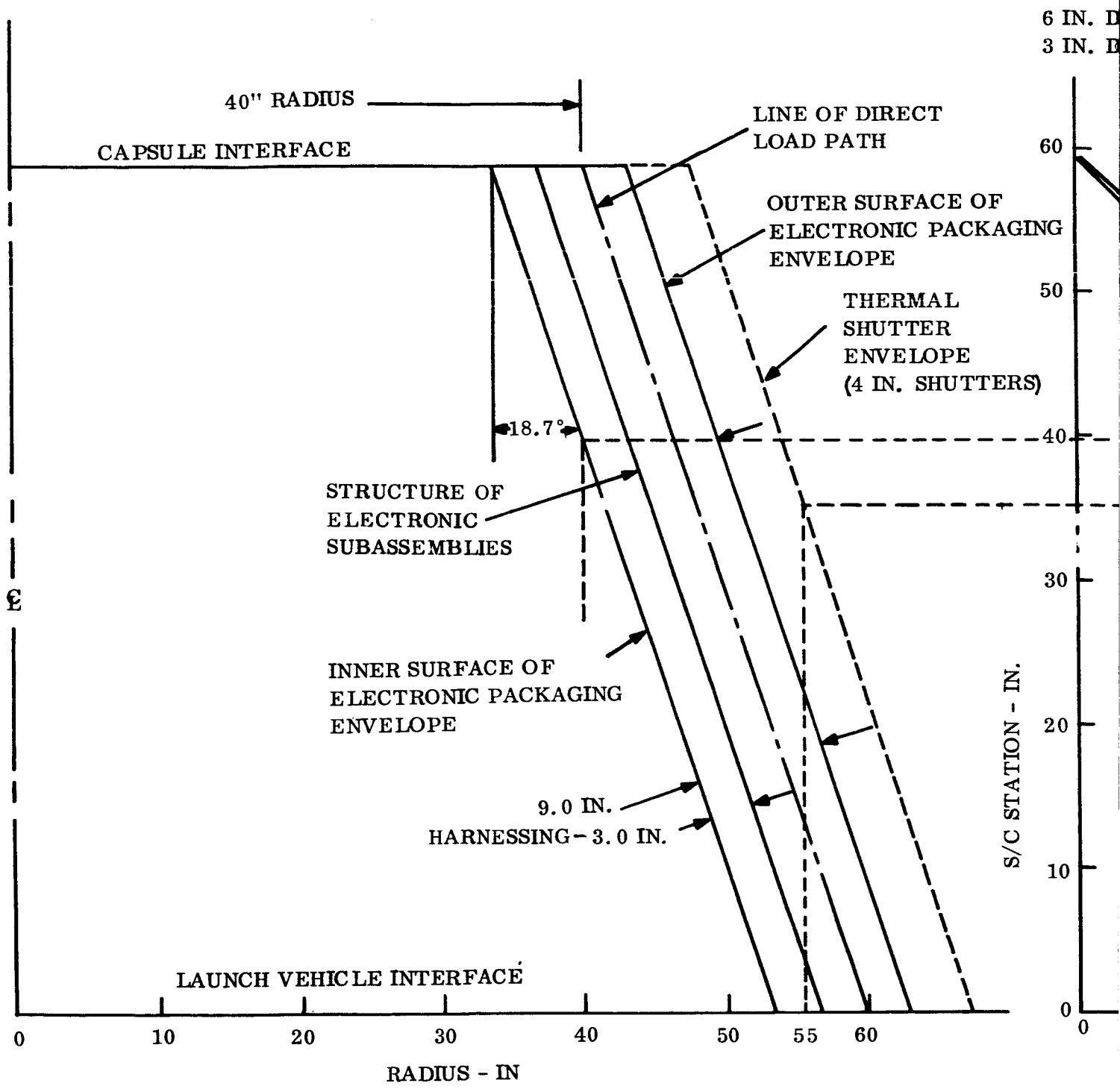

[redacted]

25 of 30

EEP ELECTRONIC SUBASSEMBLY
EEP HARNESS SUBASSEMBLY

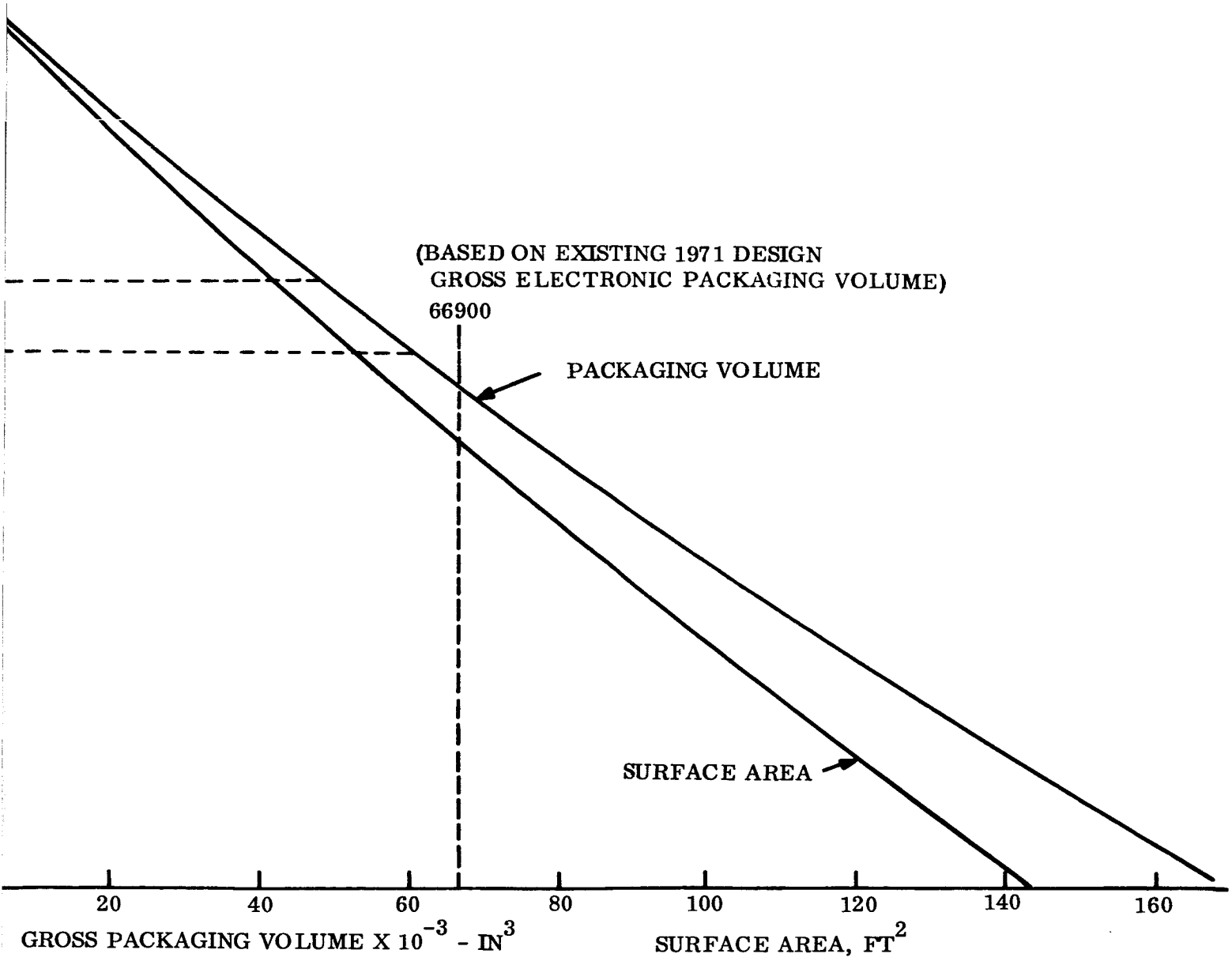

Figure 2-8. Design Geometry Parameters

Conclusion of above trade-offs was establishment of a 12-bay vertical-sided E/M with 100-inch dimension across flats. The advantages are not significant and perturbations of packaging ground rules could lead to an alternate design.

2.3.2 ANTENNA, SENSOR LOCATIONS

The general configuration is affected by the requirements for the pointing of sensing and transmitting devices and their corresponding fields of view, engine exhaust plume envelopes, and cold gas nozzle plume dimensions. Some of these devices are located by their function requirement (e.g. retro engine, cold gas nozzles, etc.). The components which are not critical in their exact location but only their orientation are those which can vary and thus affect the configuration. Major of these are the telecommunications antennas, the various attitude control position sensors, the magnetometer, and the planet scan platform (which is discussed separately here and in VB234FD109).

2.3.2.1 TELECOMMUNICATION ANTENNAS

a. High-gain antennas

The high-gain antenna is deployed so that it clears the solar array structure during the large excursions required for maneuver. The only variable is the location on the vehicle, and the requirement for the major axis of rotation to be parallel to the Y axis.

b. Medium-gain antenna

The medium gain antenna has pointing requirements as defined in VB233FD101 and may be located anywhere on the vehicle that physical obstruction with the antenna wave pattern does not exist. The location out from bay 3 in the proxmity of the high gain antenna was made due to desirability of combining the support structure of the two antennas into one, and the pointing requirement orients the elongated direction of the antenna nearly along an element line, resulting in less interference with the solar array.

c. VHF Relay Antenna

The VHF relay antenna pointing requirement and alignment are as shown in VB233FD104 and thus require a location in the vicinity of the high-gain and medium-gain antennas. The existing location is as far over in Quadrant I as it can be without interference of its wave pattern by the high gain antenna.

2.3.2.2 MAGNETOMETER

The only constraint on magnetometer location is the deployed position with respect to the spacecraft and the alignment requirement of 1° to the Z axis. Initial studies indicated the requirement for a maximum length non-folding boom which could be stowed on the spacecraft and this was a boom of approximately 170 inches in length. However,

the alignment requirement and the decision to keep the magnetometer deployed during retrofire necessitates a much shorter boom and the present 63 inch length was selected.

2.3.2.3 SENSORS

The optical sensors have requirements for orientation, accurate alignment and no surface contamination, but no specific location requirements other than having a clear optical field of view. Consequently they have been placed at satisfactory locations with no particular problems.

2.3.2.4 ROLL NOZZLE LOCATION

The pitch and yaw nozzles are located in planes which go through the C.G., while the thrust vectors from the roll nozzles lie in a plane which is displaced about 24 inches from the C. G. This displacement could result in cross-coupling in the pitch plane in the event that one of the nozzles fails to exhaust. (Actually any imbalance of the opposed forces causes cross-coupling, but of negligible degree). Consideration was given to placing the roll nozzles on standoffs to bring them closer to a C. G. plane and the following considerations entered into final location (on the solar array structure):

a. C. G. motion after lander separation rendering impossible the complete elimination of cross-coupling.

b. Moment arm would decrease as roll nozzles move upward due to slope of spacecraft envelope thus requiring additional gas for normal operation with no failed valves.

c. Reliability of proper valve-nozzle operation is very high.

d. Additional structure required for standoff would add weight (probably in excess of the additional gas requirements)

e. The nozzles would create more interference with other components if mounted on standoffs.

2.3.3 PLANET SCAN PLATFORM

The planet scan platform has presented the most problems with respect to location and orientation due to its requirement for motion combined with no blockage. The orbit change effects, articulation requirements and desired coverage are traded-off in VB234AA108. The major perturbation that the spacecraft configuration has gone through is establishment of the deployed position of the planet scan platform, so that the optical axes clear the extended solar cell panels, the flight capsule sterile canister,

and the spacecraft structure. This final position affects the platform boost support structure, length of supporting arm and subsequent rigidity, spacecraft moment of inertia, and C. G. location.

In general the Y axis intersection with the edge of the spacecraft has been a satisfactory location due to the range of Mars orbit inclinations studied, and the requirement is to deploy the platform so that the optical axes are parallel to the orbit plane and a rotation axis exists which is normal to the orbit plane so that the optical axes may remain on the local vertical during orbit.

The planet scan platform has therefore been positioned at the Y axis intersection with the outer edge of the fixed solar panels with the high-gain antenna being approximately diametrically opposite (they could be reversed without any difference). When the requirement for deployed solar cell panels was removed, the remaining major blockage to planet scan view became the Capsule sterile canister.

The decision to jettison the lower portion of the sterile canister (which was partially influenced by the planet scanner requirements) then essentially solves the blockage problem. The final stowage and deployed location was selected because of the existence of an empty bay (#9) and the following advantages associated with locating the platform closer to the equipment module behind the fixed solar array:

a. Shorter electrical cable runs for science instruments

b. Further away from cold gas nozzles and thus less likelihood of contamination.

c. Better structural support available for boost support and deploying mechanism.

d. Reduced spacecraft roll moment of inertia.

e. Easier thermal control of platform since it is shaded.

f. Lens cover may be incorporated with tie-down structure.

g. Angle of rotation in orbit plane is increased some before blockage by fixed solar array.

Disadvantages are (1) the absolute reliance upon the separation of the sterile canister for planet scanner operation, i. e. there is no partial operation mode in case the separation does not occur, (2) the proximity of the platform to the capsule separation systems and the possible detrimental effects from the associated shock pulse, and (3) requirement for design modification if the bay #9 is ever desired to be used for equipment.

2.3.4 SOLAR ARRAY LOCATION

The station location of the fixed solar array is predicated upon several considerations as shown in Table 2-1 and the only additional consideration would be a design which would move the solar array lower but be supported from a higher location, i.e. it could satisfy the constraints 11, 12, and 13 all at the same time. Figure 2-9 shows this type of configuration.

This configuration would cost some structural weight and complicate the OSE handling fixture somewhat.

2.3.5 SEPARATION OF LOWER PORTION OF STERILIZATION CANISTER

The considerations concerning jettisoning of the capsule adapter/sterile canister structure which remain after capsule separation are tabulated as a list of advantages and disadvantages of jettisoning in Table 2-3 below:

Table 2-3. Capsule Adapter Jettisoning Considerations

Advantages	Disadvantages
Reduces weight into orbit, thus decreasing propellant requirement for a given ΔV, and subsequent general decrease in spacecraft weight.	Requires additional separation which is in series with the science data gathering function orbital mission requirements, and thus decreases probability of success by some amount.
Permits final position of planet scan platform and the associated advantages (see section 2.3.3)	Additional shock impulse to spacecraft components.
	Removes the upper meteoroid protection provided by this structure being jettisoned.

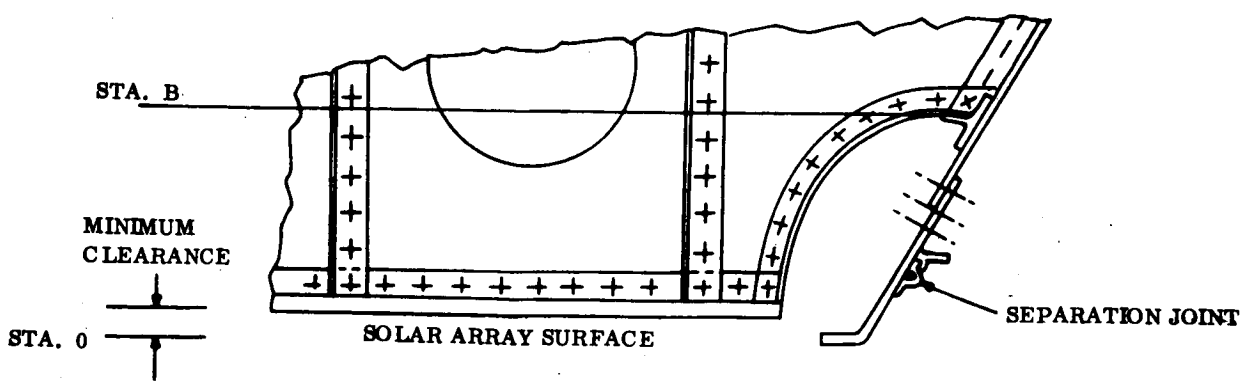

Figure 2-9. Solar Array Configuration

CII - VB220AA112

ALTERNATE SYSTEM PHILOSOPHIES AND SYSTEM MECHANIZATIONS CONSIDERED

ALTERNATE MISSION SEQUENCES

Index

1 Introduction
2 Capsule Separation and Final Guidance Correction Timing
3 Time of Arrival Separation Between Capsule and Spacecraft
4 Capsule-Spacecraft Separation

1.0 INTRODUCTION

Selection of the propulsion subsystem and the means of controlling spacecraft attitude during engine firings involves consideration of the overall vehicle configuration and has a major influence on the total system design. A wide range of possibilities was considered in arriving at the design solution described.

A first consideration was location of the thrust vector relative to spacecraft axes for both midcourse corrections and orbit injection. For midcourse, it is clear that thrusting should be along the vehicle roll axes since corrections may be made both with and without the Capsule attached. The shift in center of mass between these two cases dictates thrusting along the roll axis.

Location of the retro propulsion engine is not quite as clear. "Side" mounted retro engines were considered and were found to have the following disadvantages:

a. Modularization of the propulsion system i.e., building it as an assembly to be attached to the spacecraft, is extremely difficult.

b. Use of mid-course engines for steering, if desirable, is not possible.

c. Interference of the plume with the spacecraft becomes aggravated.

d. Control of the spacecraft center of mass under thrusting in two directions is difficult. For example, the midcourse propellants should have a center of mass along the roll axis during midcourse corrections, and along the retro thrust axis during orbit injection, which is difficult to achieve.

e. Incompatibility with the '69 flight on Atlas/Centaur.

f. Use of the high gain antenna for communication during both midcourse and orbit injection will require greater antenna freedom if the two thrust axes are not coincident.

The only advantages for a side mounted engine are somewhat greater separation between the center of mass and the point of application of thrust, and a potential capability for mounting a larger antenna in the area occupied by the thrust chamber.

Comparing these advantages and disadvantages, it is clear that the optimum location for the retro propulsion engine is on the roll axis.

The propulsion systems considered and the associated means of controlling the thrust vector are described in VB238FD101. Three major systems that were considered in detail are a single gimballed bi-propellant engine, a fixed bi-propellant engine using mono-propellant engines for steering, and a solid retropropulsion motor using mono-propellant engines for steering. Results of this study show that each of these systems have the potential for successfully performing the Voyager propulsion function.

The advantages and problems associated with each of these systems is discussed briefly in the following.

2.0 SINGLE BI-PROPELLANT LIQUID ENGINE FOR RETRO AND MIDCOURSE

The single engine for accomplishing both guidance corrections and orbit injection is the lightest and least complex (and consequently, the potentially most reliable) propulsion system considered. In the approach considered most fully, the engine would be gimballed to provide pitch and yaw control and roll control would be achieved using the cold gas system.

The thrust level for this engine would be determined by the maximum burn time allowed for an ablative chamber. As discussed in VB238AA101, 1000 pounds is a conservative minimum level from this standpoint. This does not allow the smallest velocity increment of 0.1 meter/sec. for guidance corrections, but as discussed in VB220AA102, a minimum correction of 1 meter/sec. presents no real guidance problems. A more likely thrust level, considering the development status of such engines, is 2200 pounds. This still allows a minimum correction of less than 1 meter/sec.

During the study, difficulties were encountered in establishing a satisfactory system for control of vehicle attitude during engine firing using a single gimballed engine. The "pancake" configuration of the spacecraft gave rise to this difficulty and the problem is indicated partially in Figure 2-1. The range of the location of the center of mass is shown for the vehicle described in Volume A for both the Capsule on and off. For an engine gimballed at the injector end, it can be seen that the center of mass with the Capsule attached may lie at, or very near, the gimbal point, and may cross the gimbal point when the Capsule separates. A gimbal ring on the expansion nozzle likewise has fairly small separation with Capsule detached, and is a less desirable location from a propulsion standpoint.

If the spacecraft body is held to a fixed attitude in inertial space during thrusting, large gimbal angles associated with small separation of the gimbal point and the center of mass result in very undesirable guidance errors.

In addition to the guidance accuracy concern, initial investigations indicated that achieving dynamic stability with this approach, while achieving the desired frequency response, was difficult. The coupling of the engine inertia with the vehicle for this particular configuration produces a different effect than in the case of the long slender body encountered in a launch vehicle.

The transfer function representing vehicle dynamics of a launch vehicle is minimum phase. Zeroes in the open loop function occur at relatively high frequencies. In the case of a configuration such as Voyager, two conditions may be considered.

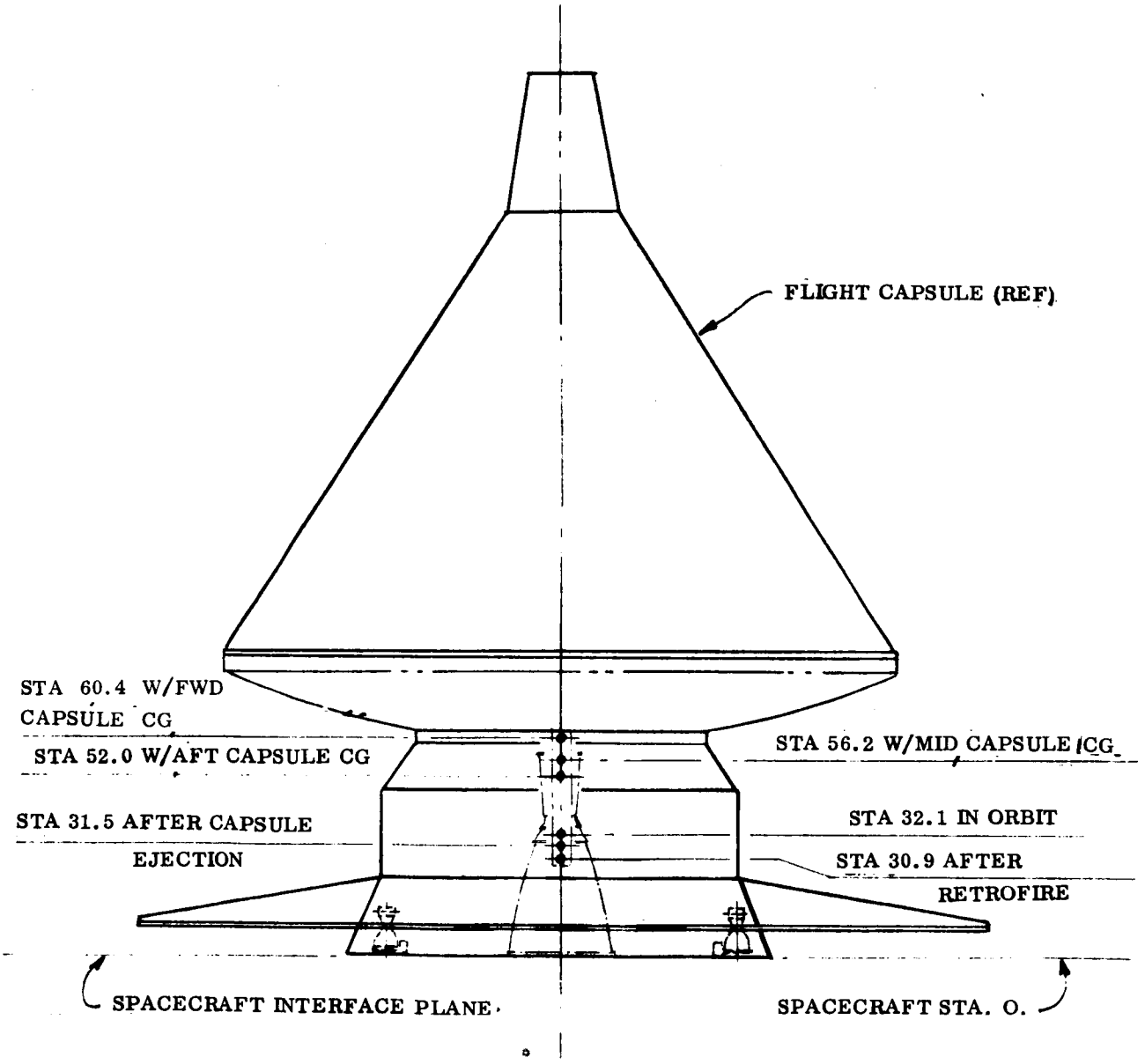

Figure 2-1. Spacecraft Nominal Center of Gravity Locations

a. Engine gimballed at the injection end.

In this case, a non-minimum phase system results for all possible Voyager configurations. The frequency of the zero is primarily dependent upon the separation distance between the gimbal pivot and the system center of mass. With the capsule separated, this frequency is approximately 35 radians per second. With the capsule attached, this value goes down considerably and with a 5-inch separation between the center of mass and the gimbal point, the frequency of the zero is 7 rad/sec.

b. Engine gimballed at the nozzle end.

Capsule removal results in a significantly different condition:

1. With capsule on, the system is non-minimum pahse and the frequency of the zero is about 50 radians/sec. for a practical configuration.

2. With capsule off, a minimum phase system exists and the real frequency zero occurs at about 20 radians/second.

Prior to encountering the control problem, the single gimballed engine was the preferred propulsion subsystem configuration. The only major concern regarding this choice was a potential problem of propellant acquisition for the oxidizer, N_2O_4. It was felt that this could be solved by

a. Use of surface tension screens,

b. Use of cold gas to settle propellants, perhaps as a back-up to (a)

c. Improvements that are being pursued in bladder design, or

d. Use of partial bellows or rupture diaphragms.

Faced with the control uncertainties and the short time available to produce an integrated system design, a decision was made to change the propulsion configuration to that described in Volume A. Specifically, the bi-propellant engine was fixed to the vehicle and a mono-propellant system with four (4) throttlable engines was added to provide steering during retropropulsion. This system is discussed in the next section.

With further effort, satisfactory solutions were subsequently found to the single gimballed engine guidance and control problem. The guidance accuracy problem associated with small separation between the gimbal point and the center of mass can be handled in two ways:

a. The engine can be mounted on a four bar linkage and translated rather than rotate with the mechanization suggested by Rocketdyne.

b. Use of gimbal angle measurement in the control loop allows the thrust vector direction to be maintained at a fixed heading in space rather than the vehicle body axes. This solution still requires some reasonable separation of gimbal point and center of mass so that a problem may exist for an injector end gimbal depending upon the specific location of the Capsule center of mass.

As shown in the autopilot analysis, VB234AA105, control system stability can be achieved without undue complexity. This system is, therefore, competitive with the other two approaches.

3.0 BI-PROPELLANT LIQUID SYSTEM FOR RETRO WITH MONO-PROPELLANT SYSTEM FOR MIDCOURSE

This combination was originally considered as essentially independent systems with control during orbit injection by means of gimballed bi-propellant engine and cold gas, while control during midcourse correction was by jet vanes. The advantages of such a system were felt to be:

a. Lower thrust and hence better accuracy for midcourse corrections.

b. Allows the bi-propellant system to be sealed until required for use.

c. Provides a potential for use of the mono-propellant system for settling of the retro-propellants should propellant acquisition for N_2O_4 be a major problem.

It was determined that the increased guidance accuracy was not justifiable, and the other factors were not sufficient reason to incorporate the added complexity of the separate mono-propellant system.

However, when the difficulty of control with the large liquid engine arose, the mono-propellant system was re-examined from a standpoint of providing steering during main engine burn. In this configuration, the retroengine is rigidly attached to the spacecraft and three or four mono-propellant engines at some distance from the roll axis are throttled to balance out disturbances due to misalignment of the main thrust vector with the center of mass. Roll control can be achieved by use of jet vanes in one or more of the mono-propellant engines, or in the case of four engines, each engine can be mounted with a slight circumferential thrust and differential throttling used for roll control.

Such a system has the following advantages as well:

a. Location of the center of mass along the roll axis is of no real concern from a control standpoint, which allows greatest flexibility in dealing with an unknown capsule center of mass location.

b. At the expense of some weight, rather wide tolerances on center of mass shifts normal to the roll axis can be handled relatively easily.

c. Obtaining the desired frequency response is no problem.

d. Guidance errors associated with rotating the thrust vector off the roll axis for control purposes are eliminated.

e. The low thrust mono-propellant system can be used for settling the retro-propellants, and also for making small midcourse and orbit adjust corrections.

f. The 1975 and 1977 missions can be conducted by removing the large retro system.

The choice of mono-propellant versus bi-propellant for the small engines was made on the basis of demonstrated reliability, no storage/acquisition problem, and throttling of only one propellant versus two. The weight penalty associated with the lower performance mono-propellant is small.

The choice of three versus four small engines is not of great significance. Four engines were selected since they lend themselves better to packaging in the vehicle configuration.

Similarly, the choice of canted engines versus jet vanes for roll control is not crucial. Jet vanes were selected since they uncouple the torques applied to the vehicle and are flight proven. A jet vane is included on each engine to provide redundancy.

4.0 SOLID ROCKET FOR ORBIT INJECTION PLUS MONO-PROPELLANT FOR MIDCOURSE

With the preferred design described, a solid rocket for orbit injection could be substituted for the liquid engine with no major difficulty. This would provide somewhat increased reliability in the main engine and reduce somewhat the center of mass shift due to reduced uncertainty in propellant location (and thereby reduce the requirements for mono-propellant engine fuel).

The disadvantages associated with the solid are:

a. Some loss in flexibility in the orbit injection velocity increment to be provided. Trajectory studies indicate that a fixed increment throughout the launch period could probably be tolerated in 1971. The 1973 opportunity has not been studied in as great detail.

b. The spacecraft is subjected to loadings of approximately 3g's during orbit injection. This imposes a design penalty on deployable devices such as the high gain antenna, magnetometer boom, relay antenna, etc. The penalty is

most severe in the high gain antennas and the actuators required to hold it under the 3g load.

c. The response time required of the mono-propellant system is increased for control purposes to compensate for the approximately seven-fold increase in thrust level.

Results of this study have not shown that any of these three systems can be excluded. All have the potential for successfully performing the propulsion function required for Voyager.

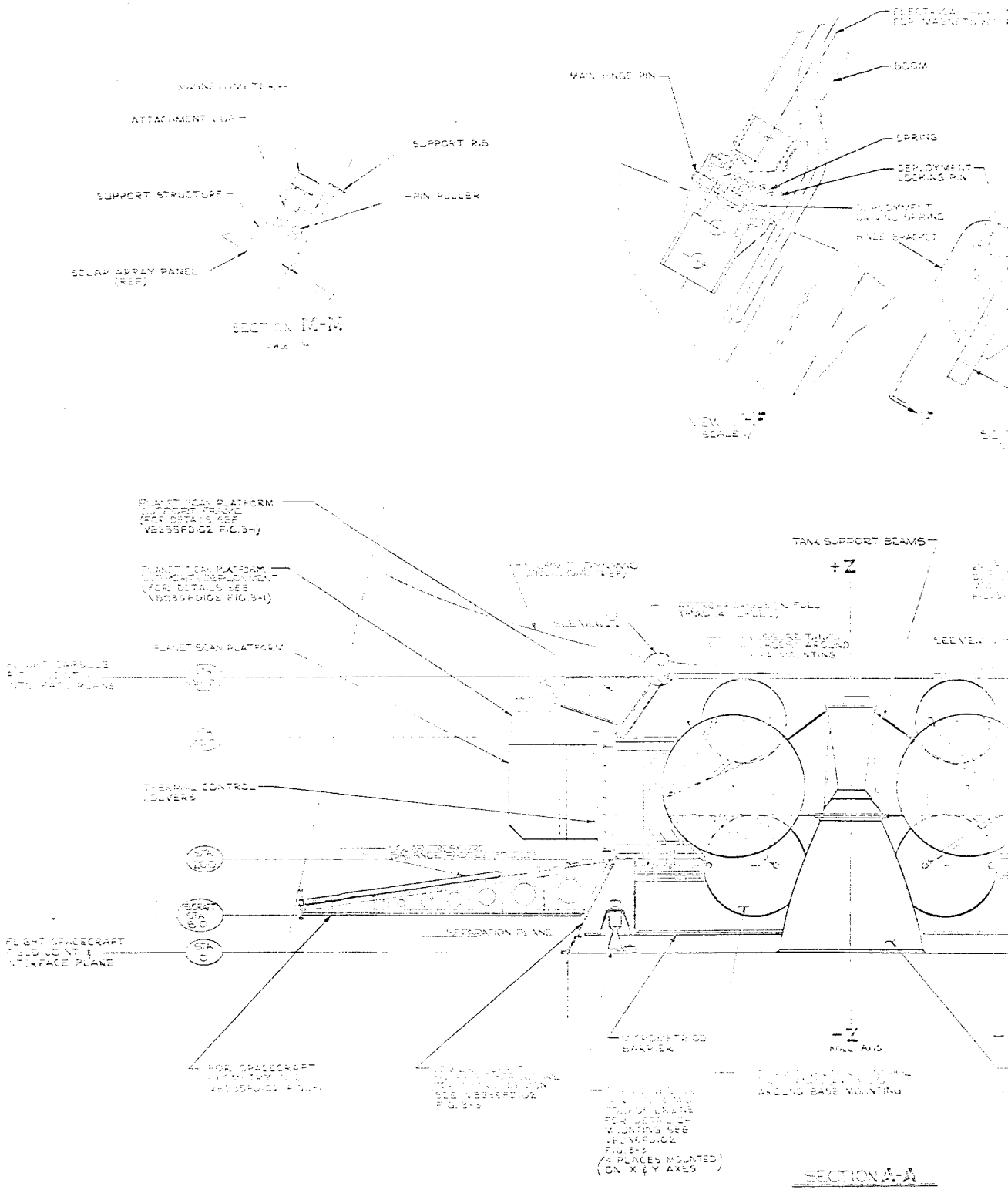
SUPPORT RIB
SUPPORT STRUCTURE
PIN PULLER
SOLAR ARRAY PANEL (REF)
SECTION M-M
MAIN HINGE PIN
BOOM
SPRING
DEPLOYMENT LOCKING PIN
HINGE BRACKET
PLANETARY PLATFORM (SUPPORT FRAME) (FOR DETAILS SEE VB1355F0102 FIG.3-1)
PLANETARY PLATFORM (SUPPORT ENCLOSURE) (FOR DETAILS SEE VB1355F0106 FIG.3-1)
PLANET SCAN PLATFORM
THERMAL CONTROL LOUVERS
TANK SUPPORT BEAMS
+Z
SLEEVE
INTERFACE PLANE
FLIGHT SPACECRAFT FIELD JOINT & INTERFACE PLANE
-Z
ROLL AXIS
SECTION A-A

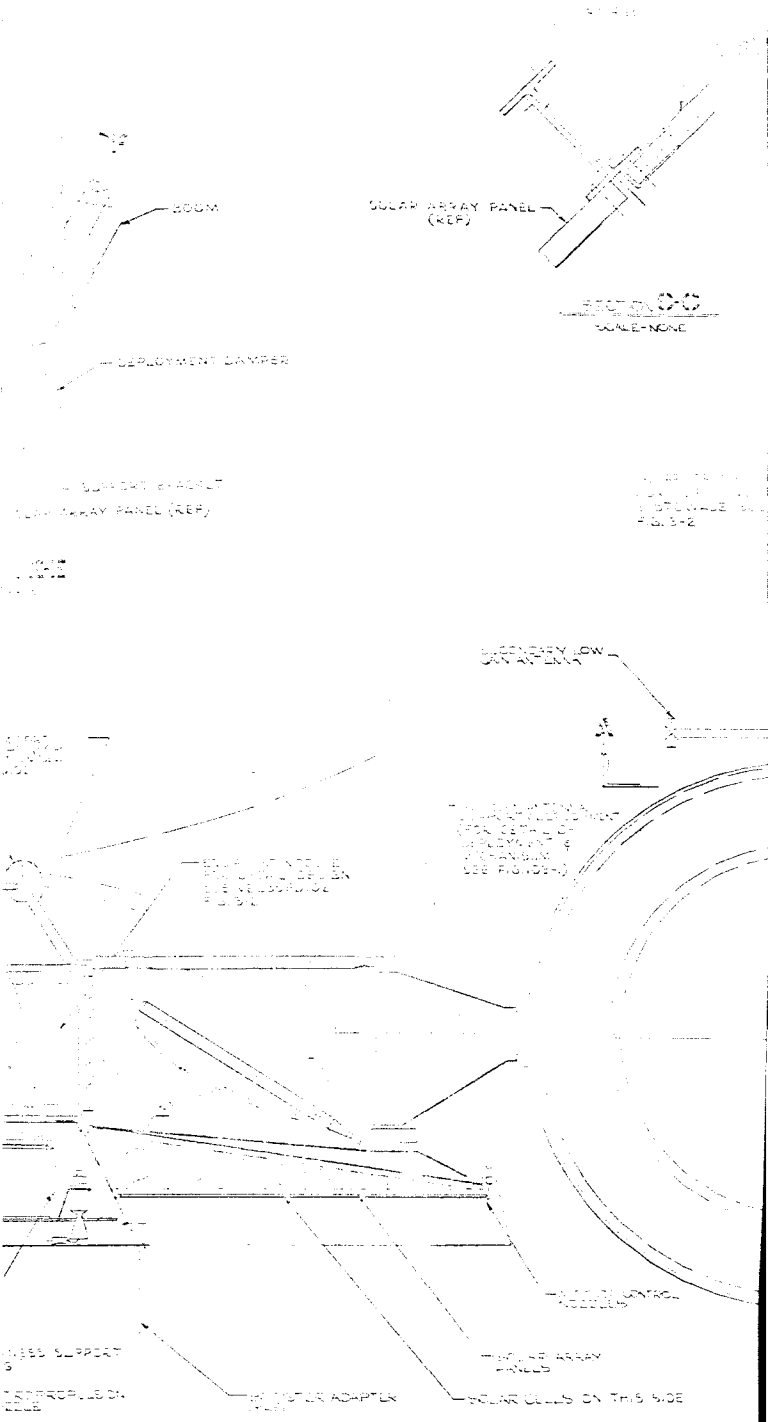
BOOM
DEPLOYMENT DAMPER
SOLAR ARRAY PANEL (REF)
SECTION C-C
SCALE-NONE
SOLAR ARRAY PANEL (REF)
SOLAR CELLS ON THIS SIDE

2

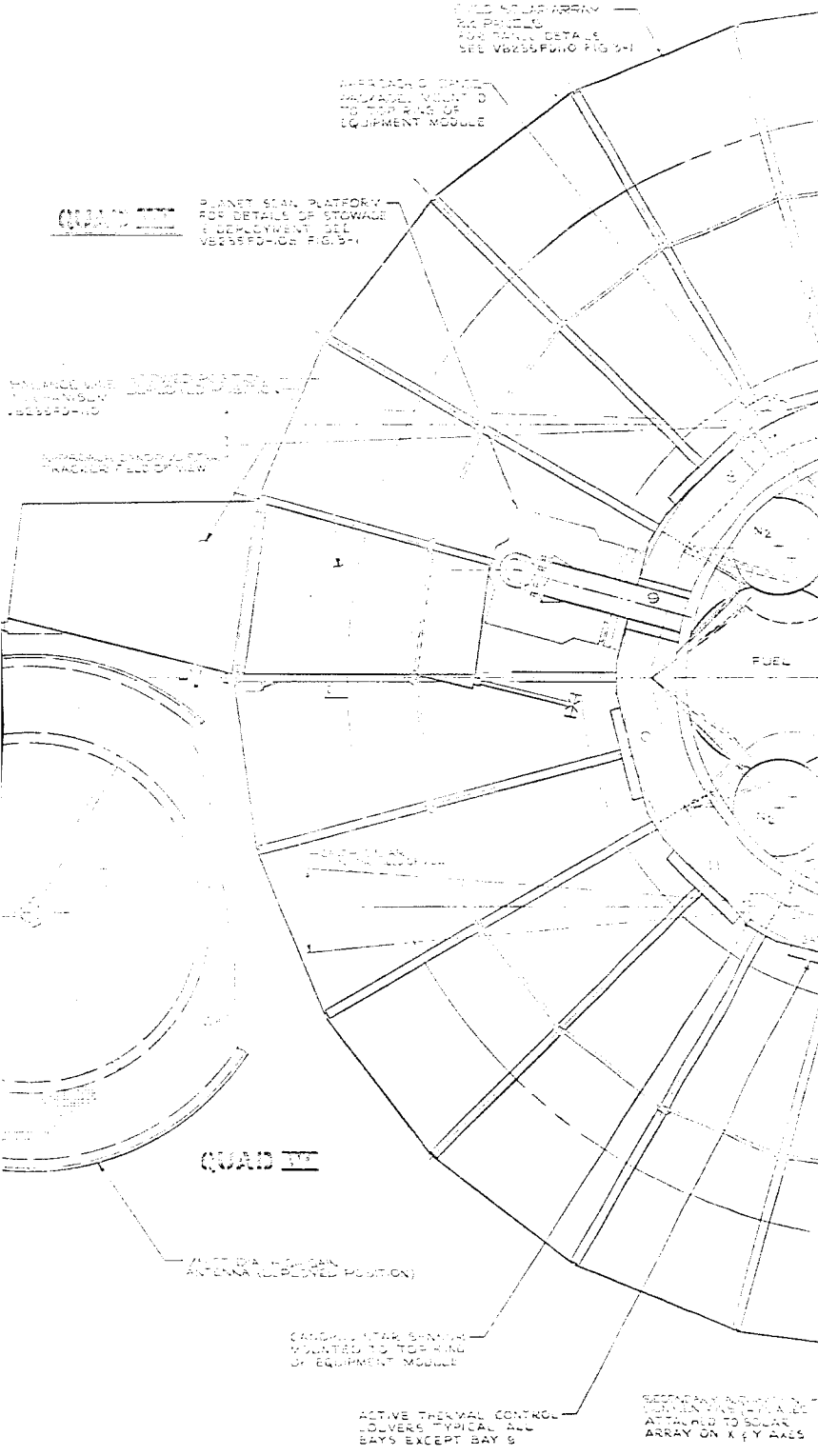
FOR DETAILS OF STOWAGE & DEPLOYMENT SEE
FUEL
QUAD III
ACTIVE THERMAL CONTROL
LOUVERS TYPICAL ALL
BAYS EXCEPT BAY 9

3

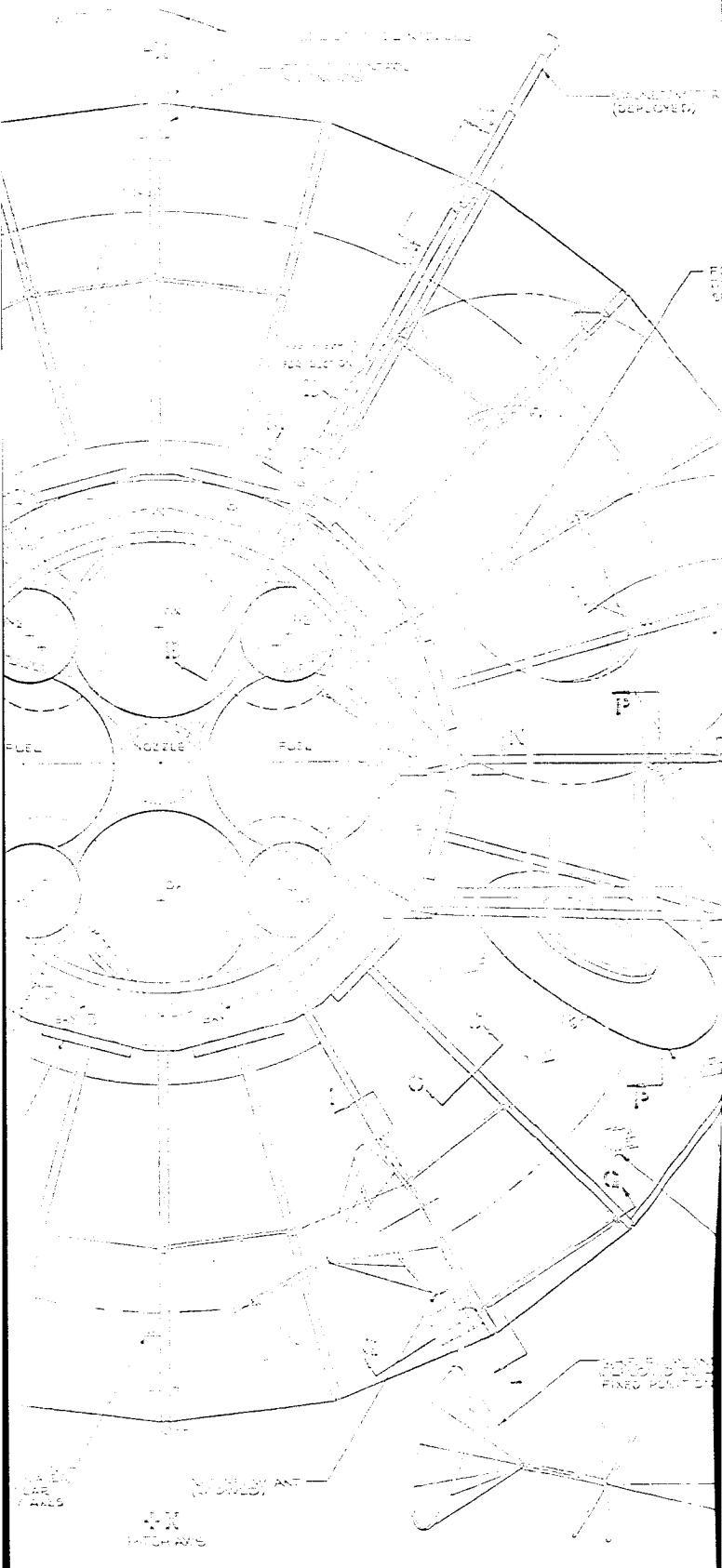

4

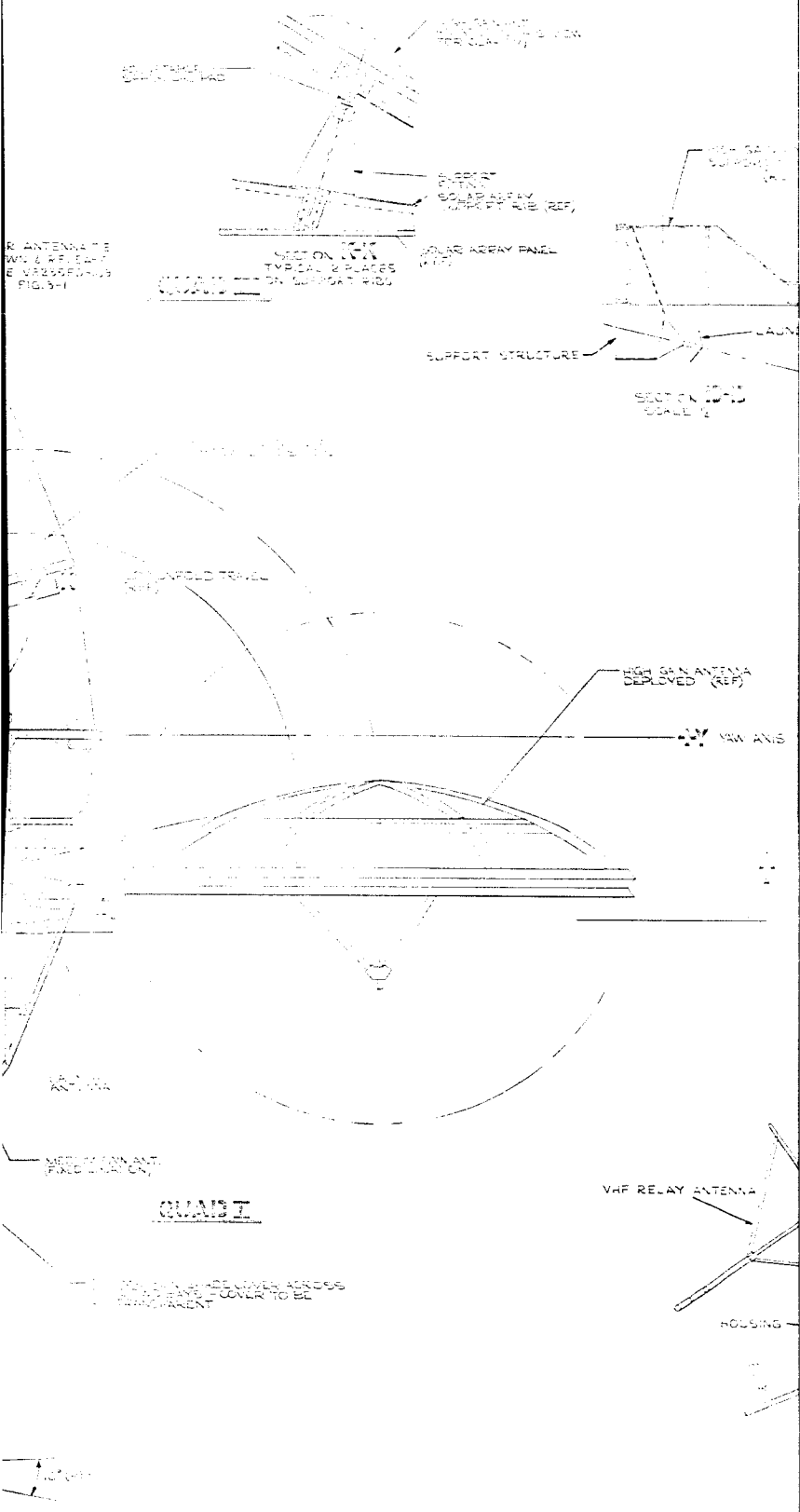
SOLAR ARRAY SUPPORT RIB (REF)
SOLAR ARRAY PANEL
SUPPORT STRUCTURE
HIGH GAIN ANTENNA DEPLOYED (REF)
YAW AXIS
VHF RELAY ANTENNA
HOUSING

5

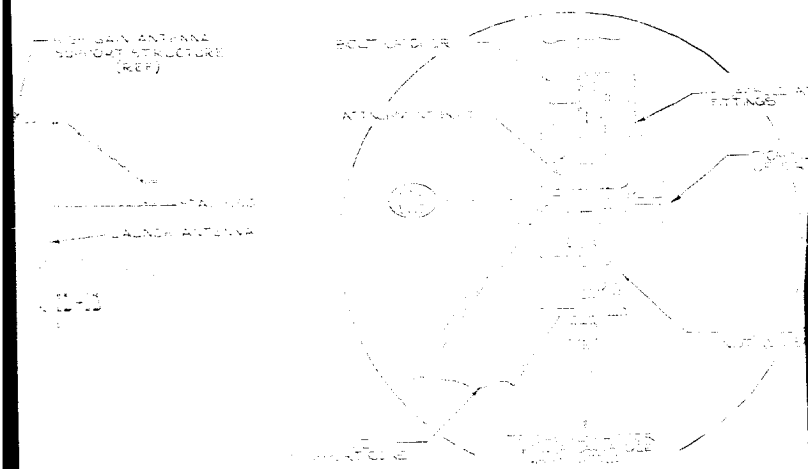
FITTINGS
VIEW
TYPICAL 6 PLACES
SCALE 1/1

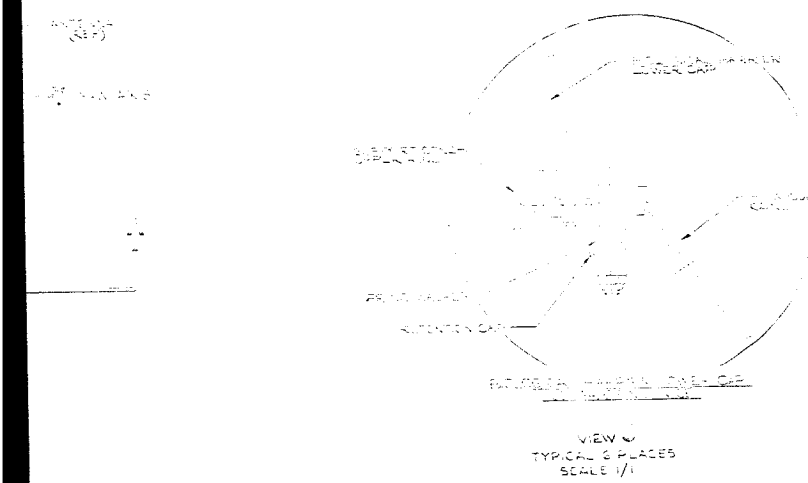
VIEW
TYPICAL 6 PLACES
SCALE 1/1

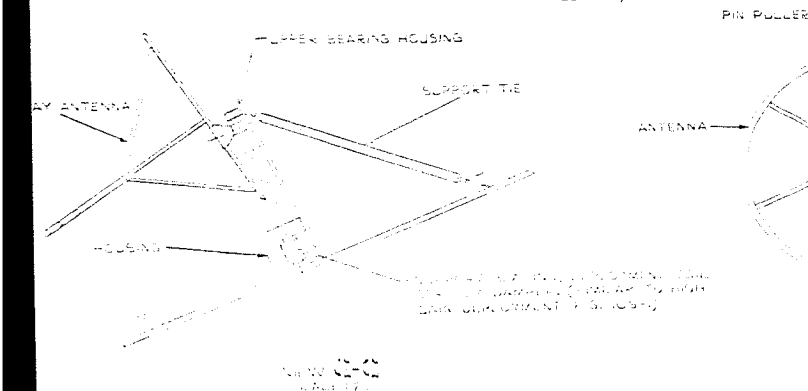
PIN PULLER
UPPER BEARING HOUSING
SUPPORT TIE
ANTENNA
HOUSING

6

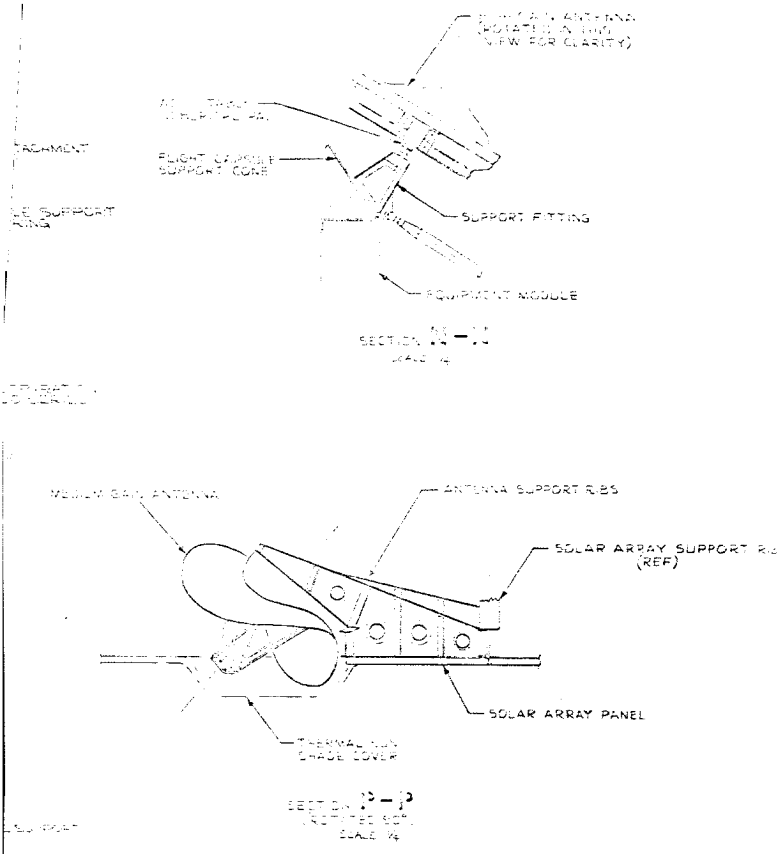

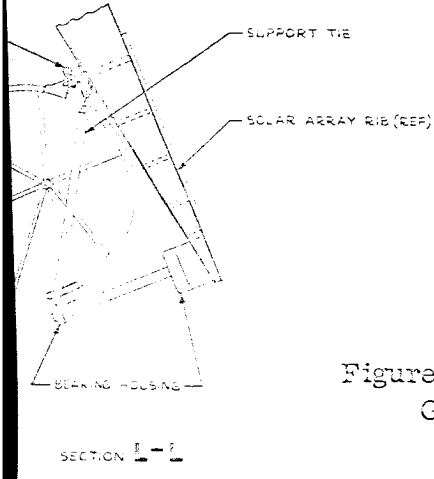

Figure 2-2. Spacecraft Structure General Arrangement

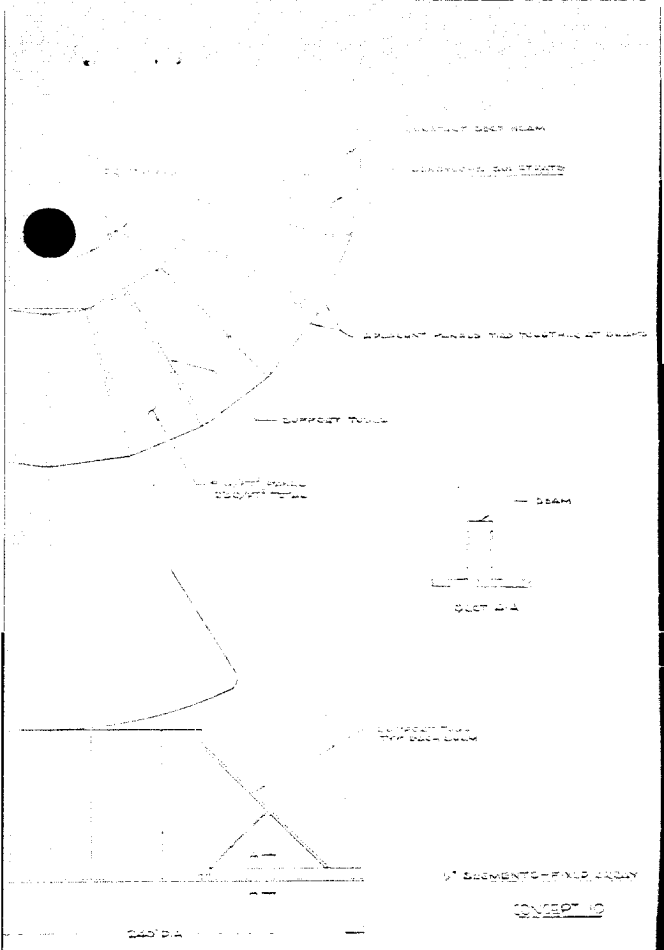
SUPPORT TRUSS
BEAM
SECT A-A
SUPPORT TRUSS
TYP DOUBLE BEAM
SEGMENTS-FIXED ARRAY
CONCEPT 10
240' DIA

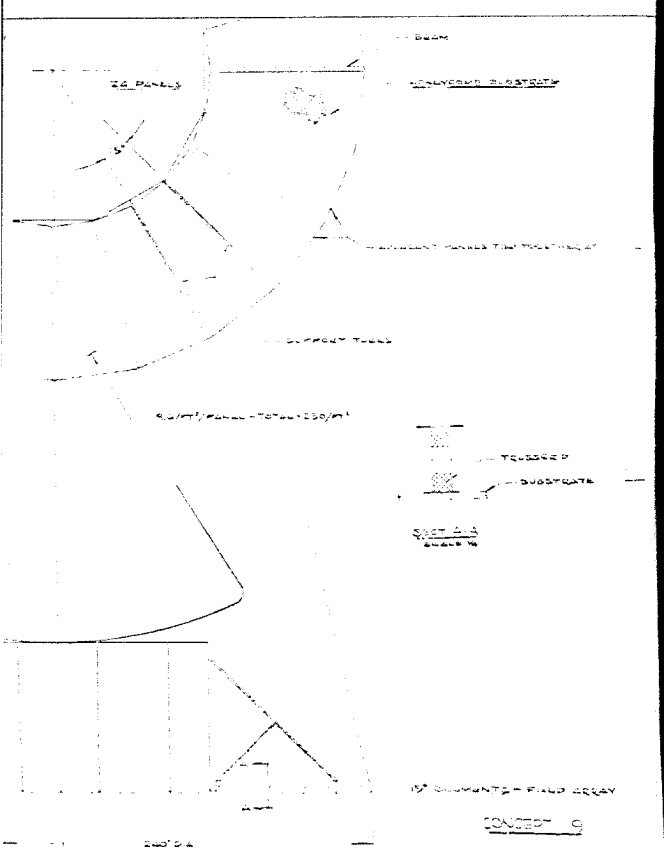
BEAM
26 PANELS
HONEYCOMB SUBSTRATE
SUPPORT TRUSS
TRUSSES
SUBSTRATE
SECT A-A
SEGMENTS-FIXED ARRAY
CONCEPT 9
240' DIA

/

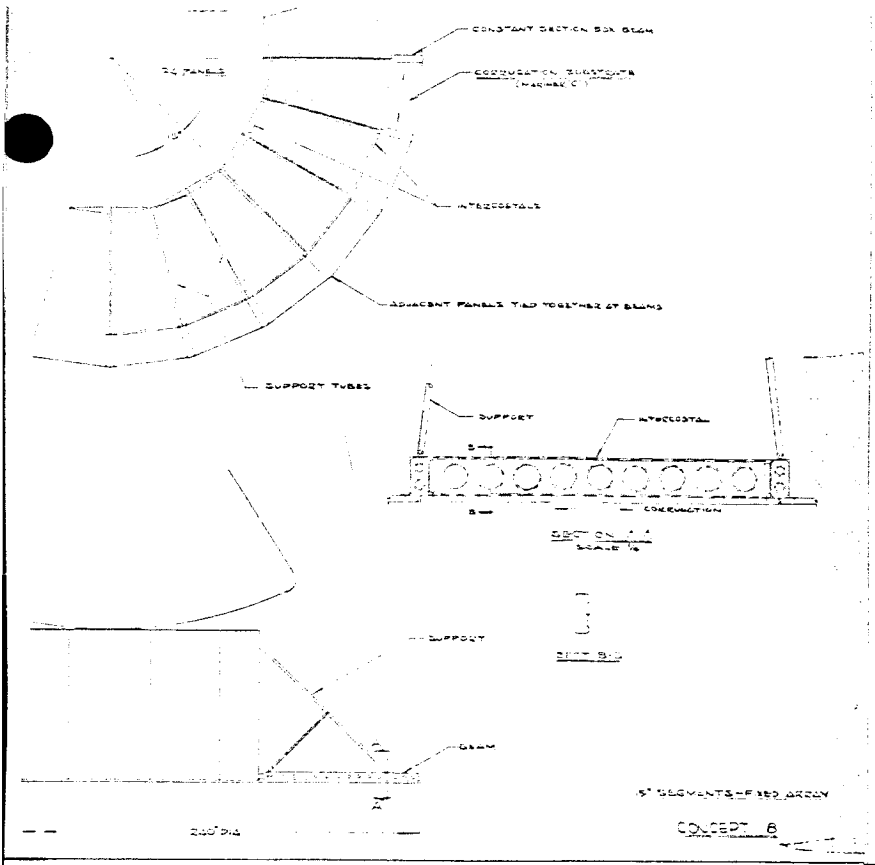
CONSTANT SECTION BOX BEAM
24 PANELS
CORRUGATION SUBSTRATE
(MARMAC C)
INTERCOSTALS
ADJACENT PANELS TIED TOGETHER AT BEAMS
SUPPORT TUBES
SUPPORT
INTERCOSTAL
CORRUGATION
SECTION A-A
SCALE 1/8
SUPPORT
BEAM
A
A
15° SEGMENTS - FIXED ARRAY
240' DIA
CONCEPT 6

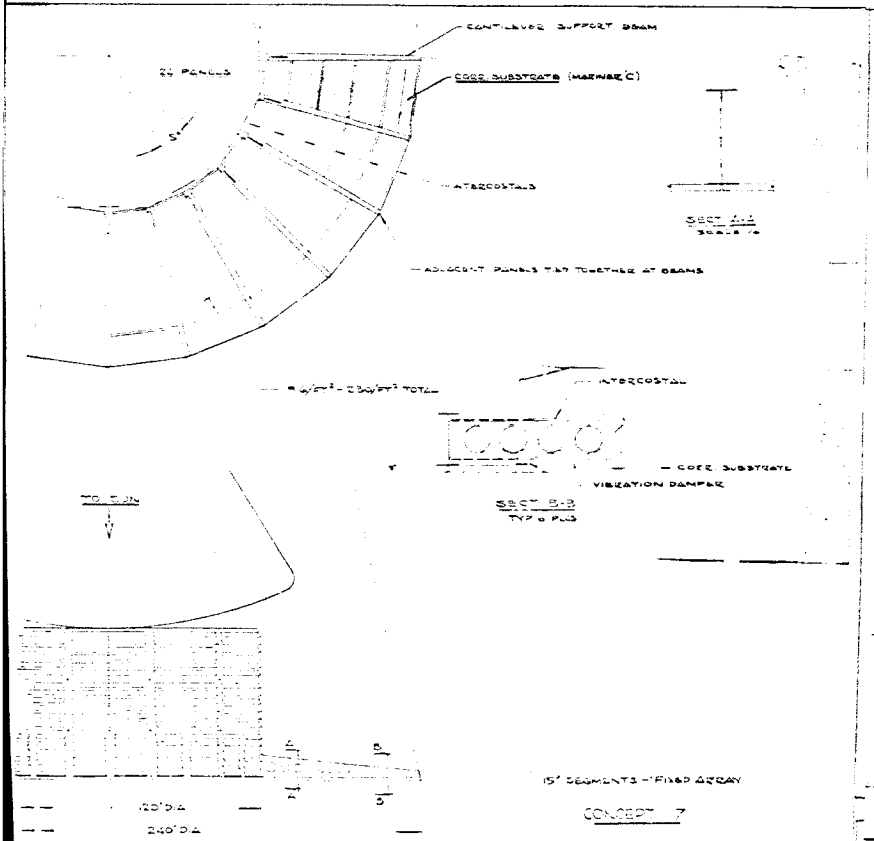
CANTILEVER SUPPORT BEAM
24 PANELS
CORR. SUBSTRATE (MARMAC C)
INTERCOSTALS
SECT A-A
SCALE 1/8
ADJACENT PANELS TIED TOGETHER AT BEAMS
INTERCOSTAL
CORR. SUBSTRATE
VIBRATION DAMPER
SECT B-B
TYP 6 PLS
A
B
A
B
15° SEGMENTS - FIXED ARRAY
120' DIA
240' DIA
SCALE 1/20 (TYP)
CONCEPT 7

2

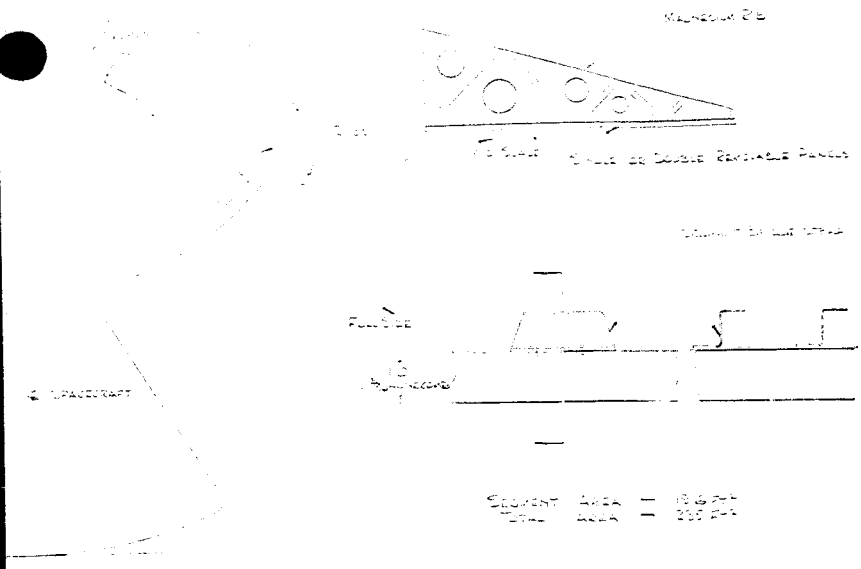

CONCEPT 6

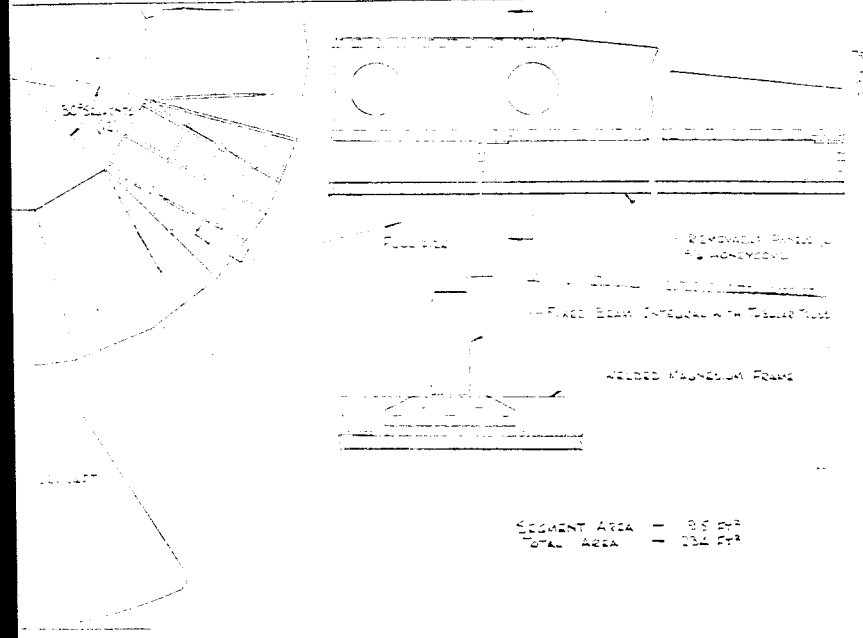

CONCEPT 5

3

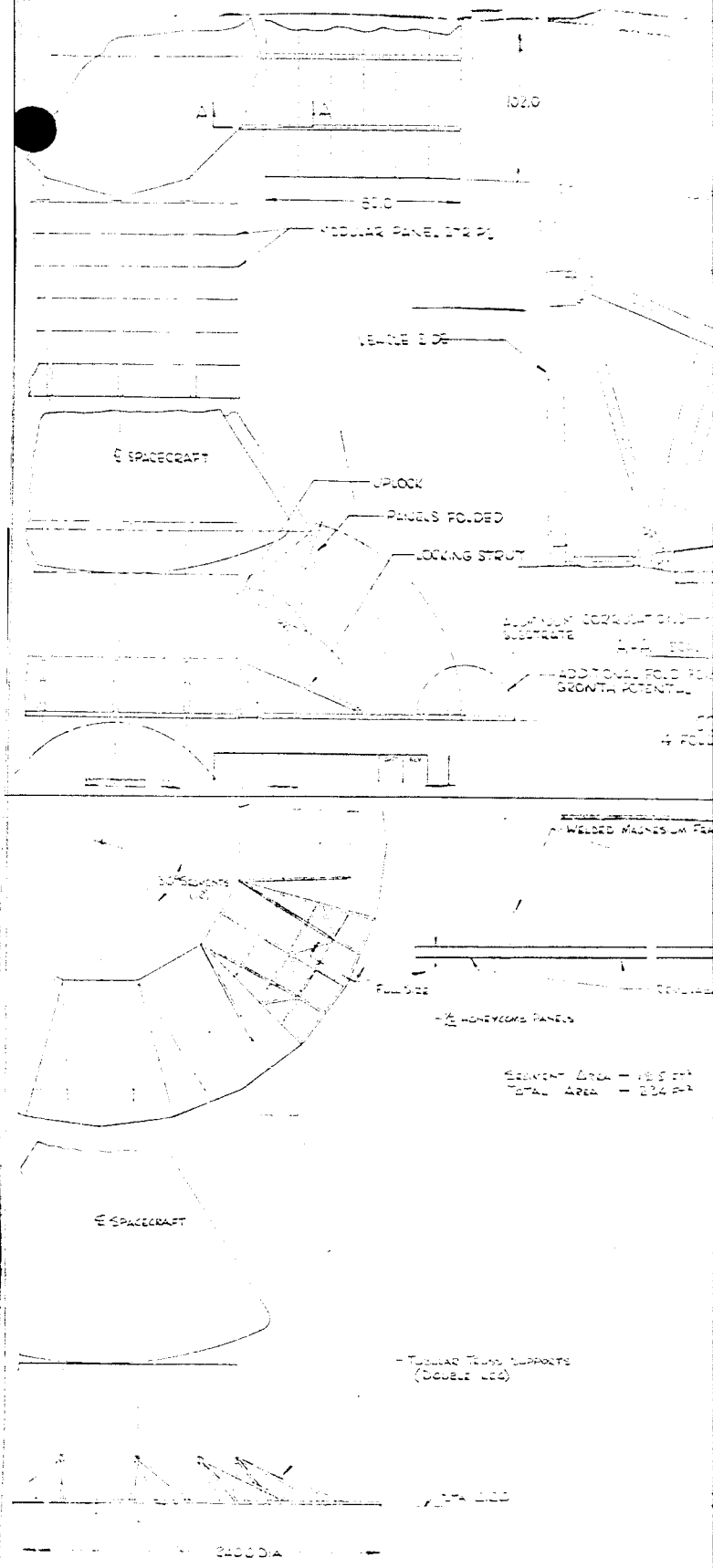
102.0
60.0
MODULAR PANEL
℄ SPACECRAFT
UPLOCK
PANELS FOLDED
LOCKING STRUT
SUBSTRATE
ADDITIONAL FOLD
GROWTH POTENTIAL
WELDED MAGNESIUM
SEGMENTS
FULL SIZE
½ HONEYCOMB PANELS
SEGMENT AREA
TOTAL AREA
℄ SPACECRAFT
TUBULAR TRUSS SUPPORTS
(DOUBLE LEG)
2400 DIA

4

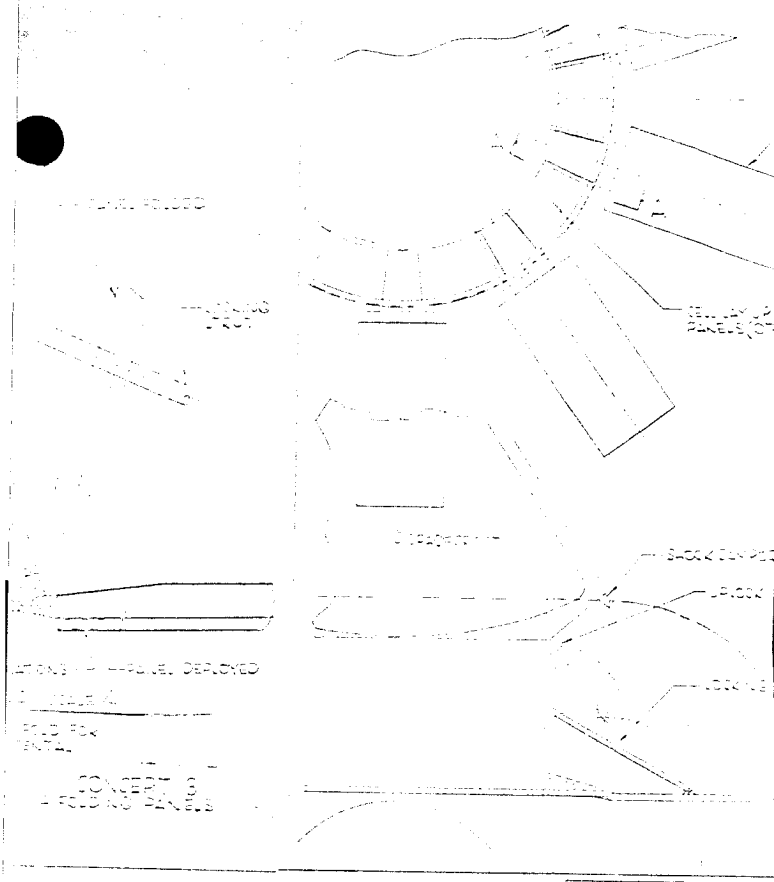
SHOCK DAMPER
UPLOCK
CONCEPT 3
FOLDING PANELS

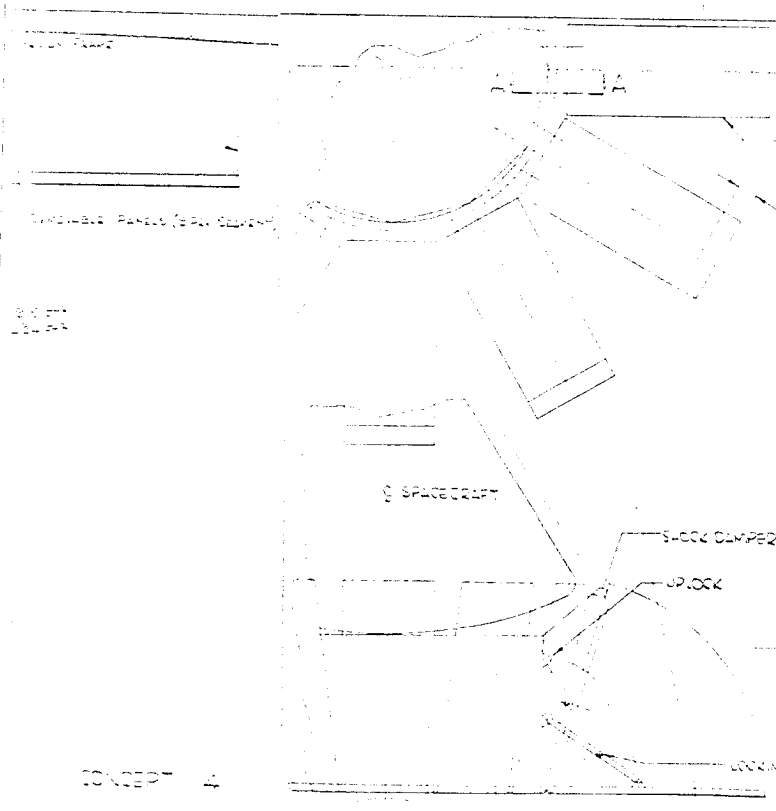
SPACECRAFT
SHOCK DAMPER
UPLOCK
CONCEPT 4

5

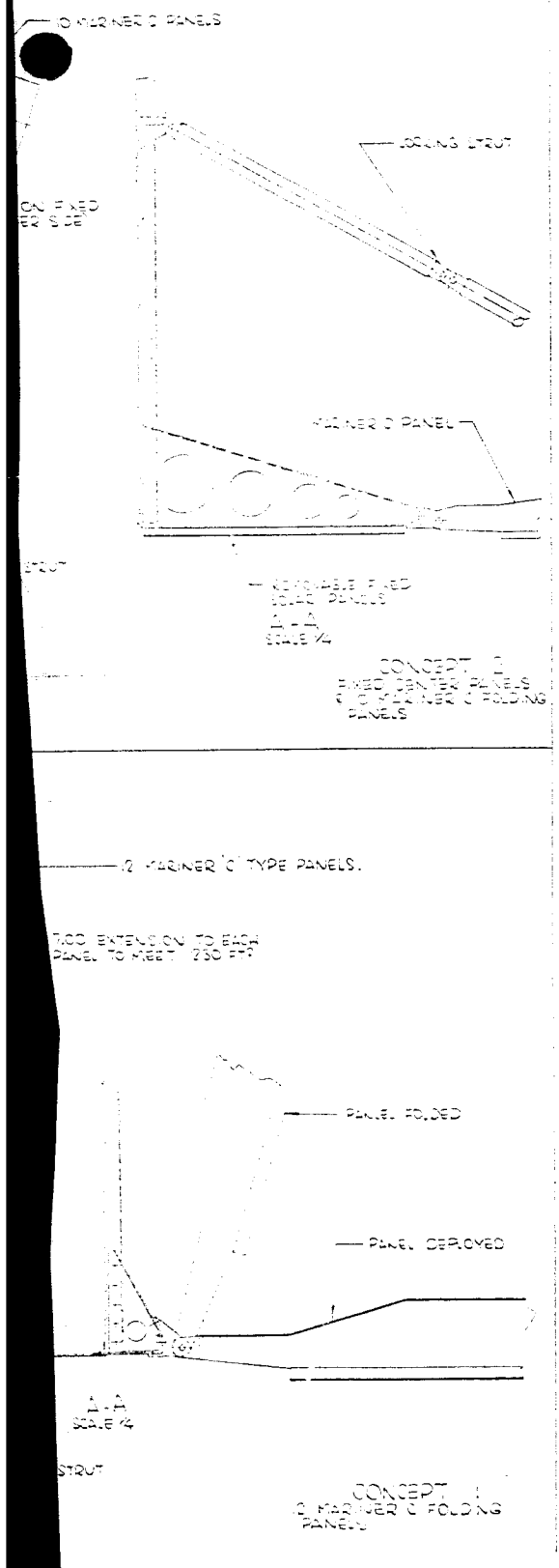

Figure 3-1. Spacecraft Structural Configuration

6

CII - VB220AA020

ALTERNATE DESIGN CHARACTERISTICS AND RESTRAINTS CONSIDERED

FLIGHT SPACECRAFT UTILIZING MARS LOCAL VERTICAL STABILIZATION

Index

1.0 General Description
1.1 Guidance and Control
1.2 Thermal Control
1.3 Summary and Conclusions

1.0 GENERAL DESCRIPTION

The feasibility of using two axis attitude stabilization to Mars during the mission orbital phase was examined with the general conclusion that the approach is possible, but not very practical in light of Voyager mission requirements. Study of this system was confined to examination of attitude control and temperature control implications. Results of these studies are that this system configuration compares poorly to all other techniques examined. Therefore, no integrated Flight Spacecraft concept was developed.

Articulation of solar panels to the Sun from a two-axis Mars vehicle is considered impractical and this stabilization concept would require radioisotope thermoelectric generator (RTG) power. Pointing of the high-gain antenna to the Earth could be accomplished using an azimuth-elevation arrangement and rolling the vehicle body about the local vertical to eliminate the azimuth gimbal. Antenna elevation would then require a gimbal with 180-degree rotation capability. This single gimbal antenna articulation technique has a significant problem due to a control reference singularity when Mars, the Flight Spacecraft, and Earth are nearly in a straight line. When this singularity is approached, the required vehicle angular rates increase drastically (several orders of magnitude) and, very likely, it will not properly track the Earth. The control problems associated with this reference singularity are reduced if a second rotational degree of freedom is added to the antenna articulation control system.

1.1 GUIDANCE AND CONTROL

The recommended control axis configuration for a Flight Spacecraft using two-axis Mars stabilization is symbolically represented by Figure 1-1. Stabilization references for the transit phase of the mission are Canopus and the Sun. Reference vectors for body axis alignment during the orbital mission phase are: the local vertical, and the perpendicular to the orbit plane. Antenna articulation is obtained using two mechanical gimbals. The body fixed (outer) gimbal axis lies in the orbit plane, while the inner gimbal axis is perpendicular to the outer gimbal axis and the Mars-Earth line.

Local vertical reference is supplied by means of a pair of IR horizon scanners which provide voltage outputs proportional to angular displacements about two orthogonal axes lying in the local horizontal plane. The angular displacement about the local vertical vector (rotational error about the yaw axis) is determined by a semi-open loop technique in which the Mars-Earth line is utilized as the prime reference. As the perpendicular to the orbit plane and the Mars-Earth line are inertial on a day-to-day basis, and a heuristic relation exists between them; the perpendicular to the orbit plane can be determined from the Mars-Earth line. Furthermore, the Mars-Earth line is known in body axes through the antenna gimbal angles. Construction of the body yaw control reference is a difficult implementation problem.

The primary antenna pointing reference is an Earth sensor. Two general types have been considered for this application: an optical star tracker, and RF simultaneous lobing equipment associated with the high-gain antenna. The choice between these sensors is examined in VB220AA010 with the conclusion that the prime Earth sensor

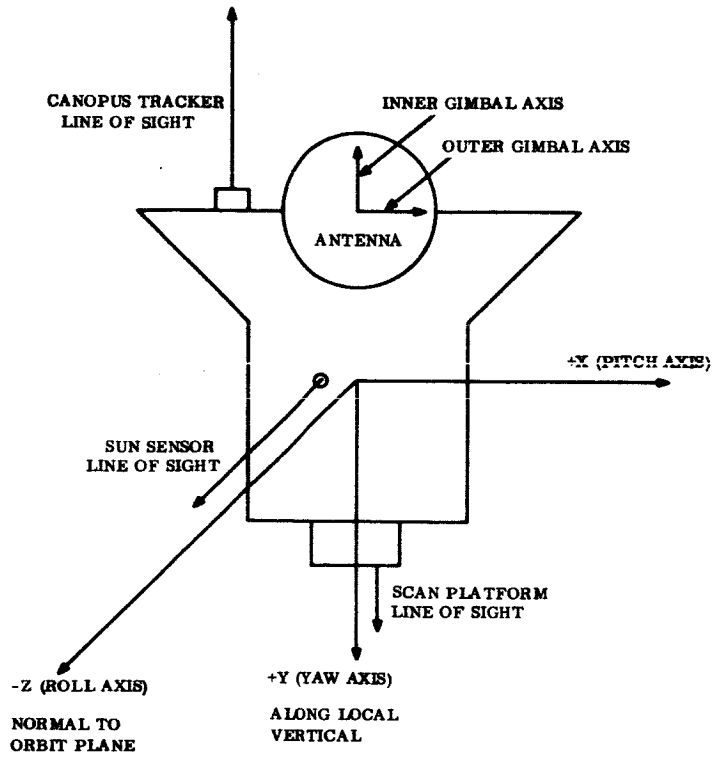

Figure 1-1. Conceptual Control Axis Configuration, Two-Axis Mars Stabilization

should be optical with the RF technique implemented for use during times of optical interference (for example, a conjunction of Venus and Earth as seen from Mars), or in case of failure of the optical sensor. This approach causes minimal degradation of the reliability of the telecommunications subsystem and makes low the probability that the DSIF will be required to provide an RF beacon signal for an extensive time interval. Both sensing techniques will experience short periods of Earth occulation during certain orbits. The limited acquisition-capability of these sensors makes a second shorter term reference necessary to avoid an antenna search mode after each occultation. Further, antenna reference must be continuous since this reference supplies information for body yaw control. To provide continuous reference, two single degree-of-freedom precision gas bearing (for long life) rate integrating gyros are mounted on the antenna to sense angular displacements about the same axes as the prime Earth sensor. These gyros are torqued by the prime reference sensor to maintain orientation. When loss of reference occurs, the torquing loop is opened and the antenna is pointed inertially.

1.2 THERMAL CONTROL

A two-axis Mars oriented vehicle creates very difficult temperature control problems in that it can assume any orientation with respect to the Sun. A simple thermal analysis assuming no conduction around the equipment module, 480 watts of heat dissipation, 48 square feet of radiating area, and temperature limits of 40° F to 80° F within the

equipment module (these values are typical of the recommended 1971 design), was performed. The zero conduction assumption is not too bad for a worst-case analysis as the narrow temperature range and light-weight construction preclude efficient heat conduction. This analysis indicates that active shutters could not maintain the part of the equipment module which is illuminated by the Sun below 80° F.

The equipment module can be maintained within the 40° F to 80° F range using a thermal coating with absorptivity of 0.1 and emissivity of 0.39, but about 100 watts of heater power is required whenever the equipment module is completely shaded. These very gross thermal studies permit only the conclusion that a two-axis Mars oriented vehicle is undesirable from a temperature control standpoint.

1.3 SUMMARY AND CONCLUSIONS

When compared with the other system concepts studied, the two-axis Mars vehicle is unattractive. A list of specific advantages and disadvantages of this system concept follows:

a. Advantages

1. Planet sensors may be body mounted. This provides flexibility in changing or adding experiments and simplifies field-of-view problems.

2. Out-of-orbit-plane pointing is easily accomplished by biasing the planet sensor.

3. Antenna pointing error is independent of limit cycle deadband. Larger vehicle deadbands are permissible resulting in control gas savings.

b. Disadvantages

1. Requires five long-life precision gyros.

2. Solar power cannot be used.

3. Requires a continuous Earth reference.

4. Requires a very complex yaw control loop.

5. Extreme dependence on proper gyro function.

6. Thermal control may impose unreasonable heater power requirements.

Table 2-3. Advantages of Final Alternate Configuring Elements

Method	Advantages
Engine Positions #1 - Engine thrust axis on Z-axis. E1	1. Compatible with 1969 Atlas-Centaur shroud diameter of 10 feet. 2. Lower roll inertia 3. Pitch and yaw inertia are more equal. 4. General symmetry about thrust axis. 5. Less travel of high-gain antenna required. 6. Less plume impingement problem. 7. Permits possible accomplishment of mid-course function and retro fire function with single engine or use of mid-course engines for thrust vector control of main retro engine. 8. Modularity is more easily effected. 9. No blockage of radiation surfaces of equipment submodules. 10. Does not encroach upon packaging volume (E2 removes 1 or 2 bays). 11. With multiple midcourse engines aligned parallel to the Z-axis longitudinal C.G. location can have large limits, thus providing greater packaging flexibility.
#2 - Engine thrust axis off to side. E2	1. Two propellant tanks in place of four and subsequent advantages: a. More usable propellant. b. Less tank weight. c. Less support weight. d. Less surface area and greater tank thickness, consequently less meteoroid bumper weight required. 2. Better alignment of propellant with thrust vector, and subsequent less steady-state and oscillatory motion of C.G. during engine burning. 3. Engine gimbal position can be farther away from C.G., thus giving longer control arm and a better situation for engine stability.
Antenna Storage Positions #1 - Antenna outside shell. A_3	1. Less interference with accessibility to components within basic shell. 2. Greater packaging volume within shell. 3. No interference with engine operation.

Table 2-3. Advantages of Final Alternate Configuring Elements (Continued)

Method	Advantages
#1 - Antenna outside shell.	4. No interference with spacecraft booster separation joint (Position 2 would restrict choice of separation systems). 5. Does not require stowage of antenna feed in engine nozzle.
#2 - Antenna inside shell. A_1	1. Larger antenna size possible. (9 1/2 feet vs. 7 1/2 feet diameter). 2. Two (2) antenna gimbals rather than three (3). 3. Better support arrangement for boost loads. 4. No interference with thermal control during ascent. 5. Greater packaging volume outside of shell.

[illegible] (cont'd)

2. Page 35 of 114, Figure 8B: Reverse encounter points for trajectories B and C.

3. Page 37 of 114, Table at top of page.

Change	31.20	to	-31.2^0
Change	-0.088	to	8.8 $(km/sec)^2$

4. Page 38 of 114, Table at bottom of page.

0.12 $(km/sec)^2$	to	18 $(km/sec)^2$

5. Page 51 of 114. Interchange titles of Figures 4-2 and 4-3.

[illegible]

1. Page 35 of 42, Table 5-3, Column 2. Change -0.01 to 0.01.

[illegible]

1. Page 2 of 30, Paragraph 2.1a, Line 6. Change 100:1 to 60:1.

2. Page 11 of 30, Figure 2-2. Replace with new Figure 2-2. New title 1971 Preferred Design Configuration A.

3. Page 29, Paragraph 3, Line 1. Change has therefore intitially to was therefore [illegible].

[illegible] B

[illegible] I

[illegible]

1. [illegible] 1 of 5, Paragraph 2.0, Line 7. Change "latudes" to "latitudes of".

[illegible]010

1. [illegible] 5 of 15, Figure 1-2. In title, change Plane to Planet.

2. [illegible] 15 of 15, Paragraph 2, Lines 12 and 13. Remove parenthesis after "essential" and insert after "[illegible]".

[illegible]

1. [illegible] 4-1 and 4-2. Insert asterisk after table heading.

2. [illegible] of 21, [illegible]. Paragraph is a footnote, place asterisk at beginning.

[illegible]070

1. Page 2 of 59, Paragraph 1, Line 7. Change Section 3 to Section 4.

2. Page 3 of 59, Paragraph 2.1. Change title from INTERNAL to [illegible].

3. [illegible] of 59, Table 3-1, Column 3, Line 5. Change 5.2 x 10^9 x 10^7 to 5.2 x 10^9/1.9 x 10^1.

4. [illegible] of 59, [illegible] 4.1. Change title from [illegible] to [illegible].

5. Page 14 of 59, Paragraph 4.0, Line 11. Change 3.1 to 4.1 and 3.2 to 4.2.

6. Page 16 of 59, Lines 4 and 5. Change part 3.13(a) to Section 4.1.3.1.

7. Page 37 of 59, Line 20. Change 1.3 to 2.3.

8. Page 46 of 59, Paragraph 4.2.1.3, Lines 5 and 6. Delete base-emitter and add collector base junction and 3 volts reverse bias on the base emitter.

9. Page 58 of 59, Reference 4. Change R. M. Smits to F. M. Smith.

[illegible]101

1. Page 5 of 114, Line 12. Change 0.234 to 0.24.

Figure 2-2. Spacecraft Structures General Arrangement